

Variability of the chalk background velocity in the South Arne area

Peter Japsen, Ida L. Fabricius, Lars Gommessen, Gary Mavko, Anders Bruun,
Torben Bidstrup, Finn Jacobsen, Dan Olsen, S. H. Nguyen,
Rasmus Rasmussen, Niels Springer & Ole V. Vejbæk

Reports included in this volume:
GEUS report 2004/106, 2005/7, 2005/16, 2005/23
DTU E&R report E&R-1, E&R-2
Ødegaard report 03.24033.01, 03.24033.02



Variability of the chalk background velocity in the South Arne area

Peter Japsen¹, Ida L. Fabricius², Lars Gommesen³, Gary Mavko⁴, Anders Bruun³,
Torben Bidstrup¹, Finn Jacobsen¹, Dan Olsen¹, Sihn H. Nguyen²,
Rasmus Rasmussen¹, Niels Springer¹ & Ole V. Vejbæk¹

¹GEUS, ²DTU, ³Ødegaard A/S, ⁴Stanford University

Reports included in this volume:

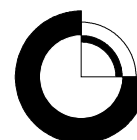
GEUS report 2004/106, 2005/7, 2005/16, 2005/23

DTU E&R report E&R-1, E&R-2

Ødegaard report 03.24033.01, 03.24033.02

For further details see next page

Released 15.04.2010



Variability of the chalk background velocity in the South Arne area

Reports included in this volume:

Danmarks og Grønlands Geologiske Undersøgelse Rapport 2004/106:
Special core analysis for Chalk Background Velocity Project
Dan Olsen

Danmarks og Grønlands Geologiske Undersøgelse Rapport 2005/7:
Lithostratigraphy and physical properties of the Chalk Group from Danish North Sea wells
Peter Japsen, Finn Jacobsen & Torben Bidstrup

Danmarks og Grønlands Geologiske Undersøgelse Rapport 2005/16:
Rock physics analysis of velocity differences in the chalk of wells Jette-1 and Isak-1
Gary Mavko & Peter Japsen

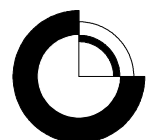
Danmarks og Grønlands Geologiske Undersøgelse Rapport 2005/23:
Seismic velocities in the chalk, NE part of the South Arne Field
Ole Vejbæk & Peter Japsen

Rapport E&R-1. E&R DTU 2003
Selection of samples. Chalk Background Velocity
Ida L. Fabricius & Niels Springer

Rapport E&R-2. E&R DTU 2005
Sample characterisation report for the Chalk Velocity project
Ida L. Fabricius. & Sihn H. Nguyen

Ødegaard Report 03.24033.01 2005
Chalk background velocity. Well log analysis.
Lars Gommesen

Ødegaard Report 03.24033.02 2005
Inversion for acoustic impedance with low-frequency information based on the CBV model.
Testing predictions of Jette-1 and Modi-1
Anders Bruun, Rasmus Rasmussen & Ole Vejbæk



Contents

Abstracts and reports enclosed	3
Abstracts	3
Reports	3
Introduction	4
Summary	5
Effective stress and porosity reduction in chalk	5
Clay and quartz content and velocity-porosity relations for chalk.....	6
Evaluation of velocities estimated from seismic processing	8
Testing low frequency modelling	8
Acknowledgements	18
Abstracts of reports	19
Inversion for acoustic impedance with low-frequency information based on the CBV model. Testing predictions of Jette-1 and Modi-1	19
Selection of samples. Chalk background velocity	19
Sample characterisation report for the chalk background velocity project	20
Chalk background velocity. Well log analysis	20
Lithostratigraphy and physical properties of the Chalk Group from Danish North Sea wells	21
Rock physics analysis of velocity differences in the chinks of wells Jette-1 and Isak-1..	21
Special core analysis for chalk background velocity project. Ultrasonic velocity measurements on plug samples of chalk from the wells Q-1, Otto-1, T-3, Gert-1, West Lulu-1, Baron-2, I-1 and Cecilie-1B.....	22
Seismic velocities in the chalk, NE part of the South Arne Field	23
Selected references	24

Abstracts and reports enclosed

Abstracts

Fabricius, I.L., Gommesen, L., Olsen, D., Springer, N., Japsen, P., Jakobsen, F. & Schiøtt, C.R. 2005. Mineralogical and textural control on chalk background velocity and porosity. EAGE 67th Conference & Exhibition - Madrid, Spain, 13 - 16 June 2005. 4 pp.

Japsen, P., Mavko, G., Gommesen, L., Fabricius, I.L., Jakobsen, F., Vejbæk, O.V., Rasmussen, R. & Schiøtt, C.R. 2005. Chalk background velocity: Influence of effective stress and texture. EAGE 67th Conference & Exhibition - Madrid, Spain, 13 - 16 June 2005. 4 pp.

Reports

Bruun, A., Rasmussen, R. & Vejbæk, O.V. 2005. Inversion for acoustic impedance with low-frequency information based on the CBV model. Testing predictions of Jette-1 and Modi-1. Ødegaard Report 03.24033.02 (confidential), 10 pp.

Fabricius, I. & Springer, N. 2003. Selection of samples. Chalk background velocity, E&R-1. E&R DTU (confidential), 19 pp.

Fabricius, I.L. & Nguyen, S.H. 2005. Sample characterisation report for the Chalk Background Velocity project. E&R-2. E&R DTU (confidential), 65 pp.

Gommesen, L. 2005. Chalk background velocity. Well log analysis. Ødegaard Report 03.24033.01 (confidential), 31 pp (1 cd).

Japsen, P., Jakobsen, F. & Bidstrup, B. 2005. Lithostratigraphy and physical properties of the Chalk Group from Danish North Sea wells. GEUS Rapport 2005/ 7, 114 pp. (1 cd).

Mavko, G. & Japsen, P. 2005 Rock physics analysis of velocity differences in the chalks of wells Jette-1 and Isak-1. GEUS Rapport 2005/16, 31 pp.

Olsen, D. 2004. Special core analysis for Chalk Background Velocity Project. GEUS Rapport 2004/106, 36 pp. (1 cd).

Vejbæk, O.V. & Japsen, P. 2005. Seismic velocities in the chalk, NE part of the South Arne Field. GEUS Rapport 2005/23 (confidential), 12 pp.

Introduction

The project “Variability of the chalk background velocity in the South Arne area” had three main aims. First, quantification of how the chalk background velocity (the low-frequency velocity variations which define the absolute level of the chalk velocity) in the South Arne area is affected by effective stress, presence of hydrocarbons as well as porosity, composition, texture and cementation of chalk. Second, estimation of upper and lower bounds on chalk porosity estimated from seismic inversion based on the analysis of these factors. Third, evaluation of the usefulness of velocities estimated from seismic processing as a supplement to well log data for establishing chalk background velocity.

Summary

We have studied the relations between velocity, porosity and depth for the Chalk Group based on data from Danish wells centred around the South Arne Field in the central North Sea (Figure 1). The Chalk Group in 29 wells was subdivided into lithostratigraphic units and the log data were quality controlled, and porosity and water saturation estimated. All wells had sonic log data and seven also shear-wave velocity logs. Temperature and formation pressure for the chalk interval were also investigated across the study area. Twenty core samples from water saturated chalk in eight wells were studied in detail; acoustic, textural, mineralogical and chemical properties were investigated and a compositional model was made by including data from image analysis of backscatter electron micrographs. Results from investigations of samples from the SA-1 and Rigs-1, -2 wells were available from previous studies and were included in the interpretation.

Effective stress and porosity reduction in chalk

Log data (especially from thick sequences) reveal the well-known increase of chalk velocity with depth (and the corresponding decrease of porosity) (Figure 2). The velocity-depth trends for the chalk sections in the individual well do, however, only line up if the depths are corrected for the effect of overpressure of the pore fluids. In the central North Sea, the dominant part of the overpressure in the chalk is caused by dis-equilibrium compaction so we can compute an approximate expression for the effective depth, Z_{eff} , of relatively high-porosity chalk. The effective depth is the burial depth where the chalk would be subject to the same effective stress during normal compaction (hydrostatic formation pressure):

$$Z_{eff} \approx Z - 100 \cdot \Delta P \quad (1)$$

where Z is true vertical depth in metres below sea bed and ΔP is the overpressure in MPa (1 MPa = 145 psi). The alignment of velocity data versus effective depth underlines that effective stress is a first-order control on chalk velocity even for velocities up to 5 km/s (porosities down to 5%).

Mechanical compaction of sedimentary rocks is a stress-dependent process that leads to porosity reduction and velocity increase (Figure 3). This process is dominant in pelagic carbonate deposits during their initial compaction from c. 70% to some 45-40%. At this stage of compaction another stress-dependent process takes over, viz. pressure dissolution of calcite at local silicate-enriched intervals. This process leads to the formation of stylolites that start to form at around 45% porosity. The combination of mechanical and chemical compaction thus leads to stress-dependent porosity reduction in chalk even to very small porosities.

We have observed a pronounced drop in chalk porosity (and a corresponding increase in velocity) over a narrow interval in effective depth around 1700-1800 m (Figures 2, 3). For simplicity we refer to this sharp change in chalk properties as the 'cementation front', because this change corresponds to a sudden increase in the degree of cementation of the chalk that leads to pore-filling cementation and stiffening of the grain contacts. The front is

observed in the Tor as wells as Hod Formations where (minimum) velocity cross c. 4.5 km/s and (maximum) porosity cross c. 15%.

Petrography reveals no sign of pressure dissolution at contacts between calcite particles, so the cementation front is apparently not caused by a change in pressure dissolution regime. Rather we suggest that the 'cementation front' can be explained by a drop in the Biot factor when chalk porosity is less than 20% porosity. The Biot factor, β (or the coefficient of internal deformation), determines the relation between total stress (S), effective stress (S_{eff}) and formation pressure (P) as defined by Terzaghi's equation:

$$S = S_{eff} + \beta \cdot P \quad (2)$$

β equals 1 for high-porosity sediments, so a reduction in β will lead to an increase in the effective stress exerted on the chalk for constant pressure. The exact value of β can be difficult to determine, but geomechanical tests show that β is reduced below c. 20% porosity in agreement with our observation of increased cementation around that porosity. One interpretation of the cementation front is thus that it represents the limit where β becomes less than 1 and thus causes a sudden increase in effective stress and a corresponding reduction in porosity. This reduction leads to further decline in β and the chalk thus experiences a kind of 'snowball' effect where the acoustic properties are drastically altered.

Deviations between the general relation between chalk porosity and effective depth occur e.g. in the Rigs-2 well where a porosity of 45% corresponds to a c. 400 m more shallow effective burial than the present (in contrast to the SA-1 well where porosity and effective depth match). One explanation of this deviation is introduction of hydrocarbons in the chalk at an early stage when the effective burial was less than today, leading to a blocking of the pressure dissolution process and thus to preservation of porosity. Correspondingly, the porosity of 45% appears to correspond to the limit of mechanical compaction of chalk.

Clay and quartz content and velocity-porosity relations for chalk

There is a clear separation between the lithostratigraphic formations in terms of the relation between velocity and porosity (Figure 4). The Tor data plot along a long and narrow trend, whereas Hod data typically plot as a cluster of points with low porosity and Ekofisk data either plot along the Tor trend (Ekofisk porous) or as data points with low velocity-porosity values (Ekofisk tight). This distinction corresponds to the differences in the gamma log: low gamma in Tor and parts of Ekofisk and typically higher values for most of Hod and Ekofisk (pure Hod chalk occurs in the southern part of the Danish Central Graben).

The gamma ray log thus gives important information for evaluating the acoustic properties of the chalk. The typical level for the GR readings is just below 10 API for pure chalk with maxima up to c. 20 API in the less pure chalk (depending on calibration). Differences in hole size, mud type, and calibration of the gamma tool may be the reason why the same relative variations are found for chalk in other wells – only with a much higher base level. The true variations of the gamma radiation in the chalk may also be obscured by potassium

content of the drilling mud. Comparison between nearby wells may reveal what level and variation that represent the true gamma response of the chalk in an area.

We have observed differences between the sonic log data from wells across the study area (Figure 5). These differences are particularly clear when shear-wave data are available, and thus we found that both P- and S-wave velocities in the Jette-1 well tend to be larger at same porosity levels than in the Isak-1 and Sine-1 wells, while the V_p/V_s ratio is smaller in Jette-1 (relative to the South Arne Field, Jette-1 is located c. 10 km west, Isak-1 c. 35 km to the west and Sine-1 c. 110 km towards south-east. The chalk sections in Jette-1 and Sine-1 are c. 1 km thick, in Isak-1 c. 0.3 km; the overburden for the chalk in Isak-1 and Jette-1 is c. 3 km, whereas the overburden for Sine-1 is only c. 2 km).

Depositional differences are not likely to cause the different velocity-porosity relations that we observe between log data from thick sections of chalk: The chalk originates from pelagic carbonates that were deposited in an open marine environment where large variations do not persist over small distances over million of years such as when we consider sedimentary sections that were deposited during the Late Cretaceous, a time span of c. 40 million years. Post-depositional differences between the development of the chalk in these wells are thus likely causes, but neither effective stress nor temperature can explain the differences: The chalk in Jette-1 and Isak-1 is found at about the same temperature and stress regime.

Chalk originates from a pelagic sediment with varying content of biogenic opal, which will be transformed to quartz upon burial. Petrographical data show that diagenetic quartz may reside in the chalk in two ways: Where the quartz is dispersed in the pores it only contributes little to the stiffness of the chalk (Figure 6); whereas where quartz is integrated in the supporting frame of the chalk it has a significant effect on the chalk stiffness (Figure 7). Quartz may thus have significant effect in some wells, in others not, even when the overall lithological composition is the same. The acoustic properties of the investigated samples depend on the mineral composition (Figure 8), and they may be modelled from an isotropic rock physics iso-frame model by taking these effects into consideration (Figure 9).

Alternatively the velocity-porosity log data can be compared with rock physics ellipsoidal pore models (Figure 5). This comparison suggests that the chalk in Jette-1 have stiffer pores than in Isak-1 and that the mineral end-point properties are different for the two wells. The end-point moduli were adjusted to find model predictions consistent with both P- and S-wave velocity data. Taking the properties of the Isak-1 mineral as the calcite end-member, the Jette-1 properties correspond to the theoretically expected value for a mixture of 80% calcite and 20% quartz. If the quartz is integrated in the supporting frame, the result would be a more rigid pore space and thus explain that the chalk in Jette-1 has stiffer pores than in Isak-1.

It is a possibility that the fluid history of the chalk could hold the key to understanding the different velocity-porosity relations that appear to occur at random relative to depositional environment and overburden properties. Expulsion of brine from the deep, high-pressure and high-temperature source rocks of Jurassic age along active faults and fracture systems could lead to the introduction of additional quartz into the chalk and thus to the observed

differences. The Jette-1 well is thus located close to a major fault that is connected to an active hydrocarbon kitchen further towards northwest, whereas the Isak-1 and the Sine-1 well are far from areas where hydrocarbons and brine are actively being expelled.

Evaluation of velocities estimated from seismic processing

We have analysed a subset of a seismic velocity cube from the north eastern quadrant of the South Arne Field and compared it with a normal velocity-depth trend for the chalk (Figure 10). The chalk velocities in this cube show a clear depth-dependency that corresponds to the normal trend, but the absolute velocity level is, however, clearly tied up with well data from the Rigs-2 well, and this may result in down-flank propagation of the properties of the chalk in this well. The Rigs-2 well (and immediate vicinity) is, however, probably a local anomaly due to porosity preservation from early hydrocarbon invasion. Chalk velocities in the well are too low compared to the normal trend even when the overpressure is taken into account (eq. 1), and the present effective burial of the chalk is thus c. 400 m deeper than predicted after correction for fluid effects (oil content) on velocity. The down flank velocity prediction from the seismic velocity cube is therefore expected to be wrong.

Testing low frequency modelling

A test on possible improvements on low frequency models for seismic inversion based on CBV studies has been performed on a random 2-D line connecting the Jette-1, Rigs-2 and Modi-1 wells. It was found that construction of pseudo wells based on porosity reduction with effective stress to support construction of the low frequency model caused noticeable improvements in the predictive capability of inversion results. In the selected case, the "cementation front" (as mentioned above) caused non-linear effects in the spatial variation of acoustic properties that could be remedied by inserting pseudo wells. At the Modi-1 well which lack sonic logs, conversion of porosity to acoustic impedance and creation of a pseudo well based on Jette-1 proved equally powerful as support for low frequency modelling.

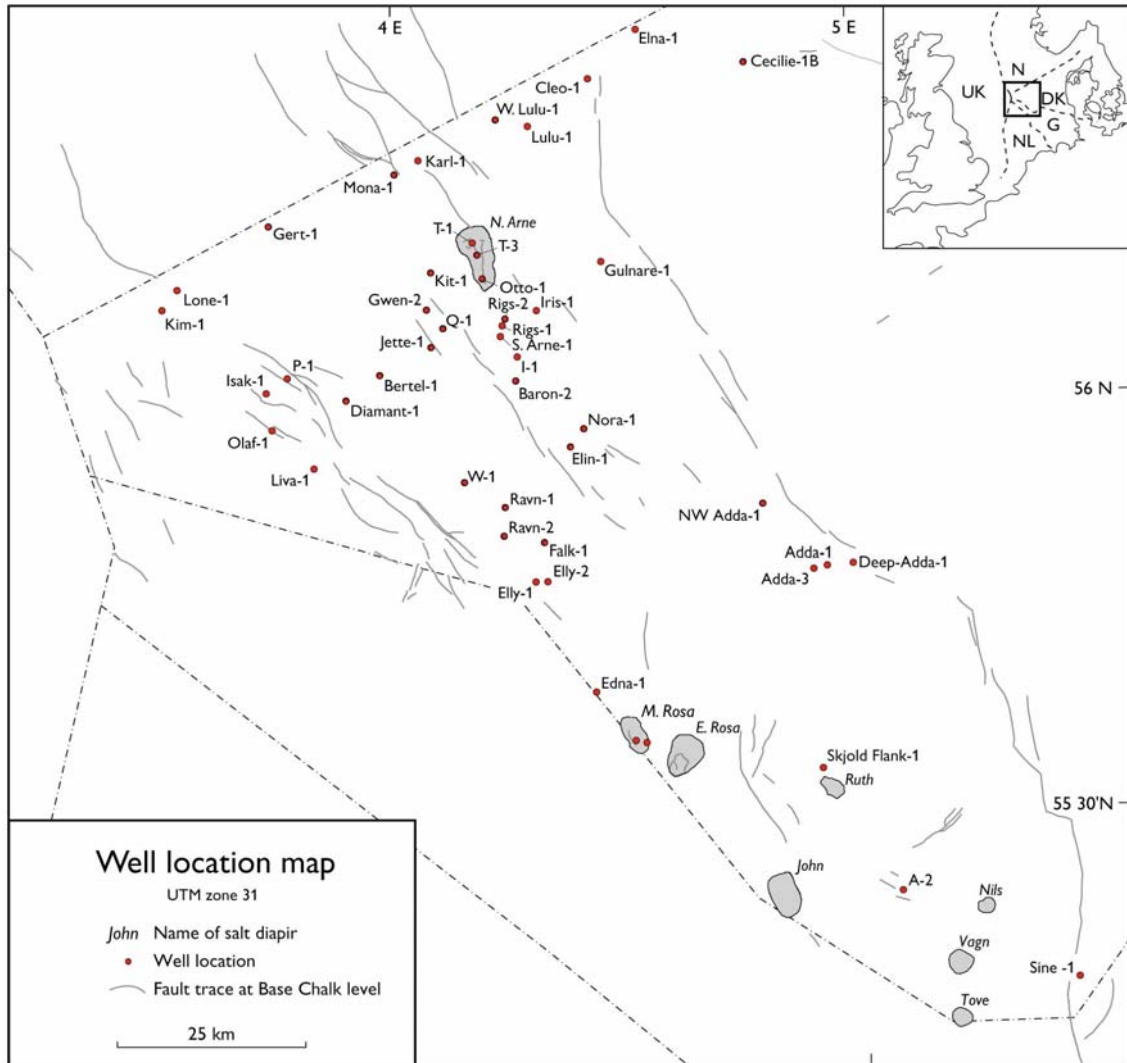


Figure 1. Location map for wells in this report. Fault pattern after Britze et al. 1995.

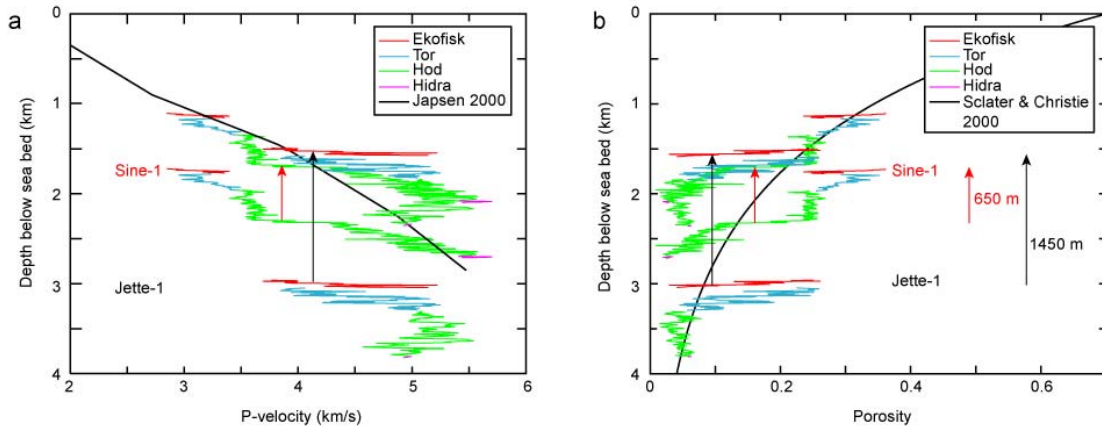


Figure 2. Sonic and porosity log data versus actual depth and effective depth for the Jette-1 and Sine-1 wells (colorcoded by formation). After correction for the effect of overpressure (arrows corresponding to chalk formation overpressure of 6.5 and 14.5 MPa; see eq. 1) the log data overlap and reveal a pronounced change for effective depths around c. 1.8 km (the cementation front). These observations indicate that porosity-reduction in chalk is controlled by effective stress. Note that the shown reference lines do not predict the changes below the cementation front. The data are averaged over 20 m intervals.

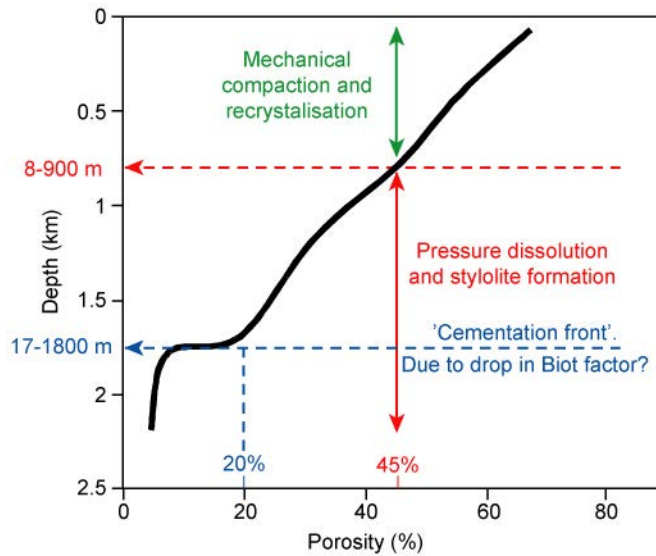


Figure 3. Sketch of porosity reduction in chalk versus effective depth (depth corrected for overpressure, equation 1). Mechanical compaction is the dominating porosity-reducing process during the more shallow burial of pelagic carbonates, whereas stress-induced dissolution are dominates at greater burial (porosities less than c. 45%). A pronounced drop in porosity occurs at an effective depth of c. 1700 – 1800 m. This may be explained by rapidly increasing effective stress due to a drop in the Biot factor around a porosity of c. 20% (eq. 2).

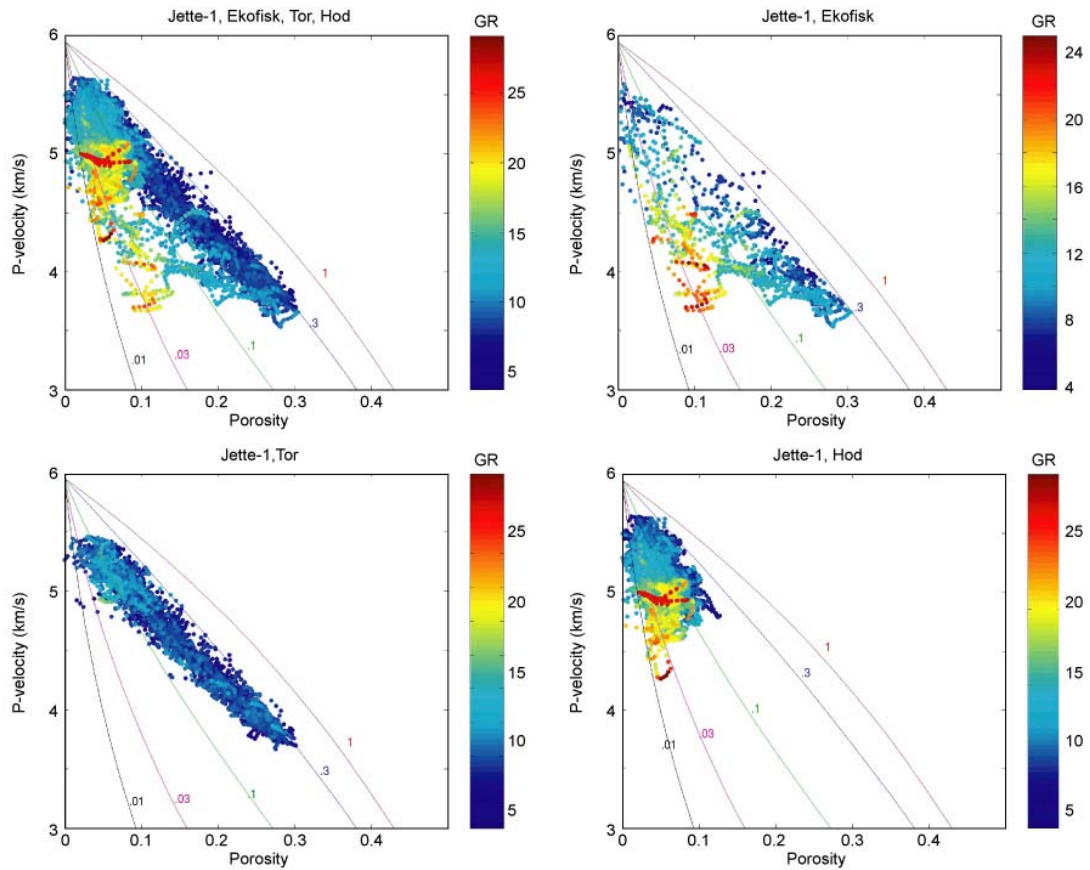


Figure 4. Plots of P-velocity versus porosity in Jette-1, color-coded by gamma ray. The clean Tor Formation has little variation with gamma ray, whereas the clay-bearing Ekofisk and Hod Formations have a large variation in gamma ray and a corresponding spread in V_p vs porosity (apparent aspect ratios). This spread thus probably reflects the presence of clay. Plots of Ekofisk, Tor, and Hod formations are shown together (upper left) and separately. Superimposed: Ellipsoidal pore models for different aspect ratios (Berryman 1995).

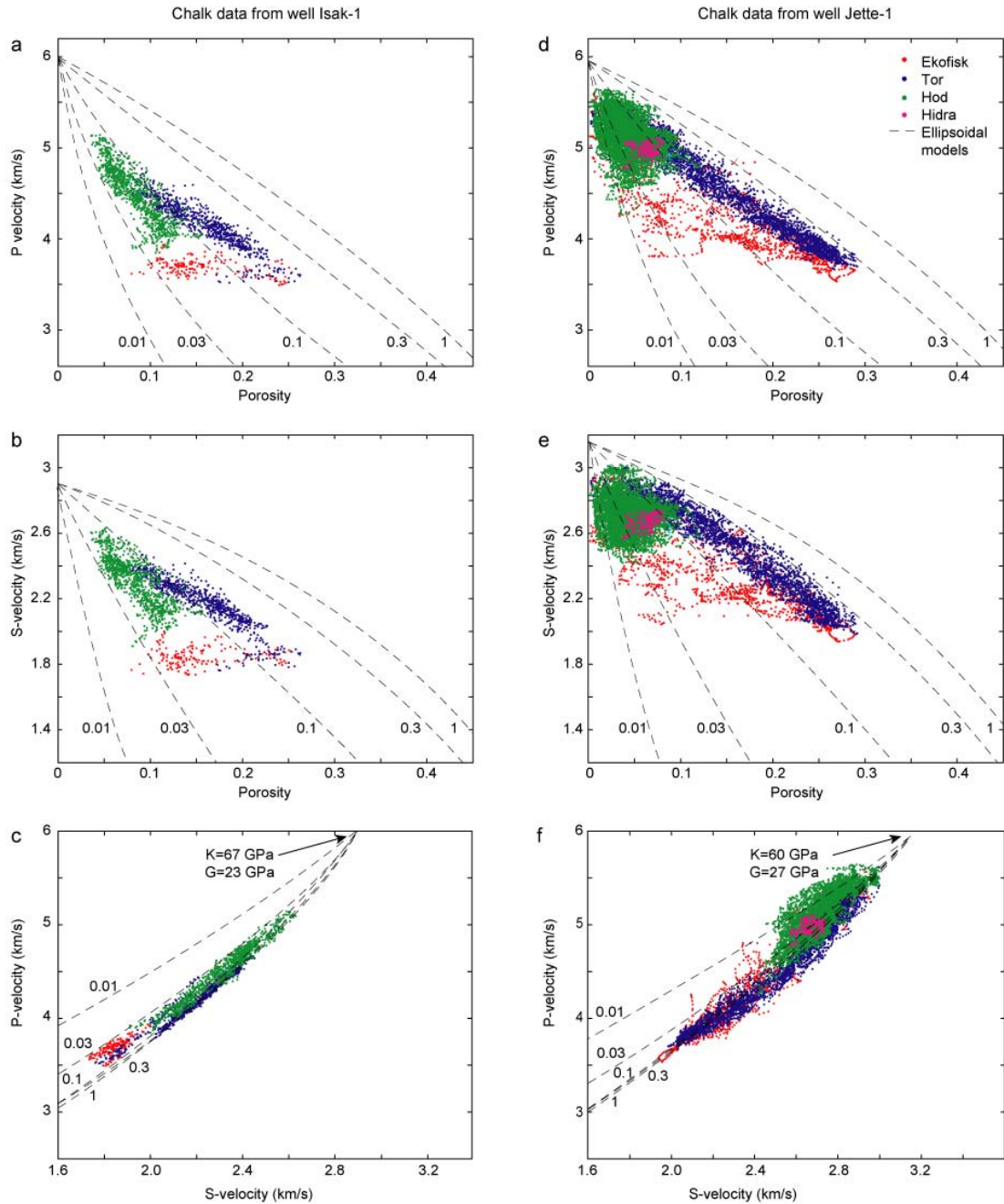


Figure 5. Plots for the Ekofisk, Tor, and Hod Formations of wells Isak-1 (left) and Jette-1 (right). Comparison with rock physics ellipsoidal pore models suggest that the chalk in Jette-1 have stiffer pores than in Isak-1 and that the mineral end-point properties are different for the two wells. Taking the properties of the Isak-1 mineral as the calcite end-member, the Jette-1 properties correspond to a mixture of 80% calcite and 20% quartz. If the quartz is integrated in the supporting frame, the result would be a more rigid pore space and thus explain that the chalk in Jette-1 have stiffer pores than in Isak-1. Mineral bulk and shear moduli used in the modeling are labelled in the bottom figures. Superimposed: Ellipsoidal pore models for different aspect ratios (Berryman 1995).

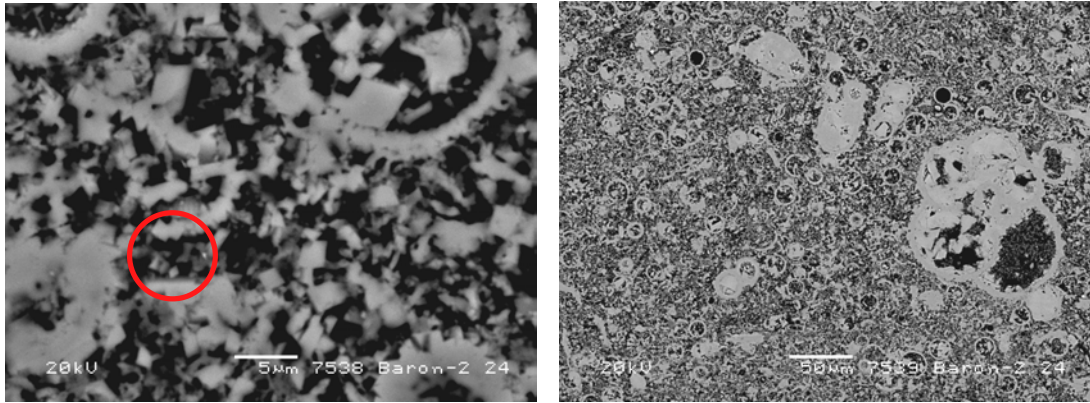


Figure 6. Baron-2 sample 24. Backscatter electron micrographs, Depth 2844 m effective depth 1716 m ($\beta=0.8$ based on acoustic data), Ekofisk Formation, Mudstone, 79% calcite, 12% quartz, 3% feldspar <1% clay (smectite) He-porosity 22.31%. The quartz is seen as tiny grey particles (e.g. within the red circle) mainly disseminated in the pores (calcite white, porosity black). Iso-frame modelling indicates that 8% out of the 12% quartz does not contribute to the supporting frame.

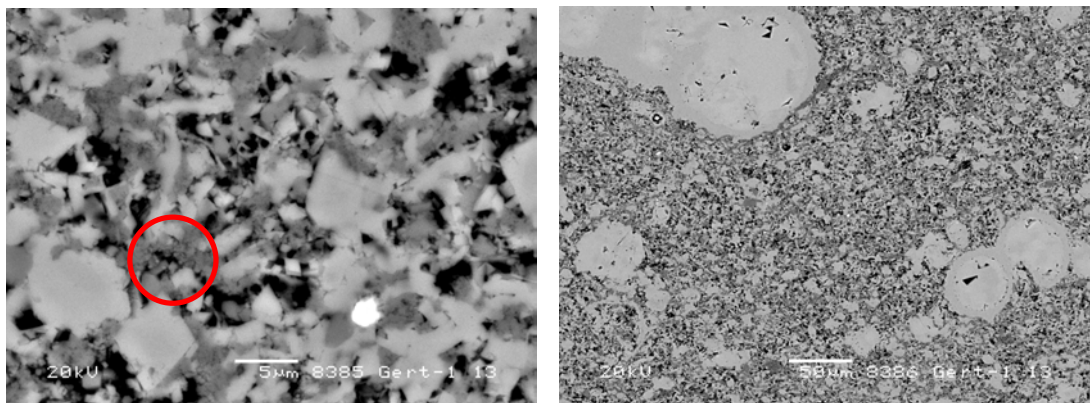


Figure 7. Gert-1 sample 13. Backscatter electron micrographs. Depth 3875 m effective depth 3220 m ($\beta=0.6$ based on acoustic data). Hidra Formation, Mud-wackestone, 69% calcite (Fe-bearing cement) 18% quartz, 4% feldspar, tr. TiO_2 He-porosity 11.58%. The quartz (light grey; e.g. within the red circle) is integrated in the solid frame -17% out of the 18% according to iso-frame modeling (calcite white, porosity black).

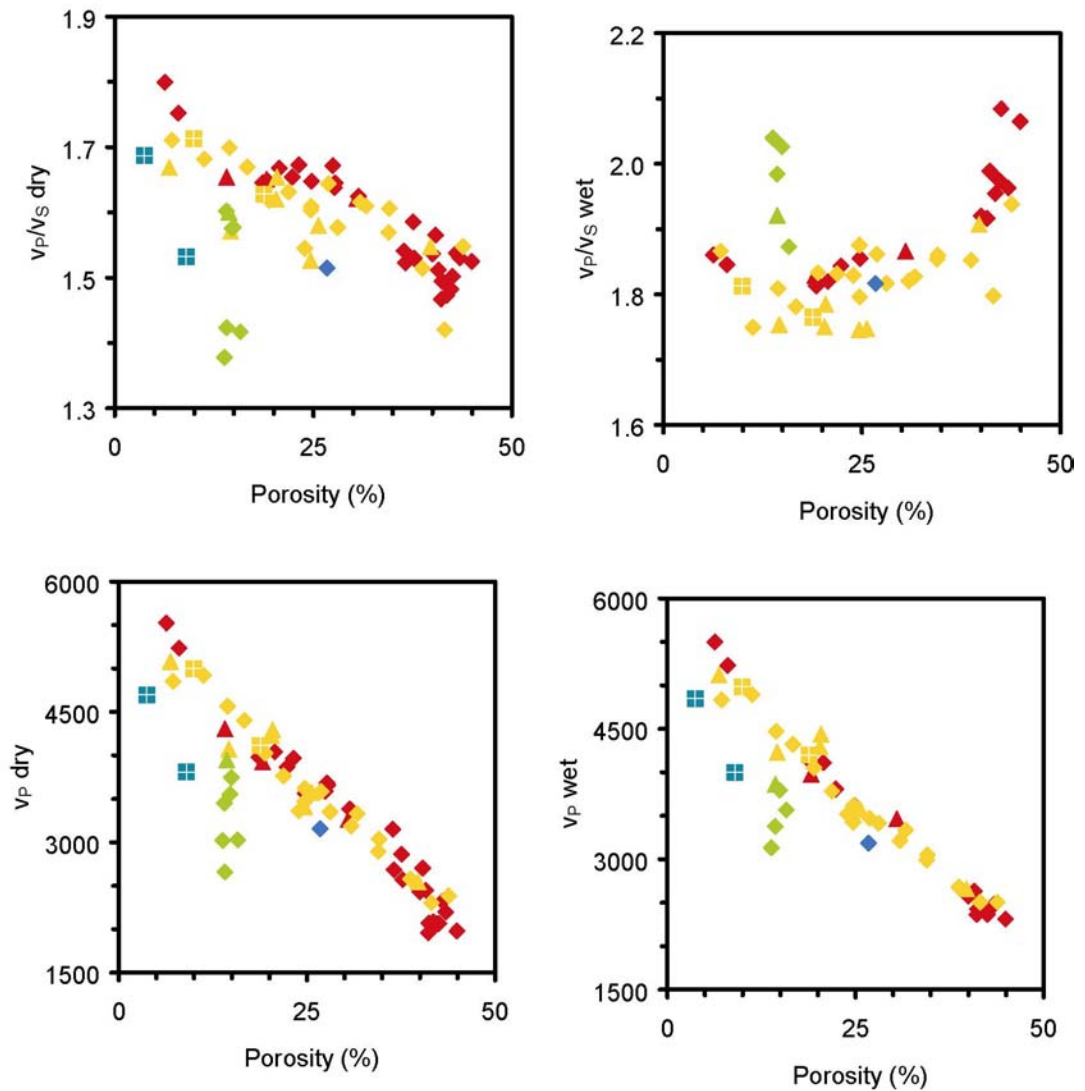


Figure 8. Plot of V_p - V_s ratio versus porosity (upper part) and V_p versus porosity (lower part) for chalk samples investigated in this study plus South Arne samples (dry samples to the left and water saturated samples to the right). A very high correlation is observed between V_p and porosity for clay-free samples (non-green) and a high dependency on fluid content of V_p/V_s . The V_p - V_s ratio also reflects the mineral composition of the chalk: high values are observed for clay-rich wet samples and low values for quartz-rich samples (yellow). Legend in Figure 9.

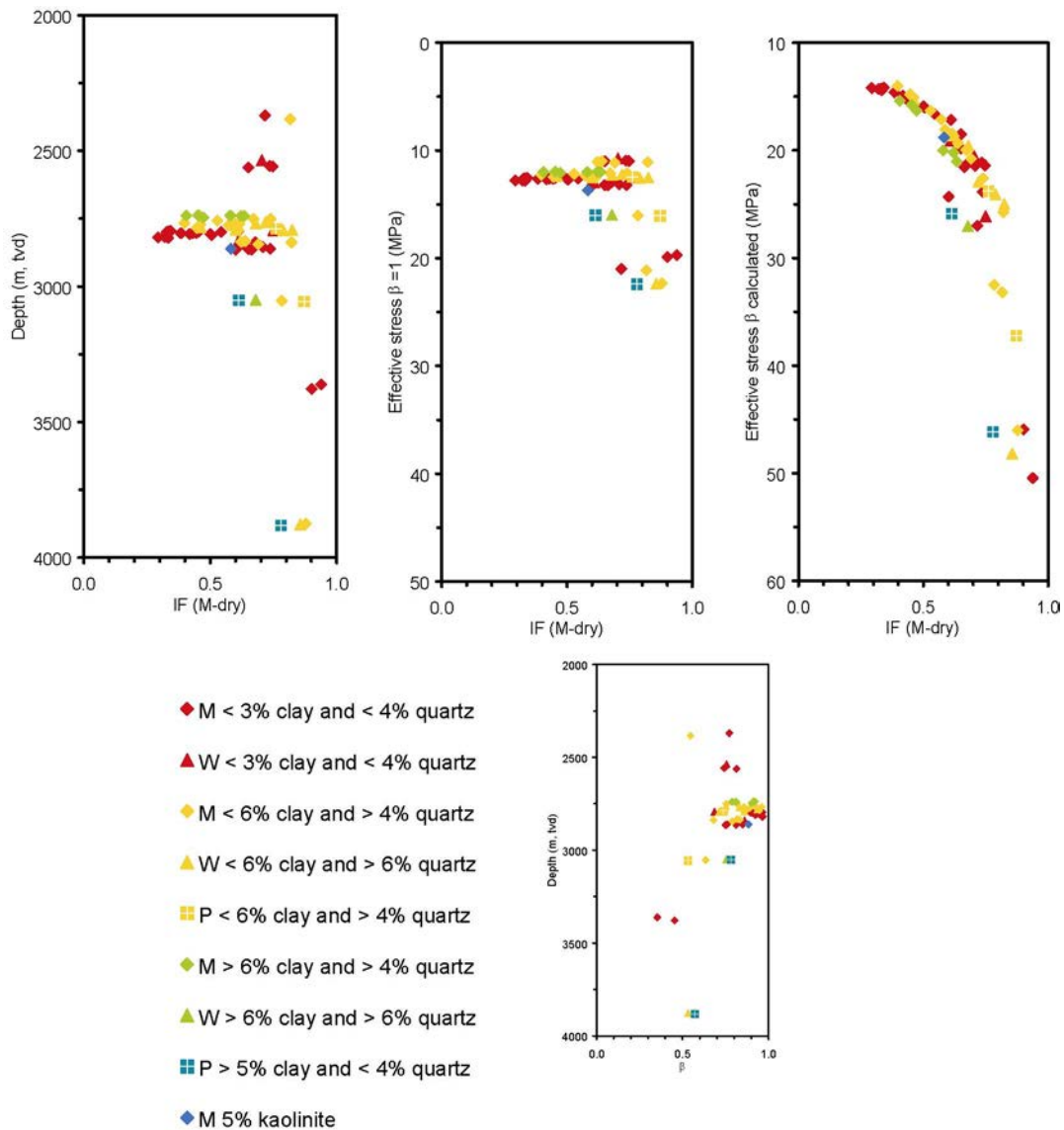


Figure 9. Isoframe (*IF*) modelling of core data (high *IF*-value corresponds to high degree of cementation). *IF* (dry) versus depth (left panel); *IF* (dry) versus effective stress calculated for the Biot factor, $\beta=1$ (middle panel: maximum β giving minimum effective stress); *IF* (dry) versus effective stress calculated for β based on acoustic data (right panel: minimum β giving maximum effective stress). Effective stress calculated from Equation (2) with two estimates of β results in a range of possible values of effective stress. Wet *P*-wave and shear data indicate the same *IF* as dry *P*-wave data (*M*-dry), whereas dry shear data indicate *IF*'s generally higher by 0.05. Plot of depth versus β calculated from acoustic data (lower right). *M*: mudstone; *P*: packstone; *W*: wackestone.

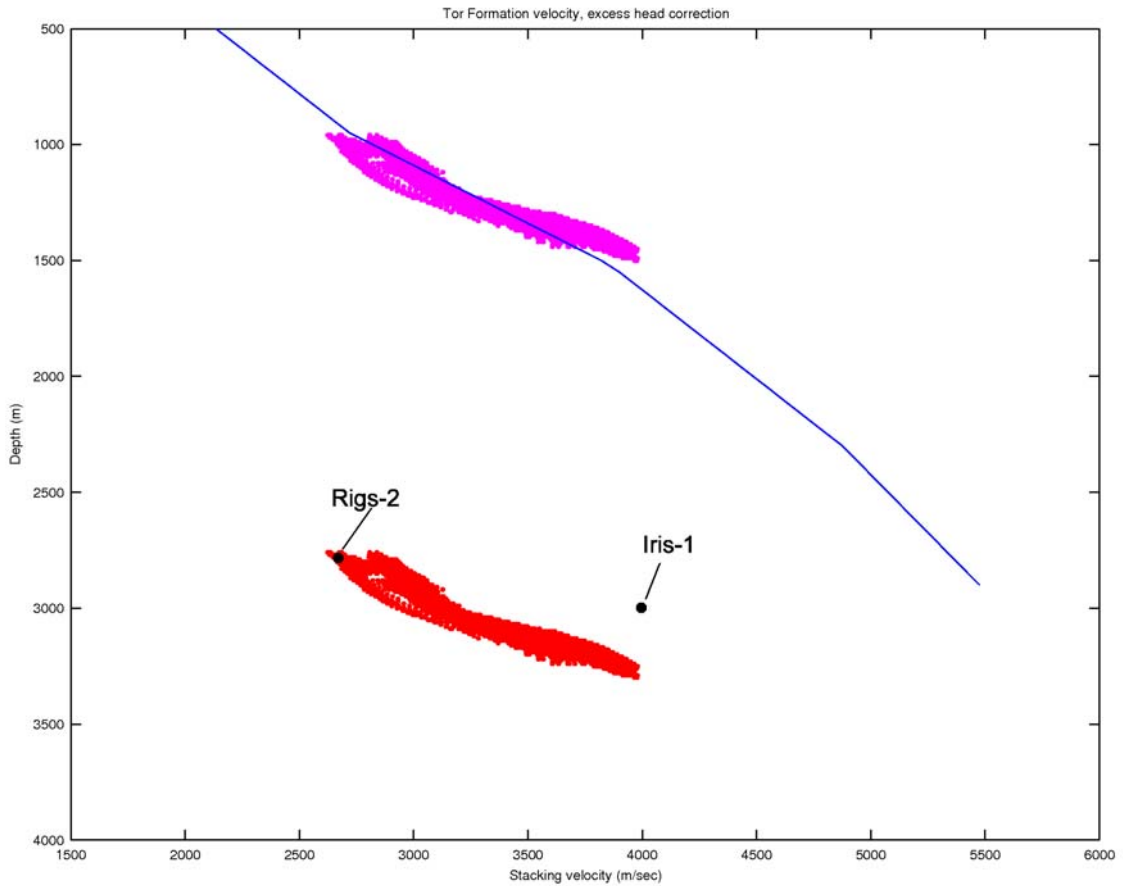


Figure 10. Original stacking velocities for Tor Formation (red dots) from the north eastern quadrant of the South Arne Field. After a depth shift of 1800 m, the population (magenta) falls on the normal velocity-depth trend (blue line; Japsen 2000). This depth shift is larger than predicted by equation (1) for the South Arne chalk overpressure of c. 15 MPa. This is probably because the stacking velocities have been tied to the Rigs-2 wells where porosities are high due to early hydrocarbon entry. The stacking velocities thus fails to match the velocity of the down-flank Iris-1 well.

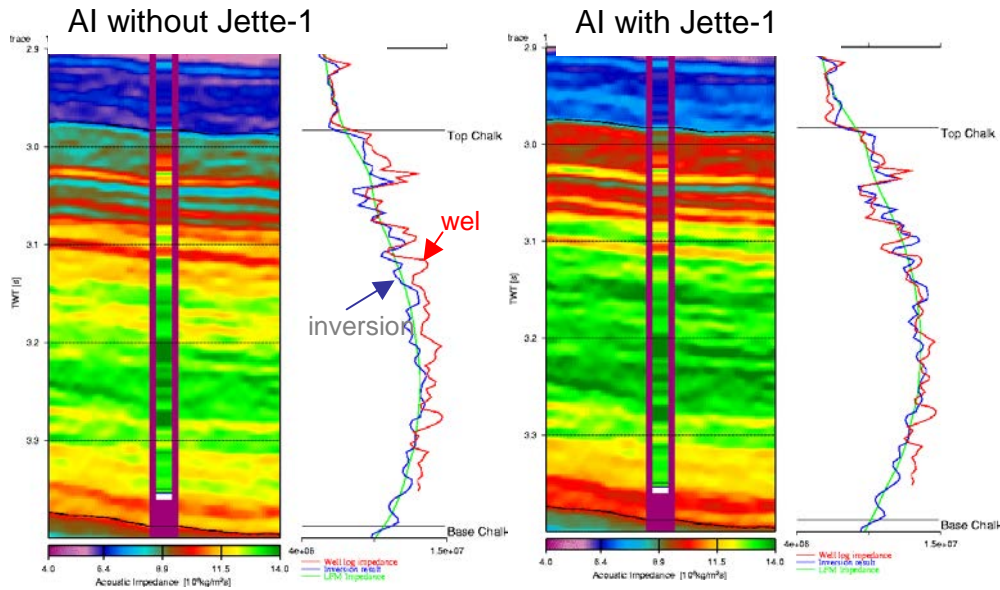


Figure 11. Acoustic impedance (AI) from inversion of seismic data near the Jette-1 well (inserted). Left panel shows blind test result for Jette-1; right panel shows the result where Jette-1 is included. The blind test is based on depth-dependent porosity reduction, but does not include the extra porosity reduction related to the ‘cementation front’ at c. 1800 m effective depth (c. 3.1 s TWT for the Jette-1 well). The blind test thus predicts too low impedance (too high porosity) particularly in the deep part of the chalk (left panel).

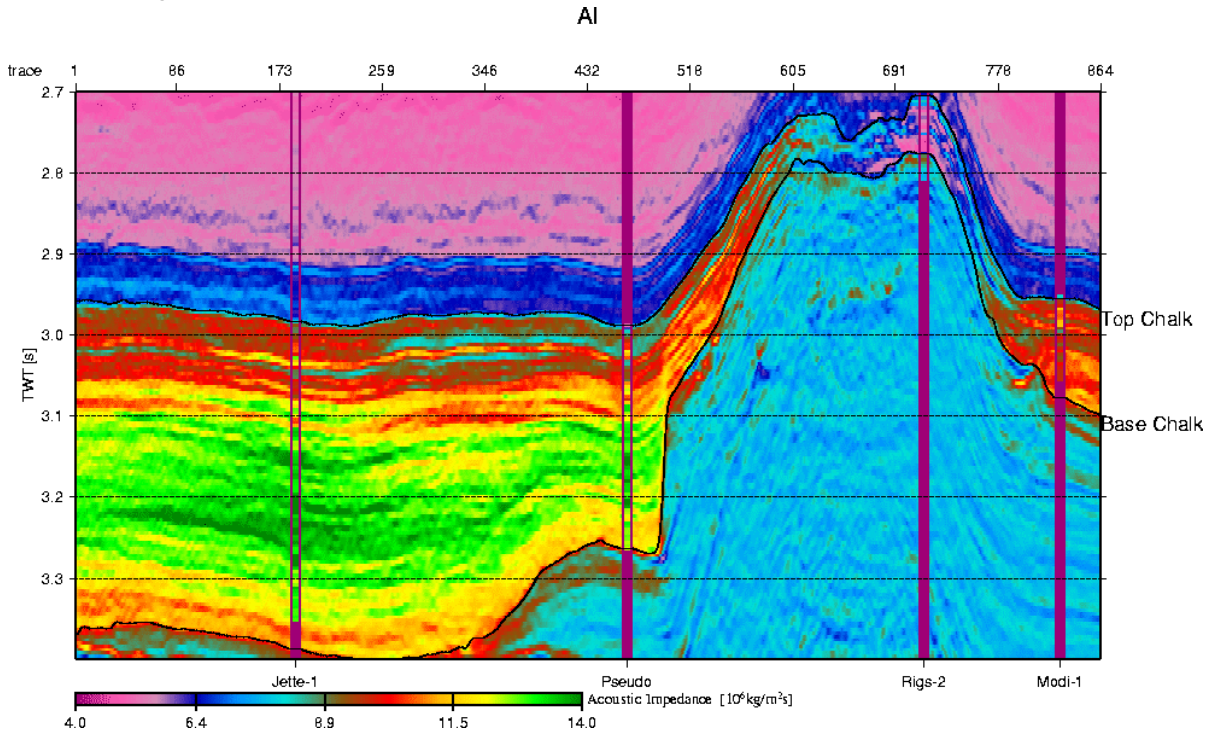


Figure 12. Acoustic impedance section across the South Arne Field. The result of the inversion shows good match with Modi-1 to the east and the adjusted result based on inclusion of the Jette-1 well to the west. Note the change in seismic character below c. 3.1 s TWT west of South Arne, where the predicted high impedance (low porosity) corresponds to the ‘cementation front’ at that depth.

Acknowledgements

The authors greatly appreciate the financial support of the South Arne Group (Amerada Hess, Dong and Denerco). The log data from the chalk in the Jette-1 well are courtesy of Amerada Hess.

Abstracts of reports

Inversion for acoustic impedance with low-frequency information based on the CBV model. Testing predictions of Jette-1 and Modi-1

Anders Bruun, Rasmus Rasmusen and Ole V. Vejbæk
Ødegaard Report 03.24033.02, 2005

Abstract. A test on possible improvements on low frequency models for seismic inversion based on CBV studies has been performed on a random 2-D line connecting the Jette-1, Rigs-2 and Modi-1 wells. It was found that construction of pseudo wells to support construction of the low frequency model caused noticeable improvements in the predictive capability of inversion results. In the selected case, the “cementation front” causes non-linear effects in the spatial variation of acoustic properties that could be remedied by inserting pseudo wells. At the Modi-1 well which lack sonic logs, conversion of porosity to acoustic impedance and creation of a pseudo well based on Jette-1 proved equally powerful as support for low frequency modelling.

Selection of samples. Chalk background velocity

E&R-1. E&R DTU 2003
Ida F. Fabricius and Niels Springer

Abstract. In order to evaluate the variation in background velocity in chalk for seismic interpretation, we need to address the influence of mineralogy and texture. For this purpose we sampled cores from the water zone of eight wells in the North Sea. The sampling intervals were selected based on available conventional core analysis data, ensuring the maximal variation in depth, effective depth, porosity, and permeability. Four 1½ inch vertical plugs were sampled from each of the wells: Q-1, Otto-1, T-3, Gert-1, West Lulu-1, Baron-2, I-1, and Cecilie-1B. Oil stained intervals, fractures, marly zones and stylolites were avoided, except for in well I-1, where no unstained intervals were found. The 32 core samples were characterised by conventional core analysis before final sampling. Final sampling was based on plug condition and so as to avoid duplication of properties. The number of samples was hereby reduced to 21, of which one failed during sonic measurements. Stratigraphy was not taken into account in the process of sampling. The resulting 20 samples represent the Ekofisk Formation, Tor Formation, Hod Formation, Hidra Formation, and Sola Formation.

Sample characterisation report for the chalk background velocity project

Ida L. Fabricius and Sinh H. Nguyen
E&R-2. E&R DTU 2005

Abstract. The 21 samples resulting from final selection were characterised with respect to petrography, mineralogy, chemistry, and selected physical properties: Specific surface by nitrogen adsorption (BET) and stable isotopes. The samples have texture varying from mudstones to packstones. Calcite is the dominating mineral, but the solid phase contains up to 11% clay and up to 19% quartz. In some samples, the quartz may be fine-grained and dispersed in the pore space, in others the quartz is integrated into the solid frame. Image analysis was done on backscatter electron micrographs of polished thin sections, and a textural-mineralogical model was made for each samples. This model formed the basis for iso-frame (IF) modeling of shear- and P-wave moduli of dry and water saturated samples. Wet P-wave and shear data as well as dry P-wave data for each sample could be modeled by the same IF. Shear data for dry samples indicate a c. 0.05 higher IF-value than for the corresponding water-saturated sample. Data from the South Arne field from earlier rock physics projects were included in the interpretation and trends in properties versus depth and versus effective vertical stress were compared. Whereas clear depth trends were difficult to define, trends with respect to vertical effective stress could be seen for porosity, IF, $\delta^{18}\text{O}$, acoustic impedance, and Poisson's ratio. In addition porosity is controlled by texture and mineralogy. The effective stress was calculated from Terzaghi's equation with minimum estimates of the Biot factor based on acoustic data (resulting in maximum estimates of effective stress). This indicates that the burial diagenesis is primarily controlled by stress (effective burial), rather than temperature (depth). Data from the South Arne field are distinctly anomalous when plotted versus depth, but fall into the general trend when plotted versus effective vertical stress.

Chalk background velocity. Well log analysis

Lars Gommesen
Ødegaard Report 03.24033.01, 2005

Abstract. A database of quality controlled well log data originating from the Danish North Sea has been established for 29 wells with focus of the chalk interval. Based on these data dry rock properties have been derived. All wells have bulk density and compressional slowness provided and seven wells also had shear slowness provided (+ one side track). Volume of clay, porosity or water saturation interpretations were provided for 24 wells and for seven wells core measurements (e.g. porosity and density). The quality of the well log data is generally good and corrections were only necessary for few wells: Minor edits were performed for five wells and depth alignments for three wells. The petrophysical analysis was aimed at performing consistent interpretations of the volume of clay, porosity and brine saturation. This analysis showed a good match between the provided interpretation of clay and that carried out in this study, and between the provided porosity and brine saturation curves and those established in this study. Differences between the porosity estimates in

some cases may be explained by choice of method (e.g. density derived estimates versus neutron porosity derived estimates) or by difference in choice of matrix density for the density derived estimates. The rock physics analysis was aimed at estimating Biot's coefficient from log data (bulk density, and dry-rock compressional and shear velocity) in order to estimate the effective stress.

Lithostratigraphy and physical properties of the Chalk Group from Danish North Sea wells

Peter Japsen, Finn Jacobsen and Torben Bidstrup
GEUS Rapport 2005/7

Abstract. The Chalk Group in 29 Danish North Sea wells centred around the South Arne Field has been subdivided into lithostratigraphic units based on bio- and log-stratigraphy. The subdivision includes the Ekofisk, Tor, Hod, Blodøks and Hidra Formations. The interface between the Tor and Hod Formations is defined by referring the surface to the major, Intra-Chalk Unconformity associated with the Late Campanian inversion of the Central Graben area. Chalk formation pressure was estimated based on available well data that are generally from the uppermost chalk. The data agrees with the pattern of overpressure due to disequilibrium compaction in the central North Sea. In Danish waters chalk formation overpressure exceeds 15 MPa towards the north (e.g. the South Arne Field) and decreases towards the south where 8 MPa is estimated for the Skjold Flank-1 well. Temperature at top and base chalk was estimated based on the temperature gradient calculated from available down-hole temperature measurements and a reduced chalk temperature gradient. Minimum temperature at top chalk for the wells studied was c. 70°C and maximum temperature at base chalk c. 125°C. The relations between velocity, porosity and depth for the chalk was studied based on log data (seven wells had S-wave logs). Plots of porosity versus porosity indicate a separation between the formations correlated with the gamma readings and there is an overall drop in porosity with depth and a corresponding increase in velocity. Moreover, there is a pronounced change in velocity and porosity over a narrow depth interval (the 'cementation front') corresponding to c. 1700-1800 m effective depth (depth corrected for overpressure). Different relations between velocity and porosity were observed for chalk at similar effective depth and temperature conditions.

Rock physics analysis of velocity differences in the chinks of wells Jette-1 and Isak-1

Gary Mavko and Peter Japsen
GEUS rapport 2005/16

Abstract. Differences between the sonic log data from wells Jette-1 and Isak-1 have been observed in the chinks of the Ekofisk, Tor, and Hod Formations. Both P- and S-wave velocities in Jette-1 tend to be larger than in Isak-1, while the V_p/V_s ratio is smaller in Jette-1. Comparison with rock physics ellipsoidal pore models suggest that the chalk in Jette-1 have stiffer pores than in Isak-1 and that the mineral end-point properties are different for

the two wells. The moduli were adjusted empirically to find model predictions consistent with both P- and S-wave velocity data because the ellipsoidal inclusion model is very sensitive to the choice of mineral properties. The mineral moduli for Isak-1 were found to be $K=67$ GPa, $G=23$ GPa and those for Jette-1 $K=60$ GPa, $G=27$ GPa. Taking the properties of the Isak-1 mineral as the calcite end-member, the Jette-1 properties correspond to the theoretically expected value for a mixture of 80% calcite and 20% quartz. If the quartz fills the thinnest cracks and grain contacts the result would be a more rigid pore space and thus explain that the chalk in Jette-1 have stiffer pores than in Isak-1. The clean Tor Formation has little variation with gamma ray, whereas the clay-bearing Ekofisk and Hod Formations have a large variation in gamma ray and a corresponding spread in V_p vs porosity (apparent aspect ratios). This spread thus probably reflects the presence of clay, rather than a systematic change in pore shape. Velocities in Isak-1 increase monotonically with depth without a significant change of pore shape (porosities decreasing from 25% to less than 10%), while in Jette-1 the velocities are not well correlated with depth.

Special core analysis for chalk background velocity project. Ultrasonic velocity measurements on plug samples of chalk from the wells Q-1, Otto-1, T-3, Gert-1, West Lulu-1, Baron-2, I-1 and Cecilie-1B

Dan Olsen
GEUS Rapport 2004/106

Abstract. GEUS Core Laboratory has carried out ultrasonic velocity measurements on twenty 1.5" plug samples from 8 wells in the Danish Central Graben. The stratigraphic position of the samples ranges from the Tuxen Formation to the Ekofisk Formation (Lower Cretaceous–Paleocene). The sample porosity ranges from 3.7% to 26.9% and the permeability from 0.002 to 0.86 mD. P- and S- wave velocities were measured at a hydrostatic confining pressure of 75 bar and 23°C on dry samples in humidity controlled state (60°C, 40%RH) as well as on water saturated samples. Two of the samples were also measured at hydrostatic confining pressures of 125 and 200 bar. For measurements in the water-saturated state, estimates of pore volume compression and length reduction were obtained by quantification of the amount of water expelled during sample loading. Centre frequencies of 700 kHz were used for the measurements. Precision and reproducibility of the ultrasonic velocity determinations are considered to be better than 1% (1 σ level). This is estimated from replicate measurements, standard measurements and repeat measurements on two chalk samples where measurements from a previous project existed. For some samples in humidity controlled state reproducibility may have deteriorated to 2%, probably due to difficulty with controlling the saturation state of clay minerals. The equilibration at humidity controlled conditions increased the weight of the samples by from nil to 0.5 g, corresponding to S_w increases between 0 and 19%, the reference state being drying at 60°C without humidity control. The measured ultrasonic velocities appear to be in reasonable agreement with the modified upper Hashin-Shtrikman model for chalk. Both P- and S-velocities increased 0.3% for a sample with 11% porosity after increasing hydrostatic pressure from 75 to 200 bar. P-

velocity increased 1.9% and S-velocity 1.3% for a sample with 22% porosity after a similar pressure increase.

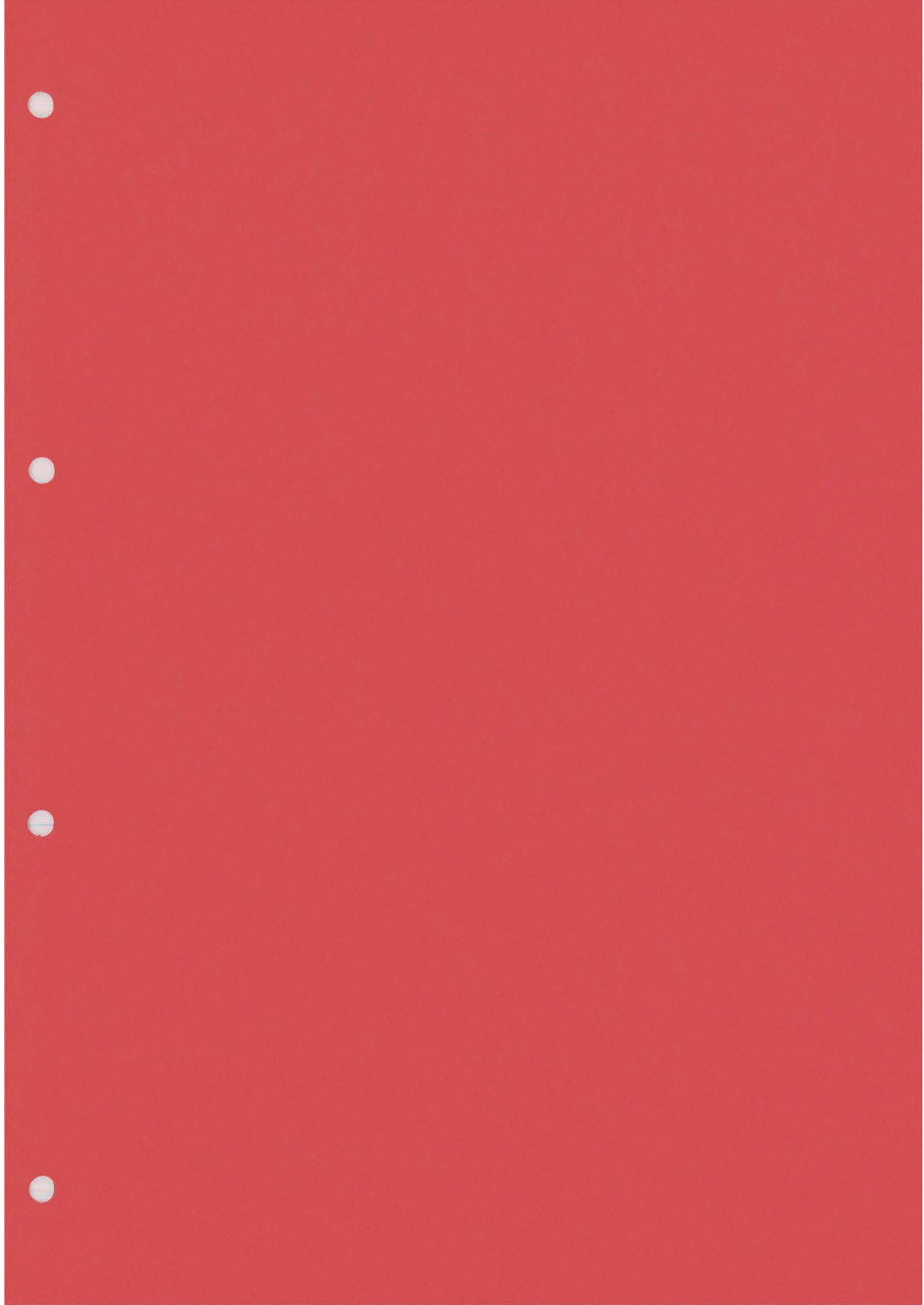
Seismic velocities in the chalk, NE part of the South Arne Field

Ole Vejbæk and Peter Japsen
GEUS Rapport 2005/23

Abstract. A subset of a seismic velocity cube from the north eastern quadrant of the South Arne Field has been analysed for consistency with general chalk velocity models. The cube covers the Rigs-2 and Modi-1 well among others. The chalk velocities in this cube show a clear depth-dependency that corresponds to the prediction of the general model. The absolute level of the velocities are, however, clearly tied up with well data from the Rigs-2 well, and this may result in down-flank propagation of the properties of the chalk in this well. The velocity at the Rigs-2 well location is seen to be smoothly continuous with the entire east flank velocity distribution such that only gradual depth dependencies are seen. However, the Rigs-2 well (and immediate vicinity) is probably a local anomaly due to porosity preservation from early hydrocarbon invasion (resulting in high porosity and low velocity in both Tor and Ekofisk Formations). Velocities in the Rigs-2 well are over 1000 m/sec too low compared to a normal velocity-depth trend even considering observed excess fluid pressures. Of these 1000 m/sec about 200 may be attributed to fluid effects (oil content) leaving about 800 m/sec to be attributed to porosity preservation from early hydrocarbon invasion. This corresponds to a c. 400 m shallower burial than the present. The down flank velocity prediction from the seismic velocity cube is therefore expected to be wrong.

Selected references

- Berryman, J.G., 1995. Mixture theories for rock properties, *In: A Handbook of Physical Constants*, Ahrens, T.J., ed., American Geophysical Union, Washington, 236 pp.
- Britze, P., Japsen, P. & Andersen, C. 1995. Geological map of Denmark 1:200,000. The Danish Central Graben. "Base Chalk" and the Chalk Group (two-way traveltime and depth, interval velocity and isochore). Geological Survey of Denmark Map Series **48**.
- Engstrøm, F. 1992. Rock mechanical properties of Danish North Sea chalk. *In: Fourth North Sea Chalk symposium*. Joint Chalk Research, Deauville. 23 pp.
- Fabricius, I. L. 2003. How burial diagenesis of chalk sediments controls sonic velocity and porosity. *AAPG Bulletin* **87**, 1755–1778.
- Gommesen, L. 2003. Prediction of porosity and fluid in chalk from acoustic measurements. Technical University of Denmark (DTU). PhD Thesis.
- Japsen, P. 1998. Regional velocity-depth anomalies, North Sea Chalk: a record of overpressure and Neogene uplift and erosion. *AAPG Bulletin* **82**, 2031–2074.
- Japsen, P. 2000. Investigation of multi-phase erosion using reconstructed shale trends based on sonic data. Sole Pit axis, North Sea. *Global and Planetary Change* **24**, 189–210.
- Mackertich, D. S. & Goulding, D. R. G. 1999. Exploration and appraisal of the South Arne Field, Danish North Sea. *In: Fleet, A. J. & Boldy, S. A. R. (eds) Petroleum Geology of Northwest Europe: Proceedings of the 5th Conference*. Geological Society, London. 959–974.
- Mavko, G., Mukerji, T. & Dvorkin, J. 1998. *The rock physics handbook*. Cambridge University Press, Cambridge.
- Sclater, J. G. & Christie, P. A. F. 1980. Continental stretching; an explanation of the post-Mid-Cretaceous subsidence of the central North Sea basin. *Journal of Geophysical Research* **85**, 3711–3739.
- Surlyk, F., Dons, T., Clausen, C.K. & Highan, J. 2003: Upper Cretaceous. *In: Evans, D., Graham, C., Armour, A. & Bathurst, P. (eds), 2003. The Millennium Atlas. Petroleum geology of the Central and Northern North Sea*.
- Terzaghi, K. & Peck, R.P. 1968. *Soil mechanics in engineering practice*, John Wiley and Sons, New York.
- Vejbæk, O. V., Rasmussen, R., Japsen, P., Pedersen, J. M., Fabricius, I. L. & Marsden, G. *in press*. Modelling seismic response from North Sea Chalk reservoirs resulting from changes in burial depth and fluid saturation. *In: Doré, A. G. & Vining, B. (eds) Petroleum Geology: NW Europe and Global Perspectives: Proceedings of the 6th Conference*. Geological Society, London.



Z-99 Mineralogical and textural control on chalk background velocity and porosity

IDA L. FABRICIUS¹, LARS GOMMESEN², DAN OLSEN³, NIELS SPRINGER³, PETER JAPSEN³, FINN JAKOBSEN³, CHRISTIAN SCHIØTT⁴

¹ Technical University of Denmark (E&R DTU) (if@er.dtu.dk), Bygningstorvet 115, DK-2800 Kgs. Lyngby, Denmark; ²Ødegaard AIS, Copenhagen, Denmark; ³GEUS, Copenhagen, Denmark; ⁴Amerada Hess, Copenhagen, Denmark.

Introduction

In order to evaluate the variation in background velocity in chalk for seismic interpretation, we need to address the influence of mineralogy and texture. For this purpose we sampled cores from the water zone of eight wells in the North Sea. The sampling intervals were selected based on available conventional core analysis data, ensuring the maximal variation in depth, effective depth, porosity, and permeability. The effective depth was estimated in two ways: 1. by simply subtracting the overpressure from the overburden stress, and 2. by taking Biot's coefficient into account (see abstract by Japsen et al., this volume, for overpressure data refer Japsen (1998)). The Biot coefficient, β , was calculated from data for dry samples as: $\beta = \rho(v_p^2 - 4/3v_s^2)/K_{\text{calcite}}$, where ρ is density, v_p is P-wave velocity, v_s is shear wave velocity, and K_{calcite} is bulk modulus of calcite. The progressing sample stiffening with effective depth was described by an isoframe model (Fabricius 2003). For this purpose a critical porosity of 60% was chosen (Anderson 1999).

Core samples		Depth	Thin section	Over-pressure	He-porosity	75 bar hydrostat. pressure				Selected solid phase components, from XRD and AAS		
Well	Formation	TVD	Dunham texture	ΔP		Air dried		Water sat.		Chlo-rite	Kao-linite	Quartz
		m		MPa	%	v_p	v_s	v_p	v_s	%	%	%
Q-1	Ekofisk	3049	Wackes.	14.5	14.35	3948	2467	3863	2011	6.6		5.8
Q-1	Ekofisk	3051	Packs.	14.5	8.97	3809	2486	4001		11.0		3.8
Q-1	Ekofisk	3053	Muds.	14.5	14.43	4566	2687	4470	2471	3.9		19.3
Q-1	Ekofisk	3056	Packs.	14.5	9.91	4999	2917	4984	2749			13.7
Otto-1	Hod	2555	Muds.	14.6	19.23	4011	2434	4106	2265	2.1		1.1
Otto-1	Hod	2558	Muds.	14.6	20.72	4043	2424	4112	2259	0.7		0.6
T-3	Tor	2535	Wackes.	14.60	19.1	3924	2377	3974	2173	1.2		0.5
T-3	Tor	2561	Muds.	14.60	24.77	3560	2161	3620	1951	1.1		0.7
Gert-1	Hidra	3875	Muds.	16.4	11.28	4921	2926	4892	2797			17.8
Gert-1	Hidra	3877	Wackes.	16.4	6.85	5079	3044	5119				15.1
Gert-1	Hidra	3881	Packs.	16.4	3.7	4700	2785	4850		5.2		3.2
WLulu-1	Hod	3361	Muds.	13.90	6.32	5525	3070	5498	2955	1.4		1.9
WLulu-1	Hod	3378	Muds.	13.90	8.01	5235	2988	5228	2833	1.9		1.5
Baron-2	Ekofisk	2833	Muds.	17.30	26.9	3588	2182	3471	1865	2.0		8.9
Baron-2	Ekofisk	2836	Muds.	17.30	24.69	3470	2164	3425	1826	3.0		10.8
Baron-2	Ekofisk	2837	Muds.	17.30	16.68	4405	2638	4319	2425			18.3
Baron-2	Ekofisk	2844	Muds.	17.30	21.87	3765	2308	3784	2066	0.3		11.5
I-1	Tuxen	2861	Muds.	14.9	26.73	3156	2083	3185	1753	0.6	5.2	1.6
Cecilie-1B	Ekofisk	2365	Muds.	2.70	14.9					4.1		9.1
Cecilie-1B	Ekofisk	2370	Muds.	2.70	22.36	3868	2338	3807	2065	2.3		3.8
Cecilie-1B	Ekofisk	2383	Muds.	2.70	7.21	4853	2837	4832	2589	2.1		12.7

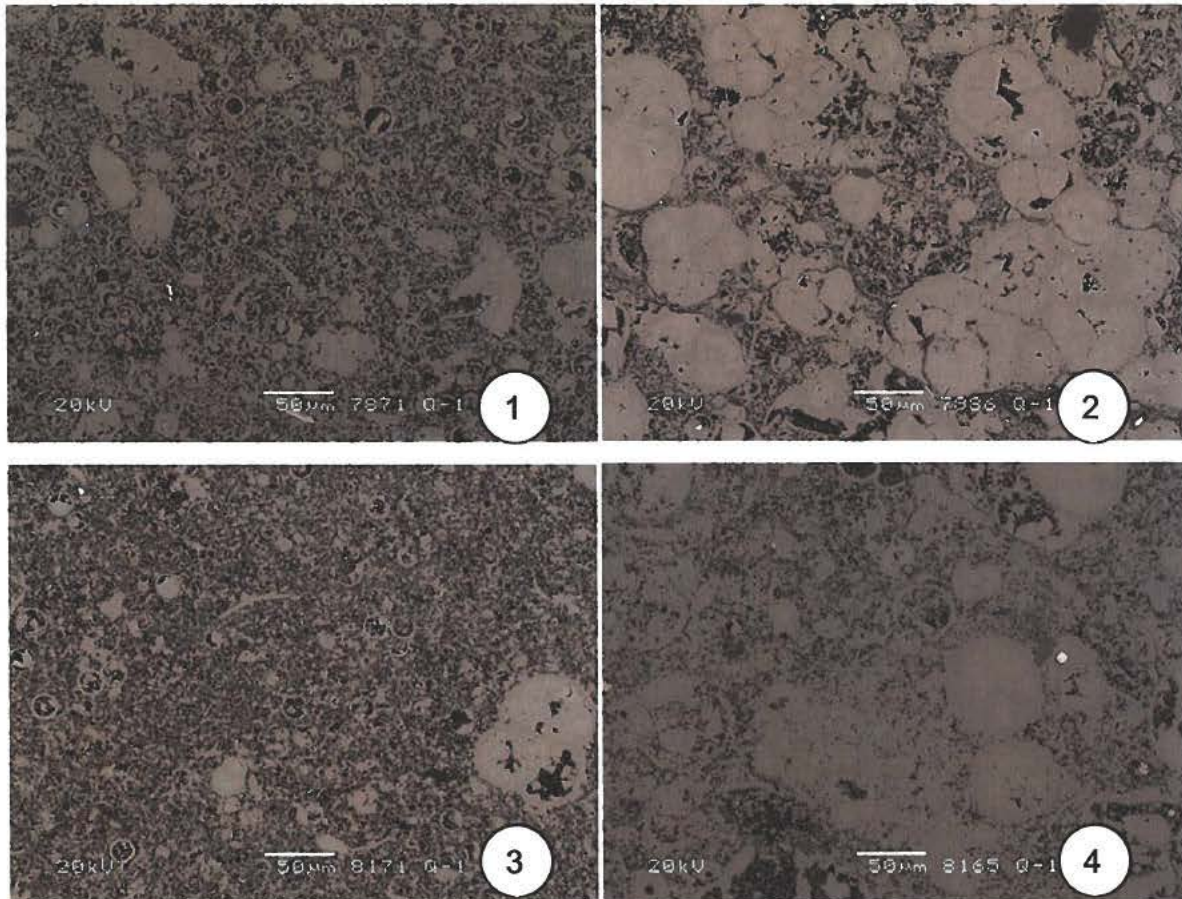


Figure 1. Control of texture on porosity and of quartz content on sonic velocity. Backscatter electron micrographs of samples from well Q-1. Light patches are cemented microfossils, pore-space is black. The well sorted samples (1 and 3) have higher porosity (14%) than the less well sorted samples (2 and 4) (porosity: 9%-10%). The quartz rich samples (3 and 4) have higher sonic velocity than the quartz poor samples (1 and 2). The samples are collected within a 7 m depth range. Refer to table.

Method

The samples were studied by conventional core analysis and P- and S-wave velocities were measured on dry and on water saturated samples under hydrostatic pressure (table). The texture and mineralogy were studied in thin section, backscatter electron micrography combined with EDS, X-ray diffraction, and wet chemical analysis (AAS).

Results

Porosity and sonic velocity are both primarily controlled by effective burial, so that velocity increases and porosity declines with depth. In order to clearly see this effect, the Biot coefficient must be taken into account. For a given burial depth, the Biot coefficient varies with texture and mineralogy, so that samples with low porosity tend to have higher Biot coefficient and consequent deeper effective burial. For a given (effective) burial, porosity is mainly controlled by texture, sonic velocity mainly by mineralogy: Mudstones tend to have higher porosity than wackestones and packstones. Calcite rich samples tend to have high v_p , quartz-bearing samples tend to have high v_s , and clay rich samples tend to have low velocity (Figure 1, 2).

For each dominating mineralogy, elastic moduli increase and porosity decreases with effective depth (Figure 3). From 30% to 20% porosity, IF increases from 0.8 to 0.9, and depth trends representing different mineralogy are close. From 20% to 5% porosity the moduli follow different trends depending on mineralogy. For P-wave modulus, purely calcitic samples follow the highest trend, quartz-rich samples a lower trend, and clay-rich samples the lowest trend. For shear moduli, quartz rich

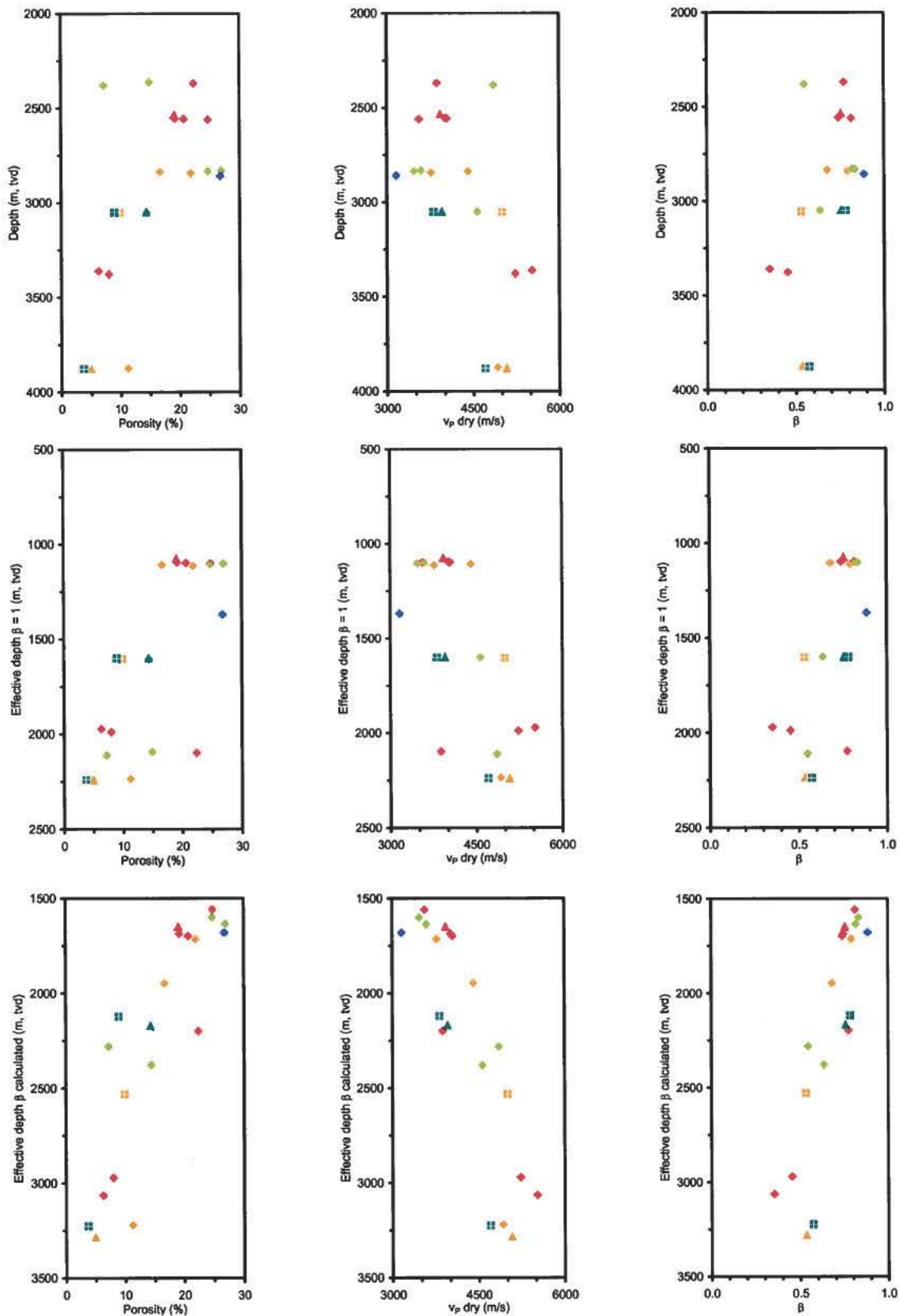


Figure 2. Porosity, P-wave velocity, v_p , of dry samples, and Biot's coefficient, β , as function of vertical depth (top), effective depth under assumption of $\beta = 1$ (middle) or β calculated from dry velocities (base). For a given depth, porosity, v_p and β are all controlled by texture and mineralogy, but porosity is primarily controlled by texture, whereas v_p and β are primarily controlled by mineralogy. Depth trends for porosity and v_p are only vague. When depth is replaced by effective depth assuming $\beta = 1$, the trends are slightly more visible, but when a β calculated from velocity is used, marked depth trends appear. For legend see Figure 3.

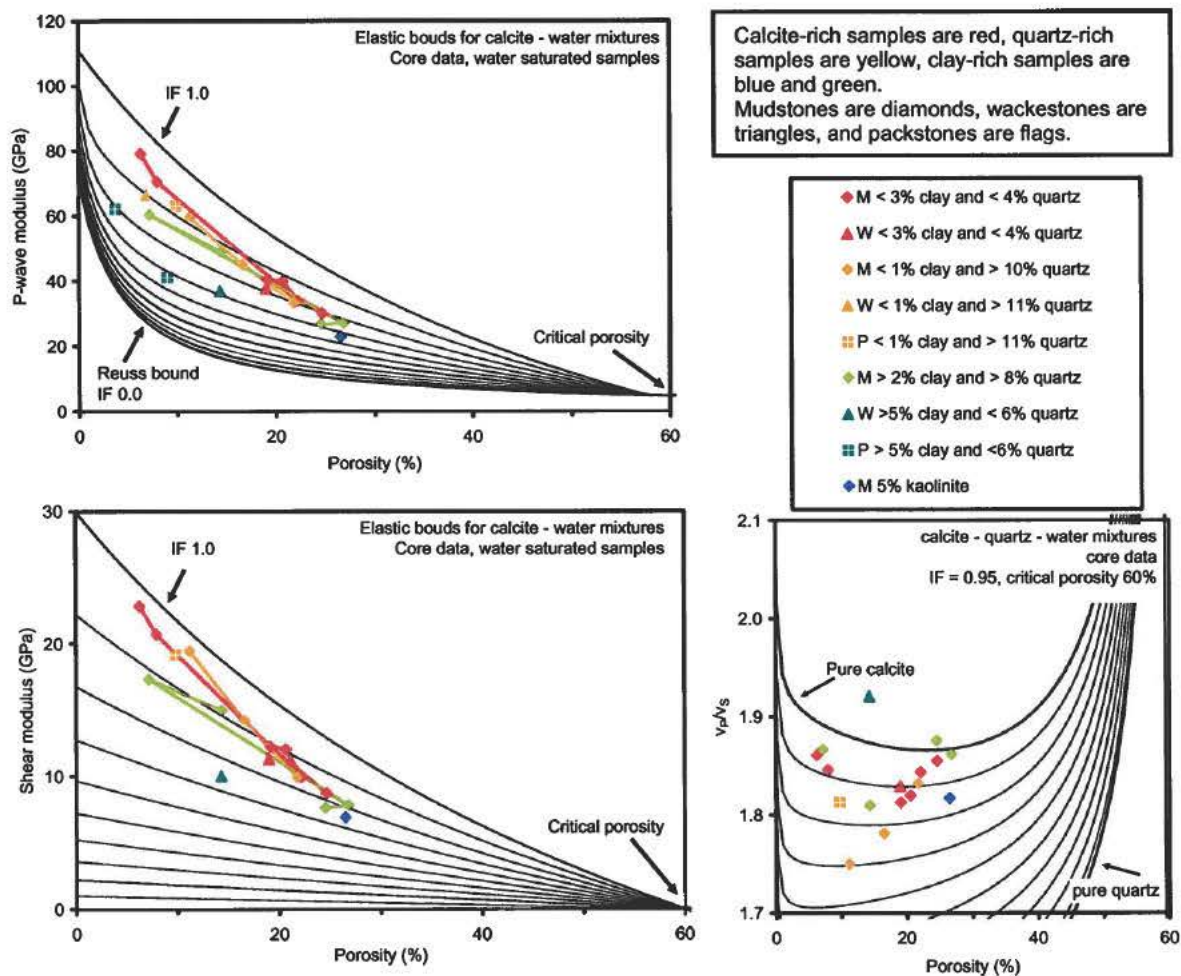


Figure 3. Iso-frame modeling of elastic moduli of water saturated samples. The modified Hashin-Shtrikman bounds for P-wave modulus (ρv_p^2) and shear modulus (ρv_s^2) are modeled under assumption of a pure calcite mineralogy. Each black IF-curve represents a constant proportion of the solid in the supporting frame. The colored lines connect samples of increasing effective depth assuming varying β . v_p/v_s is modeled under assumption of a constant proportion of solid in the supporting frame (IF) and a varying proportions of calcite and quartz.

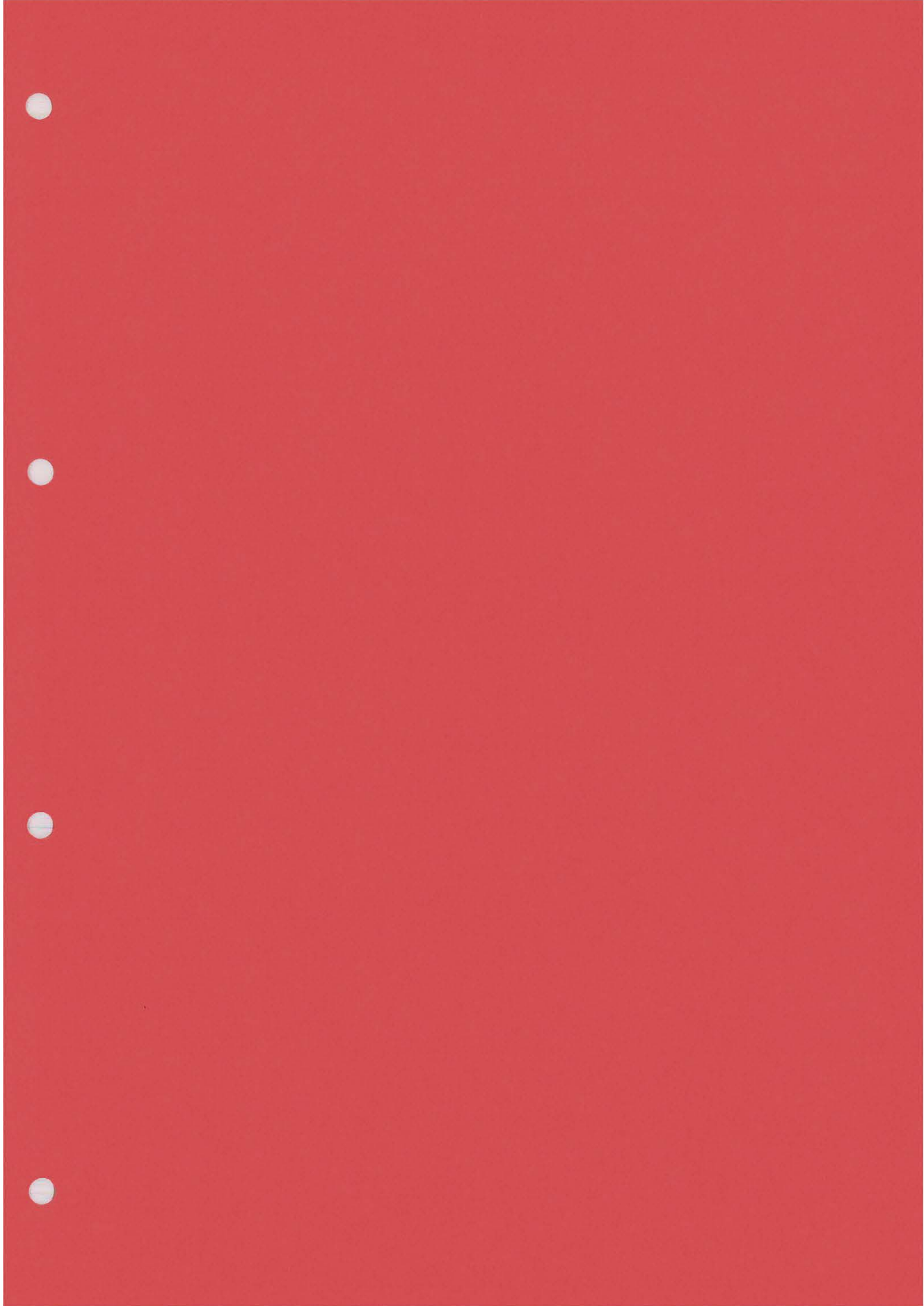
samples follow the highest trend, purely calcitic samples a lower trend, and clay-rich samples the lowest trend. This is probably a consequence of quartz having the highest shear modulus, calcite the highest P-wave modulus, and clay the lowest moduli. v_p/v_s exposes the effect of mineralogy (Figure 3). Quartz rich samples have lower v_p/v_s than calcite rich, which again have lower v_p/v_s than clay rich samples. Whereas modeling P-wave modulus and shear moduli from an iso-frame concept is relatively robust, modeling v_p/v_s is more delicate. The presented model seems to over-predict the quartz content.

Acknowledgement

This study was funded by the South Arne Group (Amerada Hess Denmark, Dong E&P, Denerco Oil).

References

- Anderson, J. K., 1999, The capabilities and challenges of the seismic method in chalk exploration, in A. J. Fleet, A. J., and S. A. R. Boldy, eds., Petroleum geology of Northwest Europe, Proceedings of the 5th conference: London, Geological Society, p. 939-947.
- Fabricius, I. L. 2003. How burial diagenesis of chalk sediments controls sonic velocity and porosity. *AAPG Bulletin*, 87, 1755–1778.
- Japsen, P. 1998. Regional velocity-depth anomalies, North Sea Chalk: a record of overpressure and Neogene uplift and erosion. *AAPG Bulletin*, 82, 2031–2074.



Z-99 Chalk background velocity: Influence of effective stress and texture

PETER JAPSEN¹, GARY MAVKO², LARS GOMMESEN³, IDA L. FABRICIUS⁴, FINN JACOBSEN¹, OLE VEJBÆK¹, RASMUS RASMUSSEN¹, CHRISTIAN RAU SCHIØTT⁵

¹ Geological Survey of Denmark and Greenland (GEUS) (pj@geus.dk), Øster Voldgade 10, DK-1350 Copenhagen; ² Stanford University, California, USA; ³ Ødegaard A/S, Copenhagen, Denmark; ⁴ Danish Technical University (DTU); ⁵ Amerada Hess Aps.

Abstract

The relative variations in acoustic impedance and hence porosity may be determined by inversion of seismic data. The estimation of the absolute level of these parameters, however, requires a priori knowledge about the low-frequency, background velocity. We find that the background velocity of the North Sea chalk is primarily controlled by effective stress: velocity and porosity log data for chalk in two wells plotted versus effective depth match published reference lines for normally compacted chalk above c. 1.8 km. Effective depth is depth corrected for the effect of overpressure. Below that depth we observe a significant drop in porosity and an increase in velocity that possibly may be explained by a decrease in the Biot factor leading to an increase in effective stress and hence in pore-filling cementation originating from pressure dissolution along stylolites. Moreover, we observe different velocity-porosity relation for the chalk in the two wells leading to differences in porosity of some 5% for identical values of velocity for apparently pure chalk. These variations may be related to differences in contact cementation between the poorly cemented and stiffer pore shapes (possibly affected by quartz-overcoating). The non-unique velocity-porosity relation for chalk will lead to variability in the estimation of porosity from seismic data because one impedance value may represent a range of porosities.

Introduction

The background velocity of a depth interval – or the low-frequency velocity variations – define the absolute level of the sonic velocity. This background velocity cannot be resolved from reflection seismic data that depend on relatively high-frequency variations of the acoustic impedance. Consequently, the background velocity has to be estimated from e.g. near-by wells before seismic data can be inverted to porosity of the right magnitude. Here we investigate the controls on the regional variations of the background velocity of the Upper Cretaceous-Danian Chalk Group in the central North Sea.

Terzaghi's principle states that the weight of the overburden per unit area, S , is borne partly by the rock matrix and partly by the pore fluid: $S = S_{eff} + \beta \cdot P$, where S_{eff} is the effective stress transmitted through the matrix, P is the formation pressure and β the Biot factor that ranges between 0 and 1 ($\beta=1$ for high-porosity rocks). If a rock is more deeply buried without change in effective stress, the added load is carried by an increase in pore pressure, ΔP . We can rewrite Terzaghi's equation in terms of the gravitational acceleration, $g=9.807 \text{ m/s}^2$, average bulk density, $\rho_b \approx 2 \text{ g/cm}^3$, and pore fluid density, $\rho_f \approx 1 \text{ g/cm}^3$, of the added overburden:

$$Z_{eff} = Z - \frac{\beta}{g(\rho_b - \beta \cdot \rho_f)} \Delta P \quad (1)$$

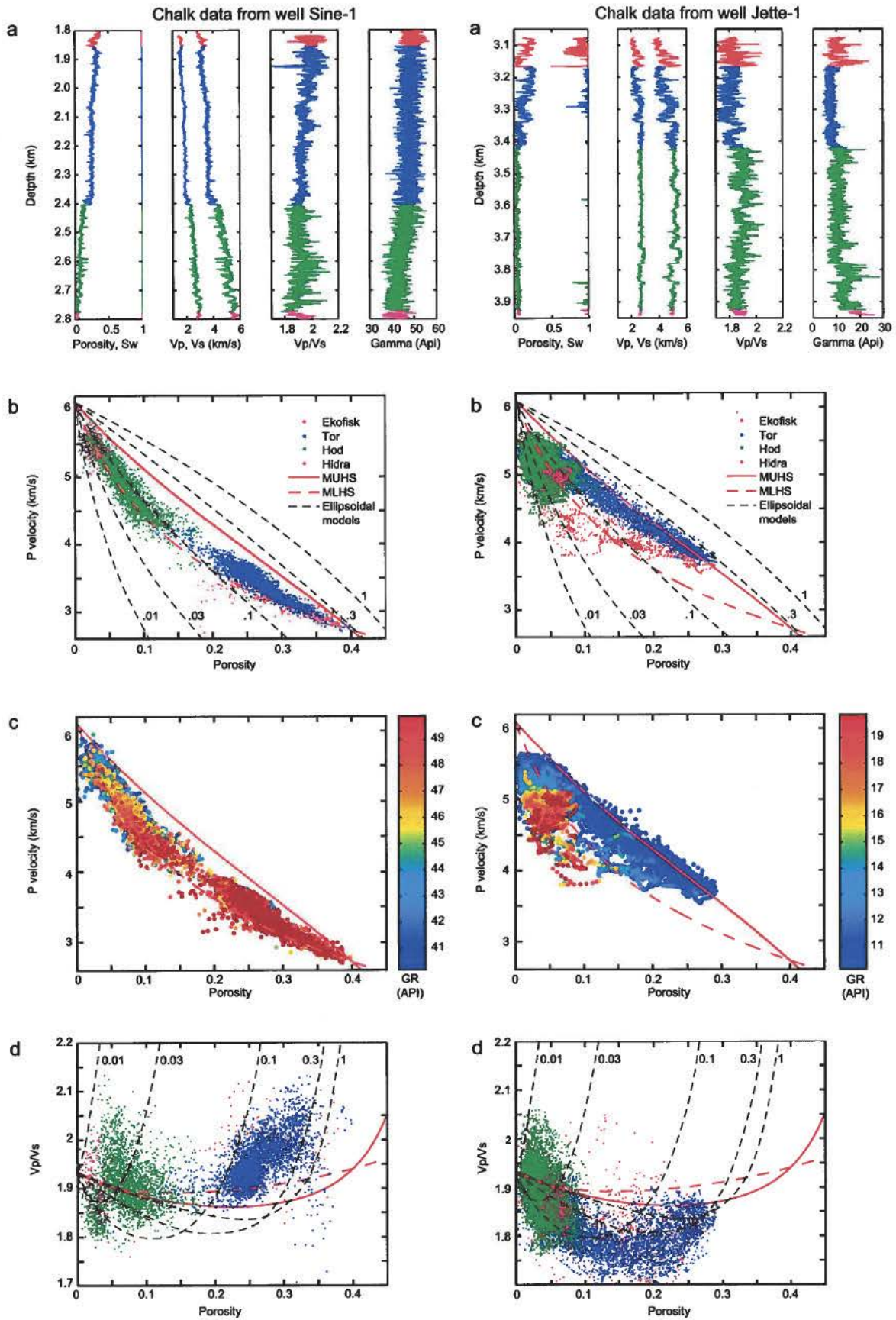


Figure 1 (left). Log data from the chalk in the Sine-1 well: a. Log data vs depth; b. and c. V_p vs porosity; d. V_p/V_s vs porosity. **Figure 2 (right).** Log data from the chalk in the Jette-1 well. Same panels as in Fig. 1. Figs a, b, d color-coded by formation and Fig. c by gamma. Superimposed: Ellipsoidal pore models for different aspect ratios (Berryman 1995) and empirical modified upper and lower Hashin-Shtrikman chalk models (Walls et al. 1998).

where Z is the actual depth of the rock and Z_{eff} is the effective depth corresponding to the depth where the effective stress would occur during normal compaction. For $\beta=1$ we get $Z_{eff} \approx Z - \Delta P \cdot 100$, and for $\beta=0.5$ we get $Z_{eff} \approx Z - \Delta P \cdot 33$ (Z in metres, ΔP in MPa) (cf. Japsen 1998).

Data

We have analyzed the variation of the acoustic properties of chalk based on log data from 29 Danish wells in the central North Sea. All wells had P-wave sonic logs and 8 also S-wave logs. Of these wells we present data from the Sine-1 and Jette-1 wells both penetrating c. 1 km thick, dry chalk sections (Figs 1, 2). The absolute level of the gamma-readings in the wells is not comparable because of insufficient calibration of the gamma tools. Chalk formation overpressure was 6.5 MPa in the Sine-1 well, whereas the overpressure in the 1.2 km more deeply buried chalk in the Jette-1 well is estimated to be 14.5 MPa as in a near-by well.

Results

Figure 3 shows a plot of the sonic and porosity logs for the chalk in the Sine-1 and Jette-1 wells versus actual depth and effective depth assuming $\beta = 1$ (eq. 1). We observe that for effective depths less than c. 1.8 km, the data plot along the $V-Z$ and $V-\phi$ reference curves for normally compacted chalk of Japsen (1998) and Sclater & Christie (1980). Below that depth a pronounced porosity drop and a corresponding velocity increase is observed over a short depth interval for both data sets. These observations imply that porosity reduction and velocity increase for chalk is governed by the effective stress for porosities less than c. 40% and that below some 20% a rapid increase in pore-filling cementation takes place.

Figs. 1 and 2 show different $V-\phi$ relations for the chalk in the two wells. Chalk with low gamma-response has higher porosity for a given velocity in the Jette-1 well than in the Sine-1 well; e.g. for $V=4.5$ km/s, porosity is c. 15% and only c. 10% in the two wells, respectively. The difference between the two data sets is clear from the much lower V_P-V_S ratios measured in the Jette-1 well compared to the Sine-1 well (Figs 1d, 2d). There is a general symmetry between gamma log and the V_P/V_S log: low gamma readings for the Tor Formation in the Jette-1 well correspond to low values of V_P/V_S , and high values of these parameters for the Ekofisk and Hod formations (Figs 1a, 2a). This indicates that both gamma readings and V_P-V_S ratios are indicators of the mineralogical composition.

Discussion

Pore-filling cementation

Mechanical compaction is limited in chalk with porosity less than 40%, whereas porosity reduction due to cementation originating from pressure dissolution at stylolites starts around that porosity (Fabricius 2003). The match seen in Fig. 3 between velocity and porosity data versus effective depth and the reference curves (that were defined by identifying normally compacted chalk) above c. 1.8 km implies that the Biot factor must be close to 1 for chalk with porosities between c. 40 and 20%. The drop in porosity below that depth could imply the initiation of a new process related to pressure dissolution, but the drop could also be explained by a sharp reduction in the Biot factor for chalk with porosities less than some 20%: equation (1) shows that such a reduction would lead to an increase in effective depth as well as effective stress, and thus to accelerated pressure dissolution. A reduction of the Biot factor below 20% porosity has been observed for chalk based on acoustic (Gommessen et al. *in review*) and geotechnical data (Engstrøm 1992). A similar behavior may be expected for the Biot factor estimated from loading of chalk across a geological basin over million of years.

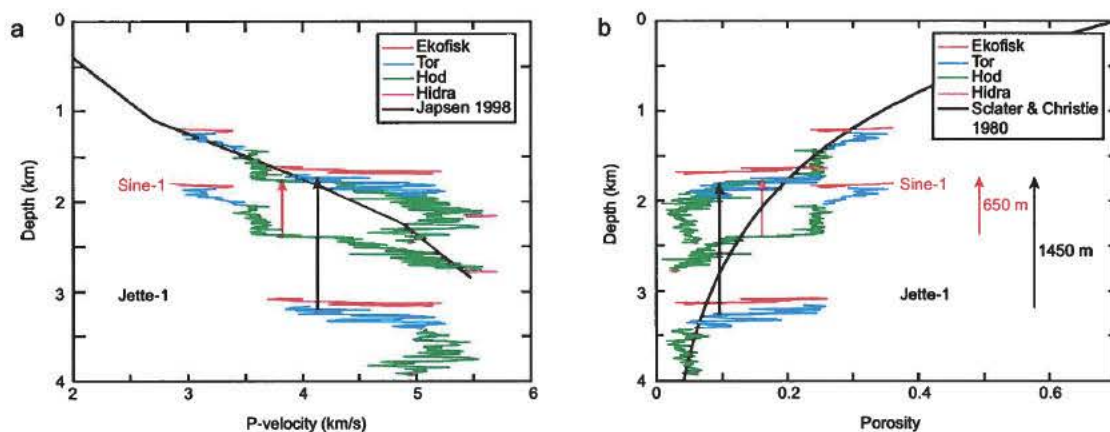


Figure 3. Sonic and porosity log data vs actual depth and effective depth for $\beta=1$ (colorcoded by formation). The data are averaged over 20 m intervals. After correction for the effect of overpressure (arrows; see eq. 1) the log data overlap and reveal a pronounced change for effective depths around c. 1.8 km. These observations indicate that porosity-reduction in chalk is controlled by effective stress.

Contact cementation

We can compare the $V\text{-}\phi$ data with models that represent the pore space as a collection of ellipsoidal inclusions, ranging from flat penny-shaped cracks to spherical pores (Figs 1, 2; Berryman 1995). The comparison suggests that the Jette-1 chalk has rounder, stiffer pores whereas the Sine-1 chalk has more compliant pores. The fact that the Sine-1 data are consistent with a penny-shaped crack model does not mean that there must be cracks in the rock; poorly cemented, compliant grain contacts will yield the same elastic behavior.

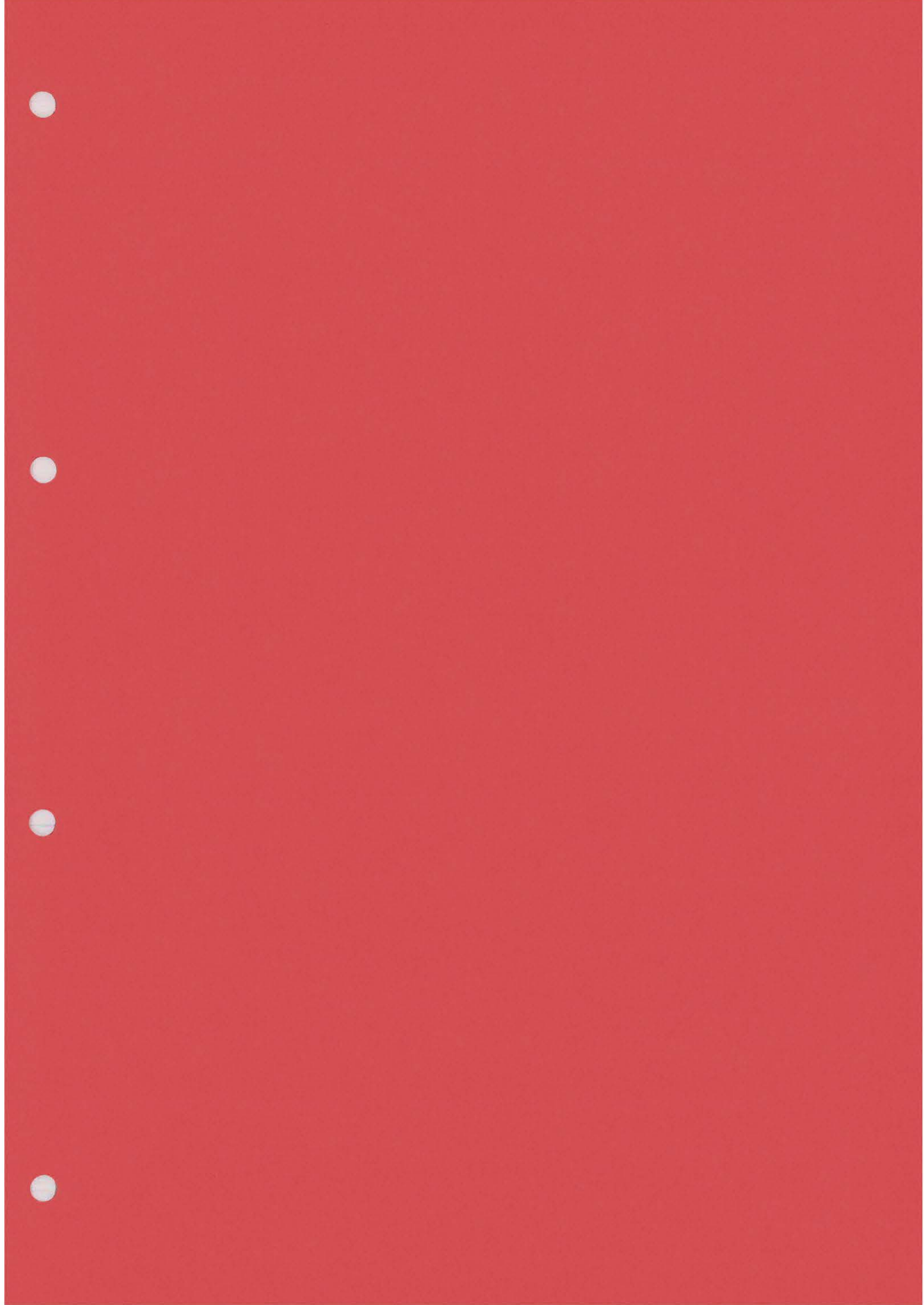
The causes behind these differences in pore stiffness are neither related to effective stress nor temperature. The chalk in the Sine-1 and Jette-1 wells are subjected to effective stress in the same range (Fig. 3) and the Jette-1 chalk differs from chalk in wells in the same temperature interval as it does relative to the more shallow and hence cooler Sine-1 chalk.

One hypothesis for explaining the differences is that earlier in their burial history, chalk from both wells had similar microstructures with compliant grain-to-grain contacts, but that the Jette-1 chalk later gained more cement preferentially deposited at grain contacts. An alternative hypothesis is that the greater stiffness of the chalk in the Jette-1 well is due to quartz-coating of the calcite grains and consequently that the observed low $V_P\text{-}V_S$ ratio reflects the mineral properties of quartz. Both hypotheses thus suggest that the post-depositional development of the chalk in the Jette-1 well differs from that in the Sine-1 well.

Acknowledgement

This study was funded by the South Arne Group (Amerada Hess Aps, Dong E&P, Denerco Oil). Data from the Jette-1 well are courtesy of Amerada Hess.

- Berryman, J.G. 1995. Mixture theories for rock properties. In: Ahrens, T. J. (ed.) *A Handbook of Physical Constants*. American Geophysical Union, Washington. 236 pp.
- Engström, F. 1992. Rock mechanical properties of Danish North Sea chalk. In: *Fourth North Sea Chalk symposium*. Joint Chalk Research, Deauville. 23 pp.
- Fabricius, I. L. 2003. How burial diagenesis of chalk sediments controls sonic velocity and porosity. *AAPG Bulletin*, 87, 1755–1778.
- Gommesen, L., Fabricius, I. L., Mukerji, T., Mavko, G., and Pedersen, J. M. in review Elastic behaviour of North Sea chalk: A well log study. *Geophysical Prospecting*.
- Japsen, P. 1998. Regional velocity-depth anomalies, North Sea Chalk: a record of overpressure and Neogene uplift and erosion. *AAPG Bulletin*, 82, 2031–2074.
- Slater, J. G. & Christie, P. A. F. 1980. Continental stretching; an explanation of the post-Mid-Cretaceous subsidence of the central North Sea basin. *Journal of Geophysical Research*, 85, 3711–3739.
- Walls, J. D., Dvorkin, J. & Smith, B. A. 1998. Modeling seismic velocity in Ekofisk Chalk. *Society of Exploration Geophysicists 68th annual conference*. 1016–1019.



Inversion for acoustic impedance with
low-frequency information based on
the CBV model

Blind test of Jette-1 and Modi-1

Ødegaard A/S





Ødegaard A/S

A Company in the Ødegaard & Danneskiold-Samsøe Group

Report 03.24033.02

**Inversion for acoustic impedance with low-frequency information based on the CBV model.
Blind test of Jette-1 and Modi-1.**

GEUS
Denmark

April 2005

Prepared by

Anders Bruun, Ødegaard A/S; Rasmus Rasmusen, GEUS and Ole V. Vejbæk, GEUS.



This document is confidential.

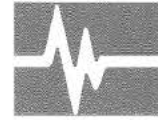
This document has been published by Ødegaard A/S.

Inversion for acoustic impedance with low-frequency information based on the CBV model. Blind test of Jette-1 and Modi-1.

**Report No: 03.24033.02
2005**

Copyright © 2005 Ødegaard A/S.

This document includes some words, which are or are not asserted to be proprietary names. The presence or absence of such assertions should not be regarded as affecting the legal status of any proprietary name or trademark.



Summary

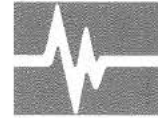
This report describes seismic inversion of a 2-D random line extracted from a 3-D data set covering the South Arne Field. The selected line connects the Jette-1, Rigs-2 and Modi-1 wells.

A low frequency model is important input for seismic inversion. The aim of this work was to investigate if different ways of constructing the low frequency model needed for the inversion and test them by comparison to existing wells that are not used or only indirectly used as input to the inversion.

The low frequency model is constructed either via standard model based extrapolation from existing wells or via insertion of supplementary calculated pseudo wells in combination with the standard extrapolation method. The novelty compared to a standard method is thus the construction and use of pseudo-wells.

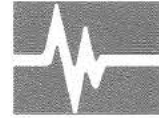
The results of the work show that:

- Low frequency models for the South Arne field may be improved by incorporating pseudo wells constructed on the basis of rock physics knowledge of North Sea chalk.
- Simple depth trends supplemented with existing wells may be dangerous, if effects such as for instance the postulated “cementation front” causes non-linear effects on acoustic property – depth trends.



Contents

Inversion for acoustic impedance with low-frequency information based on the CBV model. Blind test of Jette-1 and Modi-1.....	ii
Chapter 1	3
Introduction	3
1.1 Seismic data.....	4
1.2 Well data.....	5
1.3 Horizon data	5
Chapter 2	6
Seismic inversion	6
2.1 Log Alignment.....	6
2.2 Least squares constant phase wavelet estimation	8
2.3 Seismic inversion.....	8
2.4 Determination of inversion parameters	10
2.5 Inversion results.....	10
2.6 Conclusion.....	12
2.7 References	13



List of Figures

Figure 1. Location of the 2-D test line shown in red. Contours are Top Chalk depths in metres. Blue polygons are approximate field outlines	3
Figure 2. Seismic random line used in the inversion. Vertical lines represent the location of Jette-1, Rigs-2 and Modi-1 wells. The extra pseudo well is located at about x-line 11900 and in-line 23160.	4
Figure 3. Least squares wavelet estimation at the I-1x well. Bottom: Wavelet suite. The lengths of the depicted wavelets range from 20 to 44 samples (80 ms to 176 ms, horizontal axis. Left: Synthetic seismic trace obtained by convolution of the selected wavelet with the reflectivity log from the well inserted into the seismic data. Top right: Amplitude spectra in the wavelet estimation window of the seismic trace at the well position and the synthetic seismic trace. Middle right: Phase and amplitude spectra of the selected wavelet. Bottom right Akaike's misfit criterion.	7
Figure 4. Filter used to low pass filter the extrapolated well log data.	8
Figure 5. Low frequency model used in the first inversion model. Shown are the wells - Jette-1, Pseudo well, Rigs-2 and a Pseudo Modi-1 - which have been extrapolated along the seismic horizons. The pseudo well and Modi-1 logs are calculated on basis of the Jette-1 well (see introduction).	9
Figure 6 Low frequency information when using the Pseudo, Rigs-2 and Pseudo Modi-1 well log data.	9
Figure 7. Acoustic impedance log from the wells Rigs-2 (left) and Modi-1 (right) inserted into the acoustic impedance inversion result with low-frequency information. The inversion result shown is extracted in the in-line direction through the well. The log is repeated five times. To the right of the acoustic impedance section, curves of the following are plotted: the calibrated acoustic impedance log, the low-frequency model extracted along the well trajectory and the acoustic impedance inversion result extracted along the well trajectory.	11
Figure 8. The left panel is an inversion using a low frequency model with information from the Jette-1 well and the right panel is without. The well is shown inserted into the acoustic impedance inversion result with low-frequency information. The inversion result shown is extracted in the in-line direction through the well. The log is repeated five times. To the right of the acoustic impedance section, curves of the following are plotted: the calibrated acoustic impedance log, the low-frequency model extracted along the well trajectory and the acoustic impedance inversion result extracted along the well trajectory.	11
Figure 9. Acoustic impedances inversion results along the random line where the low frequency model includes the Jette-1 well information.	12



List of Tables

Table 1. <i>Surface locations of wells in terms of UTM co-ordinates and in-line and cross-line numbers.</i> ..5
Table 2. <i>Seismic inversion parameter values for the ISIS global seismic inversions.</i>10



Chapter 1

Introduction

This report describes seismic inversion of a 2-D random line extracted from a 3-D data set covering the South Arne Field.

The purpose of the inversion exercise is to investigate different ways of constructing the low frequency model needed for the inversion and test them by comparison to existing wells that are not used or only indirectly used as input to the inversion. The low frequency model is constructed either via standard model based extrapolation from existing wells or via insertion of supplementary calculated pseudo wells in combination with the standard extrapolation method. The novelty compared to a standard method is thus the construction and use of pseudo-wells.

The selected line connects the Jette-1, Rigs-2 and Modi-1 wells (Figure 1).

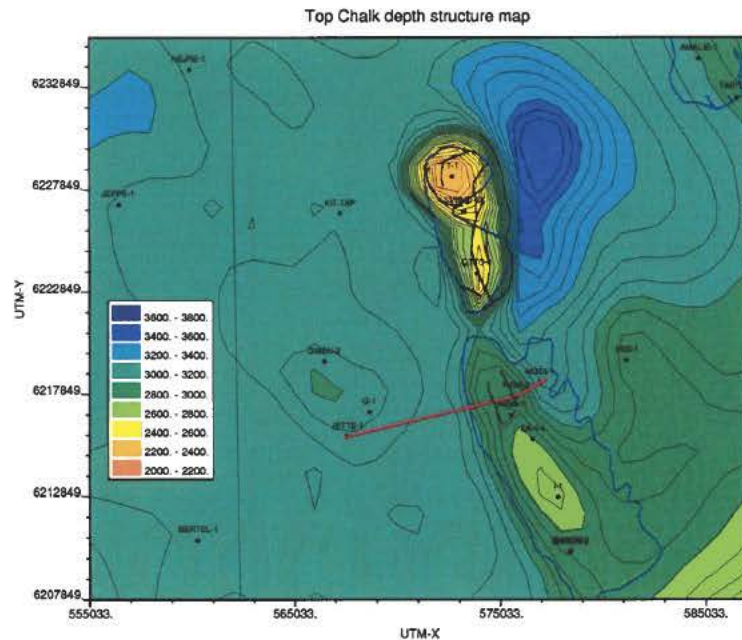


Figure 1. Location of the 2-D test line shown in red. Contours are Top Chalk depths in metres. Blue polygons are approximate field outlines



CHAPTER 1

The pseudo well construction method uses an existing well that is modified in terms of degree of compaction and fluid content is altered to match expected conditions outside well control. The difference in depth between the original well site and a new site is used to calculate differences in the general porosity level as well as log sampling scale porosity variation. Subsequently changes in acoustic properties resulting from these porosity changes and possible differences in fluid content are calculated. Further detail in the modelling approach may be obtained from Vejrbæk et al (2005). In this study we use the Jette-1 well to construct two pseudo well locations along the seismic profile. These locations are on the profile:

1. The immediate down-flank position west of the South Arne structure.
2. The Modi-1 well position on the east flank of the South Arne structure; hereafter referred to as Pseudo Modi-1.

1.1 Seismic data

The 2-D random line was cut out from the near stack 3-D data of the FEDA_PAM99 survey. Amerada Hess Denmark (see Figure 1 for location) supplied the seismic data.

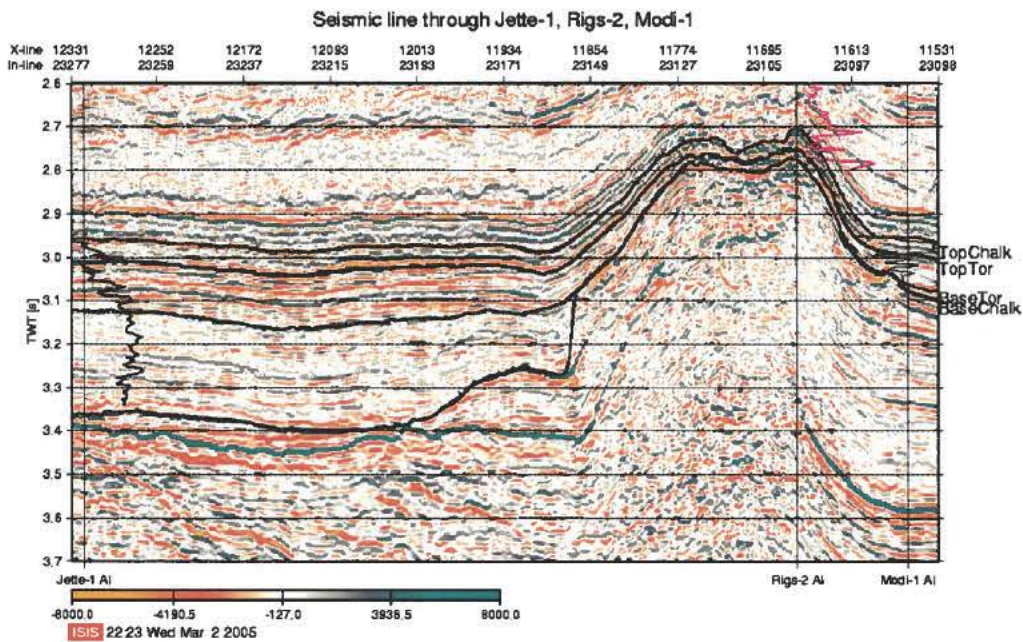


Figure 2. Seismic random line used in the inversion. Vertical lines represent the location of Jette-1, Rigs-2 and Modi-1 wells. The extra pseudo well is located at about x-line 11900 and in-line 23160.



CHAPTER 1

1.2 Well data

Sonic logs, density logs, check shot data and deviation surveys were available for the wells Jette-1, Rigs-2 and Modi-1. The Modi-1 well is only supplied with synthetic sonic log constructed on the basis of the porosity log (and density log) via a porosity - acoustic impedance relationship. In the inversion procedure the Pseudo Modi well constructed on the basis of Jette-1 was used. The Modi-1 well may thus be used as a test on the procedure for constructing pseudo wells.

The I-1x well is not located on the 2-D random line but only nearby within the 3-D cube. This well was used for wavelet extraction.

Well	UTM-X	UTM-Y	In-Line	X-Line
I-1X	577802	6212763	2671	1721
Jette-1	567598	6215798	3277	2319
Modi-1	576989	6218405	3098	1560
Rigs-2	575835	6217754	3097	1666

Table 1. *Surface locations of wells in terms of UTM co-ordinates and in-line and cross-line numbers.*

1.3 Horizon data

Amerada Hess supplied four horizons for guiding low frequency model building. These were Top Chalk, Top Tor, Base Tor and Base Chalk.



Chapter 2

Seismic inversion

The seismic inversion included the following steps:

- Logs from the wells were checked, converted from depth to TWT and calibrated against the seismic data.
- Suites of wavelets were estimated from the I-1X well on the basis of a time domain-based least squares constant phase estimation method.
- Two versions of 2D low-frequency acoustic impedance models were constructed on the basis of the acoustic impedance well logs and horizon data.

The optimum inversion parameters were determined and the ISIS seismic inversion results computed.

2.1 Log Alignment

The sonic, density and check shot data were used to derive a calibrated acoustic impedance log and a calibrated reflectivity log for each well. During the calibration, the log data were resampled to the same sample interval of 4 ms as the seismic data. The wells were treated as vertical wells because of no available deviation surveys.

The well logs within the seismic surveys were calibrated to the seismic data by comparing the synthetic seismic trace from each well with the seismic trace at the well location.



CHAPTER 2

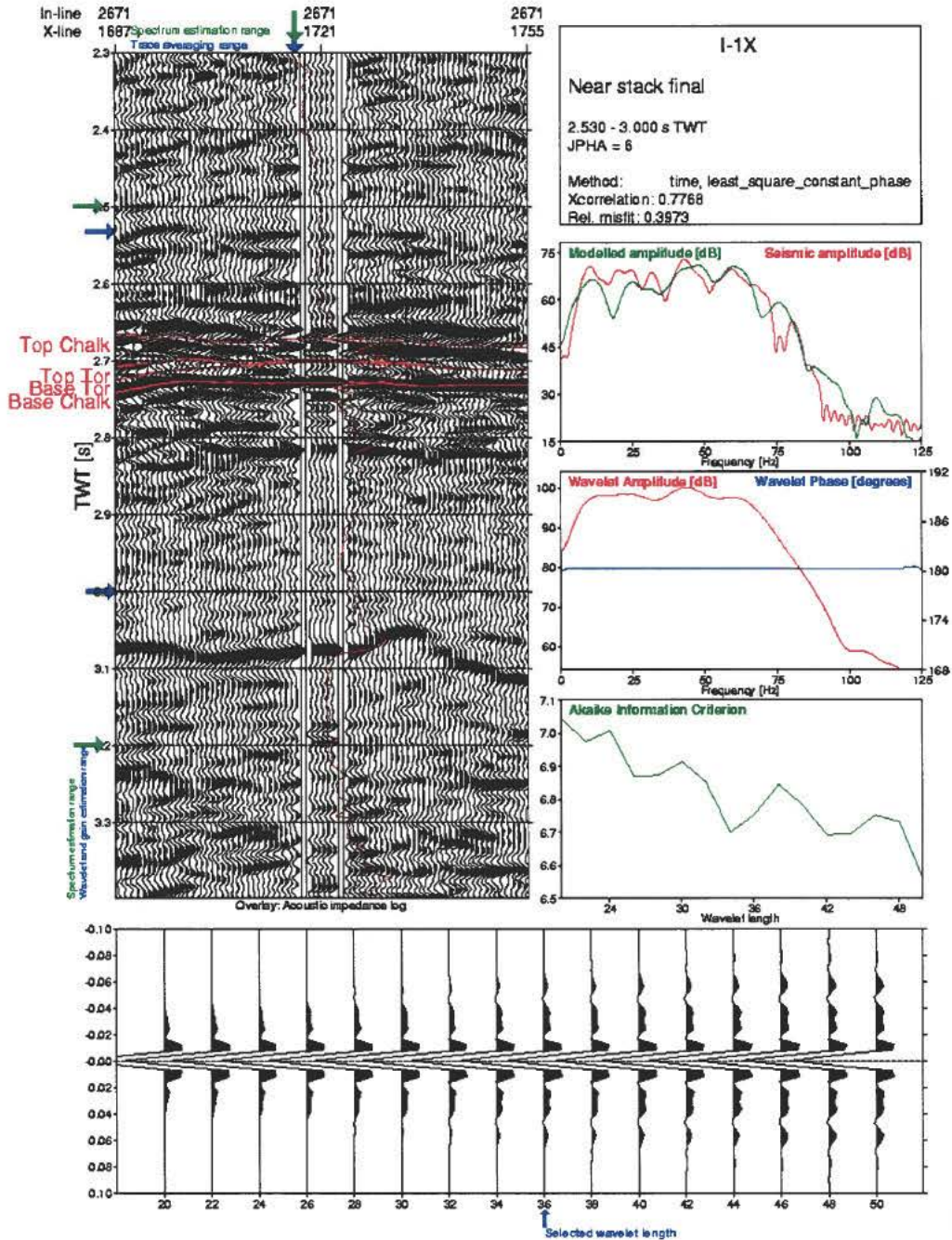


Figure 3. Least squares wavelet estimation at the I-1x well. Bottom: Wavelet suite. The lengths of the depicted wavelets range from 20 to 44 samples (80 ms to 176 ms, horizontal axis). Left: Synthetic seismic trace obtained by convolution of the selected wavelet with the reflectivity log from the well



inserted into the seismic data. Top right: Amplitude spectra in the wavelet estimation window of the seismic trace at the well position and the synthetic seismic trace. Middle right: Phase and amplitude spectra of the selected wavelet. Bottom right Akaike's misfit criterion.

2.2 Least squares constant phase wavelet estimation

Wavelets were estimated for the I-1x well using the least squares estimation method in the time domain with constraints on phase. A number of estimation windows were tested. The wavelet experiments were performed for wavelet lengths from 20 to 200 ms using a step length of 4 ms in both cases. The wavelet suite containing the optimum wavelets estimated for the I-1x well are plotted in *Figure 3*. Also plotted are spectra of the optimum wavelet; the amplitude spectra of the seismic data trace and the synthetic seismic trace in the wavelet estimation window; and the synthetic seismic trace inserted into the seismic data. The cross-correlations and relative misfit values are good.

2.3 Seismic inversion

This section describes the inversion parameters used for the final inversions and the seismic inversion results. The inversion window consists of 824 traces from the random line where inversion is performed in a window between 2.500 and 3.600 s TWT. Prior knowledge is needed for low frequencies not contained in the seismic data in the form of low frequency models (Figure 4). Two versions of a 2D low-frequency model were created.

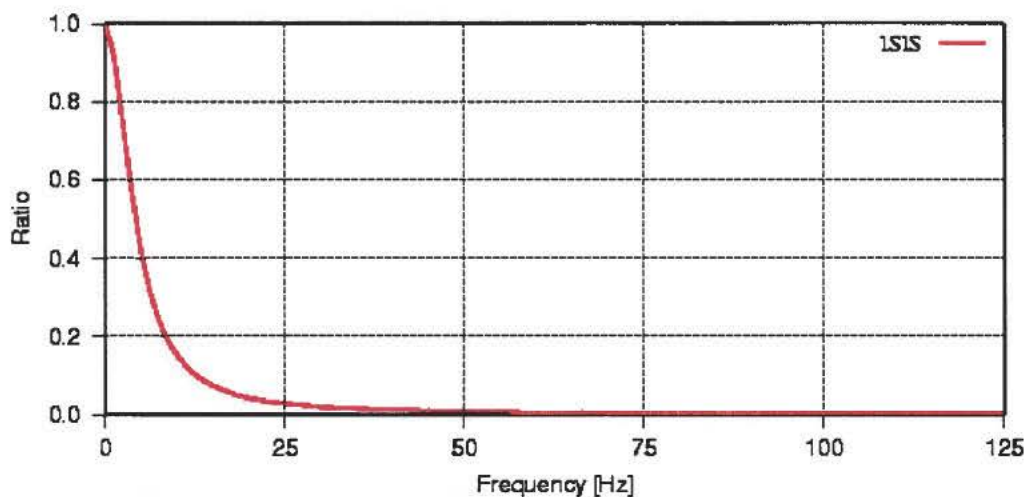


Figure 4. Filer used to low pass filter the extrapolated well log data.

The first model uses input of the well logs from Jette-1 and Rigs-2 together with the pseudo wells described in the introduction (Figure 5). The well log data and pseudo well log acoustic impedances were extrapolated using the Top and Base Chalk horizons. The low frequency model was filtered using the filter showed in Figure 4. This case may serve as reference for model two, but a test in the form of a prediction of Modi-1 via the pseudo-well technique is also provided.



CHAPTER 2

The second model uses the same approach but excluding the Jette-1 well log data (see Figure 6).

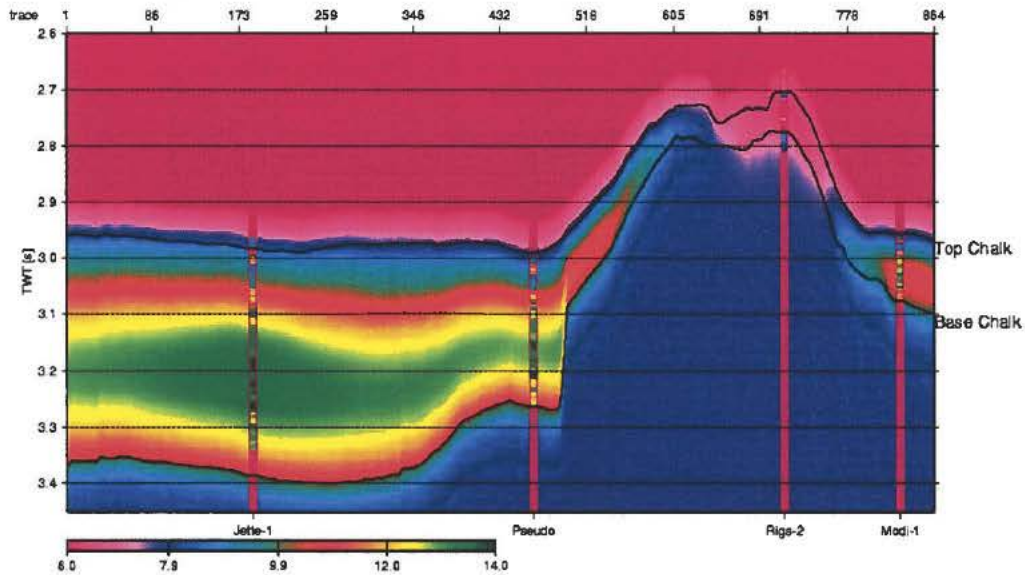


Figure 5. Low frequency model used in the first inversion model. Shown are the wells - Jette-1, Pseudo well, Rigs-2 and a Pseudo Modi-1 - which have been extrapolated along the seismic horizons. The pseudo well and Modi-1 logs are calculated on basis of the Jette-1 well (see introduction).

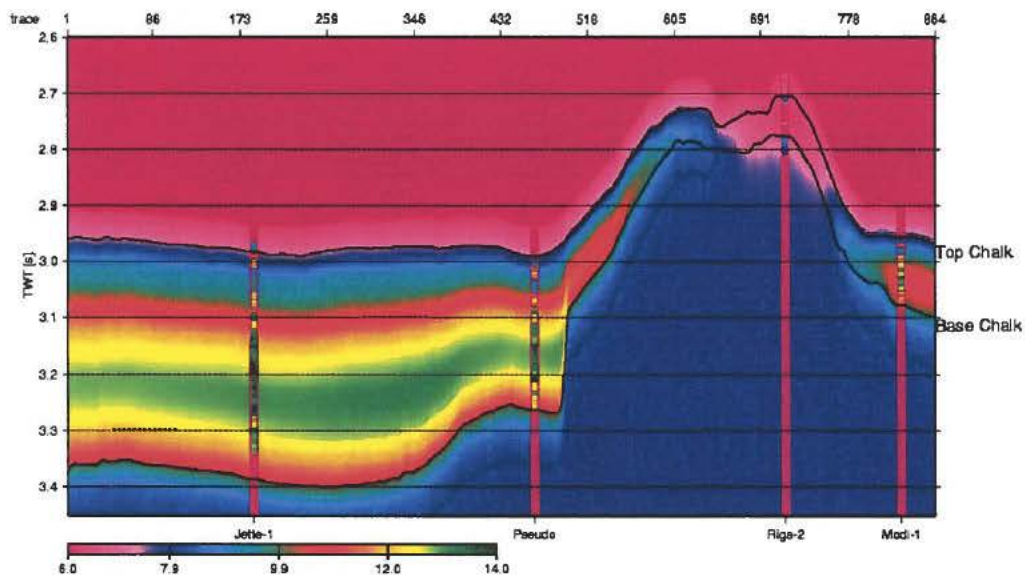
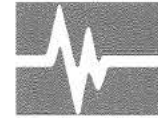


Figure 6 Low frequency information when using the Pseudo, Rigs-2 and Pseudo Modi-1 well log data.



2.4 Determination of inversion parameters

Table 2 shows the values of the seismic inversion parameters, which were determined by a parameter study and used in the final inversions. The inversion results are stable in the neighbourhood of the selected parameter values.

The final seismic inversion modelled 87.5 % of the seismic energy.

The match between the acoustic impedance results with low-frequency information and the acoustic impedance logs is considered to be good.

Inversion parameter	Value
Signal-to-noise Ratio, RSNR	5
Horizontal Continuity, RALPHA	0.06
Deviation of the Prior Model, RSIGMA	0.08
Threshold for Reflection Coefficients, R1	0.015

Table 2. *Seismic inversion parameter values for the ISIS global seismic inversions.*

2.5 Inversion results

The results obtained in the low frequency model tests are given as Figure 7 to Figure 9.

The pseudo well to replace Modi-1 is included in both models. It is seen that the absolute level of the Modi-1 well is the same as seen in the log readings (Fig. 7). The log readings in this well are based on a back transformation of porosity to seismic impedance, whereas the seismic inversion and low frequency model is constrained by a pseudo well log constructed on the basis of Jette-1.

The Rigs-2 well fits the inversion result excellently, but this well was also used as constraints on the low frequency model (Figure 7)

The Jette-1 well was included in one model and left out in the other (Fig. 8). Ideally the pseudo well on the South Arne west flank should help constrain the low frequency model on the western portion as it is only moderately shallower than the Jette-1 well location. Results show that if Jette-1 is taken out of the low frequency model, the absolute level of the acoustic impedances becomes too low equivalent to too high porosities, especially in the deeper portions of the chalk. This is interpreted to be related to rather non-linear (fairly abrupt) increases in velocity (and density) and associated porosity reductions caused by the “cementation front” occurring at effective depths of around 1800 m (Japsen et al. 2005). The lower two thirds of the chalk in this well is estimated to be deeper than the cementation front and thus to have very low porosity and high velocities.



CHAPTER 2

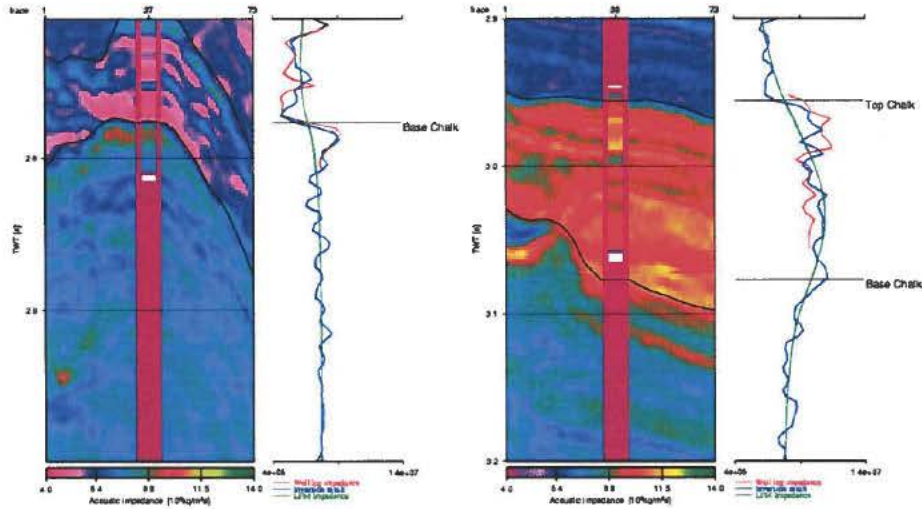


Figure 7. Acoustic impedance log from the wells Rigs-2 (left) and Modi-1 (right) inserted into the acoustic impedance inversion result with low-frequency information. The inversion result shown is extracted in the in-line direction through the well. The log is repeated five times. To the right of the acoustic impedance section, curves of the following are plotted: the calibrated acoustic impedance log, the low-frequency model extracted along the well trajectory and the acoustic impedance inversion result extracted along the well trajectory.

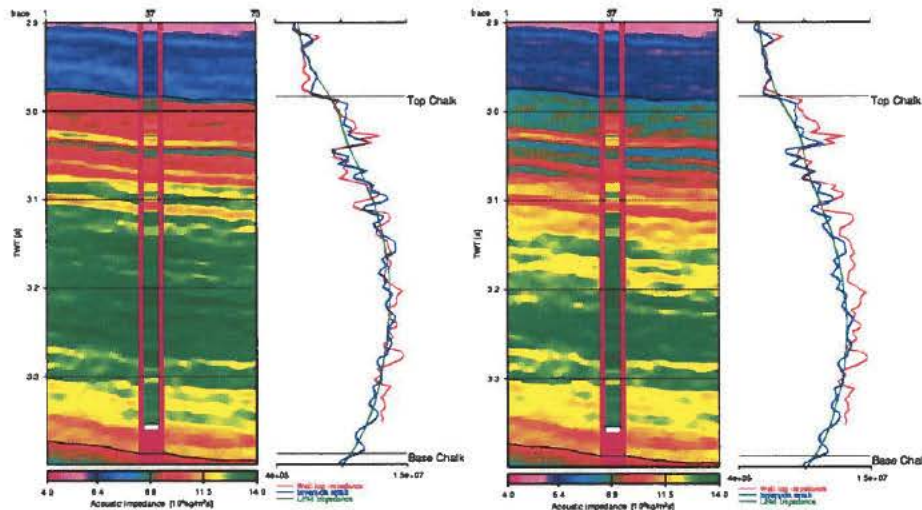


Figure 8. The left panel is an inversion using a low frequency model with information from the Jette-1 well and the right panel is without. The well is shown inserted into the acoustic impedance inversion result with low-frequency information. The inversion result shown is extracted in the in-line direction



CHAPTER 2

through the well. The log is repeated five times. To the right of the acoustic impedance section, curves of the following are plotted: the calibrated acoustic impedance log, the low-frequency model extracted along the well trajectory and the acoustic impedance inversion result extracted along the well trajectory.

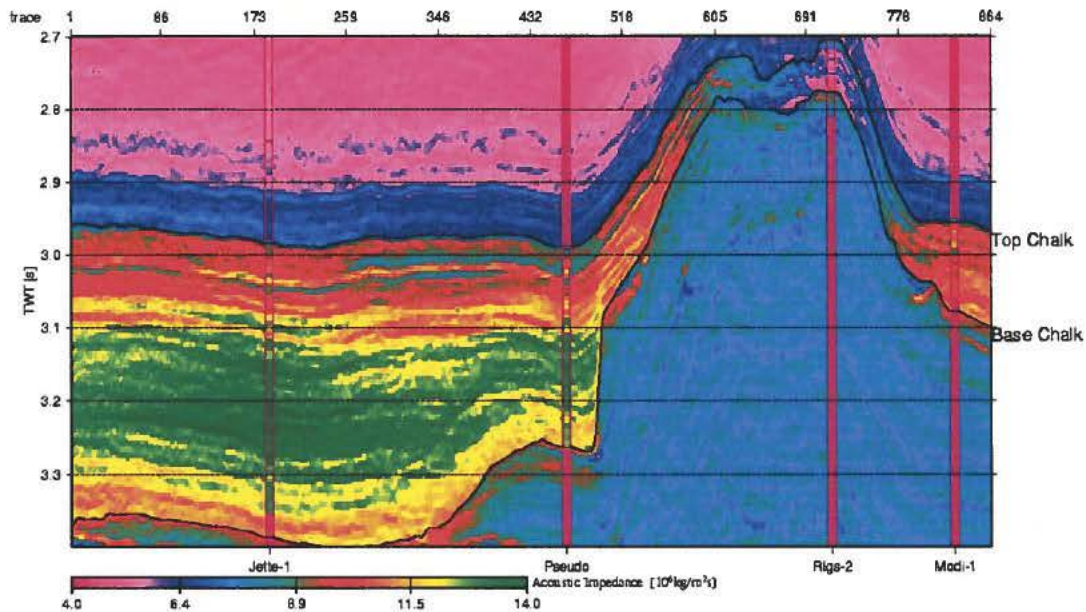


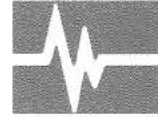
Figure 9. Acoustic impedances inversion results along the random line where the low frequency model includes the Jette-1 well information.

2.6 Conclusion

This report shows test of the Jette-1 and Modi-1 well sites. Although the purpose was to perform blind tests, it is strictly not a blind test for the Jette-1 location since this well is indirectly incorporated via the pseudo well location. The Modi-1 site comes closer to a blind test, since this well was not directly included in the inversion. However, missing velocity logs for this well makes this test more indirect, as the comparison is done via an acoustic impedance – porosity relationship.

Results show that low frequency models may be improved by incorporating pseudo wells constructed on the basis of rock physics. Simple depth trends supplemented with existing wells may be dangerous, if effects such as for instance the postulated “cementation front” causes non-linear effects on acoustic property – depth trends. This is thought to occur at the Jette-1 well site, where the deeper two thirds are likely to be below this “cementation front”. On the conclusive inversion profile, this front is located roughly at 3.1 sec depth.

With respect to the Modi-1 location a good prediction was made owing to the constructed Pseudo Modi well. Without this well, it may be asserted that major prediction problems would have been encountered there, because the low frequency model would have to rely on extrapolation from the Rigs-



CHAPTER 2

2 well, which is an anomaly due to porosity preservation from early hydrocarbon invasion (see Vejbæk & Japsen, this volume). The success for the Modi-1 location presented here relies on the availability of a well for pseudo well construction that also lacks abnormal porosity preservation effects. Alternatively the Rigs-2 well could be corrected for this effect according to the quantification given in Vejbæk & Japsen (this volume) or similar estimates.

2.7 References

Japsen, P., Mavko, G., Gommesen, L., Fabricius, I. L., Jacobsen, F., Vejbæk, O. V., Rasmussen, R., & Schjøtt, C. R. 2005: Chalk background velocity: Influence of effective stress and texture. EAGE 67th Conference & Exhibition, Madrid, Spain 13- 16 June 2005, 4 p.

Vejbæk, O. V., Rasmussen, R., Japsen, P., Bruun, A., Pedersen, J. M., Marsden, G., & Fabricius, I. L. 2005: Modelling seismic response from North Sea chalk reservoirs resulting from changes in burial depth and fluid saturation. 6th Petroleum Geology Conference: North West Europe and Global Perspectives.



Ødegaard A/S

A Company in the Ødegaard & Danneskiold-Samsøe Group

Report 03.24033.02

Appendices for

**Inversion for acoustic impedance with low-frequency information based on the CBV model.
Blind test of Jette-1 and Modi-1.**

GEUS
Denmark

April 2005

Prepared by

Signe Bagger on request of Anders Bruun, Ødegaard A/S.



This document is confidential.

This document has been published by Ødegaard A/S.

Appendices for: Inversion for acoustic impedance with low-frequency information based on the CBV model. Blind test of Jette-1 and Modi-1.

**Report No: 03.24033.02
2005**

Copyright © 2005 Ødegaard A/S.

This document includes some words, which are or are not asserted to be proprietary names. The presence or absence of such assertions should not be regarded as affecting the legal status of any proprietary name or trademark.



Contents

A	AVO inversion theory	1
A.1	AVO attribute data	1
A.2	Calculation of intercept and gradient data	1
A.3	AVO inversion of intercept and gradient data	2
A.4	Calculation of shear reflectivity seismic	2
A.5	AVO inversion of angle stack data	3
A.6	AVO inversion of offset stacks	4
A.7	Logs for angle stacks and offset stacks	4
A.8	Calculation of supplementary physical properties	5
A.9	Simultaneous AVO inversion	6
A.10	Lithological identification by cross-plotting	6
B	Wavelet estimation theory	10
B.1	Log calibration	10
B.2	Deviated wells	11
B.3	Multi versus single well wavelet estimation	11
B.4	Least squares wavelet estimation in the time domain	12
B.5	Least square wavelet estimation in the frequency domain	12
B.6	Least squares constant phase wavelet estimation	13
B.7	Estimated Constant Phase wavelet estimation	13
B.8	Amplitude corrections to wavelets	14
B.9	Vertically-varying wavelet estimation	14
B.10	Zero-phasing	14
B.11	Mean wavelet	15

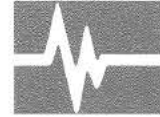


C	Seismic inversion theory	16
C.1	Introduction	16
C.2	ISIS seismic inversion algorithm	16
C.3	ISIS seismic inversion input	17
C.4	Horizon interpolation	18
C.5	Addition of low-frequency information	18
C.6	ISIS seismic inversion results	19
C.7	ISIS seismic inversion for porosity	20
C.8	Alignment	20
C.9	Spectral balancing	21
D	Stratigraphic Correlation Cube theory	22
D.1	Introduction	22
D.2	Dip and Layer Sequence Field calculation	22
D.3	Stratigraphic Correlation Cube calculation	23



List of Figures

A.1	Empirical relations between acoustic velocity and density.	8
A.2	Empirical relations between acoustic impedance and Poisson's ratio.	9



List of Tables

C.1 Permitted ranges of seismic inversion parameter values	18
----------------------------------------------------------------------	----



APPENDIX A

AVO inversion theory

This chapter describes how seismic Amplitude Versus Offset (AVO) attribute data are used in the ISIS seismic inversion. It is also described how Poisson's ratio and other petrophysical and direct hydrocarbon indicators are computed from the AVO inversion results.

A.1 AVO attribute data

The analysis of seismic AVO variation provides the possibility of obtaining both acoustic and shear information from acoustic data and thus obtaining information regarding pore fluid variation for a more detailed reservoir description.

The implementation of inversion methods in the analysis of AVO attribute data provides the ability to derive estimates of the real physical parameters which control the AVO, acoustic impedance and shear impedance which can be compared directly with well log data. Not only do the volumes derived in the inversions have real physical meaning, they also benefit from the removal of the effect of the wavelet and damping of random noise.

The following AVO attribute data can be inverted:

- Intercept and gradient data. (Section A.3).
- Angle stack data. (Section A.5).
- Offset stack data. (Section A.6).

The acoustic, shear and angle impedance inversion results (Z_P , Z_S and Z_θ) can be interpreted directly and direct comparison of the inversion results with well log values is possible.

A.2 Calculation of intercept and gradient data

The AVO attributes, intercept and gradient are commonly used to quantify the variation of amplitude with offset. The attributes are calculated on the basis of the Shuey's approximation (Equation (A.1)) to the full Zoeppritz equations [Shuey, 1985].



$$R_P(\theta) = I + G \sin^2(\theta) \quad (\text{A.1})$$

where R_P is the acoustic reflection coefficient, θ is the angle of incidence, and I and G are the intercept and gradient as defined in Equations (A.2) and (A.3).

The I and G attributes are calculated using the NMO-corrected, true amplitude processed and pre-stack migrated data in conjunction with an interpreted interval velocity model which is used to convert offset to angle.

A.3 AVO inversion of intercept and gradient data

The intercept and gradient data are used to calculate acoustic and shear reflection seismic (R_P and R_S) (see Section A.4). These seismic data are then inverted for acoustic and shear impedance (Z_P and Z_S). For the inversion of the shear reflection seismic the wavelet is derived using a shear reflectivity log rather than the normal acoustic reflectivity log, and the low-frequency model is derived using shear impedance logs rather than acoustic impedance logs. The same depth-to-time relationship is used for the acoustic and shear logs from each well.

The acoustic impedance (Z_P) and shear impedance (Z_S) inversion results can be interpreted directly, or supplementary physical properties such as V_P/V_S , Poisson's ratio and fluid factor can be calculated from them (see Section A.8). In all cases, direct comparison of the inversion results with well log data is possible, and use of cross-plotting techniques enables quantitative lithological and pore fluid determination.

A.4 Calculation of shear reflectivity seismic

When inverting intercept and gradient data using the ISIS global seismic inversion package, a shear reflection volume (R_S) is calculated by implementing a variant of Shuey's approximation [Shuey, 1985; Castagna and Backus, 1993; Smith and Gidlow, 1987], which takes into account a slowly varying V_S/V_P ratio and an estimated exponential constant for Gardner's relationship. The intercept and gradient can be expressed as:

$$I = R_P \quad (\text{A.2})$$

$$G = \frac{R_P}{1+a} - 2 \left(\frac{2V_S}{V_P} \right)^2 \left(R_S - \frac{a}{2} \frac{R_P}{1+a} \right) \quad (\text{A.3})$$



where a is Gardner's exponential constant. It should be noted that V_S/V_P in Equation (A.3) refers to the low-frequency content only of the V_S/V_P variation.

From Equations (A.2) and (A.3) the following equations for acoustic reflection seismic (R_P) and shear reflectivity seismic (R_S) in the acoustic time domain can be derived.

$$R_P = I \quad (\text{A.4})$$

$$R_S = \frac{\frac{I}{1+a} - G}{2 \left(\frac{2V_S}{V_P} \right)^2} + \frac{a}{2} \frac{I}{1+a} \quad (\text{A.5})$$

A.5 AVO inversion of angle stack data

A frequently used method for examining AVO effects is to compute angle stacks and analyze them qualitatively. In order to perform a quantitative analysis, the angle stacks can be inverted using the concept of the effective impedance at a constant angle of incidence. This impedance we have called angle impedance (see Section A.7).

The implementation of angle impedance in ISIS, makes it possible to invert angle stacks as if the data were ordinarily stacked seismic data. Using angle reflectivity and angle impedance logs computed for the effective angle of the angle stack makes the application of the convolution model valid for inversion of the angle stacks. The angle reflectivity logs are used for the wavelet estimation (see Appendix B). The angle impedance logs are used in the prior model generation (see Section C.5) and for quality-control of the inversion result. The same depth-to-time relationship is used for all logs from each well.

The effective angle of the angle stack is the single angle corresponding to the arithmetic mean of the reflection coefficient over the traces in the angle stack. Using an unweighted mean, of course, assumes that the traces in the angle stack have been equally weighted. As the reflection coefficient according to Shuey's approximation (Equation (A.1)) is approximately linear related to $\sin^2(\theta)$, the effective angle, θ_{eff} , is given by

$$\sin^2(\theta_{\text{eff}}) = \frac{\sin^2(\theta_{\text{min}}) + \sin^2(\theta_{\text{max}}) + \sin(\theta_{\text{min}}) \sin(\theta_{\text{max}})}{3} \quad (\text{A.6})$$

where θ_{min} and θ_{max} denote the minimum and maximum angle of the angle stack, respectively. The effective angle can be up to 16% larger than the arithmetic mean of the minimum and maximum angle of the angle stack.

Estimating a separate wavelet for each angle stack decreases the influence of many kinds of errors. Effects of NMO stretch, frequency variation with offset and energy variation with offset can be compensated for by using separate wavelets in the inversions.

The angle impedance inversion results can either be interpreted directly, for example for differentiation of sands and shales, or can be combined to derive more classical AVO indicators, for instance V_P/V_S and Poisson's ratio (see Section A.8).



A.6 AVO inversion of offset stacks

A variation of angle stacks is offset stacks. Offset stacks are generated by stacking receivers according to offset rather than angle of incidence. For offset stacks the angle of incidence is a function of depth and horizontal position. Angle stacks are therefore preferred to offset stacks. However, it is possible to invert offset stacks using the ISIS global seismic inversion package. Inversion of offset stacks is done by computing the variation of the angle with depth and using it instead of a constant angle in all the equations originally developed for angle stacks.

The effective offset, x_{eff} , of an offset stack is computed in a similar way as the effective angle of an angle stack:

$$x_{\text{eff}}^2 = \frac{x_{\text{min}}^2 + x_{\text{max}}^2 + x_{\text{min}}x_{\text{max}}}{3} \quad (\text{A.7})$$

where x_{min} and x_{max} denote the minimum and maximum offset of the offset stack, respectively. The effective offset can be up to 16% larger than the arithmetic mean of the minimum and maximum offset of the offset stack.

Neglecting formation dip, the angle of incidence, θ can be computed by

$$\sin(\theta) = \frac{v_{\text{int}}x}{v_{\text{rms}}\sqrt{(v_{\text{rms}}t)^2 + x^2}} \quad (\text{A.8})$$

where v_{int} is the interval velocity, v_{rms} is the root-mean-square velocity, x is the source-receiver offset, and t is the zero-offset two-way travel-time [Castagna and Backus, 1993].

A.7 Logs for angle stacks and offset stacks

Angle impedance (Z_θ) is a function of the acoustic impedance (Z_P), the shear impedance (Z_S) and the angle of incidence (θ).

The angle impedance is based on the Shuey's approximation and is defined as

$$Z_\theta = Z_P \exp\left([\log(Z_P) - 2\log(Z_S) + \log(5.0 \cdot 10^6)] \sin^2(\theta)\right) \quad (\text{A.9})$$

The constant $5.0 \cdot 10^6$ in Equation A.9 above could be replaced by any other arbitrary constant and the equation would still possess the following properties:

- The angle impedance is identical to the acoustic impedance for normal incidence.
- The reflection coefficient, derived in the same way as for normal incidence but using angle impedance instead of acoustic impedance, is identical to the reflection coefficient for a P-P reflection at the given angle.

In the derivation of Equation A.9, it has been assumed that:



- The low-frequency V_S/V_P ratio is approximately 0.5, and that density variations are small.
- The angle of incidence is reasonably low (less than about 33°).

A.8 Calculation of supplementary physical properties

Acoustic impedance (Z_P) and shear impedance (Z_S) inversion results can be converted to Poisson's ratio, V_P/V_S and fluid factor:

$$\text{Poisson's ratio} = \frac{\frac{(Z_P)^2}{2} - (Z_S)^2}{(Z_P)^2 - (Z_S)^2} \quad (\text{A.10})$$

where Z_P and Z_S are the acoustic impedance and shear impedance inversion results with low-frequency information.

$$V_P/V_S = \frac{Z_P}{Z_S} \quad (\text{A.11})$$

where Z_P and Z_S are the acoustic impedance and shear impedance inversion results with low-frequency information.

$$\text{Fluid factor} = Z_S - Z_P \quad (\text{A.12})$$

where Z_P and Z_S are the acoustic impedance and shear impedance inversion results with the same constant low-frequency value (see Appendix C). Fluid factor as defined here highlights changes in fluid properties, without adding any empirical relations between shear and acoustic velocities as in the conventional fluid factor calculation.

From angle stack and offset stack inversion results, acoustic impedance, shear impedance, V_P/V_S and Poisson's ratio can be derived by estimating the optimum linear relation in the $(\log(Z_\theta), \sin^2(\theta))$ -domain using all angle impedance inversion results. The V_P/V_S and Poisson's ratio estimates are calculated from the angle impedance at $\theta = 90^\circ$ computed using the estimated optimum linear relation. In order to obtain reliable V_P/V_S and Poisson's ratio volumes it is therefore essential to use angle stacks with large differences between the effective angles. The estimation of V_P/V_S , Poisson's ratio and shear impedance can be additionally constrained by low-frequency angle impedance models calculated for $\sin^2(\theta) = 1$ and $\sin^2(\theta) = -1$. The constraints are introduced to avoid unphysical fluctuations appearing in the estimated V_P/V_S values, Poisson's ratio and shear impedance values.



A.9 Simultaneous AVO inversion

Separate AVO inversion which is the approach described above in Section A.7 and Section A.8 is characterized by independent inversion of the various partial stacks with respect to angle impedance and subsequent post-processing to true layer quantities like acoustic impedance, shear impedance, Poisson's ratio, and/or density. In this section an alternative approach named simultaneous AVO inversion will be described. It is characterized by that all partial stacks are inverted simultaneously directly with respect to the desired true layer quantities. Consequently, the need for defining a problematic quantity like angle impedance is eliminated as the reflection coefficient as a function of incidence angle is computed directly from the true layer quantities using for instance the Aki & Richards approximation [Aki and Richards, 1980]. With respect to estimation of true layer quantities, the inherent problems with angle impedance and for the matter any alternative formulation of the same concept like Connolly elastic impedance [Connolly, 1999] for instance are due to that it is in fact not a true layer quantity. Angle impedance is not a true layer quantity as it is assumed that the average Poisson's ratio for the layer interfaces are known in advance.

Simultaneous AVO inversion is implemented by extending the individual terms of the non-linear cost function mentioned in Section C.2. The penalty for differences between the seismic data and the synthetic seismic is to be accumulated over all partial stacks. The penalty for horizontal and vertical changes in the estimated impedance model and for deviations from the prior model are all to be accumulated over all layer quantities. A consequence of this modified cost function is that some of the inversion parameters mentioned in Section C.3 are multiplied. More specific, each partial stack has an associated **RSNR** inversion parameter, and each layer quantity has associated **RALPHA** and **RSIGMA** inversion parameters.

The ISIS simultaneous AVO inversion algorithm has been programmed such that it allows for a selection of more or less advanced seismic forward modeling algorithms. The most simple forward seismic modeling algorithm implemented is a constant coefficients AVO model essentially corresponding to the angle impedance concept. The most advanced forward modeling implemented is a varying coefficients AVO model essentially corresponding to the so called Aki & Richards approximation which is more accurate for high angles of incidence and for V_P/V_S ratios significant different from 2. Optimal inversion results are of course achieved only if the reflection series used in the wavelet estimation for each partial stack has been computed using the same forward seismic modeling algorithm as the one used in the inversion part.

The layer quantity parameterization and consequently what prior models that have to be specified is partly independent of the forward seismic modeling algorithm. Acoustic impedance and either shear impedance or Poisson's ratio are always included. In the case of the Aki & Richards AVO model, density is also included in the parametrization.

A.10 Lithological identification by cross-plotting

Cross-plotting of the well log data can be used to aid interpretation of the inversion results. The well log data can be used to establish relationships between lithology and the physical parameters determined in the seismic inversions, e.g. acoustic impedance and Poisson's ratio.



These relationships can then be used to predict lithology from the inversion results.

Figure A.1 shows a cross-plot of acoustic velocity versus density with general curves for some common lithologies [Castagna, 1993]. Contours of acoustic impedance are drawn on the plot. The plot shows the following:

- Acoustic impedances of sand and shale is similar.
- Limestone and sand-shale lithologies can be separated in acoustic impedance.
- Low porosity lithologies tend to have a large acoustic impedance while high porosity lithologies have low values of acoustic impedance.

Figure A.2 shows a cross-plot of acoustic impedance versus Poisson's ratio. Empirical sand and shale lines are plotted, and general trends of varying pore-fluid and compaction are indicated. Poisson's ratio is, generally, very sensitive to sand-shale and pore-fluid variations, while the acoustic impedance is sensitive to porosity and pore-fluid variations (see Section A.1). The plot also indicates that by using a combination of acoustic impedance and Poisson's ratio gas sands can be separated from water filled sands and sands can be separated from shales.

Identification of lithologies using cross-plots of log data and subsequent correlation to the inversion results makes it possible to make regional lithology interpretations and increase confidence in hydrocarbon detection.

References

- Aki, Keiiti and Richards, Paul G., 1980, Quantitative Seismology - Theory and Methods, Volume 1, *W. H. Freeman and Company*.
- Castagna, John P. and Backus, Milo M., 1993, Offset-dependent reflectivity - Theory and practice of AVO analysis. *Society of Exploration Geophysicists*.
- Connolly, P., 1999, Elastic impedance: The Leading Edge, 18, no. 4, 438-452.
- Shuey, R.T., 1985. A simplification of the Zoeppritz equations. *Geophysics*, **50**, 609-614.
- Smith, G.C. & Gidlow, P.M., 1987. Weighted Stacking for Rock Property Estimation and Detection of Gas. *Geophysical Prospecting*, **35**, 993-1014.

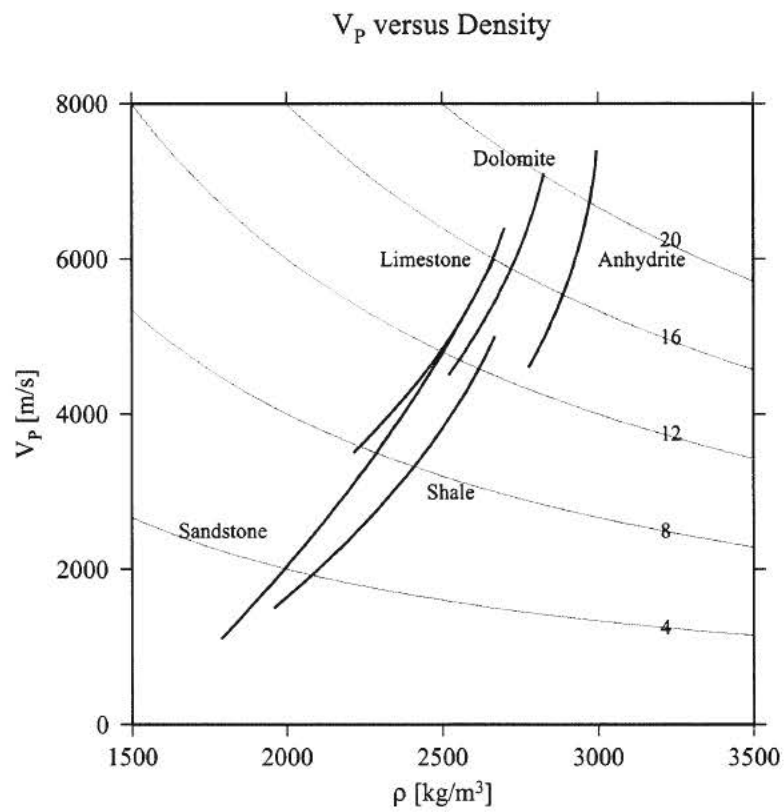


Figure A.1: Empirical relations between acoustic velocity and density for major lithologies [Castagna, 1993]. Contours of acoustic impedance ($\times 10^6$) have been plotted on top.

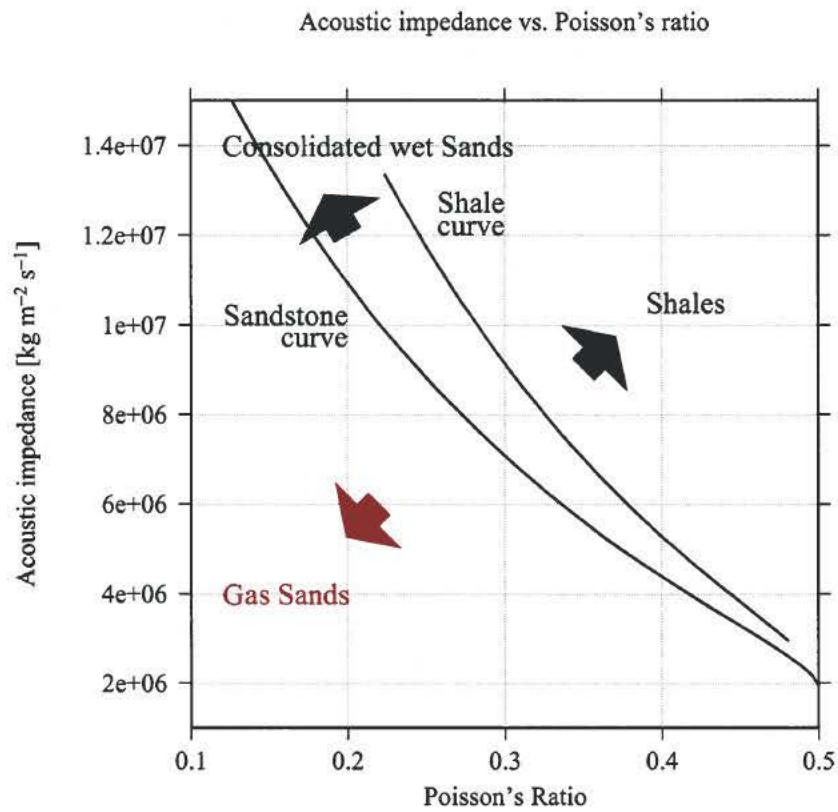


Figure A.2: Empirical relations between acoustic impedance and Poisson's ratio for sand and shale. Poisson's ratio is generally highly sensitive to sand-shale and pore-fluid variations, while the acoustic impedance is sensitive to porosity and pore-fluid variations.



APPENDIX B

Wavelet estimation theory

This chapter outlines the theory behind the log calibration and the wavelet estimation.

B.1 Log calibration

The purpose of the log calibration is usually to create:

1. A reflectivity series with the same sampling rate as the seismic data for use in the wavelet estimation.
2. An acoustic impedance series for use in construction of the low-frequency model.

Using available check-shots, the sonic and density logs are converted from the depth domain to the two-way travel-time domain. The acoustic impedance series is computed by multiplication of the calibrated density log and the velocity log derived from the calibrated sonic log. The reflectivity series is then derived by differentiating the acoustic impedance series. If necessary, visual ties are added to shift, stretch or squeeze the logs. Visual ties are determined by comparing the calibrated logs directly with the seismic data, or by comparing the seismic trace at the well location with the synthetic seismic trace derived by convolving a wavelet with the calibrated reflectivity log. Visual ties may be required for the following reasons:

1. The well logs are measured at much higher frequencies than the seismic data. Consequently, the well log velocities can be up to 10% higher than the reflection seismic velocities. This error is largely compensated for by using check-shots.
2. The filters used in the seismic processing may introduce a static time shift into the seismic data. It is therefore sometimes necessary to apply a compensatory static shift using the visual ties.
3. The seismic migration does not perfectly move the reflectors back to their correct position as the migration velocities and the migration algorithms are imperfect. This will introduce a varying time shift dependent on depth and dip of the reflectors.



4. The normal move-out correction for the check-shots is imperfect, particularly for deep and dipping reflectors.

Once the optimum wavelet for the inversion has been chosen, synthetic seismic traces are calculated by convolving the wavelet with the reflectivity series derived from the well logs. The resulting synthetic traces are compared with the seismic traces at the well locations. The well logs are then finally calibrated (stretched and squeezed) for optimum match.

B.2 Deviated wells

In order to compare logs from a deviated well with the seismic data, the seismic data along the well trajectory are extracted from the seismic cube. The resulting seismic trace is called a super-trace.

In order to evaluate the significance of individual events in a super-trace, a super-section passing through the super-trace is also extracted from the seismic data. For plotting, super-traces and super-sections are projected onto vertical lines or planes.

For a deviated well, whenever the depth-to-time relationship is changed by applying a visual tie, the deviation of the well needs to be adjusted. Hence, after applying a visual tie, a new super-trace must be extracted from the seismic data along the new well trajectory. Hence, the calibration of deviated wells involves considerably more steps than the calibration of vertical wells.

For deviated wells, the super-trace along the well trajectory is used for wavelet estimation, rather than the trace at the well-head location. The deviation of wells is also fully utilized when constructing 3D low-frequency impedance models.

B.3 Multi versus single well wavelet estimation

Wavelet estimation may be performed either (i) at each well location one at a time (single-well wavelet estimation), or (ii) simultaneously using several wells to determine the best overall wavelet for the wells (multi-well wavelet estimation).

For multi-well wavelet estimation, the estimation is performed over an arbitrary number of well log segments. Such an approach can be advantageous, for example, where:

- Although there are several wells, the well log data for each well are reliable only over a restricted interval covering the reservoir zone and are too short for reliable wavelet estimation at each individual well.
- The well log data for a single well contain intervals of poor log data or where the seismic data is contaminated by noise, e.g. multiples.



B.4 Least squares wavelet estimation in the time domain

The time domain based least squares wavelet estimation process is divided into two parts. A least squares method is first used to estimate a suite of wavelets with different lengths. The optimum wavelet length is then determined by using Akaike's Final Prediction Error (FPE) criterion (Ljung, 1987) in combination with visual inspection of the wavelet and synthetic seismic. Vertical variations of the wavelet (see Section B.9) can be specified as part of the least squares estimation.

The least squares method in the time domain minimizes the sum of squared differences (the misfit) between the seismic trace and a synthetic trace obtained by convolution of the well log reflectivity series and a wavelet. Wavelets are estimated using the least squares method for a range of lengths and a range of initial delays. For each wavelet length, the best initial delay is determined by using the misfit criterion.

Akaike's FPE is a function of the misfit, which decreases as a function of wavelet length, and the relative number of parameters, which increases as a function of wavelet length. The relative number of parameters is equal to the length of the wavelet divided by the length of the window within which the misfit between the synthetic trace and the seismic data is calculated. The optimum wavelet length, and thereby the optimum wavelet, is determined by finding the minimum value for the wavelet suite of Akaike's FPE. The wavelet with the minimum value of Akaike's FPE models as much of the coherent signal as is possible without modelling a significant amount of the local noise. Wavelets, which are too long and model large amounts of local noise, are unlikely to be representative of the seismic data away from the well location.

B.5 Least square wavelet estimation in the frequency domain

The frequency domain least square wavelet estimation method is in principle based on the same object function as its time domain counterpart, although computed in the frequency domain instead of in the time domain. Consequently, the wavelet is derived from the correlation between the seismic data and the well log. The main difference between the two methods is that the wavelet is parameterized in its frequency domain response rather than directly in its time domain response.

The advantages of this method compared with the time domain least squares method is:

- The wavelet looks more realistic with more gradually decaying wiggles, and the wavelet is therefore longer without being sensitive to noise.
- The approach is much easier to use as it is much less sensitive to specified wavelet length and because it is not necessary to specify the search interval for the initial delay.

A disadvantage of this method compared with the time domain least squares method is that the fit between the real and synthetic data is slightly worse.



B.6 Least squares constant phase wavelet estimation

The least squares wavelet estimation method is sensitive to additive noise in the seismic data and in the reflectivity log if the length of the reflectivity log is too short compared with the length of the true wavelet even if there are no alignment errors between the reflectivity log and the seismic data. In this case we propose the least squares constant phase wavelet estimation method.

The least squares constant phase wavelet estimation method sets the amplitude spectrum of the wavelet equal to the estimated amplitude spectrum of the seismic data. The phase spectrum of the wavelet is assumed constant. The constant phase, the gain (including the sign), and the delay of the wavelet are estimated by computing the values which minimize the misfit between the synthetic trace and the seismic data in a least squares sense.

The amplitude spectrum of the seismic data is estimated by using Welch's method (Welch, 1970; Oppenheim, 1989). In Welch's method the seismic data are divided into data segments with 50% overlap between each segment and weighted with a Welch window function. The Welch spectral estimate is the mean of the squared Fourier transform amplitude for each segment.

The optimum least squares constant phase wavelet length can be determined using Akaike's Information Theoretic Criterion; a technique similar to Akaike's Final Prediction Error in the least squares wavelet estimation.

B.7 Estimated Constant Phase wavelet estimation

The least squares wavelet estimation method is sensitive to alignment errors between the reflectivity log and the seismic data, especially for the higher frequencies, and the method can not be implemented if a reflectivity log is not available. In these cases other wavelet estimation approaches have to be used. We propose the estimated constant phase wavelet estimation method.

The estimated constant phase wavelet estimation method sets the amplitude spectrum of the wavelet equal to the estimated amplitude spectrum of the seismic data. The phase spectrum of the wavelet is either assumed known, e.g. zero phase or minimum phase, or is estimated from the seismic data. Given the amplitude and the phase spectrum, the wavelet itself can be computed using the inverse Fourier transform. The remaining gain (including the sign) and delay of the wavelet are computed by convolving the wavelet with either the noisy reflectivity log or the guessed reflection coefficient of a significant reflector in the seismic section, and finally comparing this synthetic trace with the seismic data.

The amplitude spectrum of the seismic data is estimated by Welch's method (Welch, 1970; Oppenheim, 1989). In Welch's method the seismic data is divided into data segments with 50 % overlap between each segment and weighted with a Welch window function. The Welch spectral estimate is the mean of the squared Fourier transform amplitude for each segment.

The estimated constant phase wavelet length can be determined using the Akaike's Information Theoretic Criterion, a technique similar to Akaike's Final Prediction Error in the



least squares wavelet estimation.

B.8 Amplitude corrections to wavelets

In some instances it may be desirable to correct the amplitudes of a computed optimum wavelet, e.g. in order to improve the match of the amplitudes of the seismic data in the reservoir zone. When computing the scaling constant it is necessary to disregard possible noise in the seismic data, so that only true amplitudes are considered. This is done by computing the *energy ratio* of the seismic data and the synthetic data modelled by the wavelet. The main assumption is that the pre-processing of the seismic data leaves an energy distribution that is monotonously decreasing or increasing with two-way travel time. Therefore we expect that the energy ratio too will be monotonous. However, the optimum wavelet will (hopefully) not model the noise in the seismic data; therefore the energy ratio will be too large in a time window dominated by noise. So when computing the scaling constant, the energy ratio is found in different sub-windows in time in order to exclude sub-windows of extensive noise.

B.9 Vertically-varying wavelet estimation

To compensate for variations of the wavelet in the vertical direction, it is possible to utilize a vertically-varying wavelet in the inversion. The computation of the vertically-varying wavelet requires as input the optimum constant wavelet at a given depth (see Section B.4).

The model used for the frequency dependent part of the vertical variation of the wavelet is the well-known Q model. It says that the attenuation of the wavelet in dB is proportional to the product of the frequency and the depth measured in two-way travel-time. The proportional factor, in this report named RATTF, is determined by examining the change in the mean frequency of the seismic data with depth. A single value for RATTF is usually sufficient to characterize the whole seismic survey. The phase spectrum of the wavelet is in most cases not changed although it is indeed possible to do so.

The model used for the frequency independent part of the vertical variation of the wavelet is an exponential amplitude gain. The exponential gain factor, in this report named RATT, is determined by comparing the power of the reflectivity well logs with the power of the seismic traces at the well locations, both as a function of depth. As with RATTF, a single value for RATT is usually sufficient to characterize the whole seismic survey.

B.10 Zero-phasing

Zero-phasing seismic data can be implemented by first estimating a wavelet using one of the methods described elsewhere in this report. The phase spectrum of the wavelet is then subtracted from the phase spectrum of the seismic data. The amplitude spectrum of the seismic data is left untouched. The main advantage of zero-phased seismic data is that the events are compressed as much as possible without modifying the amplitude spectrum and thereby potentially, but not necessarily, decreasing the signal to noise ratio.



B.11 Mean wavelet

If a number of almost equally trustworthy wavelets have been estimated and it is decided not to vary the wavelet horizontally between the wells a good alternative is to use a mean wavelet for the whole area. The mean wavelet is computed as a linear interpolation independently for the amplitude spectrum and for the phase spectrum, rather than using a simple linear interpolation in the time domain. An advanced phase unwrapping algorithm is applied to ensure comparable phases of the original wavelets in the mean wavelet calculation.

References

- Ljung, L., 1987. *System Identification: Theory for the User*. Prentice-Hall.
- Oppenheim, A. V. and Schafar, R. W., 1989. *Discrete-Time Signal Processing*. Prentice-Hall.
- Welch, P. D., 1970. *The Use of the Fast Fourier Transform for Estimation of Power Spectra*. IEEE Trans. Audio Electroacoustics, Vol. AU-15.



APPENDIX C

Seismic inversion theory

C.1 Introduction

The ISIS seismic inversion algorithm is based on a unique combination of an advanced global search algorithm and a non-linear cost function. A global search algorithm is employed in order not to get trapped in sub-optimum models close to the starting model which local methods frequently are. ISIS inversion uses the convolutional model for generating the synthetic seismic data that are compared with the original seismic data. ISIS inversion can consequently be implemented on migrated full-stack, offset-stack, or angle-stack reflection seismic data. The wavelet in the convolutional forward model can be varied both horizontally and vertically.

ISIS seismic inversion improves the resolution as the wavelet includes both amplitude and phase spectrum information. Further improvement in the resolution is due to the spectral expansion caused by the non-linear inversion (Cooke & Schneider, 1983).

The inversion can be constrained by a so-called prior model. In the simplest case, the prior model consists of one constant background impedance value. For such a prior model, the inversion gives an unbiased result called the plain ISIS result. The prior model may also consist of the low-frequency components of the impedance variations, which cannot be resolved from the seismic data. These low-frequency components can be determined by extrapolating the impedance logs using horizons and faults as a guide followed by low-pass filtering. Seismic velocities, e.g. stacking velocities, and dip information from the seismic data can also be used to constrain the prior model.

C.2 ISIS seismic inversion algorithm

The ISIS seismic inversion algorithm uses an advanced global search algorithm to estimate the impedance subsurface model that minimizes a non-linear cost function containing the following terms:

- Penalty for differences between the seismic data and the synthetic seismic determined



from the estimated impedance model by convolutional forward modelling.

- Penalty for horizontal variations in the estimated impedance model.
- Penalty for deviation of the estimated impedance model from the prior model.
- Penalty for the presence of significant reflectors. Significant reflectors are places in the estimated impedance model where the reflection coefficient exceeds a predefined threshold.
- Penalty for vertical changes in impedance between the significant reflectors.

The inversion algorithm therefore finds a subsurface impedance model which gives synthetic seismic that approximates the seismic data while also satisfying the other constraints in the cost function which provide damping of random noise, incorporation of the prior model and correct location of significant reflectors.

C.3 ISIS seismic inversion input

The inversion algorithm requires as input: the migrated seismic data, a wavelet, a prior model and values for four inversion parameters that appear in the cost function. These four inversion parameters are:

- **Signal-to-noise ratio (RSNR)**: controls to what degree differences between the synthetic seismic and the seismic data are penalized. The greater RSNR, the greater the penalty, so the inversion algorithm models more of the seismic energy.
- **Horizontal continuity (RALPHA)**: controls to what degree horizontal variations in the impedance model are penalized. RALPHA is the standard deviation of neighbouring impedance traces. The greater the value given to RALPHA, the lesser the penalty, so the inversion algorithm imposes less horizontal continuity.
- **Relative standard deviation of the prior model (RSIGMA)**: controls to what degree deviation of the estimated impedance model from the prior model is penalized. The greater RSIGMA, the lesser the penalty, so the further the estimated acoustic impedance model is allowed to deviate from the prior model.
- **Threshold for reflection coefficient (R1)**: all points in the estimated impedance model with a reflection coefficient greater than R1 are interpreted as significant reflectors. The penalty for the presence of significant reflectors is strongly influenced by the value of R1. The greater R1, the greater the penalty for each significant reflector present in the model, but the lesser the probable total number of significant reflectors.

Values for the above inversion parameters are estimated initially using available information. To find the best set of values, a parameter study is conducted. The value of each parameter is varied and each result evaluated by inspection of the inversion result and by statistical analysis.

The allowed ranges of the four inversion parameters are given in Table C.1.



Parameter	Lower limit	Upper limit
Signal-to-noise ratio, RSNR	>0	∞
Horizontal continuity, RALPHA	>0	1
Deviation of prior model, RSIGMA	>0	1
Threshold for reflection coeff., R1	>0	1

Table C.1: *Permitted ranges of the seismic inversion parameter values.*

C.4 Horizon interpolation

In order to generate the prior model it is necessary that the original horizons are interpolated and extrapolated such that the whole section, which is to be inverted, is covered.

The horizons are interpolated in succession based on their degree of coverage and starting with the one with the highest degree of coverage. The linear interpolation of each horizon is guided by the nearest horizon above and the nearest horizon below that already have been wholly interpolated if such horizons are available. Pinching-out of horizons is handled by letting them follow the horizons on which they truncated.

C.5 Addition of low-frequency information

For a constant prior model, the ISIS inversion result lacks the very low-frequency components as they also are missing in the seismic data. These components can only be introduced into the inversion result by using a non-constant prior model. Such a prior model can be constructed by extrapolating laterally the calibrated impedance logs using a number of interpreted horizons and faults as a guide and then by low-pass filtering the resulting model. Each well log is weighted by one divided by the distance squared to the well plus a constant. The prior model is also called the low-frequency model due to the low-pass filtering that in most cases is applied.

The extrapolation of the well log values can be modified by a depth trend. It is done by multiplying the well log values before the weighted averaging by $\exp(\mathbf{RDEPTH}\Delta T/t_s)$ where the depth trend constant \mathbf{RDEPTH} denotes the relative increase per sample, ΔT denotes the increase in two-way travel time when going away from the well along horizon slices, and t_s denotes the sample period. The depth trend is applied only in between the two horizon slices that intersect the top and bottom of the well log.

In the present implementation, the depth trend constant is allowed to change when crossing a horizon as long as it is constant in between the horizons. Proper depth trend constants can be estimated by performing a statistical analysis of the depth trends of the available well logs. This, of course, requires that at least two well logs with significant depth differences between the layers when going from one well to the other are available.

Seismic velocity data can also be used to constrain the low-frequency model. Velocity values are computed for each trace by linear interpolation using the nearest defined grid points.



The resulting 3D velocity model is low-pass filtered laterally parallel to the interpreted horizons and vertically to remove anomalies. The velocity model is finally transformed to acoustic impedance using Gardner's relation. In the case of multiple crossing 2D lines, sometimes referred to as the 2.5D case, the velocity data is treated as 3D and only at the very end, 2D lines are extracted. This procedure ensures that incompatible information is not introduced where two 2D lines crosses.

The acoustic impedance well log information, extrapolated along the interpreted horizons, is then used in combination with the velocity-derived low-frequency acoustic impedance model to generate a detailed acoustic impedance model, which is then low-pass filtered to produce the final low-frequency model. The velocity-derived low-frequency acoustic impedance model is used to guide the acoustic impedance changes between the well locations. This guidance is such that only lateral variations in the seismic velocities have an influence on the final low-frequency model between the wells. The degree of guidance is specified by a parameter, RGUIDE, for which the value zero corresponds to no guidance by the velocity-derived low-frequency acoustic impedance model and the value 1 corresponds to proportional or full guidance. The absolute level of the velocity-derived acoustic impedance model has no influence between the well logs.

Dip information from the seismic data can also be used to help guide the extrapolation of the well logs. Dips estimated from the seismic data are converted to horizon like information called a layer sequence field. The layer sequence field is then used to guide the extrapolation of the well logs either with or without interpreted horizons and faults and seismic velocity information (Rasmussen, 1999).

The degree to which the resulting impedance model is low-pass filtered is represented by a filter constant: the higher the value of the constant, the greater the degree of filtering. If the filter constant is too high, the final inversion result will not contain variations with frequencies between the lowest frequency resolvable from the seismic data and the very low frequencies introduced by the prior model. However, if the filter constant is too low, the frequency content of the prior model will overlap significantly with that of the seismic and the detail in the inversion result will not be independent of the well log information.

C.6 ISIS seismic inversion results

The primary results produced by the ISIS seismic inversion are two impedance models; one with and one without low-frequency information.

The impedance result without low-frequency information enables the interpreter to carry out an interpretation of a fully unbiased result as neither well logs nor seismic horizons have been utilized. However, only the relative impedance level can be interpreted. In the inversion result with low-frequency information, the absolute impedance level may also be interpreted.



C.7 ISIS seismic inversion for porosity

Inversion of the seismic data for porosity is performed in exactly the same way as the inversion for acoustic impedance. The inputs to the ISIS seismic inversion algorithm are, however, different. Rather than the normal acoustic impedance wavelet, a porosity wavelet is used, and the prior model consists of a low-frequency porosity model. The method is described in more detail in Rasmussen & Maver (1996).

C.8 Alignment

Misalignment of events in a number of different areas can to the degree that it is representing errors in the different simplified models used in the seismic processing have a degrading influence on the results and extracting the displacement information can to the degree that it is not representing the above mentioned errors be valuable in itself. The areas that this concerns are:

- **Well log calibration:** Misalignment between synthetic and original seismic data at the well position due to for instance migration inaccuracies can lead to loss of especially the high frequency components in the least square wavelet. An alignment should therefore be performed either manually or automatically.
- **Time lapse:** Misalignment between the different seismic vintages can be due to a number of reasons: acquisition and processing inaccuracies, changed layer thicknesses due to compaction, changed wave velocities due to compaction, fluid, temperature, and/or pressure changes. The different seismic vintages should be aligned before sample by sample differencing. The displacement information could furthermore be a valuable attribute in itself.
- **AVO:** Due to inaccurate NMO, DMO, and/or migration some misalignment in depth is often present between the events in the different angle- or offset-stacks. The misalignment is less, but still present, in the inverted data as separate wavelets have been used for the different angle- or offset-stacks. The misalignment can degrade the results that are obtained by combining the different separate angle- or offset-stacks inversion results, e.g. Poisson's ratio and Shear impedance, and to a lesser degree the computed Acoustic Impedance. An alignment should therefore be performed if the misalignment is not due to that acoustic and shear reflection coefficients simply are not fully correlated.
- **4C:** Misalignment of the PP and PS seismic data due to for instance inaccurate estimated Poisson's ratio can degrade the results obtained by combining the two data sets. An alignment as in the AVO case should therefore be performed.

If it for some technical or economic reason is not possible to correct the misalignment using an improved deterministic seismic processing scheme then one is left with the less reliable statistical approaches. Statistical approaches work by modifying one of the two data sets by a constrained mathematical transformation such that the data set in some mathematical sense becomes more like the other data set. The reason why statistical approaches are



less reliable than deterministic approaches is that they cannot directly distinguish between misalignment due to the simplified models used and misalignment bearing useful information. The way they attempt to distinguish the two contributions is by using a very constrained mathematical transformation.

Our implementation of statistical alignment is a pure single trace algorithm meaning that the data is stretched and squeezed vertically only, and that there is no requirements with respect to horizontal continuity of the vertical displacement. Furthermore are the amplitudes not modified. Our algorithm is fully automatic in the sense that the only interaction required by the user is to choose a parameter describing how much vertical displacement that is allowed in the search for maximum cross-correlation.

C.9 Spectral balancing

When comparing two signals visually or arithmetically as for instance in statistical alignment algorithms, it is in some cases advantageous that they have approximately identical amplitude spectra. This amplitude spectra has to be the common frequency interval of the two input signals of the spectral balancing in order not to introduce noise in either of the two output signals. Denoting the amplitude spectrum as a function of the frequency f before spectral balancing of signal 1 as $A_1(f)$ and of signal 2 as $A_2(f)$, one way to obtain spectral balancing is to compute the filter $H_1(f)$, which is to be applied to signal 1, and the filter $H_2(f)$, which is to be applied to signal 2, as follows

$$H_1(f) = \frac{A_2(f)}{\sqrt{A_1(f)^2 + A_2(f)^2}} \quad (\text{C.1})$$

$$H_2(f) = \frac{A_1(f)}{\sqrt{A_1(f)^2 + A_2(f)^2}} \quad (\text{C.2})$$

The common amplitude spectrum $A(f)$ after the spectral balancing is simply

$$A(f) = \frac{A_1(f)A_2(f)}{\sqrt{A_1(f)^2 + A_2(f)^2}} \quad (\text{C.3})$$

which means that the common power spectrum is the harmonic mean of the two input power spectra.

References

- Cooke, D.A. & W.A. Schneider, 1983. Generalized linear inversion of reflection seismic data. *Geophysics*, **48**, 665–676.
- Rasmussen, K. B. & K.G. Maver, 1996. Direct inversion for porosity of post stack seismic data. **SPE35509**. *Society of Petroleum Engineers*.
- Rasmussen, K. B. 1999. Use of dip in seismic inversion. *61th Mtg.: Eur. Assoc. Expl. Geophys., Session 4049*.



APPENDIX D

Stratigraphic Correlation Cube theory

The theory for the calculation of the Layer Sequence Field and the Stratigraphic Correlation Cube is described in this appendix.

D.1 Introduction

Dips measured in the seismic data can be used either alone or together with interpreted horizons and faults to constrain the extrapolation of the impedance logs in the low-frequency model building (see Section C.5). However, before measured seismic dips can be used in the low-frequency model building, they are converted from a vector field to a scalar field, which we have called the Layer Sequence Field.

The Stratigraphic Correlation Cube shows the trace-to-trace coherence of either the seismic data or of the inversion results. The Layer Sequence Field is used as input in the Stratigraphic Correlation Cube calculation, where it is used to constrain the orientation of the layering.

D.2 Dip and Layer Sequence Field calculation

The calculations for dip and the Layer Sequence Field are described below. They are presented in a little more detail in Rasmussen (1999).

The seismic dip in the in-line direction is estimated as

$$S_x = -\frac{\frac{\partial d}{\partial t} \frac{\partial d}{\partial x} + \frac{\partial d_h}{\partial t} \frac{\partial d_h}{\partial x}}{\left(\frac{\partial d}{\partial t}\right)^2 + \left(\frac{\partial d_h}{\partial t}\right)^2} \quad (\text{D.1})$$

where $d(t,x,y)$ denotes the seismic signal, $d_h(t,x,y)$ denotes the Hilbert transform of the seismic signal, t denotes the depth measured in two-way travel-time (TWT), x denotes the



horizontal distance in the in-line direction, and y denotes the horizontal distance in the cross-line direction. Equation (D.1) is exact for a sine signal. In order to stabilize the estimation for real signals, both the numerator and denominator are low-pass filtered before the division. The dip S_y in the cross-line direction is estimated using a similar procedure.

The estimated dips, however, cannot be used directly in the low-frequency model generation. They have to be converted to a scalar field, $h(t,x,y)$, which is used to extrapolate the well logs. We have named this scalar field the Layer Sequence Field. The Layer Sequence Field has the property that a given layer is characterized by the same value in the whole seismic volume. Furthermore, in the absence of faults, the Layer Sequence Field increases as a function of depth. The Layer Sequence Field satisfies the following two partial differential equations as closely as possible such that dips calculated from the Layer Sequence Field match the dips estimated from the seismic data as closely as possible:

$$\frac{\partial h}{\partial x} = -S_x \frac{\partial h}{\partial t} \quad (\text{D.2})$$

$$\frac{\partial h}{\partial y} = -S_y \frac{\partial h}{\partial t} \quad (\text{D.3})$$

In order to stabilize the estimation of the Layer Sequence Field, the additional constraints that the Layer Sequence Field is smooth and increases as a function of depth are applied. The estimated layer sequence field can then be used as a guide together with or replacing interpreted horizons in the extrapolation of the well log information away from the well positions.

D.3 Stratigraphic Correlation Cube calculation

The Stratigraphic Correlation Cube provides a measure of the trace-to-trace coherence in either the seismic data or in the inversion result. The result is the coherence between one trace and two neighbouring traces; one in the in-line direction and one in the cross-line direction. The coherence is calculated in a vertically sliding window. The effective size of the window acts as a "smoothing" constraint, thereby low-pass filtering the result.

The dip of the geological layering is accounted for in the Stratigraphic Correlation Cube calculation by using the Layer Sequence Field. The Layer Sequence Field is used to shift neighbouring traces before calculation of the coherence.

References

Rasmussen, K. B., 1999. Use of dip in seismic inversion. 61st Meeting Eur. Assoc. Expl. Geophys., 4-49. *EAGE abstract*.

Selection of samples

Chalk Background Velocity, E&R-1

Ida L. Fabricius, DTU
Niels Springer, GEUS

confidential

Selection of samples

Ida L. Fabricius, DTU and Niels Springer, GEUS

This note contains a brief description of the procedure applied in selecting twenty-one core samples from water zone chalk in the northern part of the Danish Central Graben. The purpose of the sampling is to measure the sonic velocities of the samples and to investigate their textural properties as part of the Chalk Background Velocity study funded by the South Arne Group. We also summarise data for the sampled material with respect to porosity, permeability, and lithostratigraphy.

Selection of wells

In the northern part of the Danish Central Graben, several wells penetrate chalk, but only a limited number of wells are cored in this section (Figure 1). In order to select which wells to sample, we plotted the depth and effective depth vs. porosity of core plugs from each well (Figure 2, 3) and also plotted permeability versus porosity (Figure 4). Effective depth is calculated as depth in meters minus 10 times the overpressure in MPa. The effective depth is thus a measure of the effective stress exerted on the sample in situ. The core data were extracted from the GEUS data base and from operator's completion reports. This project focuses on background velocity, so we limited the study to the water zone to wells where cores can still be plugged. This left us with eight wells (Figure 5, 6, 7, 8).

Selection of samples

From each of the eight wells we sampled four new vertical 1½ inch plugs. The plugging depths were chosen with the aim of representing the variation in porosity in each well. Oil stained intervals, fractures, marly zones and stylolites were avoided, except for in well I-1, where no unstained intervals were found. This sampling resulted in 32 core samples, which were characterised by conventional core analysis (see Appendix) before final sampling. The resulting data are presented in Table 1 and on Figures 9, 10, and 11.

Final sampling

Final sampling was done from plug condition and from inspection of Figures 9, 10, and 11. First small or fractured samples were left out. Then only one sample was selected if two samples from one well have similar porosity and permeability. Then, in most cases where samples from two wells have similar porosity, permeability, depth and effective depth, one sample was left out. The resulting number of samples is 21 (Figure 12, 13, 14). Stratigraphy was not taken into account in the process of sampling. The samples represent the Ekofisk Formation, Tor Formation, Tuxen Formation and GEUS stratigraphic unit Chalk-2 (Table 1 and Figure 15).

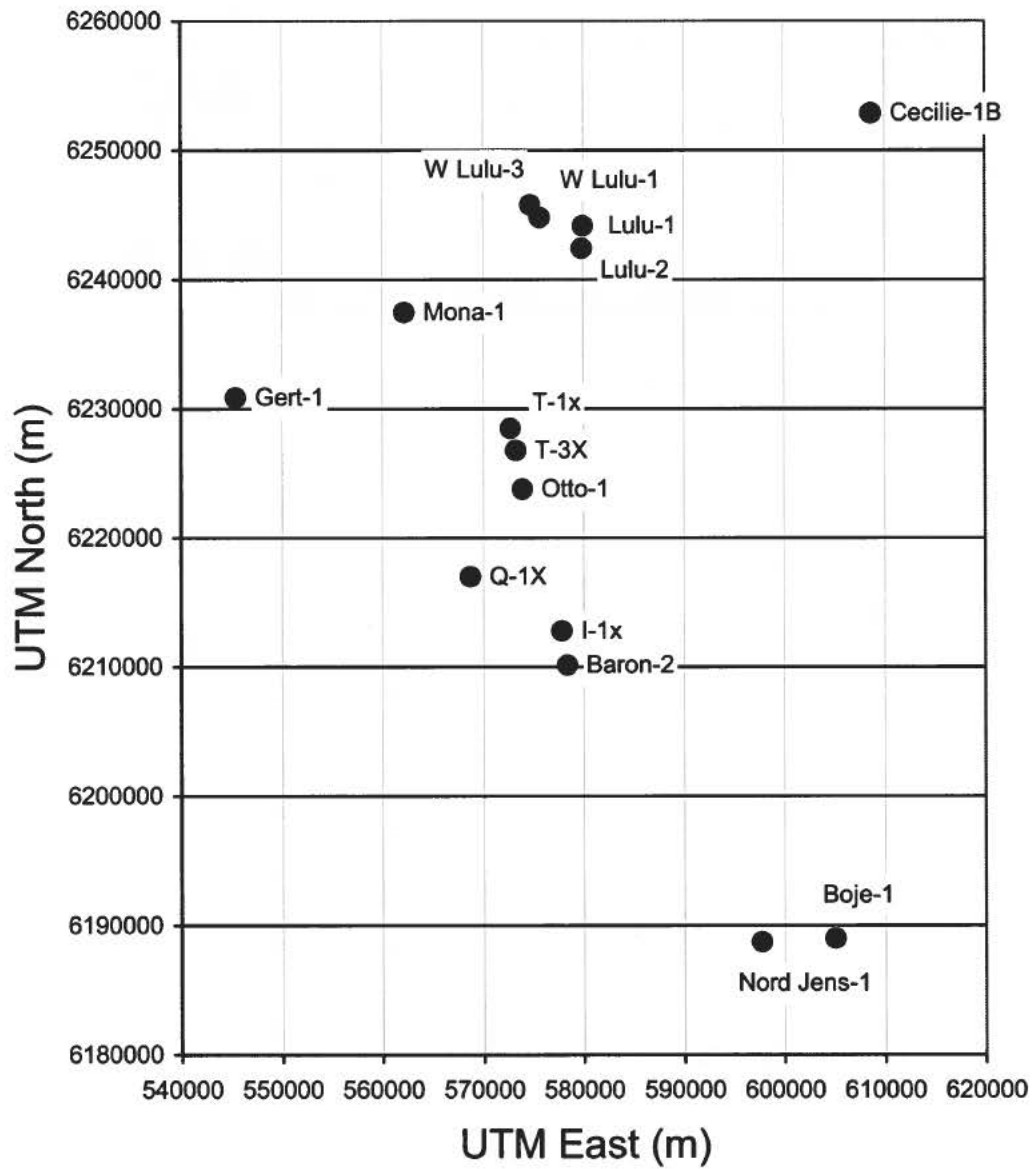


Figure 1. Wells with chalk cores, located in the Northern part of the Danish Central Graben.

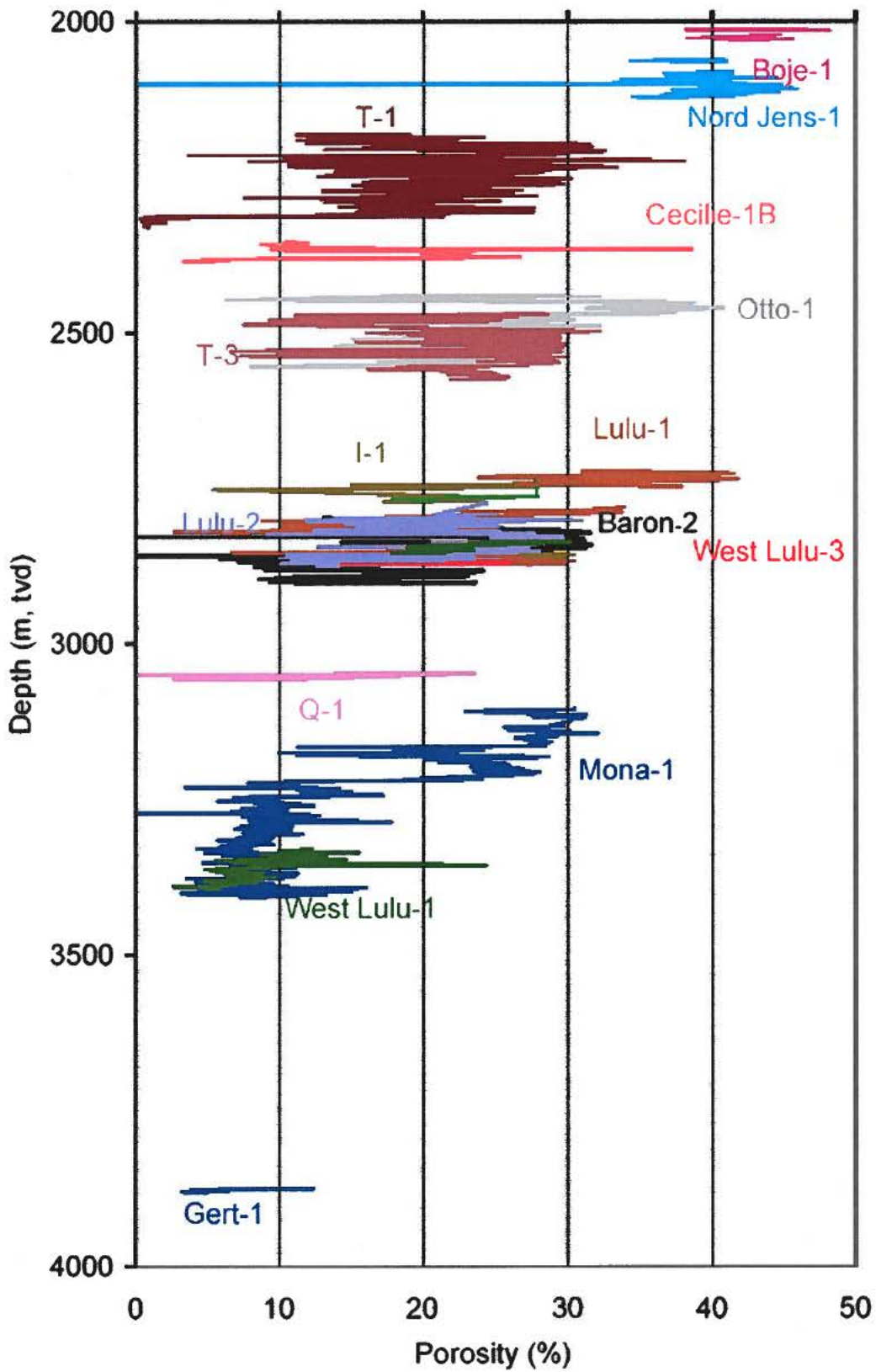


Figure 2. Porosity vs. depth. All core data.

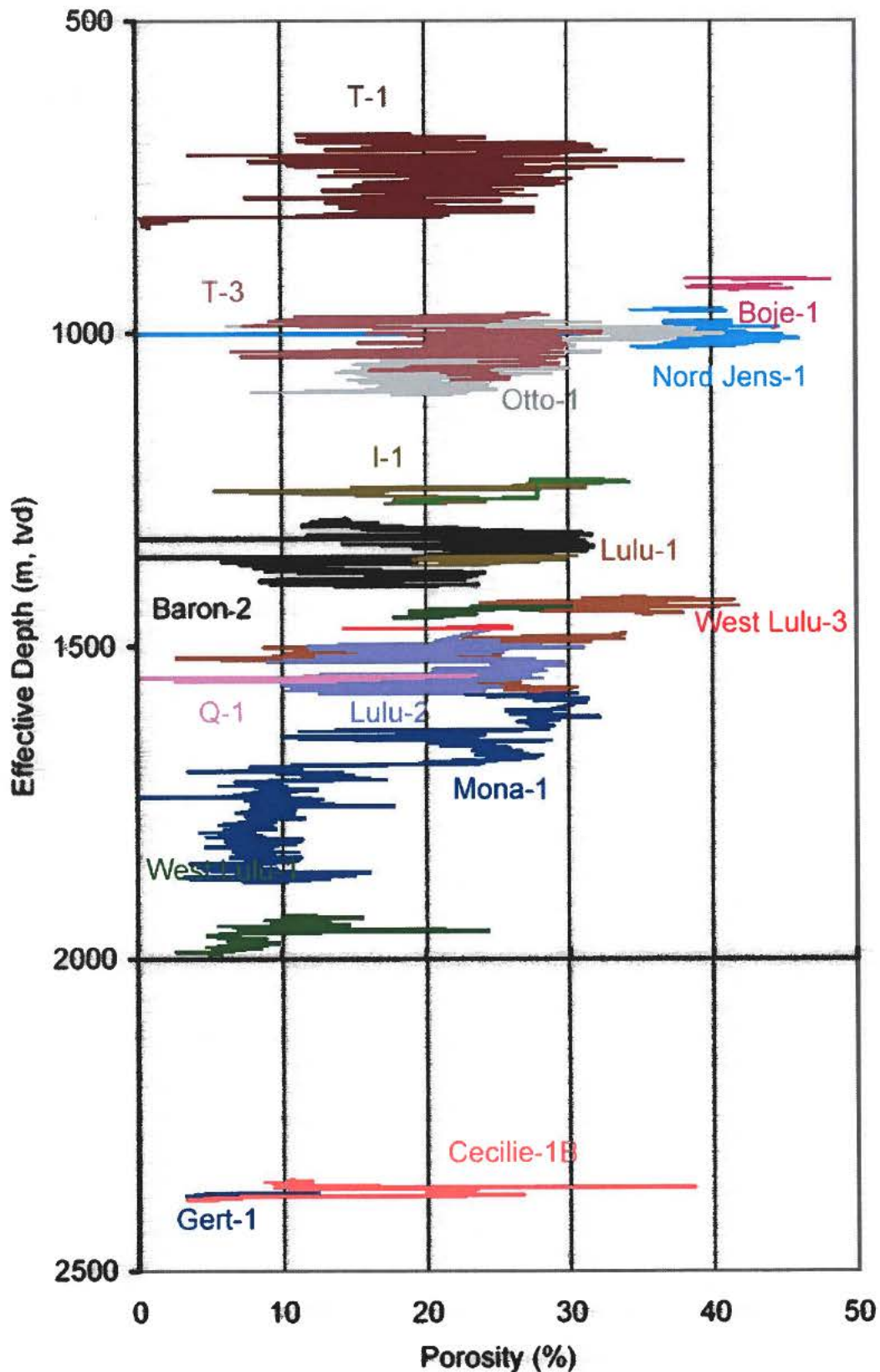


Figure 3. Porosity vs. effective depth. All core data. Pore pressures from Japsen, P. 1998: Regional velocity-depth anomalies, North Sea chalk: a record of overpressure and Neogene uplift and erosion, AAPG Bulletin, v. 82, p. 2031-2074.

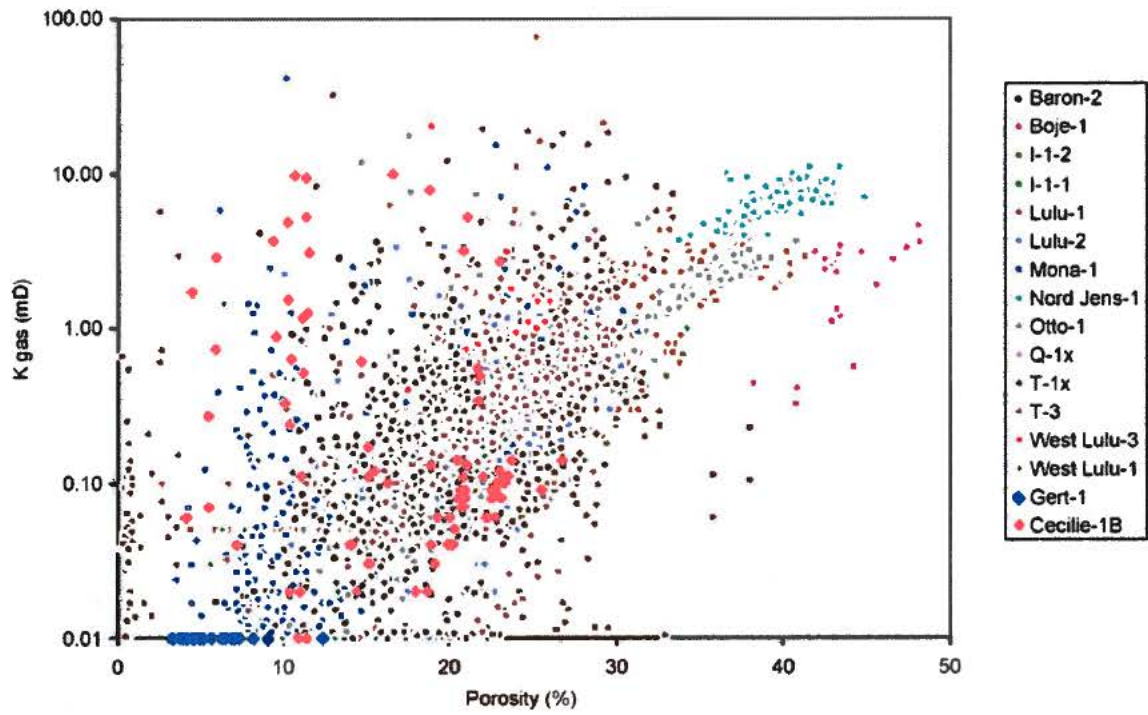


Figure 4. Permeability vs. porosity. All core data.

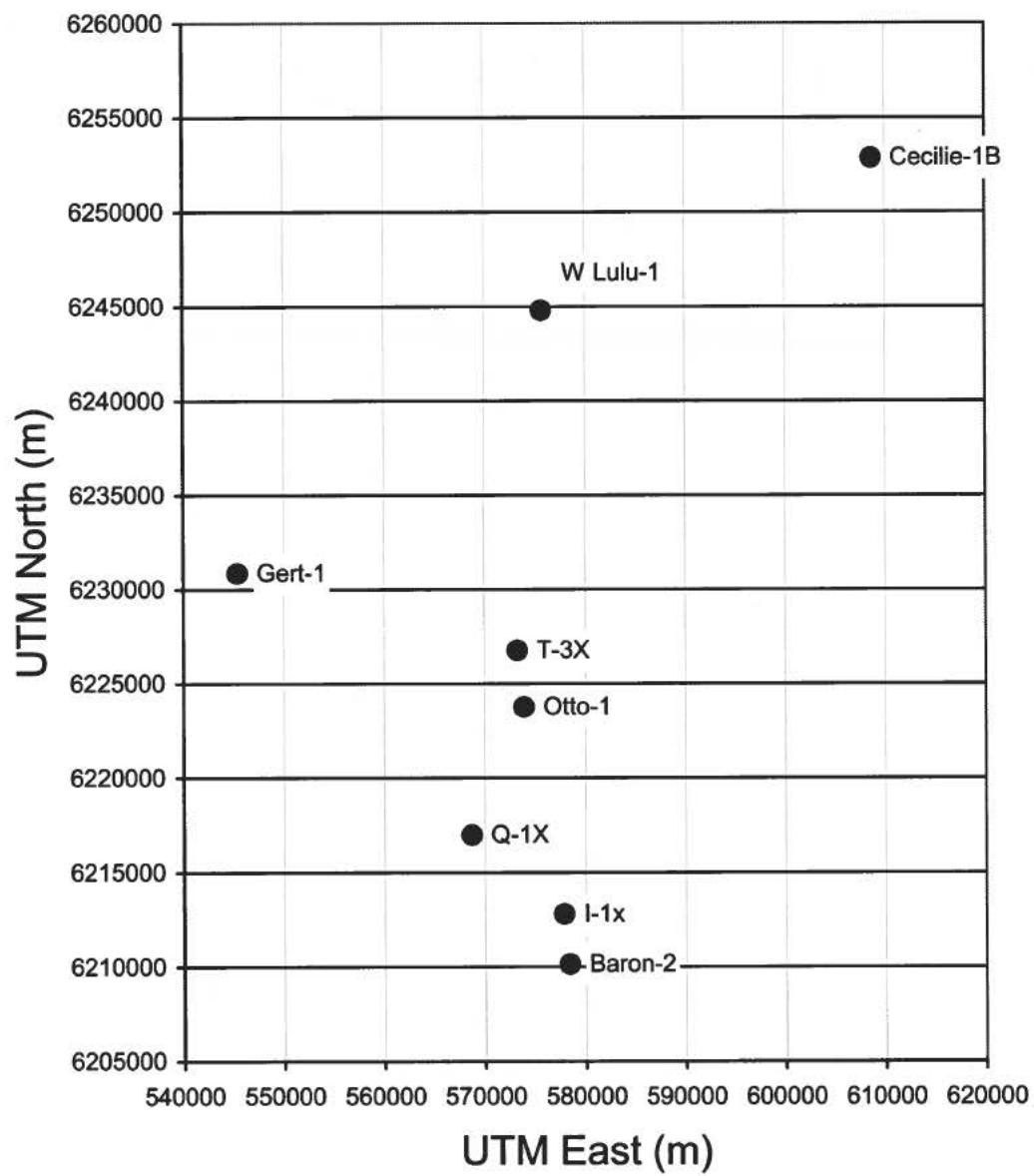


Figure 5. Wells selected for sampling.

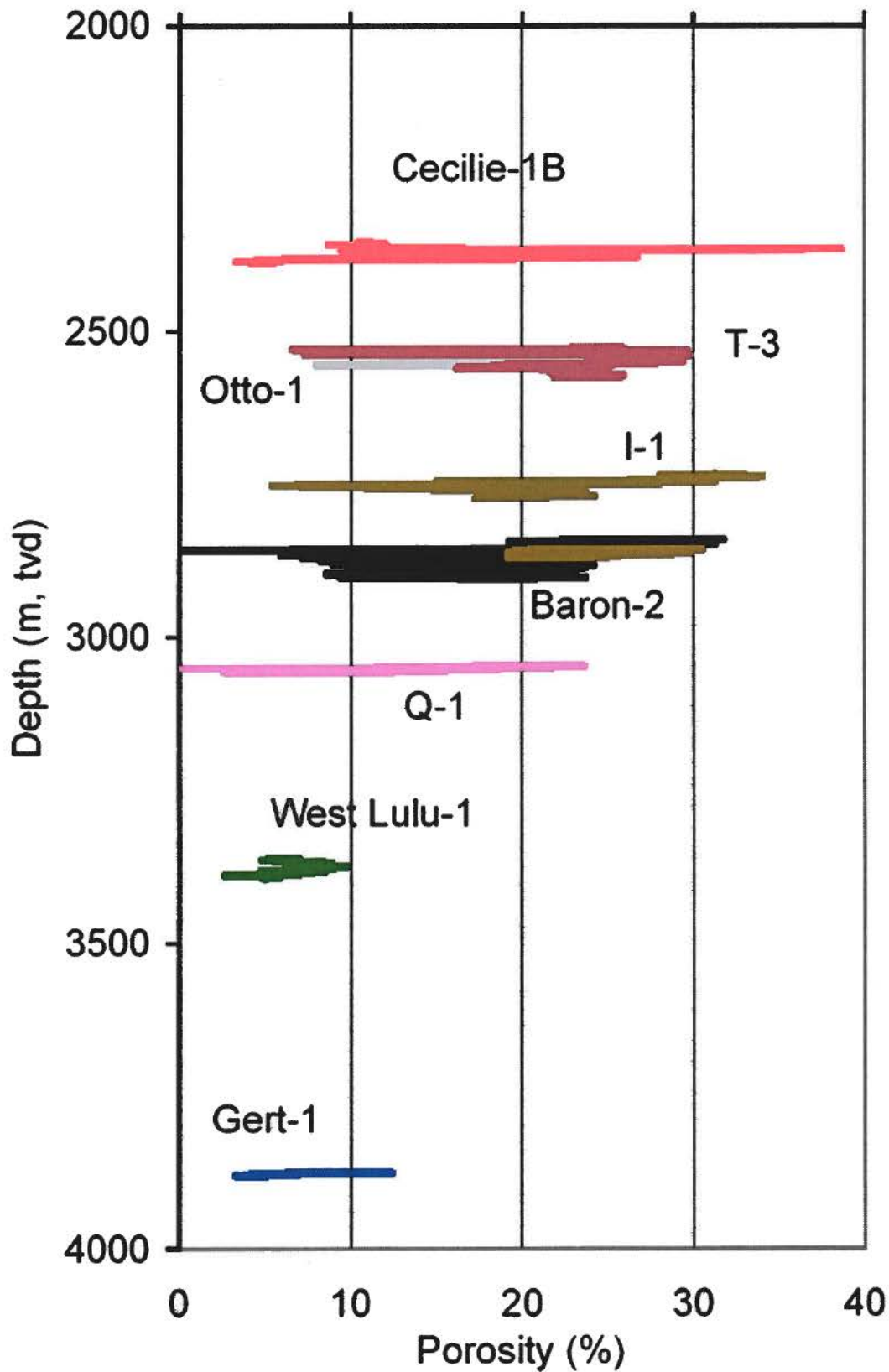


Figure 6. Porosity vs. depth. Water zone core data from selected wells.

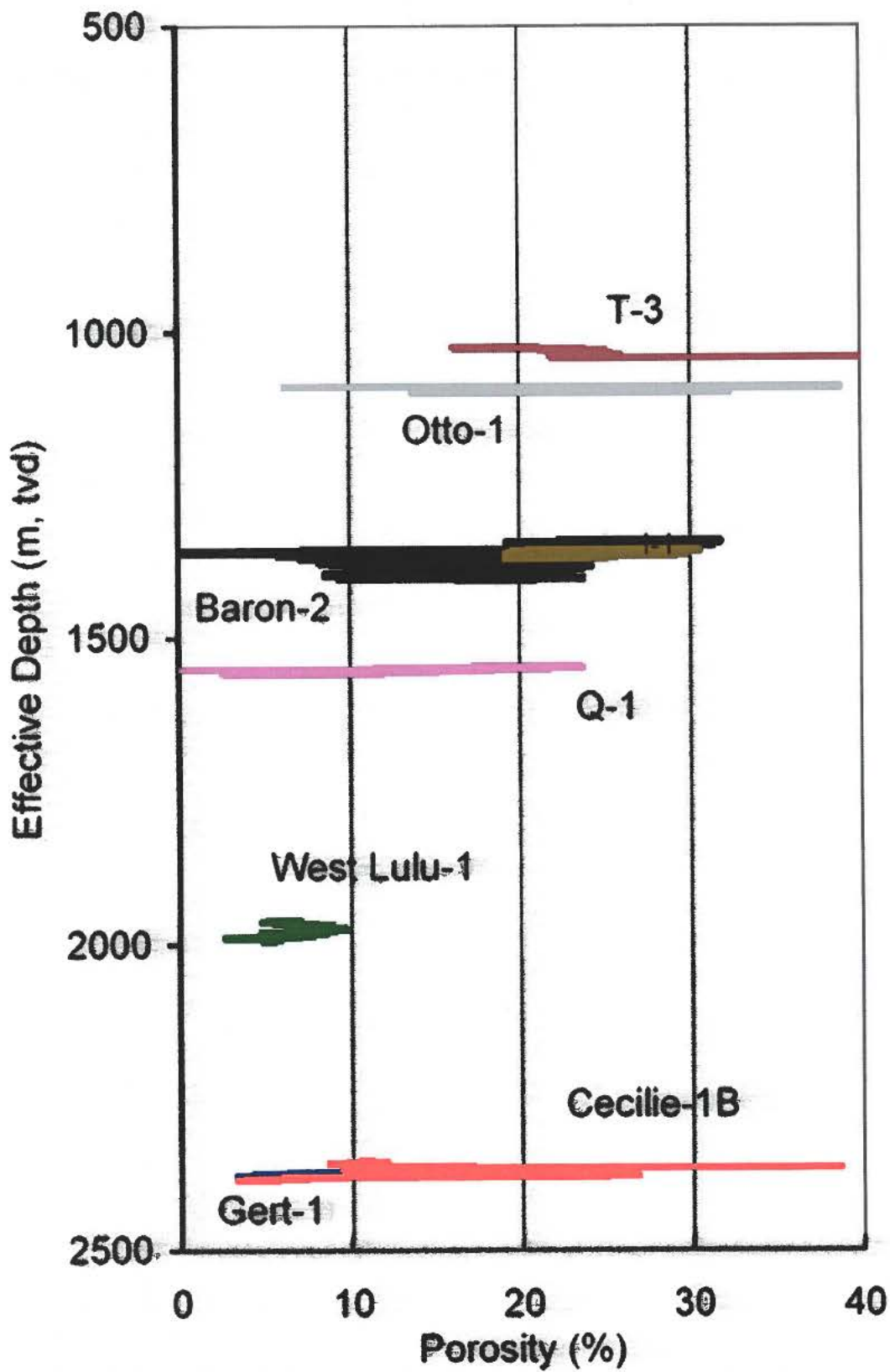


Figure 7. Porosity vs. effective depth. Water zone core data from selected wells.

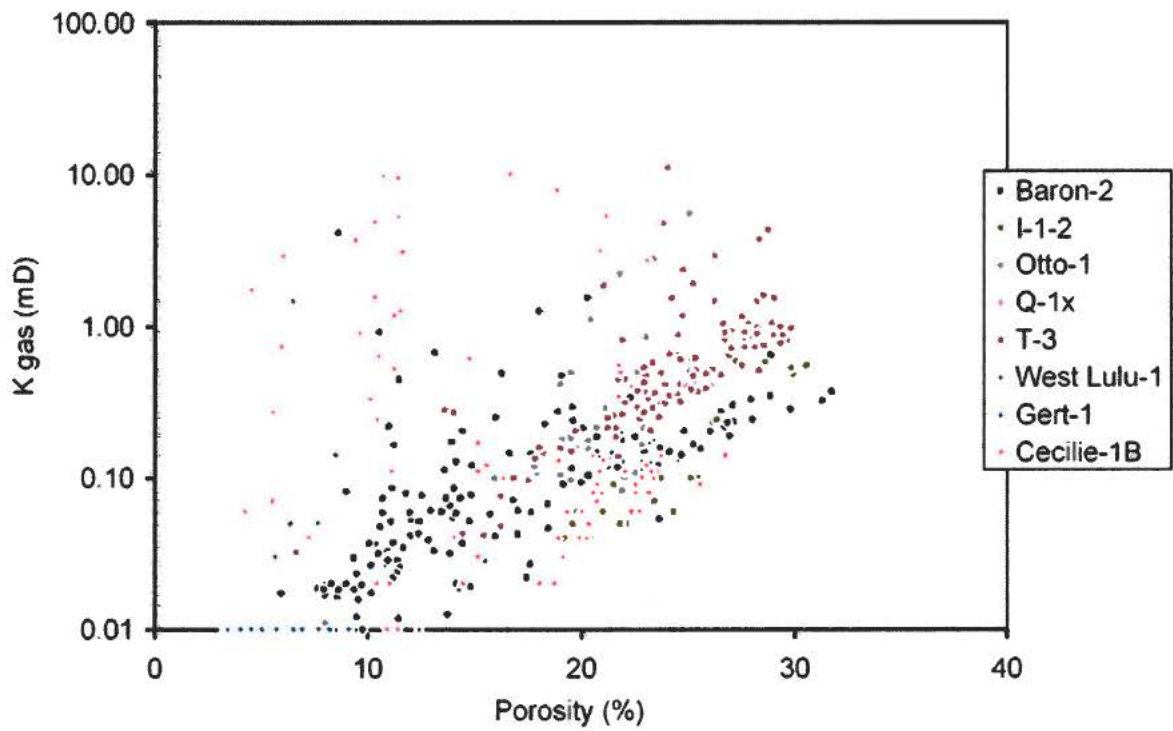


Figure 8. Permeability vs. porosity. Water zone data from selected wells.

Sample ID	Depth m/f	Gas Perm mD	Por %	Dens g/ccm	Well ID	Final sampling	Formation	GEUS Unit
Q1-1	10125.25	0.003	14.35	2.72	Q-1	x	Ekofisk	Chalk-6
Q1-2	10132.50	0.002	8.97	2.72	Q-1	x	Ekofisk	Chalk-6
Q1-3	10138.08	0.018	14.43	2.70	Q-1	x	Ekofisk	Chalk-6
Q1-4	10147.25	0.009	9.91	2.71	Q-1	x	Ekofisk	Chalk-6
Otto1-5	8473.84	0.430	19.06	2.72	Otto-1		Tor	Chalk-3
Otto1-6	8495.00	0.330	19.23	2.72	Otto-1	x	Tor	Chalk-3
Otto1-7	8497.00	4.390	21.96	2.72	Otto-1		Tor	Chalk-3
Otto1-8	8504.00	0.520	20.72	2.72	Otto-1	x	Tor	Chalk-3
T3-9	8440.33	0.420	19.1	2.72	T-3	x	Tor	
T3-10	8526.75	0.860	24.77	2.72	T-3	x	Tor	
T3-11	8532.08	0.770	24.69	2.72	T-3		Tor	
T3-12	8568.33	1.620	24.24	2.72	T-3		Tor	
Gert1-13	12838.90	0.009	11.28	2.68	Gert-1	x	Hod	Chalk-2
Gert1-14	12846.42	0.030	4.96	2.65	Gert-1	x	Hod	Chalk-2
Gert1-15	12854.50	0.005	3.99	2.70	Gert-1		Hod	Chalk-2
Gert1-16	12858.58	0.005	3.7	2.70	Gert-1	x	Hod	Chalk-2
WL1-17	11159.51	0.002	6.32	2.73	West lulu-1	x	Hod	Chalk-2
WL1-18	11187.33	0.003	6.68	2.72	West lulu-1		Hod	Chalk-2
WL1-19	11213.33	0.004	8.01	2.72	West lulu-1	x	Hod	Chalk-2
WL1-20	11246.42	0.003	7.11	2.72	West lulu-1		Hod	Chalk-2
Ba2-21	2855.55	0.170	26.9	2.71	Baron-2	x	Ekofisk	
Ba2-22	2858.55	0.060	24.69	2.71	Baron-2	x	Ekofisk	
Ba2-23	2860.48	0.050	16.68	2.70	Baron-2	x	Ekofisk	
Ba2-24	2867.03	0.070	21.87	2.70	Baron-2	x	Ekofisk	
I1-25	9504.00	0.050	24.8	2.70	I-1		Sola	
I1-26	9508.50	0.080	26.73	2.70	I-1	x	Tuxen	
I1-27	9523.90	0.015	17.43	2.73	I-1		Tuxen	
I1-28	9538.50	0.020	16.95	2.72	I-1	Fractured	Tuxen	
Ce1B-29	2393.81		12.29	2.71	Cecilie-1B	Fractured	Ekofisk?	
Ce1B-30	2402.61	0.010	14.9	2.71	Cecilie-1B	x	Ekofisk?	
Ce1B-31	2407.50	0.410	22.36	2.71	Cecilie-1B	x	Ekofisk?	
Ce1B-32	2420.76	0.015	7.21	2.71	Cecilie-1B	x	Ekofisk?	

Table 1. Conventional core analysis data of 32 vertical 1½ inch samples.

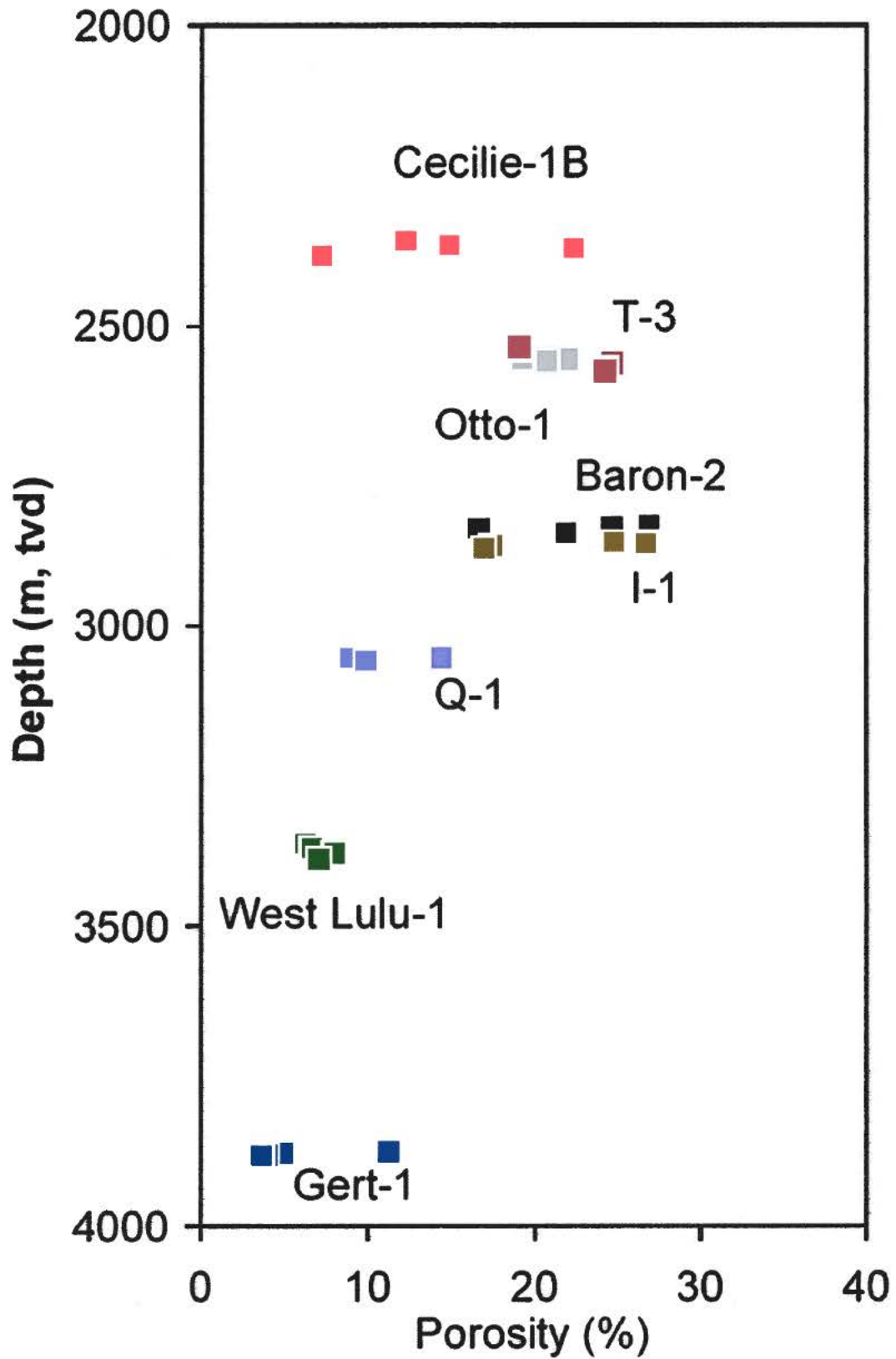


Figure 9. Porosity vs. depth. The 32 1½ vertical core samples.

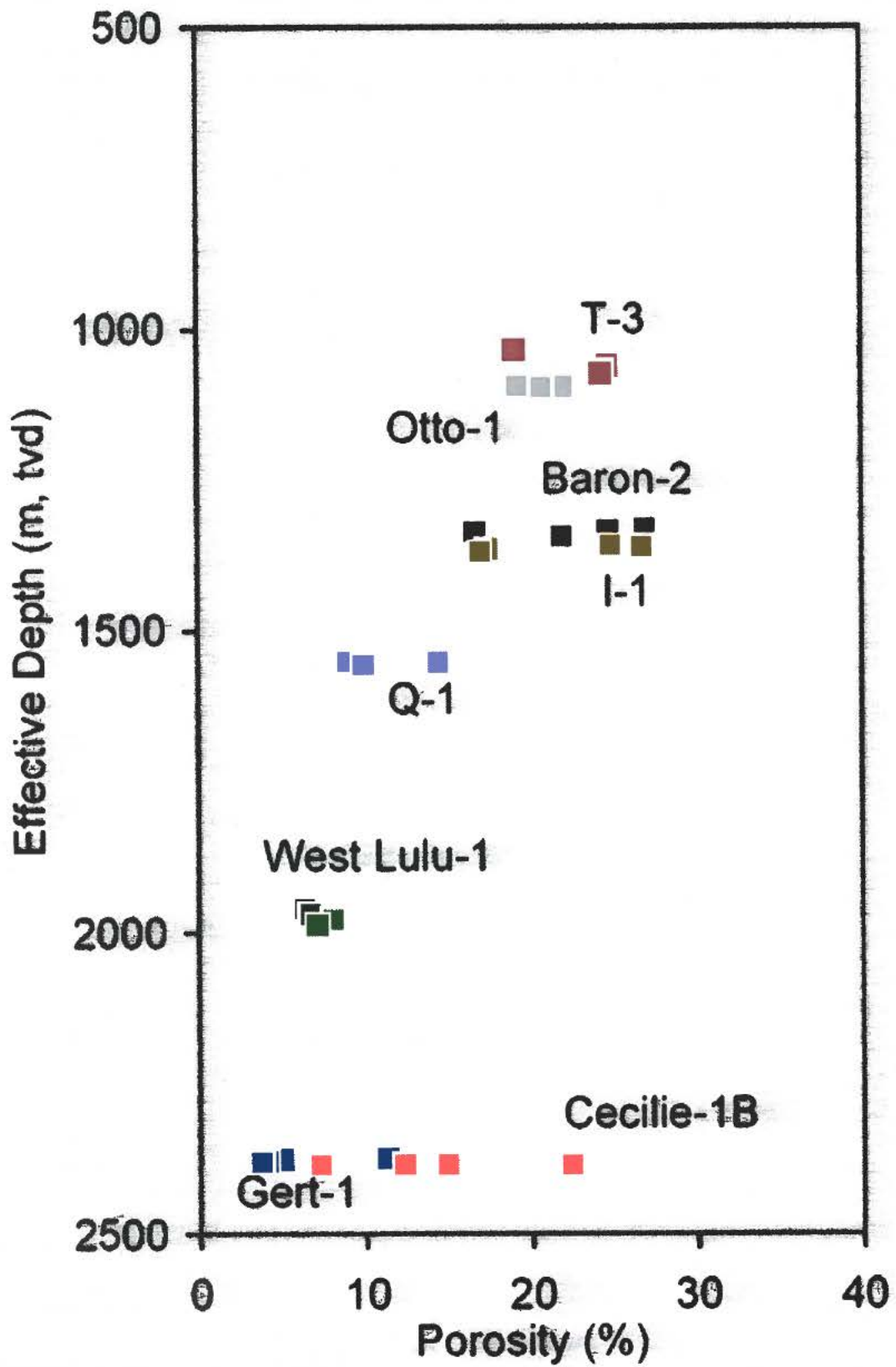


Figure 10. Porosity vs. effective depth. The 32 1½ vertical core samples.

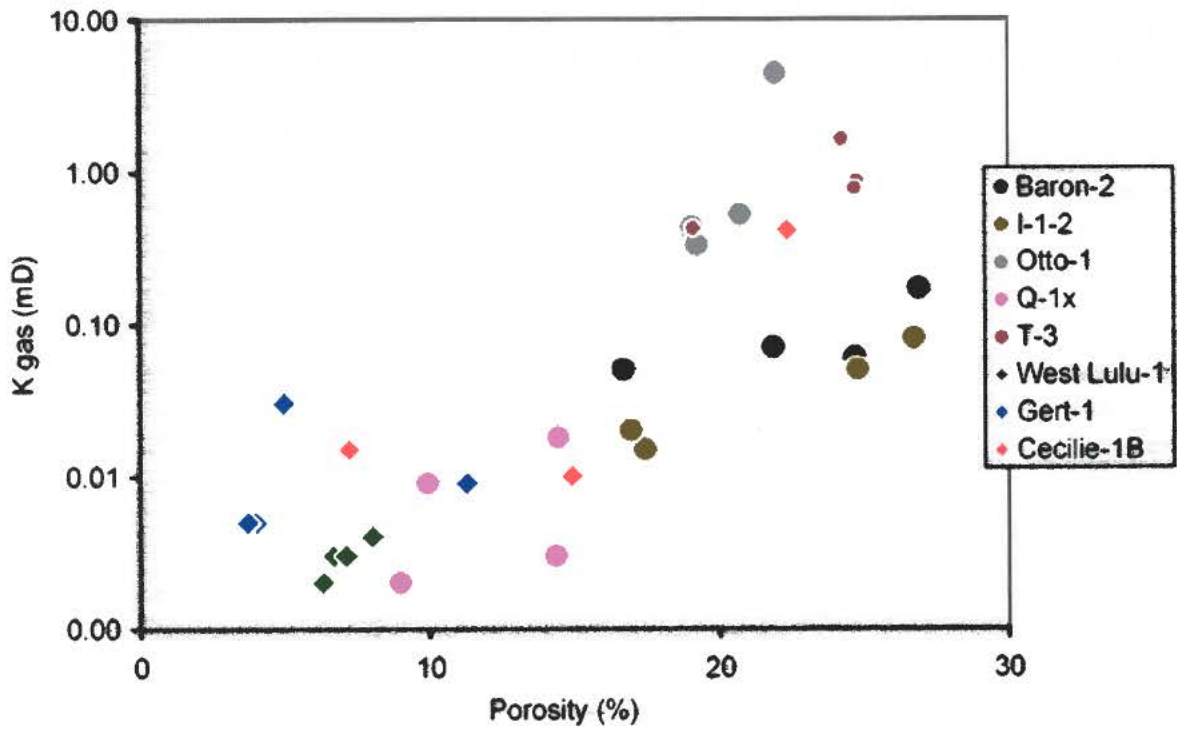


Figure 11. Permeability vs. porosity. Thirty-three 1½ vertical core samples. One sample were broken so that no permeability data were obtained.

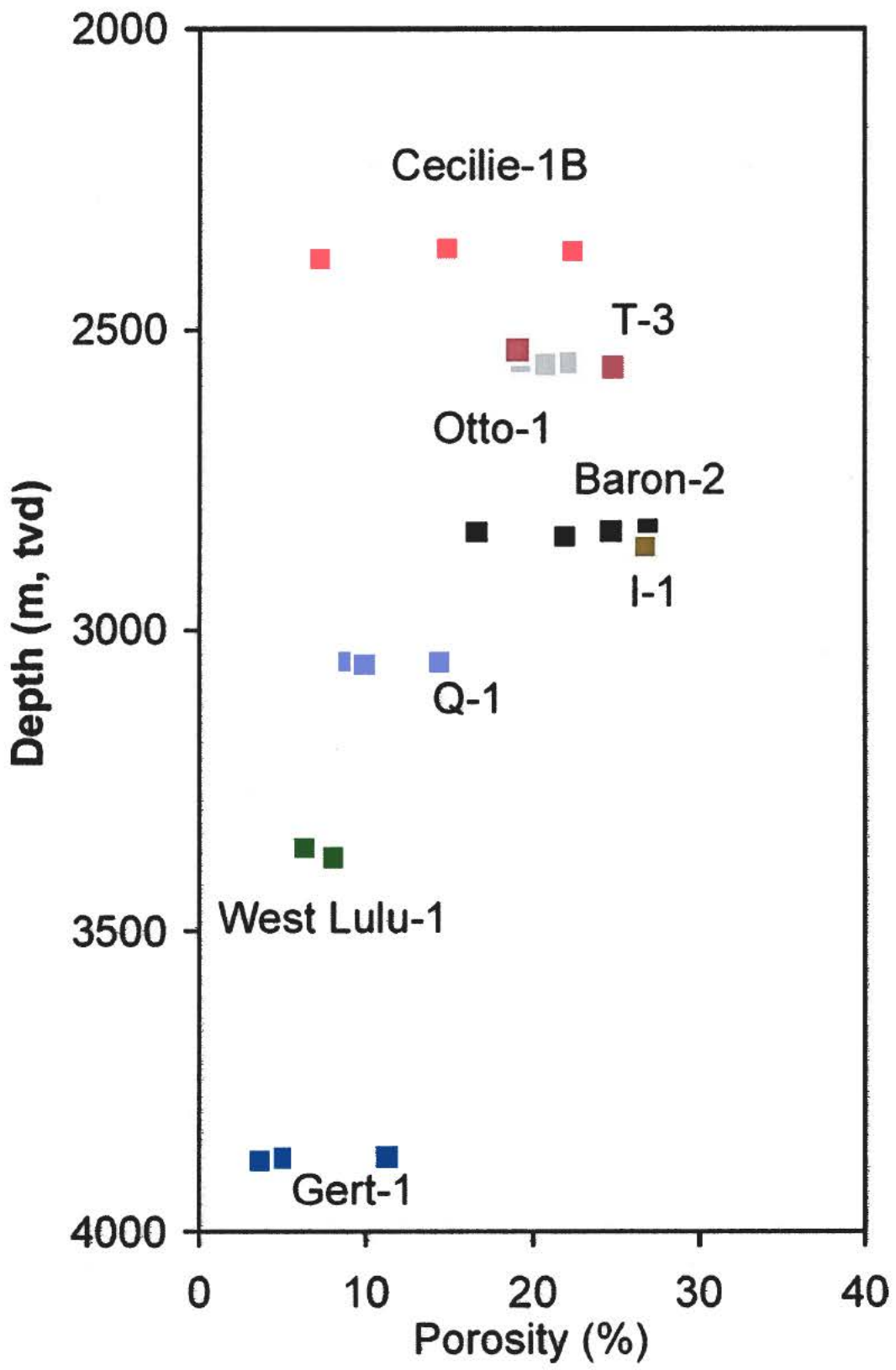


Figure 12. Porosity vs. depth. The 21 selected 1½ vertical core samples.

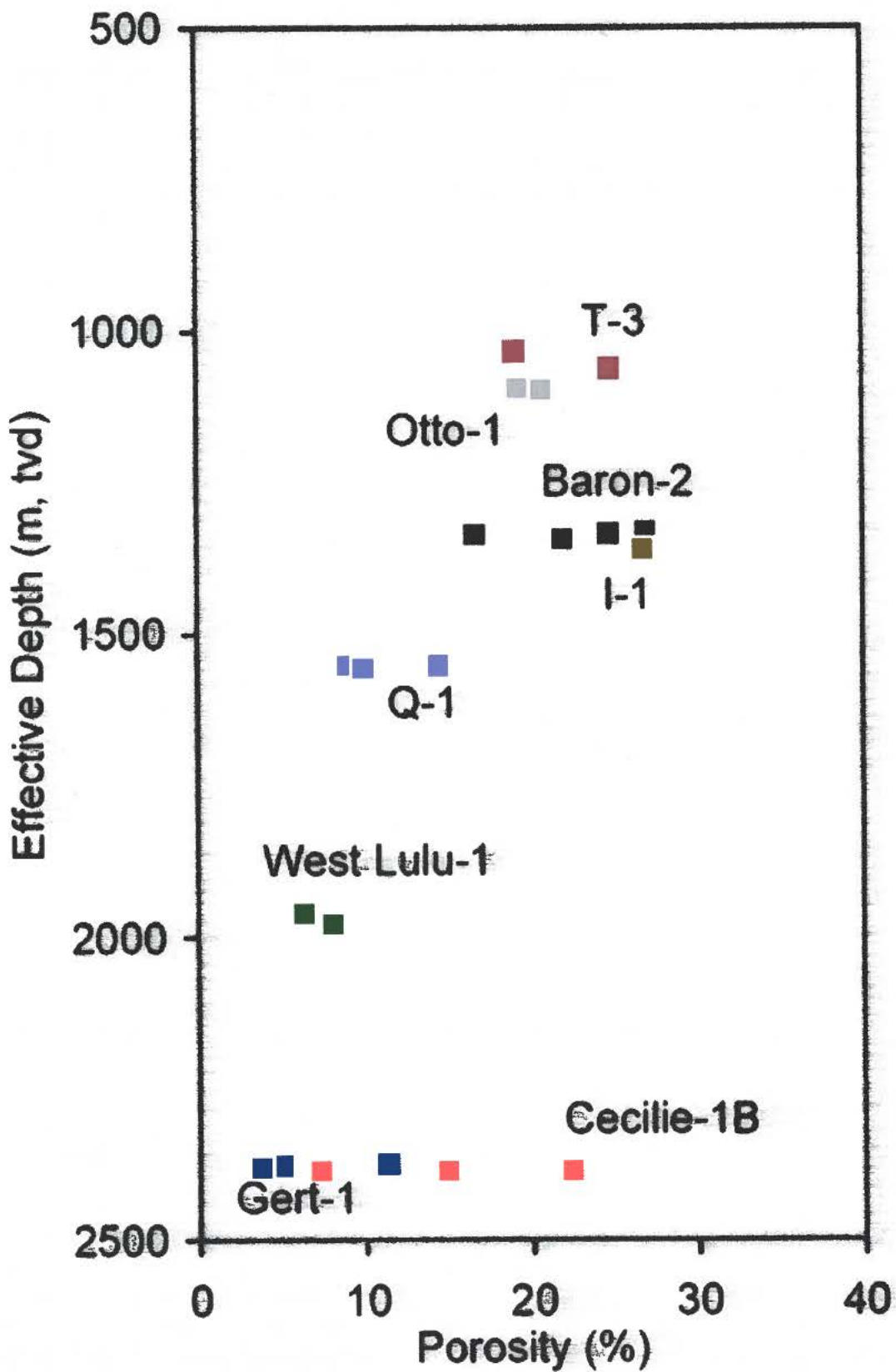


Figure 13. Porosity vs. effective depth. The 21 selected 1½ vertical core samples.

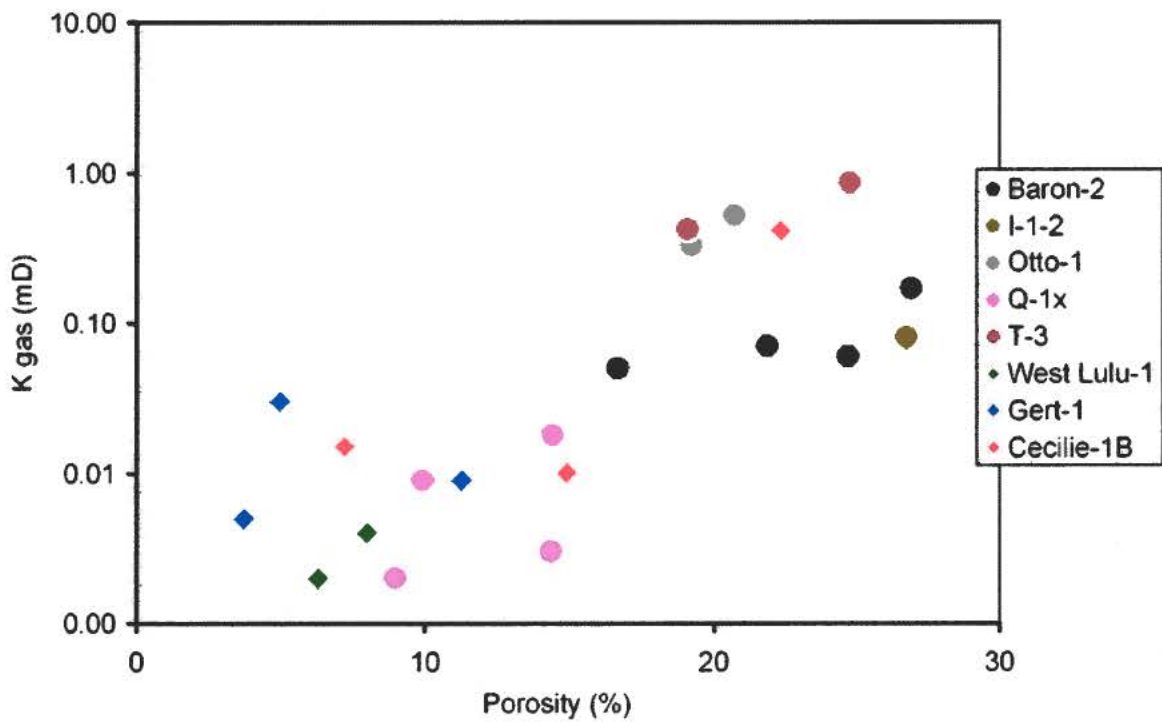


Figure 14. Permeability vs. porosity. The 21 selected 1½ vertical core samples.

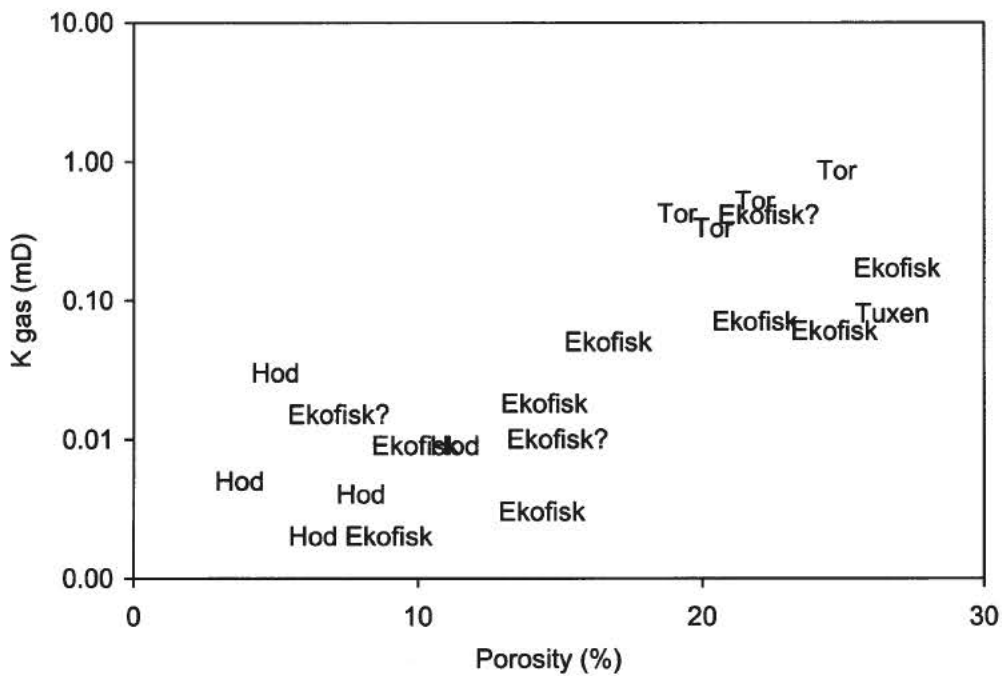


Figure 15. Permeability vs. porosity. Lithostratigraphic origin of the 21 selected 1½ vertical core samples.

Appendix

4 Analytical Methods

The following is a short description of the methods used by GEUS Core Laboratory. For a more detailed description of methods, instrumentation and principles of calculation the reader is referred to API recommended practice for core-analysis procedure (API RP 40, 2nd ed. 1998).

4.3 Conventional cleaning and drying

Plugs of diameter 38 mm are drilled and trimmed carefully. The samples are then placed in a Soxhlet extractor, which continuously soaks and washes the samples with methanol. This process removes water and dissolves salt precipitated in the pore space of the rock. Extraction is terminated when no chloride ions are present in the methanol. Samples containing hydrocarbons are then cleaned in toluene until a clear solution is obtained. Samples are finally dried at 110 °C and passed on for measurement of conventional porosity and permeability.

4.5 Gas permeability (GEUS steady state instrument)

The plug is mounted in a Hassler core holder, and a confining pressure of 400 psi applied to the sleeve. The specific permeability to gas is measured by flowing nitrogen gas through a plug of known dimensions at differential pressures between 0 and 1 bar. No back pressure is applied. The readings of the digital gas permeameter are checked regularly by routine measurement of permeable steel reference plugs (Core Laboratories™ gas permeability reference plug set).

4.7 He-porosity and grain density (GEUS He-porosimeter)

The porosity is measured on cleaned and dried samples. The porosity is determined by subtraction of the measured grain volume and the measured bulk volume. The Helium technique, employing Boyle's Law, is used for grain volume determination, applying a double chambered Helium porosimeter with digital readout, whereas bulk volume is measured by submersion of the plug in a mercury bath using Archimedes principle. Grain density is calculated from the grain volume measurement and the weight of the cleaned and dried sample. The Helium porosimeter is calibrated using a set of steel plugs (Core Laboratories™ volume reference plug set) before the measurement of plug samples are initiated.

4.8 Archimedes porosity

Samples that are saturated to 100% with a liquid can have their bulk volume determined by Archimedes test, i.e. by submersion in a jar containing the saturating liquid and weighing of the buoyancy. If the sample grain density is known (e.g. from a He-porosity measurement) or can be estimated with good precision, the sample pore volume and porosity can be calculated.

4.10 Precision of analytical data

The table below gives the precision (= reproducibility) at the 68% level of confidence (+/- 1 standard deviation) for routine core analysis measurements performed at the GEUS Core Laboratory.

Measurement	Range, mD	Precision
Grain density		0.003 g/cc
Porosity		0.1 porosity-%
Permeability: (Klinkenberg)	0.01-0.1	15%
	0.1-1	10%
	> 1	4%
Permeability: (Conventional)	0.001-0.01	25%
	0.01-0.1	15%
	> 0.1	4%



**Sample characterisation report
for the Chalk Background Velocity project**

**Ida Lykke Fabricius, E&R DTU
Sinh Hy Nguyen, E&R DTU**

Confidential

Chalk Background Velocity, E&R-2

**Sponsored by: Amerada Hess A/S,
Denerco Oil A/S, and DONG A/S**

This report contains results from geological characterization of 21 samples from the water zone of wells in the Northern part of the Danish sector (Figure 1). The applied methods are described below.

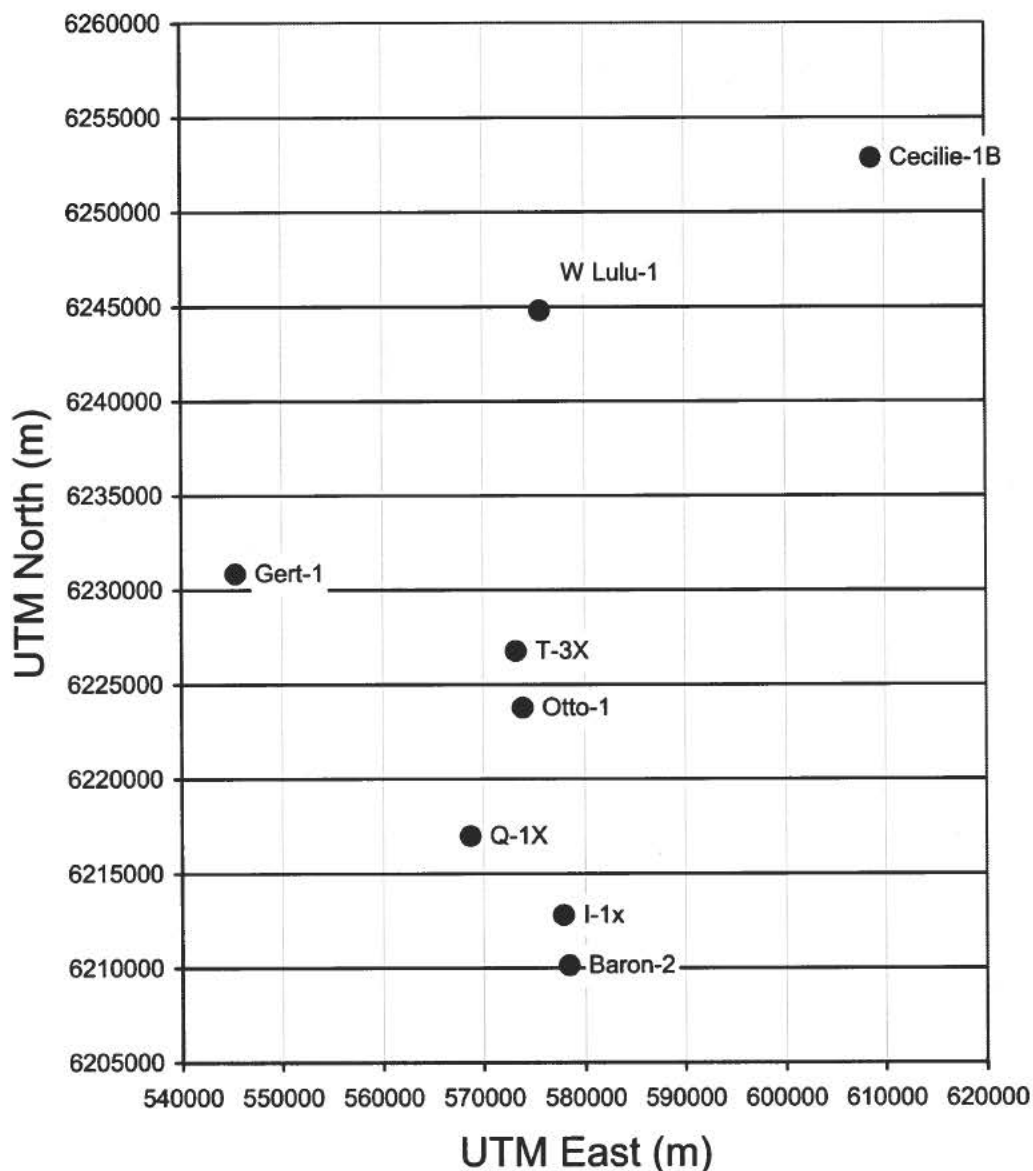


Figure 1. Location of sampled wells.

1. Samples

The samples were selected from a set of 32 samples collected for preliminary study (Table 1, Fabricius & Springer, 2003).

Table 1. All samples.

Sample ID	Depth m/f	Gas Perm mD	Por %	Grain density g/ccm	Well ID	Final sampling	Formation
Q1-1	10125.25	0.003	14.35	2.72	Q-1	x	Ekofisk
Q1-2	10132.50	0.002	8.97	2.72	Q-1	x	Ekofisk
Q1-3	10138.08	0.018	14.43	2.70	Q-1	x	Ekofisk
Q1-4	10147.25	0.009	9.91	2.71	Q-1	x	Ekofisk
Otto1-5	8473.84	0.430	19.06	2.72	Otto-1		Hod
Otto1-6	8495.00	0.330	19.23	2.72	Otto-1	x	Hod
Otto1-7	8497.00	4.390	21.96	2.72	Otto-1		Hod
Otto1-8	8504.00	0.520	20.72	2.72	Otto-1	x	Hod
T3-9	8440.33	0.420	19.1	2.72	T-3	x	Tor
T3-10	8526.75	0.860	24.77	2.72	T-3	x	Tor
T3-11	8532.08	0.770	24.69	2.72	T-3		Tor
T3-12	8568.33	1.620	24.24	2.72	T-3		Tor
Gert1-13	12838.90	0.009	11.28	2.68	Gert-1	x	Hidra
Gert1-14	12846.42	0.003	6.85	2.65	Gert-1	x	Hidra
Gert1-15	12854.50	0.005	3.92	2.70	Gert-1		Hidra
Gert1-16	12858.58	0.005	3.7	2.70	Gert-1	x	Hidra
WL1-17	11159.51	0.002	6.32	2.73	West lulu-1	x	Hod
WL1-18	11187.33	0.003	6.68	2.72	West lulu-1		Hod
WL1-19	11213.33	0.004	8.01	2.72	West lulu-1	x	Hod
WL1-20	11246.42	0.003	7.11	2.72	West lulu-1		Hod
Ba2-21	2855.55	0.170	26.9	2.71	Baron-2	x	Ekofisk
Ba2-22	2858.55	0.057	24.69	2.71	Baron-2	x	Ekofisk
Ba2-23	2860.48	0.047	16.68	2.70	Baron-2	x	Ekofisk
Ba2-24	2867.03	0.070	21.87	2.70	Baron-2	x	Ekofisk
I1-25	9504.00	0.056	24.8	2.70	I-1		Sola
I1-26	9508.50	0.075	26.73	2.70	I-1	x	Sola
I1-27	9523.90	0.016	17.43	2.73	I-1		Tuxen
I1-28	9538.50	0.020	16.95	2.72	I-1	Fractured	Tuxen
Ce1B-29	2393.81		12.29	2.71	Cecilie-1B	Fractured	Ekofisk?
Ce1B-30	2402.61	0.011	14.9	2.71	Cecilie-1B	x	Ekofisk?
Ce1B-31	2407.50	0.410	22.36	2.71	Cecilie-1B	x	Ekofisk?
Ce1B-32	2420.76	0.002	7.21	2.71	Cecilie-1B	x	Ekofisk?

A part of each sample was used for preparation of polished thin sections. Another part was used for chemical and physical characterization.

2. – 5. Analytical procedure as preparation for chemistry, X-ray, and BET

Before chemical and physical characterization, each cleaned and dried chalk sample was subjected to the following procedures:

2.1 Crushing of samples

Coarse crushing: c. 5 g of total chalk sample was crushed in agate mortar to size below 2 mm.
Fine grinding: remaining sample was ground in agate ring mortar (SiebTechnik) for 1 min. at 960 rot./min.

BET was measured on coarsely crushed samples.

The finely ground samples were used for:

- Carbonate content
- insoluble residue
- dissolution by 2 M HCl for chemical analysis (Si, Al, K)
- stable isotopes of oxygen and carbon
- X-ray diffraction (bulk)

2.2 Carbonate removal by HCl 2 M (insoluble residue)

c. 0.5 g – 20 g (depends on concentration of carbonate) dry, finely ground sample was weighed (to 2 decimals) directly into plastic centrifugal container, and 50 ml distilled water was added, HCl 2 M was gradually added until all carbonate was dissolved and pH reached 2, and the sample rested overnight. Next the sample was centrifuged at 3000 rot./min., clear fluid was removed, the sample was washed in distilled water until no indication of chloride, and the sample finally was dried to constant weight at 50°C.

After removal of all carbonate the insoluble residue was used for:

- dissolution by LiBO_2 for chemical analysis (Si, Al, K)
- X-ray diffraction (oriented sample) water-saturated – ethylene-glycol saturated at 60°C - heated to 350°C - and to 550°C
- BET

3. Chemical Analysis

Results from the chemical analysis are summarized in Table 2.

3.1 Carbonate content by titration

c. 0.3 g dry, finely ground sample was weighed (to 4 decimals) directly in a conical flask, 175 ml dist. water and 25.00 ml HCl 0.5000M were added together with c. 10 glass balls. Delicate boiling for 20 minutes to remove carbon dioxide totally. After cooling to room temperature, surplus HCl was titrated back with NaOH 0.5M to faint red color by phenolphthalein indicator.

The concentration of NaOH was checked daily.

3.2 LiBO₂ dissolution and AAS analysis of insoluble residue

c. 0.15 g dry, finely ground sample was weighed (to 4 decimals) directly into Pt- crucible and mixed with 1g LiBO₂ + 0.4g H₃BO₃. The crucible was heated slowly to 800°C and complete melting, and temperature was kept for 40 minutes.

After cooling, the melt was heated and transferred to beaker by a mixture of 20 ml dist. water and 10 ml HNO₃ 1:1 until all was dissolved.

The contents of the beaker were moved quantitatively to a 100 ml volumetric flask and distilled water was added to fixed volume.

This solution was used for measurement of Si, Al, K by atomic absorption spectral photometry, Perkin-Elmer model 5000.

4. X-ray diffractometry

X-ray diffractometry was done on bulk chalk sample as well as on the insoluble residue, and a qualitative interpretation was done (Table 3).

4.1 On finely ground sample (bulk)

c. 0.5 g finely ground total chalk sample was placed in a hole in a brass container, the surface of powder was smoothed by glass plate, and X-ray analysis was done. A Philips 1730/10 X-ray diffractometer was used using Cu K- α radiation and automatic divergent slit.

4.2 On insoluble residue

c. 0.03 g ins. residue was pulverized and mixed with 1.5 ml dist. water by a pipette. The suspension was placed on object glass and left to dry overnight, and X-ray analysis was done.

4.3 Glycolation

The sample from 4.2 was glycolated at 60°C for two days in desiccator and X-ray analysis was done.

4.4 Heating

The sample was heated to 350°C and X-ray analysis was done. The sample was subsequently heated to 550°C and X-ray analysis was done.

5. BET (specific surface)

A suitable amount of sample (for chalk: 1g – 2g) was transferred into a BET-tube, which had been dried and weighed dry already.

The sample was subsequently degassed under nitrogen at 70°C for 5 hrs. The tube with the sample was cooled and weighed.

BET was measured by a Micromeritics Instrument, model Gemini III 2375 by using He gas for measurement of free-space multi pointer with nitrogen as adsorbing gas.

Data are listed in Table 2.

Table 2. Laboratory characterization data.

Total sample						Insoluble residue				
Sample ID	BET* m ² /g	$\delta^{13}\text{C}$ ‰	$\delta^{18}\text{O}$ ‰	CaCO ₃ ** wt %	Insoluble residue wt %	BET* m ² /g	SiO ₂ wt %	K ₂ O wt %	Al ₂ O ₃ wt %	total wt %
Q1-1	3.33	0.71	-6.24	84.5	13.1	35.03	64.2	1.2	11.5	76.9
Q1-2	4.37	1.22	-7.23	83.5	15.5	46.48	54.0	2.1	16.7	72.7
Q1-3	3.82	1.14	-5.22	70.2	26.6	12.35	78.8	0.4	3.4	82.5
Q1-4	2.42	1.25	-5.93	78.2	17.6	9.34	79.2	0.3	2.5	82.0
Otto1-6	1.69	2.12	-5.16	95.0	3.2	26.33	59.4	0.9	14.2	74.5
Otto1-8	1.50	2.01	-4.89	97.1	1.4	24.09	61.9	1.0	12.1	75.0
T3-9	1.49	1.77	-5.64	96.7	2.0	40.68	52.1	1.9	14.4	68.4
T3-10	1.52	2.20	-4.21	96.1	2.2	35.52	54.7	1.8	11.7	68.3
Gert1-13	2.65	2.22	-4.57	69.2	28.9	5.61	70.1	0.3	2.6	73.1
Gert1-14	3.05	1.81	-4.49	74.3	22.7	11.30	70.1	0.5	3.3	73.9
Gert1-16	2.94	1.98	-2.89	84.9	12.8	22.00	48.3	2.0	11.3	61.6
WL1-17	2.08	2.30	-3.59	93.3	5.1	31.31	70.5	1.8	12.9	85.3
WL1-19	2.72	2.26	-3.45	92.7	5.9	39.74	65.9	2.4	15.7	84.0
Ba2-21	3.32	1.35	-3.51	83.0	14.4	21.96	78.1	0.7	6.3	85.0
Ba2-22	4.18	1.37	-3.48	78.3	19.3	25.69	74.8	0.9	7.3	83.0
Ba2-23	3.35	0.75	-4.65	70.8	25.6	14.27	80.2	0.4	3.3	83.9
Ba2-24	3.05	1.02	-4.79	79.2	18.1	16.09	76.1	0.4	3.9	80.4
I1-26	4.68	2.75	-3.64	84.7	11.7	24.62	45.5	2.4	22.0	69.9
Ce1B-30	3.00	0.89	-3.87	82.9	14.9	22.89	72.1	0.7	6.3	79.1
Ce1B-31	2.84	1.33	-3.90	90.7	7.2	28.33	68.0	0.9	8.0	76.8
Ce1B-32	2.79	1.39	-4.08	79.1	18.6	12.60	72.8	0.3	2.6	75.8

*multipoint

**by titration

When BET of insoluble residue is multiplied by grain density it can be compared to BET of bulk sample (Figure 2). A linear relationship is found, which indicates that the variation in BET between samples is controlled by content of clay and silica, and that the calcite has a near constant contribution of 1.37 m²/g. This is a significantly lower number than the 1.85 m²/g which was found from the South Arne field samples by Fabricius et al. (2003). The difference is probably caused by more extensive cementation in the present samples, causing the area of calcite exposed to pores to be relatively small.

In accordance with this interpretation, an anomalously high BET of the bulk sample was found for the kaolinite bearing sample from the relatively uncemented Sola Formation of well I-1 (Figure 2).

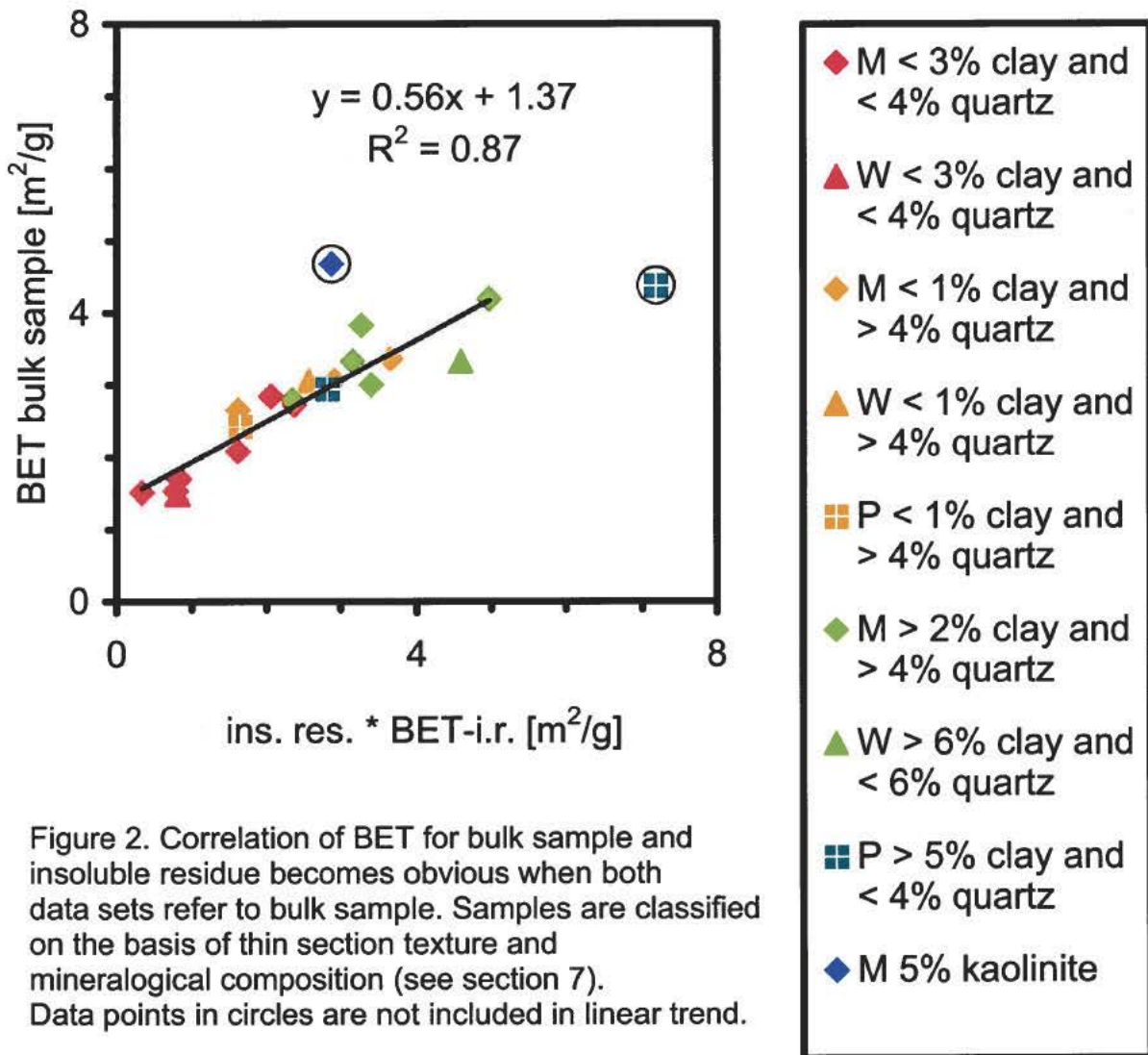


Figure 2. Correlation of BET for bulk sample and insoluble residue becomes obvious when both data sets refer to bulk sample. Samples are classified on the basis of thin section texture and mineralogical composition (see section 7). Data points in circles are not included in linear trend.

6. Backscatter electron microscopy

Backscatter electron microscopy was done on polished epoxy-impregnated and carbon coated samples.

A JEOL 3SM-5900 microscope was used with the following settings: 20kV acceleration voltage, and 10 mm working distance.

The images were sampled as rectangular images at two magnifications: 400 by 300 microns and 40 by 30 microns. On each sample four sets of images were sampled at regular intervals along a vertical line. The 400 by 300 micron images give information of the bulk composition of the sample, whereas the 40 by 30 micron images give information on the fine grained matrix of the typically bi-modally sorted chalk. The images were stored as bitmap files.

Each image is composed of 1280 by 960 square pixels, so that the pixel dimensions are 0.3125 by 0.3125 microns at the low magnification and 0.03125 by 0.03125 microns at the high magnification.

7. Model of mineralogical composition

The mineralogical composition of the samples was modeled based on X-ray diffraction, wet chemical analysis, thin section microscopy, backscatter electron microscopy, and EDAX-data (Table 3). The strategy was as follows:

- 1) Solids dissolvable in 2 M HCl were assumed to be calcite
- 2) All K goes to K-feldspar,
- 3) Remaining Al is distributed among clay-minerals and albite based on X-ray diffraction data.
- 4) Remaining Si in insoluble residue goes to quartz,

Table 3. Mineralogical model.

Sample ID	Texture*	Calcite wt %	Quartz wt %	K-feldspar wt %	Albite wt %	Clay-type**	Clay wt %	Present	Trace	Trace	Total wt %
Q1-1	w	84.47	5.80	0.98		ch-sm	6.58	Fe-calcite	pyrite		97.84
Q1-2	p	83.51	3.75	1.98		ch-sm	10.99	Fe-calcite	pyrite	apatite	100.24
Q1-3	m-w	70.18	19.34	0.64		ch?	3.89		pyrite	TiO ₂	94.04
Q1-4	p	78.21	13.74	0.31	1.94				pyrite	apatite	94.20
Otto1-6	m	95.01	1.14	0.17		ch-il	2.08		pyrite	apatite	98.40
Otto1-8	m	97.05	0.55	0.09	0.08	ch-il	0.69	Dolomite			98.46
T3-9	w	96.69	0.52	0.23		sm-il-ch	1.21		pyrite		98.65
T3-10	m	96.07	0.73	0.25		sm-il-ch	1.06	Dolomite	pyrite		98.11
Gert1-13	m-w	69.15	17.77	0.53	3.29			Fe-calcite		TiO ₂	90.74
Gert1-14	w	74.32	15.09	0.69	3.12					TiO ₂	93.22
Gert1-16	p	84.92	3.22	1.58	0.57	sm-il-ch	5.17			TiO ₂	95.46
WL1-17	m	93.25	1.89	0.59	1.38	sm-il-ch	1.38				98.49
WL1-19	m	92.73	1.46	0.90	1.92	sm-il-ch	1.92	Fe-calcite	TiO ₂	apatite	98.92
Ba2-21	m	82.97	8.91	0.63	1.95	sm-il-ch	1.95				96.42
Ba2-22	m-w	78.33	10.80	1.07	3.03	sm-il-ch	3.03		pyrite		96.26
Ba2-23	m-w	70.84	18.31	0.56	3.66					apatite	93.38
Ba2-24	m	79.15	11.51	0.46	2.77	sm	0.31				94.20
l1-26	m	84.67	1.59	1.74		kaolinite	5.23	sm-il-ch 0.56 wt%			93.80
Ce1B-30	m	82.90	9.10	0.63		sm	4.11		pyrite	apatite	96.74
Ce1B-31	m	90.73	3.81	0.40	0.25	sm	2.25		TiO ₂	apatite	97.45
Ce1B-32	m	79.11	12.72	0.33			2.14	Fe-calcite			94.30

* from thin sections, p: packstone, w: wackestone, m: mudstone, Dunham (1962).

** clay type, ch: chlorite, sm: smectite, il: illite

8. Image analysis

The scanning procedure leaves the images skewly illuminated in the left right direction. This skewness is barely visible with the unaided eye. The skewness was removed by a mat-lab routine kindly provided by Keld Dueholm, IMM, DTU.

Image analysis was done by the free software UTHSCSA Image Tool (Table 4). The procedure was as follows: On the 400 by 300 micron images the amounts of large porosity and of large grains were assessed from the grey level distribution of the image after applying a 9 by 9 averaging filter three times. Large porosity, ϕ_{large} , and large grains, G_{large} , were chosen so that they have a diameter of above c. 5 microns in cross section.

From large porosity and large grain content together with insoluble residue, $G_{\text{i.r.}}$, and He-porosity, small grains, G_{small} , small porosity, ϕ_{small} , and matrix porosity, ϕ_{matrix} , were calculated under assumption of grain density of insoluble residue equal to grain density of bulk sample. This is not strictly true, but has insignificant influence on resulting image analysis data. From the same data, matrix calcite content, C_{matrix} , was calculated.

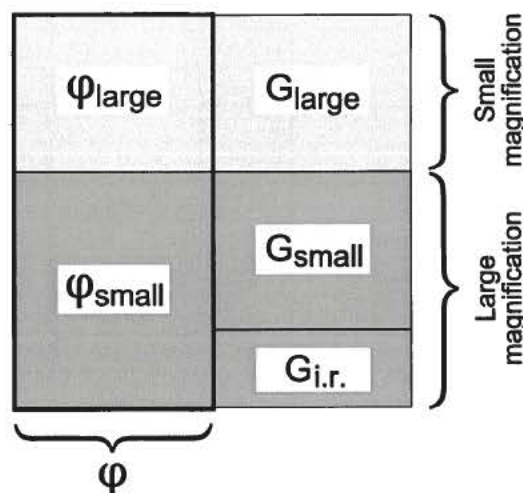


Figure 3. Schematic representation of chalk composition. The light grey components (large porosity, ϕ_{large} , and large grains, G_{large}) are measured by image analysis of 300 by 400 micron backscatter electron images. The dark grey components are seen at high magnification backscatter electron images (30 by 40 microns). (Røgen et al. 2001).

The 40 by 30 micron images were used for measuring the specific circumference, S_{par} of the calcite crystals composing the nannofossils and fossil debris. In order to smooth away the noise at pore-crystal interfaces, the images were first smoothed by applying a 9 by 9 averaging filter one time. The calcite phase was then selected as one grey level with an eye on the matrix calcite content calculated above, and the remaining image as another grey level. This binary image was then used for measuring the specific circumference of the calcite crystals by applying a 3 by 3 cross filter according the procedure of Borre et al. (1997). Specific circumference with respect to bulk area, S , and specific circumference with respect to pores, S_{ϕ} , was calculated from S_{par} and the matrix calcite content.

Table 4. Image analysis data.

Sample ID	Core analysis data		Image analysis data, 300 by 400 microns							Image analysis data, 30 by 40 microns			
	He-por	G _{l.r.}	Φ _{large}	G _{large}	G _{small}	Φ _{small}	Φ _{matrix}	C _{matrix}	C _{matrix}	S	S _g	S _{par}	
	%	%	%	%	%	%	%	%	%	1/my	1/my	1/my	
Q1-1	14.45	13.29	2.3	15.1	57.2	12.2	17.5	69.2	68.6	0.94	2.99	1.37	
st.dev.			1.6	3.7	3.7	1.6	1.7	1.4	1.4	0.07	0.17	0.12	
Q1-2	8.88	15.03	1.4	52.2	23.9	7.5	24.3	51.1	51.3	0.96	2.00	1.88	
st.dev.			0.3	4.5	4.5	0.3	3.4	4.9	5.4	0.11	0.39	0.22	
Q1-3	15.11	25.31	0.4	6.2	53.4	14.7	21.6	57.2	57.0	1.22	2.83	2.14	
st.dev.			0.1	1.5	1.5	0.1	0.5	0.7	0.9	0.11	0.26	0.19	
Q1-4	9.4	19.74	1.3	30.6	40.2	8.1	16.9	58.9	60.4	0.86	2.18	1.43	
st.dev.			0.6	5.5	5.5	0.6	1.7	3.1	3.6	0.14	0.38	0.25	
Otto1-6	19.78	4.00	0.7	7.6	68.6	19.1	21.8	74.8	75.0	0.82	3.27	1.09	
st.dev.			0.1	3.4	3.4	0.1	0.9	1.0	1.1	0.03	0.06	0.06	
Otto1-8	20.74	2.34	1.5	5.0	71.9	19.2	21.1	76.9	76.9	0.77	3.35	1.01	
st.dev.			1.0	3.4	3.4	1.0	1.5	1.5	1.5	0.03	0.13	0.05	
T3-9	19.1	2.68	0.3	3.1	75.1	18.8	20.0	77.8	77.8	0.76	3.44	0.98	
st.dev.			0.1	2.3	2.3	0.1	0.5	0.6	0.4	0.05	0.18	0.06	
T3-10	24.8	2.96	0.5	5.1	67.2	24.3	26.6	71.1	70.9	0.95	3.26	1.34	
st.dev.			0.2	3.6	3.6	0.2	1.1	1.2	1.1	0.06	0.11	0.10	
Gert1-13	11.58	27.28	0.3	11.8	49.3	11.3	18.8	56.0	56.1	1.01	2.30	1.80	
st.dev.			0.1	4.9	4.9	0.1	1.6	2.5	2.5	0.09	0.26	0.16	
Gert1-14	6.99	23.88	0.2	22.6	46.5	6.7	12.8	60.1	60.4	0.96	2.46	1.60	
st.dev.			0.2	7.0	7.0	0.2	1.8	3.7	3.8	0.05	0.35	0.03	
Gert1-16	5.19	14.30	1.0	69.6	10.9	4.2	31.0	35.4	68.0	0.83	2.80	1.37	
st.dev.			0.5	5.5	5.5	0.5	11.5	12.2	16.7	0.25	0.63	0.82	
WL1-17	6.41	6.32	0.1	5.5	81.8	6.3	7.1	86.6	86.6	0.65	4.82	0.75	
st.dev.			0.0	1.8	1.8	0.0	0.2	0.3	0.3	0.03	0.20	0.04	
WL1-19	8.12	6.68	0.1	5.3	79.9	8.0	9.1	84.5	84.5	0.74	4.78	0.88	
st.dev.			0.0	3.3	3.3	0.0	0.3	0.5	0.5	0.03	0.21	0.03	
Ba2-21	24.31	12.89	1.5	7.4	55.4	22.8	29.2	60.8	60.7	1.22	3.09	2.01	
st.dev.			0.8	1.4	1.4	0.8	0.9	0.8	0.7	0.13	0.33	0.23	
Ba2-22	24.3	16.40	4.1	10.1	49.2	20.2	29.2	57.3	57.1	1.32	3.09	2.31	
st.dev.			1.6	5.1	5.1	1.6	3.5	3.4	3.7	0.08	0.36	0.16	
Ba2-23	17.7	24.00	6.8	11.5	46.8	10.9	18.9	57.2	57.2	1.10	2.58	1.93	
st.dev.			0.9	4.2	4.2	0.9	2.6	2.7	2.5	0.05	0.23	0.09	
Ba2-24	22.31	16.20	4.4	9.9	51.6	17.9	25.8	60.1	60.3	1.10	2.78	1.83	
st.dev.			0.8	2.9	2.9	0.8	0.9	1.1	1.1	0.09	0.27	0.14	
I1-26	28.12	11.02	0.8	2.0	58.8	27.4	31.7	60.5	60.7	1.25	3.18	2.06	
st.dev.			0.4	0.9	0.9	0.4	0.5	0.5	0.6	0.18	0.43	0.31	
Ce1B-30	15.38	14.47	1.9	5.5	64.7	13.4	17.2	69.8	70.1	1.03	3.45	1.47	
st.dev.			0.9	2.7	2.7	0.9	1.3	1.3	1.1	0.06	0.26	0.09	
Ce1B-31	22.57	7.18	1.1	3.9	66.3	21.5	24.5	69.8	69.9	1.17	3.88	1.67	
st.dev.			0.4	1.1	1.1	0.4	0.5	0.5	0.3	0.07	0.23	0.11	
Ce1B-32	6.69	19.49	2.4	32.1	41.7	4.3	9.1	63.6	63.8	0.80	2.22	1.26	
st.dev.			2.3	3.8	3.8	2.3	4.7	2.2	2.6	0.06	0.05	0.14	

9. Combined textural-mineralogical model, iso-frame

Based on mineralogical, textural and image analysis data a combined textural-mineralogical model can be defined by using an iso-frame concept (Fabricius, 2003, Figure 4, Table 5). Large grains as measured by image analysis were assumed to be part of the supporting frame. Fine-grained silicates observed by petrography to be non-supporting were defined as in suspension. The remaining solids were assigned to be part of the frame or the suspension, so as to match core analysis data on P-wave, M and Shear-moduli, G (Olsen, 2004).

$$M = \rho v_p^2 \quad \text{and} \quad G = \rho v_s^2,$$

where ρ is bulk density and v_p and v_s are P-wave- respectively shear-wave velocities. All data were modeled by using a Modified Hashin Shtrikman model for a multi-component system as formulated by Berryman (1995, as cited in Mavko et al. 1998) and Fabricius (in review). A critical porosity of 70% was assumed.

Table 5. Composition modeled from wet data shear modulus. Air content is modeled from P-wave modulus and shear-model.

	Frame						suspension				IF
	air	water	calcite	quartz	feldspar	kaolinite	calcite	quartz	kaolinite	smectite	
	(%)	(%)	(%)	(%)	(%)	(%)	(%)	(%)	(%)	(%)	
Q1-1	0.0002	14.45	49.51	1.52	0.91	0.00	24.62	3.69	0.00	5.59	0.61
Q1-2	0.0002*	8.88	50.20	0.83	1.92	0.00	25.99	2.67	0.00	9.71	0.58
Q1-3	0.0002**	15.11	49.42	13.51	0.61	0.00	13.70	4.28	0.00	3.38	0.75
Q1-4	0.0002	9.40	65.51	10.57	2.24	0.00	9.71	2.94	0.00	0.00	0.86
Otto1-6	0.0022	19.78	61.91	0.74	0.15	0.00	15.83	0.22	0.00	1.65	0.78
Otto1-8	0.0016	20.74	62.12	0.36	0.14	0.00	16.29	0.10	0.00	0.54	0.79
T3-9	0.0015	19.10	58.36	0.31	0.20	0.00	21.23	0.12	0.00	0.96	0.73
T3-10	0.0008	24.80	49.93	0.37	0.21	0.00	23.98	0.20	0.00	0.79	0.57
Gert1-13	0.0095	11.57	59.47	15.22	3.82	0.00	7.17	2.29	0.00	0.00	0.89
Gert1-14	0.0005*	6.99	67.78	6.81	3.86	0.00	4.73	8.24	0.00	0.00	0.86
Gert1-16	0.0005*	5.19	70.57	1.46	2.24	0.00	13.46	1.79	0.00	4.95	0.79
WL1-17	0.0004	6.41	84.50	1.75	1.97	0.00	4.77	0.11	0.00	1.28	0.93
WL1-19	0.0013	8.12	79.66	1.27	2.73	0.00	6.79	0.12	0.00	1.73	0.91
Ba2-21	0.0009	24.31	41.59	2.12	2.11	0.00	23.54	5.04	0.00	1.48	0.60
Ba2-22	0.0004	24.30	36.75	4.50	3.35	0.00	24.85	8.53	0.00	2.31	0.59
Ba2-23	0.0025	17.70	56.60	7.31	3.85	0.00	5.61	9.13	0.00	0.00	0.82
Ba2-24	0.0009	22.31	48.05	3.35	2.75	0.00	16.99	6.33	0.00	0.24	0.70
I1-26	0.0032	28.12	39.01	1.24	1.40	2.43	25.64	0.00	1.69	0.41	0.61
Ce1B-31	0.0008	22.57	52.99	1.11	0.54	0.00	19.11	1.98	0.00	1.73	0.71
Ce1B-32	0.0002	6.69	67.67	4.96	0.35	0.00	10.61	7.91	0.00	2.05	0.78

* No shear data, air content estimated from comparison with similar samples.

** Modeled by assuming quartz to provide maximal mineral shear modulus.

For this model the mineral phase with the highest bulk modulus ($K = M - 4/3G$) and the highest shear modulus must be chosen. Feldspar has the highest bulk modulus (Table 6), but is sparse, so calcite was in all cases chosen to represent the phase with the highest bulk modulus. The choice of the phase representing the highest shear modulus was more difficult, because quartz has the highest shear modulus and in several samples has a significant contribution to the supporting frame, but at the same time calcite is the dominating phase. For each sample, both possibilities were tested to see where the best match could be found between modeling based on water saturated shear wave modulus and modeling based on water saturated P-wave modulus. In only one case quartz was chosen to be the dominating phase with respect to shear modulus.

Table 6. Elastic moduli of components.

	P-wave modulus M	Shear modulus G	Bulk modulus K	
	(GPa)	(GPa)	(GPa)	
calcite	111.3	30.4	70.8	Citations in Mavko, Mukerji, and Dvorkin, 1998, p. 307-308.
quartz	97.0	44.8	37.3	Citations in Mavko, Mukerji, and Dvorkin, 1998, p. 307-308.
feldspar	109.7	25.6	75.6	Citations in Mavko, Mukerji, and Dvorkin, 1998, p. 307-308
kaolinite	42.1	10.5	28.1	*Tröger, W.E. (1971) Optische Bestimmung der gesteinsbildenden Minerale.
smectite	43.0	10.8	28.7	*Tröger, W.E. (1971) Optische Bestimmung der gesteinsbildenden Minerale.
air	0.00014		0.00014	Calculated from data in CRC Handbook of Chemistry and Physics, 1986.
equilibrated tap water	2.22		2.22	Calculated from citations in Mavko, Mukerji, and Dvorkin, 1998.

Modeling of water saturated P-wave modulus is dependent of possible residual air saturation, so water saturated shear modulus was chosen as the basis for defining the IF-value, indicating to which extent the solid phase may be imagined as in the supporting frame of the sediment. In order to model water saturated P-wave modulus, air-saturation was subsequently modeled so as to match P-wave and shear-data. In every case the modeled air-saturation was below the detection limit reported by Olsen (2004) (Table 5). When water saturated P-wave modulus is modeled under assumption of 100% water saturation, IF values are lowered by 0.01 to 0.07 (Table 7). IF modeled on the basis of dry P-wave modulus tend to match the IF based on wet data, whereas IF based on dry shear moduli tend to be higher by up to around 0.1 (Table 7, Figure 5).

IF values tend to increase with depth, and as might be expected IF tends to be relatively high for well sorted (mudstone) textures and relatively low for poorly sorted (clay rich) textures (Figure 6).

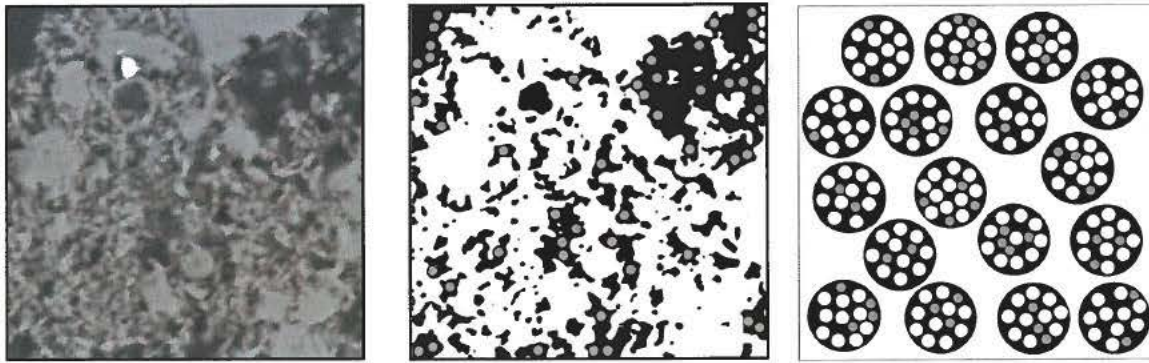


Figure 4. Iso-frame (IF) model for chalk. (a) Chalk mudstone with 28.1% porosity. Of the bulk volume 5.9% is fine grained silicates. (b) By petrographic image analysis the fine-grained calcite (including a pyrite crystal) is marked as white and the pore space as black. The fine grained silicates are symbolized by grey circles. The specific perimeter of the white phase is calculated to be 2.9 micron^{-1} . From correlation with elastic data, this specific perimeter corresponds to an IF value of 0.65 for the fine-grained calcite. When taking large pores and grains (not visible at this magnification) and fine-grained silicates into account, we obtain an IF value of 0.6 for the sample. (c) Model: of the solid phase 70% is forming a frame with spherical pores. The remaining solids are suspended in the fluid within the pores.

Table 7. Isoframe models based on different data sets.

	Wet samples		Dry samples		IF dry-G	IF dry-M	IF wet (G)	IF wet-M, no air
	air	water	air	water				
	(%)	(%)	(%)	(%)				
	modeled		measured					
Q1-1	0.0002	14.45	13.51	0.94	0.78	0.68	0.61	0.59
Q1-2	0.0002	8.88	7.67	1.21	0.75	0.61	0.58	0.54
Q1-3	0.0002	15.11	14.35	0.76	0.81	0.78	0.75	0.74
Q1-4	0.0002	9.40	8.99	0.41	0.91	0.87	0.86	0.85
Otto1-6	0.0022	19.78	19.64	0.14	0.82	0.73	0.78	0.74
Otto1-8	0.0016	20.74	20.62	0.12	0.82	0.75	0.79	0.75
T3-9	0.0015	19.10	18.97	0.13	0.78	0.70	0.73	0.68
T3-10	0.0008	24.80	24.70	0.10	0.72	0.65	0.67	0.64
Gert1-13	0.0095	11.57	11.16	0.42	0.92	0.88	0.89	0.86
Gert1-14	0.0005	6.99	6.21	0.78	0.93	0.86	0.86	0.84
Gert1-16	0.0005	5.19	4.22	0.97	0.85	0.78	0.79	0.74
WL1-17	0.0004	6.41	6.03	0.38	0.97	0.94	0.93	0.92
WL1-19	0.0013	8.12	7.67	0.45	0.95	0.90	0.91	0.89
Ba2-21	0.0009	24.31	23.92	0.39	0.70	0.64	0.60	0.57
Ba2-22	0.0004	24.30	23.72	0.58	0.71	0.62	0.59	0.56
Ba2-23	0.0025	17.70	17.10	0.60	0.88	0.82	0.82	0.78
Ba2-24	0.0009	22.31	21.60	0.71	0.77	0.69	0.70	0.66
I1-26	0.0032	28.12	27.53	0.59	0.74	0.58	0.61	0.54
Ce1B-31	0.0008	22.57	22.57	0.00	0.79	0.72	0.71	0.68
Ce1B-32	0.0002	6.69	5.74	0.95	0.86	0.82	0.78	0.76

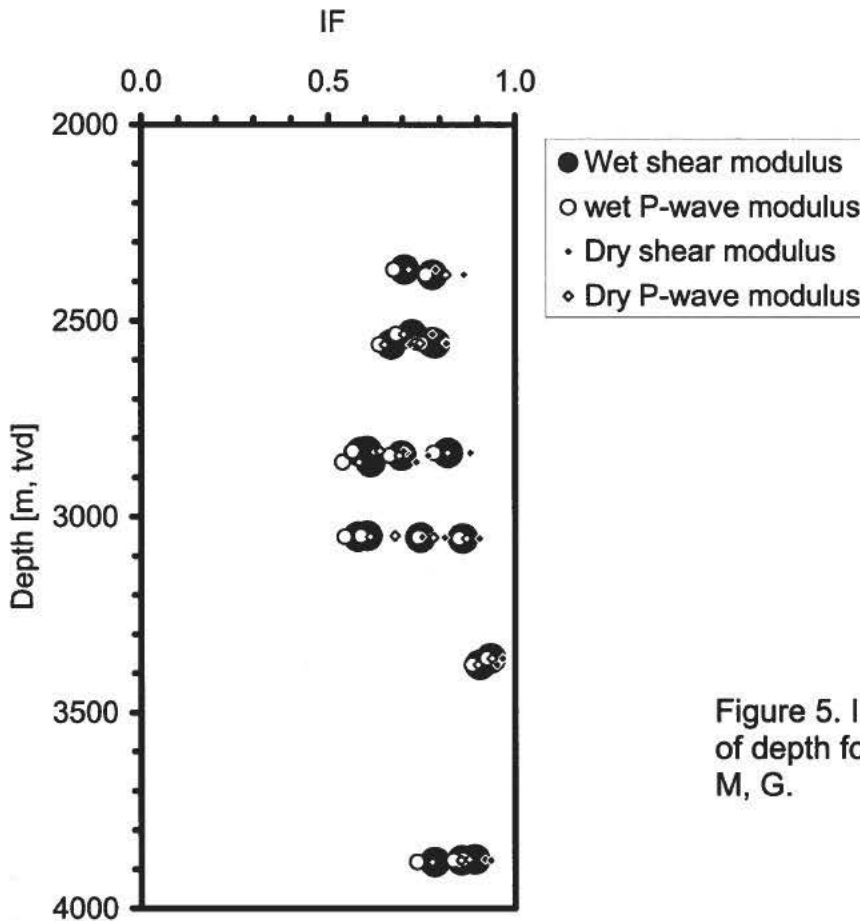


Figure 5. IF values as function of depth for dry M, G, and wet M, G.

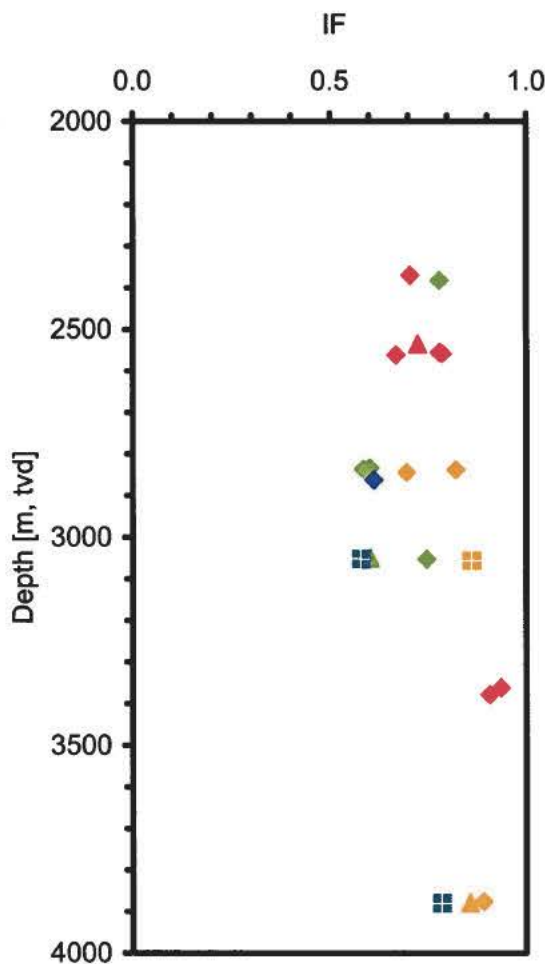


Figure 6. IF values calculated from water saturated core data. IF values tend to increase with depth and to be relatively high for well sorted (mudstone) texture and to be low for clay-bearing samples. (For legend see Figure 2).

10. Effect on elastic properties of texture and mineralogy, including South Arne data.

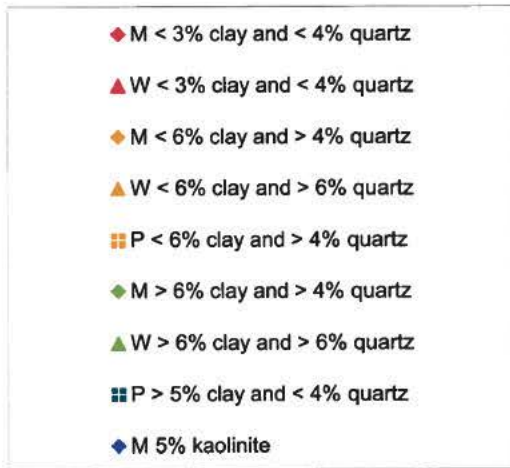
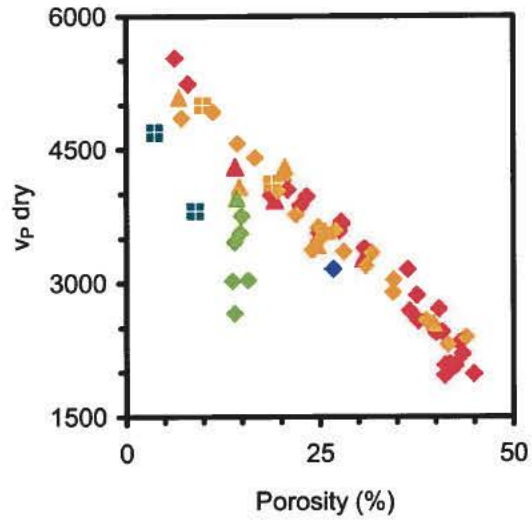
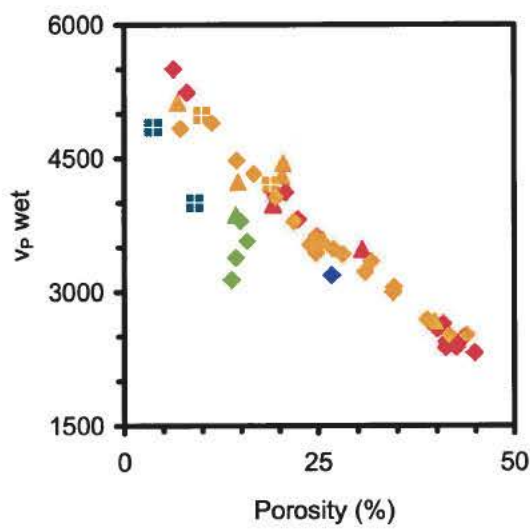


Figure 7. P-wave velocity for water saturated and for dry samples. Data from South Arne field from the earlier rock physics projects are included. Please observe that legend is different from that of Figure 2 and 7.

Porosity and elasticity is controlled by texture and mineralogy in different ways. Whereas porosity is primarily controlled by texture, acoustic velocity is controlled by porosity and mineralogy. Poorly sorted textures

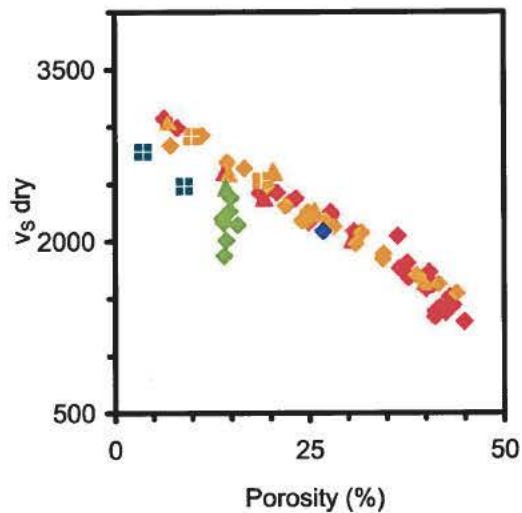
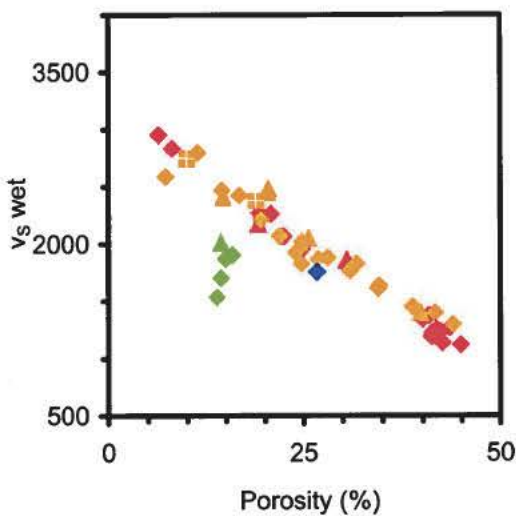


Figure 8. Comparison of v_s vs. porosity for dry and for water saturated samples. For legend please see Figure 7.

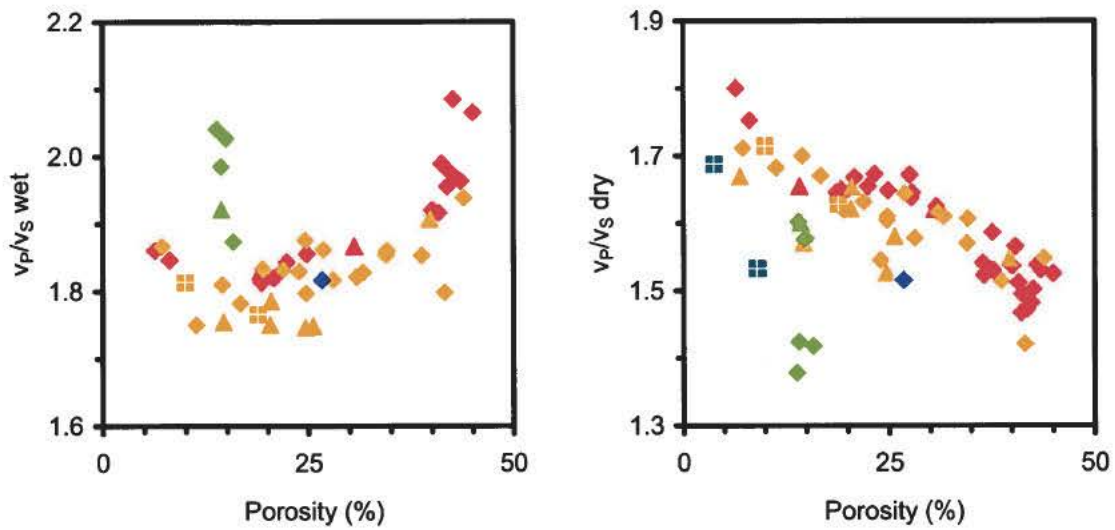


Figure 9. Comparison of v_p/v_s ratio vs. porosity for dry and for water saturated samples. For legend please see Figure 7.

(wackestone and packstone –especially clay-bearing) tend to have low porosity, whereas well sorted textures (mudstone) tend to have high porosity (Figure 7, we have included existing data from the South Arne field (Japsen et al., 2001 and Japsen et al., 2003)).

Quartz-rich samples fall slightly below calcite-rich samples on the P-wave-velocity v_p – porosity trend (Figure 7), for wet as well as dry samples; and quartz rich samples fall slightly above the calcite rich samples in the v_s -porosity trends (Figure 8). This mineralogical effect is enhanced in v_p/v_s plots (Figure 9).

The extremely clay rich samples are clay-supported samples from the top layers of the South Arne field (Fabricius et al. in review). For a given porosity they tend to have low v_p and v_s for wet and for dry samples (Figure 7, 8). But the clay effect is not equal resulting in high v_p/v_s for wet samples and low v_p/v_s for dry samples (Figure 9).

Similar to v_p/v_s , Poisson’s ratio for water saturated samples exhibit relatively high values for low and for high porosities (or low and high acoustic impedance) in accordance with the observation of Gommesen et al. (2003).

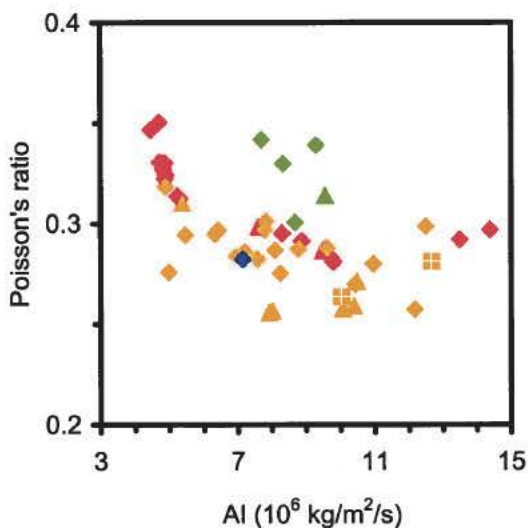


Figure 10. Poisson’s ratio, ν , versus acoustic impedance, AI, for water saturated samples. $\nu = (v_p^2 - 2v_s^2)/2(v_p^2 - v_s^2)$. $AI = \rho v_p$. For legend please see Figure 7.

11. Cementation vs. depth and stress curves

One of the purposes of the present project was to discuss which burial-related factor controls the elastic properties of the rock: temperature or effective stress. By assuming a generally uniform geothermal gradient, we use depth as a proxy for temperature, whereas effective vertical stress, σ' , was calculated from Terzhagi's equation:

$$\sigma' = \sigma - \beta P$$

where the total overburden stress, σ , was estimated by assuming an average overburden bulk density, ρ , of 2000 kg/m³ and an acceleration of gravity, g , of 10 m/s²:

$$\sigma = \text{depth } \rho g$$

The pore pressure, P , was obtained from well test data (P. Japsen, personnel communication) and the factor describing the effectiveness of the pore pressure, β . β has 1 as its upper bound, whereas its lower bound may be approximated by Biot's coefficient:

$$\beta = 1 - K_{\text{dry}}/K_0$$

where K_{dry} is bulk modulus of the dry sample, and K_0 is bulk modulus of solid phase, in this case assumed to be calcite: $K_0 = 71$ MPa. Biot's coefficient is near 1 at shallow depth, but in the studied depth interval it reaches values as low as 0.3 (Figure 11). When β is plotted versus effective vertical stress calculated using Biot's coefficient, it declines with stress along a trend independent of texture and mineralogy (Figure 11).

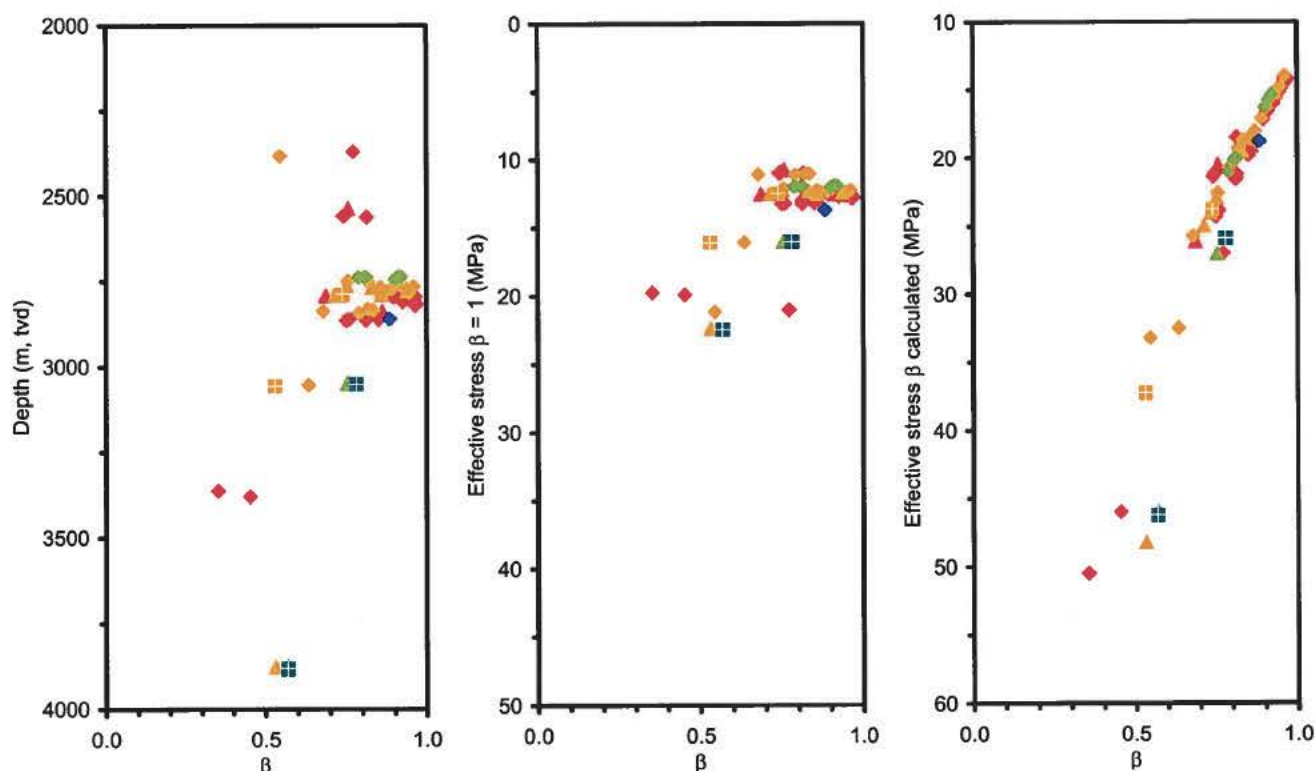


Figure 11. Biot's coefficient, β , as a function of vertical depth, and as function of vertical effective stress. For legend see Figure 7.

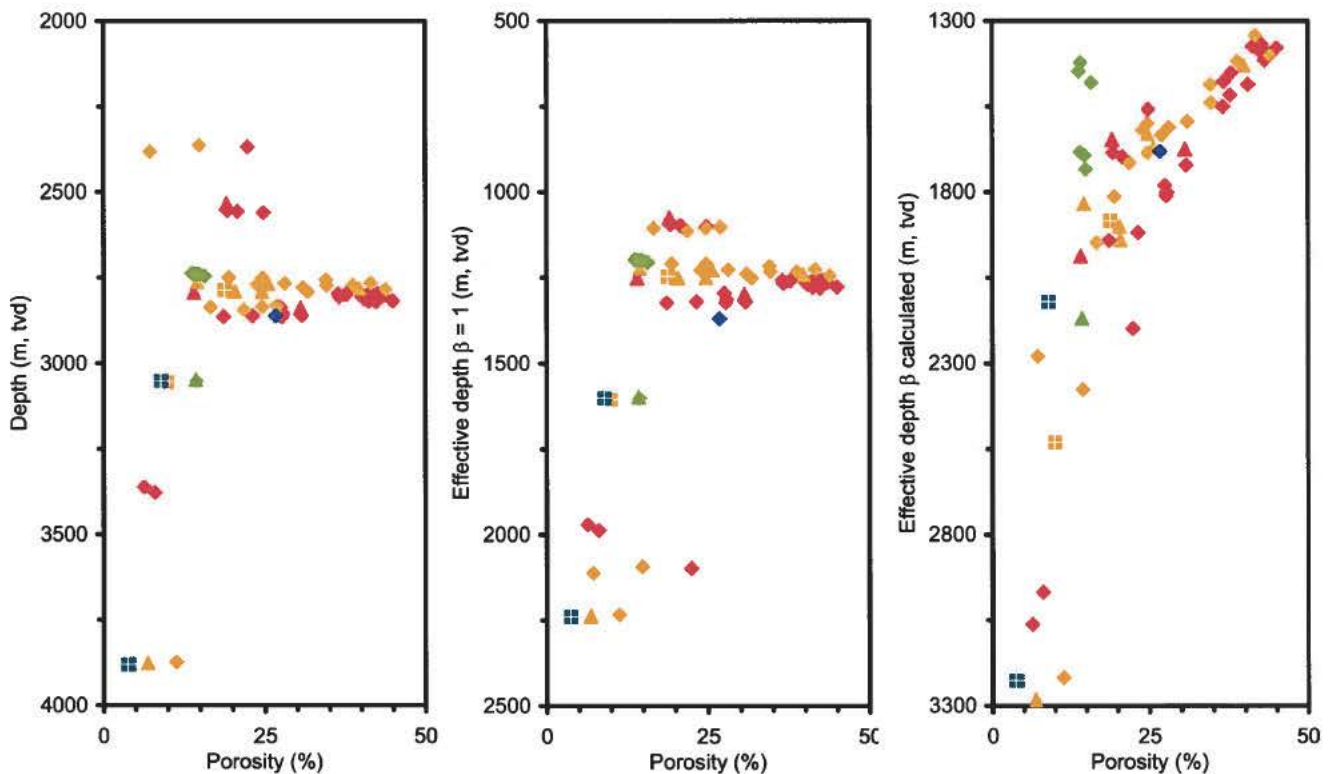


Figure 12. Porosity as a function of vertical depth, and as function of vertical effective stress. For legend see Figure 7.

We find that porosity is more clearly related to effective stress than to burial depth (Figure 12), but clay-bearing poorly sorted lithologies tend to have relatively low porosity for a given effective stress, and the well sorted, calcite rich lithologies tend to have relatively high porosity for a given effective stress (Figure 12). The degree of cementation may be estimated from the following parameters: the iso-frame value, IF, and the ratio of stable oxygen isotopes, $\delta^{18}\text{O}$. IF is supposed to increase with cementation, $\delta^{18}\text{O}$ to decrease. Neither exhibit a clear depth trend (Figures 13, 14), but versus effective vertical stress calculated by using Biot's coefficient, $\delta^{18}\text{O}$ decreases until an effective stress of 22 MPa and IF increases monotonously in the entire depth interval (Figures 13, 14). Clay rich and poorly sorted lithologies have relatively low IF (Figure 13).

When turning to classical acoustic properties, we find that the acoustic impedance for wet samples overall increases with depth, but that the margin of variation is large, especially for samples from the reservoir section of the South Arne field around 2800 m TVD (Figure 15). When AI is plotted versus vertical effective stress. The data seem to fall along two linear trends: one for samples under less than 22 MPa effective stress, one for samples under effective stress of more than 22 MPa (Figure 15). Data from the reservoir section do not stand out as anomalous when plotted against vertical effective stress.

Poisson's ratio for dry samples tends to increase with vertical effective stress (Figure 16): Clay-bearing and poorly sorted lithologies tend to have low values. For water saturated samples, Poisson's ratio decreases with depth. Clay rich samples tend to have high values (Figure 16).

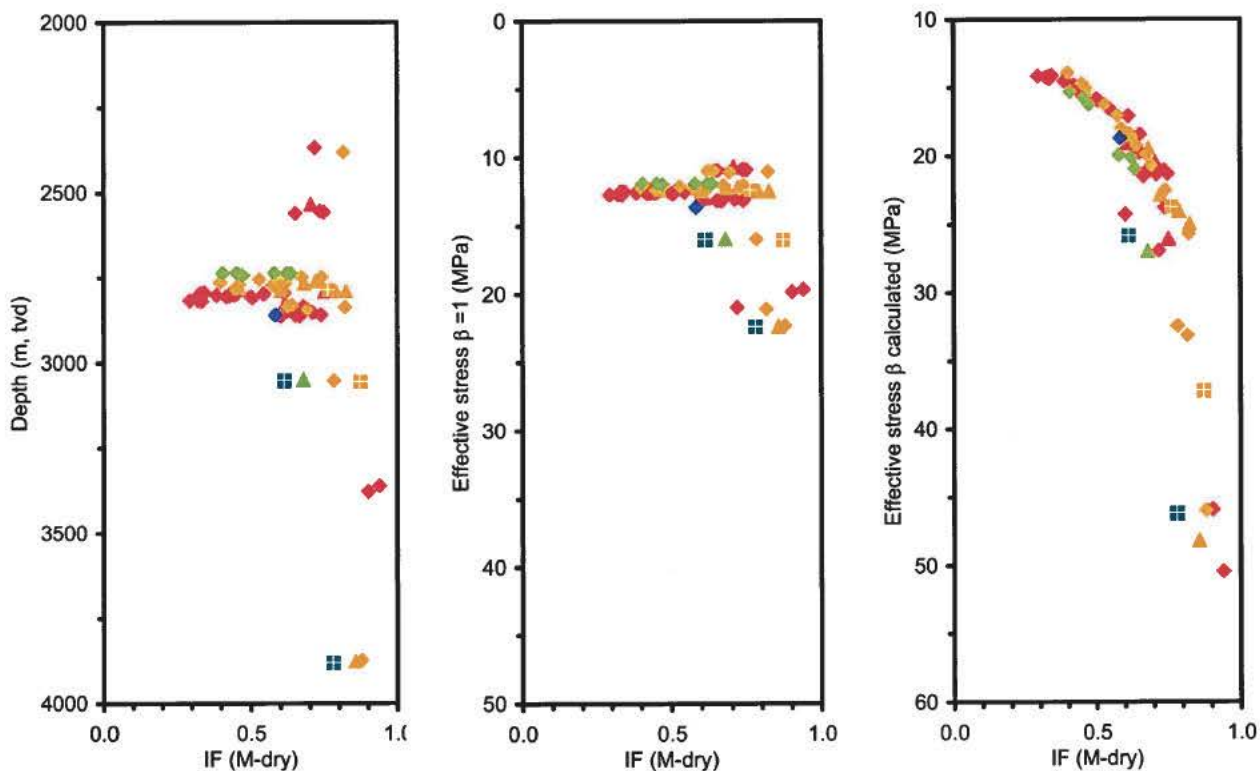


Figure 13. Iso-frame value, IF, as a function of vertical depth, and as function of vertical effective stress. For legend see Figure 7.

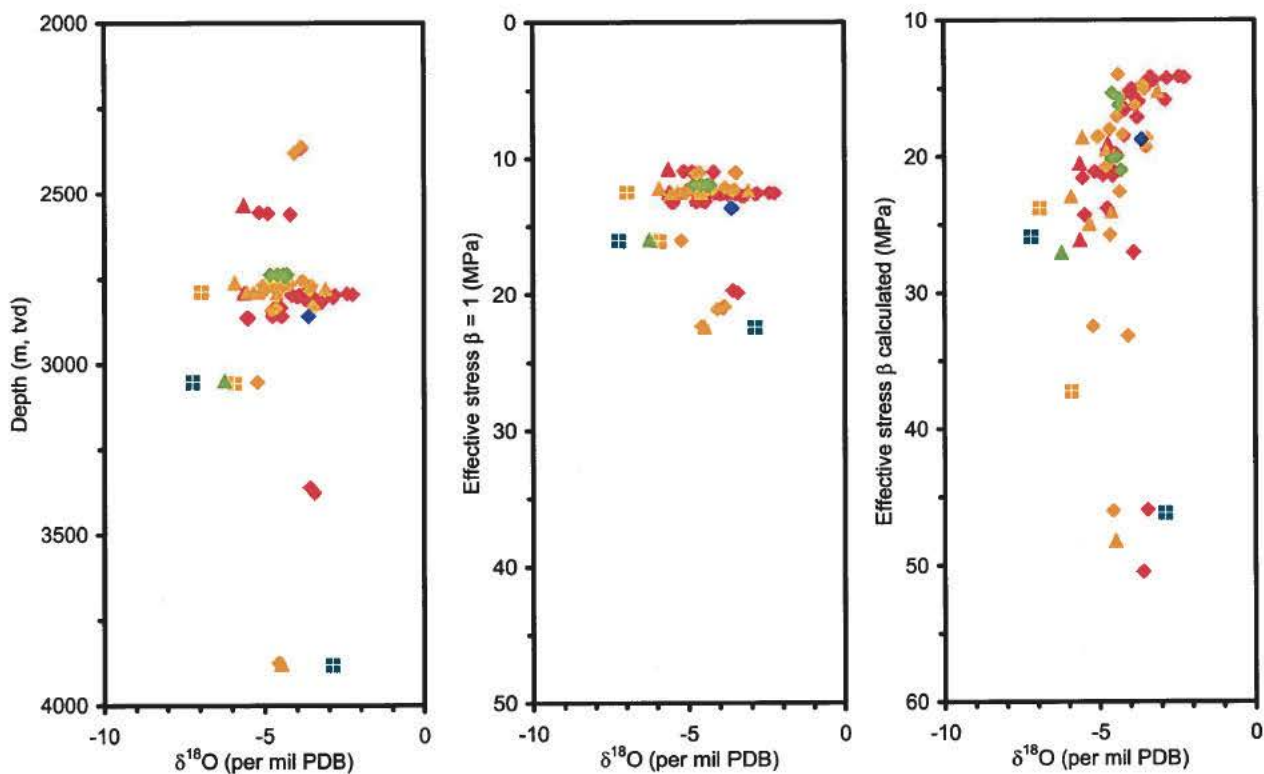


Figure 14. The ratio of stable oxygen isotopes, $\delta^{18}\text{O}$, as a function of vertical depth, and as function of vertical effective stress. For legend see Figure 7.

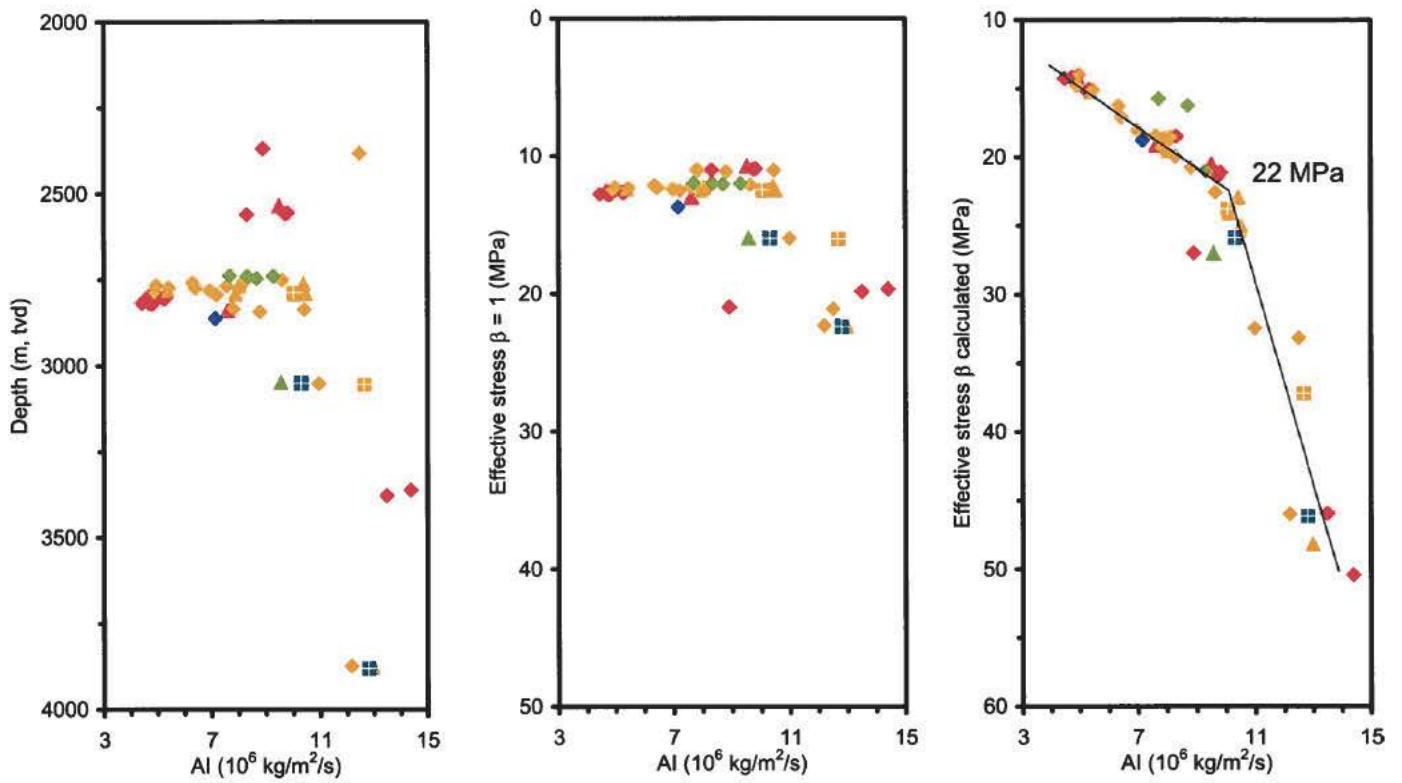


Figure 15. Acoustic impedance for wet samples, $AI = \rho v_p$, as a function of vertical depth, and as function of vertical effective stress. For legend see Figure 7.

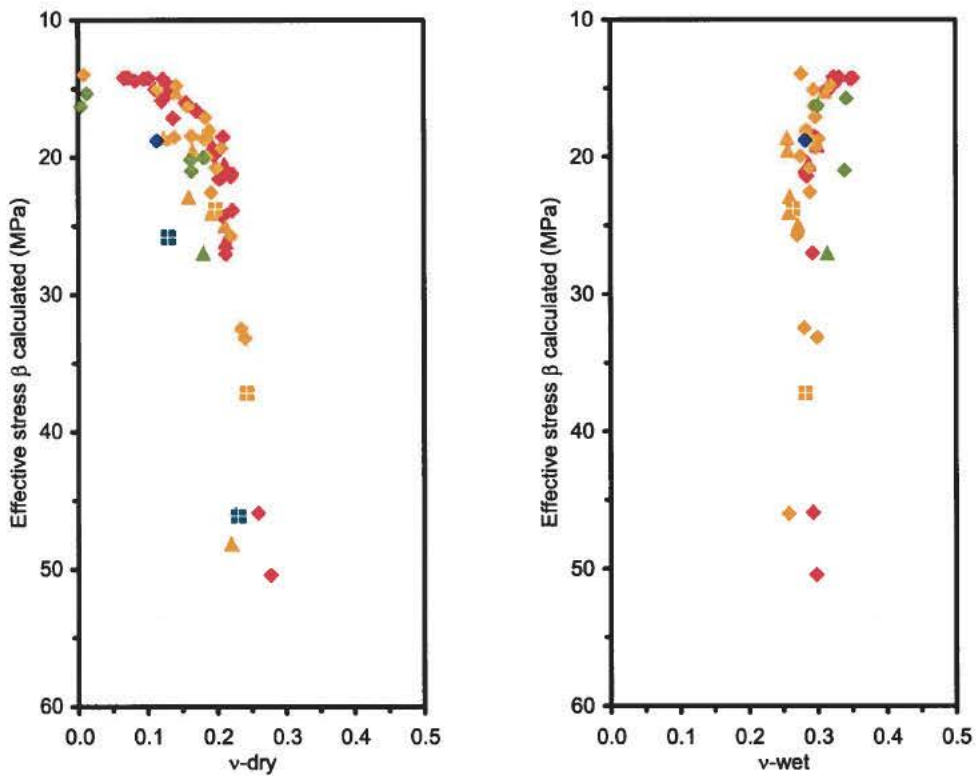


Figure 16. Poisson's ratio for dry and for wet samples versus vertical effective depth. For legend see Figure 7.

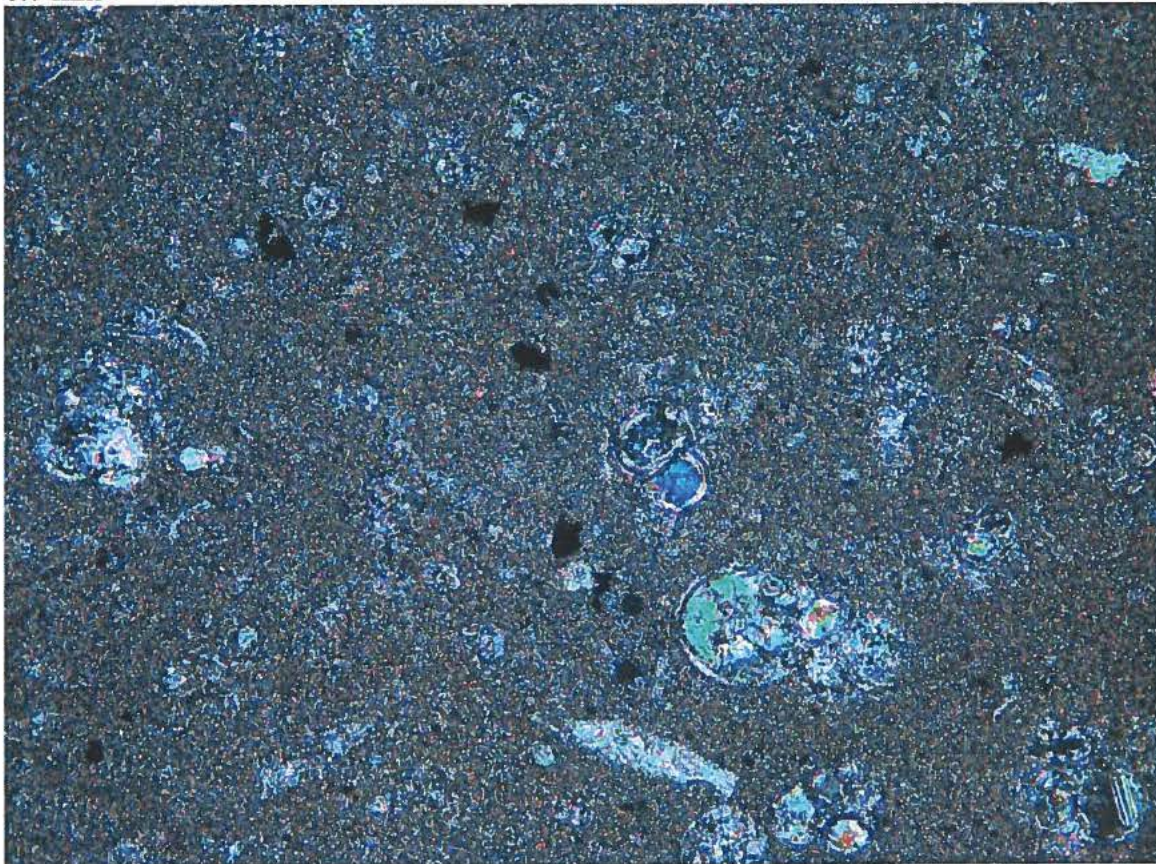
12. References

- Borre, M., Lind, I. L., and Mortensen, J. 1997: Specific surface as a measure of Burial Diagenesis of Chalk. *Zbl. Geol. Paläont. Teil 1 1995*, 1071-1078.
- Dunham, R. J. 1962: Classification of carbonate rocks according to depositional texture. In: Ham, W. E. (ed.) *Classification of Carbonate Rocks*. American Association of Petroleum Geologists Memoir, 1, 108-123.
- Fabricius I.L. 2003: How burial diagenesis of chalk sediments controls sonic velocity and porosity: *AAPG Bulletin* 87, 1755-1778.
- Fabricius, I.L., Høier, C., Japsen, P., & Korsbech, U.: Modelling elastic properties of impure chalk from the South Arne field, North Sea. submitted to *Geophysical Prospecting*.
- Fabricius, I. L., Nguyen, S. H. & Korsbech, U. 2003: Sample characterization report. EFP 2001 rock physics of impure chalk. In: Japsen, P., Bruun, A., Fabricius, I. L., Høier, C., Mavko, G., Mogensen, C., Pedersen, J. M., Rasmussen, R. & Vejrbæk, O. V. (eds.), EFP-01 Rock Physics of Impure Chalks. Final report. ENS J. nr. 1313/01-0006, Geological Survey of Denmark and Greenland, GEUS, Copenhagen (Confidential).
- Fabricius, I. L. and Springer, N. 2003: Selection of samples Chalk Background Velocity; E&R DTU and GEUS Core Laboratory 25-10-2003.
- Gommesen, L, Fabricius, I.L., Pedersen, J.M. 2003: Elastic behaviour of North Sea Chalk 65th EAGE Conference and Exhibition, 2-5 June 2003, Stavanger, Paper C-11, CD-ROM, 4 pages.
- Japsen, P., Espersen, T.B., Fabricius, I., Gommesen, L., Høier, C., Mavko, G., Nielsen E.B., Pedersen, J. M., Røgen, B., Stentoft, N., Wagner, H., Zhu, D. 2001: EFP-98 Rock Physics of Chalk: Final report to the Danish Energy Agency, GEUS (Confidential).
- Japsen, P., Bruun, A., Fabricius, I. L., Høier, C., Mavko, G., Mogensen, C., Pedersen, J. M., Rasmussen, R. & Vejrbæk, O. V., 2003: EFP-01 Rock Physics of Impure Chalks. Final report. Geological Survey of Denmark and Greenland, GEUS, Copenhagen (Confidential), ENS J. nr. 1313/01-0006.
- Olsen, D, 2004: Special Core Analysis fro Chalk Background Velocity Project. Ultrasonic velocity measurements on plug samples of chalk from the wells Q-1, Otto-1, T-3, Gert-1, West Lulu-1, Baron-2, I-1, and Cecilie-1B. GEUS Report 2004/106.
- Mavko G., Mukerji T. & Dvorkin, J. 1998: *The Rock Physics Handbook*: Cambridge University Press.
- Røgen, B., Gommesen, L. & Fabricius, I.L. 2001: Grain size distributions of Chalk from Image analysis of Electron Micrographs: *Computers & Geosciences* 27, 1071-1080.

13. Electron micrographs and thin section photos.

Q-1 sample 1

0.7 mm



Thin section micrograph

Depth 3049 m effective depth 1599 m ($\beta = 1$) - 2170 m (β calculated).
Ekofisk Formation

Wackestone

84% calcite (Fe-bearing cement)

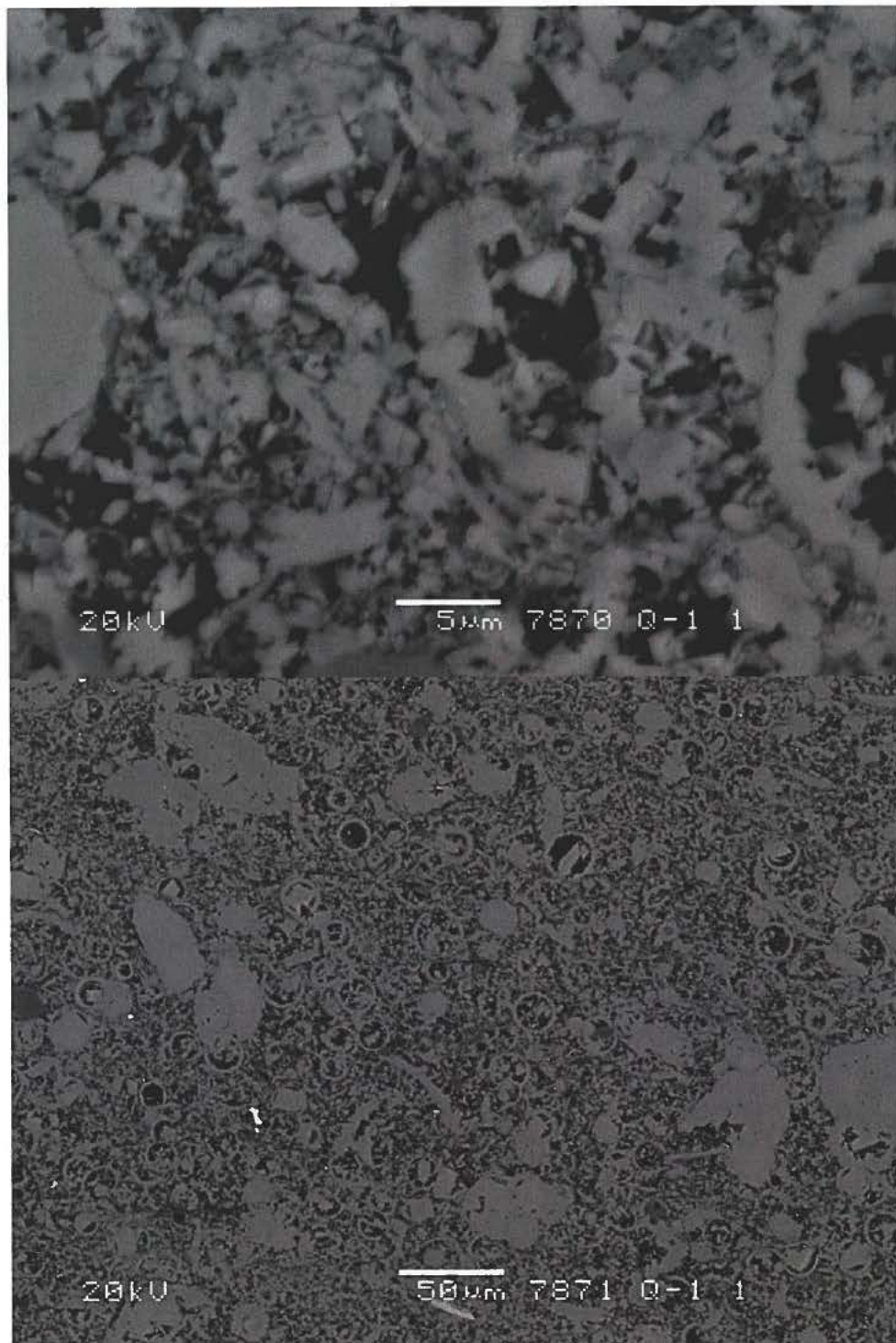
6% quartz, mainly fine-grained disseminated in pores

1% feldspar

7% clay (chlorite-smectite)

tr. pyrite

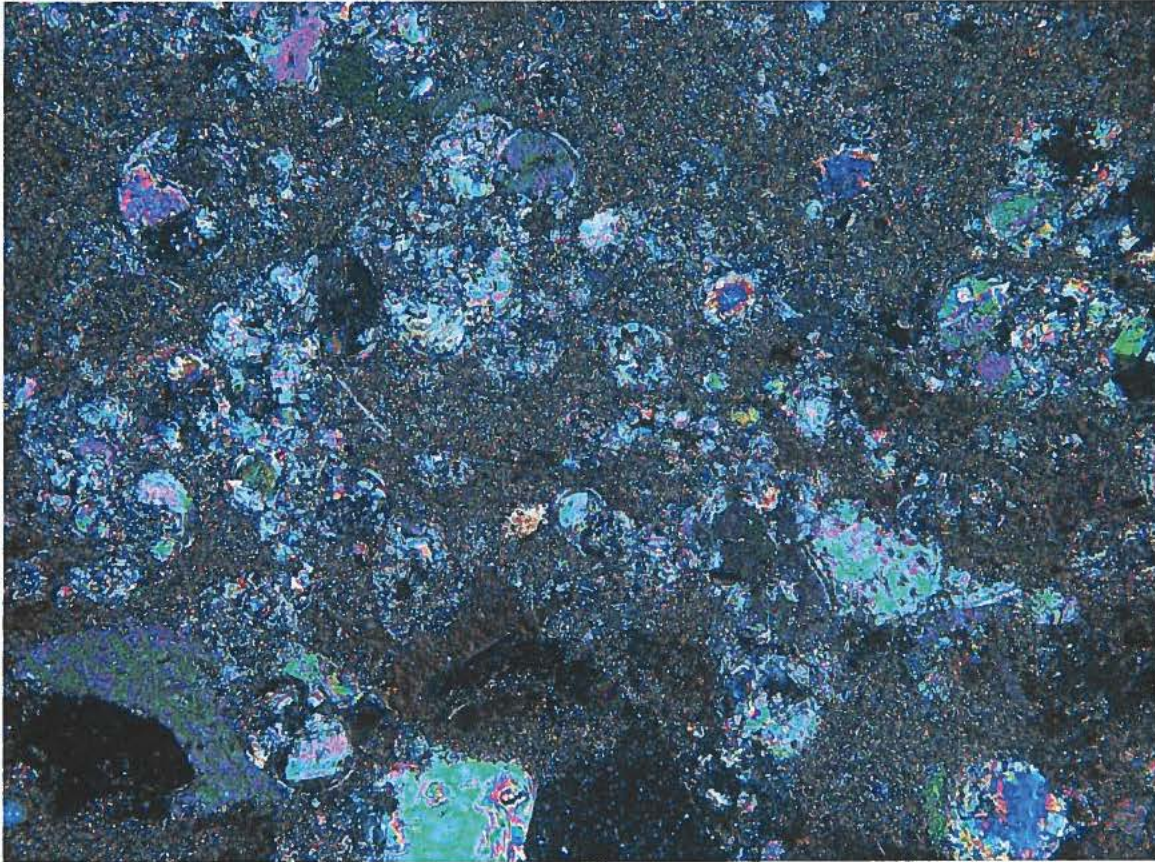
He-porosity 14.45%



Q-1 sample 1. Backscatter electron micrographs

Q-1 sample 2

0.7 mm



Thin section micrograph

Depth 3051 m effective depth 1601 m ($\beta = 1$) - 2122 m (β calculated).

Ekofisk Formation

Packstone

84% calcite (Fe-bearing cement)

4% quartz

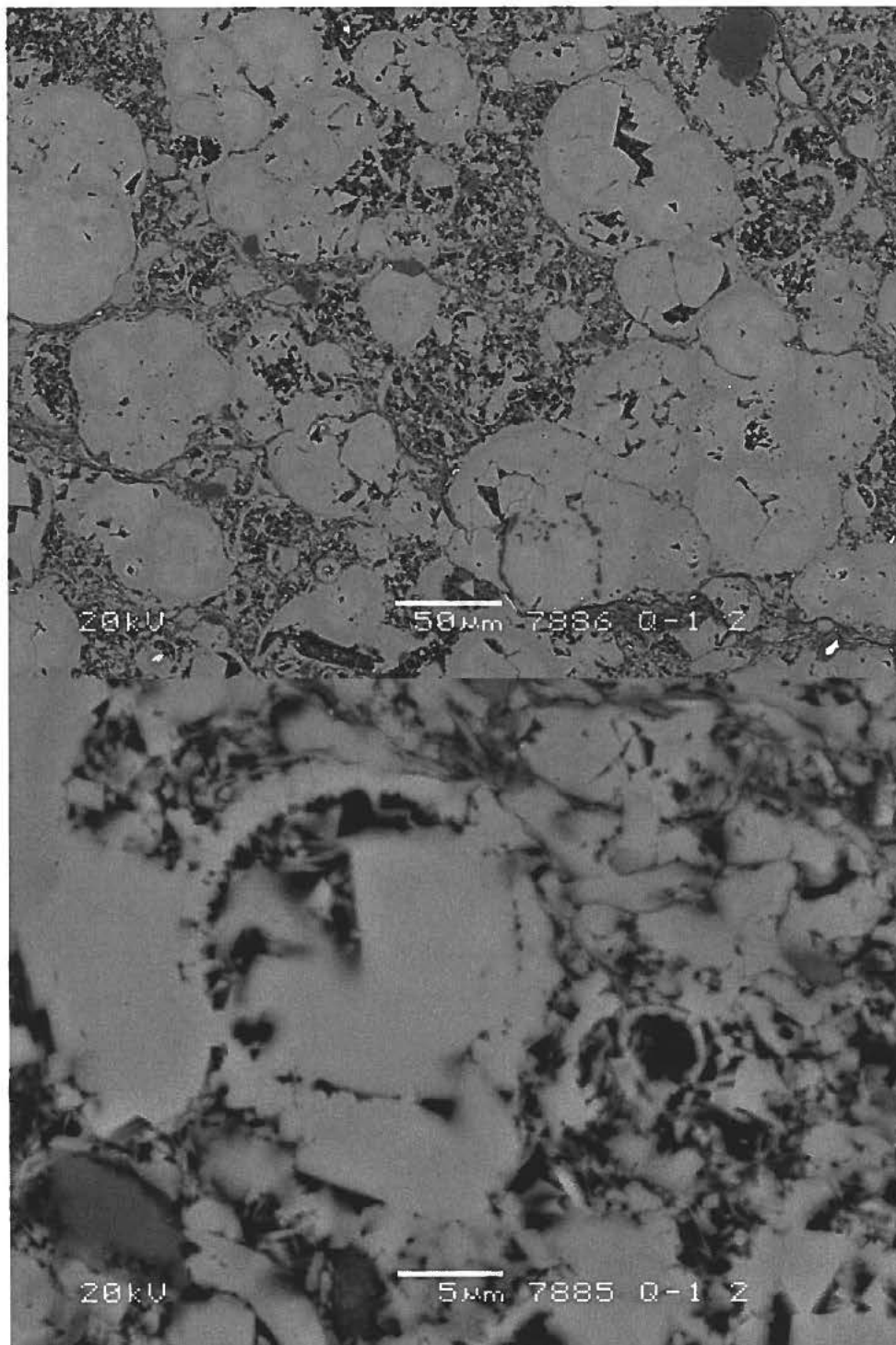
2% feldspar

11% clay (chlorite-smectite)

tr. pyrite

tr. apatite

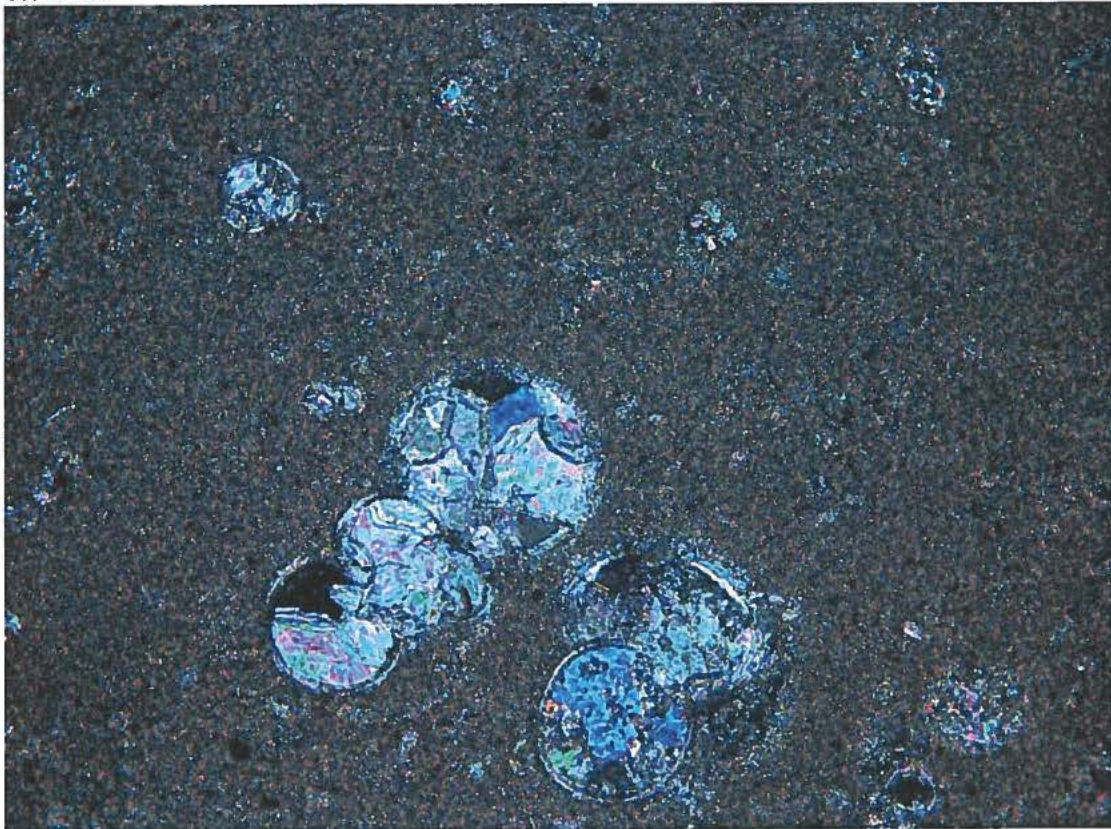
He-porosity 8.88%



Q-1 sample 2. Backscatter electron micrographs. Large gray grains are quartz.

Q-1 Sample 3

0.7 mm



Thin section micrograph

Depth 3052 m effective depth 1603 m ($\beta = 1$) - 2379 m (β calculated).

Ekofisk Formation

Mud-wackestone

70% calcite

19% quartz, mainly fine-grained

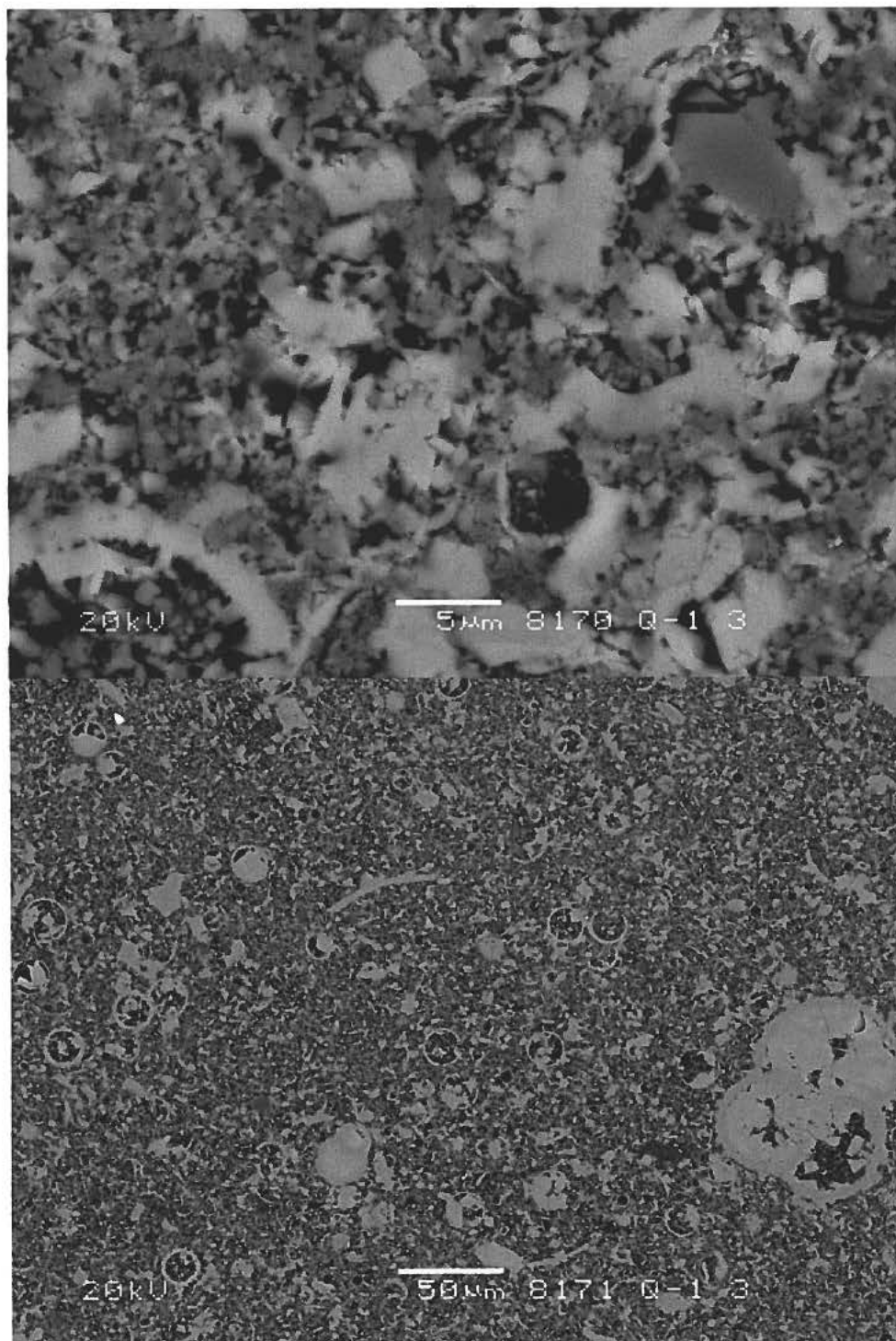
<1% feldspar

4% clay (chlorite-smectite)

tr. pyrite

tr. TiO_2

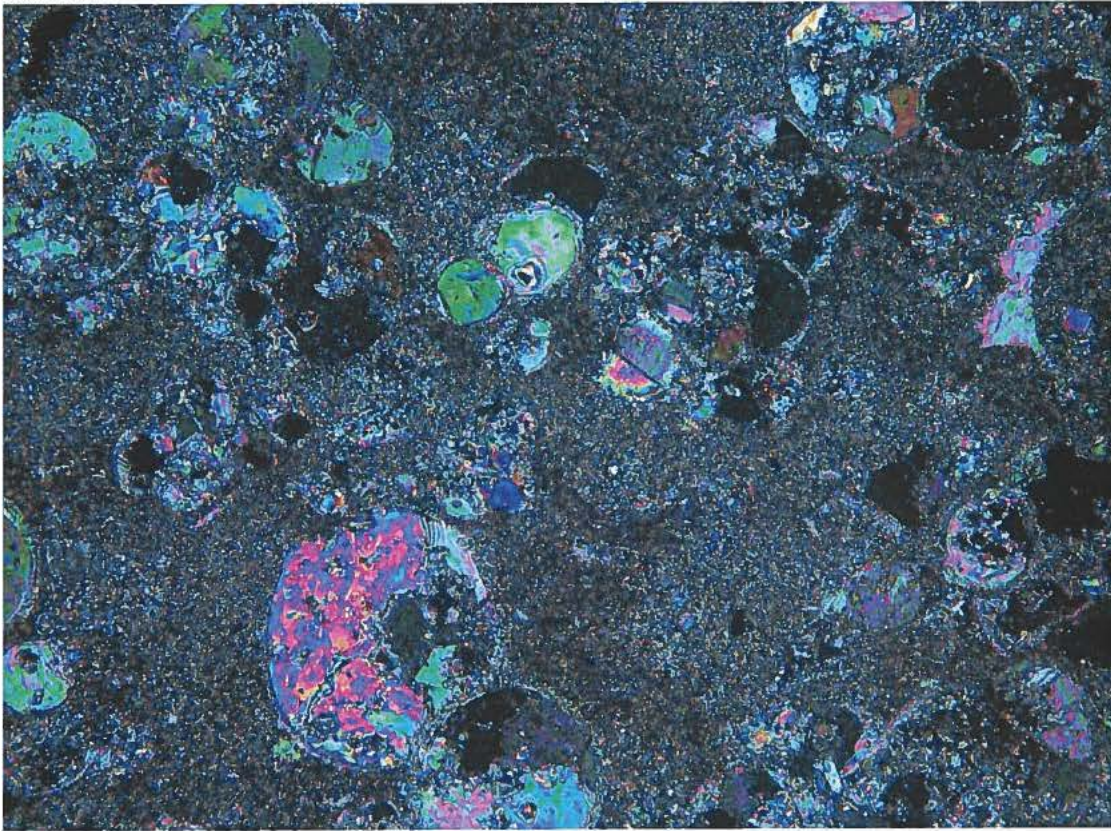
He-porosity 15.11%



Q-1 sample 3. Backscatter electron micrographs

Q-1 Sample 4

0.7 mm



Thin section micrograph

Depth 3056 m effective depth 1607 m ($\beta = 1$) - 2532 m (β calculated).

Ekofisk Formation

Packstone

78% calcite

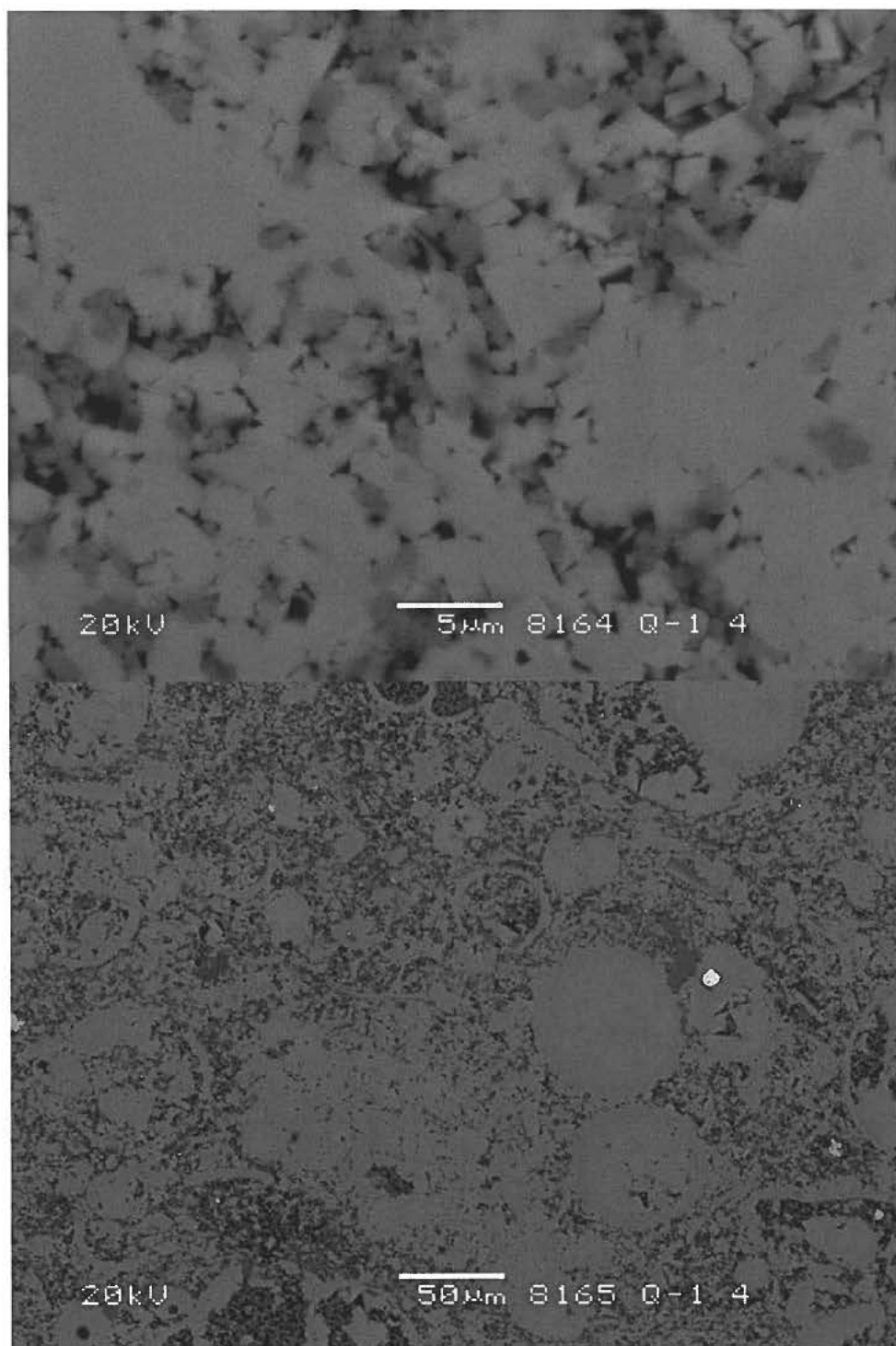
14% quartz, mainly fine-grained

2% feldspar

tr. pyrite

tr. apatite

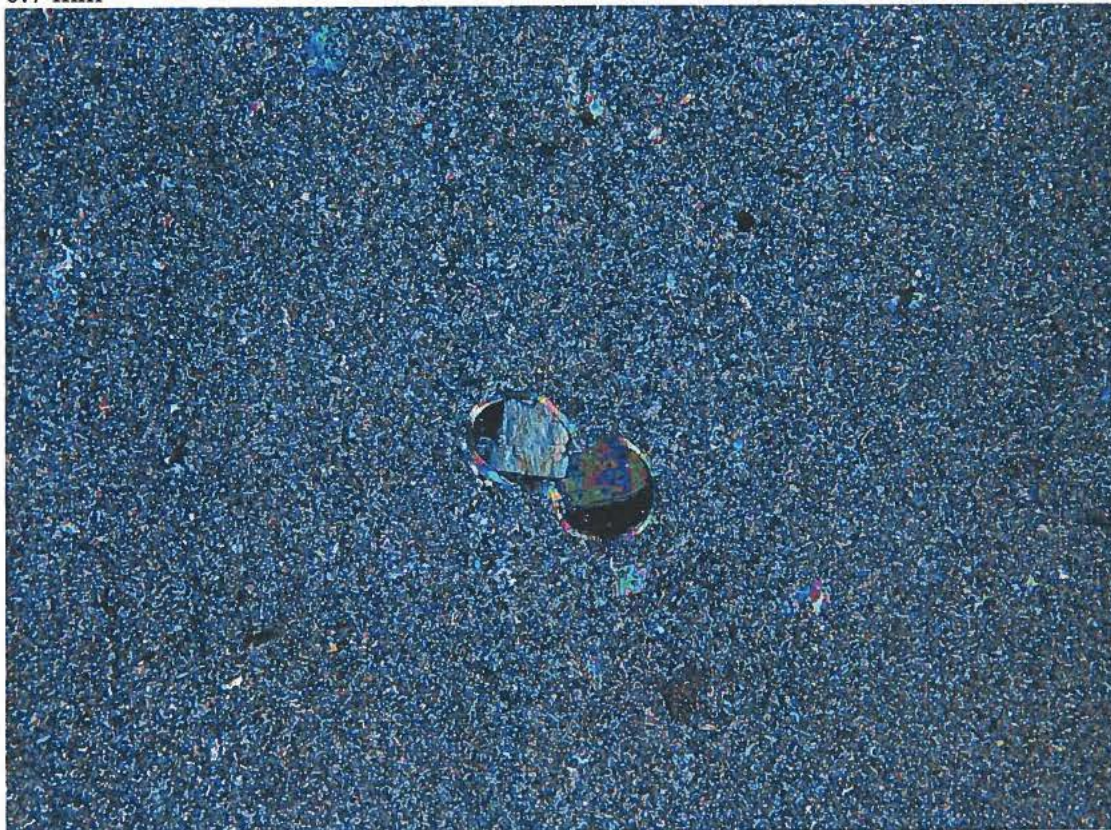
He-porosity 9.40%



Q-1 sample 4. Backscatter electron micrographs

Otto-1 Sample 6

0.7 mm



Thin section micrograph

Depth 2555 m effective depth 1095 m ($\beta = 1$) - 1686 m (β calculated).

Hod Formation

Mudstone

95% calcite

1% quartz, mainly fine-grained

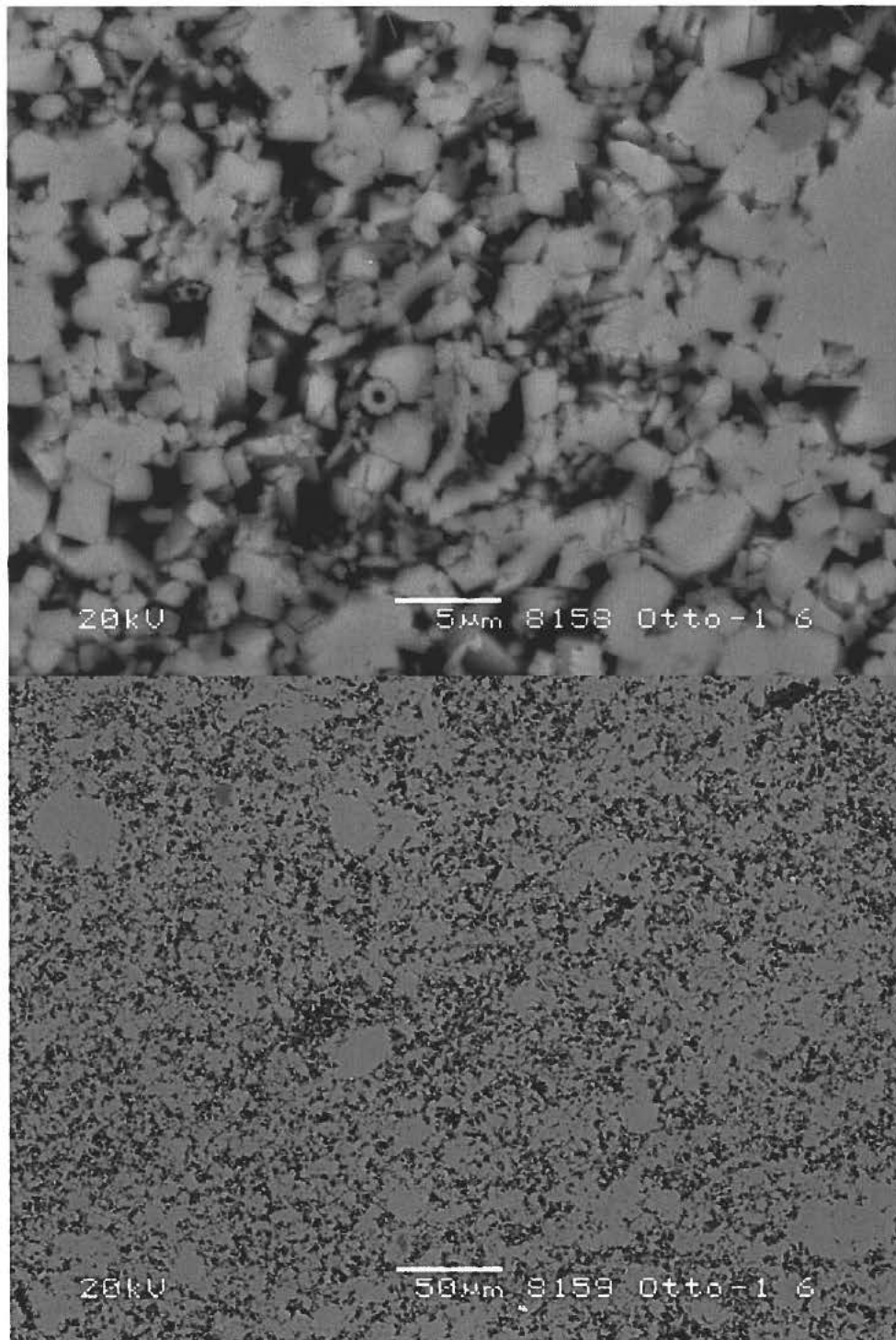
2% clay (chlorite-illite)

<1% feldspar

tr. pyrite

tr. apatite

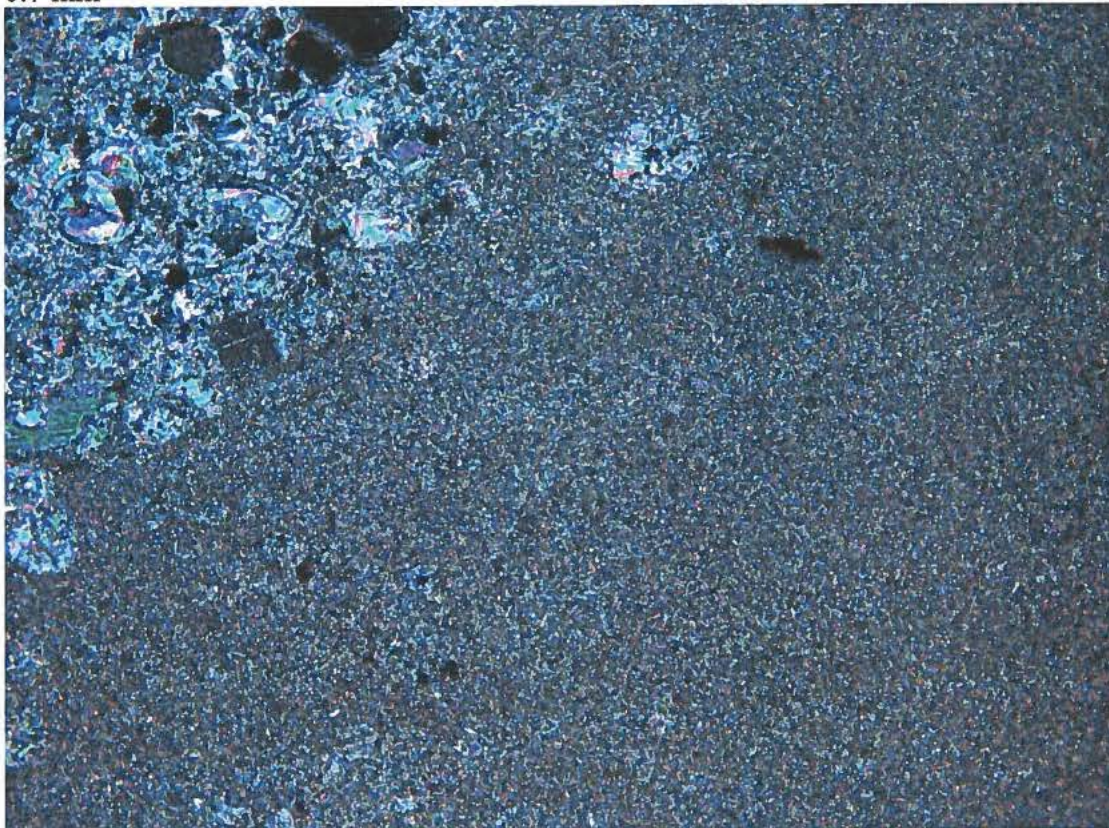
He-porosity 19.78%



Otto-1 sample 6. Backscatter electron micrographs

Otto-1 Sample 8

0.7 mm



Thin section micrograph

Depth 2558 m effective depth 1098 m ($\beta = 1$) – 1698 m (β calculated).

Hod Formation

Mudstone

97% calcite

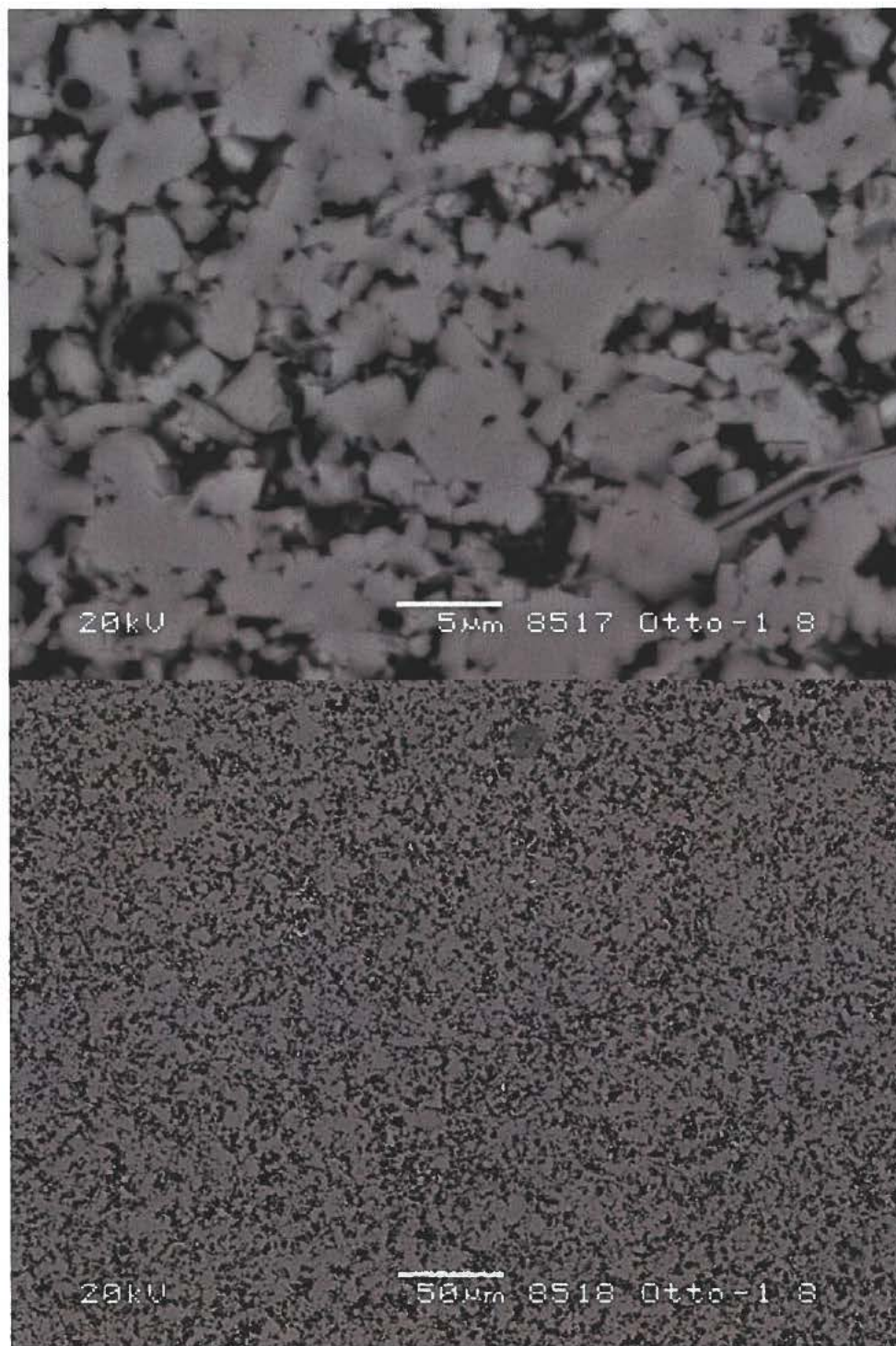
<1% quartz, mainly fine-grained

<1% clay (chlorite-illite)

<1% feldspar

tr. dolomite

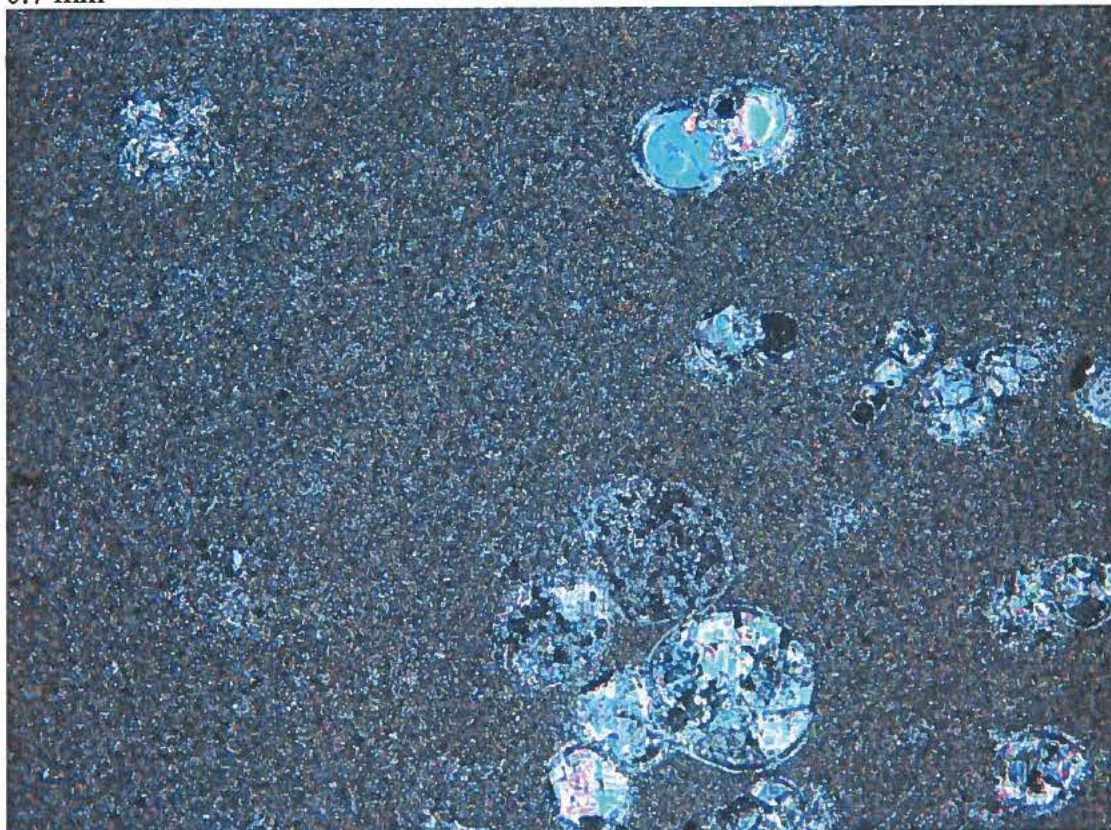
He-porosity 20.74%



Otto-1 sample 8. Backscatter electron micrographs

T-3 sample 9

0.7 mm



Thin section micrograph

Depth 2535 m effective depth 1075 m ($\beta = 1$) - 1648 m (β calculated).

Tor Formation

Wackestone

97% calcite

<1% quartz, mainly fine-grained

<1% feldspar

1% clay (chlorite-illite-smectite)

tr. pyrite

He-porosity 19.10%



T-3 sample 9. Backscatter electron micrographs

T-3 sample 10

0.7 mm



Thin section micrograph

Depth 2561 m effective depth 1101 m ($\beta = 1$) - 1559 m (β calculated).

Tor Formation

Mudstone

96% calcite

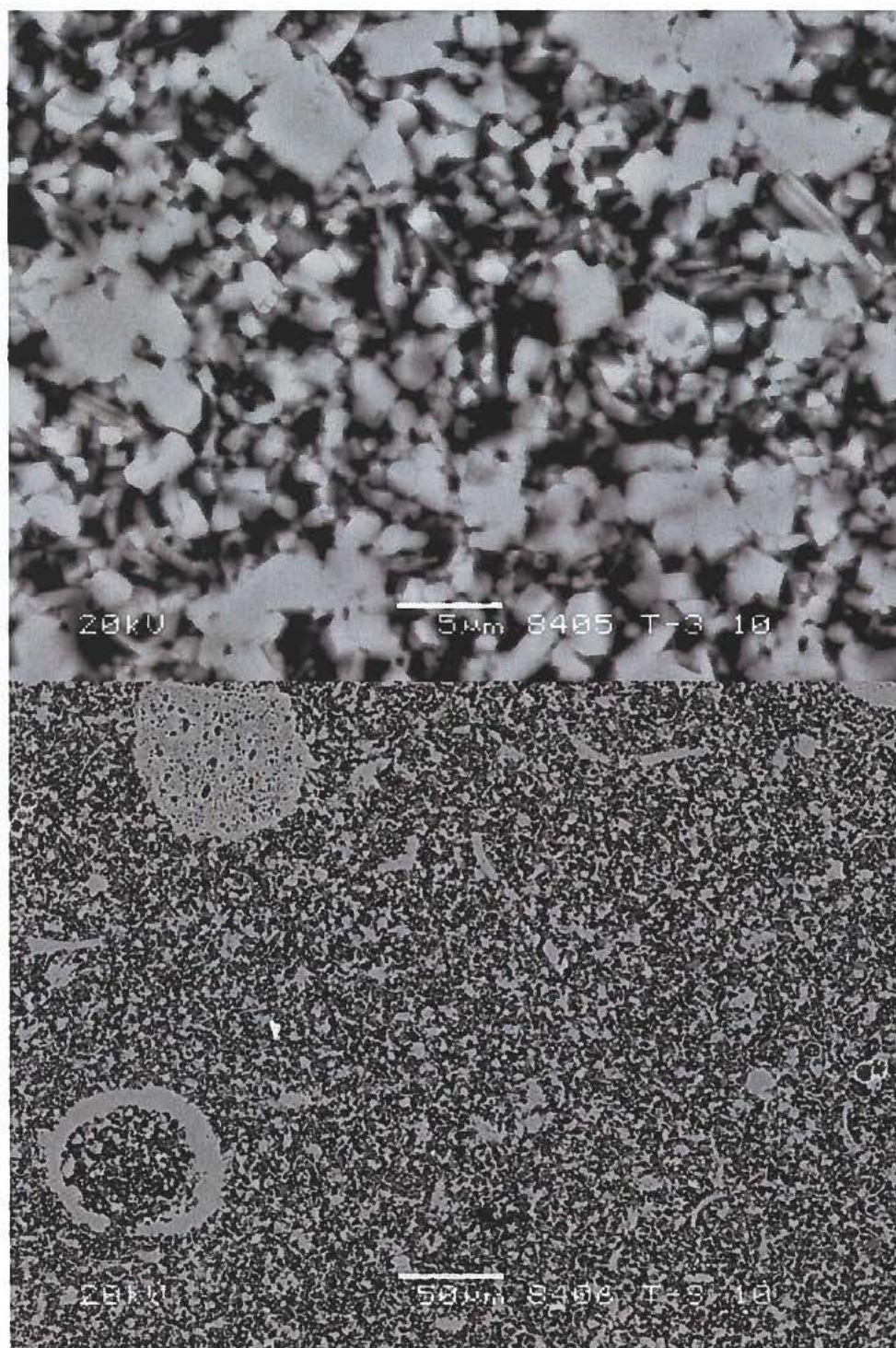
<1% quartz, mainly fine-grained

<1% feldspar

1% clay (chlorite-illite-smectite)

tr. pyrite

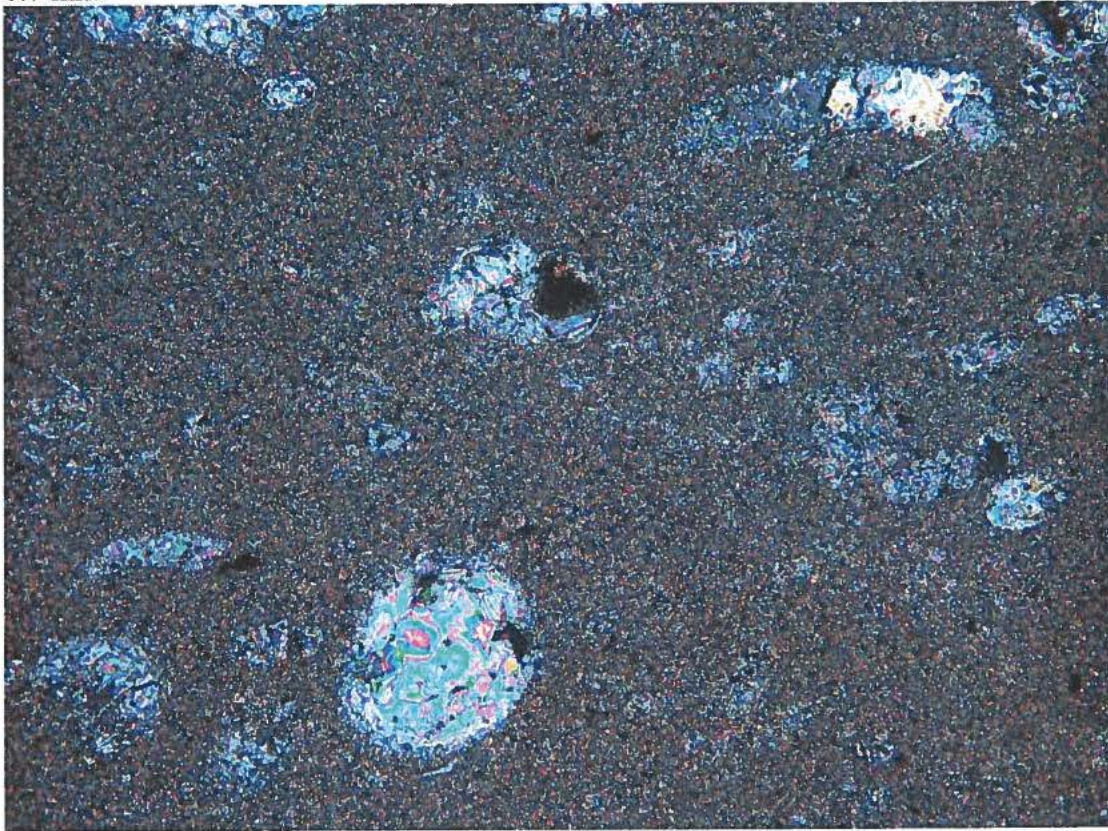
He-porosity 24.80%



T-3 sample 10. Backscatter electron micrographs

Gert-1 sample 13

0.7 mm



Thin section micrograph

Depth 3875 m effective depth 2235 m ($\beta = 1$) - 3220 m (β calculated).

Hidra Formation

Mud-wackestone

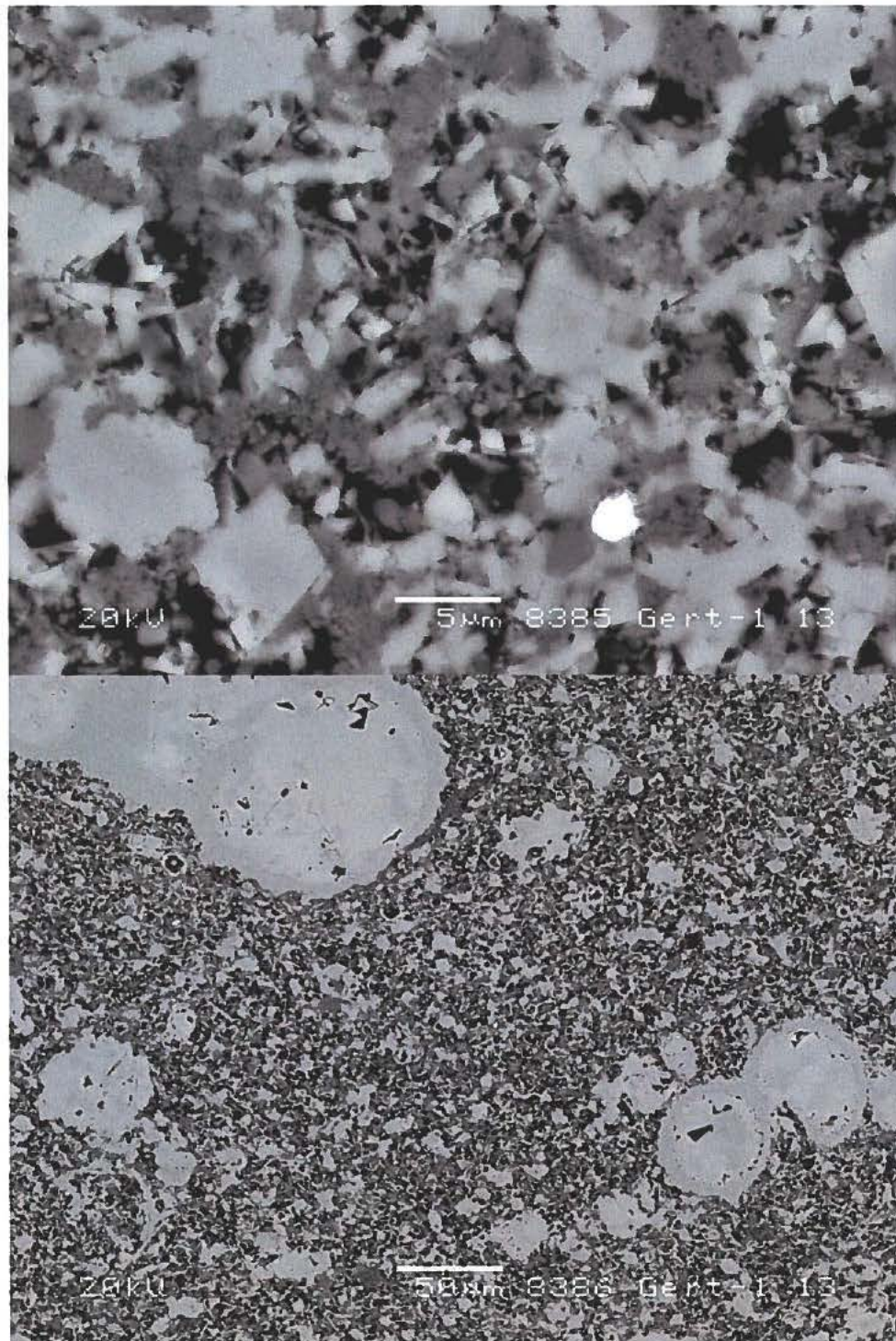
69% calcite (Fe-bearing cement)

18% quartz, mainly fine-grained

4% feldspar

tr. TiO_2

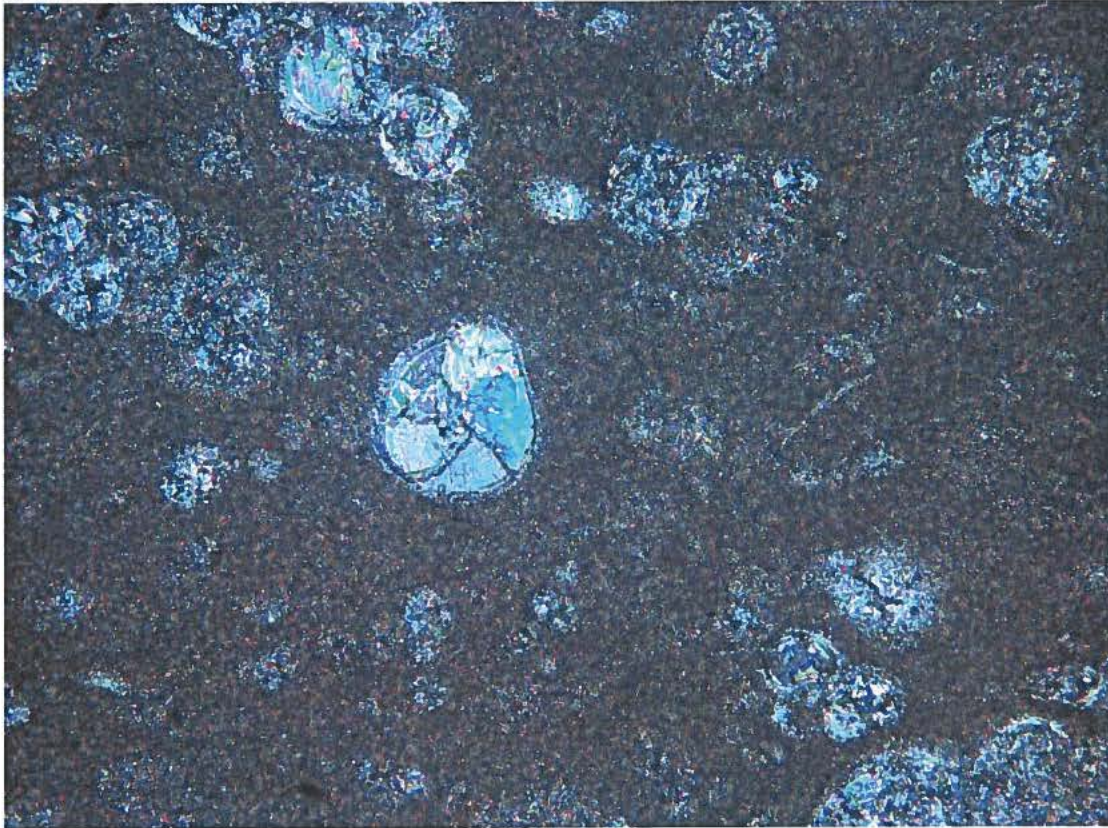
He-porosity 11.58%



Gert-1 sample 13. Backscatter electron micrographs

Gert-1 sample 14

0.7 mm



Thin section micrograph

Depth 3877 m effective depth 2237 m ($\beta = 1$) - 3282 m (β calculated).

Hidra Formation

Wackestone

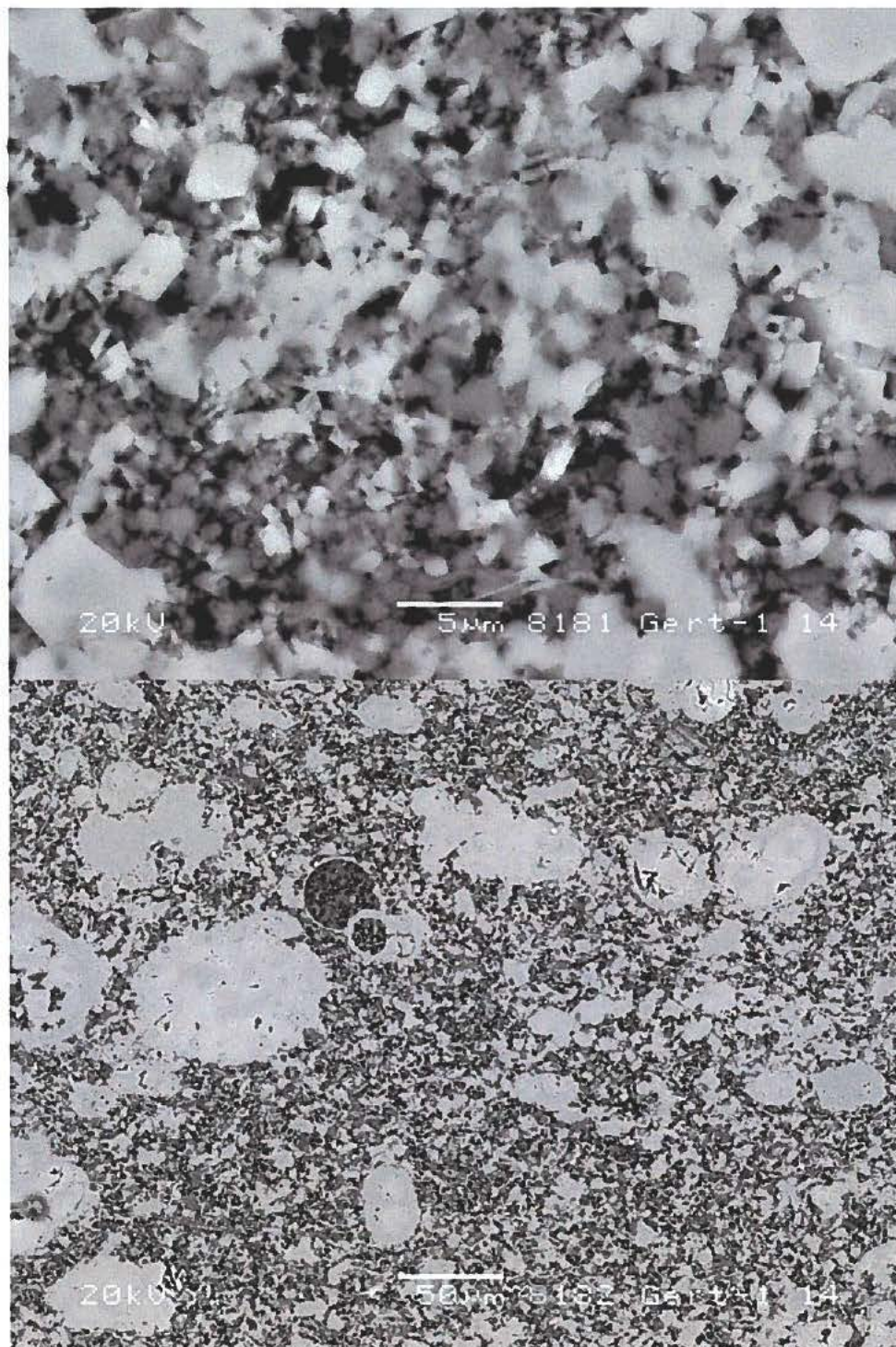
74% calcite

15% quartz, mainly fine-grained desiminated in pores

4% feldspar

tr. TiO_2

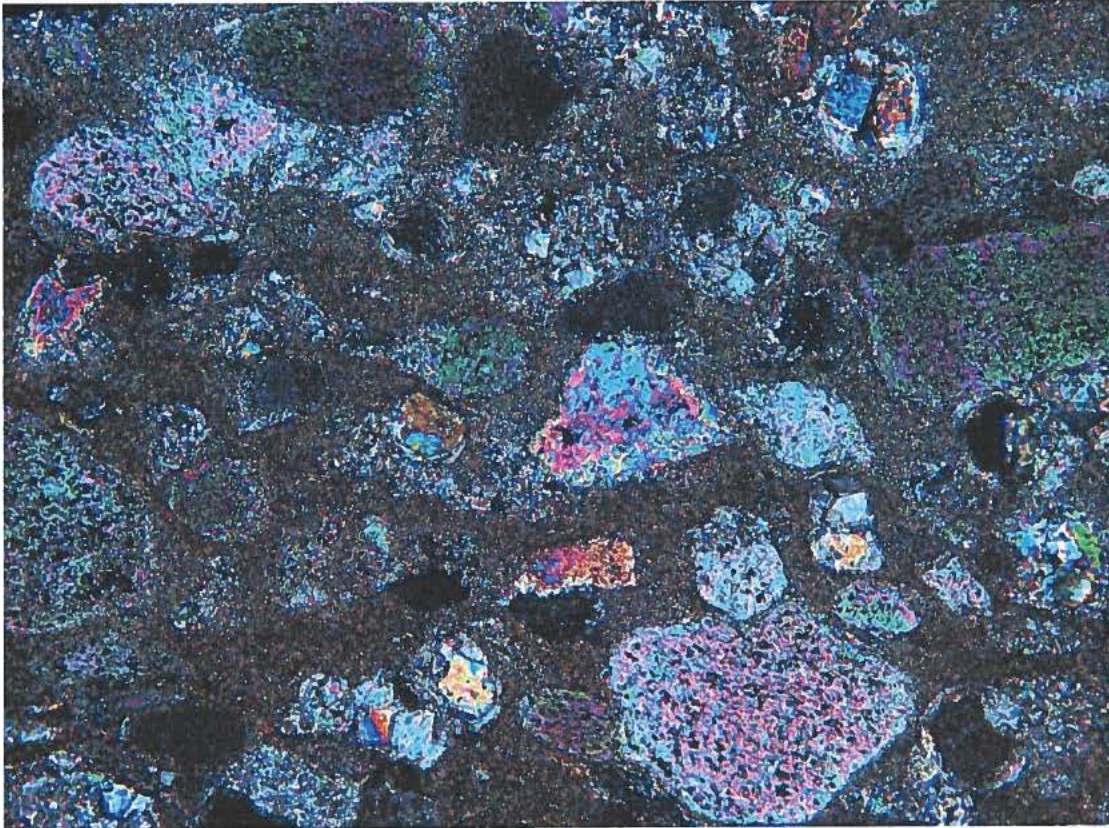
He-porosity 6.99%



Gert-1 sample 14. Backscatter electron micrographs

Gert-1 sample 16

0.7 mm



Thin section micrograph

Depth 3881 m effective depth 2241 m ($\beta = 1$) - 3227 m (β calculated).

Hidra Formation

Packstone

85% calcite (Fe-bearing cement)

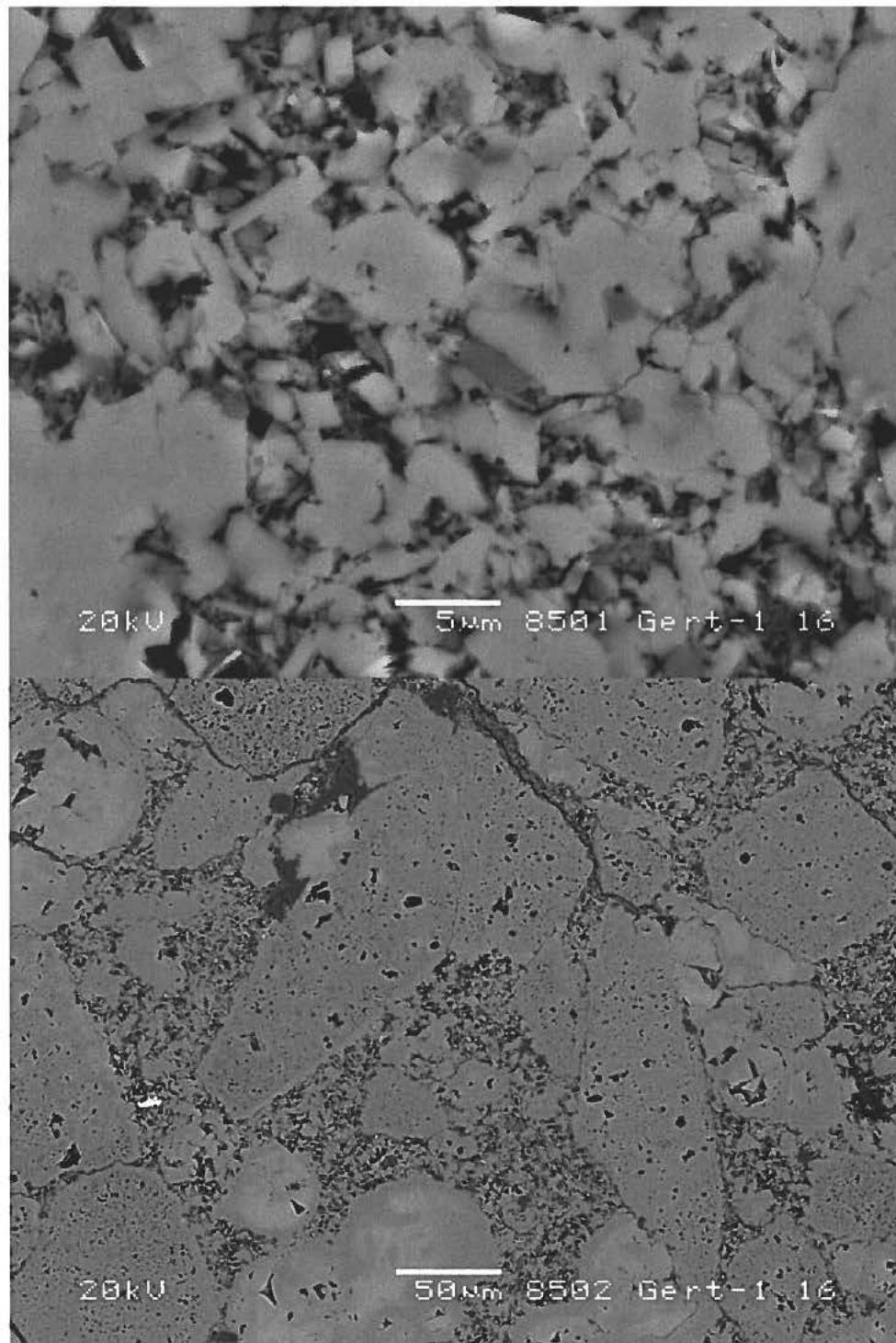
3% quartz, mainly fine-grained

2% feldspar

5% clay (chlorite-illite-smectite)

tr. TiO_2

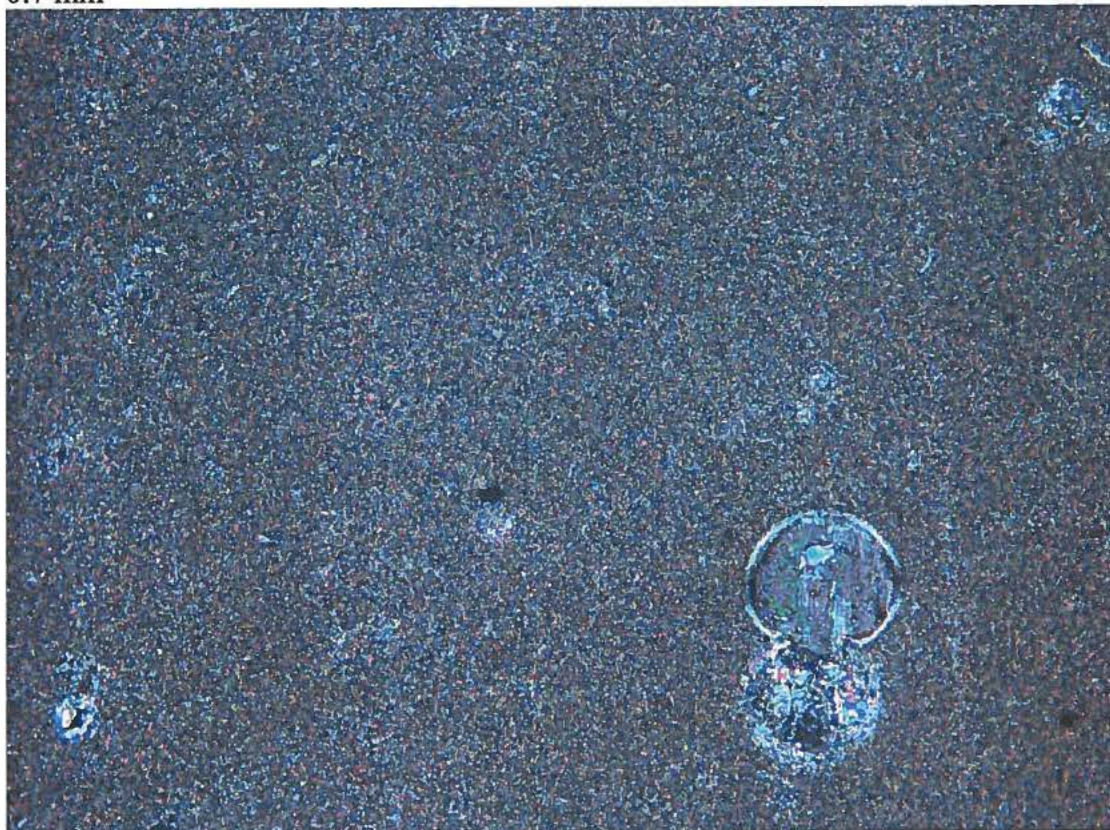
He-porosity 5.19%



Gert-1 sample 16. Backscatter electron micrographs

West Lulu-1 sample 17

0.7 mm



Thin section micrograph

Depth 3361 m effective depth 1971 m ($\beta = 1$) - 3064 m (β calculated).

Hod Formation

Mudstone

93% calcite

2% quartz, mainly fine-grained

2% feldspar

1% clay (chlorite-illite-smectite)

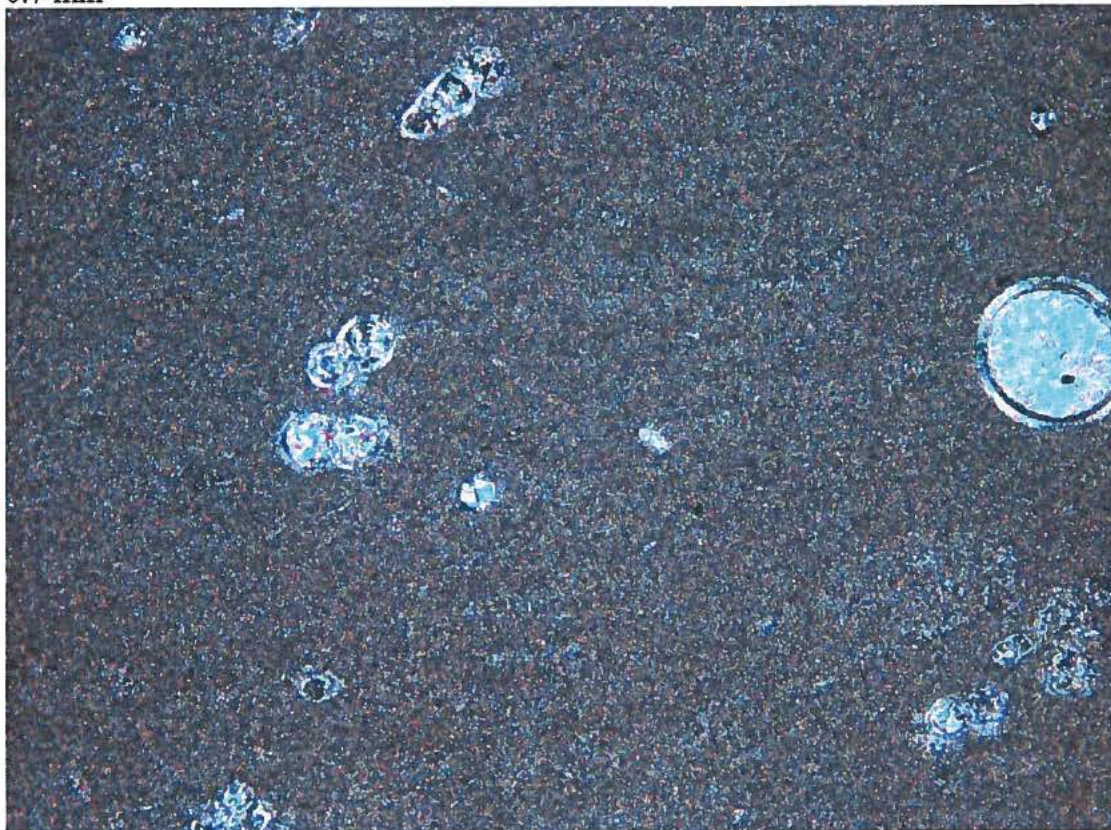
He-porosity 6.41%



West Lulu-1 sample 17. Backscatter electron micrographs

West Lulu-1 sample 19

0.7 mm



Thin section micrograph

Depth 3378 m effective depth 1988 m ($\beta = 1$) - 2970 m (β calculated).

Hod Formation

Mudstone

93% calcite (Fe-bearing cement)

1% quartz, mainly fine-grained

3% feldspar

2% clay (chlorite-illite-smectite)

tr. apatite

tr. TiO_2

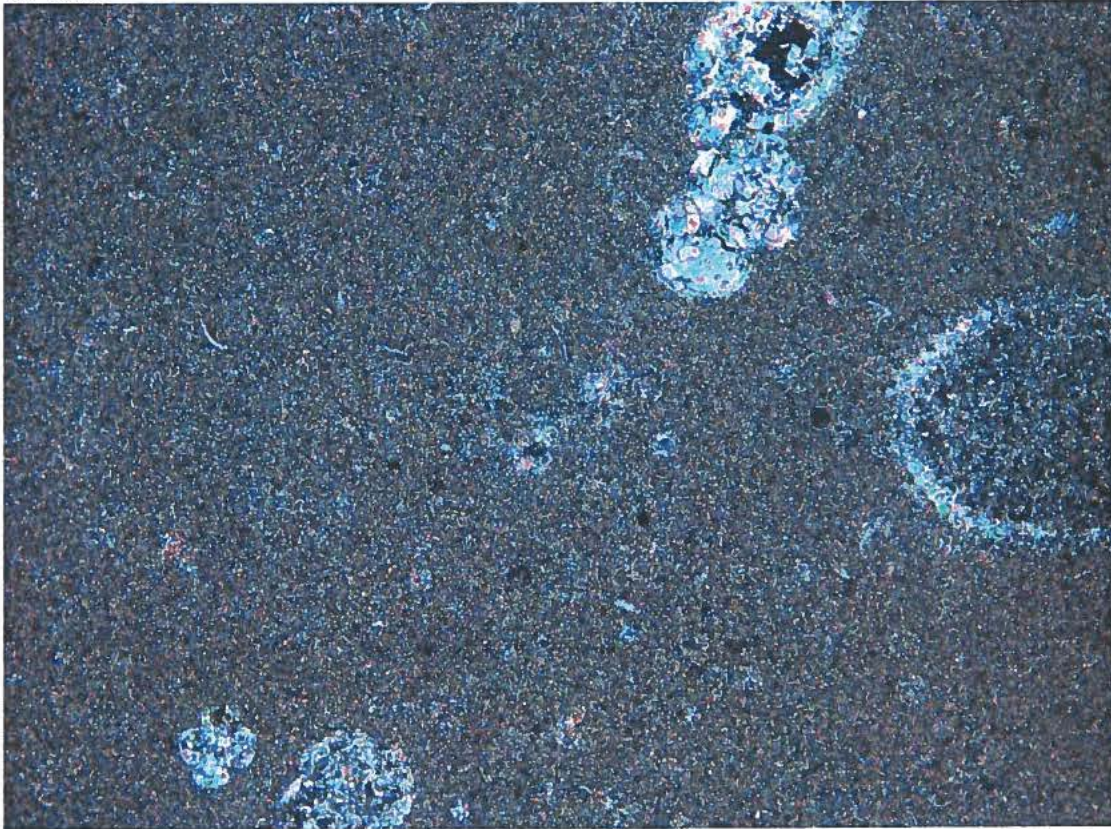
He-porosity 8.12%



West Lulu-1 sample 19. Backscatter electron micrographs

Baron-2 sample 21

0.7 mm



Thin section micrograph

Depth 2833 m effective depth 1103 m ($\beta = 1$) - 1636 m (β calculated).

Ekofisk Formation

Mudstone

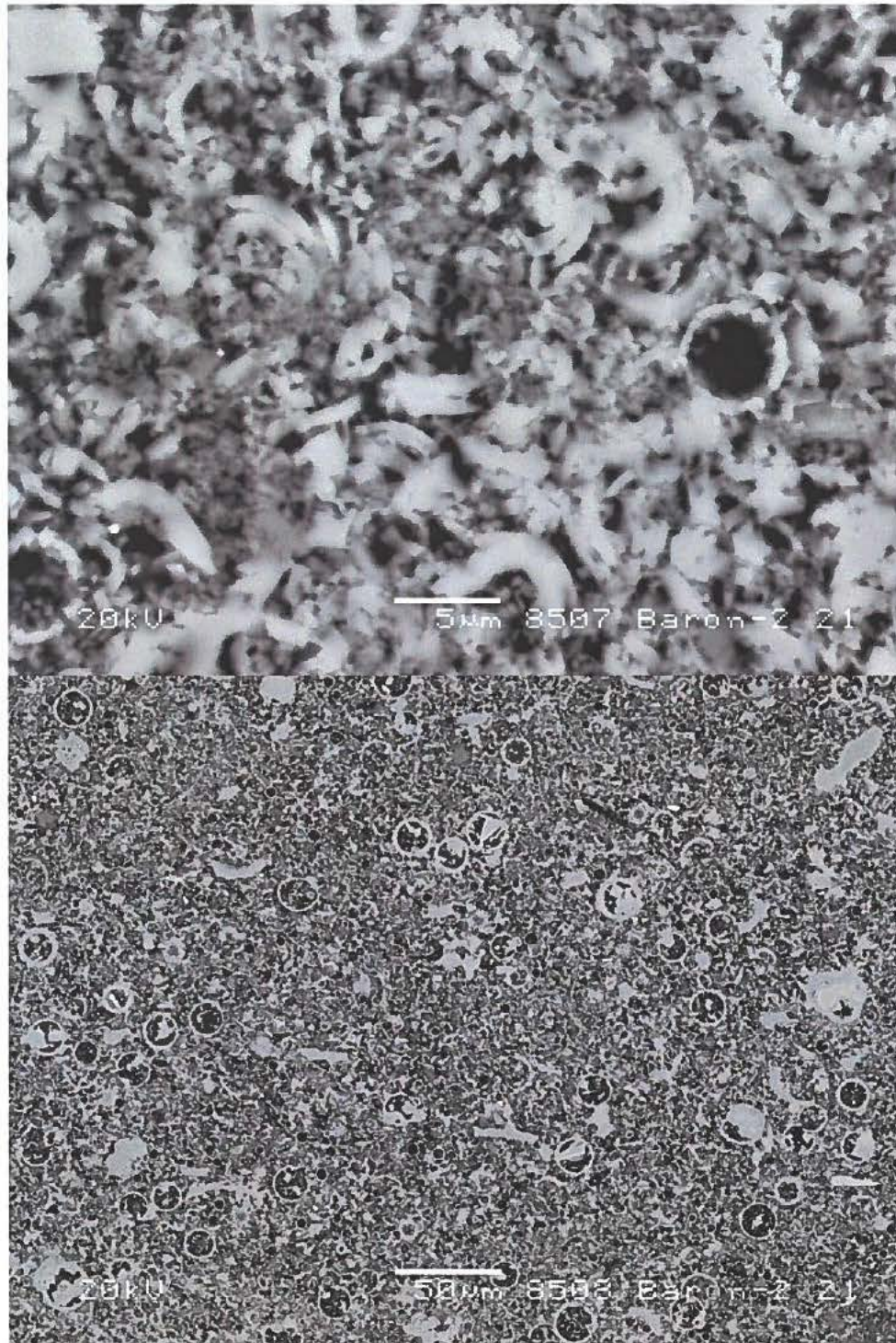
83% calcite

9% quartz, mainly fine-grained disseminated in pores

3% feldspar

2% clay (chlorite-illite-smectite)

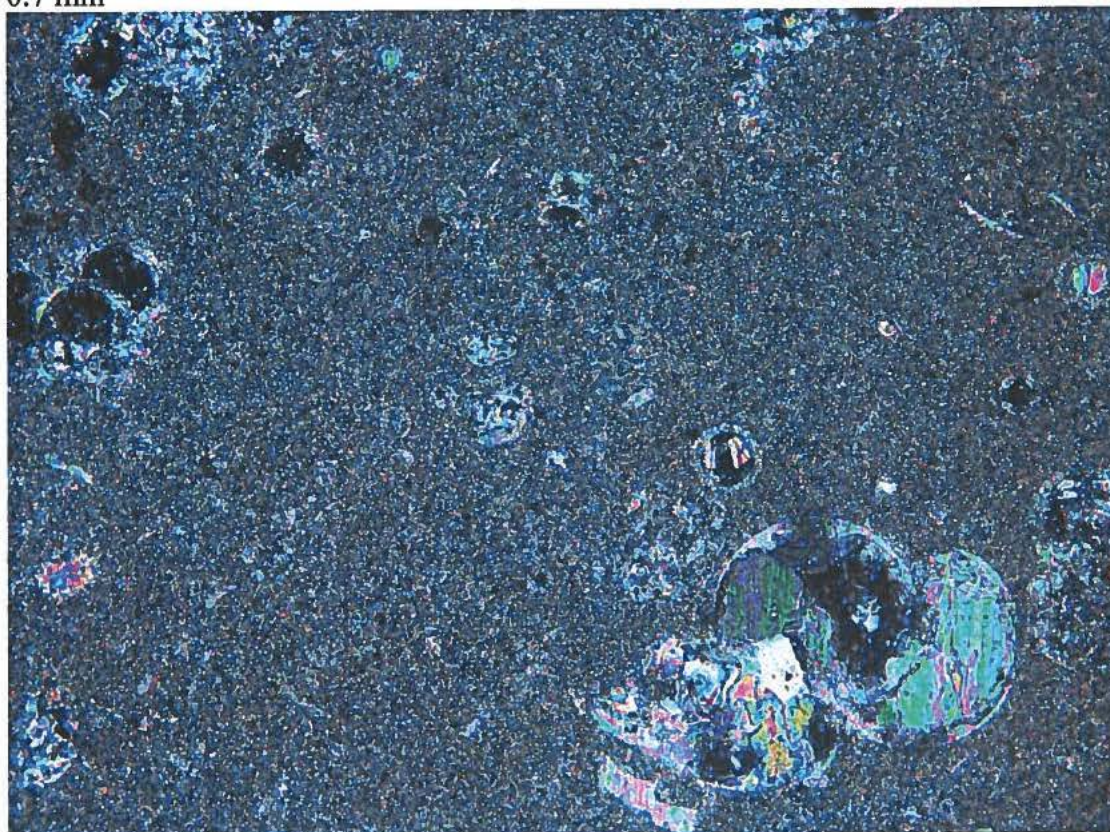
He-porosity 24.31%



Baron-2 sample 21. Backscatter electron micrographs

Baron-2 sample 22

0.7 mm



Thin section micrograph

Depth 2836 m effective depth 1106 m ($\beta = 1$) - 1601 m (β calculated).

Ekofisk Formation

Mud-wackestone

78% calcite

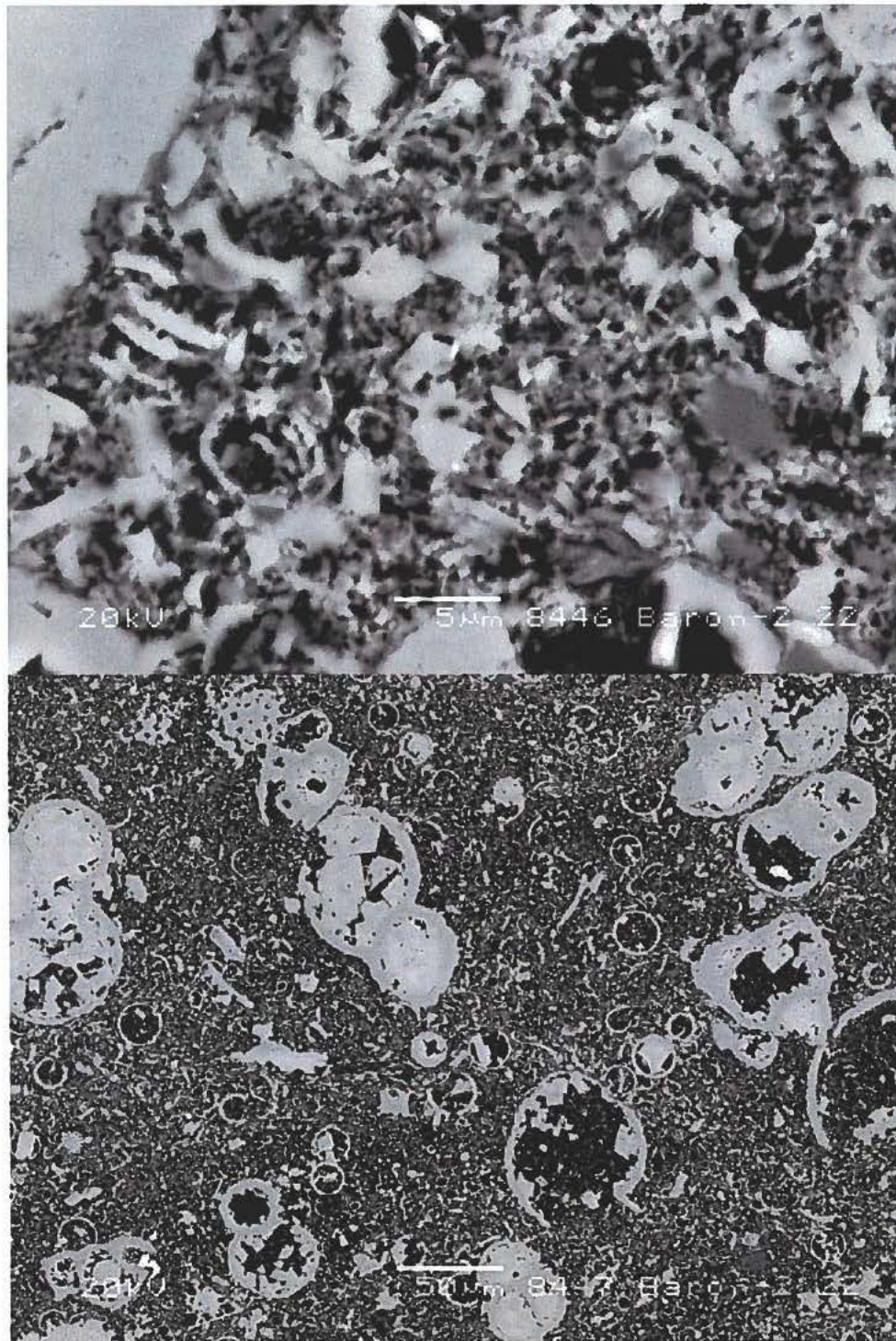
11% quartz, mainly fine-grained desiminated in pores

4% feldspar

3% clay (chlorite-illite-smectite)

tr. pyrite

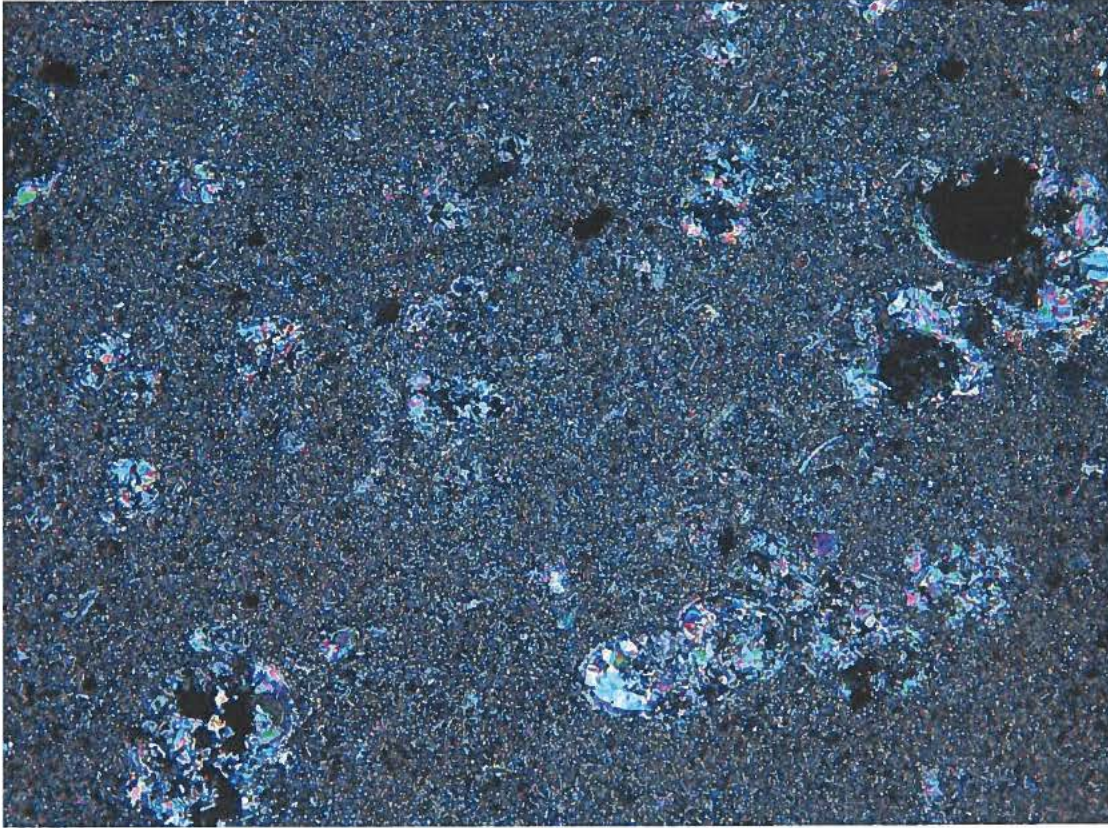
porosity 24.30%



Baron-2 sample 22. Backscatter electron micrographs

Baron-2 sample 23

0.7 mm



Thin section micrograph

Depth 2837 m effective depth 1107 m ($\beta = 1$) - 1948 m (β calculated).

Ekofisk Formation

Mud-wackestone

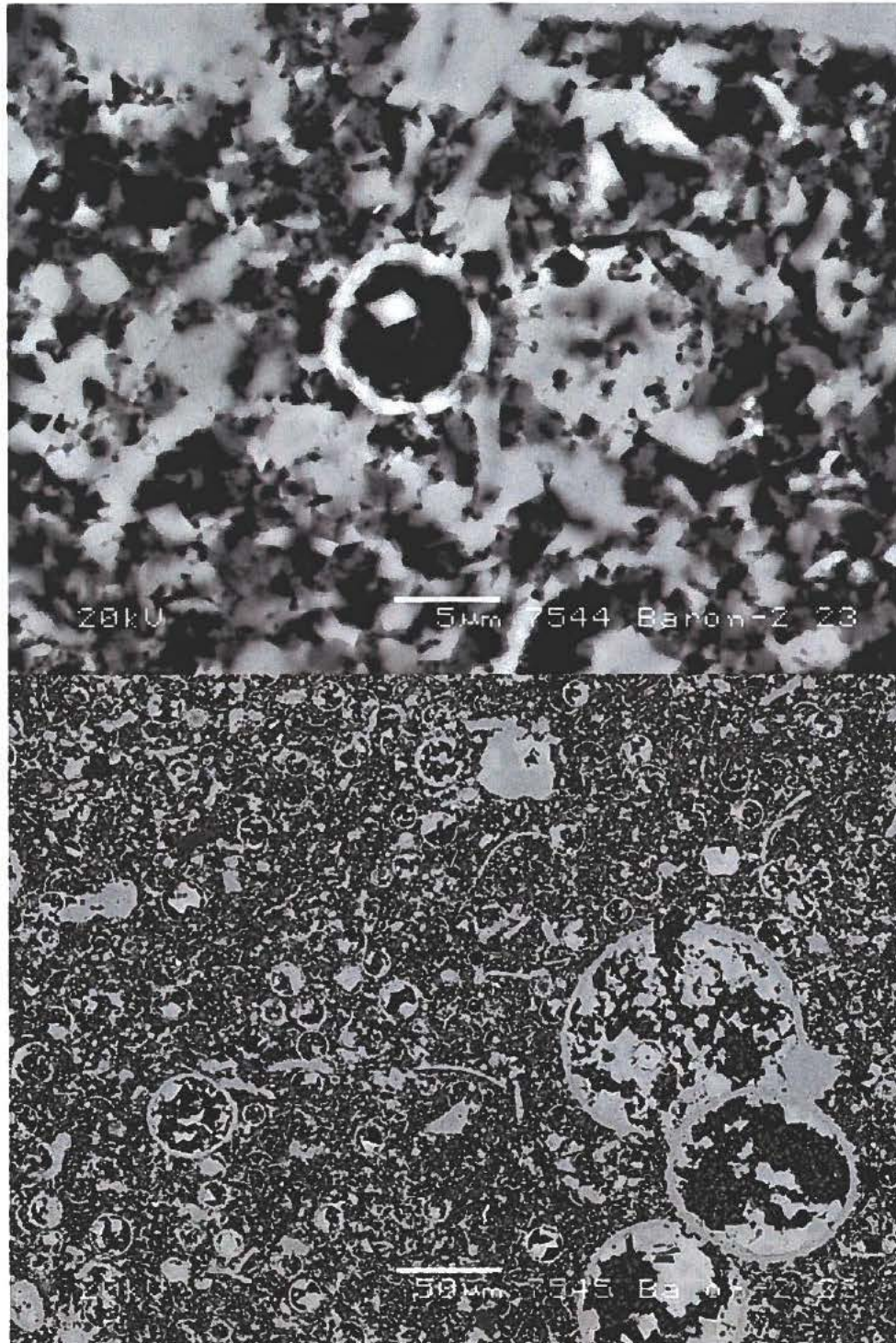
71% calcite

18% quartz, mainly fine-grained desiccated in pores

4% feldspar

tr. apatite

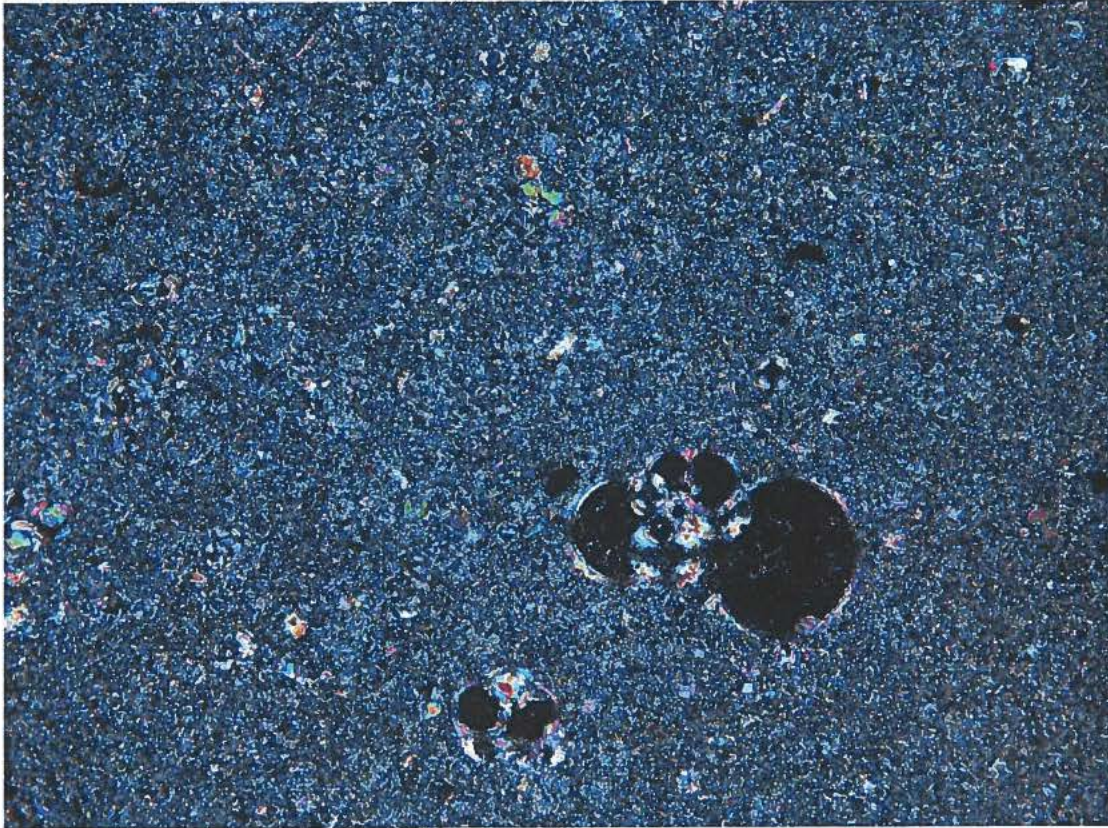
He-porosity 17.70%



Baron-2 sample 23. Backscatter electron micrographs

Baron-2 sample 24

0.7 mm



Thin section micrograph

Depth 2844 m effective depth 1114 m ($\beta = 1$) - 1716 m (β calculated).

Ekofisk Formation

Mudstone

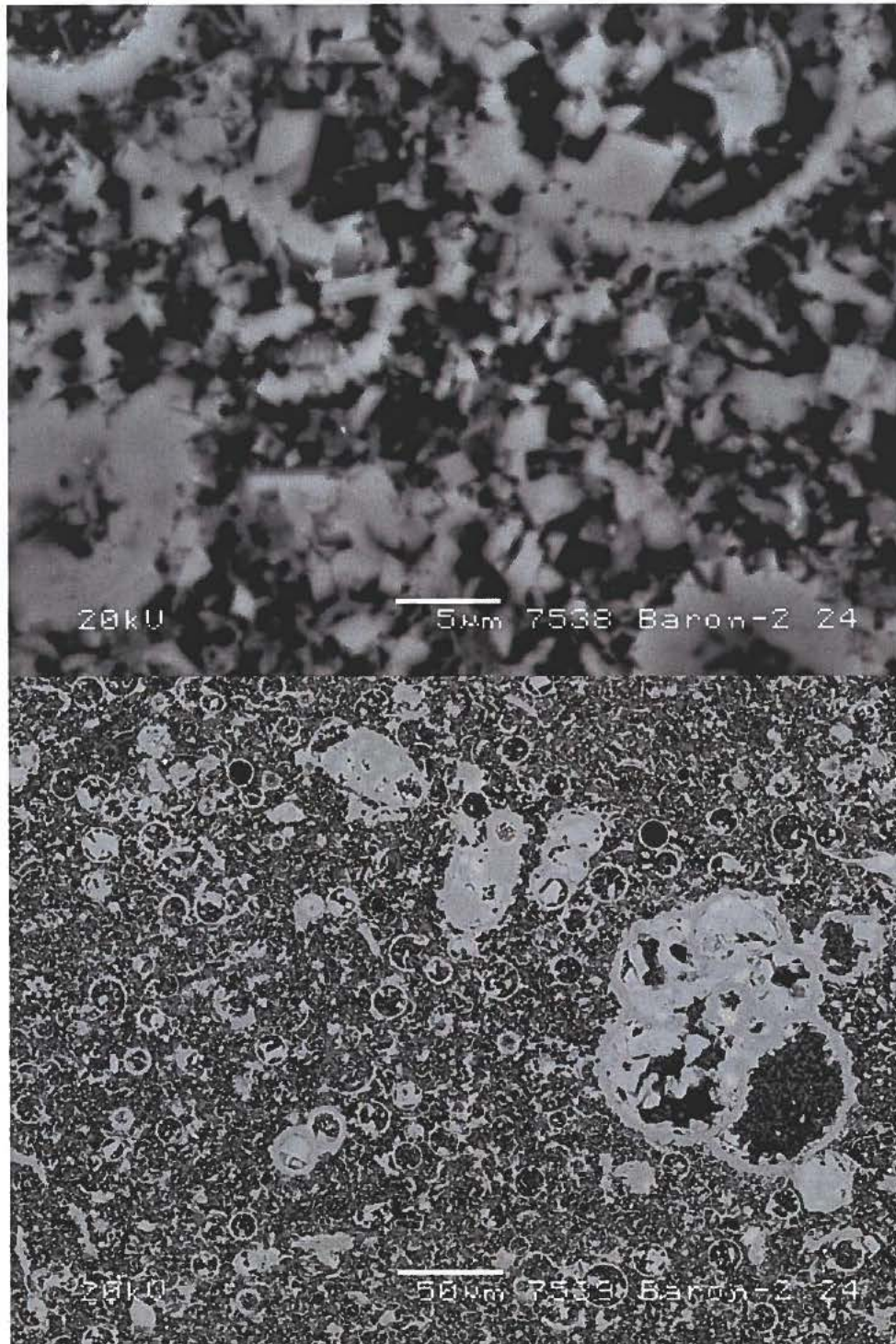
79% calcite

12% quartz, mainly fine-grained desiminated in pores

3% feldspar

<1% clay (smectite)

He-porosity 22.31%



Baron-2 sample 24. Backscatter electron micrographs

I-1 sample 26

0.7 mm



Thin section micrograph

Depth 2861 m effective depth 1371 m ($\beta = 1$) - 1682 m (β calculated).

Tuxen Formation

Mudstone

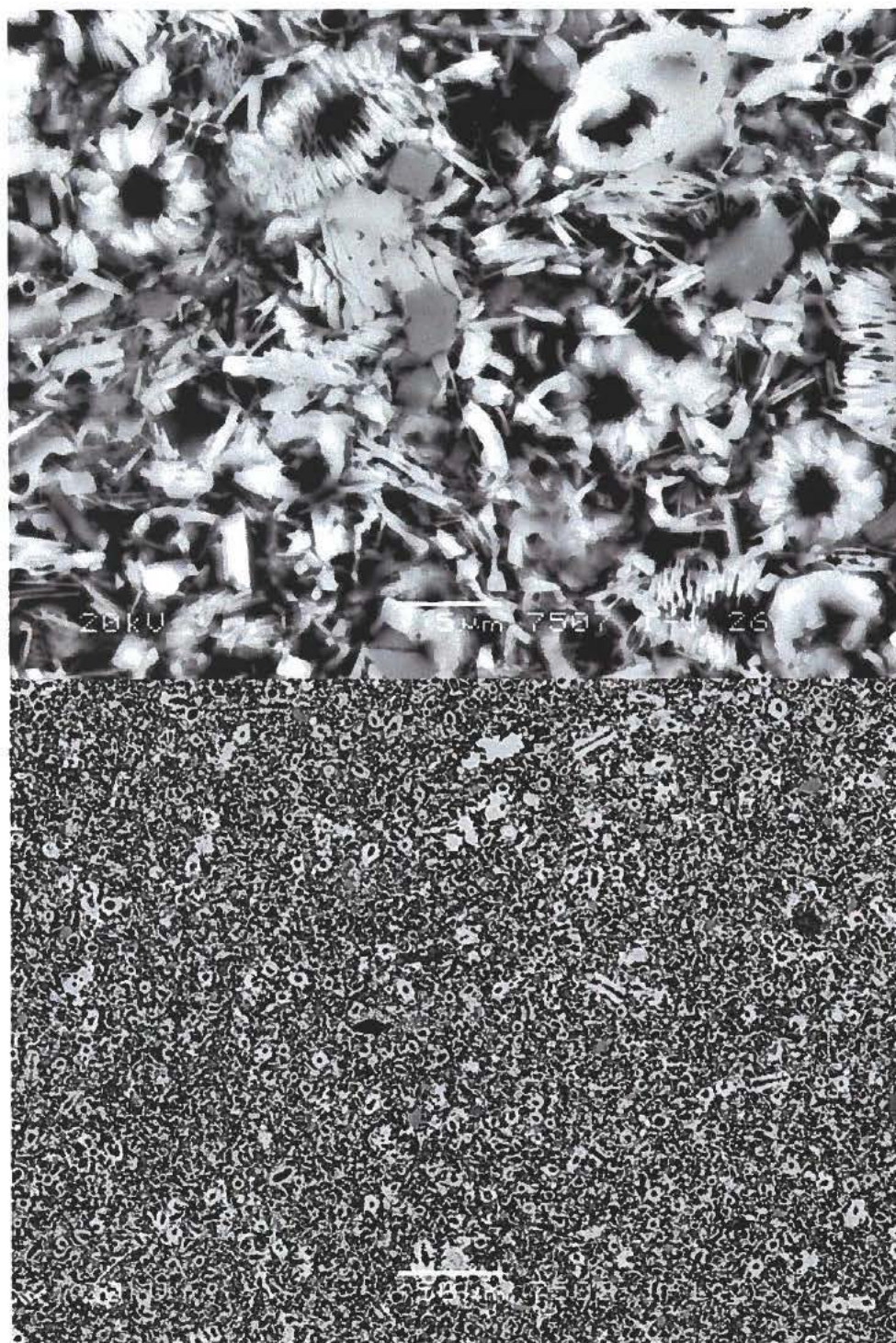
85% calcite

2% quartz, mainly fine-grained

2% feldspar

6% clay (kaolinite plus minor smectite-illite-chlorite))

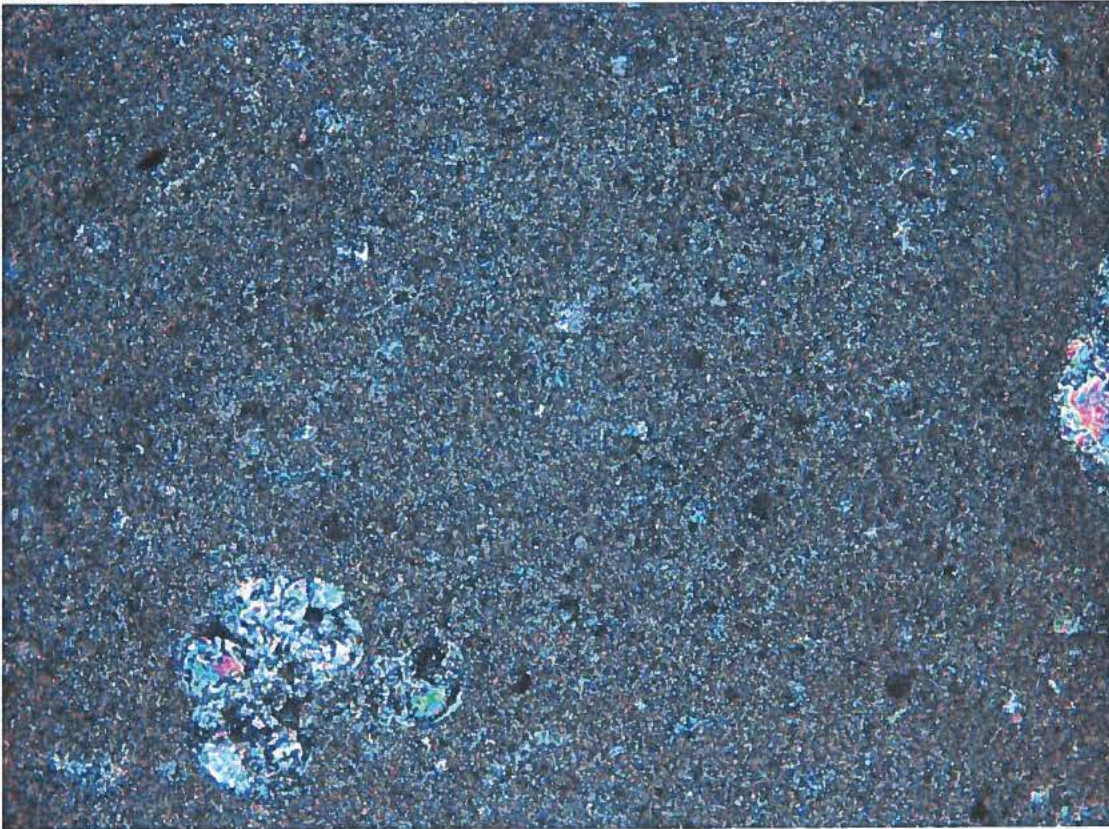
He-porosity 28.12%



I-1 sample 26. Backscatter electron micrographs

Cecilie-1B sample 30

0.7 mm



Thin section micrograph

Depth 2365 m effective depth 2095 m ($\beta = 1$).

Ekofisk Formation

Mudstone

83% calcite

9% quartz, mainly fine-grained disseminated in pores

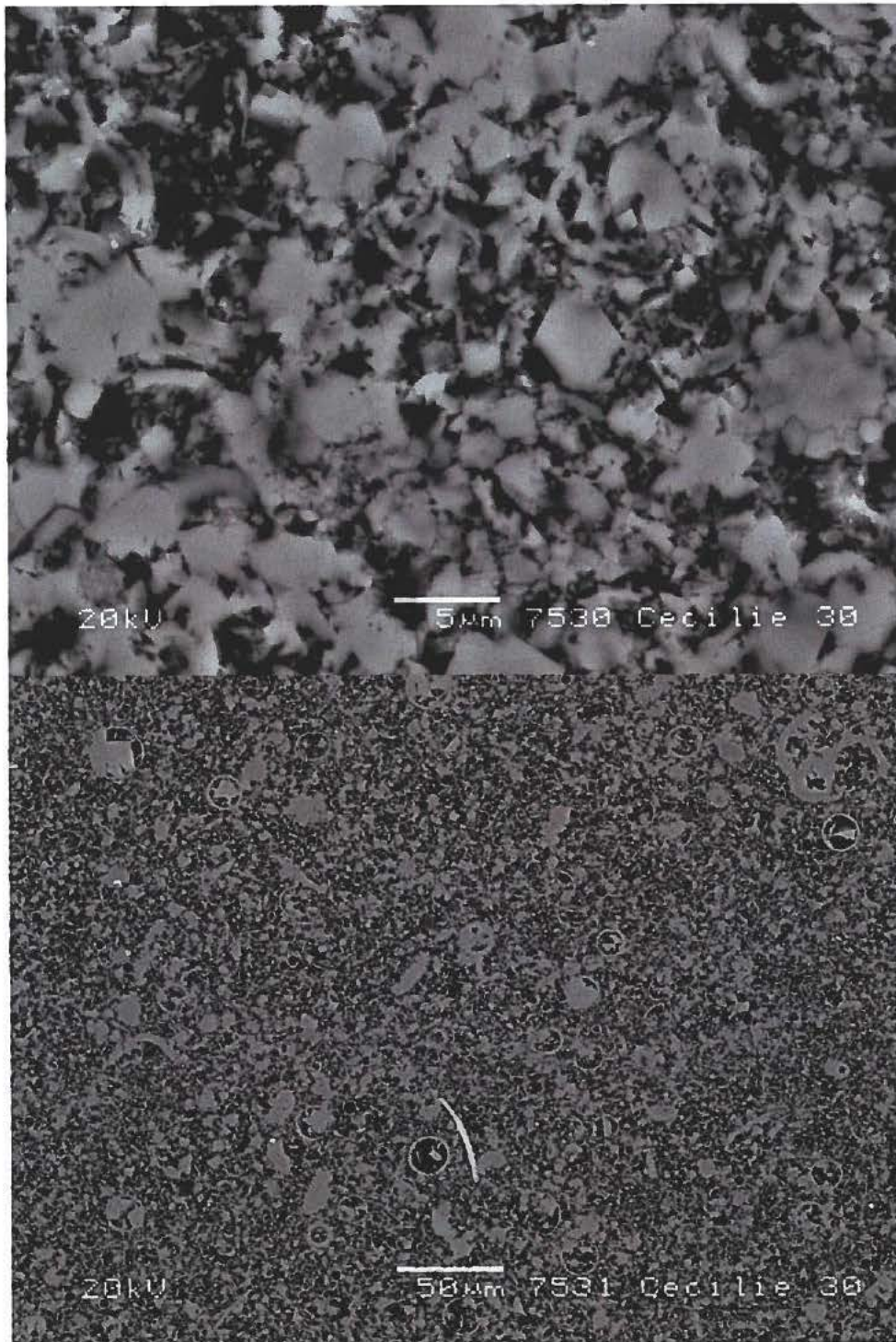
<1% feldspar

4% clay (smectite)

tr. pyrite

tr. apatite

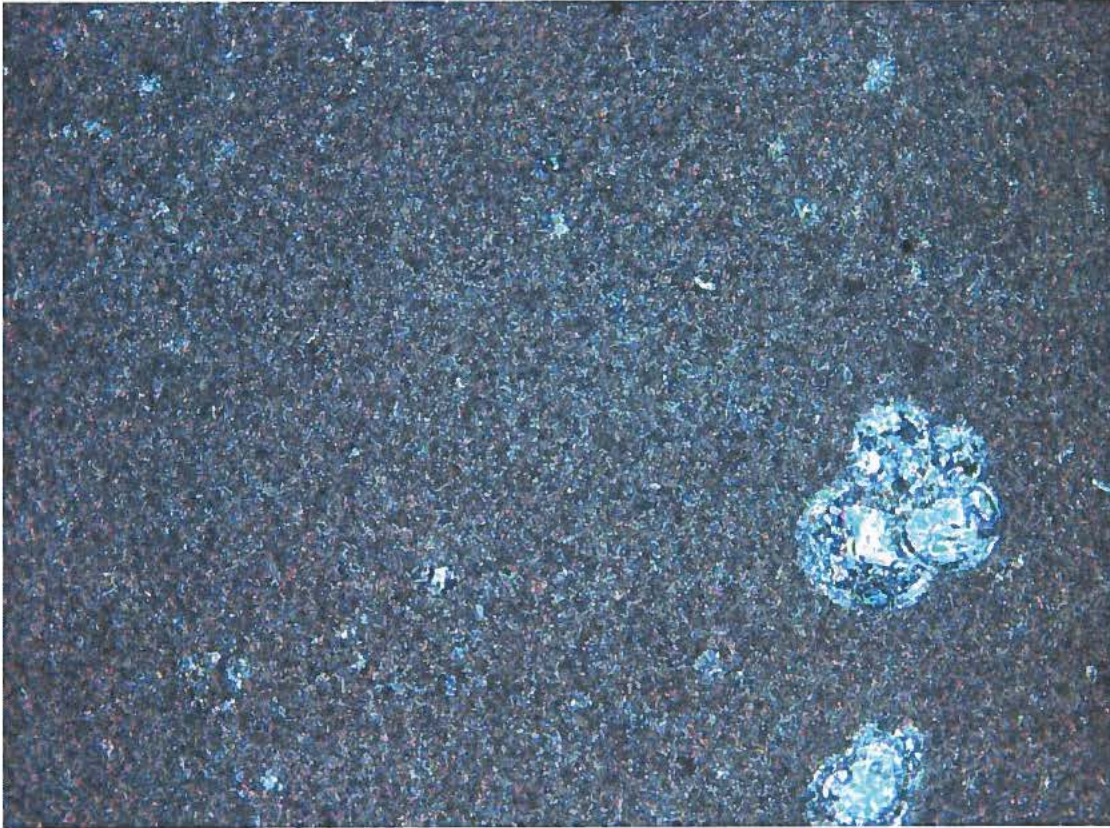
He-porosity 15.38%



Cecilie-1B sample 30. Backscatter electron micrographs

Cecilie-1B sample 31

0.7 mm



Thin section micrograph

Depth 2370 m effective depth 2100 m ($\beta = 1$) - 2200 m (β calculated).

Ekofisk Formation

Mudstone

91% calcite

4% quartz, mainly fine-grained disseminated in pores

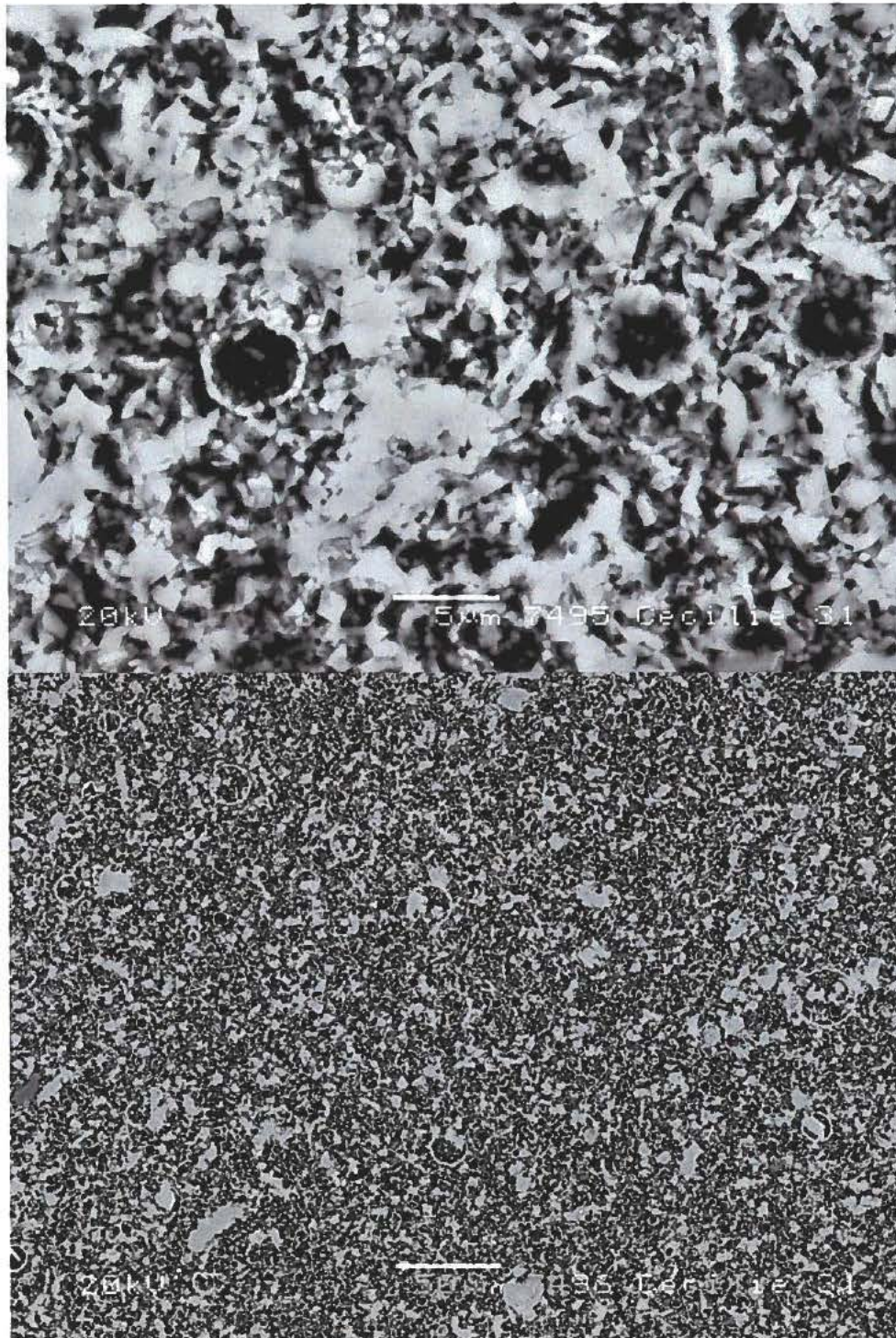
<1% feldspar

2% clay (smectite)

tr. apatite

tr. TiO_2

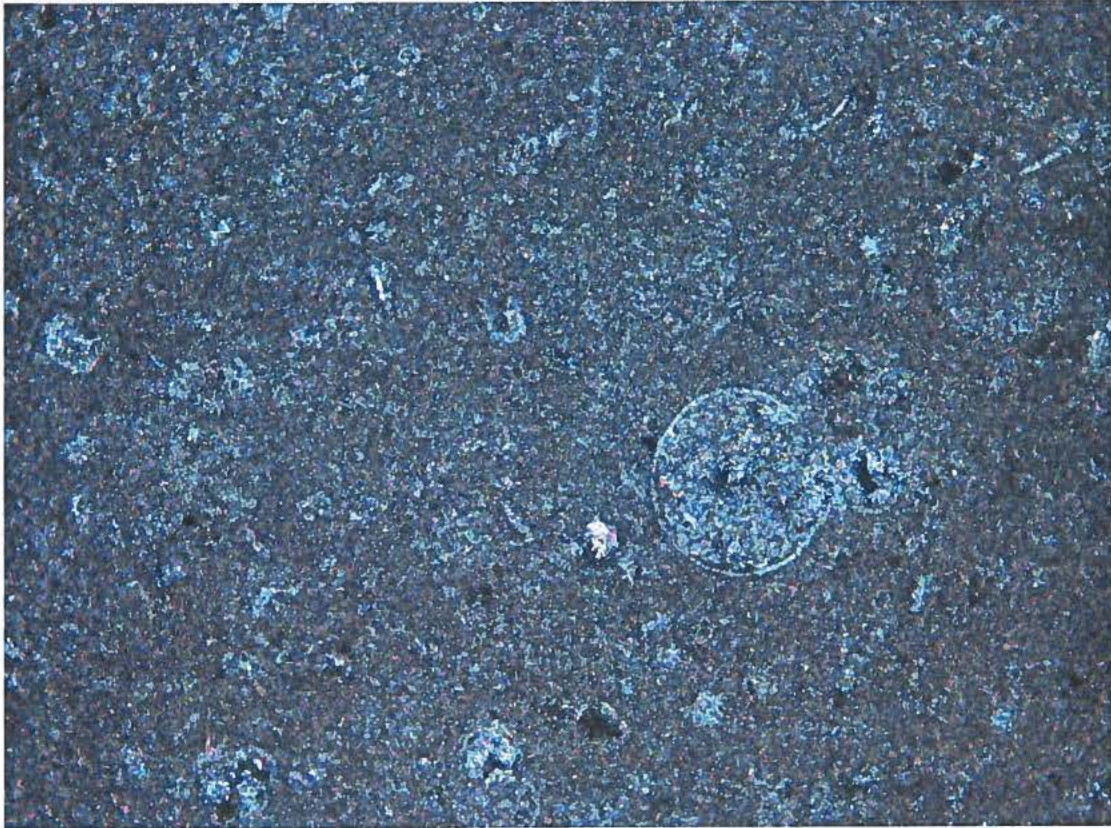
He-porosity 22.57%



Cecilie-1B sample 31. Backscatter electron micrographs

Cecilie-1B sample 32

0.7 mm



Thin section micrograph

Depth 2383 m effective depth 2113 m ($\beta = 1$) - 2282 m (β calculated).

Ekofisk Formation

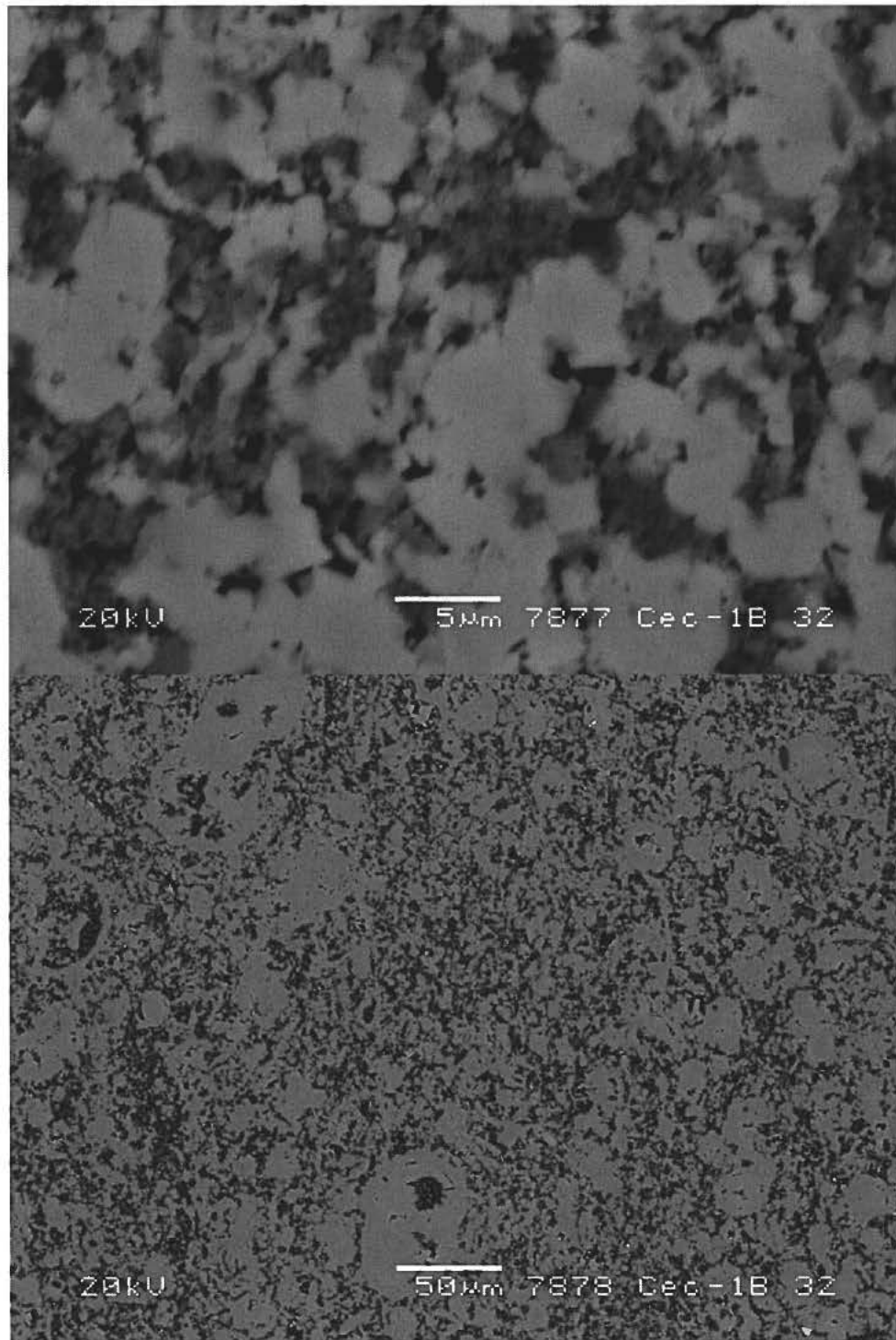
Mudstone

79% calcite (Fe-bearing cement)

13% quartz, mainly fine-grained desiminated in pores

<1% feldspar

He-porosity 6.69%

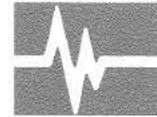


Cecilie-1B sample 32. Backscatter electron micrographs

Chalk Background Velocity Well log analysis

Ødegaard A/S





Report 03.24033.01

Chalk Background Velocity

Well log analysis

GEUS
Denmark

April 2005

Prepared by

Lars Gommesen



This document is confidential.

This document has been published by Ødegaard A/S.

Chalk Background Velocity: Well log analysis

**Report No: 03.24033
2005**

Copyright © 2005 Ødegaard A/S.

This document includes some words, which are or are not asserted to be proprietary names. The presence or absence of such assertions should not be regarded as affecting the legal status of any proprietary name or trademark.



Summary

The main objective of this project is to build a database of quality controlled well log data originating from the Danish North Sea. The database consists of 29 wells and focuses on the logged chalk sections of each well which includes the Ekofisk, Tor, Hod and Hidra formations down to Base Chalk. The secondary objective is to derive dry rock properties from well log data.

The study includes several phases: 1) loading of data, 2) well log quality control and basic editing, 3) petrophysical analysis, where the volume of clay, the porosity and the brine saturation are estimated and compared to corresponding client provided curves and 4) rock physics analysis, where the elastic properties of chalk are derived.

For all wells bulk density and compressional slowness are provided. A total of eight wells have in addition shear slowness provided. Volume of clay, porosity or water saturation interpretations are provided for a total of 24 wells. A total of seven wells had core measurements, such as porosity and density available.

The well log analysis shows that:

- The quality of the well log data is generally good and corrections were only necessary in a limited number of wells: For five wells minor edits were performed. For three wells depth alignments were carried out.
- The petrophysical analysis aims to perform consistent interpretations of the volume of clay, porosity and brine saturation so that intra-well comparison of the elastic properties versus petrophysical properties can be carried out. The analysis shows that a) the provided clay interpretations were in general similar to the interpretations carried out in this study, b) the provided porosity and brine saturation curves were in general similar to the corresponding curves established in this study. The porosity distributions generally fall within three groups: lower (0 to c. 0.15), mid (c. 0.15 to 0.3) and upper (c. 0.35 to 0.4). In some cases, the provided porosity estimates differ from the QC estimates established by Ødegaard A/S. This difference is in some cases explained by choice of method (e.g. density derived estimates versus neutron porosity readings) and in some cases due to difference in choice of matrix density for the density derived estimates.
- The rock physics analysis aims to estimate Biot's coefficient from log data so that effective stress calculations may be carried out. This is done through fluid substitution from the in situ conditions to a dry rock state. The analysis shows that this is possible from dynamic (log) data such as bulk density, compressional and shear velocity.



Contents

Chalk Background Velocity: Well log analysis	ii
Chapter 1	3
Introduction	3
1.1 Well log data.....	3
1.2 Nomenclature.....	4
Chapter 2	5
Well log editing.....	5
2.1 Methods	5
2.2 Results.....	8
2.3 References.....	8
Chapter 3	9
Petrophysical analysis	9
3.1 Volume of clay.....	9
3.2 Porosity	12
3.3 Saturation	16
Chapter 4	19
Rock physics analysis	19
4.1 Fluid substitution	19
4.2 Biot's coefficient.....	20
4.3 References.....	21
Chapter 5	22
List of final products delivered	22
Appendix A. Rock physics theory	23
A.1 General equations.....	23
A.2 Empirical V_p - $RHOB$ relations	23
A.3 Empirical V_p - RT - TVD relations	24
A.4 Empirical V_p - V_S relations.....	24
A.5 Matrix mixture	24
A.6 Fluid mixture.....	25
A.7 V_p -only fluid substitution.....	25
A.8 Gassmann fluid substitution.....	26
A.9 Effective Stress	27
A.10 General lithological identification by cross-plotting	28
A.11 References.....	30



List of Figures

Figure 1. Example of depth alignment. The provided slowness curve (DT, red curve) is replaced by the depth corrected compressional slowness curve (DT_C, black curve).	6
Figure 2. Example of density correction in Bertel-1A. The provided bulk density curve (RHOB, red curve) is replaced by the synthetic empirically derived density curve. The corrected bulk density curve (RHOB_C, black curve) replaces the recorded curve.	6
Figure 3. Bulk density (g/cc) versus compressional slowness (us/ft) for Hod Fm. data of Bertel-1A (blue). The regression applied to predict density from slowness in the example of Figure 2 is included as a red curve. Black data trend is the limestone trend of Castagna et al. [1993], given in the Rock physics theory Appendix. Note the outliers of low density (>2.15 g/cc): The high compressional slowness indicates together with high caliper values that density readings suffer from poor bore hole conditions.	7
Figure 4. Schematic cross-plot of the neutron-density clay estimation principle.	10
Figure 5. Overview comparison of the distributions for the provided volume of clay (VCL) and the estimated volume of clay (VCL_C) (left and right, respectively).	11
Figure 6. Overview of final volume of clay (VCL_C) for the Ekofisk and the Tor intervals. (left and right, respectively). Colors indicate the different wells (unspecified).	11
Figure 7. Overview of final volume of clay (VCL_C) for the Hod 3 and the Hod 2 intervals (left and right, respectively). Colors indicate the different wells (unspecified).	12
Figure 8. Overview of final volume of clay (VCL_C) for the Hod 1 and the Hidra intervals (left and right, respectively). Colors indicate the different wells (unspecified).	12
Figure 9. Overview of effective porosity (PHIE) and total porosity (PHIT) distributions (left and right, respectively).	14
Figure 10. Overview of provided porosity (PHI) and approximate density porosity (PHIT_STD) distributions (left and right, respectively).	14
Figure 11. Overview of estimated total porosity distributions (PHIT_C) for the Ekofisk and the Tor intervals (left and right, respectively).	15
Figure 12. Overview of estimated total porosity distributions (PHIT_C) for the Hod 3 and the Hod 2 intervals (left and right, respectively).	15
Figure 13. Overview of estimated total porosity distributions (PHIT_C) for the Hod 1 and the Hidra intervals (left and right, respectively).	15
Figure 14. Overview comparison of provided water saturation (SW) and the estimated water saturation (SW_C) distributions (left and right, respectively).	17
Figure 15. Example of input parameter file for the porosity-saturation interpretation for Otto-1.	18
Figure 16. Biot's coefficient porosity color-coded by volume of clay and by well (left and right, respectively).	20



- Figure A-1: Empirical relations between acoustic velocity and density for major lithologies [Castagna, 1993]. Contours of acoustic impedance ($\cdot 10^6$) have been plotted on top..... 29
- Figure A-2: Empirical relations between acoustic impedance and Poisson's ratio for sand and shale. Poisson's ratio is generally highly sensitive to sand-shale and pore-fluid variations, while the acoustic impedance is sensitive to porosity and pore-fluid variations..... 30



List of Tables

<i>Table 1. List of wells included in the project.</i>	<i>3</i>
<i>Table 2. Important input parameters for the porosity estimations.</i>	<i>13</i>
<i>Table 3. Mud filtrate resistivity and resistivity tools for wells included in the report entitled South Arne – Petrophysical Chalk Study (Amerada Hess A/S). (*) indicates that Rmf calculated from log data is of a smaller value than reported on the field prints headers. (**) indicates oil based mud.</i>	<i>16</i>
<i>Table 4. Formation water resistivity and salinities for wells included in the report entitled South Arne – Petrophysical Chalk Study (Amerada Hess A/S). (*) indicates min. and max. values calculated from SP. (**) indicates values for Ekofisk and Tor/Hod, respectively.</i>	<i>17</i>
<i>Table 5. Elastic properties of fluid used for the fluid substitution.</i>	<i>19</i>
<i>Table 6. Elastic properties of the matrix used for the fluid substitution.</i>	<i>20</i>
<i>Table A-1: Coefficients for Gardner’s equation as presented by Castagna et al. [1993].</i>	<i>23</i>
<i>Table A-2: Regression coefficients for different lithologies for Greenberg-Castagna V_S prediction.</i>	<i>24</i>



Chapter 1

Introduction

1.1 Well log data

Well log data from a total of 29 wells are included in this project. The 29 wells are well-distributed throughout the Danish sector of the North Sea.

In addition to the primary geophysical logs, bulk density, compressional slowness and shear slowness, other relevant log curves were applied for each well (if available): Caliper, bit size, gamma ray, neutron porosity and resistivity (deep, medium and shallow). In addition, interpreted curves were provided for the majority of the wells: Volume of clay, porosity and water saturation.

A list of the well names and important input is given in *Table 1*.

No.	Well Name	Provided VCL/PHI/SW	Core POROSITY	Measured RHOB/DT	Measured DTS
1	BERTEL-1A	yes	no	yes	no
2	DIAMANT-1	yes	no	yes	no
3	ELIN-1	yes	no	yes	no
4	ELLY-1	yes	no	yes	no
5	ELLY-2	yes	no	yes	no
6	FALK-1	yes	no	yes	no
7	GWEN-2	yes	no	yes	no
8	IRIS-1	yes	yes	yes	no
9	ISAK-1	yes	no	yes	yes
10	NORA-1	yes	no	yes	no
11	OTTO-1	yes	yes	yes	no
12	P-1X	yes	no	yes	no
13	Q-1X	yes	yes	yes	no
14	RAVN-1	yes	no	yes	no
15	RAVN-2	yes	no	yes	no
16	T-1X	yes	yes	yes	no
17	T-3X	yes	yes	yes	no
18	W-1X	yes	no	yes	no
19	BARON-2	yes	no	yes	no
20	I-1X	yes	no	yes	no
21	RIGS-2	yes	yes	yes	yes
22	RIGS-2A	yes	no	yes	yes
23	SA-1	yes	yes	yes	yes
24	NWADDA-1X	no	no	yes	yes
25	SKJOLDFLANK-1	no	no	yes	yes
26	JETTE-1	no	no	yes	yes
27	GERT-1	yes	no	yes	no
28	WESTLULU-1	no	no	yes	yes
29	SINE-1XP	no	no	yes	yes

Table 1. List of wells included in the project.



The lithostratigraphy used in this work was provided by Finn Jacobsen, GEUS. Following picks were considered: Top Ekofisk, Top Tor, Hod 3, Hod 2, Hod 1, Top Hidra and based Chalk.

1.2 Nomenclature

The provided curves are renamed to Ødegaard's standard. All exported data are delivered as LAS files with descriptions in the file header. The most important log curve names are:

Geophysical curves: Bulk density (*RHOB*), Compressional slowness (*DT*), shear slowness (*DTS*).

Additional curves: Caliper (*CAL*), bit size (*BS*), gamma ray (*GR*), neutron porosity (*NPHI*), Resistivity (*RES*, *RESM* and *RESS*) and true vertical depth (*TVDS*).

Interpreted curves: Volume of clay (*VCL*), porosity (*PHIE* and *PHIT*), water saturation (*SW*) and flushed zone saturation (*SXO*). In addition a simple density derived porosity was considered (*PHIT_STD*).

Selected curves: A set of preferred curves were selected from either the client-provided database or the curve sets established during the present work. These curves are: Volume of clay (*VCL_C*), porosity (*PHIE_C* and *PHIT_C*), water saturation (*SW_C*) and flushed zone saturation (*SXO_C*).



Chapter 2

Well log editing

The aim of the well log editing is to quality control and correct the density and acoustic logs, such that these are suitable as input for the rock physics study and the geophysical analysis.

The geophysical well logs are characterized by shallow readings and may therefore be influenced by, for example, borehole rugosity. Accordingly, the logs are corrected, for example around the casing shoes and intervals of washouts. Furthermore, the logs are analysed for apparent malfunctions, such as cycle skipping in the sonic readings, and for missing readings. In both cases, synthetic log data were calculated using numerical approaches such as regression methods or published empirical relationships.

This project focuses only on the chalk interval and the interfaces above and below the chalk interval. For this reason, the final curves may not include the full logged interval of the overburden as well as the full logged interval below the chalk.

2.1 Methods

Various methods were applied to quality control and edit the well log data. This section presents the general methods used in the actual quality control process followed by examples from the actual editing.

Generally, the log readings are deleted at the top of the hole, around the casing shoes or when the logging stops. The log readings are in some cases also deleted in the very bottom of the hole before the tool starts moving.

The geophysical logs are corrected for stretch so that the logs correspond to additional logs such as the gamma ray and the resistivity logs. For West Lulu 1 we have performed depth alignment (*Figure 1*).

In intervals where log readings are identified to suffer from malfunction in the tool, log values were estimated instead. A standard quality control is to analyse the velocity-density relationship. From rock physics theory we know that this relationship among others varies with lithology. The empirical relationships of Gardner et al. [1974] as presented by Castagna et al. [1993] may be used for either quality-checking or predicting density where sonic readings are available, and density readings are not (see Appendix A, Section A.2).

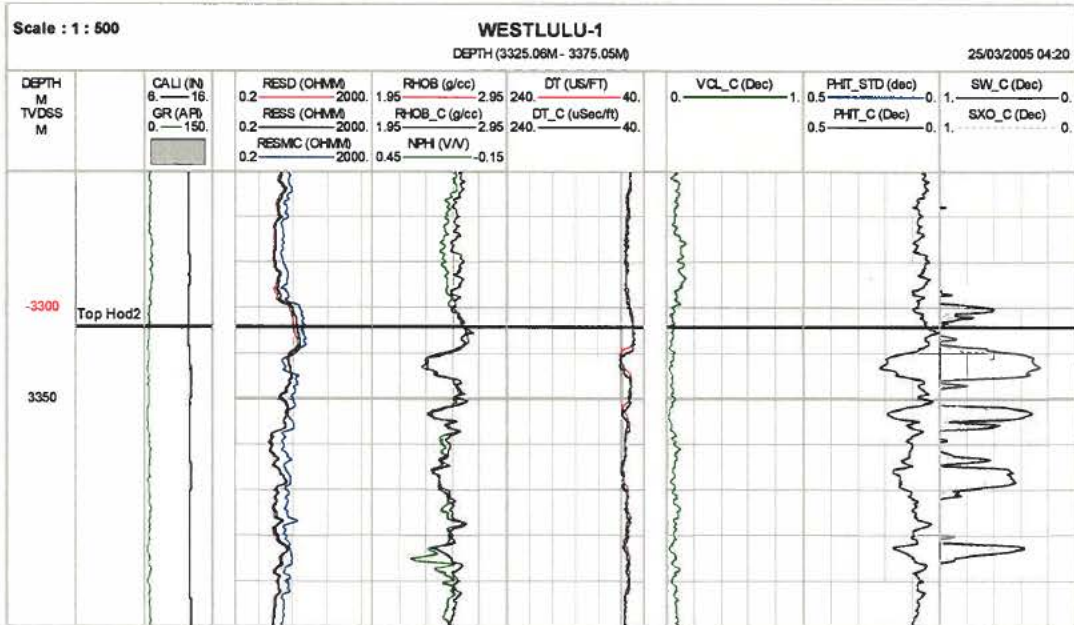


Figure 1. Example of depth alignment. The provided slowness curve (DT, red curve) is replaced by the depth corrected compressional slowness curve (DT_C, black curve).

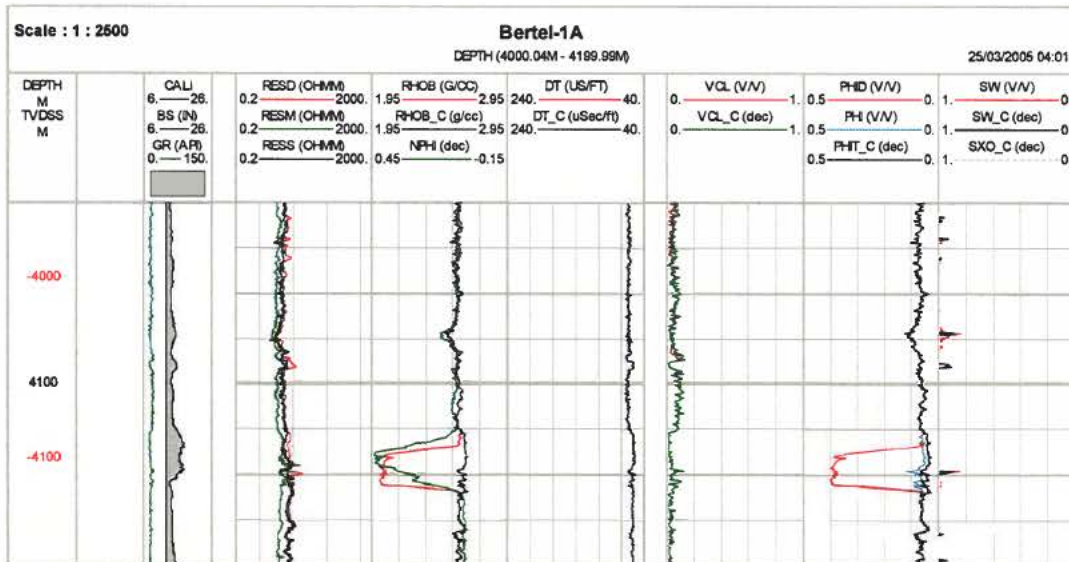


Figure 2. Example of density correction in Bertel-1A. The provided bulk density curve (RHOB, red curve) is replaced by the synthetic empirically derived density curve. The corrected bulk density curve (RHOB_C, black curve) replaces the recorded curve.



Despite the usefulness of the lithology dependent coefficients of Castagna et al. [1993], these do not always predict the density well. Therefore, one may establish an empirical relationship from an appropriate interval within the same well or using a well nearby. Generally, an empirical relationship is established from a linear regression trend established from the *DT-RHOB* cross-plot for the relevant lithologies.

An example of density prediction from the sonic measurements using an empirical relation is found in Bertel-1A in the interval between c. 4125 to 4160 m MD (*Figure 2*). A synthetic density estimate replaces the measured density (*RHOB*) over a minor interval to represent the edited density log (*RHOB_C*). The synthetic density was here based on a linear function obtained on selected Hod Fm. data of Bertel-1A. *Figure 3* shows the *RHOB-DT* cross of selected Hod Fm. data (blue), the empirical linear relation based on the encircled data ($RHOB = 3.0799 - 0.0079DT$) and the limestone trend of Castagna et al. [1993] (black).

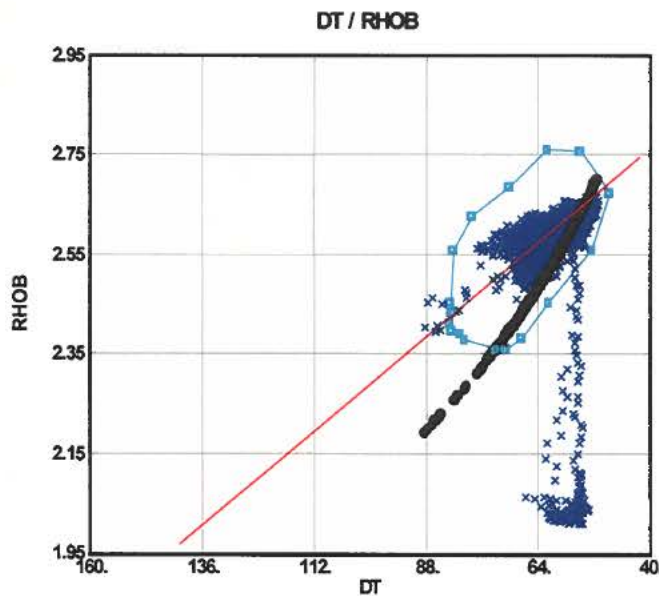


Figure 3. Bulk density (g/cc) versus compressional slowness (us/ft) for Hod Fm. data of Bertel-1A (blue). The regression applied to predict density from slowness in the example of Figure 2 is included as a red curve. Black data trend is the limestone trend of Castagna et al. [1993], given in the Rock physics theory Appendix. Note the outliers of low density (>2.15 g/cc): The high compressional slowness indicates together with high caliper values that density readings suffer from poor bore hole conditions.

The sonic tool readings may be affected by e.g. washouts. The readings of the deeper looking resistivity tool are in some cases applied for editing the sonic log. The so-called Faust relation [Faust, 1953] is used for predicting the acoustic response (see Appendix A, Section A.3). The Faust relation was used to quality control the sonic logs of the wells of this project. However, it was not used to correct any sonic curves.



2.2 Results

The well log editing is presented included on the delivered data CD (03.24033.CD01). Here, the panel plots display the final, corrected geophysical log overlying the corresponding provided logs. Accordingly, the user may see if corrections have been carried out at a given depth.

2.3 References

Castagna J. P., Batzle M. L. and Kan T. K. 1993. Rock Physics – The Link Between Rock Properties and AVO Responce. In: *Offset-dependent reflectivity – Theory and practice of AVO analysis, Investigations in geophysics; no. 8* (eds. Castagna, J. P. & Backus, M. M.), p. 135-171. Society of Exploration Geophysicists.

Gardner, G. H. F., Gardner, L. W. and Gregory, A. R. 1974. Formation velocity and density- The diagnostic basics for stratigraphic traps. *Geophysics*, 39, p. 770-780.

Faust, L. Y. 1953. A Velocity Function Including Lithologic Variation, *Geophysics*, 18, p. 271-297



Chapter 3

Petrophysical analysis

The objective of the petrophysical analysis is to estimate the volume of clay, porosity and saturation in order to either evaluate the provided corresponding interpretations or to simply populate the database.

The client-provided petrophysical work was carried out within Amerada Hess A/S by Jørgen Jensenius and Søren Amdi Christensen. Within Ødegaard A/S the petrophysical work was carried out by David D. Jackson and Lars Gommesen.

3.1 Volume of clay

The estimation of the volume of clay (*VCL*) is a cornerstone in the overall well log interpretation as it influences the porosity estimation and accordingly also the saturation interpretation, which in combination are important input parameters to cross-plot studies and shear slowness prediction.

In this study the volume of clay is based on a combination of two methods:

- Clay interpreted from gamma ray readings (*VCLGR*).
- Clay interpreted from neutron porosity and bulk density (*VCLND*).

The *VCLGR* is based on establishment of chalk and shale base lines defined for specific interval, where the fraction of clay is calculated from a linear relation between the two baselines.

$$VCLGR_e = \frac{GR - GR_{clean}}{GR_{clay} - GR_{clean}} \quad \text{Equation 3-1}$$

The *VCLND* is based on lithology points with zero porosity (chalk and shale) defined in the *RHOB-NPHI* cross-plot. The *VCLND* is accordingly estimated from the grid that these lithology points generate with increasing porosity (*Figure 4*).



$$VCLND_e = \frac{(RHO_{clean2} - RHO_{clean1})(NPHI - NPHI_{clean1}) - (RHO - RHO_{clean1})(NPHI_{clean2} - NPHI_{clean1})}{(RHO_{clean2} - RHO_{clean1})(NPHI_{clay} - NPHI_{clean1}) - (RHO_{clay} - RHO_{clean1})(NPHI_{clean2} - NPHI_{clean1})}$$

Equation 3-2

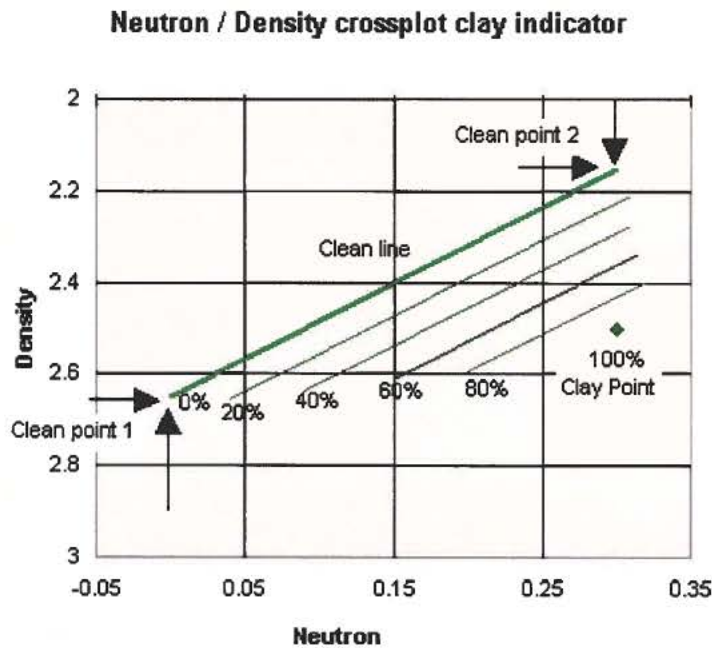


Figure 4. Schematic cross-plot of the neutron-density clay estimation principle.

A fundamental problem with the clay estimation in North Sea chalk is definition of the shale baseline for the *VCLGR* estimation and the 100% clay point for the *VCLND* estimation because of the very low clay volume throughout the chalk interval. However, the clay interpretations are calibrated based on general experience and on the volume of clay curves provided by the client.

The two independent clay estimates are compared to each other as well as to the provided curve for all the wells. Generally, there is a good correspondence between the interpretations and the provided curve as observed from the distributions given in *Figure 5*. Here the x-axis indicates the volume of clay in fractions. The curves represent the normalised distributions of the interpreted volume of clay for the different wells, where the area below each curve is equal (normalised) for all wells.

The final volume of clay (*VCL_C*) of this study is equal to the *VCLGR* interpretation. The *VCLND* is for this project only used as independent qualitative double indicator. The magnitude of the volume of clay is similar, when comparing the client-provided and the interpreted curves. This is illustrated by *Figure 5*. Here the curves represent the normalised distributions for the different wells similarly as the previous figures. For a comparison versus depth, it is recommended to study the panel plots on the delivered data CD (03.24033.CD01).

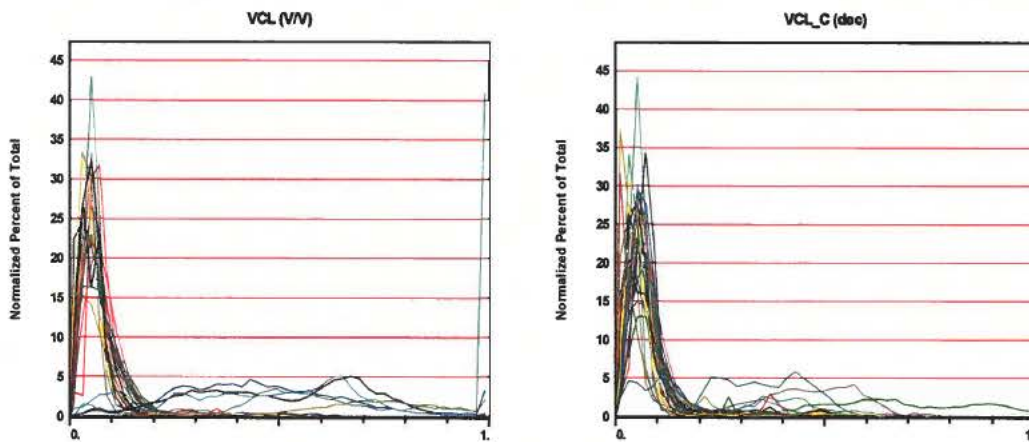


Figure 5. Overview comparison of the distributions for the provided volume of clay (VCL) and the estimated volume of clay (VCL_C) (left and right, respectively).

The histograms of the final volume of clay interpretation (VCL_C) are given for Ekofisk and Tor, Hod 3 and Hod 2, Hod 1 and Hidra respectively in the figures series *Figure 6* to *Figure 8*. From the histograms it is observed that the clay content of the Ekofisk Fm. varies between zero and up to c. 0.2, whereas the Tor Fm. is generally pure and varies between zero and 0.1. The clay volumes of the different units of the Hod Fm. vary internally relatively little and are generally defined within zero and 0.15. The clay volume of the Hidra Fm. varies to the same degree as for the Ekofisk Fm.

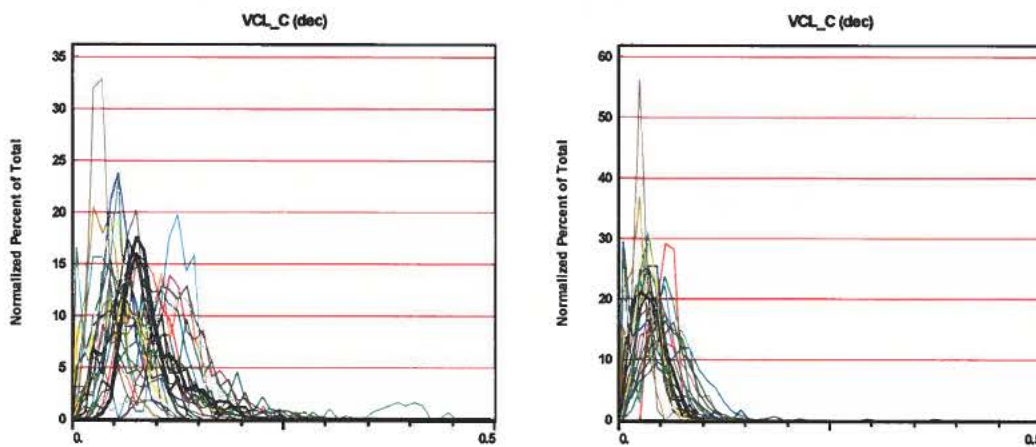


Figure 6. Overview of final volume of clay (VCL_C) for the Ekofisk and the Tor intervals. (left and right, respectively). Colors indicate the different wells (unspecified).

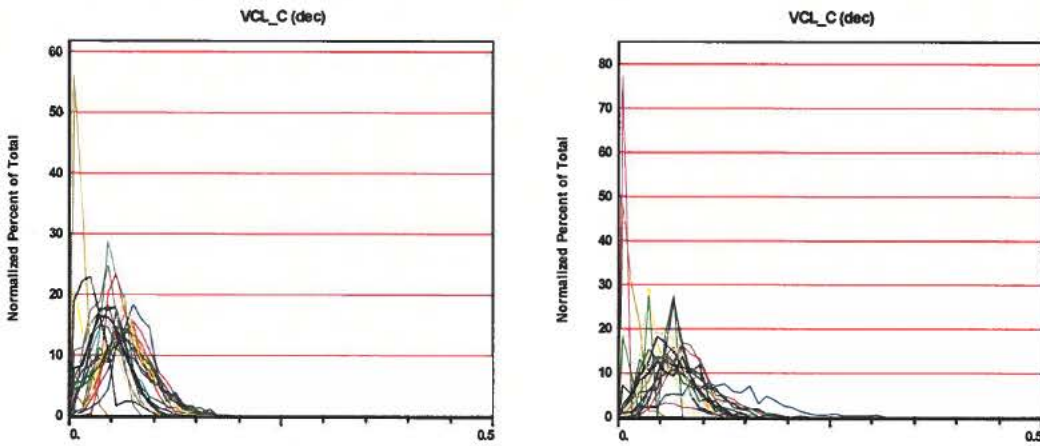


Figure 7. Overview of final volume of clay (VCL_C) for the Hod 3 and the Hod 2 intervals (left and right, respectively). Colors indicate the different wells (unspecified).

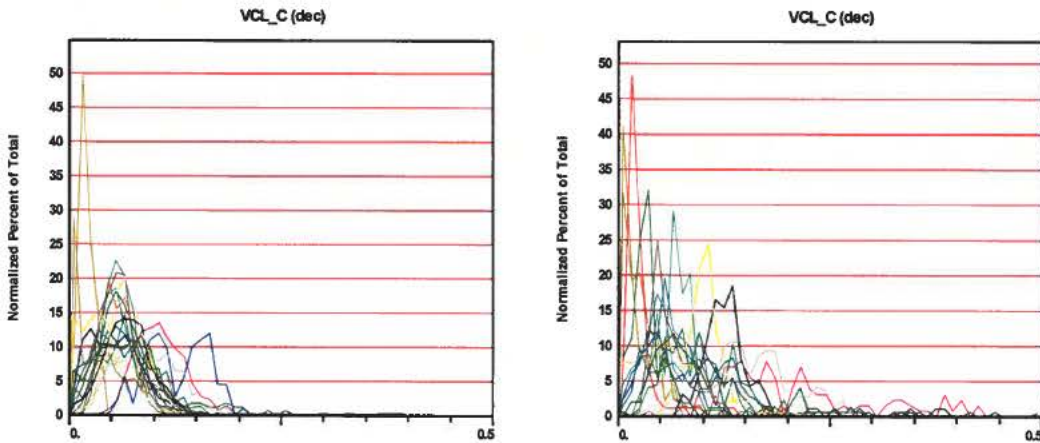


Figure 8. Overview of final volume of clay (VCL_C) for the Hod 1 and the Hidra intervals (left and right, respectively). Colors indicate the different wells (unspecified).

3.2 Porosity

The effective and the total porosity ($PHIE$ and $PHIT$, respectively) are calculated from the bulk density curve ($RHOB$) using the volume of clay, the matrix density and the density of the fluid (or gas) of the flushed zone. As fluid density goes into the calculations, porosity is estimated simultaneously together with saturation.

The effective porosity ($PHIE$, φ_e) is calculated for all wells from the matrix density (ρ_{matrix}), the bulk density (ρ_b), the volume of clay (VCL), wet clay density (ρ_{clay}) and the fluid density (ρ_{fluid}):

$$\varphi_e = \frac{\rho_{matrix} - \rho_b - VCL(\rho_{matrix} - \rho_{clay})}{\rho_{matrix} - \rho_{fluid}} \tag{Equation 3-3}$$



The total porosity (*PHIT*, φ_t) is calculated for all wells. *PHIT* is calculated from the *VCL*, total porosity of the clay (φ_{tclay}) and *PHIE*:

$$\varphi_t = \varphi_e + VCL\varphi_{tclay} \quad \text{Equation 3-4}$$

where total porosity of the clay is calculated from the dry clay density ($\rho_{dryclay}$), the wet clay density ($\rho_{wetclay}$) and the fluid density (ρ_{fluid}):

$$\varphi_{tclay} = \frac{\rho_{dryclay} - \rho_{wetclay}}{\rho_{dryclay} - \rho_{fluid}} \quad \text{Equation 3-5.}$$

Finally, one may do an approximate porosity estimate using only a matrix density excluding the clay component:

$$\varphi_{t_STD} = \frac{\rho_{matrix} - \rho_b}{\rho_{matrix} - \rho_{fluid}} \quad \text{Equation 3-6.}$$

The input parameters for the porosity estimation are given in *Table 2*. On purpose these are kept constant for consistency and for comparison with e.g. curve estimates calibrated to core porosity.

MATRIX	CLAY		FLUIDS		
RHOmatrix	RHOwetclay	RHOdryclay	RHOsxo	RHOhc	RHOhc_min
2.71 g/cc	2.45 g/cc	2.60 g/cc	1.055 g/cc	0.75 g/cc	0.1 g/cc

Table 2. Important input parameters for the porosity estimations.

An overview of the effective and total porosity distributions for all the wells is given as *Figure 9*. Here the curves represent the normalised distributions for the different wells. The x-axis indicates the porosity in fractions. The curves represent the normalised distributions of the interpreted porosity for the different wells, where the area below each curves is equal (normalised) for all wells.

Because of the small fraction of clay generally observed in the chalk interval of these wells, the total and effective porosity estimates are relatively close to each other. Also we observe that the porosity distributions group in three: a low porosity end member ranging from just above zero to c. just above 0.15, an intermediate member from c. just above 0.15 to c. 0.3, and high end members from c. 0.35 to c. just above 0.4. The high end members are Rigs-2 and Rigs-2A. This pattern is also observed from the distributions of the provided porosity interpretations (*Figure 10*). From the same figure it is also observed that the approximate porosity estimate (*PHIT_STD*) is overall acceptable, because of the low volume of clay.

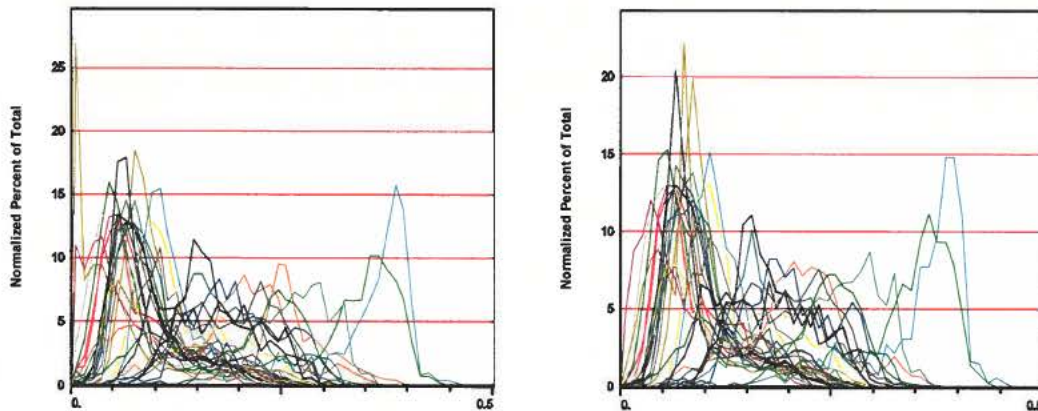


Figure 9. Overview of effective porosity (PHIE) and total porosity (PHIT) distributions (left and right, respectively).

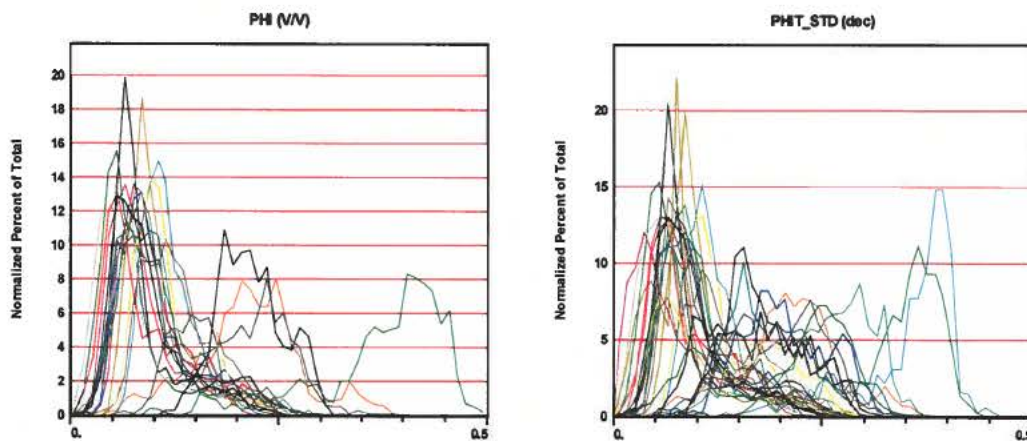


Figure 10. Overview of provided porosity (PHI) and approximate density porosity (PHIT_STD) distributions (left and right, respectively.)

A set of preferred porosity curves was selected from either the client-provided database or the curve sets established during the present work. The curves were selected from a comparison of core porosity trends and trends from cross-plots of log data. The selected curves are named *PHIE_C* and *PHIT_C*.

Studying the total porosity distributions from a lithostratigraphic approach a different pattern is observed. The porosity distributions of the Ekofisk and Tor Fm.s cover a wide spectrum from c. 0.05 to c. just above 0.3 together with the high porosity end members seen in Rigs-2 and Rigs-2A (Figure 11). Generally, the three Hod Fm. sections cover the low to mid range (Figure 12), whereas the Hidra Fm. covers the low end member (Figure 13).

The parameters that are input for the porosity (and saturation) calculations are included on the delivered CD (03.24033.CD01) as text files. An example of the input parameter file of the porosity interpretation is given in Figure 15.

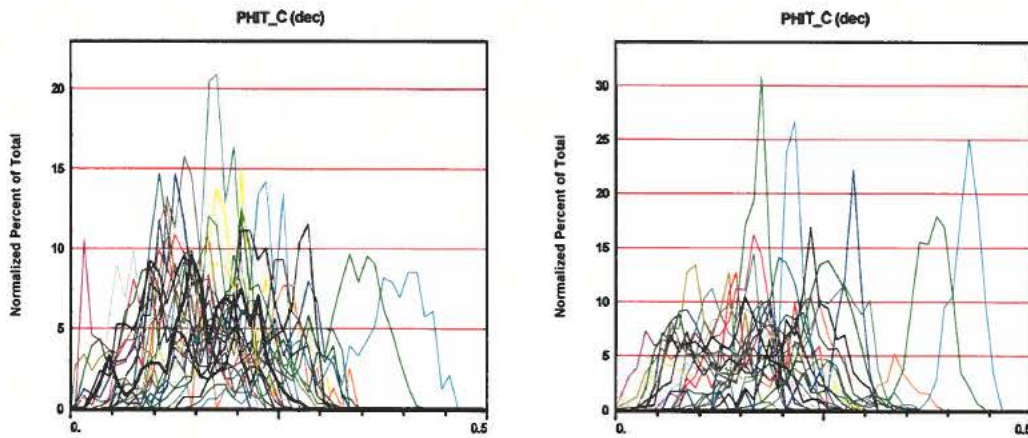


Figure 11. Overview of estimated total porosity distributions (PHIT_C) for the Ekofisk and the Tor intervals (left and right, respectively).

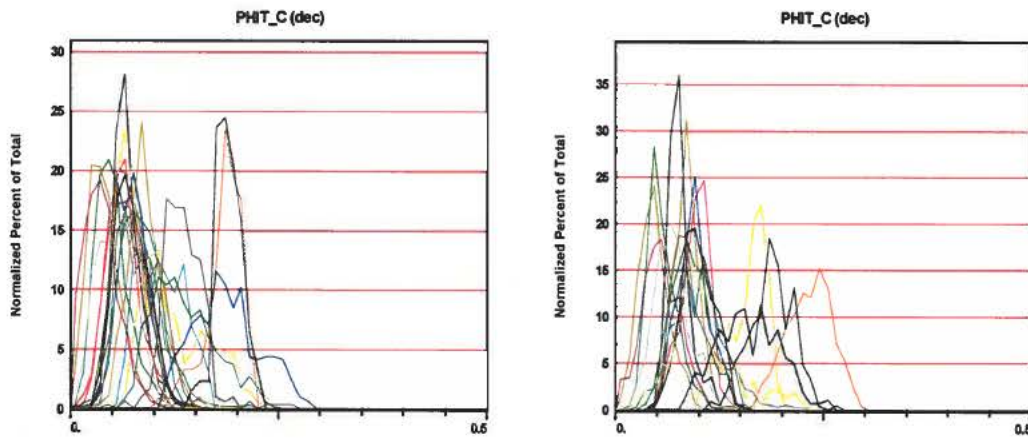


Figure 12. Overview of estimated total porosity distributions (PHIT_C) for the Hod 3 and the Hod 2 intervals (left and right, respectively).

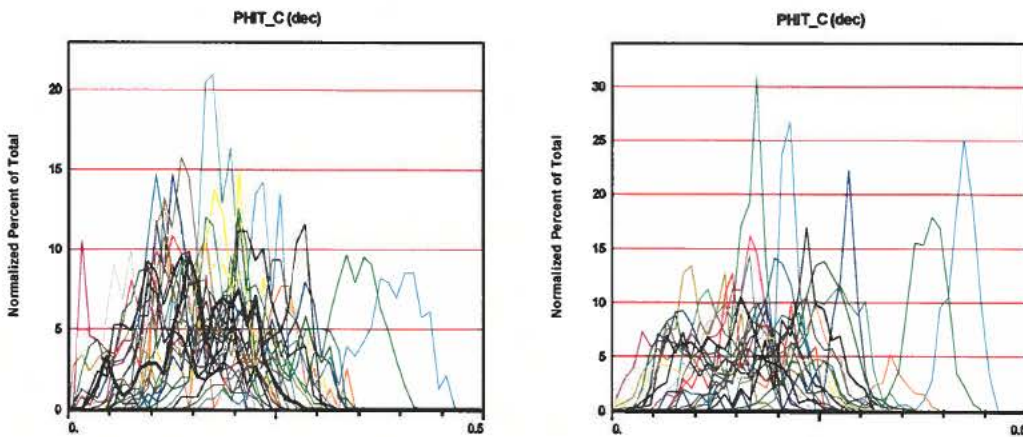


Figure 13. Overview of estimated total porosity distributions (PHIT_C) for the Hod 1 and the Hidra intervals (left and right, respectively).



It is clear that factors such as compaction due to increased effective stress influence the porosity variations of the chalk sequence. However in this work we focus on the actual QC and population of the well log database. The issues of depth-porosity and effective stress-porosity trends are discussed in other contributions to the Chalk Background Velocity project.

3.3 Saturation

Because of the relatively low volumes of clay observed in the wells, we chose to use Archie's equation for estimations of water saturation. Hereby we assume that the impact of the water bound in the clay only influences the total resistivity insignificantly. The brine saturation (S_w) is calculated from the total resistivity (R_T), the formation water resistivity (R_w), and the porosity (ϕ) using Archie's equation:

$$\frac{1}{(R_T)} = \left[\frac{\phi^m}{(aR_w)} \right] \cdot S_w^n \quad \text{Equation 3-7,}$$

where a , m and n in this project are kept constant and equal to 1, 2 and 2, respectively.

As porosity goes into the calculations, saturation is estimated simultaneously together with porosity. Due to the assumptions stated above, the total porosity was used as input to the estimation of saturation. Other important inputs for the saturation estimation are formation water and mud filtrate resistivity. As far as possible this information was extracted from the report *South Arne – Petrophysical Chalk Study* by Søren Amdi Christensen, Amerada Hess A/S. This information is duplicated here as *Table 3* and otherwise, the formation water resistivity is determined from Picket plots.

Well	Rmf Ohmm @ degF	Rmf@75 degF ohmm	Rmf/Rw @ 75 degF	Pref. Res. tool	Used	Problems
Q-1X	0.278 @ 50	0.193	2.40	Induction	6FF40	Poor resolution
T-1X	0.130 @ 57	0.101	0.80	Laterolog	LLD	
OTTO-1	0.068 @ 62	0.057	0.40	Laterolog	LLD	
ELIN-1	0.096 @ 50	0.067	0.48	Laterolog	LLD	
T-3X	0.068 @ 60	0.056	0.35	Laterolog	LLD	
NORA-1	0.151 @ 54	0.112	0.74* (0.76)	Laterolog	LLD	
IRIS-1	0.344 @ 68	0.315	1.25* (2.1)	Induction!	DIL-D	Possibly
GWEN-2	0.114 @ 68	0.104	1.6* (3)	Induction!	DIL-D	Possibly
P-1X	0.343 @ 50	0.238	3.3	Induction	6FF40	
W-1X	0.273 @ 60	0.223	1.64	Laterolog	LLD	
DIAMANT-1	0.330 @ 40	0.189	3.38	Induction	DIL-D	
RAVN-1	0.365 @ 63	0.311	2.55	Induction	DIL-D	
RAVN-2	4**	4	4	Induction	DIL-D	
ELLY-1	0.45 @ 64	0.222	2.44	Induction	DIL-D	
ELLY-2	0.331 @ 56	0.239	2.09	Induction	DIL-D	
FALK-1	4**	4	4	Induction	DIL-D	
BERTEL-1A	0.197 @ 64	0.17	2.65	Induction	DIFL	
ISAK-1	0.063 @ 66	0.09	0.83	Laterolog	HALS	

Table 3. Mud filtrate resistivity and resistivity tools for wells included in the report entitled South Arne – Petrophysical Chalk Study (Amerada Hess A/S). () indicates that Rmf calculated from log data is of a smaller value than reported on the field prints headers. (**) indicates oil based mud.*



Well	Rw(a) @ RESCON ohmm	Formation Water Salinity ppm NaCl
Q-1X	0.044 – 0.076	70500 – 37400*
T-1X	0.051	50200
OTTO-1	0.051	50200
ELIN-1	0.062	46300
T-3X	0.051	50200
NORA-1	0.063	43800
IRIS-1	0.064	46600
GWEN-2	0.035 / 0.026	84000 / 116800**
P-1X	0.030	102400
W-1X	0.060	47800
DIAMANT-1	0.022	144600
RAVN-1	0.046 / 0.035	59800 / 81000**
RAVN-2	0.047	48600
ELLY-1	0.038	64800
ELLY-2	0.038	64800
FALK-1	0.053	42700
BERTEL-1(A)	0.047 / 0.033	55000 / 64000**
ISAK-1	0.045	68600

Table 4. Formation water resistivity and salinities for wells included in the report entitled *South Arne – Petrophysical Chalk Study (Amerada Hess A/S)*. (*) indicates min. and max. values calculated from SP. (**) indicates values for Ekofisk and Tor/Hod, respectively.

An overview of the saturation curves provided by the client and the curves interpreted in this project is given in *Figure 14*. Here the curves represent the normalised distributions for the different wells. The x-axis indicates the water saturation in fractions. From the figure it is observed that the majority of wells have a brine-saturated chalk sequence. It is also observed that for hydrocarbon-bearing chalk with water-saturations less than c. 0.3 the distributions are similar.

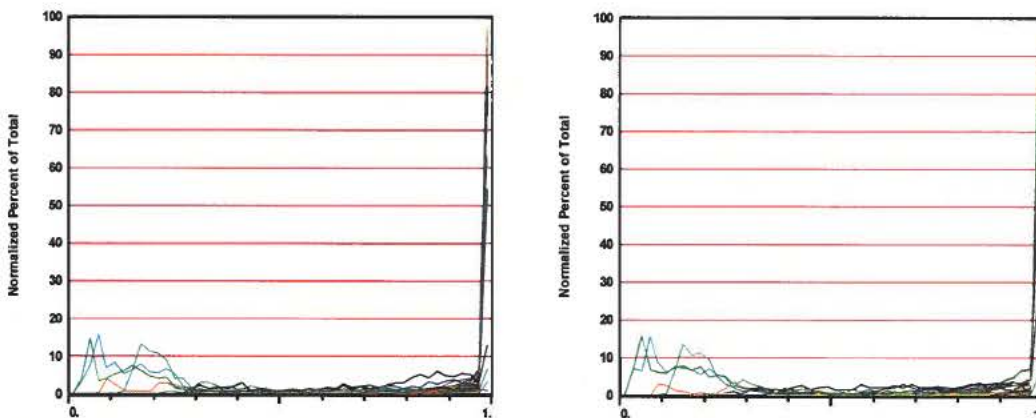


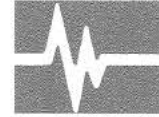
Figure 14. Overview comparison of provided water saturation (SW) and the estimated water saturation (SW_C) distributions (left and right, respectively).

The parameters that are input for the saturation (and porosity) calculation are included on the delivered CD (03.24033.CD01). An example of the input parameter file of the porosity-saturation interpretation is given in *Figure 15*.



POROSITY WATER SATURATION PARAMETERS			
Well : OTTO-1			
Date : 10-08-2004 09:44:53]			
Zone number 1 Vale Top : 2464.50 Bottom : 2475.00			
Rw	: 0.04	Rw Temp	:
Rmf Temp	: 75.	Rho Sxo zone	: 1.055
Rho Dry Clay	: 2.6	Hc Den	: 0.75
GD source	: Param	Rho GD	: 2.71
OBM ?	: No	Phi max	: 0.45
m vari wth vcl	: No	vcl cutoff	: 0.6
Sxo Limit	: 0.2	Sat Equation	: Archie PHT
m exponent	: 2.	n exponent	: 2.
m source	: Param	n source	: Param
Salt Logic	: No	PhIT Clay	:
Rmf	:	Rmf	: 0.057
Rho wet Clay	:	Rho wet Clay	: 2.45
Den Hc app	:	Den Hc app	:
Porosity Method	: Density	Porosity Method	: Density
Delta Phi max	: 0.15	Delta Phi max	: 0.15
Sxo Limit ?	: Yes	Sxo Limit ?	: Yes
a factor	: 1.	a factor	: 1.
Sxo Method	: Rxo	Sxo Method	: Rxo
Coal Logic	: No	Coal Logic	: No
Zone number 2 Ekofisk Top : 2475.00 Bottom : 2485.60			
Rw	: 0.04	Rw Temp	:
Rmf Temp	: 75.	Rho Sxo zone	: 1.055
Rho Dry Clay	: 2.6	Hc Den	: 0.75
GD source	: Param	Rho GD	: 2.71
OBM ?	: No	Phi max	: 0.45
m vari wth vcl	: No	vcl cutoff	: 0.6
Sxo Limit	: 0.2	Sat Equation	: Archie PHT
m exponent	: 2.	n exponent	: 2.
m source	: Param	n source	: Param
Salt Logic	: No	PhIT Clay	:
Rmf	:	Rmf	: 0.057
Rho wet Clay	:	Rho wet Clay	: 2.45
Den Hc app	:	Den Hc app	:
Porosity Method	: Density	Porosity Method	: Density
Delta Phi max	: 0.15	Delta Phi max	: 0.15
Sxo Limit ?	: Yes	Sxo Limit ?	: Yes
a factor	: 1.	a factor	: 1.
Sxo Method	: Rxo	Sxo Method	: Rxo
Coal Logic	: No	Coal Logic	: No
Zone number 3 Tor Top : 2485.60 Bottom : 2595.10			
Rw	: 0.04	Rw Temp	:
Rmf Temp	: 75.	Rho Sxo zone	: 1.055
Rho Dry Clay	: 2.6	Hc Den	: 0.75
GD source	: Param	Rho GD	: 2.71
OBM ?	: No	Phi max	: 0.45
m vari wth vcl	: No	vcl cutoff	: 0.6
Sxo Limit	: 0.2	Sat Equation	: Archie PHT
m exponent	: 2.	n exponent	: 2.
m source	: Param	n source	: Param
Salt Logic	: No	PhIT Clay	:
Rmf	:	Rmf	: 0.057
Rho wet Clay	:	Rho wet Clay	: 2.45
Den Hc app	:	Den Hc app	:
Porosity Method	: Density	Porosity Method	: Density
Delta Phi max	: 0.15	Delta Phi max	: 0.15
Sxo Limit ?	: Yes	Sxo Limit ?	: Yes
a factor	: 1.	a factor	: 1.
Sxo Method	: Rxo	Sxo Method	: Rxo
Coal Logic	: No	Coal Logic	: No

Figure 15. Example of input parameter file for the porosity-saturation interpretation for Otto-1.



Chapter 4

Rock physics analysis

A rock physics analysis was performed on selected wells aiming to estimate the Biot coefficient. The selected wells are: Sine-1XP, Jette-1, Skjold Flank 01, NW Adda-1X, Rigs-2, Isak-1. For these wells, fluid substitution to a dry rock scenario was performed. From the dry properties, the Biot's coefficient was estimated and analysed.

4.1 Fluid substitution

For porous rocks, variations in the elastic properties of the saturating fluid also influence the effective elastic properties. In this context the fluid substitution method is an important tool, because it makes it possible to predict the elastic response of a rock saturated with one type of fluid from the elastic response of the same rock saturated with another fluid. The Gassmann theory [1951] was used for substitution of fluids when both P -wave and S -wave data are available (see Appendix A).

Fluid properties and mixing:

The velocity and density of the fluid before and after fluid substitution may be estimated from Batzle and Wang's formulas [Batzle and Wang, 1992] as cited in Mavko et al. [1998]. The elastic properties of the fluid are given below (*Table 5*).

Bulk modulus and Density	Brine	Oil
K_f [GPa]	2.96	0.52
RHO [g/cm^3]	1.035	0.633

Table 5. Elastic properties of fluid used for the fluid substitution.

In order to calculate the density and velocity of the mixed fluid, the scale of mixing must be considered. In this project only the homogeneous fluid mixing approaches were applied. Fractions of different types of fluids can be assumed to be homogeneous mixed on a small scale. Accordingly, the Reuss average of the composite is used to calculate the effective bulk modulus of the mixed fluid.

Mineral properties and mixing:

The input for the fluid substitution is also depending of the elastic properties of the matrix. When substituting only to a dry rock scenario, one will notice the high sensitivity to the matrix (solid phase) properties. Although the chalk is generally very pure, we aim to include the small amounts of clay in the matrix properties estimation. The matrix properties that are input for the fluid substitutions are given in *Table 5*. The elastic properties of the matrix are estimated as the average values of the upper and lower Hashin-Shtrikmann predictions (*KAHS*) of the calcite and wet clay listed in *Table 6* (for Hashin-Shtrikmann theory, see Appendix A).



	K [GPa]	G [GPa]	RHO [g/cm ³]
Calcite	65	27	2.71
Wet clay	25	9	2.71

Table 6. Elastic properties of the matrix used for the fluid substitution.

4.2 Biot’s coefficient

From fluid substitution to a dry state the dry rock bulk modulus is estimated. From this parameter and the bulk modulus of the solid phase (K_0), Biot’s coefficient (β) can be calculated:

$$\beta = 1 - \frac{K_{dry}}{K_0} \tag{Equation 4-1}$$

We have calculated Biot’s coefficient for the chalk sequence of Sine-1XP, Jette-1, Skjold Flank 01, NW Adda-1X, Rigs-2, Isak-1. From the Biot’s coefficient–porosity cross-plot (including these wells) it is observed that Biot’s coefficient is strongly depending on porosity. This is well known [e.g. Gommessen, 2002]. We also observe that relatively small fractions of clay will introduce some noise to the estimation of Biot’s coefficient. Because data of all the included wells show a similar trend, we believe that the fluid substitution to a dry state has high validity and that we were able to calculate the elastic properties of the solid phase acceptably.

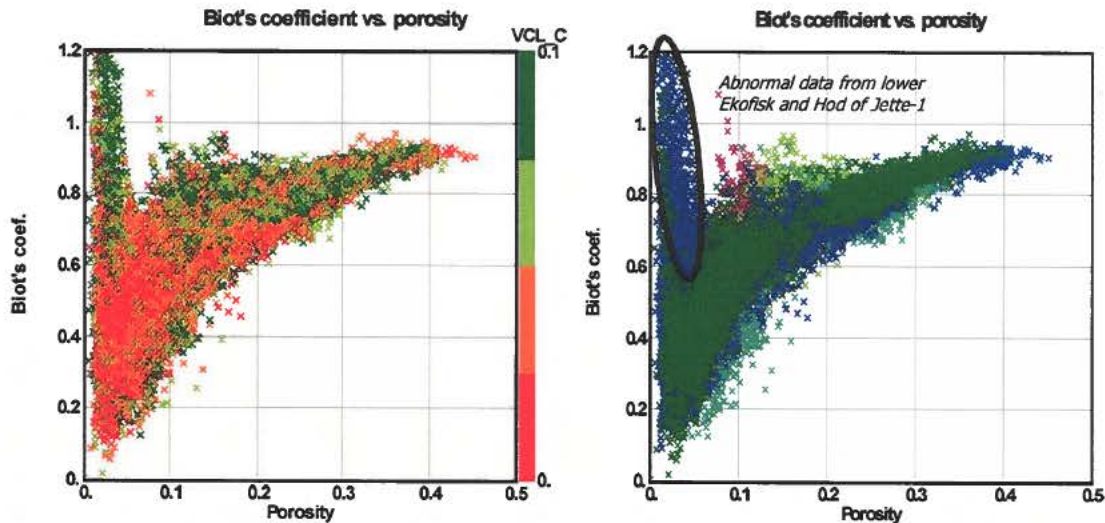


Figure 16. Biot’s coefficient porosity color-coded by volume of clay and by well (left and right, respectively).



Note the abnormal plotting data of lower Ekofisk Fm. and Hod Fm. of Jette-1. Compressional and shear velocity data of these intervals (of Jette-1) generally behave abnormally and therefore also causes abnormal Biot's coefficients.

The elastic curves (*KAHS*, *K_{dry}* and *Biot*) are included on the delivered CD (03.24033.CD01) as las files.

4.3 References

Batzle, M. and Z. Wang: Seismic properties of pore fluids. 1992. *Geophysics*, 57, 1396-1408.

Gassmann, F.: Elastic waves through a packing of spheres. 1951. *Geophysics*, 16, 673-685.

Gommesen, L.: Prediction of porosity and fluid in chalk from acoustic measurements. *PhD thesis*. Environment & Resources, Technical University of Denmark. 2002.

Greenberg, M.L. and Castagna, J.P. 1992. Shear-wave velocity estimation in porous rocks: Theoretical formulation, preliminary verification and application. *Geophysical Prospecting*, 40, 195-209.

Hashin Z. and Shtrikman S. 1963. A variational approach to the theory of elastic behavior of multiphase materials. *Journal of Mechanics and Physics of Solids*, 11, 127-140.

Mavko, G., T. Mukerji and J. Dvorkin 1998. *The Rock Physics Handbook, Tools for Seismic Analysis in Porous Media*. Cambridge University Press.



Chapter 5

List of final products delivered

Report 03.24033.01: Chalk Background velocity, Well log Analysis. CD 03.24033.CD01: Chalk Background velocity, Well log analysis. Report delivered Data delivered	 April 2005 April 2005
--------------------------------------------------------------------------------------------------------------------------------------------------------------------------------	--------------------------------------



Appendix A. ROCK PHYSICS THEORY

This chapter describes the theories applied in the geophysical well log analysis and in the rock physics study.

A.1 General equations

The shear modulus is calculated from the bulk density ($RHOB$) and the shear velocity (V_S) [Mavko et al., 1998]:

$$\mu = \rho V_S^2 \quad \text{Equation A-1}$$

The bulk modulus is calculated from the bulk density ($RHOB$) and the compressional and the shear velocity (V_P and V_S respectively) [Mavko et al., 1998]:

$$K = \rho \left(V_P^2 - \frac{4}{3} V_S^2 \right) \quad \text{Equation A-2}$$

A.2 Empirical V_P - $RHOB$ relations

For the brine-saturated rock Castagna et al. [1993] presented empirical V_P - $RHOB$ relationships for several lithologies based on the general expression established by Gardner et al. [1974]:

$$RHOB = a(V_P)^b \quad \text{Equation A-3}$$

Where V_P in [km/s], $RHOB$ in [g/cm^3].

The coefficients for shale, sandstone, limestone, dolomite and anhydrite are given in Table A-1.

Lithology	a	b	Range [km/s]
Sandstone	1.66	0.386	1.5-6.0
Shale	1.75	0.265	1.5-6.0
Limestone	1.359	0.386	3.5-6.4
Dolomite	1.74	0.252	4.5-7.1
Anhydrite	2.19	0.160	4.6-7.4

Table A-1: Coefficients for Gardner's equation as presented by Castagna et al. [1993].



A.3 Empirical V_P - RT - TVD relations

Faust [1953] established an empirical relationship between total resistivity true vertical depth and velocity:

$$V_{P_Faust} = 1945 * (TVD * RT)^{0.1667} \quad \text{Equation A-4}$$

Where TVD is true vertical depth in [ft], RT is total resistivity in [ohmm], V_{P_Faust} in [ft/s].

A.4 Empirical V_P - V_S relations

For the brine-saturated rock Greenberg and Castagna [1992] established empirical V_P - V_S relationships for several lithologies:

$$V_S = a_{i2}V_P^2 + a_{i1}V_P + a_{i0} \quad \text{Equation A-5}$$

Where V_P and V_S is in [km/s] and represent the fully brine-saturated rock. The regression coefficients a_i are given in Table A-2.

Lithology	a_{i2}	a_{i1}	a_{i0}
Sandstone	0	0.80416	-0.85588
Shale	0	0.76969	-0.86735
Limestone	-0.05508	1.01677	-1.03049
Dolomite	0	0.58321	-0.07775

Table A-2: Regression coefficients for different lithologies for Greenberg-Castagna V_S prediction.

A.5 Matrix mixture

When the matrix (solid phase) is build by more than one constituent the effective elastic moduli can be estimated from Hills average which is simply the average of the harmonic (Reuss) average and the arithmetic (Voigt) average (Equation A-6 to Equation A-8). One may alternatively use the Hashin-Shtrikmann effective medium theory to mix different constituents (Equation A-9 and Equation A-10). Here the upper (+) and the lower (-) Hashin-Shtrikmann (HS) bounds are calculated by interacting which material is named 1 and which is named 2.

$$\frac{1}{M_{Reuss}} = \sum_{i=1}^N \frac{f_i}{M_i} \quad \text{Equation A-6}$$

$$M_{Voigt} = \sum_{i=1}^N f_i M_i \quad \text{Equation A-7}$$



Equation A-8

$$M_{VRH} = \frac{M_{Voigt} + M_{Reuss}}{2}$$

$$K_{HS\pm} = K_1 + \frac{f_2}{(K_2 - K_1)^{-1} + f_1(K_1 + \frac{4}{3}\mu_1)^{-1}}$$

Equation A-9

$$\mu_{HS\pm} = \mu_1 + \frac{f_2}{(\mu_2 - \mu_1)^{-1} + \frac{2f_1(K_1 + 2\mu_1)}{5\mu_1(K_1 + \frac{4}{3}\mu_1)}}$$

Equation A-10

A.6 Fluid mixture

The bulk modulus of a gas-fluid mixture follows the Reuss (iso-stress) average of the composite whereas a gas-fluid mixture follows a harmonic average:

$$\frac{1}{K_f} = \frac{S_{gas}}{K_{gas}} + \frac{S_{oil}}{K_{oil}} + \frac{S_{brine}}{K_{brine}}$$

Equation A-11

$$RHO_f = S_{gas} RHO_{gas} + S_{oil} RHO_{oil} + S_{brine} RHO_{brine}$$

Equation A-12

A.7 V_P -only fluid substitution

The dry bulk modulus is calculated from the dry Poisson's ratio using following equations [Gregory, 1977]:

$$S = 3 \frac{1 - \nu_{dry}}{1 + \nu_{dry}}$$

Equation A-13



$$c = -\phi \left(\frac{s - \rho_b V_p^2}{K_{matrix}} \right) \left(\frac{K_{matrix}}{K_{fSxo} - 1} \right)$$

$$a = S - 1$$

Equation A-15

$$b = \phi S \left(\frac{K_{matrix}}{K_{fSxo} - 1} \right) - S + \frac{\rho_b V_p^2}{K_{matrix}}$$

Equation A-16

$$K_{dry} = K_{matrix} \left(1 - \frac{-b + \sqrt{b^2 - 4ac}}{2a} \right)$$

Equation A-17

Thus the bulk modulus of the fully brine saturated rock is calculated as:

$$K_{100} = \frac{K_{matrix} \left(\frac{K_{brine}}{\phi(K_{matrix} - K_{brine})} + \frac{K_{dry}}{K_{matrix} - K_{dry}} \right)}{1 + \frac{K_{brine}}{\phi(K_{matrix} - K_{brine})} + \frac{K_{dry}}{K_{matrix} - K_{dry}}}$$

Equation A-18

Accordingly the shear modulus is calculated as:

$$\mu = K_{dry} 1.5 \frac{1 - 2 \cdot \nu_{dry}}{1 + \nu_{dry}}$$

Equation A-19

A.8 Gassmann fluid substitution

The Gassmann theory provides a fluid substitution method which assumes that isotropically distributed pores of arbitrary shapes in a homogeneous solid phase are connected and therefore can communicate. The assumption requires sufficiently low frequencies because the pore fluid here instantaneously equilibrates in the connected pore space when the sound wave propagates through the rock. The bulk modulus increases when a stiffer pore fluid replaces a more compressible pore fluid, while the shear modulus is predicted to be independent of the saturating fluid.



The Gassmann relations may generally be written as [Gassmann, 1951]:

$$\frac{K_{sat}}{K_{matrix} - K_{sat}} = \frac{K_{dry}}{K_{matrix} - K_{dry}} + \frac{K_f}{\phi(K_{matrix} - K_f)} \quad \text{Equation A-20}$$

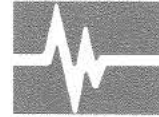
$$\mu_{sat} = \mu_{dry} \quad \text{Equation A-21}$$

A.9 Effective Stress

The effective pressure is estimated from the pore pressure (PP), Biot's coefficient (β) and the overburden stress (σ) as:

$$\sigma' = \sigma - \beta PP \quad \text{Equation A-22}$$

Note, that the Biot coefficient is here assumed to be equal to the coefficient of external stress.



A.10 General lithological identification by cross-plotting

Cross plotting of the well log data can be used to aid interpretation of the inversion results. The well log data can be used to establish relationships between lithology and the physical parameters determined in the seismic inversions, e.g. acoustic impedance and Poisson's ratio. These relationships can then be used to predict lithology from the inversion results.

Figure A-1 shows a cross-plot of acoustic velocity versus density with general curves for some common lithologies [Castagna, 1993]. Contours of acoustic impedance are drawn on the plot. The plot shows the following:

- Acoustic impedances of sand and shale are similar
- Limestone and sand-shale lithologies can be separated in acoustic impedance.
- Low porosity lithologies tend to have large acoustic impedance while high porosity lithologies have low values of acoustic impedance.

Figure A-2 shows a cross-plot of acoustic impedance versus Poisson's ratio. Empirical sand and shale lines are plotted, and general trends of varying pore-fluid and compaction are indicated. Poisson's ratio is, generally, very sensitive to sand-shale and pore-fluid variations, while the acoustic impedance is sensitive to porosity and pore-fluid variations. The plot also indicates that by using a combination of acoustic impedance and Poisson's ratio gas sands can be separated from water filled sands and sands can be separated from shales.

Identification of lithologies using cross-plots of log data and subsequent correlation to the inversion results makes it possible to make regional lithology interpretations and increase confidence in hydrocarbon detection.

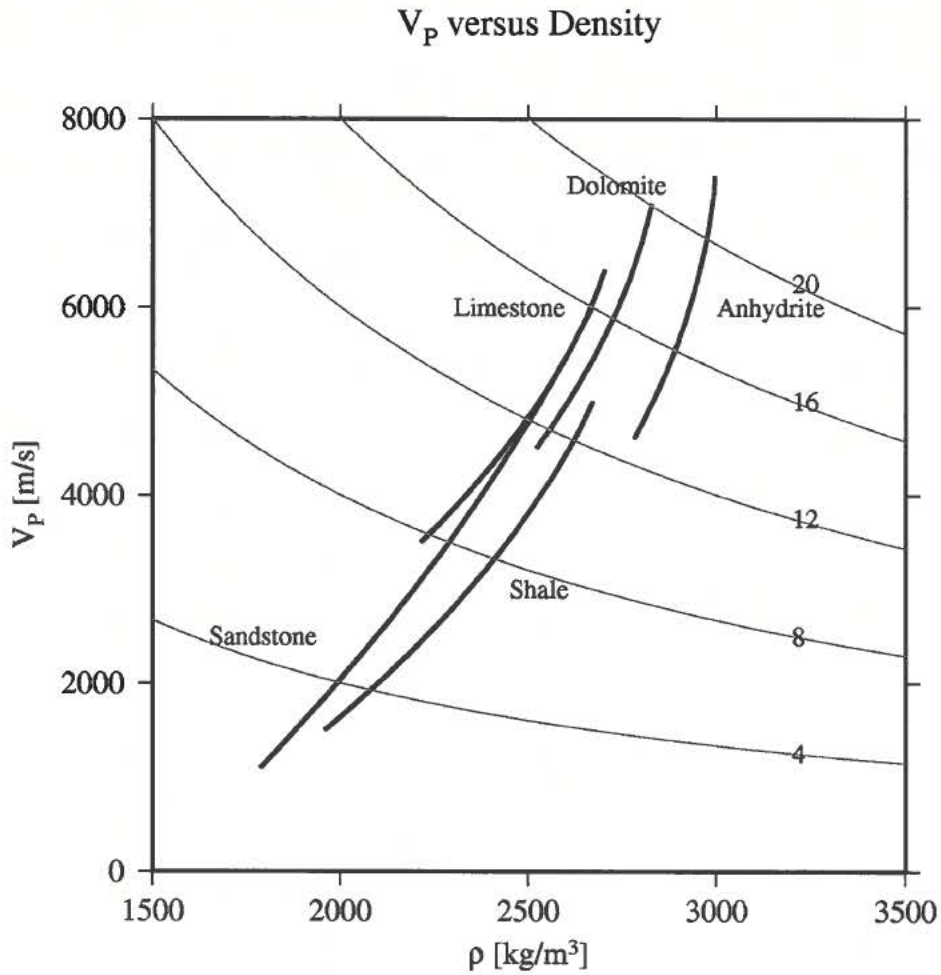


Figure A-1: Empirical relations between acoustic velocity and density for major lithologies [Castagna, 1993]. Contours of acoustic impedance ($\cdot 10^6$) have been plotted on top.

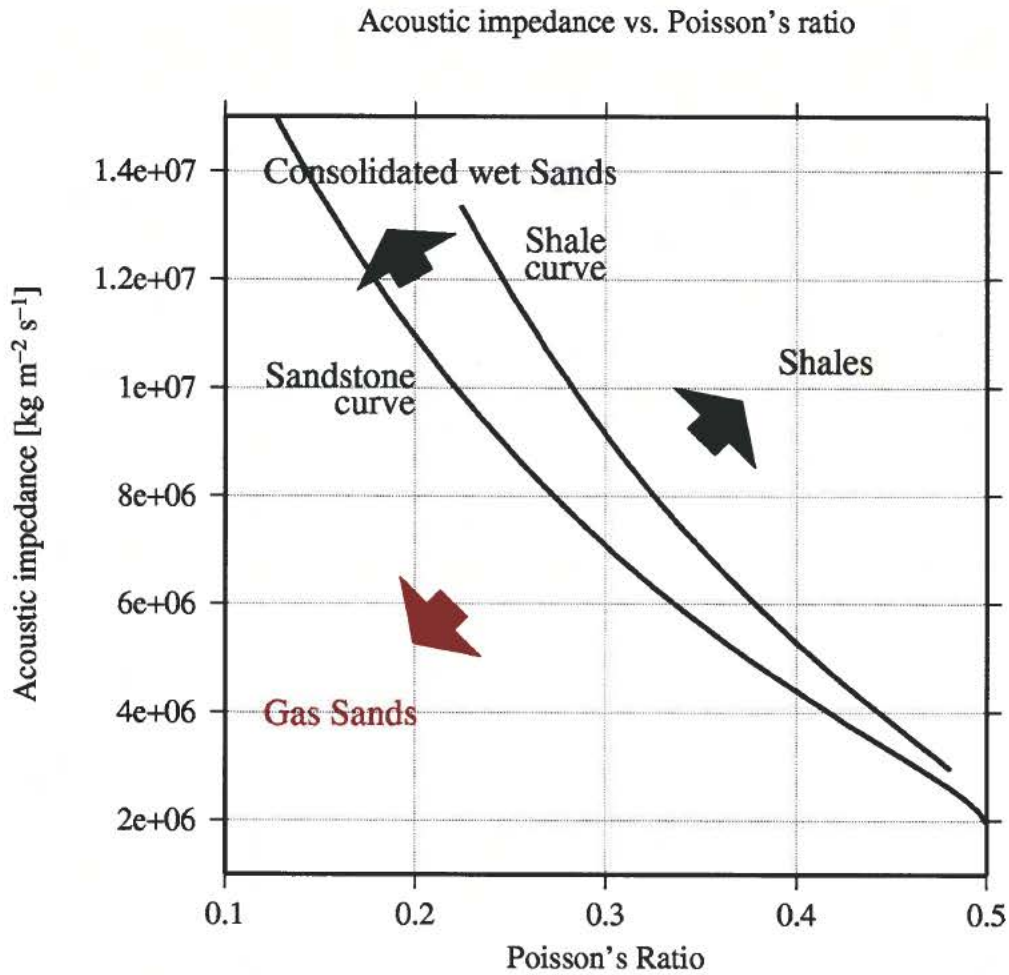


Figure A-2: Empirical relations between acoustic impedance and Poisson's ratio for sand and shale. Poisson's ratio is generally highly sensitive to sand-shale and pore-fluid variations, while the acoustic impedance is sensitive to porosity and pore-fluid variations.

A.11 References

Castagna, John P. and Backus, Milo M., 1993, *Offset-dependent reflectivity - Theory and practice of AVO analysis*. Society of Exploration Geophysicists.

Faust, L. Y. 1953. A Velocity Function Including Lithologic Variation, *Geophysics*, 18, p. 271-297.

Gassmann, F., 1951: Elastic waves through a packing of spheres. *Geophysics*, 16, 673-685.



Gregory, 1977. Hampton Russel.

Mavko, G., Mukerji, T. and Dvorkin, J.: *The Rock Physics Handbook, Tools for Seismic Analysis in Porous Media*. Cambridge University Press, 1998.

Shuey, R.T., 1985. *A simplification of the Zoeppritz equations*. *Geophysics*, **50**, 609-614.

Smith, G.C. and Gidlow, P.M., 1987. *Weighted Stacking for Rock Property Estimation and Detection of Gas*. *Geophysical Prospecting*, **35**, 993-1014.

Lithostratigraphy and physical properties of the Chalk Group from Danish North Sea wells

A contribution to the Chalk Background
Velocity project

Peter Japsen, Finn Jacobsen & Torben Bidstrup



Lithostratigraphy and physical properties of the Chalk Group from Danish North Sea wells

A contribution to the Chalk Background
Velocity project

The Chalk Background Velocity project
is funded by the South Arne Group

Peter Japsen, Finn Jacobsen & Torben Bidstrup

Contents

1. Introduction	3
2. Lithostratigraphic subdivision	4
Introduction	4
Database	4
Lithostratigraphy	4
Intra-Chalk Unconformity.....	5
3. Formation pressure	12
Overpressure due to compaction disequilibrium	12
Effective depth for $\beta=1$	12
Chalk pressure data	14
4. Temperature	19
5. Acoustic properties	24
Comments to the cross plots for the individual wells	26
6. Data CD	36
Lithostratigraphic subdivision	36
Excel file with depth to individual boundaries in the wells.....	36
CGM files with cross correlation of log data.....	36
Acoustic properties	38
Power Point files with cross plots of log data	38
MatLab files with log data for the chalk sections in each well.....	39
7. References	40
Appendix 1: The main lithostratigraphic formations	42
Appendix 2: Cross plots of log data	46
Vp plots	47
Vp-Vs plots	104

1. Introduction

The present report is a contribution to the project "Variability of the chalk background velocity in the South Arne area". The project is funded by the South Arne Group (Amerada Hess Aps, Dong E&P, Denerco Oil) and the partners in the project are GEUS, DTU E&R, Ødegaard A/S and Gary Mavko (Stanford University).

The aims of the project are the following

- Quantification of how the chalk background velocity (the low-frequent velocity variations which define the absolute level of the chalk velocity) in the South Arne area is affected by effective stress, presence of hydrocarbons as well as porosity, composition, texture and cementation of chalk.
- Estimation of upper and lower bounds on chalk porosity estimated from seismic inversion based on the analysis of these factors.
- Evaluation of the usefulness of velocities estimated from seismic processing as a supplement to well log data for establishing chalk background velocity.

The present report documents various aspects of the Chalk Group in wells in the Danish North Sea: the lithostratigraphic subdivision of the chalk (29 wells), the temperature at the top and the base of the chalk, the formation pressure and the acoustic properties estimated from well logs (28 wells). Most of the wells are located in the northern part of the Danish Central Graben. Stratigraphic correlation diagrams, log data in MatLab format and PowerPoint files with cross plots of the log data are included on a CD.

2. Lithostratigraphic subdivision

Introduction

The Chalk Group in 29 wells has been divided into lithostratigraphic units (Figure 2.1). The subdivision follows the formal lithostratigraphic nomenclature for the Chalk Group (Isakson & Tonstad 1989; Surlyk *et al.* 2003) and includes the Ekofisk, Tor, Hod, Blødøks and Hidra Formations (Figure 2.2).

The basis for the subdivision is the bio- and log-stratigraphy provided by the drilling operators. There are, however, some inconsistencies connected with the identification of the top and base of the various formations due to inadequate biostratigraphical information. Inconsistencies are often related with the determination of the top Hod Formation. In this study a consistent definition of the top of the Hod Formation is attempted by referring the surface to the major regional unconformity (the Intra-Chalk Unconformity) associated with the Late Campanian inversion in the Central Graben area.

The thickness of the chalk formations varies according to depositional basin setting and a number of hiatus are found within the different formations. In addition to the Upper Campanian Intra-Chalk Unconformity, two unconformities are encountered in the Cenomanian to Santonian succession (within the Lower and Middle Hod). These unconformities are identified from seismic interpretation and are generally overlooked in well interpretation unless detailed biostratigraphy in that section is available (among others Robertson Research International Ltd 1984). The thickness variation within the various formations is illustrated in the enclosed correlation panels (Enclosure 1-3). Hiatus identified within the various wells are indicated in Appendix 1.

Database

29 wells have been selected for the study (Table 2.1, Figure 2.1). Wire-line logs and biostratigraphic data from these wells are used for the lithostratigraphical subdivision. The stratigraphical data available for this study are primarily from final completion well reports provided by the drilling operator. When available, additional biostratigraphical reports have been included.

Lithostratigraphy

Different lithostratigraphic subdivisions of the Chalk Group are shown in Figure 2.2. The definition of the top Hod formation varies between authors and may range from being an internal Upper Campanian surface (Vejbæk & Andersen 1987) to represent the Campanian

/Maastrichtian boundary (Surlyk *et al.* 2003; Figure 2.2). In this study the lithostratigraphy given in the Millennium Atlas (Surlyk *et al.* 2003) is applied and consequently the Upper Campanian deposits are included in the Hod formation. A hiatus (the Intra-Chalk Unconformity) is found between the Hod and Tor formations. The hiatus is associated with a regional sea level fall and inversion of varying intensity within the Danish Central Graben area.

For illustration of the hiatus and thickness variations within the Tor and Hod Formations a correlation between the internal horizons/unit tops has been carried out (Enclosure 1-3). The division of the Chalk sequence into subunits is based on the log motif and biostratigraphy. The horizons/unit tops used for this correlation are listed in Table 2.2 and a correlation is shown in Figure 2.3 using the Gwen-2 and Sine-1 as reference wells. Both wells comprise a thick and a nearly complete stratigraphic section of the post-Cenomanian sequence, but are located in two different geological provinces with different subsidence history during the Late Cretaceous. The surface picks from the examined wells are listed in Appendix 1.

Intra-Chalk Unconformity

A major hiatus characterises the boundary between the Hod and the overlying Tor formations and is associated with the major sea level fall and inversion during Late Campanian (Oakman & Partington, 1998). On seismic data the top of the Hod formation is connected with an unconformity (the Intra-Chalk Unconformity). The unconformity is significant in the southern part of the Danish Central Graben and is associated with severe erosion and non-deposition. The unconformity locally represents a hiatus ranging in age from Santonian to Maastrichtian, but occasionally the hiatus represents a minor time gap ranging in age from the latest Campanian to earliest Maastrichtian (e.g. Sine-1 and Skjold Flanke-1).

Contrary to Vejbæk & Andersen (1987), the unconformity is here considered as isochronous with significant variations in the time span of the missing section in the different wells. The time gap related to the hiatus in the various wells is indicated in Appendix 1.

The Intra-Chalk Unconformity mirrors a significant change in the depositional environment and represents the boundary between two generally different lithofacies. The rock properties related to the lithofacies are controlled by the geological setting, which again is controlled by the tectonic regime. For illustration of the variation in thickness and lithotypes in the Danish Central Graben the geological setting is summarised below.

A compressional tectonic regime with inversion prevailed during the deposition of the Hydra and Hod Formations. The inversion activity ceased through the Late Upper Cretaceous and the Intra-Chalk Unconformity represents the end of the main inversion activity during Late Campanian. Contemporaneously with the tectonic activity the global sea level continued to rise throughout the Santonian and into the Campanian, reaching a high stand maximum in the late Campanian. In the Danish Central Graben the high stand is locally masked by the compressive event resulting in inversion structures (Figure 2.4). Significant parts of the

Campanian succession are absent over inversion swells suggesting considerable local erosion and redeposition in adjacent deeper sub-basins

Large thickness variations developed, as the post-inversion topography was infilled during the Maastrichtian and Danian. Deeper subbasins were filled with considerable thicknesses of mass-flow and turbiditic chalk. Thick basinal chinks, often of remarkable purity, can be mapped adjacent to the inversion area e.g. to the east of the inversion axis on the Ringkøbing Fyn High (represented by the Sine-1 well).

The difference between inversion swells with erosion and/or non-deposition and basins gives rise to significant variation in the lithofacies and thickness especially for the Hod and Tor formations; which is demonstrated by this study.

Table 2.1. *Wells used in this study*

Baron-2	Falk-1	Jette-1	Ravn-1	Skjold Flank-1
Bertel-1A	Gert-1	Nora-1	Ravn-2	T-1
Diamant-1	Gwen-2	NW Adda-1	Rigs-1	T-3
Elin-1	I-1x	Otto-1	Rigs-2	W-1
Elly-1	Iris-1	P-1x	SA-1	W. Lulu-1
Elly-2	Isak-1	Q-1	Sine-1	

Table 2.2. Correlation surfaces used in the study. The formal lithostratigraphic boundaries are marked in bold blue and unit tops are in black.

Chronostratigraphy		Correlation horizons Formation and unit tops	Abbreviations
Danian		Top Chalk Ekofisk 3 Ekofisk 2 Ekofisk 1	Top Chalk Eko3 Eko2 Eko1
Maastrichtian	Latest Maastrichtian	Top Tor Upper Tor 2 Upper Tor 1	Top Tor UT2 UT1
	Late Maastrichtian	Middle Tor 2 Middle Tor 1	MT2 MT1
	Early Maastrichtian	Lower Tor 3 Lower Tor 2 Lower Tor 1	LT3 LT2 LT1
Campanian	Late Campanian	Top Hod Upper Hod 4 Upper Hod 3	Top Hod UH4 UH3
	Early Campanian	Upper Hod 2 Upper Hod 1	UH2 UH1
Santonian		Middle Hod 4 Middle Hod 3	MH4 MH3
Coniacian		Middle Hod 2 Middle Hod 1	MH2 MH1
Turonian		Lower Hod 4 Lower Hod 3 Lower Hod 2 Lower Hod 1	LH4 LH3 LH2 LH1
Cenomanian		Top Plenus Marl	
		Top Hydra	Top Hydra
Albian		Base Chalk	Base Chalk

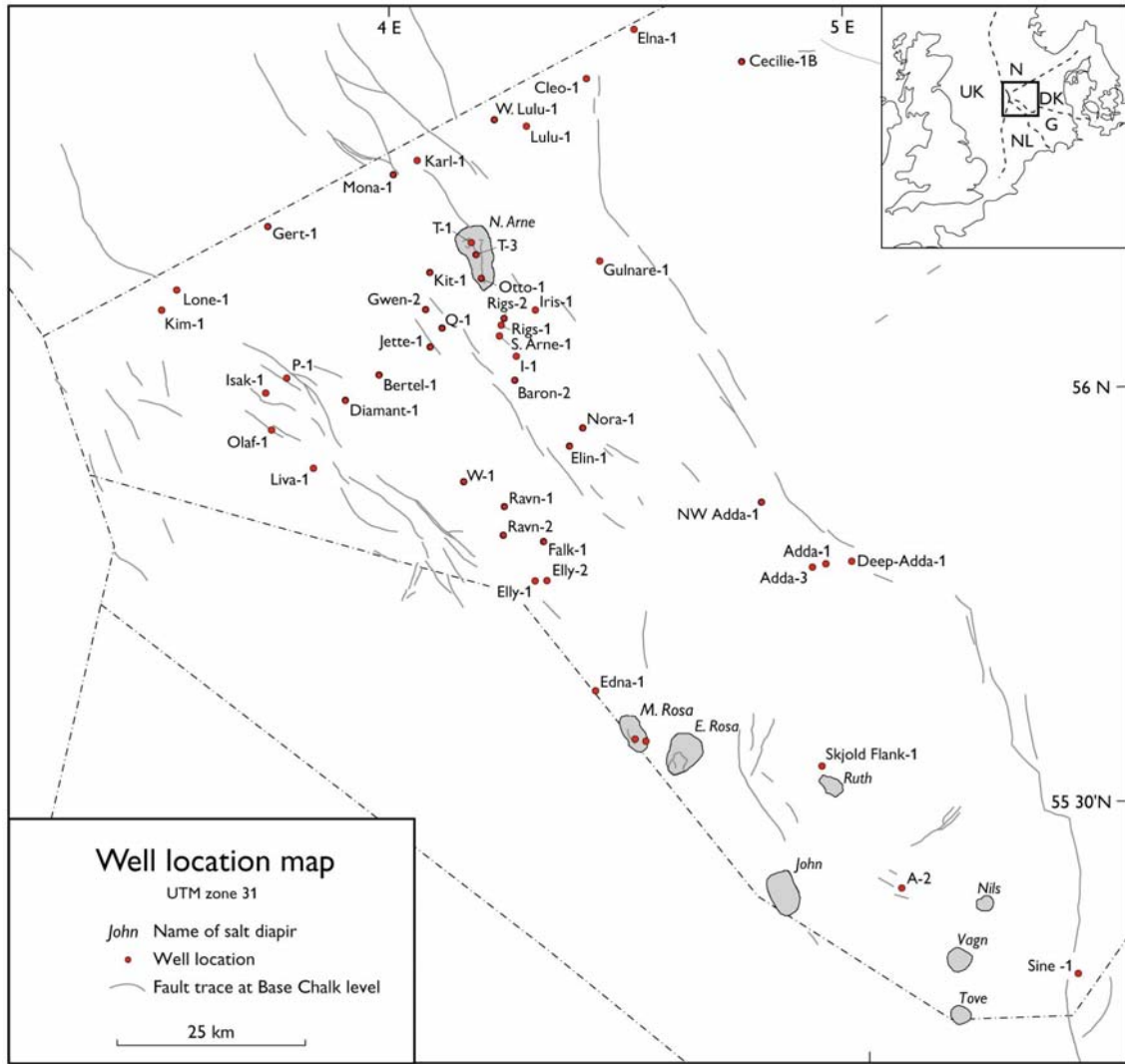


Figure 2.1. Location map for wells in this report. Fault pattern after Britze et al. 1995.

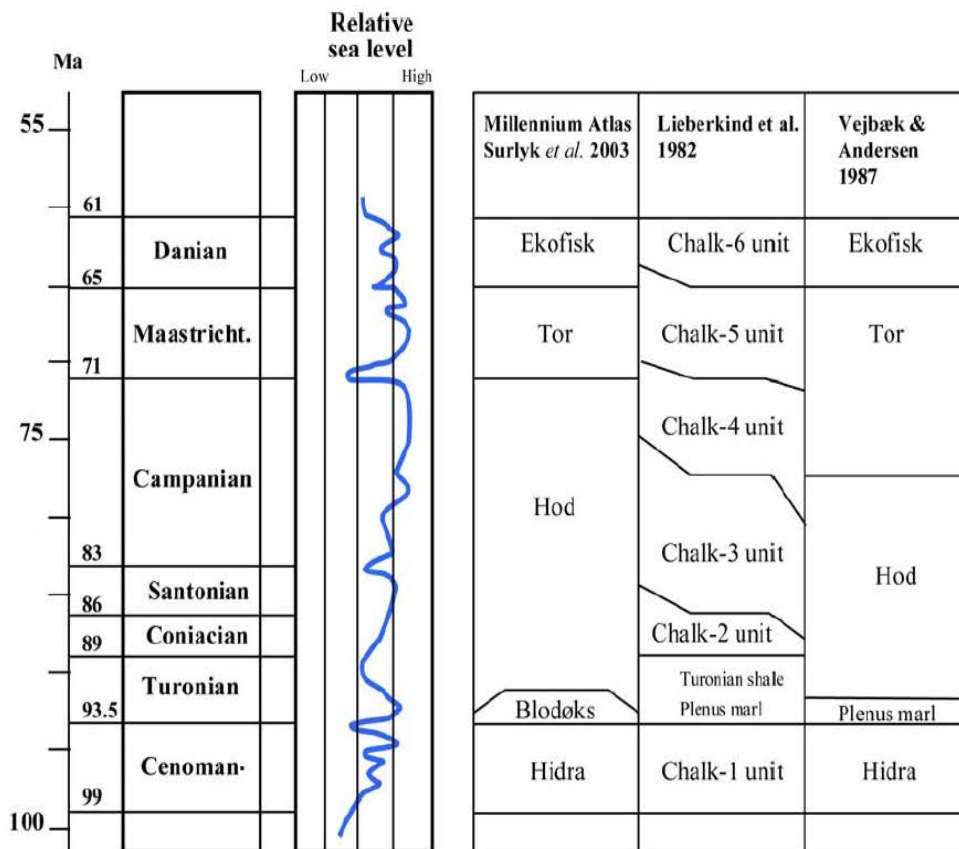


Figure 2.2. Lithostratigraphic nomenclature for the Chalk Group in Danish Central Graben. From Surlyk *et al.* 2003; Vejbæk & Andersen 1987 and Lieberkind *et al.* 1982. Time scale according to Gradstein *et al.* 1995.

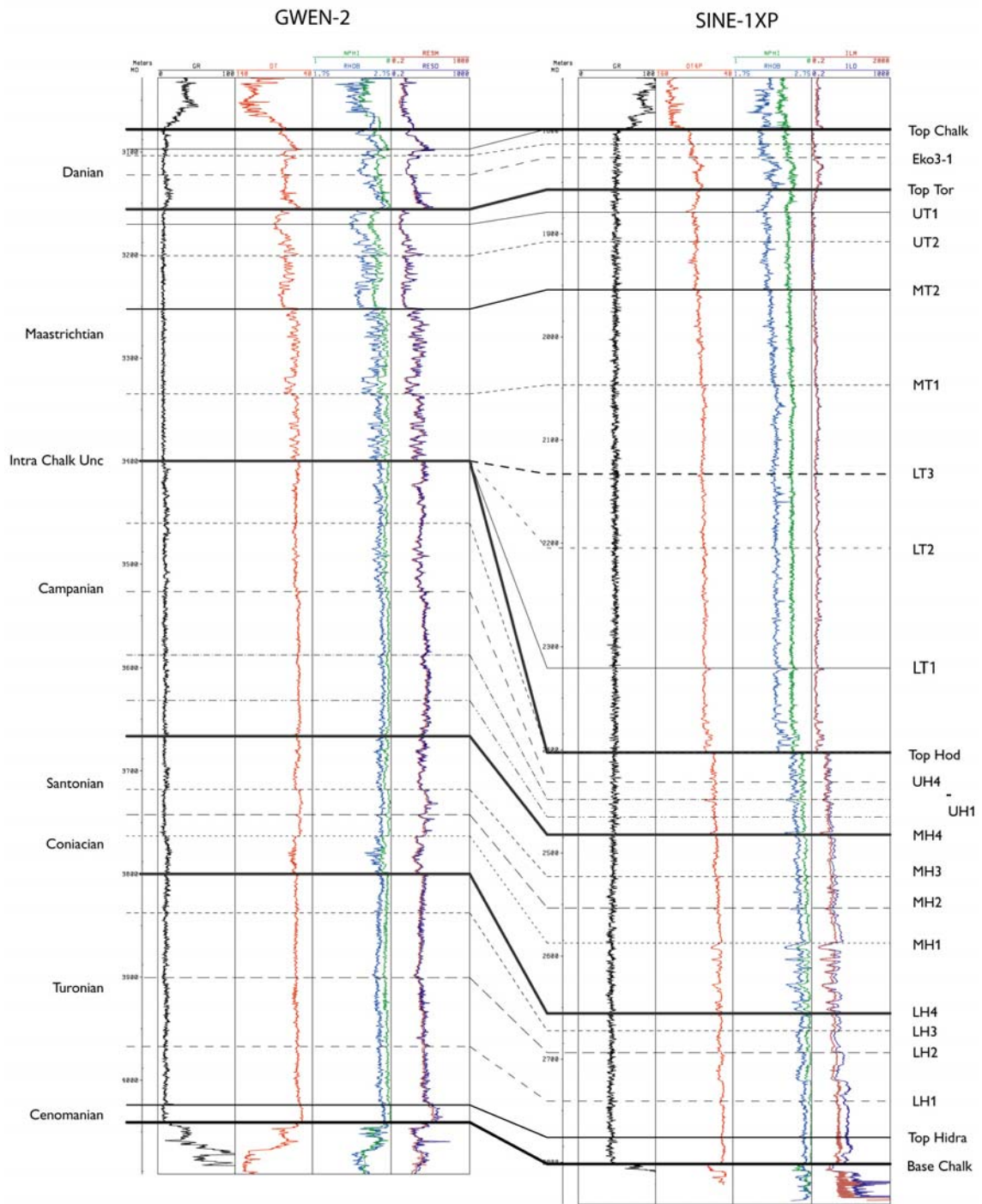


Figure 2.3. Log correlation between the Gwen-2 and Sine-1 wells. In the Sine-1 well the uppermost Hod formation is condensed or even missing. In the Gwen-2 well the lowermost Tor formation is missing.

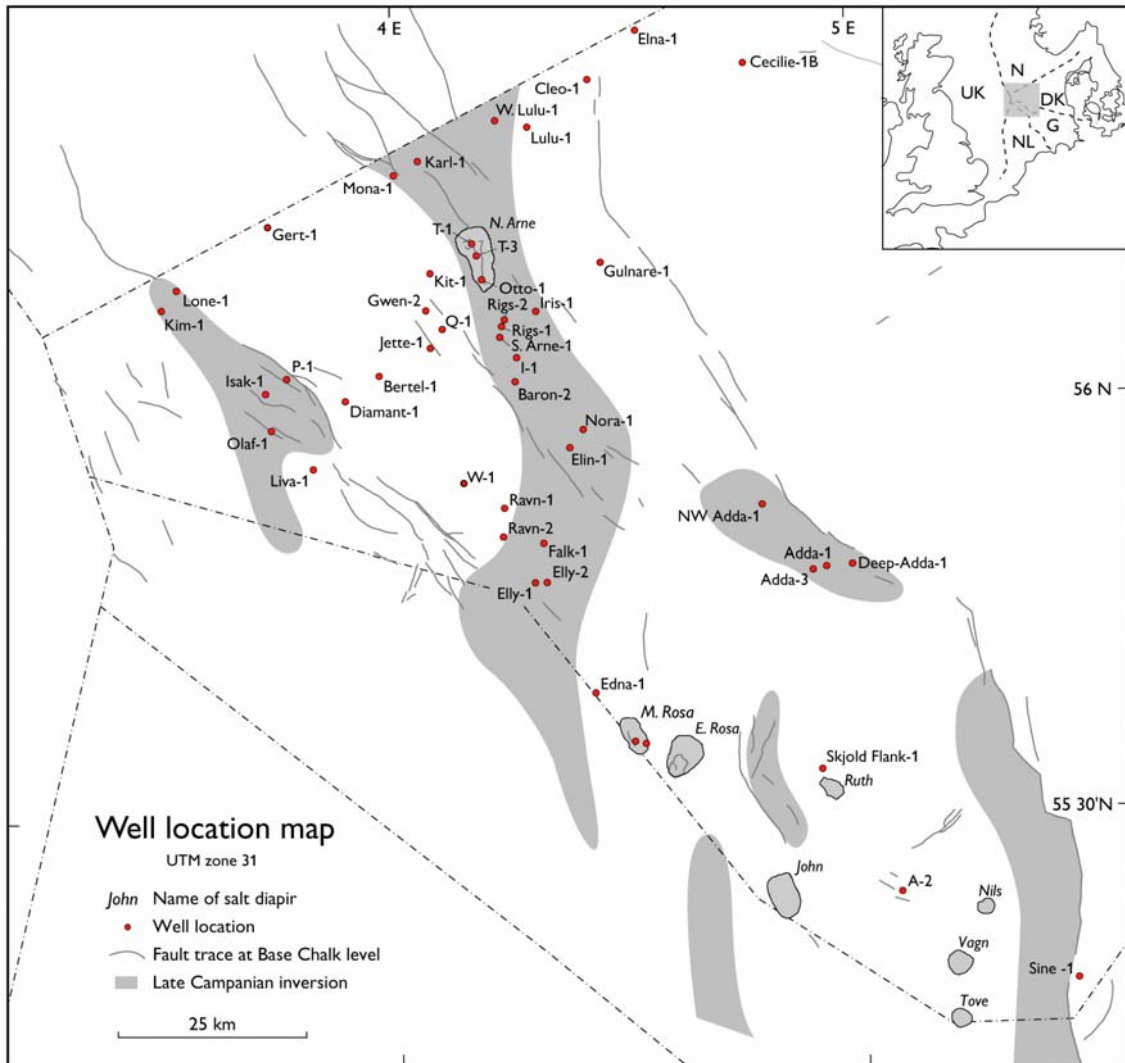


Figure 2.4. Danish Central Graben structural elements with faults at Base Chalk level. Hatching indicates areas of positive Late Campanian inversion. (From Vejrbæk & Andersen 2002). Associated with the main inversion phase during Late Campanian erosion on the swells and redeposition in adjacent deeper sub-basins took place.

3. Formation pressure

Overpressure due to compaction disequilibrium

Overpressure, ΔP (Pa; 1 MPa=145 psi) is the difference between the measured formation pressure, P , and the calculated hydrostatic pressure, P_H , at depth Z :

$$\Delta P = P - P_H = P - \rho_f \cdot g \cdot Z ,$$

where ρ_f (kg/m^3) is the mean pore fluid density of the overburden, and g is the gravitational acceleration (9.807 m/s^2). According to Japsen (1998), $\rho_f = 1.02 \text{ g/cm}^3$ at depth in the central North Sea. Overpressure is frequently given in mud weight equivalents (mwe):

$$1 \cdot 10^3 \text{ kg/m}^3 \text{ mwe} = 1 \text{ g/cm}^3 \text{ mwe} = 9.807 \text{ MPa/km} = 0.4335 \text{ psi/foot}.$$

A pore fluid density of 1.02 g/cm^3 thus corresponds to a water gradient of 10 MPa/km or 0.44 psi/f. The lithostatic pressure, S (Pa), at depth z is the stress exerted by the weight of the overburden: $S = \rho_b \cdot g \cdot z$ where ρ_b is the mean bulk density (wet). Terzaghi's principle states that the weight of the overburden per unit area, S , is borne partly by the rock matrix and partly by the pore fluid:

$$S = S_{eff} + \beta \cdot P ,$$

where S_{eff} (Pa) is the effective stress that is transmitted through the matrix (Terzaghi & Peck 1968). β is the Biot factor – or the effective stress coefficient (see Prasad & Manghnani 1997) – of the sediment and it ranges between 0 and 1 (assumed to equal 1 for high-porosity rocks). The principle implies that if a rock is more deeply buried without change in effective stress, the added load is carried by an increase in pore pressure, ΔP (for $\beta=1$).

Overpressure is generated by disequilibrium compaction when the weight of the overburden is increased by addition of sediments at the surface, and the pore fluid in the formation is sealed in the formation (Dickinson 1953; Rubey & Hubbert 1959; Osborne & Swarbrick 1997). The rock is unable to compact because the pore fluid cannot escape at the same rate as load is added to the overburden of the rock. Consequently, the additional load is carried by pore fluids, and higher than hydrostatic pressures result. The rock is said to be undercompacted, because porosity becomes high relative to depth.

Effective depth for $\beta=1$

The chalk in the central North Sea is buried below a normally compacted upper overburden and an undercompacted, sealing lower overburden. Here we will apply Terzaghi's principle to the case when a normally compacted rock is shifted to greater burial without change in porosity (nor velocity) and thus without change in effective stress. In such a case the added

load is carried by an increase in pore pressure. This may take place because the loading is so rapid compared to the low permeability of the sealing shales that no pore fluid can escape from the rock and hence no compaction can take place (Fig. 3.1). The effective stress on the rock is identical before and after overpressuring, and we refer to the initial depth as the effective depth of the rock: the depth corresponding to normal compaction of the rock for the given effective stress (reflected in a given sonic velocity).

Prior to the additional burial the rock was at its maximum burial, Z_{eff} (m below sea bed) and the formation pressure prior was hydrostatic (i.e. the rock was normally compacted) and we can write

$$S_{eff} = S - P = \rho_{low} \cdot g \cdot Z_{eff} - \rho_{fl} \cdot g \cdot Z_{eff} \quad (1)$$

where ρ is the average bulk density of the overburden,

If the rock is more deeply buried by the burial anomaly, $dZ_B = Z - Z_{eff}$, relative to the depth of normal compaction, without change in porosity or velocity of the chalk, the effective stress, S_{eff} , is unchanged because the overpressure, ΔP , carries the effective stress of the additional overburden entirely. The unchanged effective stress in the rock and the overpressure equals the effective stress of the overburden:

$$S_{eff} = S' - P' = (\rho \cdot g \cdot Z_{eff} + \rho_{up} \cdot g \cdot dZ_B) - (\rho_w \cdot g \cdot Z_{eff} + \rho_w \cdot g \cdot dZ_B + \Delta P) \quad (2)$$

where ρ_{up} is the bulk density of the added upper part of the overburden (below the later added upper overburden). We can combine the two above expressions:

$$\begin{aligned} \rho \cdot g \cdot Z_{eff} - \rho_{fl} \cdot g \cdot Z_{eff} &= (\rho_{low} \cdot g \cdot Z_{eff} + \rho_{up} \cdot g \cdot dZ_B) - (\rho_{fl} \cdot g \cdot Z_{eff} + \rho_{fl} \cdot g \cdot dZ_B + \Delta P) \\ \rho_{fl} \cdot g \cdot dZ_B + \Delta P &= \rho_{up} \cdot g \cdot dZ_B \\ \Delta P &= g \cdot dZ_B \cdot (\rho_{up} - \rho_{fl}) \end{aligned} \quad (3)$$

if $\rho_{up}=2.06 \cdot 10^3 \text{ kg/m}^3$ and $\rho_w=1.02 \cdot 10^3 \text{ kg/m}^3$ we get:

$$\begin{aligned} \Delta P &= 9.807 \cdot dZ_B \cdot (2.06 - 1.02) \cdot 10^3 \\ \Delta P &\approx dZ_B / 100 \text{ MPa} \quad (dZ_B \text{ in m}) \end{aligned} \quad (4)$$

This means that a burial anomaly of 1000 m relative to the depth of normal compaction reflects overpressure due to undercompaction of c. 10 MPa. In this simple case the load of the added kilometre (20 MPa) is carried by the formation pressure – partly by increased hydrostatic pressure (10 MPa) and partly by the overpressure (10 MPa): The effective stress exerted by the added overburden is carried by the overpressure. Reformulating the last two expressions we can estimate the effective depth in terms of the actual depth of the rock with overpressure, ΔP , due to undercompaction:

$$\begin{aligned} Z_{eff} &= Z - \Delta P \frac{1}{g \cdot (\rho_{up} - \rho_{fl})} \\ Z_{eff} &= Z - \Delta P \cdot 100 \text{ m} \quad (\Delta P \text{ in MPa}) \end{aligned} \quad (5)$$

This means that if the overpressure is 10 MPa, the effective stress at depth Z is the same as for a normally compacted rock c. 1000 m less deeply buried.

Chalk pressure data

Chalk formation pressure data from Danish central North Sea are available for the study from a number of sources (Table 3.1):

- pressure data published by Japsen (1998)
- pressure data from in-house reports
- pressure data in various completion reports

The pressure evaluations are based on drill stem and repeat formation tests, and are generally from the uppermost part of the Chalk. A few tests indicating very high pressure near the base of the Chalk are probably related to the Jurassic-Lower Cretaceous pressure regimes in the Central Graben, and are not included in the study. Mud weights have only been used to give an upper limit for the overpressure where indicated.

The general trend revealed by the chalk overpressure data given in Table 3.1 agrees with the map of chalk overpressure in the central North Sea (Fig. 3.2): Maximum overpressure is found in the Ekofisk area below the late Cenozoic depocentre. The rapid loading of sediments over the last c. 15 million years has generated undercompaction in the chalk because the sealing lower Cenozoic shales prevent the chalk from compacting at the same speed as sediments are added at sea bed. Overpressure declines away from this centre towards NNW and SSE along the depocentre axis. In Danish waters overpressure exceeding 15 MPa occurs in the northern part of the Central Graben area (e.g. the South Arne field) and decreases towards the south where 8 MPa is estimated for Skjold Flank-1 and 6.2 MPa for Sine-1. There is however some uncertainty about the decline of overpressure towards the west and east where few data are available for the chalk; e.g. west of the South Arne field and the Kit-1 well (Isak-1) and along the eastern flank of the graben.

Comments to selected overpressure estimates:

Baron-2/2a, 17.5 MPa: This value exceeds the regional level by c. 2 MPa.

Very few good estimates of the chalk formation pressure are available for the area west of the South Arne Field.

Kit-1; 14.6 MPa: This well (just north of Jette-1) provides one of the few good data points based on several pressure tests in the Maastrichtian reservoir (Tor Fm).

Gert-1; 16.4 MPa: This value based on formation tests indicates increasing pressure in the direction of the Ekofisk Field.

Olaf-1; 16.9 MPa: A very high overpressure based on an unsuccessful test in that well. Overpressure estimates based on mud weights in near-by wells indicate a more moderate level: Isak-1 (12.6 MPa), Diamant-1 (13.9 MPa), Liva-1 (14.0 MPa) and a very low value for P-1 (9.0 MPa). The data from Olaf-1 has thus not been used in the estimation, and the values for Diamant-1 and Bertel-1 (14.0 MPa) are taken as intermediate value between the estimate in Isak-1 and the test result in Kit-1. Likewise, the estimate for Jette-1 (14.6 MPa) is copied from the test result in Kit-1.

Skjold Flank-1; 8.1 MPa: This value is based an estimate of the initial pressure at the location of the well based on regional data. RFT data for the Ekofisk Formation in the well is c. 8 MPa, but RFT data for the Tor Formation give an overpressure of only c. 7 MPa. According to the completion report this drop of about 1 MPa is to be expected due to pressure depletion related to the production of the Skjold Field. The higher overpressure in the Ekofisk Formation than in the Tor Formation suggests differential depletion between these two formations.

Table 3.1. Chalk formation pressure

Well	Core *	Vs *	DP (MPa)	P (MPa)	Z (m bsl)	Source	Comment
Baron-2/2a	x		17.5	45.8	2845	RFT	Completion report
Bertel-1A			14.0			-ch	Regional estimate, Kit-1
Cecilie-1B	x	(x)	3.5		2223	-ch	Estimate from Elna-1
Diamant-1			14.0			-ch	Regional estimate, Kit-1
Elin-1			15.9			-ch	Estimate from Nora-1
Elly-1			13.4			-ch	Estimate from Elly-2
Elly-2			13.4	42.8	2941	PJ	
Falk-1			15.0	44.9	3010	Erico	
Gert-1	x		16.4	49.0	3262	PJ	
Gwen-2			14.6			-ch	Estimate from Kit-1
I-1	x		14.9	42.6	2765	PJ	
Iris-1			15.1	46.0	3111	Erico	
Isak-1		x	12.6		3200	mud weight	Completion report
Jette-1		x	14.6			-ch, mud	Estimate from Kit-1
Kit-1		x	14.6	46.3	3170	RFT	Completion report
Nora-1			15.9	41.2	2574	PJ	
NW Adda-1		x	10.0	33.0	2300	-ch	Regional estimate, Adda-1 + Bo-1
Otto-1	x		14.6	39.8	2521	PJ	
P-1			12.6			-ch	Isak-1, possibly less (cf. Erico)
Q-1	x		14.6			-ch	Regional estimate, Kit-1
Ravn-1			14.2			-ch	Regional estimate, Falk-1 + Elly-2
Ravn-2			14.2			-ch	Regional estimate, Falk-1 + Elly-2
Rigs-2	x	x	15.4	43.4	2800	Tests	Amerada
SA-1	x	x	15.4	43.4	2800	Tests	Amerada
Sine-1		x	6.5	27.4	2100	RFT	Completion report
Skjold Flank-1		x	8.1	29.0	2100	-ch	Regional estimate, Skjold-1 (Erico)
T-1			15.0	37.5	2251	PJ	
T-3	x		14.5	39.3	2494	Erico	
W. Lulu-1	x		13.8	42.8	2910	Erico	
W-1			14.2			-ch	Regional estimate, Falk-1+ Elly-2

* Availability of chalk cores and S-wave sonic log.

** Data courtesy of Amerada Hess (personal communication, Jørgen Jensenius 2003)

- P* Formation pressure.
 ΔP Overpressure relative to water gradient of 10 MPa/km.
Z Vertical depth below sea level.
RFT Repeat formation tester.
-ch No chalk pressure data.
PJ Japsen (1998).
Erico Petroleum Information (Erico) (1995).

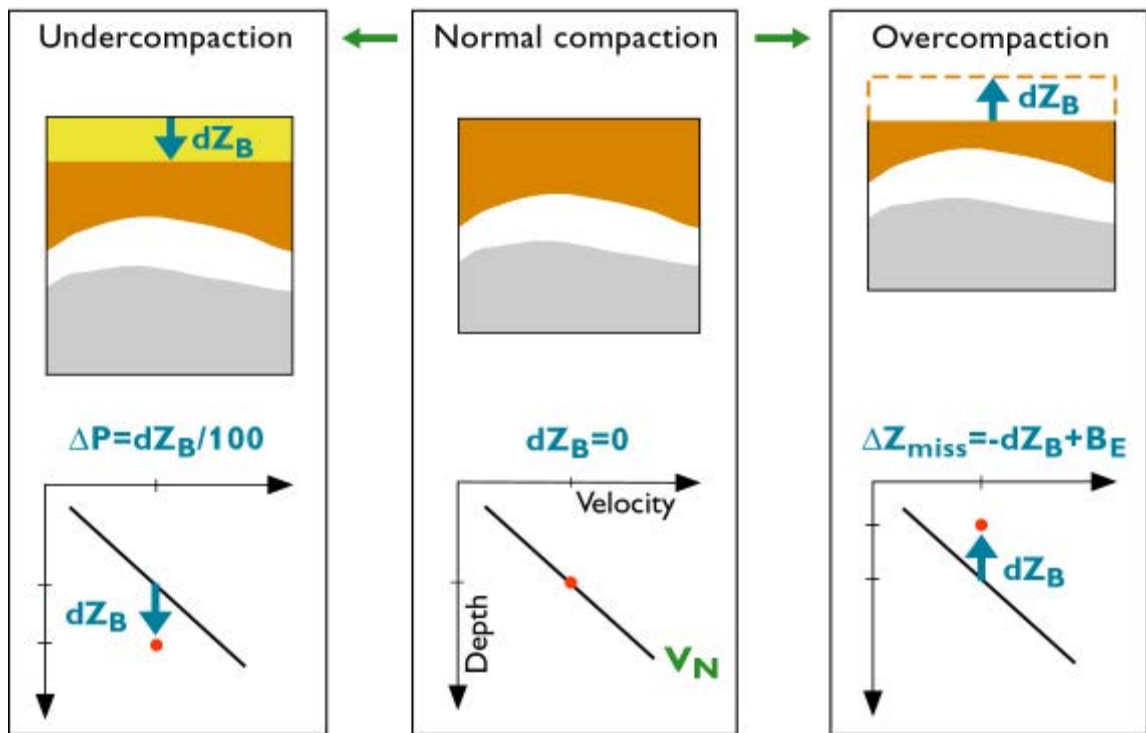


Figure 3.1. Burial anomaly, dZ_B (m), relative to a normal velocity-depth trend, V_N . Undercompaction due to rapid burial and low permeability causes overpressure, ΔP_{comp} (MPa), and low velocities relative to depth (positive dZ_B). Uplift and erosion reduce the overburden thickness and result in overcompaction expressed as anomalously high velocities relative to present-day depth (negative dZ_B). However, post-exhumational burial, B_E , will mask the magnitude of the missing section, ΔZ_{miss} . The effective depth, Z_{eff} , is the depth corresponding to normal compaction as predicted by the normal velocity-depth trend for the measured velocity. Modified after Japsen (1998).

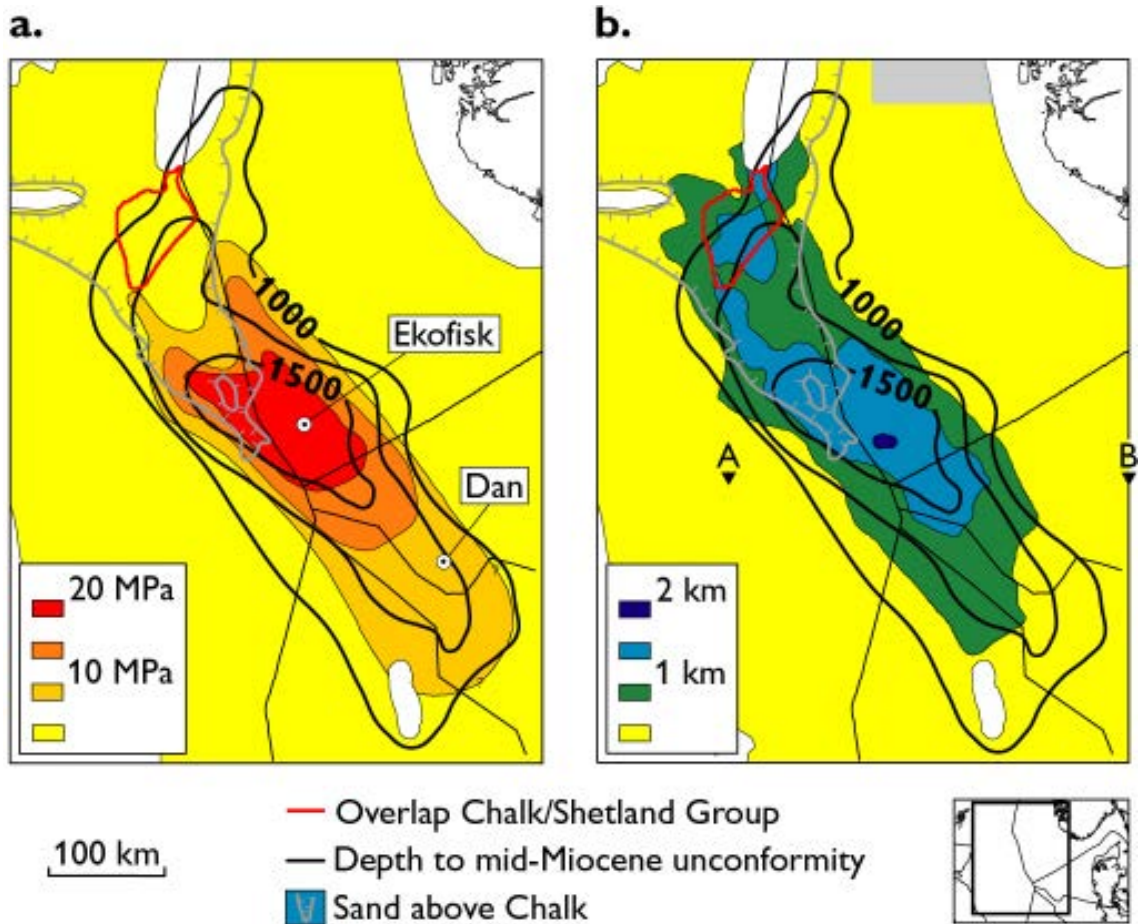


Figure 3.2. Corresponding areas of overpressured Chalk outlined from pressure measurements and from Chalk burial anomalies coincident with the late Cenozoic depocenter.

a. Chalk formation overpressure.

b. Chalk burial anomalies relative to a normal velocity-depth trend (Japsen 1998).

The overpressured zone corresponds to maximum thickness of the late Cenozoic deposits, whereas Paleocene sands overlying the Chalk to the northwest cause bleed-off of overpressure. South of the Viking Graben, shaly Chalk causes positive velocity anomalies even where the Chalk is normally compacted. Modified after Japsen (1998).

4. Temperature

The temperature at the top and the base of the chalk has been estimated for a number of wells (Table 4.1) and mapped (Figs 4.1 – 4.2). The temperatures were calculated based on the following considerations:

The temperature gradient was estimated for each well (Fig. 4.3) as the average gradient based on available down-hole temperature measurements in the well using an assumption of a surface temperature of 5°C. However, data from near-by wells were used for some wells (Jette-1, Bertel-1, Baron-2 and Rigs-1). The estimated temperature gradients are thus based on temperatures measured in different depths and in different formations depending on the TD of each well.

The temperature at Base Chalk was calculated from its depth in the well, the temperature gradient and a surface temperature of 5°C. The temperature at Top Chalk was calculated from the thickness of the chalk in the well, the temperature at Base Chalk and a temperature gradient only 77% of the estimated average gradient in the well. The factor of 77% is found from comparison of the average measured gradients and estimated gradients in the chalk based on basin modeling.

Table 4.1. *Temperature estimated at top and base chalk.*

Well	Top Chalk temp. (°C)	Base Chalk temp. (°C)	Temp. gradient (°C/km)	Top Chalk depth (m TVD)	Base Chalk depth (m TD)
A-2	71	82	35	1778	2171
Adda-1	71	76	31	2058	2256
Adda-3	68	73	30	2071	2303
Baron-2	98	101	33	2803	2928
Bertel-1	100	124	28	3107	4222
Cleo-1	91	102	30	2791	3277
Deep Adda-1	78	85	34	2128	2384
Diamant-1	94	108	28	3013	3660
Edna-1	101	109	35	2678	2966
Elin-1	98	103	34	2679	2897
Elna	88	95	35	2438	2723
Gulnare-1	95	115	28	2942	3899
Gwen-2	102	124	30	3039	4004
I-1X	95	97	33	2727	2814
Iris-1	87	94	28	2867	3171
Jette-1	92	99	29	2889	3182
Karl-1	102	127	30	3023	4147
Kim-1	105	123	30	3119	3871
Liva-1	92	112	28	2910	3793
Lone-1	94	101	30	2949	3255
Lulu-1	97	109	32	2722	3214
Nora-1	98	106	35	2560	2861
Otto-1	99	106	38	2441	2689
P-1	87	92	28	2882	3117
Q-1	100	120	29	3033	3925
Ravn-1	105	122	31	3013	3745
Rigs-1	82	84	28	2748	2812
Skjold Flank-1	78	95	32	2169	2795
T-3	95	102	36	2438	2699
W-1	97	112	29	3054	3726

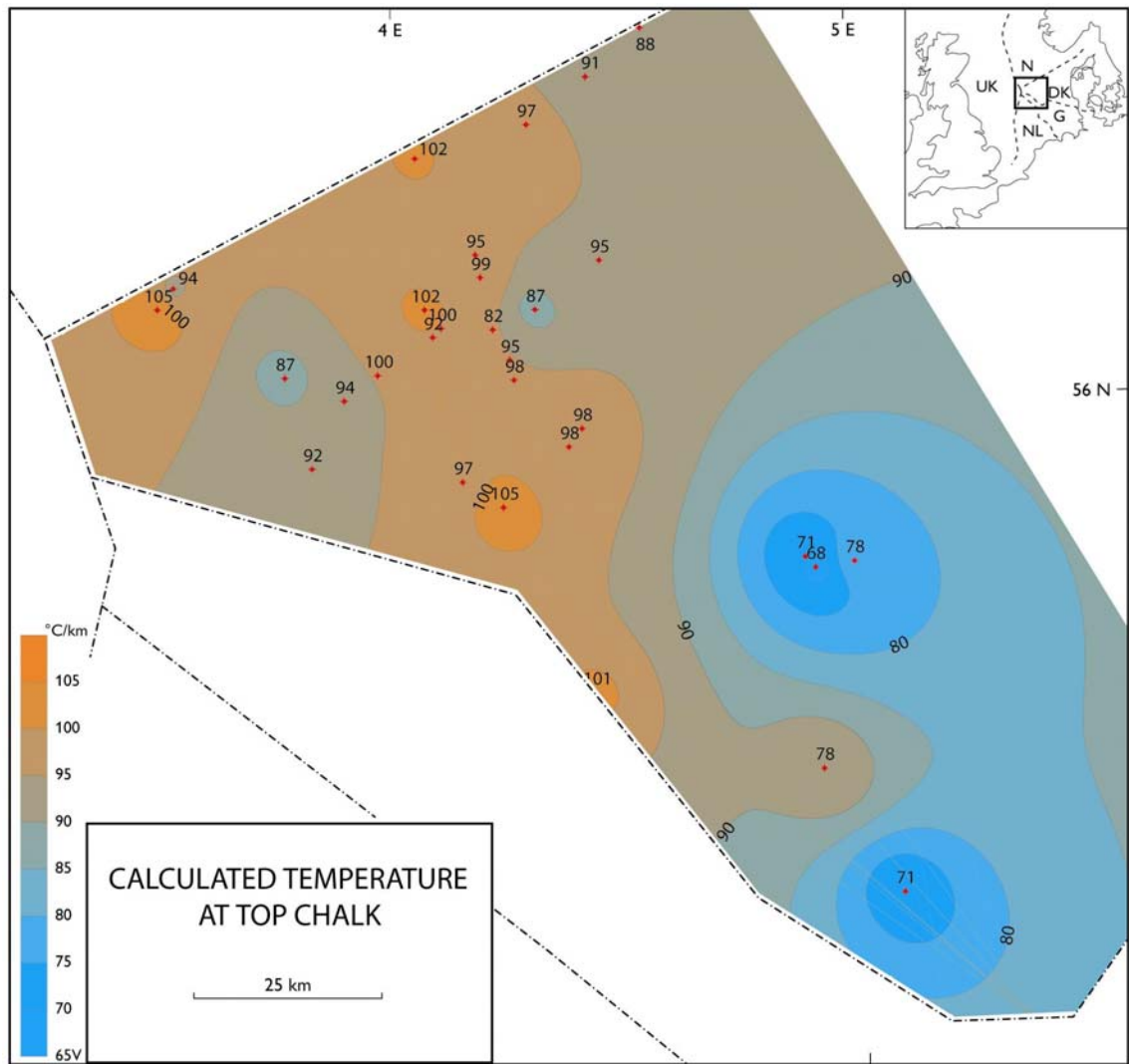


Figure 4.1. Temperature at Top Chalk estimated in wells (Table 4.1). Contours represent interpolation of the temperatures in the wells.

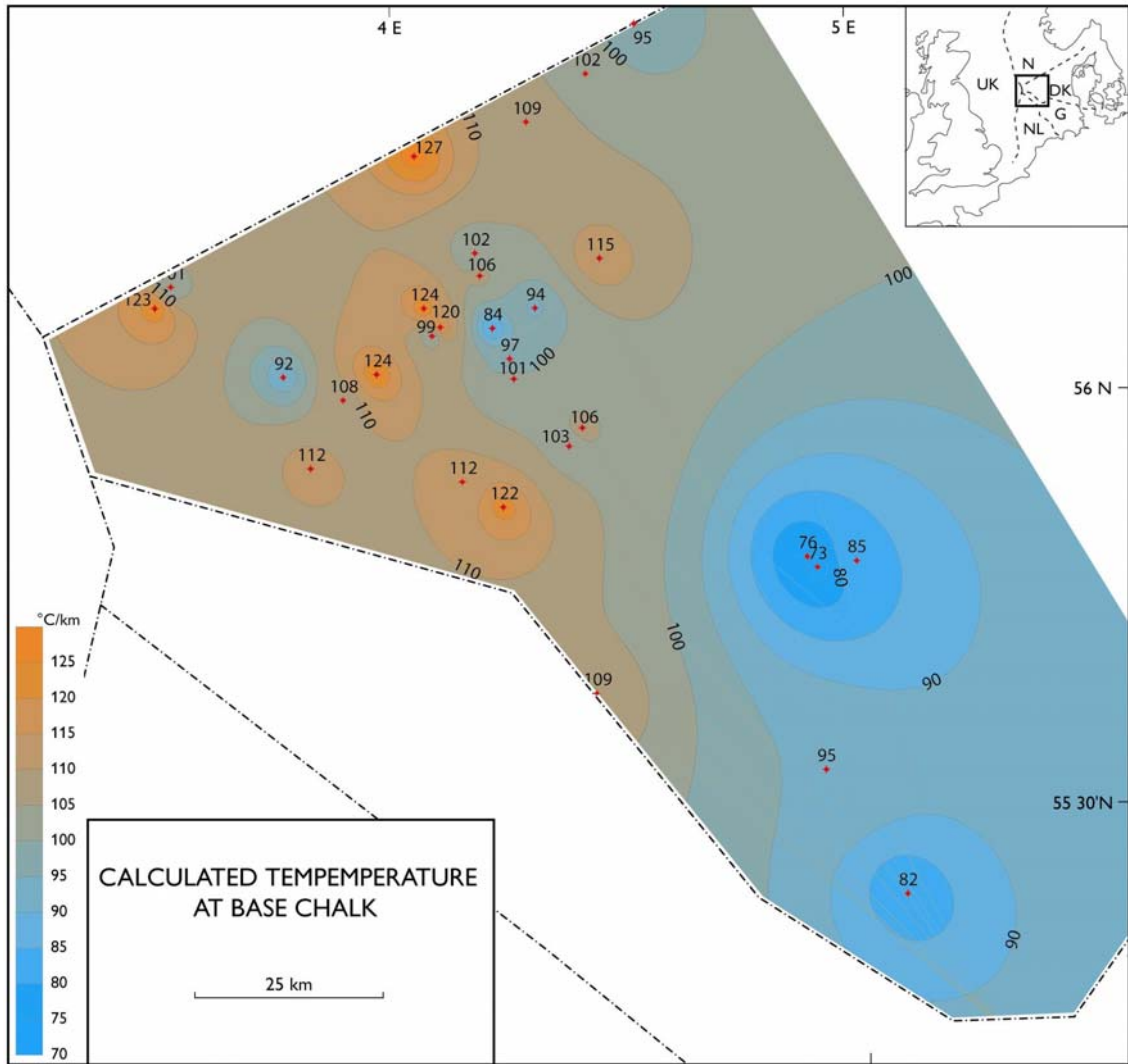


Figure 4.2. Temperature at Base Chalk estimated in wells (Table 4.1). Contours represent interpolation of the temperatures in the wells.

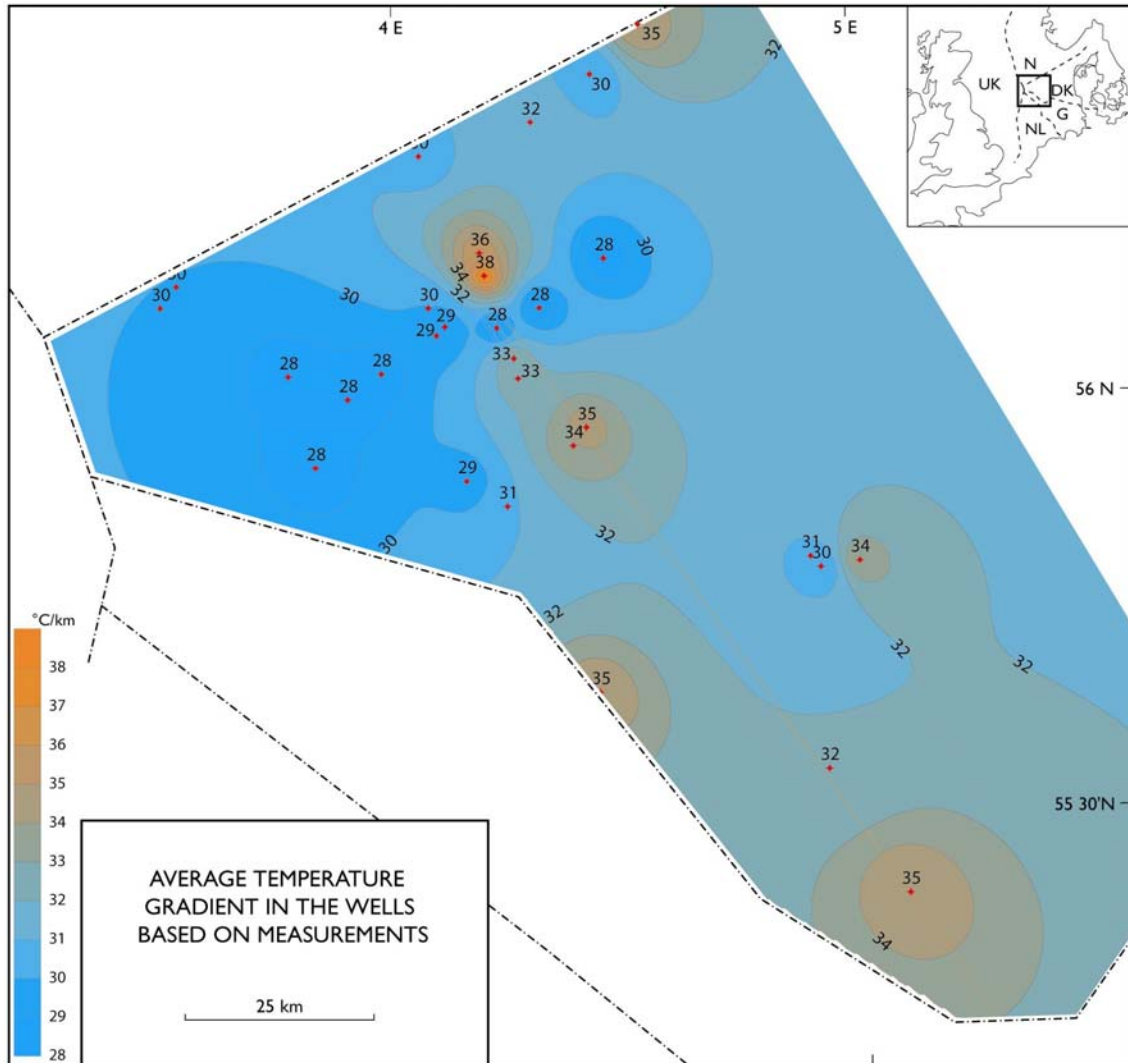


Figure 4.3. Average temperature gradient estimated for the section penetrated by the wells (Table 4.1). Contours represent interpolation of the gradients in the wells.

5. Acoustic properties

Log data from the Chalk Group in 28 wells were quality controlled and used as input for estimation of porosity and water saturation (Ødegaard 2005). The porosity and brine saturation interpretation was done simultaneously using the bulk density, deep and micro/shallow resistivity well log curves together with Archie's equation assuming $(a, n, m) = (1, 2, 2)$. Parameters such as R_w , R_{mf} and RHO_{mf} was used as input (if available) together with fixed matrix density and clay properties.

Main aspects of the chalk data are shown in cross plots of the physical parameters in Appendix 2. A larger selection of cross plots is presented in PowerPoint files on the enclosed CD together with the data files in MatLab format. Various aspects of the data for each of the wells is discussed in the section below.

Typical examples of the variation of the acoustic properties of the chalk are revealed by the plots of the thick chalk sections in the Gwen-2 and the near-by Jette-1 well (plots shown in Appendix 2):

- The plot of V_p versus porosity indicates a clear separation between the formations in these wells: Tor plots along a long and narrow trend whereas Hod plots as a cluster of points with low porosity and Ekofisk either plots along the Tor trend (Ekofisk porous) or as data points with low velocity-porosity values (Ekofisk tight). This distinction corresponds to the differences in the gamma log: low gamma ray (GR) in Tor and parts of Ekofisk and higher values for most of Hod and Ekofisk (see also cross plots colorcoded by GR values in the PowerPoint files on the enclosed CD).
- There is an overall drop in porosity with depth in the Tor Formation and corresponding increase in velocity for these wells. When the log data are plotted against depth and effective depth with compressed depth scales it is apparent that there is a drastic change in these parameters over a narrow interval in effective depth (corrected for overpressure): c. 1700 – 1800 m. We refer to this sharp drop in porosity and an increase in velocity as the 'Cementation front'. The front is where (minimum) velocity cross c. 4.5 km/s and (maximum) porosity cross c. 15%. It is only possible to judge the match between the normal trends and the data versus effective depth for chalk sections of substantial thickness.
- The plots of velocity versus porosity reveals that velocity increases as porosity is lost during greater burial; cf. the plots for the Gwen-2 and Isak-1 wells. For these wells data for the Hod Formation moves towards the upper left of the diagram when we compare the more deeply buried chalk in the Gwen-2 well (c. 3400 – 4000 m) with the Isak-1 well (c. 3100 – 3200 m). The data are moving along the MLHS trend. A similar shift of the data points can be seen for the Tor and Hod formations when comparing the Sine-1 well with the more deeply buried Skjold Flank-1 well.
- The level of V_p versus porosity is quite different for the Gwen-2 and the Jette-1 well: Jette-1 has considerably higher P-velocities for the same porosity than the Gwen-2 well. This difference would probably have been even clearer if a shear ve-

locity log had been available for the Gwen-2 well, because Jette-1 has very high S-velocities compared to porosity and a corresponding low Vp-Vs ratio (also compared to other wells with Vs data).

The analysis reveals that the gamma ray gives information that are important for evaluating the acoustic properties of the chalk. The typical level for the GR readings for the chalk is just below 10 API for the pure chalk in the Tor Formation with maxima up to c. 20 API in the less pure formations (e.g. Jette-1). Bad calibration of the gamma tool may be the reason why the same relative variations are found for chalk in other wells – only with a much higher base level (e.g. Baron-2). The true variations of the gamma radiation in the chalk may also be obscured by potassium content of the drilling mud (compare the low and systematic GR variations in the T-1 well with high and constant level in the near-by T-3 well or P-1 relative to Isak-1 or Elin-1 relative to Nora-1). The high and monotonous GR reading (c. 45 API) for the Sine-1 well could be mistaken as an erroneous measurement, but the log data from the near-by Per-1 well (not included in this report) show the same uniform GR level for the chalk – only very close to a base level of 10 API.

Plots of velocity versus porosity or Vp versus Vs show two reference curves: The modified upper and lower Hashin-Shtrikman curves (MUHS, MLHS) defined from log data for chalk on the Ekofisk Field (Walls et al. 1998; see also Japsen et al. 2004).

Plots of velocity and porosity versus depth show two other reference curves: The normal-velocity depth trend for North Sea Chalk defined by Japsen (2000) (a revision of the trend defined by Japsen 1998). The normal velocity-depth trend was based on an analysis of data from 845 wells throughout the North Sea Basin and data from outside the North Sea (Ocean Drilling Project). Normally compacted Chalk is rare in the North Sea Basin (no overpressure and no erosion of the overburden). However, in the southern, central part of the Basin, the chalk is deeply buried and overpressure is low and decreasing towards the south. Here, – in Dutch and British waters – it is thus possible to identify wells where the chalk is normally compacted in the interval with velocities ranging from c. 2.5 to 4 km/s. For smaller velocities the trend is based on ODP data and for velocities greater than 4 km/s, data representing normal compaction were identified along the upper bound in a velocity-depth plot where the effect of undercompaction due to overpressuring is a minimum. The trend is formulated as a segmented, linear function:

$$\begin{aligned}
 V_N^{Ch} &= 1550 + 1.3 \cdot z, & z < 900 \text{ m} \\
 V_N^{Ch} &= 920 + 2 \cdot z, & 900 < z < 1471 \text{ m} \\
 V_N^{Ch} &= 1950 + 1.3 \cdot z, & 1471 < z < 2250 \text{ m} \\
 V_N^{Ch} &= 2625 + z, & 2250 < z < 2875 \text{ m}
 \end{aligned}
 \tag{2}$$

The velocity increase with depth, k [m/s/m = 1/s], ranges from 1 to 2 s⁻¹ with a maximum between a depth of 1 and 1.5 km (Fig. 1b).

The normal porosity-depth trend for North Sea chalk was estimated by Sclater & Christie (1980) also by combining shallow data from outside the North Sea (Deep Sea Drilling Proj-

ect) with deep data from two normally pressured bore holes in the North Sea. The trend is formulated as exponential porosity decay (Fig. 2a):

$$\phi_N^{Ch} = 0.7 \cdot e^{-z/1408} \quad (3)$$

The porosity decay with depth, $kphi$ [$m^{-1} = 10^5$ pu/km], ranges from -50 pu/km ($=0.0005$ m^{-1}) near the surface to c. -5 pu/km at a depth of 3 km (Fig. 2b).

There is an overall agreement between the normal trends for velocity-depth and for porosity-depth of Japsen (1998, 2000) and Sclater & Christie (1980), even though they are not completely compatible. The agreement is evident from these plots for the Gwen-2 well: at shallow depths (c. 1.7 km) the minimum velocities and the maximum porosities are in agreement with normal trends when plotted against effective depth. However, at the base of the chalk velocity data match the velocity-depth trend, whereas the porosity data are much smaller than predicted by the porosity-depth trend.

Comments to the cross plots for the individual wells

Baron-2

- Thin chalk section (c. 100 m) with no GR separation between Ekofisk porous and Hod (Tor missing). Some HC in Ekofisk. Log pattern comparable to I-1. (log plot)
- Max phi c. 30% in Ekofisk (large scatter). (V-phi plot)
- Estimate of overpressure results in a poor match between normal trend and sonic data vs effective depth. Overpressure may be overestimated. Section just above 'Cementation front'. (V-Z plot)

Bertel-1

- Very thick chalk section (c. 1100 m) where GR is relatively high in Ekofisk and Hod and relatively low in Tor. Thick Tor with shift in character between Tor and Hod (GR, V and phi). No clear porosity-depth trend in Hod, but velocity variations reflect GR log. Similar log pattern as in Diamant-1, Gwen-2, Q-1 and Jette-1. Bertel more deeply buried than near-by Diamant-1 and thick chalk section down to c 4300 m. (log plot)
- Max phi c. 25% in Ekofisk and Tor. Ekofisk tight separated from clean Ekofisk and Tor. Very high Vp-values (up to 6 km/s) reflecting deep burial. Tor plot on a clearly 'stiffer' V-phi trend than Diamant-1. High GR plot in the lower left corner of the V-phi data (low V). Large phi-range for Tor and low range for Hod. (V-phi plot)
- Estimate of overpressure results in a fair match between normal trend and sonic data vs effective depth. Overpressure may be underestimated. 'Cementation front' within Tor Fm (V-Z plot)

Diamant-1

- Fairly thick chalk section (c. 600 m) where GR is relatively high in Ekofisk and Hod and relatively low in Tor. A high-porosity interval in Hod (3575 m kb) is reflected in low Vp. Similar log pattern as in W-1 and Jette-1. (log plot)
- Max phi c. 20% in Ekofisk and Tor. Ekofisk tight separated from clean Ekofisk and Tor. High GR plot in the lower left corner of the V-phi data (low V). (V-phi plot)
- Estimate of overpressure results in a good match between normal trend and sonic data vs effective depth. 'Cementation front' within Tor. (V-Z plot)

Elin-1

- Fairly thin chalk section (c. 200 m) with no GR difference between Ekofisk, Hod and Hidra (untypical high GR level – compare with near-by Nora-1 well) (Tor almost absent). Log pattern comparable to Nora-1 (and Isak-1). (log plot)
- Max phi around 20% for few recordings in Tor and Ekofisk. Rather scattered data points. (V-phi plot)
- Estimate of overpressure results in a poor match between normal trend and sonic data vs effective depth (maybe overestimated overpressure). 'Cementation front' within Hod. (V-Z plot)

Elly-1

- Fairly thick chalk section (c. 400 m) where GR is relatively high in Ekofisk and in Hod and particularly in the deepest part of Hod and in Hidra, but generally small variations. Small phi-contrast between Tor and Hod. Gradual decrease of phi corresponds to marked increase of V with depth in Hod (high porosity near base chalk). Similar to Falk-1 (and Elly-1, Ravn-1, -2) – but no high-porosity interval in Hod. (log plot)
- Max phi c. 20% in Tor. Narrow V-phi trend for Hod (near MLHS trend). Hidra reveal high GR and phi around 10-15%. High GR plot in the lower left corner of the V-phi data (low V). The deepest data points plot (Hidra) plot in the middle of the V-phi trend. (V-phi plot)
- Estimate of overpressure results in a good match between normal trend and sonic data vs effective depth. 'Cementation front' represented by gradual increase of velocity below effective depth of 1500 m within Hod Fm (similar to the changes seen in Hod in Sine-1). (V-Z plot)

Elly-2

- Fairly thick chalk section (c. 600 m) where GR is higher in Hod than in Tor, but small GR range. Small phi-contrast between Tor and Hod. Gradual decrease of phi and increase of V with depth in Tor and Hod. Hidra reveal high GR and phi around 10-15%. Similar to Elly-1 – but with high-porosity interval in Hod as in Falk-1. (log plot)
- Max phi c. 20% in Tor. Broader V-phi trend for Hod than in Elly-1. High GR plot in

the lower left corner of the V-phi data (low V). The deepest data points plot (Hidra) plot in the middle of the V-phi trend. (V-phi plot)

- Estimate of overpressure results in a good match between normal trend and sonic data vs effective depth. 'Cementation front' represented by gradual increase of velocity below effective depth of 1500 m within Hod (cf. Sine-1). (V-Z plot)

Falk-1

- Thick chalk section (c. 700 m) where GR is relatively high in Ekofisk and relatively low in the thin Tor. Sharp drop of phi (increase in V) from Tor to Hod. Gradual decrease of phi with depth in Hod. Very similar to Ravn-1 and W-1 (and Elly-1, -2) – also a high-porosity interval in Hod (3450 m kb) is reflected in low Vp. Less deeply buried than Ravn-1. (log plot)
- Max phi c. 25% in Tor and Ekofisk. Slightly higher minimum phi than in the Ravn-1 and corresponding higher max. Vp. Hidra reveals high GR and low phi. High GR plot in the lower left corner of the V-phi data (low V). (V-phi plot)
- Estimate of overpressure results in a good match between normal trend and sonic data vs effective depth. Slightly overestimated overpressure? 'Cementation front' represented by gradual increase of velocity below effective depth of 1500 m within Hod. (V-Z plot)

Gert-1

- Thick chalk section (c. 800 m) where GR is relatively high in Ekofisk and Hod and relatively low in Tor (but also low in the upper part of Hod). Thick Ekofisk and Tor. Rather gradual shift in character between Tor and Hod – e.g. decline of porosity (GR, V and phi). No clear porosity-depth trend in Hod, but velocity variations reflect variations in GR and porosity logs. Similar log pattern as in Diamant-1, Bertel-1, Gwen-2 and Jette-1. (log plot)
- Max phi c. 25% in Tor and Ekofisk. Rather scattered data, but difference between Tor and Hod. Tor plot on a rather low V-phi trend. Hod has fairly high minimum porosities (>5%) – cf. Gwen-2 (greater effective depth, more compacted Hod). High GR plot in the lower left corner of the V-phi data (low V). (V-phi plot)
- Estimate of overpressure results in a match between normal trend and sonic data vs effective depth. Velocity increase in upper Tor matches normal trend. 'Cementation front' within Tor. (V-Z plot)

Gwen-2

- Very thick chalk section (c. 1000 m) where GR is relatively high in Ekofisk and Hod and relatively low in Tor. Thick Tor with shift in character between Tor and Hod (GR, V and phi). No clear porosity-depth trend in Hod, but velocity variations reflect porosity and GR log. Similar log pattern as in Diamant-1, Bertel-1, Q-1 and Jette-1. (log plot)
- Max phi c. 25-30% in Tor. Very nice example of separation of the chalk formations

in a plot of V-phi. Ekofisk tight separated from clean Ekofisk and Tor. Tor plot on a very narrow V-phi but not as 'stiff' as in Bertel-1 (but a higher trend than in Diamant-1). Hod has low phi and high V. Hydra represent max velocities for the chalk. High GR plot in the lower left corner of the V-phi data (low V). Large phi-range for Tor and low range for Hod. (V-phi plot)

- Estimate of overpressure results in good match between normal trend and sonic data vs effective depth. 'Cementation front' within Tor. (V-Z plot)

I-1

- Thin chalk section (c. 100 m) with no GR separation between Ekofisk and Hod (Tor almost missing). Some HC in Ekofisk and thin Tor. Log pattern comparable to Baron-2. (log plot)
- Max phi c. 30% in Ekofisk (large scatter). (V-phi plot)
- Estimate of overpressure results in a match between normal trend and sonic data vs effective depth. Section above 'Cementation front'. (V-Z plot)

Iris-1

- Fairly thin chalk section (c. 300 m) with no clear GR separation between Ekofisk, Tor (thin) and Hod. High GR and low Vp for most of Hydra. Log pattern comparable to Isak-1. (log plot)
- Max phi c. 20-25% in Ekofisk. High GR plot in the lower left corner of the V-phi data (low V). (V-phi plot)
- Estimate of overpressure results in a fair match between normal trend and sonic data vs effective depth. Overpressure may be overestimated. No clear 'Cementation front' (section mainly below the front). (V-Z plot)

Isak-1

- Fairly thin chalk section (c. 300 m) without clear GR difference between Ekofisk, Tor and Hod. The clear GR difference seen for the near-by P-1 well may suggest that the GR data for Isak-1 may be of bad quality. A clear separation between the formations is seen on the Vp/Vs log. A consistent depth trend is seen for phi and Vp in the Hod formation. Log pattern comparable to e.g. P-1, Nora-1 and Elin-1. (log plot)
- Max phi c. 25% in Tor. The V-phi plot reveals a clear separation of the Ekofisk, Tor and Hod formations: Ekofisk tight separated from clean Tor, which has a well-defined trend. Hod plots towards lower phi-V and this is probably related to higher clay content (not revealed by the GR data). The data plot quite similarly to the data from the near-by Diamant-1 well, but significantly lower V-phi compared to the Jette-1 well. (V-phi plot)
- Estimate of overpressure results in a good match between normal trend and sonic data vs effective depth (maybe slightly underestimated overpressure). 'Cementation front' within Tor and Hod. (V-Z plot)

- High Vp/Vs for Ekofisk and Tor tight and elevated level for most of Hod (compared to Tor) – probably related to clay content. Vp/Vs(Tor) c. 1.9 in contrast to c. 1.8 for Jette-1. (Vp/Vs-phi plot)

Jette-1

- Thick chalk section (c. 900 m) with clear GR difference between Ekofisk, Tor and Hod. This separation is also seen on the Vp/Vs log. An overall depth trend is seen for phi and Vp in the Tor formation. High GR correlates with low Vp and Vs in the Hod Formation (c. 3720 and 3820 m) and consequently not with high Vp/Vs. Very similar to the logs from the near-by Gwen-2 well (log plot)
- Max phi c. 25-30% in Ekofisk and Tor. The V-phi plot reveals a clear separation of the Ekofisk, Tor and Hod formations: Ekofisk tight separated from clean Tor, which has a well-defined trend with a very large phi-range (over a limited depth range). High-GR Ekofisk and Hod plot towards lower phi-V. The data plot quite similarly to the data from the near-by Gwen-2 well, but along a higher V-phi trend. (V-phi plot)
- Estimate of overpressure results in a good match between normal trend and sonic data vs effective depth. 'Cementation front' within Tor. (V-Z plot)
- Low Vp/Vs for Tor and Hod – marked 'smile' with minimum for phi = 15%. Vp/Vs(Tor) c. 1.8 in contrast to c. 1.9 for Isak-1. No high Vp/Vs values for high GR (as in Isak-1), whereas high GR deviates from V-phi trend. (Vp/Vs-phi plot)

Nora-1

- Fairly thin chalk section (c. 300 m) with higher GR in Hidra than in most of Hod (Tor absent). General depth trend in Hod for phi and Vp. Log pattern comparable with Elin-1 (and Isak-1). (log plot)
- Max phi around 25% for few recordings in Ekofisk and Hod. General V-phi trend for Hod. Very low velocities for most Hidra data (but normal porosities). Could be related to transference of overpressure from deeper source rocks: $V > 3.5$ km/s for phi = 10% (original data $V > 3$ km/s). (V-phi plot)
- Estimate of overpressure results in a poor match between normal trend and sonic data vs effective depth (maybe overestimated overpressure or transference of overpressure from pre-chalk strata). 'Cementation front' near Hod. (V-Z plot)

NW Adda-1

- Fairly thin chalk section (c. 300 m) without clear GR difference between Ekofisk, Tor and Hod. The GR level is high (50 API), but it is unclear whether it represents a uniform level as that for the uniform chalk in Sine-1 or an erroneous reading. That the GR log is erroneous is indicated because a high Vp/Vs ratio in the uppermost Ekofisk is not reflected in high GR readings. Both GR and Vp/Vs-log has a very broad range. Large porosity variations are seen along the depth axis. Fairly long distance between this well and the other wells in the study, but the log pattern corresponds to Ein-1 and Nora-1 – only with higher porosities. (log plot)

- Max phi c. 30-35% in Ekofisk and Tor – a large scatter is seen in the data set. (V-phi plot)
- Estimate of overpressure results in a good match between normal trend and sonic data vs effective depth (maybe slightly underestimated overpressure). ‘Cementation front’ just below the section. (V-Z plot)
- Huge scatter in Vp/Vs – centred around a value of 1.9. (Vp/Vs-phi plot)

Otto-1

- Fairly thin chalk section (c. 200 m) with no GR separation (high API level). HC in Tor. Comparable to T-3. (log plot)
- Max phi c. 40% in Tor reservoir (low Sw and low Vp). No GR separation of the data. (V-phi plot)
- Estimate of overpressure results in a poor match between normal trend and sonic data vs effective depth. Overpressure may be overestimated or maybe salt diapirism has moved the chalk to a more shallow depth or overpressure is increased by transfer from more deeply buried chalk. Section above ‘Cementation front’. (V-Z plot)

P-1

- Fairly thin chalk section (c. 200 m) with clear GR difference between Ekofisk and Tor (thin) (similar to upper part of Hod). High GR in the lower part of Hod is reflected in low Vp. Thin Hydra has low GR and high Vp. Log pattern comparable to Isak-1 and Elin-1. (log plot)
- Max phi c. 25% in Tor and Ekofisk (few points). The V-phi plot indicates the typical separation of the Ekofisk, Tor and Hod formations (cf. Isak-1). High-GR Ekofisk and Hod plot towards lower phi-V. (V-phi plot)
- Estimate of overpressure results in a fair match between normal trend and sonic data vs effective depth (section too thin to make any further assessments). ‘Cementation front’ within Hod. (V-Z plot)

Q-1

- Thick chalk section (c. 900 m, but no data for lower part) where GR is relatively high in Ekofisk and Hod and relatively low in Tor. Thick Tor with shift in character between Tor and Hod (GR, V and phi). No clear porosity-depth trend in Hod. Similar log pattern as in Diamant-1, Bertel-1, Gwen-2 and Jette-1. (log plot)
- Max phi c. 20-25% in Tor and Ekofisk. Ekofisk tight separated from clean Ekofisk and Tor. Tor plot on a well-defined V-phi but, fairly ‘stiff’, but not as ‘stiff’ as in Bertel-1. Hod has very low phi (lower than Gwen-2). High GR plot in the lower left corner of the V-phi data (low V). (V-phi plot)
- Estimate of overpressure results in a match between normal trend and sonic data vs effective depth. ‘Cementation front’ within Tor. (V-Z plot)

Ravn-1

- Thick chalk section (c. 700 m) where GR is relatively high in Ekofisk and relatively low in Tor. Very similar to Ravn-2 and W-1 – also a high-porosity interval in Hod (3630 m kb) is reflected in low Vp. Extends deeper than Ravn-2. (log plot)
- Max phi c. 20% in Ekofisk and Tor. Slightly lower phi and higher Vp than in W-1 matches deeper burial of chalk in Ravn-1. Hidra reveal high GR and low phi, plot similarly as Hod. High GR plot in the lower left corner of the V-phi data (low V). (V-phi plot)
- Estimate of overpressure results in a good match between normal trend and sonic data vs effective depth. 'Cementation front' represented by gradual increase of velocity below effective depth of 1500 m within Hod (cf. Sine-1). (V-Z plot)

Ravn-2

- Thick chalk section (c. 700 m) where GR is relatively high in Ekofisk and relatively low in Tor. Sharp drop of phi from Tor to Hod (increase in V). Hidra reveal high GR and low phi. Very similar to Ravn-1 and W-1 – also a high-porosity interval in Hod (3600 m kb) is reflected in low Vp. (log plot)
- Max phi c. 20-25% in Tor. Lower minimum phi than in Ravn-1 even though the Ravn-1 chalk section extends to greater burial – differences in porosity estimation? High GR plot in the lower left corner of the V-phi data (low V). (V-phi plot)
- Estimate of overpressure results in a good match between normal trend and sonic data vs effective depth. 'Cementation front' represented by gradual increase of velocity below effective depth of 1500 m. (V-Z plot)

Rigs-2

- Very thin chalk section (c. 50 m) with no GR difference between Ekofisk and Tor. Clear peak in Vp and Vs at top Tor. High oil saturation in Tor. Low Vp-Vs ratio – maybe related to invasion of mud filtrate and problematic estimation of Vs in very high-porosity chalk (see Japsen et al. 2004). (log plot)
- Max phi c. 40-45% in Tor and Ekofisk. The V-phi plot reveals a separation of the Ekofisk and Tor formations with the pure Tor formation shifted towards higher porosities. No clear GR separation of the data. (V-phi plot)
- Estimate of overpressure results in a poor match between normal trend and sonic data vs effective depth. Possibly due to high porosities caused by porosity preservation due to early hydrocarbon entry. Section above 'Cementation front'. (V-Z plot)
- Vs plot above the MUHS trend – maybe data problems. (Vs-phi plot)
- Low Vp/Vs for Tor and Hod – see above. (Vp/Vs-phi plot)

SA-1 TVD ??

- Fairly thin chalk section (c. 200 m) with GR difference between Ekofisk and Tor. This separation is not seen on the Vp/Vs log because of the high oil saturation in the Tor formation (low Vp). (log plot)

- Max phi c. 30-35% in Tor. The V-phi plot reveals a clear separation of the Ekofisk and Tor formations with the pure Tor formation shifted towards higher porosities. Fluid substitution of the Tor data would shift them up towards the MUHS trend – and thus a higher trend than seen in most wells (apart from Jette-1). This argument assumes that there are no problems with invasion of mud filtrate in the well (as in the high-porosity Rigs-2 well). No clear GR separation of the data. (V-phi plot)
- Estimate of overpressure results in good match between normal trend and sonic data vs effective depth. This indicates that the porosities in SA-1 are agreement with the present effective stress (in contrast to Rigs-2 where porosities are relatively high). Section above 'Cementation front'. (V-Z plot)
- Vs plot along MUHS trend as for Jette-1 data (in sharp contrast to Isak-1). Bad Vs data for Ekofisk. (Vs-phi plot)
- Low Vp/Vs for Ekofisk and Tor – probably due to low density of hydrocarbons. Fluid substitution would result in a high Vp/Vs ratio (probably close to the MUHS trend and quite different from Jette-1). (Vp/Vs-phi plot)

Sine-1

- Very thick chalk section (c. 1000 m) without clear GR difference between Ekofisk, Tor and Hod. The GR level is high (40 to 50 API) and fairly scattered. The uniform level may correspond to that seen in Skjold Flank-1 and thus simply reflect very uniform chalk. This interpretation is also supported by the symmetry between the GR and the Vp/Vs logs. The Vp/Vs-log has a very broad range. Consistent depth trends are seen for phi and Vp in the upper part of Tor (above c 2100 m MD) and in Hod. The lower part of Tor reveals remarkably stable values of ϕ and Vp over c. 300 m. The log pattern is similar to Skjold Flank-1, but with a more clearly developed intra-chalk unconformity in Sine-1 – probably due to differences in the physical parameters across the unconformity in Sine-1. The hiatus is very small at this unconformity for both wells (see Appendix 1). (log plot)
- Max phi up to 40% in Tor – large range of both phi and Vp, and a fairly narrow trend in the data set. Apparently a slight shift in the V-phi trends for Tor and Hod, but few data points for ϕ between 15 and 20%. However, the chalk is probably very uniform and the general trend related to depth-dependent 'compaction' (cf. the Skjold Flank-1 well). (V-phi plot)
- Estimate of overpressure results in a good match between normal trend and sonic data vs effective depth (maybe slightly underestimated overpressure – or slightly to high normal velocity-depth trend). Note the relatively low P-velocities in the lower part of Tor. 'Cementation front' in uppermost part of Hod. (V-Z plot)
- Rather high Vp/Vs for Tor and Hod: plots as a smile versus phi with a range from 1.85 to 2.05 (similar to Skjold Flank-1). Data between 5 and 25% plot near the MUHS/MLHS trends. Whereas Vp plots close to the MLHS trends (Vp-phi), Vs plots slightly below the MLHS trend for the upper part of Tor (Vs-phi plot not shown). Lowest part of Hod and Hidra show relatively low Vp/Vs. (Vp/Vs plots)

Skjold Flank-1

- Fairly thick chalk section (c. 600 m) without clear GR difference between Ekofisk, Tor and Hod. The GR level is high (30 API), but the uniform level may correspond to that seen in Sine-1 and thus simply reflect very uniform chalk. This interpretation is also supported by the symmetry between the GR and the Vp/Vs logs. The Vp/Vs-log has a fairly broad range and even a cyclicity in the Tor Formation with a wavelength of about 10 m. This cyclicity is not seen on the porosity-log and may well be an artefact. A consistent depth trend is seen for phi and Vp in the Tor and especially the Hod. The log pattern is similar to Sine-1, but with a less clearly developed intra-chalk unconformity. The hiatus is very small at this unconformity for both wells (see Appendix 1). (log plot)
- Max phi c. 30% in Tor – large range of both phi and Vp, but also a large scatter in the data set. No V-phi separation between Tor and Hod in agreement with the uniform GR log for both formations: The chalk is probably very uniform and the general trend related to depth-dependent ‘compaction’ (cf. the Sine-1 well). (V-phi plot)
- Estimate of overpressure results in a good match between normal trend and sonic data vs effective depth (maybe slightly to high normal velocity-depth trend). ‘Cementation front’ in uppermost part of Hod. (V-Z plot)
- Rather high Vp/Vs for Tor and Hod: plots as a smile versus phi with a range from 1.9 to 2, but large scatter (and unlikely variations in Vs seen in plot of Vp vs Vs). Whereas Vp plots in between the MUHS and MLHS trends (Vp-phi), Vs plots towards the MLHS trend (Vs-phi plot not shown). (Vp/Vs plots)

T-1

- Thin chalk section (c. 100 m) with GR separation between Ekofisk, Tor (thin) and most of Hod. Low Sw in Tor. Log pattern a condensed version of T-3. (log plot)
- Max phi c. 30% in Ekofisk and Tor. Low Vp in Tor due to HC. High GR plot in the lower left corner of the V-phi data (low V, Ekofisk tight). (V-phi plot)
- Estimate of overpressure results in a very poor match between normal trend and sonic data vs effective depth. Maybe salt diapirism has moved the chalk to a more shallow depth or overpressure is increased by transfer from more deeply buried chalk. Section above ‘Cementation front’. (V-Z plot)

T-3

- Fairly thin chalk section (c. 300 m) with slightly higher GR for Ekofisk. Some HC in upper part of Tor. General depth trend for Vp and phi. Comparable to T-3. (log plot)
- Max phi c. 30% in Tor and Ekofisk. Separation of Ekofisk, Tor and Hod similar to Isak-1 (but higher V-phi level for T-3). No clear GR separation of the data. (V-phi plot)
- Estimate of overpressure results in a poor match between normal trend and sonic data vs effective depth. Maybe salt diapirism has moved the chalk to a more shallow depth or overpressure is increased by transfer from more deeply buried chalk. Section above ‘Cementation front’. (V-Z plot)

W-1

- Thick chalk section (c. 700 m) where GR is relatively high in Ekofisk and relatively low in Tor. A high-porosity interval in Hod (3650 m kb) is reflected in low Vp. Log pattern comparable to Diamant-1 and Jette-1. (log plot)
- Max phi c. 25% in Ekofisk and Tor. Uppermost part of Ekofisk plot outside normal V-phi chalk area, Ekofisk tight clearly separated from clean Ekofisk and Tor. (V-phi plot)
- Estimate of overpressure results in a good match between normal trend and sonic data vs effective depth. 'Cementation front' within Tor. (V-Z plot)

West Lulu-1

- Fairly thick chalk section (c. 600 m) with clear GR difference between Ekofisk, Tor and Hod. An overall depth trend is seen for phi and Vp in the thick Tor formation. High GR in the thick Ekofisk formation correlates with low phi. Similar to the logs from the Jette-1 well (log plot)
- Max phi c. 25-30% in Tor. The V-phi plot reveals a clear separation of the Ekofisk, Tor and Hod formations: Ekofisk tight separated from clean Tor, which has a well-defined trend with a very large phi-range. High-GR Ekofisk and Hod plot towards lower phi-V. The data plot quite similarly to the data from the Jette-1 well, also along a high V-phi trend. (V-phi plot)
- Estimate of overpressure results in a good match between normal trend and sonic data vs effective depth. 'Cementation front' within Tor. (V-Z plot)

6. Data CD

Lithostratigraphic subdivision

Excel file with depth to individual boundaries in the wells

Filename: lithological subdivision.xls

CGM files with cross correlation of log data

Filenames:

correl1.cgm: Arne-Elin Graben – NW Adda-1 – Sine-1

correl2.cgm: Mandal High – Svend Field – Gertrud and Feda Grabens

correl3.cgm: Inge High – Heno Plateau

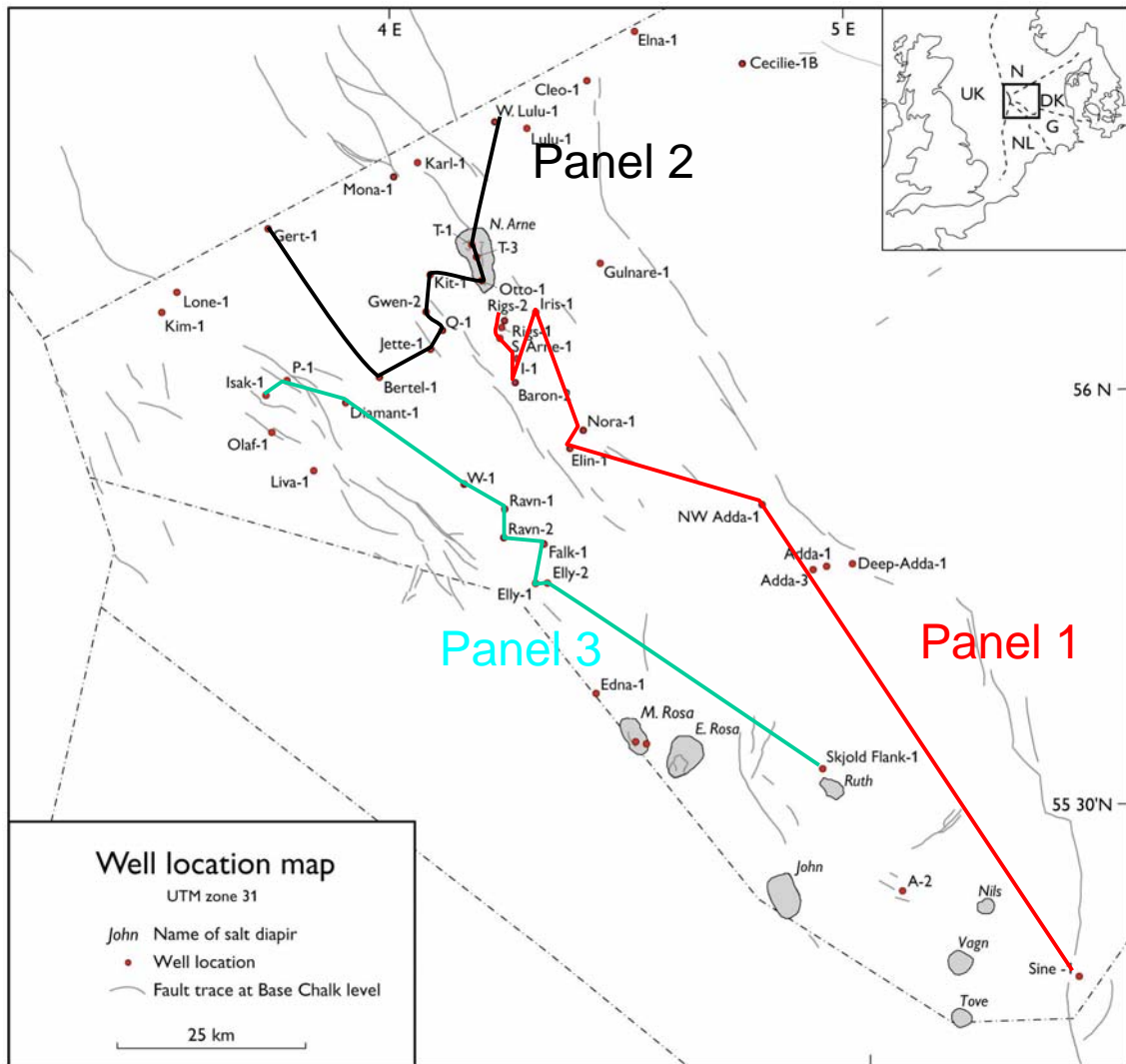


Figure 6.1. Location of the stratigraphic correlation panels

Acoustic properties

Power Point files with cross plots of log data

Filenames: <wellname<.ppt:

Baron-2
Bertel-1A
Diamant-1
Elin-1
Elly-1
Elly-2
Falk-1
Gert-1
Gwen-2
I-1
Iris-1
Isak-1
Jette-1
Nora-1
NW Adda-1
Otto-1
P-1
Q-1
Ravn-1
Ravn-2
Rigs-2
SA-1
Sine-1
Skjold Flank-1
T-1
T-3
W. Lulu-1
W-1

MatLab files with log data for the chalk sections in each well

Filenames:

v6_<wellname>.m (MatLab version 6)

v7_<wellname>.m (MatLab version 7)

Parameters:

d	depth, m below kb (array)
d1, d2,	depth to top and base chalk, m below kb (scalar)
dmax, dmin	min and max depths used in log plots (scalar)
dp	chalk formation overpressure, 100xMPa (scalar)
dref	distance between kb and sea bed, m (scalar)
dtp, dts	transit time for P- and S-waves, micro sec/foot (array)
g = g_i	shear modulus, GPa (array)
gr	gamma ray (scalar)
i, j	indices (scalar)
k_w=k_w_i	bulk modulus, GPa (array)
litho	lithology code*, - (array)
m_w	P-wave modulus, GPa (array)
nu_w	poisson's ratio. – (array)
phi	porosity, - (array)
rho	density, g/cm ³ (array)
sw	water saturation, - (array)
vp, vs	P- and S-wave velocity, m/s (array)
zb_eko, zb_hdr, zb_hod, zb_plm, zb_tor, zt_eko, zt_hdr, zt_hod, zt_plm, zt_tor	depth to top and base Ekofisk/Hidra/Hod/Plenus Marl/Tor formations

*) lithology code:

- 1 – Ekofisk Fm
- 2 – Tor Fm
- 3 – Hod Fm
- 4 – Plenus Marl
- 5 – Hidra Fm

If the thickness of any of these units is less than 1 m the unit is not present in the well but only included in the data set in this way to avoid problems with the legends in the cross plots.

7. References

- Britze, P., Japsen, P. & Andersen, C. 1995. Geological map of Denmark 1:200,000. The Danish Central Graben. "Base Chalk" and the Chalk Group (two-way travelttime and depth, interval velocity and isochore). Geological Survey of Denmark Map Series **48**.
- Chiarelli, A. and F. Duffaud, 1980, Pressure origin and distribution in Jurassic of Viking Basin (United Kingdom-Norway): AAPG Bulletin **64**, 1245–1250.
- Dickinson, G. 1953. Geological aspects of abnormal reservoir pressures in Gulf Coast Louisiana. AAPG Bulletin **37**, 410–432.
- Foged, N., A. Krogsbøll, C.F. Hansen, K. Zinck-Jørgensen, H.F. Christensen and J.-E. Jepsen, 1995, EFP-93. Modelling of stresses and fractures in a reservoir. Final report. Copenhagen, DGU/DGI, 68 pp.
- Gradstein F.M., Agterberg, F. P., Ogg, J. G., Hardenbol, J., Veen, P.v., Thierry, J. & Huang, Z. 1995: A Triassic, Jurassic and Cretaceous time scale. Geochronology time scales and global stratigraphic correlation. SEPM Special Publication **54**, 95–126.
- Isaksen, D. and Tonstad, K. (Eds.) 1989. A revised Cretaceous and Tertiary lithostratigraphic nomenclature for the Norwegian North Sea. NPD-Bulletin **5**, Oljedirektoratet, Stavanger, 59 pp.
- Japsen, P., 1994, Retarded compaction due to overpressure deduced from a seismic velocity/depth conversion study in the Danish Central Trough, North Sea: Marine and Petroleum Geology **11**, 715–733.
- Japsen, P. 1998. Regional velocity-depth anomalies, North Sea Chalk: a record of overpressure and Neogene uplift and erosion. AAPG Bulletin **82**, 2031–2074.
- Japsen, P. 2000. Investigation of multi-phase erosion using reconstructed shale trends based on sonic data. Sole Pit axis, North Sea. Global and Planetary Change **24**, 189–210.
- Japsen, P., Bruun, A., Fabricius, I.L., Rasmussen, R., Vejbæk, O.V., Pedersen, J.M., Mavko, G., Mogensen, C. & Høier, C. 2004. Influence of porosity and pore fluid on acoustic properties of chalk: AVO-response from oil, South Arne Field, North Sea. Petroleum Geoscience **10**, 319–330.
- Lieberkind, K., Bang, I., Mikkelsen, N. & Nygaard, E. 1982: Late Cretaceous and Danian Limestones. *In* Michelsen, O. (ed) Geology of the Danish Central Graben. Danmarks Geologiske Undersøgelse **B8**, 45–49.
- Knudsen, P., 1993, Integrated inversion of gravity data: National Survey and cadastre - Denmark, Geodetic Division, technical report **7**, 52 pp.
- Nielsen, L.H. and P. Japsen, 1991, Deep wells in Denmark, 1935-1990; lithostratigraphic subdivision: Geological Survey of Denmark, Series A **31**, 179 pp.
- Oakman, C. D. & Partington, M. A. 1998. Cretaceous. *In* K.W. Glennie, (ed.) Petroleum geology of the North Sea, basic concepts and recent advances, 4th edition: London, Blackwell Science Limited, 294–349.
- Ødegaard A/S 2005. Quality control and petrophysical evaluation of Danish North Sea wells. Report.
- Osborne, M.J. & Swarbrick, R.E. 1997. Mechanisms for generating overpressure in sedi-

- mentary basins: A reevaluation. AAPG Bulletin **81**, 1023–1041.
- Petroleum Information (Erico) 1995. Danish Central Trough. Formation pressure database and regional evaluation. 47 pp.
- Robertson Research International 1984: The Danish North Sea Area: The stratigraphy and petroleum Geochemistry of the Jurassic to Tertiary sediment. Robertson Report
- Prasad, M. & Manghnani 1997. Effects of pore and differential pressure on compressional wave velocity and quality factor in Berea and Michigan sandstones. Geophysics **62**, 1163–1176.
- Rubey, W.W. & Hubbert, M.K. 1959. Role of fluid pressure in mechanics of overthrust faulting, II. Geological Society of America Bulletin **70**, 167–206.
- Sclater, J.G. & Christie, P.A.F. 1980. Continental stretching; an explanation of the post-Mid-Cretaceous subsidence of the central North Sea basin. Journal of Geophysical Research **85**, 3711–3739.
- Surlyk, F., Dons, T., Clausen, C.K. & Highan, J. 2003: Upper Cretaceous. In: D.Evans, C. Graham, A. Armour & P. Bathurst (eds), 2003. The Millennium Atlas. Petroleum geology of the Central and Northern North Sea.
- Terzaghi, K. & Peck, R.P. 1968. Soil mechanics in engineering practice, John Wiley and Sons, New York.
- The Millennium Atlas. Petroleum geology of the Central and Northern North Sea. (Eds.) D.Evans, C. Graham, A. Armour & P. Bathurst, 2003. Geol.Soc. London.
- Vejbæk, O.V., Rasmussen, R., Japsen, P., Pedersen, J.M., Fabricius, I.L. & Marsden, G. *in press*. Modelling seismic response from North Sea Chalk reservoirs resulting from changes in burial depth and fluid saturation. In: Doré, A.G. & Vining, B. (eds) Petroleum Geology: NW Europe and Global Perspectives: Proceedings of the 6th Conference. Geological Society, London.
- Vejbæk, O. V. & Andersen, C. 1987: Cretaceous-Early Tertiary inversion tectonism in the Danish Central Trough. In: Ziegler, P. A. (ed.) Compressional intra-plate deformations on the Alpine foreland. Tectonophysics **137**, 221–238.
- Vejbæk, O. V. & Andersen, C. 2002: Post mid-Cretaceous inversion tectonics in the Danish Central Graben – regional synchronous tectonic events? Bulletin of Geological Society of Denmark **49**, 129–144
- Walls J.D., Dvorkin J. & Smith B.A. 1998. Modeling seismic velocity in Ekofisk Chalk. *In*: **1998**, SEG, Tulsa, 1016–1019.

Appendix 1: Lithostratigraphic subdivision

Formation tops in 29 wells. Bold numbers refer to the main lithostratigraphic formations. Normal font numbers refer to subunits. Grey pattern indicate a hiatus identified in the wells. The data indicate a regional hiatus (the Intra-Chalk Unconformity) associated with the top of the Hod formation. The time span related to with the Intra-Chalk Unconformity varies according to basin setting.

Chronostratigraphy		Correlations horizons	Short	Baron-2	Bertel-1	Diamant-1	Elin-1	Elly-1	Elly-2	Falk-1	Gert-1	Gwen-2	I-1
				m MD	m MD	m MD	m MD	m MD	m MD	m MD	m MD	m MD	m MD
Danian		Top Chalk	Top Chalk	2826	3147,5	3050	2733,5	2855	2857	2901	3150,5	3078	2764,5
		Ekofisk 3	Eko3	2841	3174	3063		2857	2858,5	2922	3179,5	3097	
		Ekofisk 2	Eko 2	2860	3196	3073	2733,5	2864	2866	2940,5	3205	3103,5	2764,5
		Ekofisk 1	Eko 1	2880	3221	3097	2746	2867,5	2874	2955	3229	3122,5	2779
Maastrichtian	Latest	Top Tor	Top Tor	2905	3259	3139	2751	2883	2900	2991,5	3277,5	3155,5	2798
		Upper Tor 2	UT2		3281	3182	2753	2891	2918,5	3012,3	3276,5	3170,5	
		Upper Tor 1	UT1		3336	3207,5	2779	2925	2947,5	3029,7	3304	3201	2798
	Late	Middle Tor 2	MT2		3401	3229	2806		2994	3054	3348,5	3252,5	2805
		Middle Tor 1	MT1		3522	3257					3406	3335	
	Early	Lower Tor 3	LT3		3460,5	3308					3453	3400	
		Lower Tor 2	LT2		3521								
Lower Tor 1		LT1											
Campanian	Late	Top Hod	Top Hod	2905	3521	3308	2806	2925	2994	3054	3453	3400	2805
		Upper Hod 4	UH4		3575	3344,5		2963	3018	3116,5		3460	
		Upper Hod 3	UH3		3646	3412,5		3006	3050	3163		3526,5	
	Early	Upper Hod 2	UH2		3694	3454		3037	3082	3224	3453	3587,5	
		Upper Hod 1	UH1		3731	3485		3055,5	3120	3280,5	3479,5	3631,5	
Santonian		Middle Hod 4	MH4		3799	3533	2806	3105,5	3137	3332	3528	3666	
		Middle Hod 3	MH3		3837	3533	2821	3179	3209	3378,5	3591,5	3718	
Coniacian		Middle Hod 2	MH2	2905	3866,5	3554	2848,5	3214	3253	3410	3626	3742	2805
		Middle Hod 1	MH1	2930	3908	3579	2868	3263	3291	3449	3671	3763	2821,5
Turonian		Lower Hod 4	LH4	2949	3949	3631	2915		3323,5	3483	3730	3800	2852
		Lower Hod 3	LH3		4010,5				3365	3495	3781	3837,5	
		Lower Hod 2	LH2		4077				3397	3516,5	3832	3900,5	
		Lower Hod 1	LH1		4181	3631			3432	3556	3870	3967	
Cenomanian		Top Plenus Marl			4238								
		Top Hydra			4248	3660	2915	3263	3467	3580,5	3906	4024	
Albian		Base Chalk	Base Chalk	2949	4264	3693,5	2943,5	3790	3486	3603,5	3930,5	4041	2852

Chronostratigraphy		Correlations horizons	Short	Iris-1	Isak-1	Jette-1	Nora-1	NW-Adda-1	Otto-1	P-1	Q-1	Ravn-1	Ravn-2
				m MD	m MD	m MD	m MD	m MD	m MD	m MD	m MD	m MD	m MD
Danian		Top Chalk	Top Chalk	2902	2925,5	3076,5	2597	2296	2477	2919,5	3070	3054	3052
		Ekofisk 3	Eko3	2907	2932	3097	2606	2312,5	2481	2931,5	3098	3054	3062
		Ekofisk 2	Eko 2	2922	2936,5	3117	2616	2329,5	2482,5	2939,5	3108	3072,5	3059
		Ekofisk 1	Eko 1	2935,5	2954,5	3135		2355	2482,5	2969,5	3126	3088	3088
Maastrichtian	Latest	Top Tor	Top Tor	2954	2960	3167	2616	2389,5	2488,5	2993	3163	3102,5	3100
		Upper Tor 2	UT2		2967	3185	2642	2421	2488,5		3185,5	3130	3125
		Upper Tor 1	UT1	2954	2984	3209	2655	2438	2498,5	2993	3210,5	3164	3149
	Late	Middle Tor 2	MT2	2980	3011	3256,5	2663	2465,5	2507	3007	3242	3184	3161
		Middle Tor 1	MT1	2989	3044	3338,5	2678,5		2555,5		3333	3228	3188
	Early	Lower Tor 3	LT3	3020	3065,5	3406	2719		2583		3400	3244	
		Lower Tor 2	LT2										
		Lower Tor 1	LT1										
Campanian	Late	Top Hod	Top Hod	3020	3065,5	3406	2719	2465,5	2583	3007	3400	3244	3188
		Upper Hod 4	UH4			3415			2583		3474	3250	3261
		Upper Hod 3	UH3			3481			2604	3007	3544,6	3314	3318
	Early	Upper Hod 2	UH2	3020		3532,5	2719		2620,5	3042,5	3600	3364	3360
		Upper Hod 1	UH1	3040		3567,5	2740		2660	3073,5	3628,5	3412,5	3392
Santonian		Middle Hod 4	MH4	3062		3626,5	2753,5				3661	3448,5	3457
		Middle Hod 3	MH3	3079		3689	2772	2465,5			3725,5	3495,5	3498
Coniacian		Middle Hod 2	MH2	3089	3065,5	3734,5	2779	2478	2660	3073,5	3757	3561	3533
		Middle Hod 1	MH1	3103,5	3083,2	3780,5	2787	2505,5	2682,5	3094,5	3790	3596	3576
Turonian		Lower Hod 4	LH4	3115	3137,8	3919	2807,5	2542,5	2722,5	3120	3830	3652	3614
		Lower Hod 3	LH3	3133	3187,5	3845	2825			3120	3855	3687	3631,5
		Lower Hod 2	LH2	3155	3218,5	3877,5	2858			3137	3890	3716	3657,5
		Lower Hod 1	LH1	3173		3908				3155	3915	3744	3692
Cenomanian		Top Plenus Marl		3173									
		Top Hydra		3175		3925	2858	2542,5			3944,5	3778,5	3712
Albian		Base Chalk	Base Chalk	3214,5	3218,5	3942	2899	2555	2722,5	3155	3963	3786	3734

Chronostratigraphy		Correlations horizons	Short	Rigs-1	Rigs-2	SA-1	Sine-1	Skjold Flanke-1	T-1	T-3	W-1	West Lulu-1
				m MD	m MD	m MD	m MD	m MD	m MD	m MD	m MD	m MD
Danian		Top Chalk	Top Chalk	2790	2782	3316	1798	2127	2219,5	2484,5	3088	2875,5
		Ekofisk 3	Eko3	2795	2782	3329	1798	2138	2235	2484,5	3102	2903
		Ekofisk 2	Eko 2	2804,5	2798	3334	1812	2145,5	2235	2494,5	3123,5	2928
		Ekofisk 1	Eko 1	2820	2820	3342	1826	2145,5	2240	2510,5	3145,5	2948,5
Maastrichtian	Latest	Top Tor	Top Tor	2837	2832,5	3360	1857	2174	2260,5	2532	3173,5	2984,5
		Upper Tor 2	UT2	2846	2838	3377	1879	2208	2271	2550	3185,5	3006,5
		Upper Tor 1	UT1	2855	2849	3413	1907,5	2232,5	2283	2576,5	3219	3023,5
	Late	Middle Tor 2	MT2		2865	3433	1954	2275		2590,5	3263,5	3064
		Middle Tor 1	MT1			3470	2046,5	2351		2630	3302	3151
	Early	Lower Tor 3	LT3			3480	2133	2391,5		2662		3190
		Lower Tor 2	LT2				2204,5	2447				
Lower Tor 1		LT1				2321	2494,5					
Campanian	Late	Top Hod	Top Hod				2403	2519	2283	2262	3302	3190
		Upper Hod 4	UH4				2403	2519			3343,5	
		Upper Hod 3	UH3				2431	2547			3423	
	Early	Upper Hod 2	UH2				2448	2575	2283	2662	3500	
		Upper Hod 1	UH1				2465	2597	2325	2686	3544	
Santonian		Middle Hod 4	MH4				2482	2620			3586	3190
		Middle Hod 3	MH3				2523	2620	2325			3278
Coniacian		Middle Hod 2	MH2				2553,5	2640,5	2342	2686	3586	3309,5
		Middle Hod 1	MH1				2587	2662		2695	3611	3345,5
Turonian		Lower Hod 4	LH4				2655,5	2685		2735	3658	3400
		Lower Hod 3	LH3				2672,5	2685				
		Lower Hod 2	LH2				2694	2691,5			3658	3400
		Lower Hod 1	LH1				2741	2720			3698,5	3455
Cenomanian		Top Plenus Marl						2743				
		Top Hidra		2855	2865	3480	2776	2749,5	2342	2735	3726	3477,5
Albian		Base Chalk	Base Chalk	2855	2865	3480	2802	2772	2342	2735	3759,5	3500

Appendix 2: Cross plots of log data

Log displays and cross plots of V_p - ϕ , V_p -Z and ϕ -Z for the chalk in 28 wells:

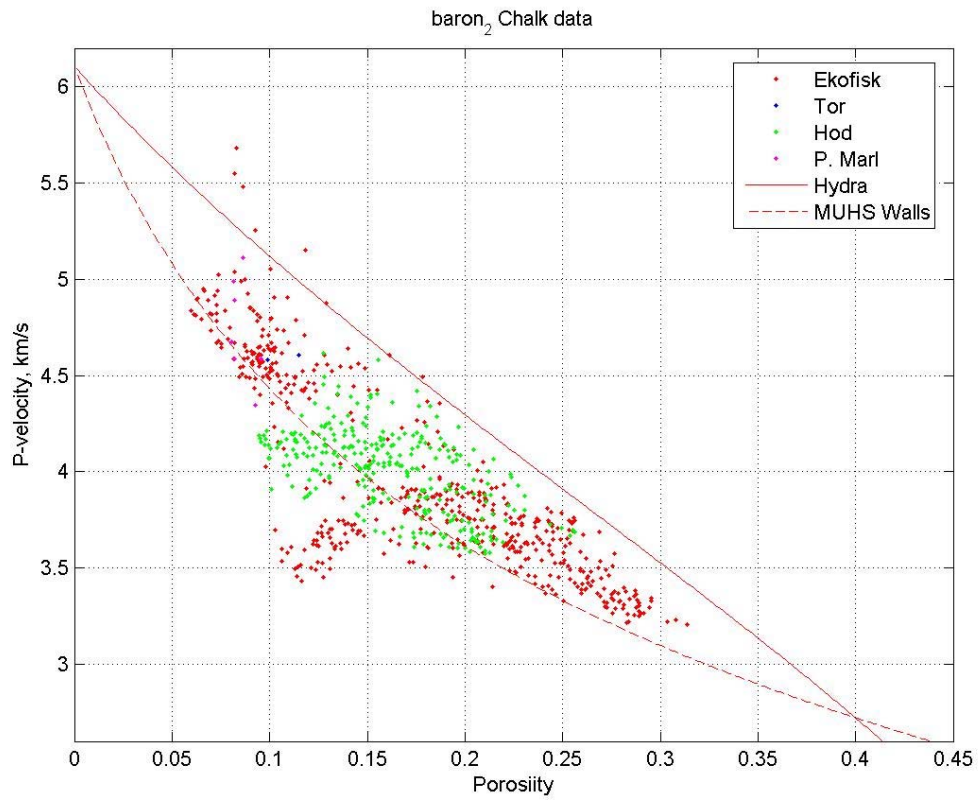
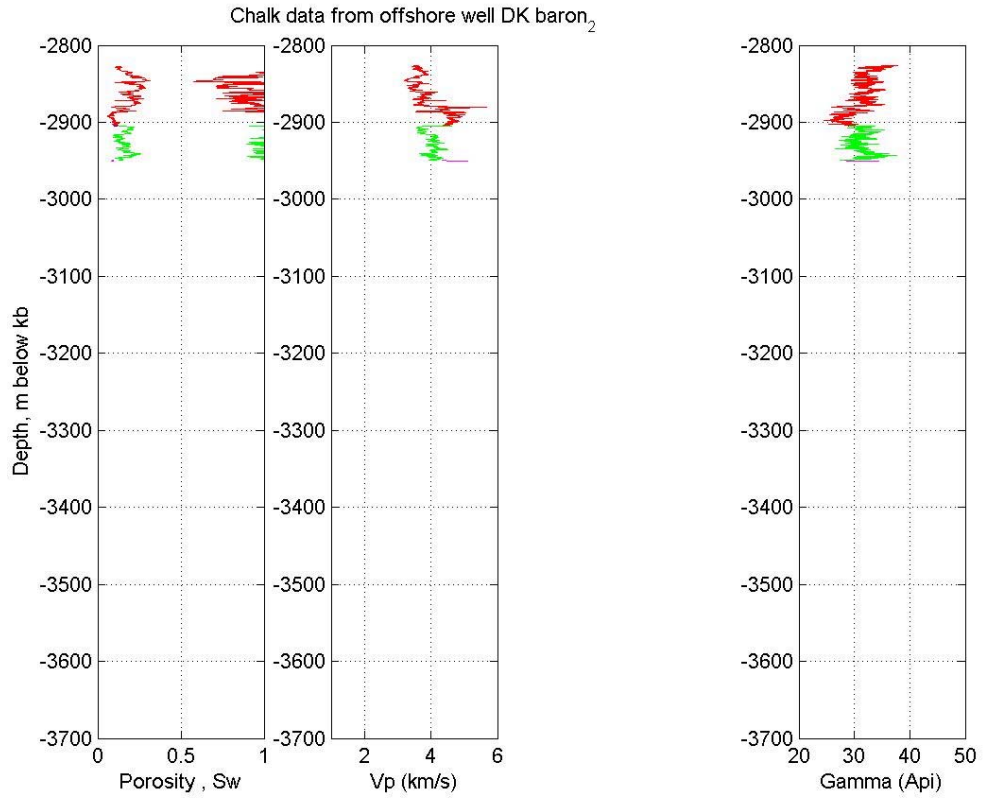
Baron-2
Bertel-1A
Diamant-1
Elin-1
Elly-1
Elly-2
Falk-1
Gert-1
Gwen-2
I-1
Iris-1
Isak-1
Jette-1
Nora-1
NW Adda-1
Otto-1
P-1
Q-1
Ravn-1
Ravn-2
Rigs-2
SA-1
Sine-1
Skjold Flank-1
T-1
T-3
W. Lulu-1
W-1

Cross plots of V_s - ϕ , V_p/V_s - ϕ and V_p - V_s for the chalk in 4 wells:

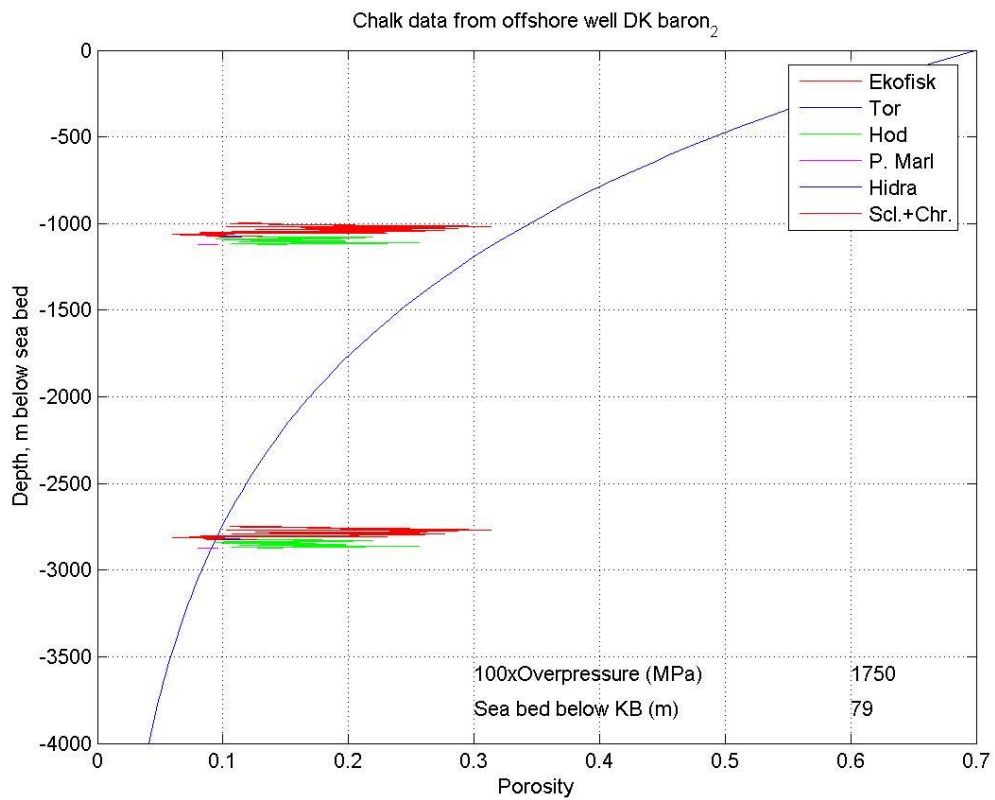
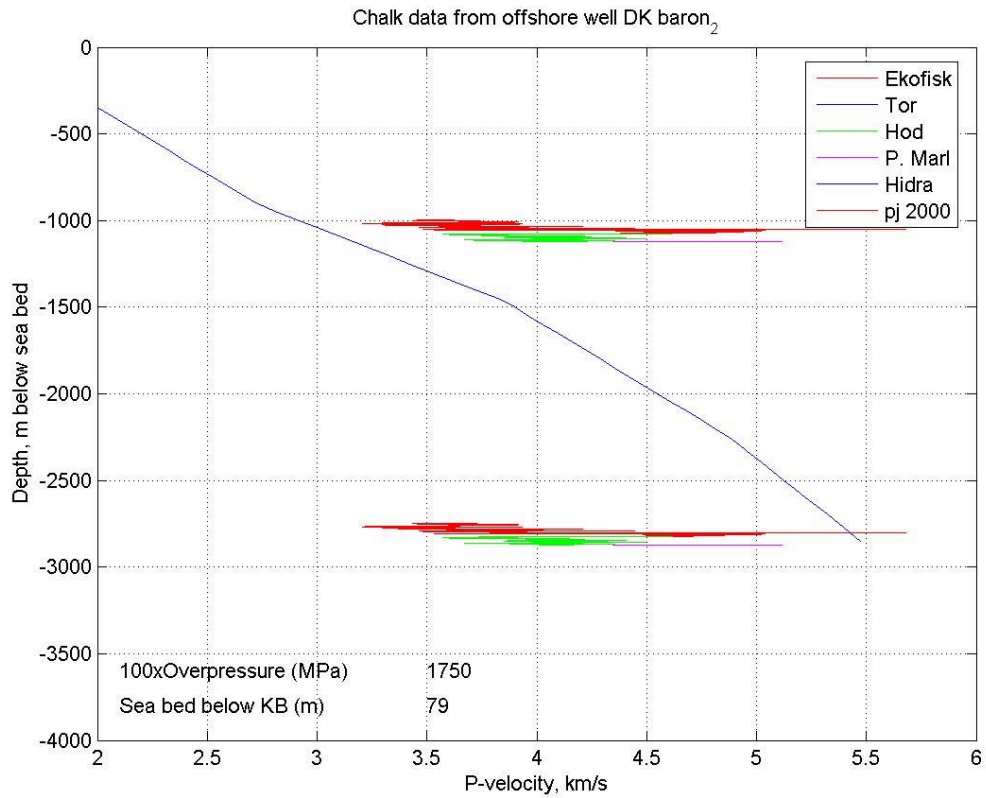
Isak-1
Jette-1
NW Adda-1
Sine-1
Skjold Flank-1

pj 2000: Japsen (2000), Scl.+Chr.: Sclater & Christie (1980), MUHS/MLHS Walls: Modified upper and Lower Hashin-Shtrikman model (Walls et al. 1998).

Vp plots

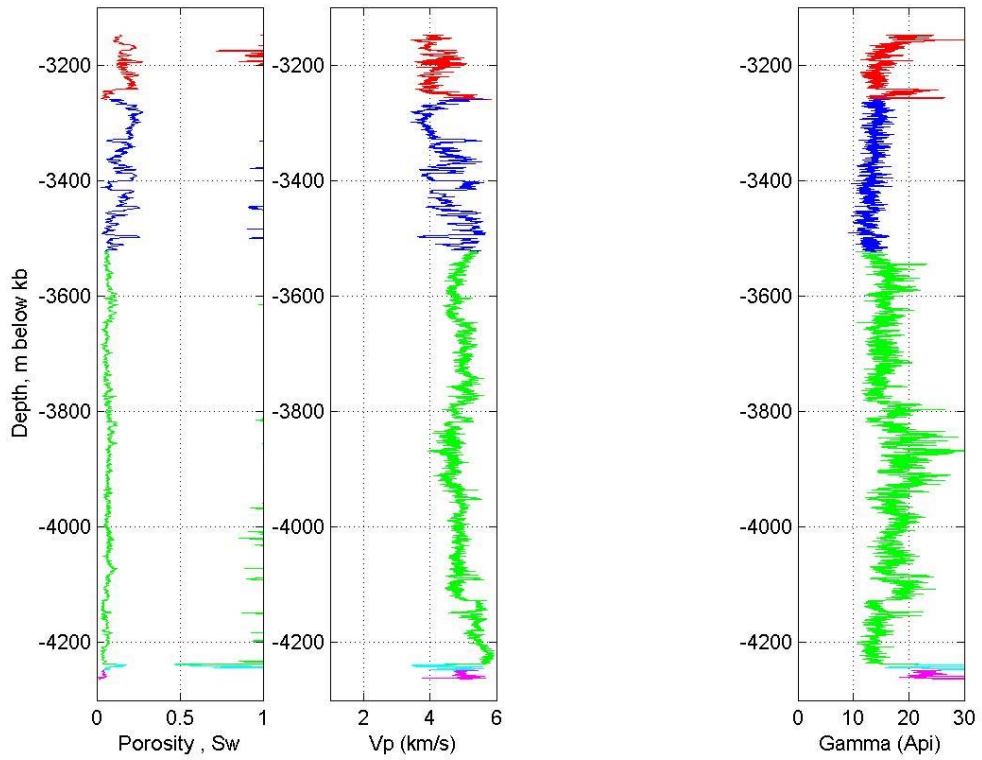


Baron-2

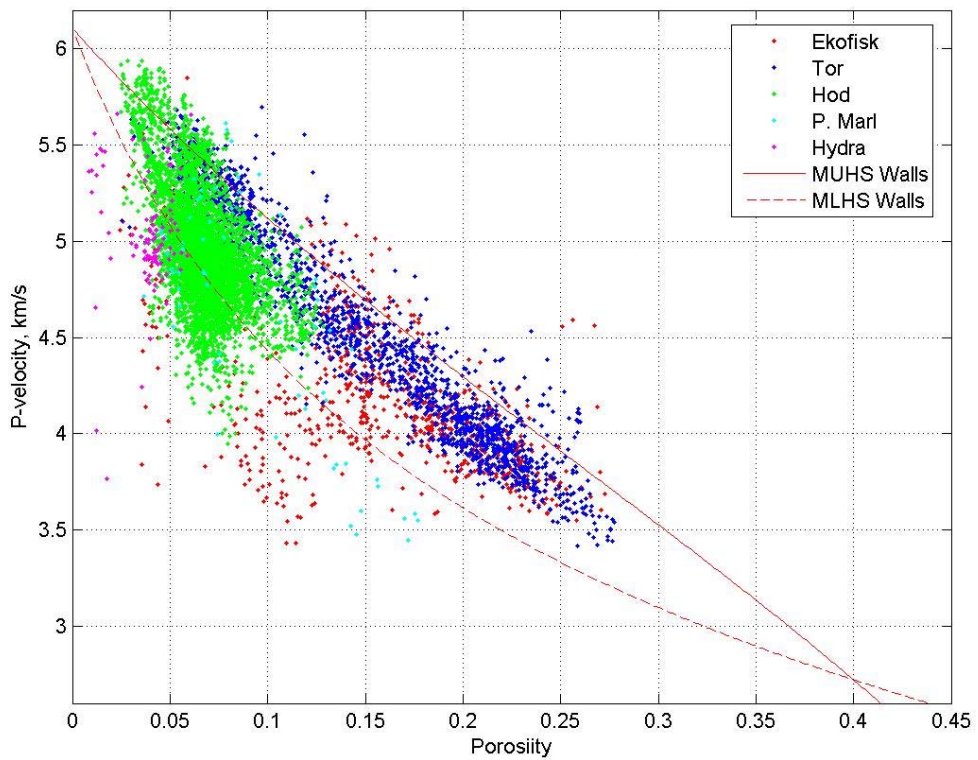


Baron-2

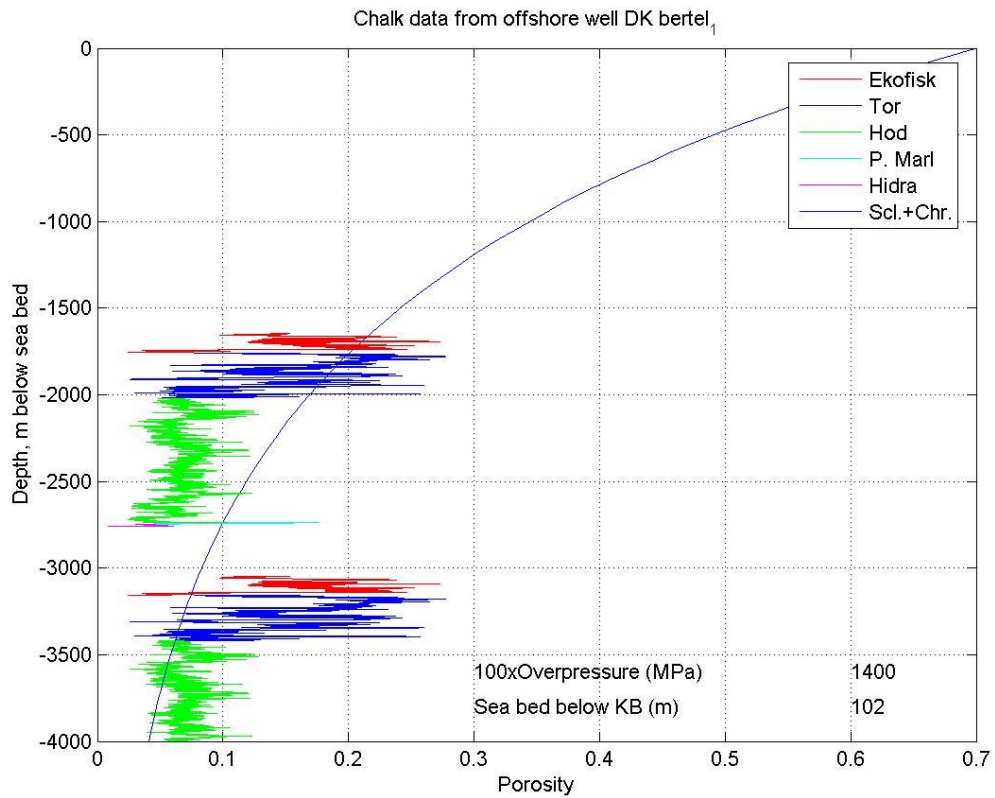
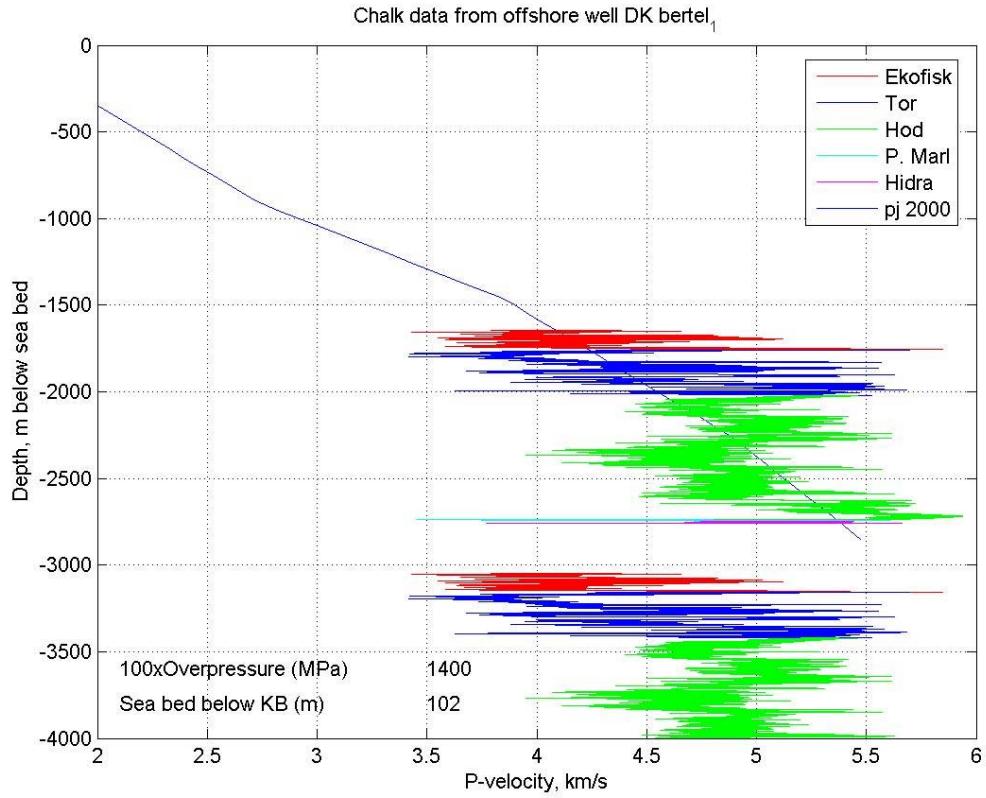
Chalk data from offshore well DK bertel₁



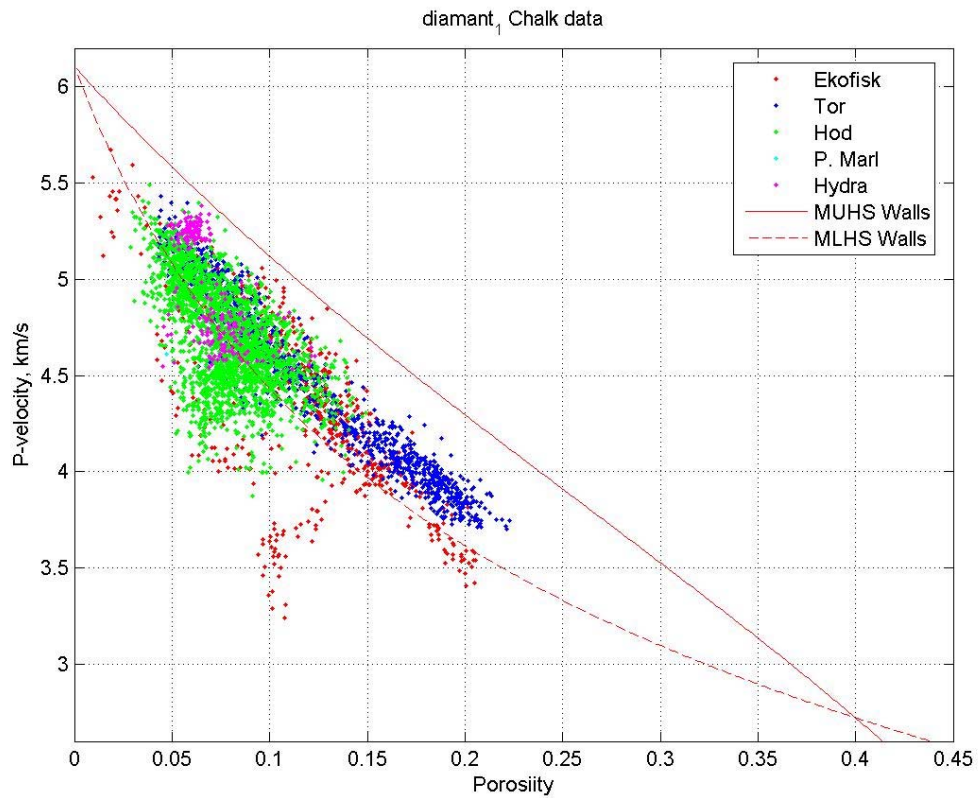
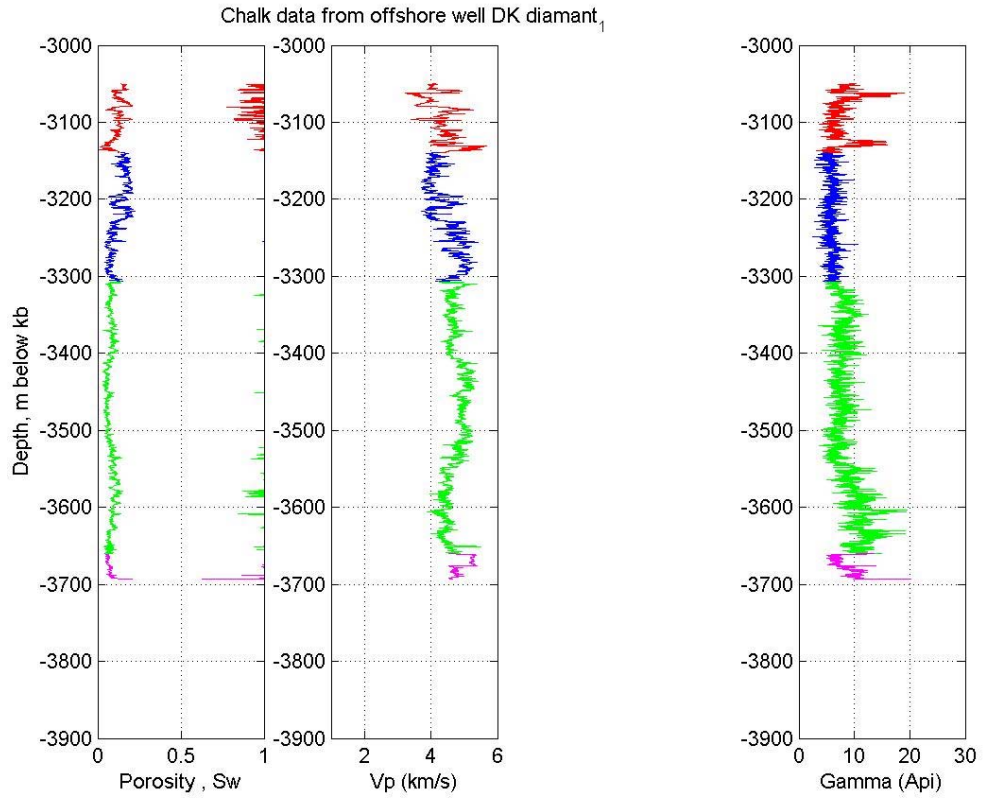
bertel₁ Chalk data



Bertel-1

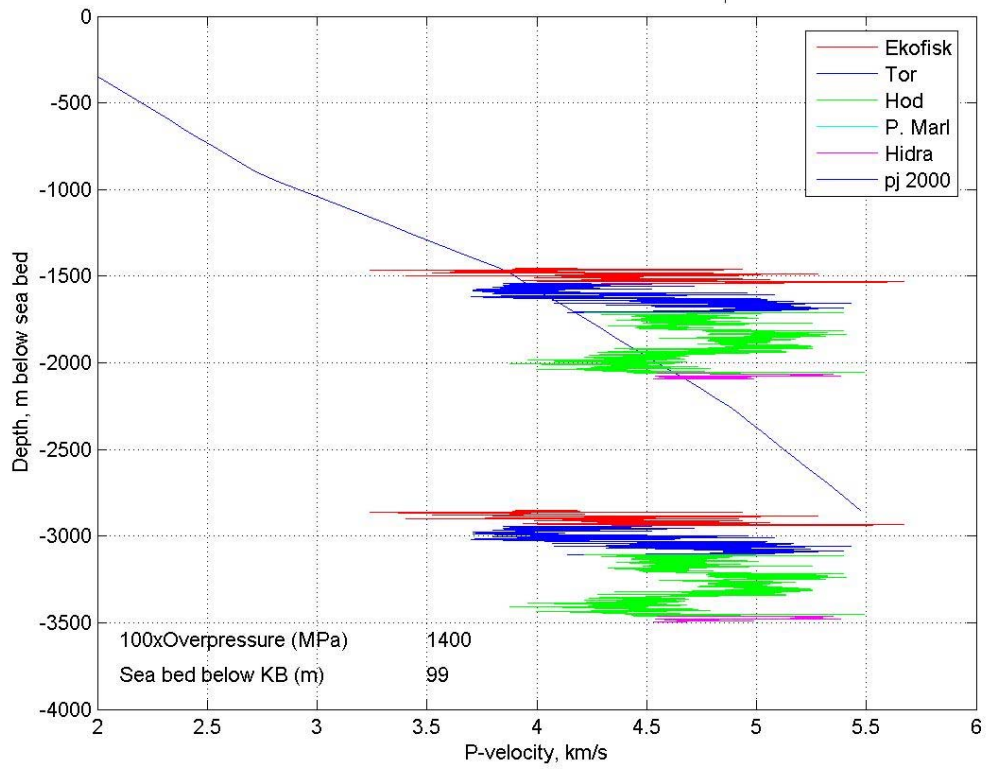


Bertel-1

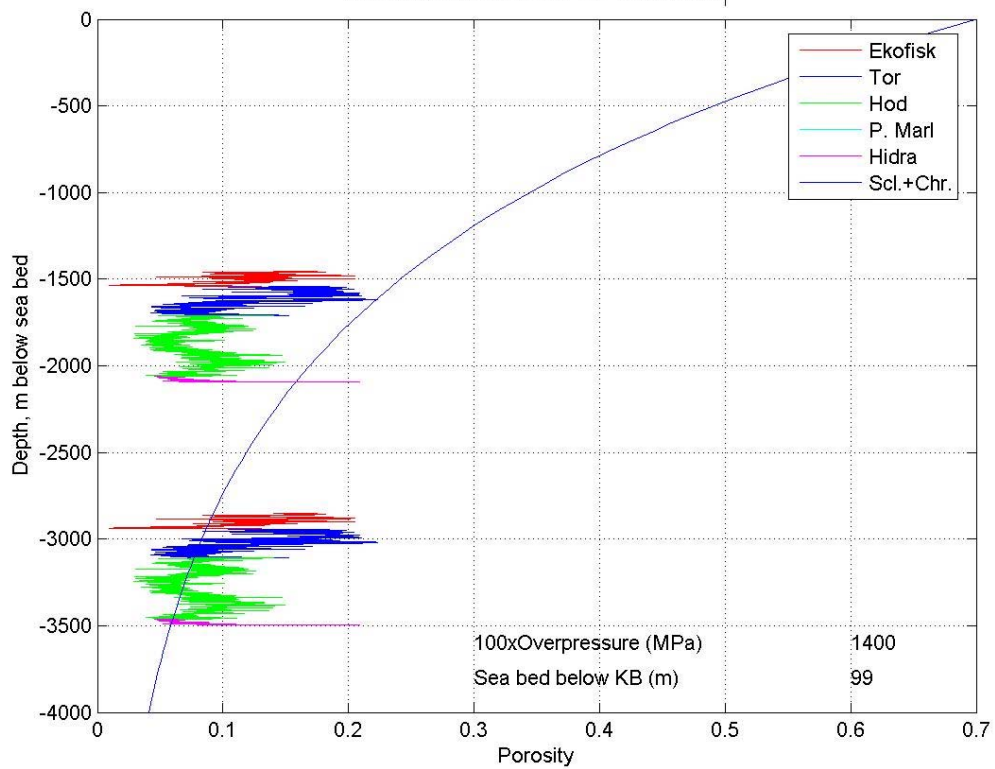


Diamant-1

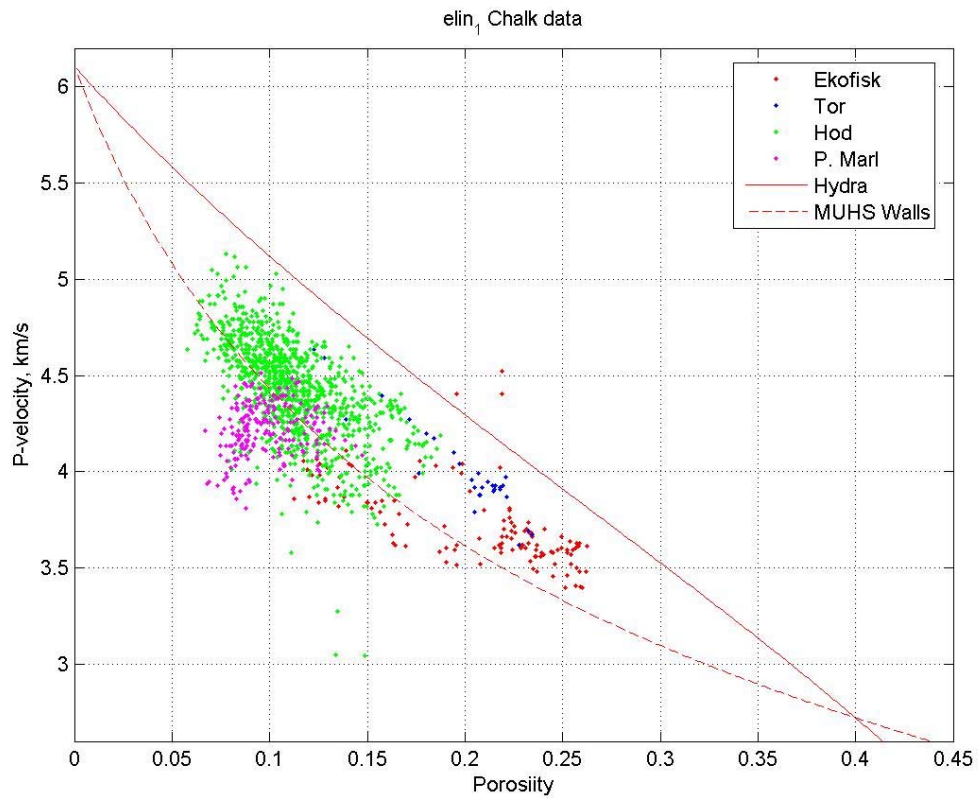
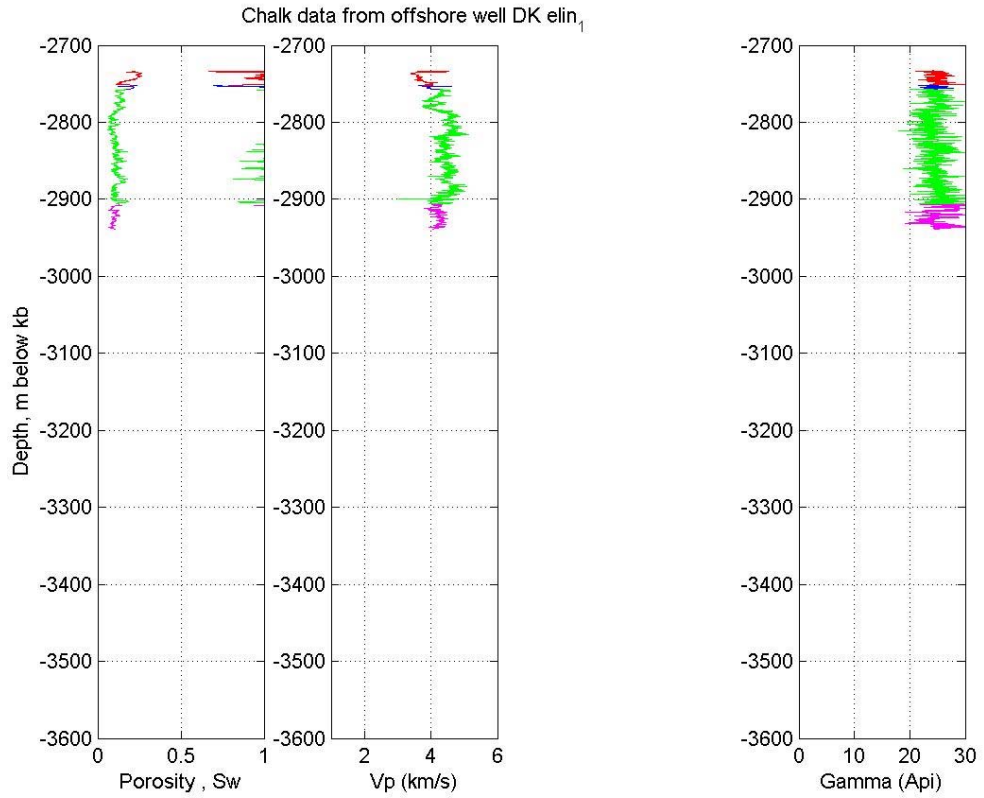
Chalk data from offshore well DK diamant₁



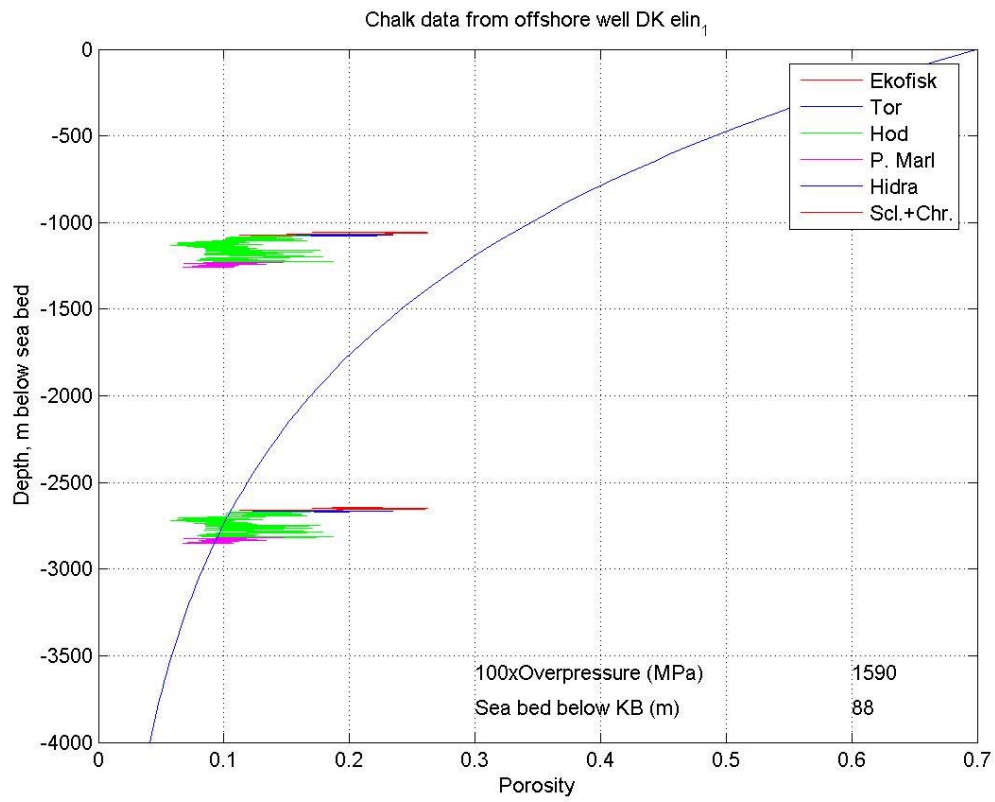
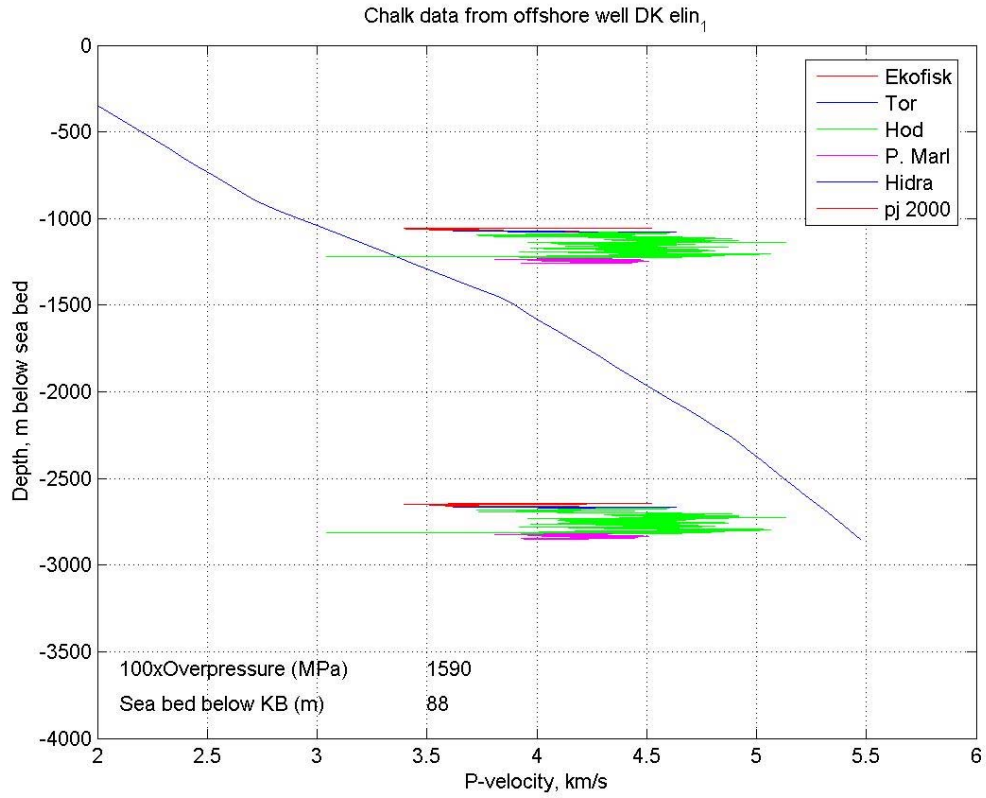
Chalk data from offshore well DK diamant₁



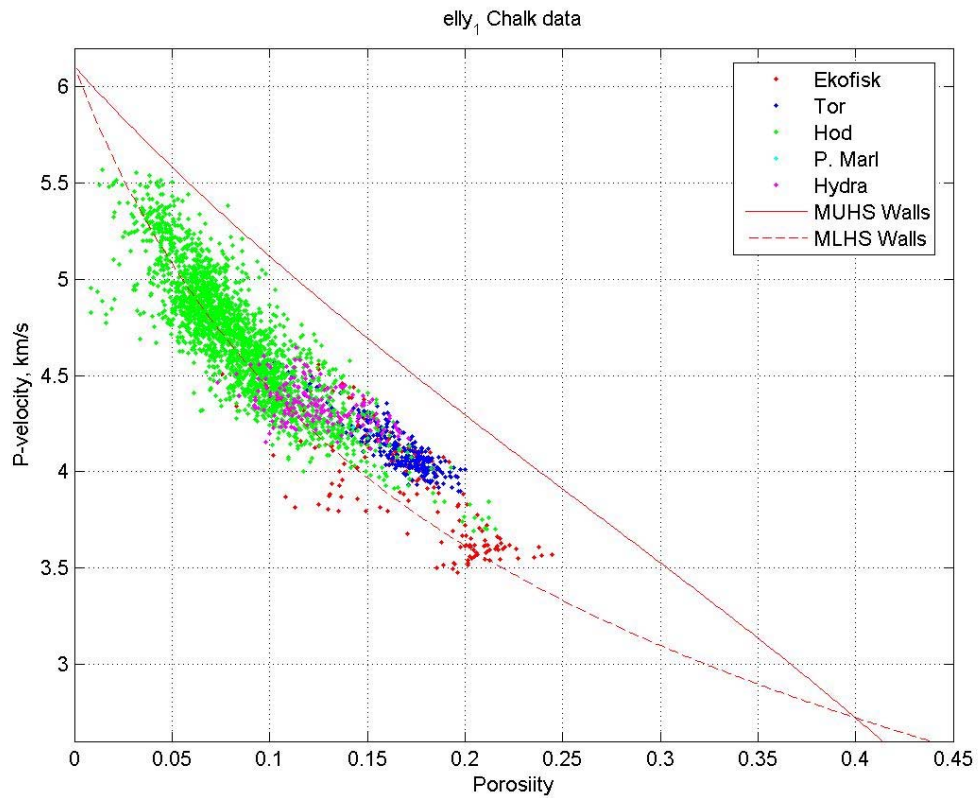
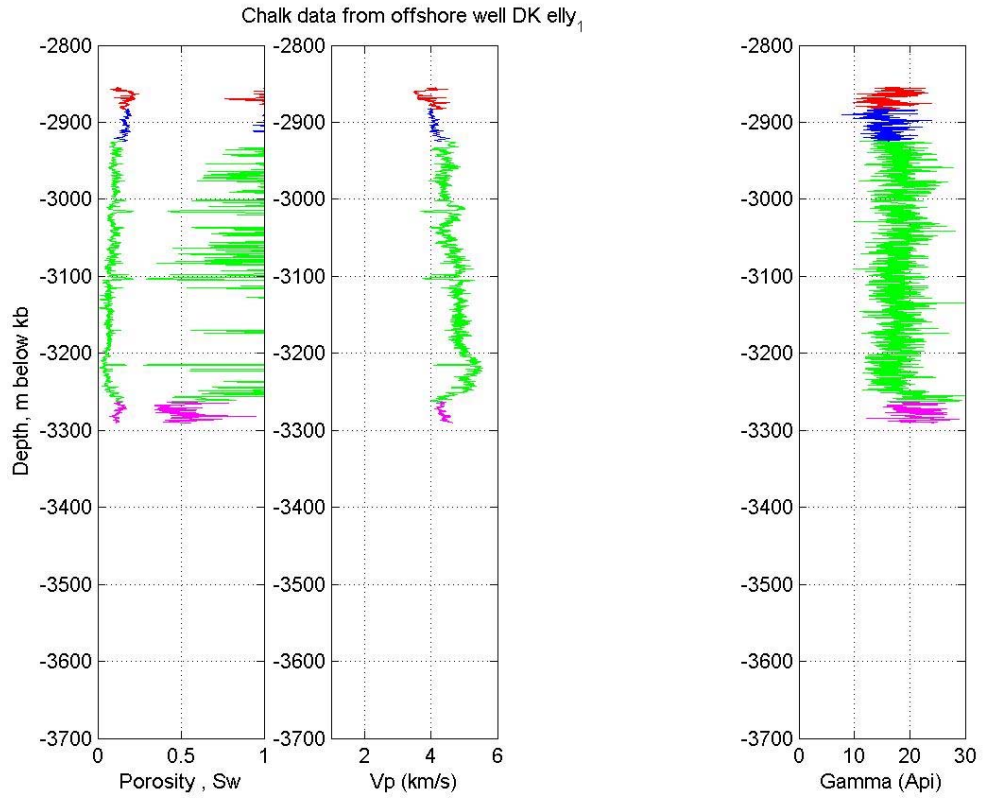
Diamant-1



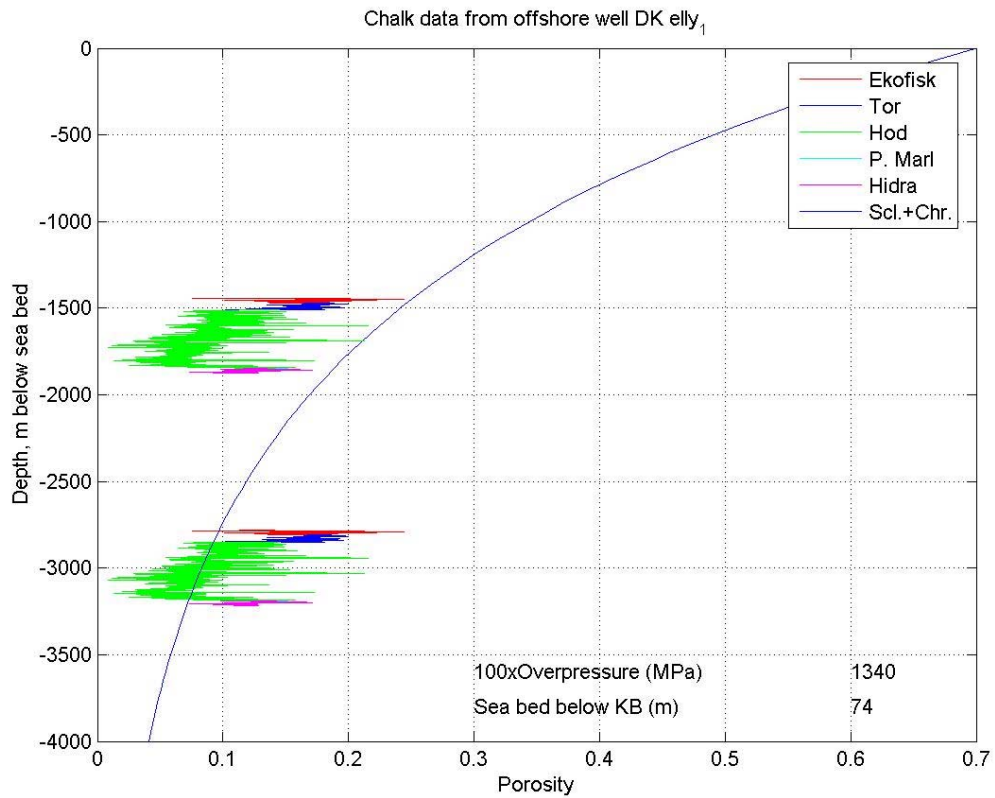
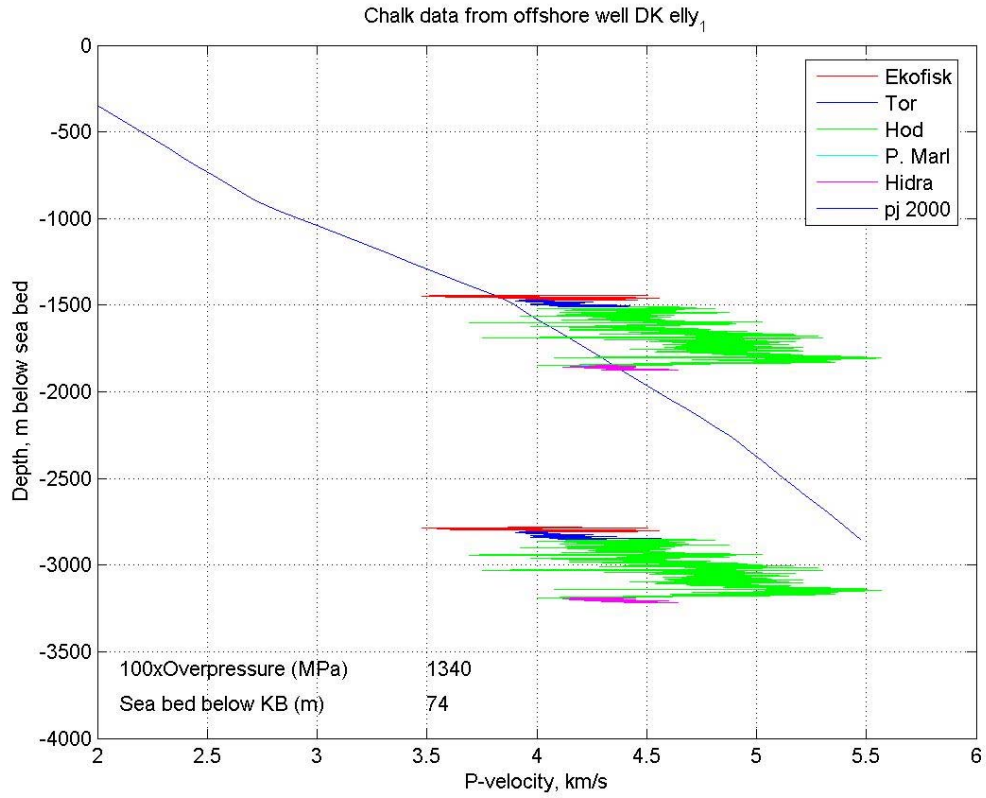
Elin-1



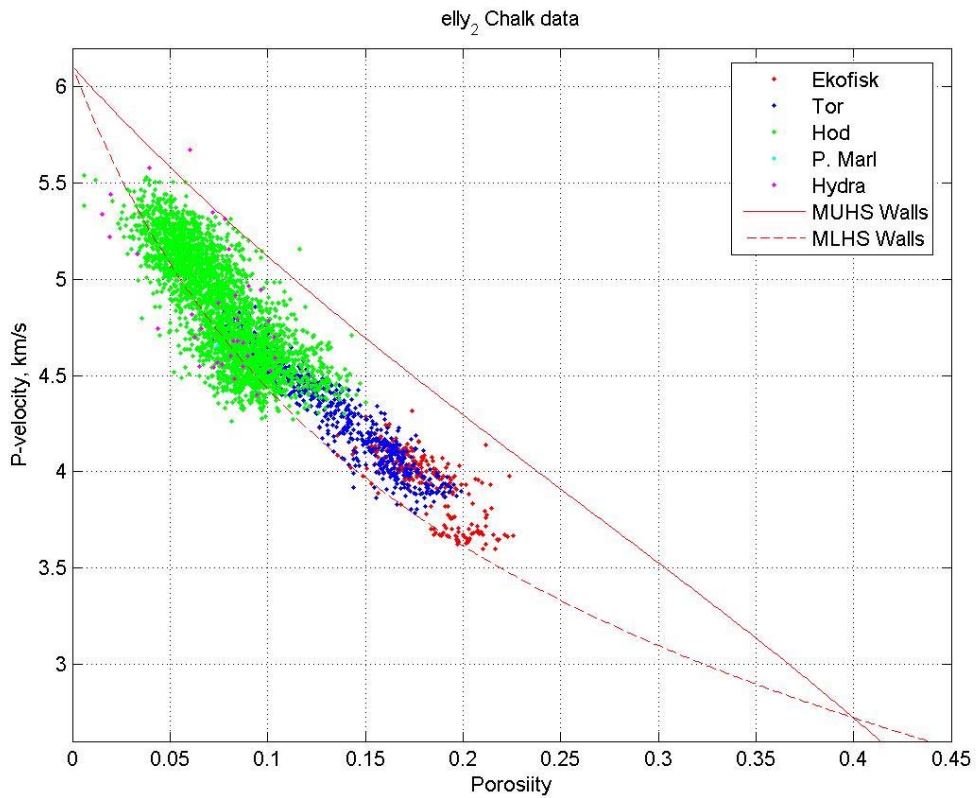
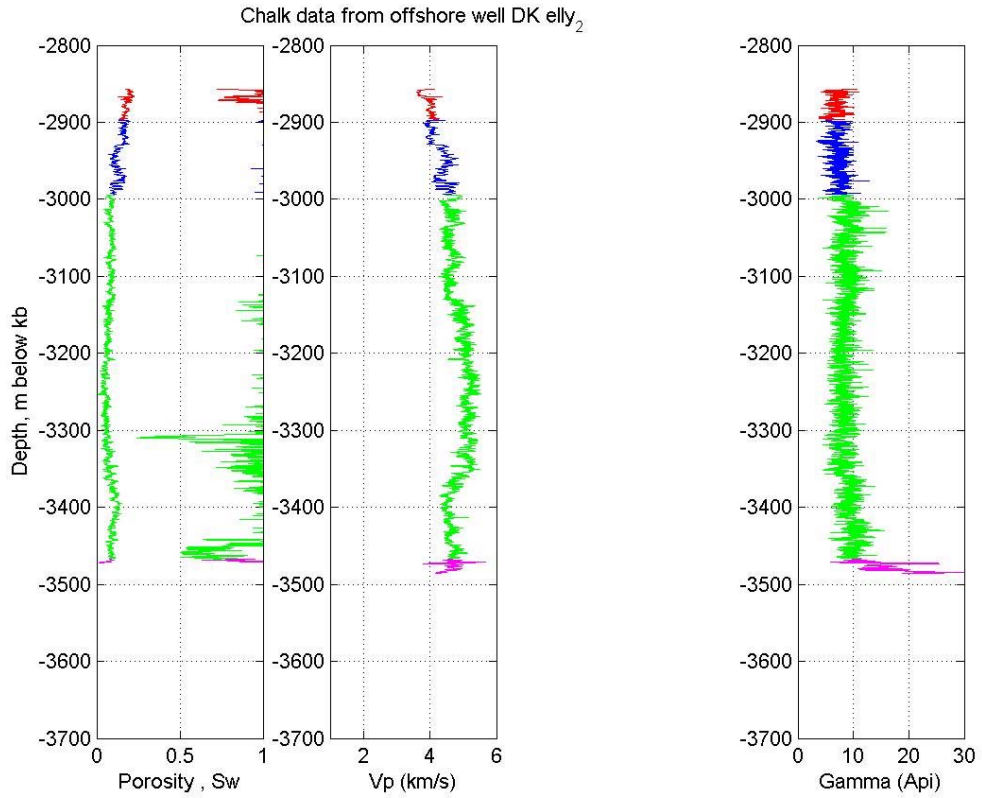
Elin-1



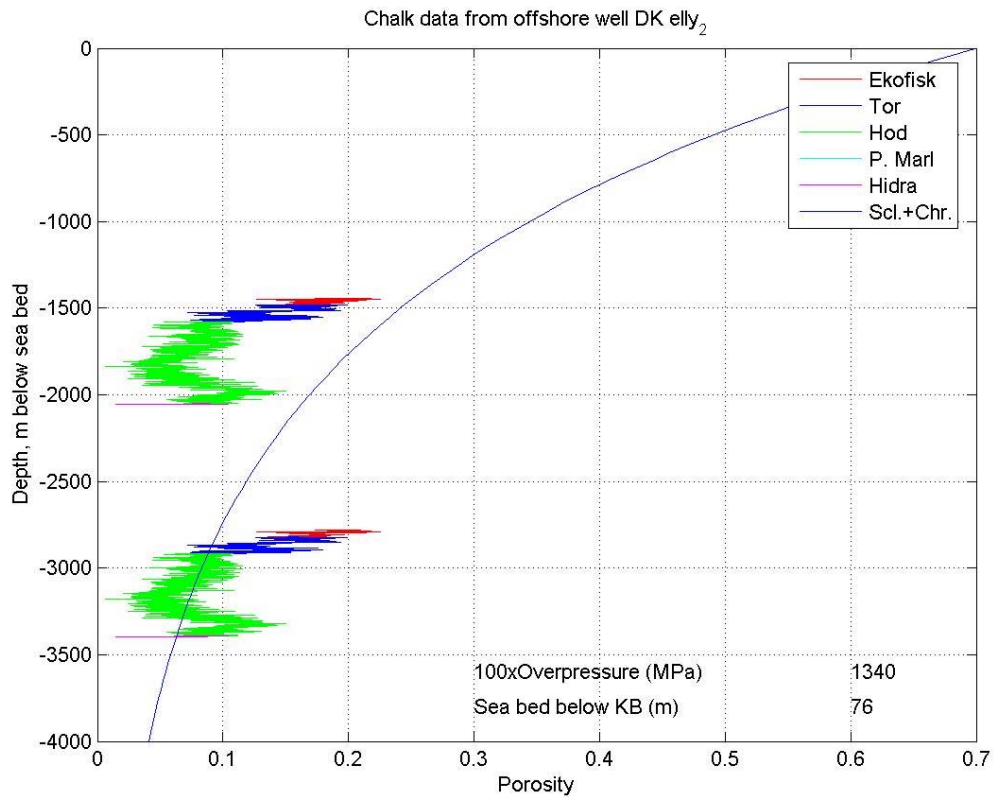
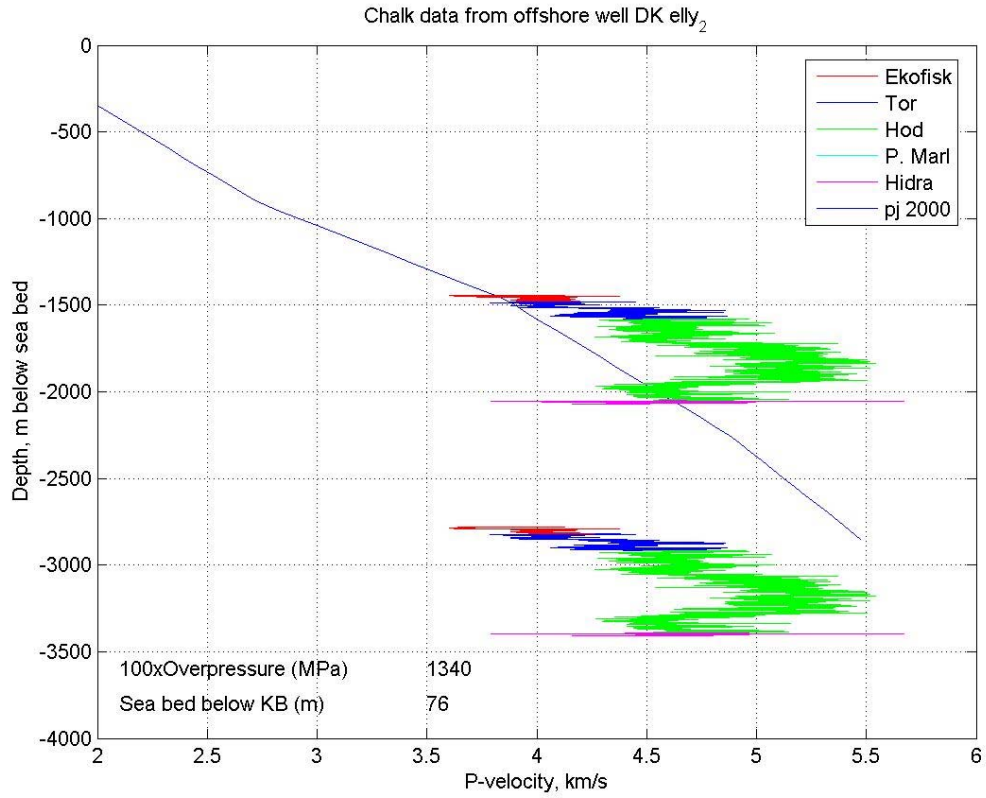
Elly-1



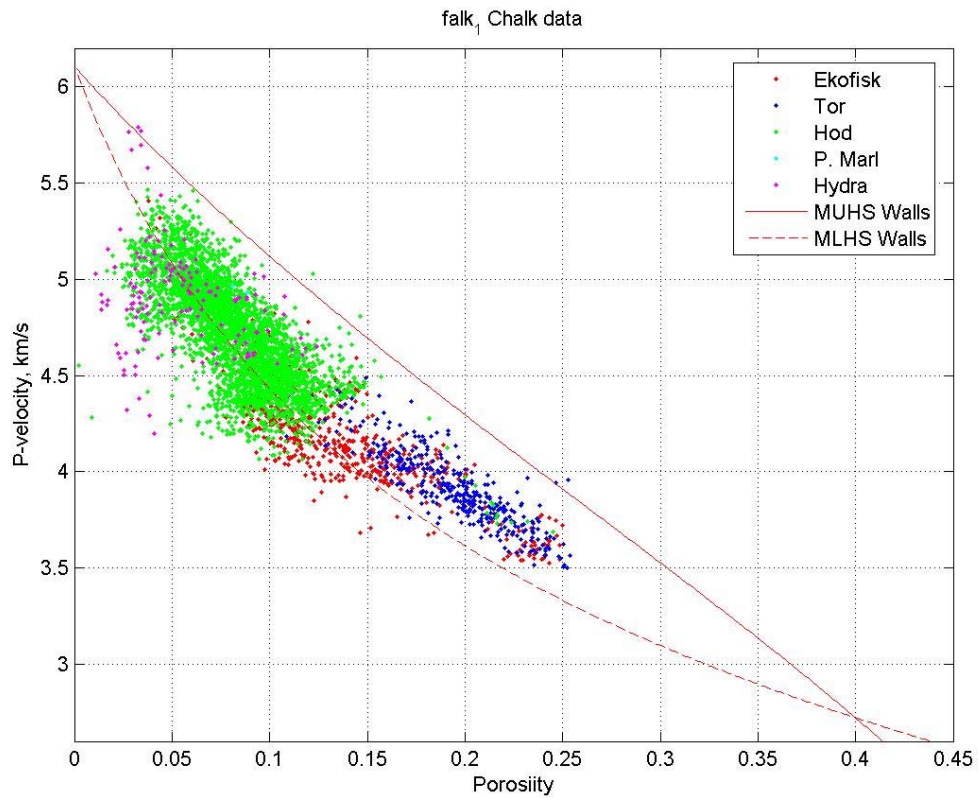
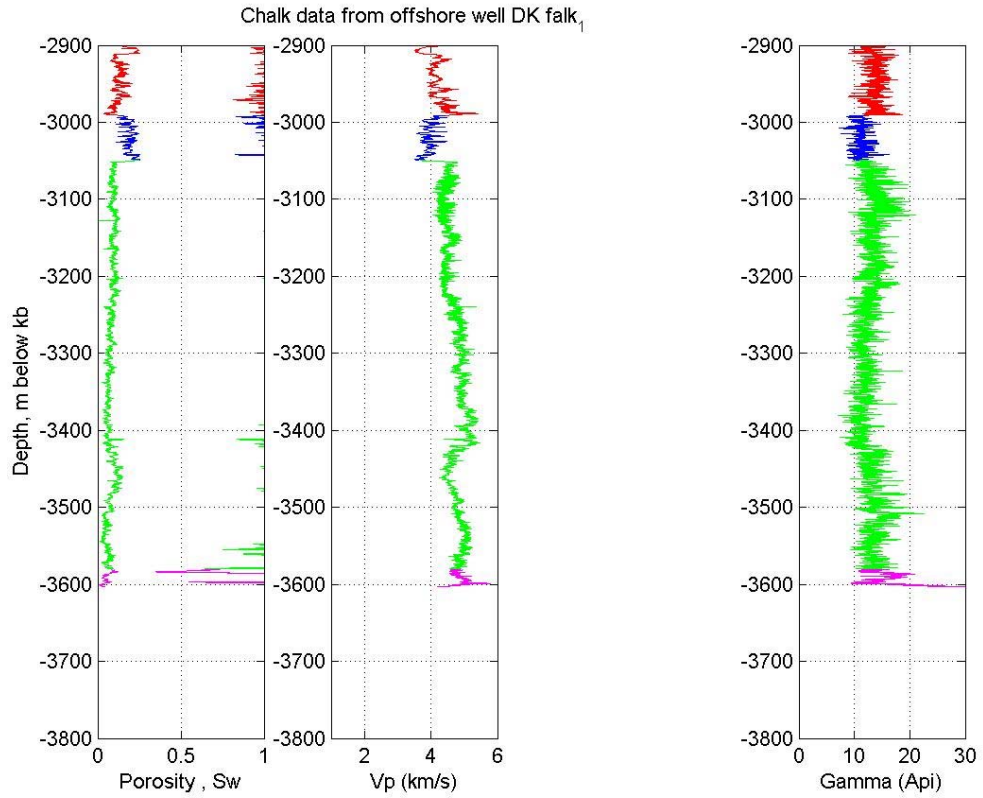
Elly-1



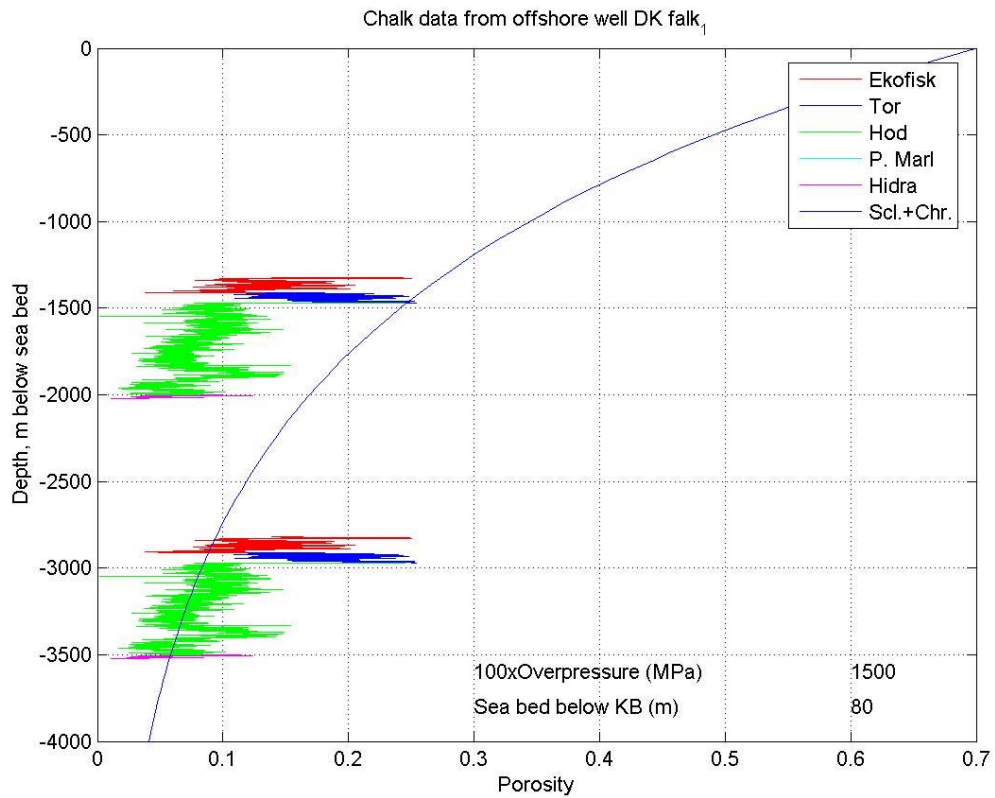
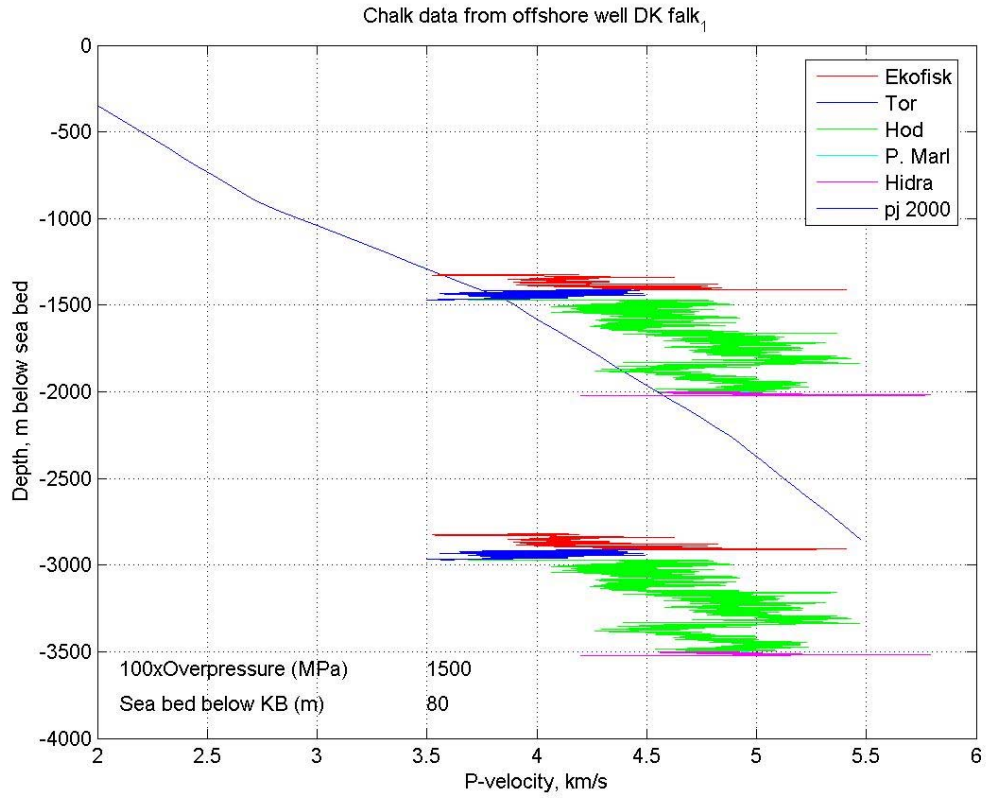
Elly-2



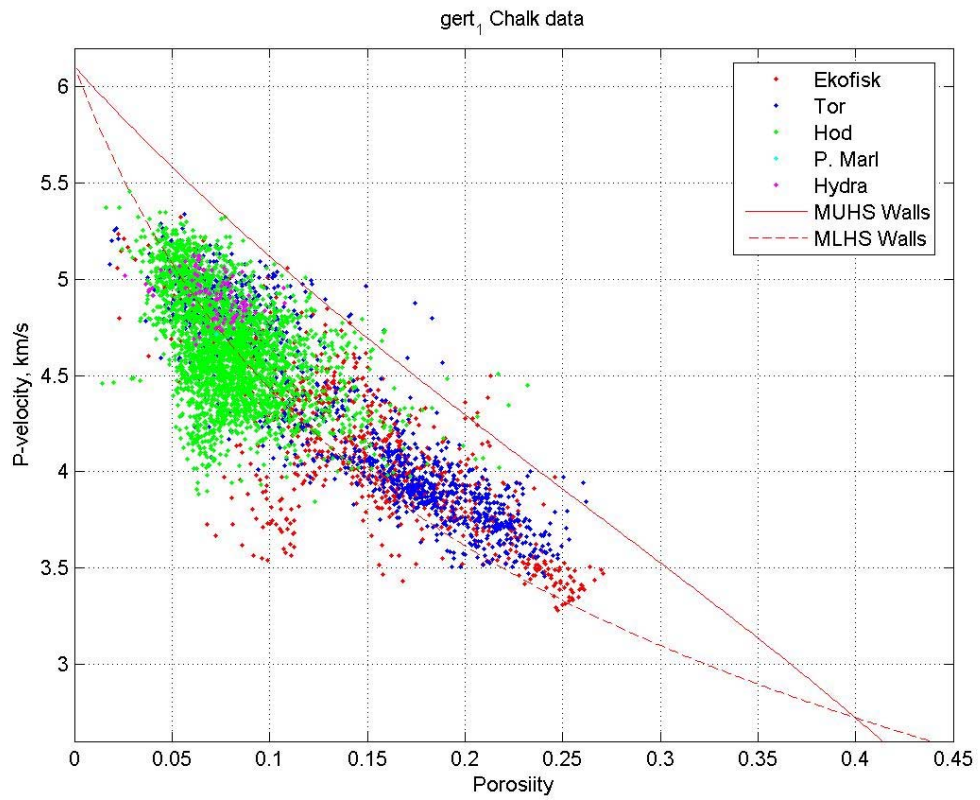
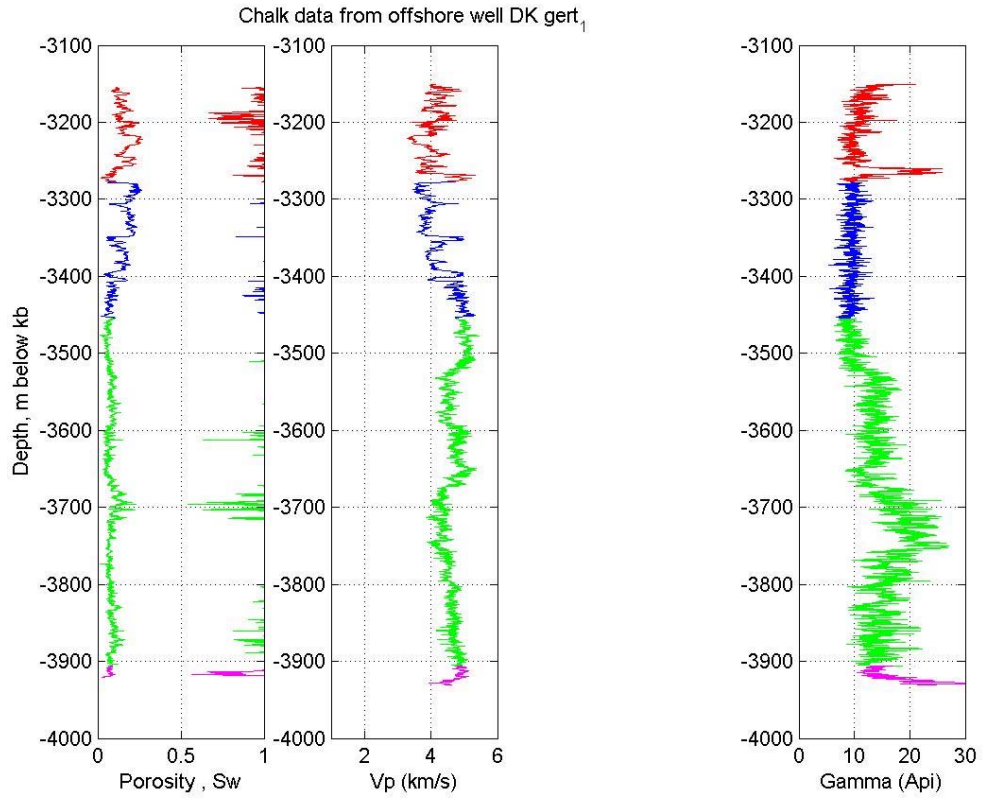
Elly-2



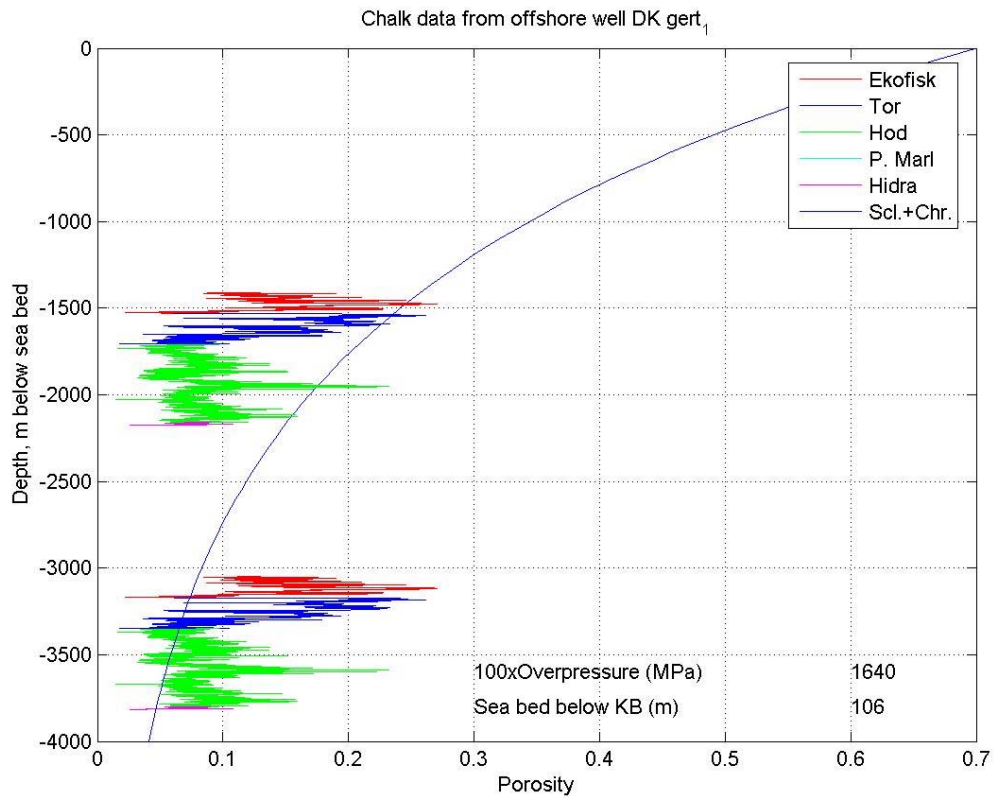
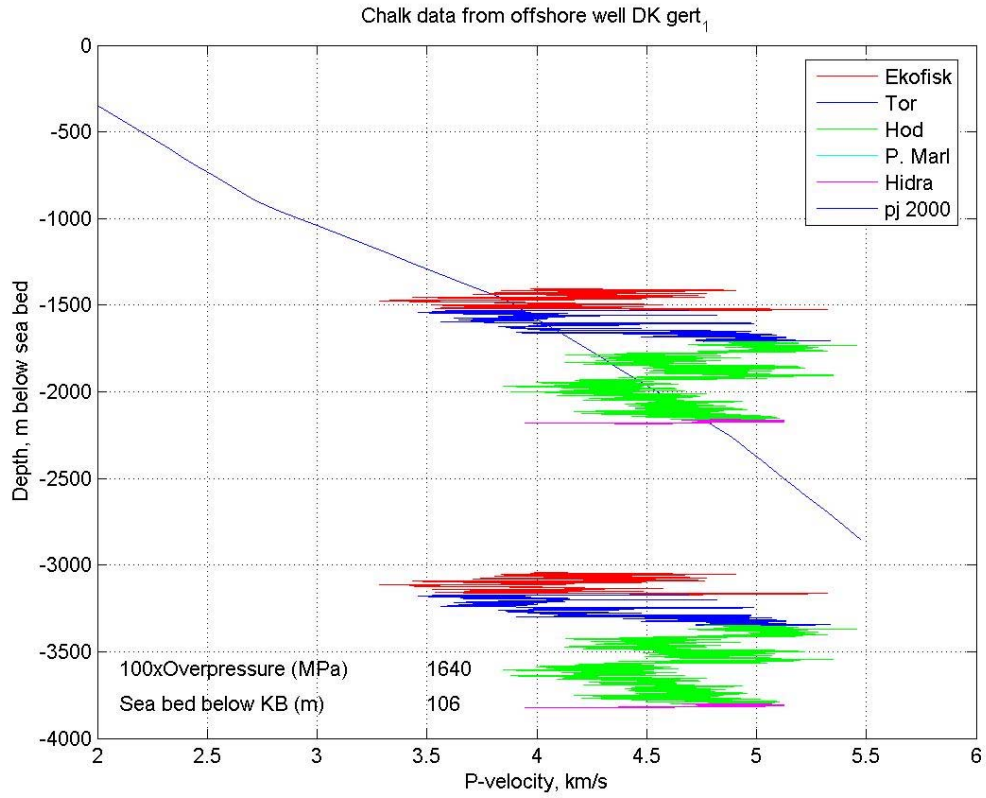
Falk-1



Falk-1

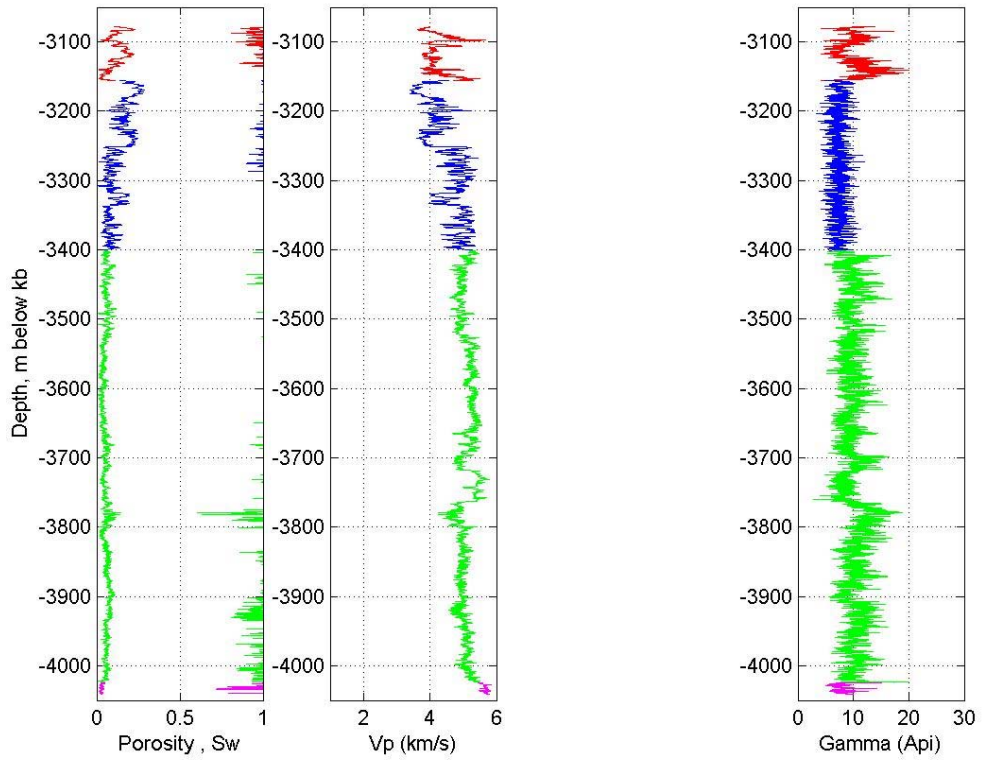


Gert-1

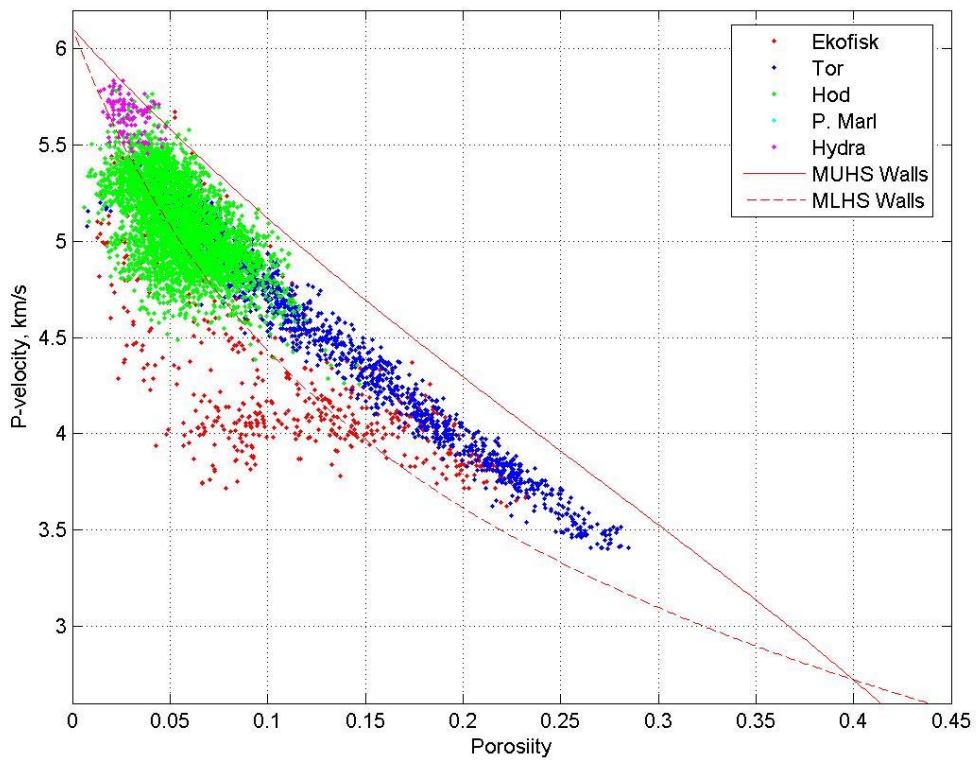


Gert-1

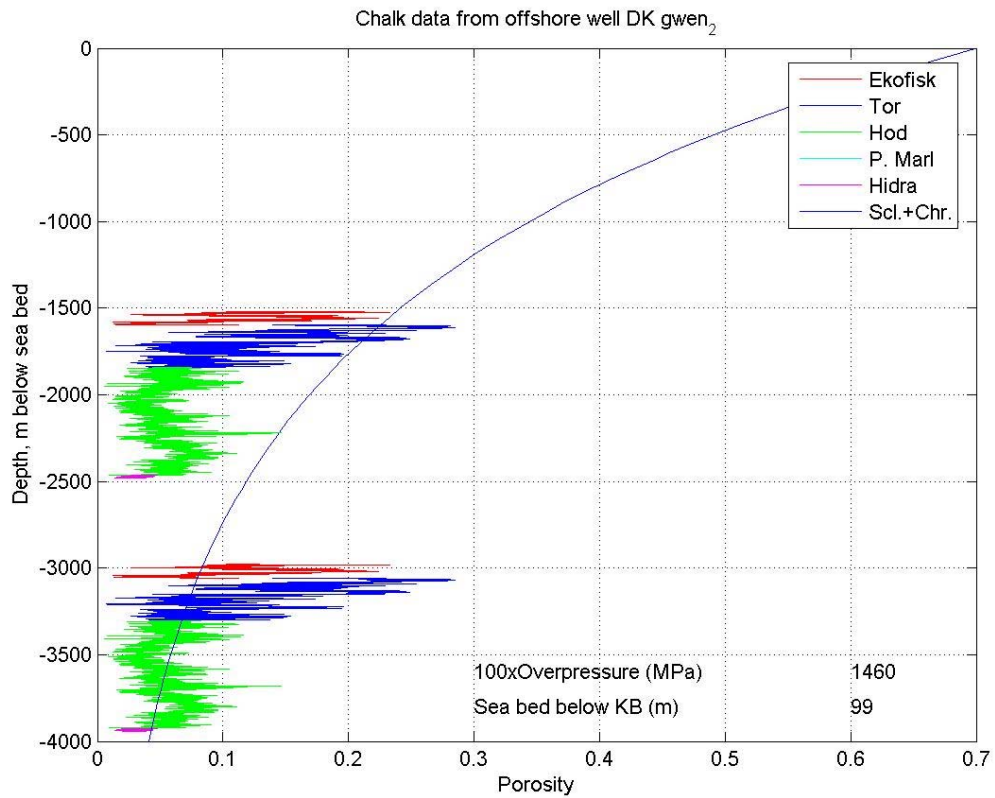
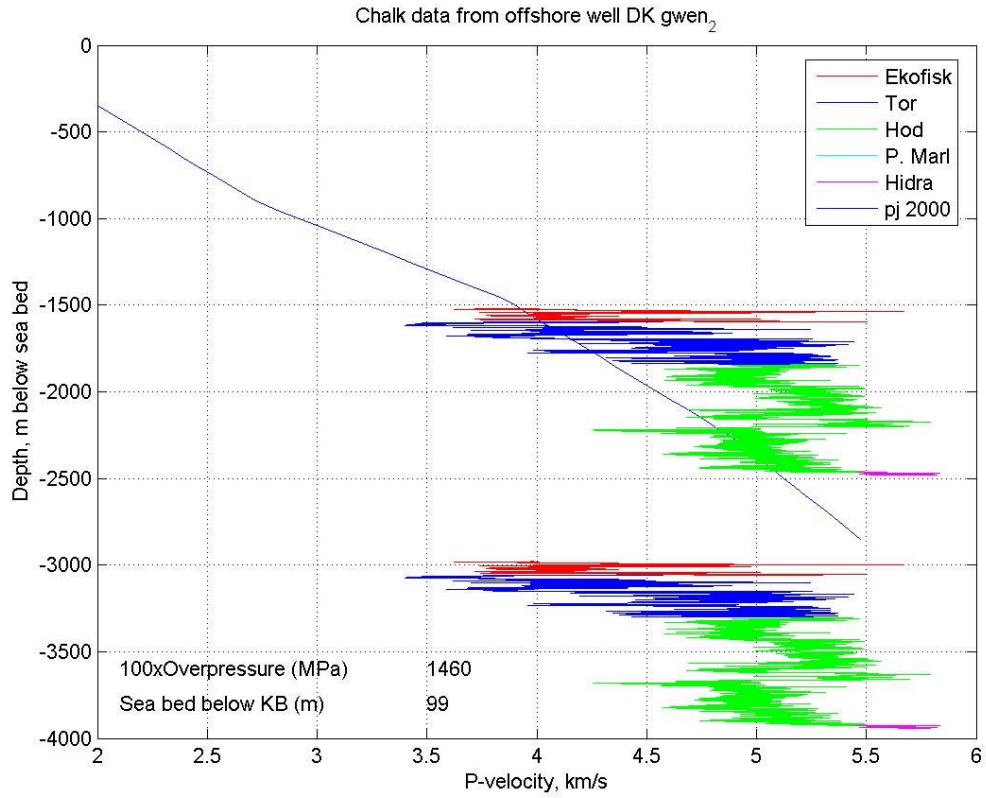
Chalk data from offshore well DK gwen₂



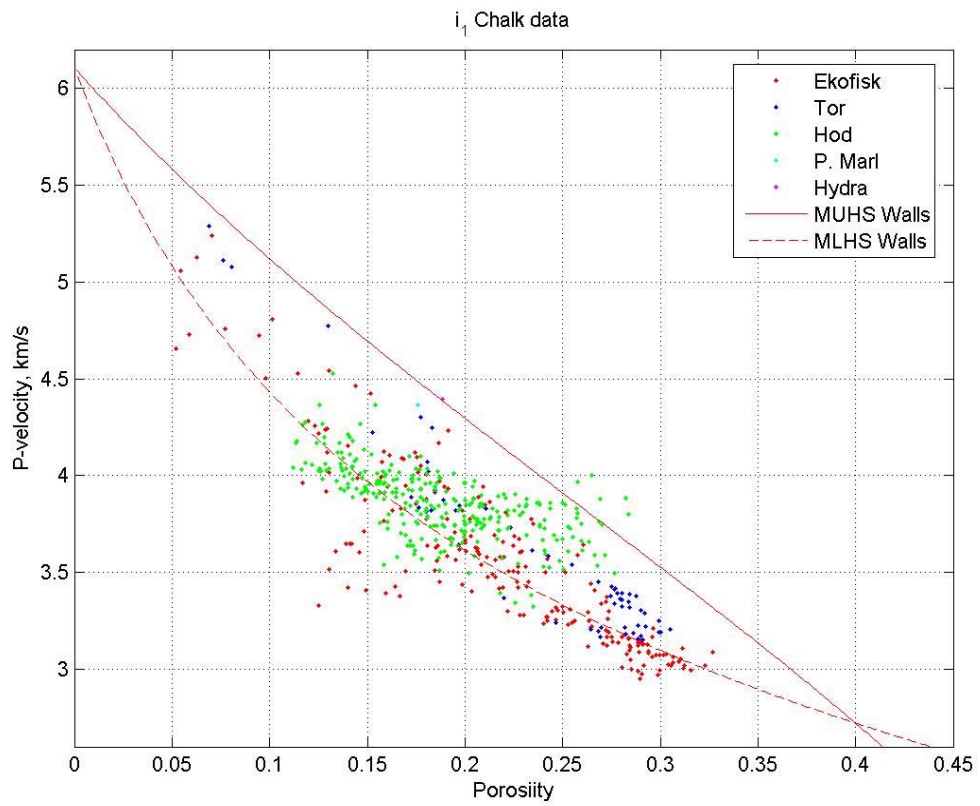
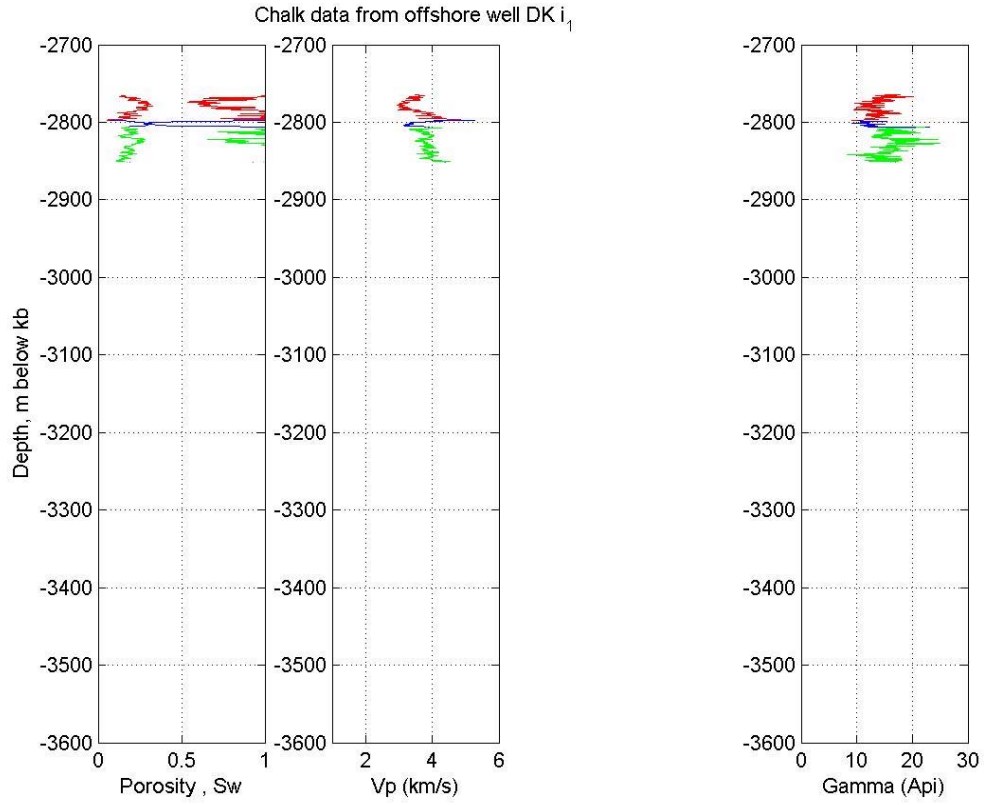
gwen₂ Chalk data



Gwen-2

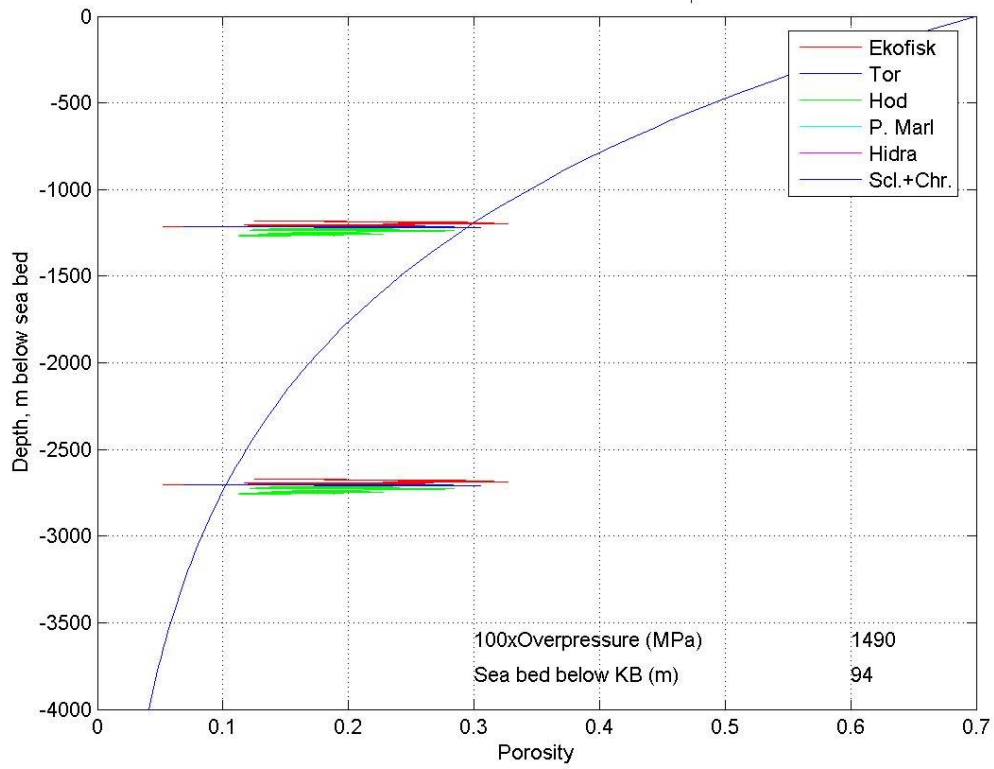


Gwen-2

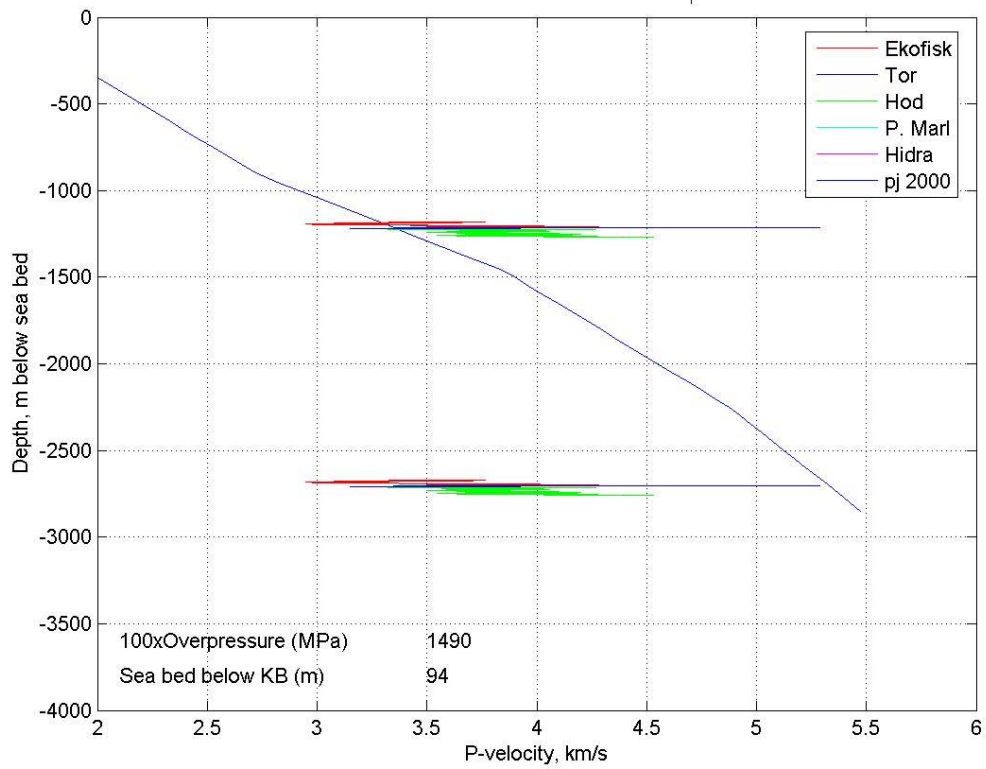


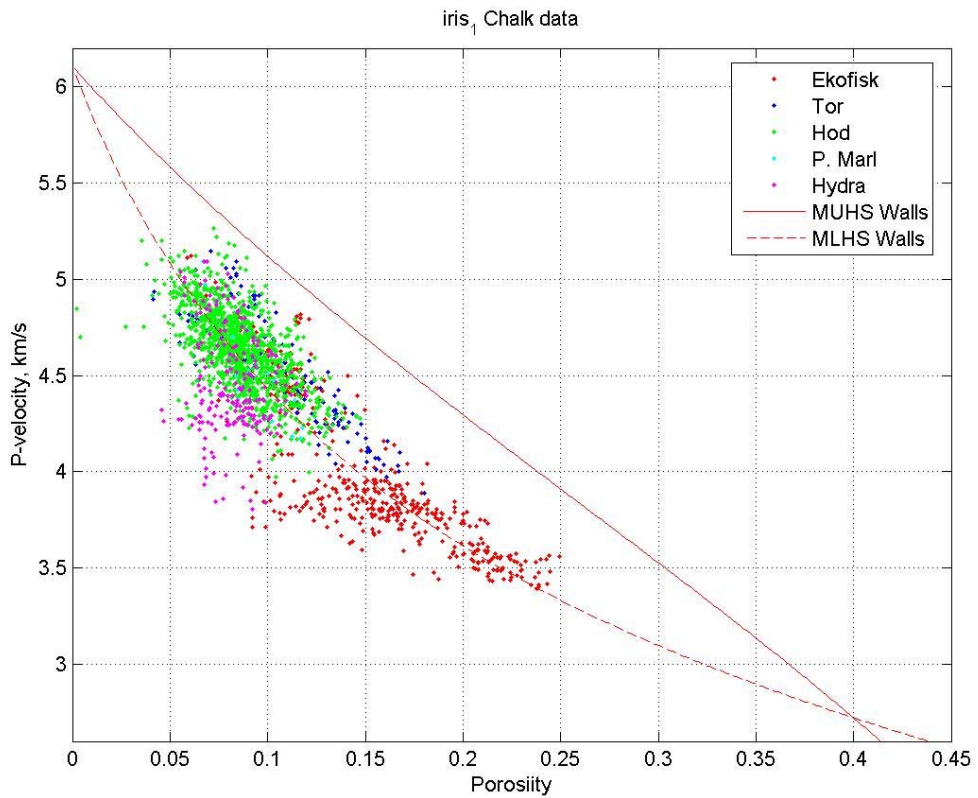
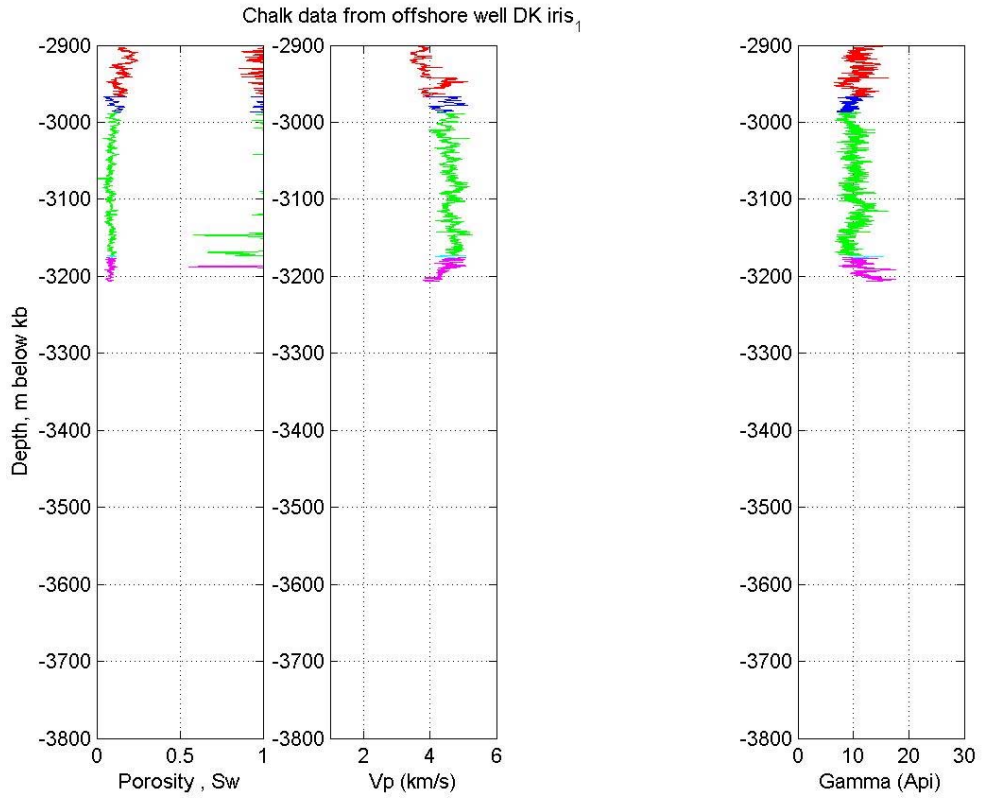
I-1

Chalk data from offshore well DK i₁

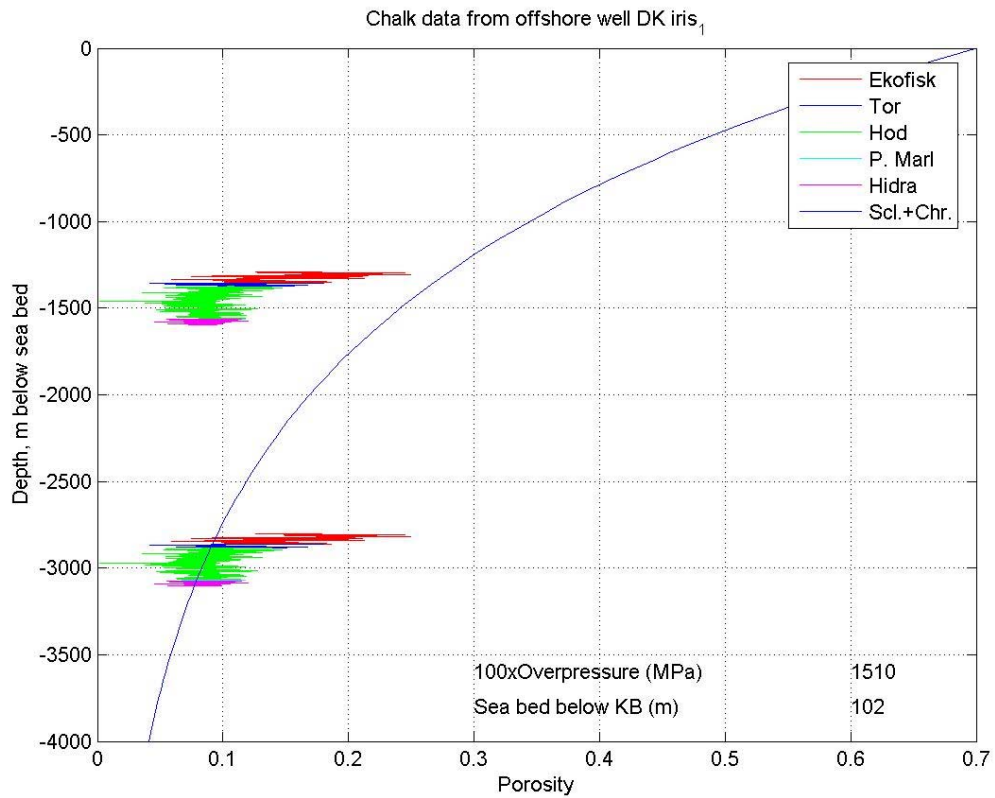
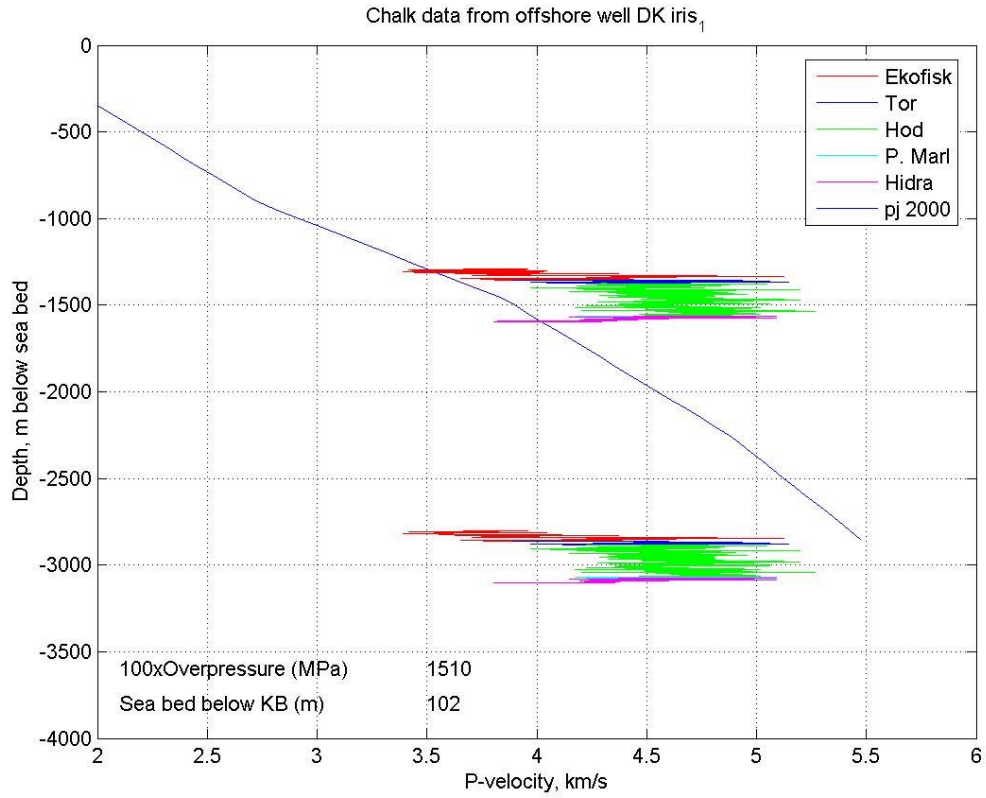


Chalk data from offshore well DK i₁

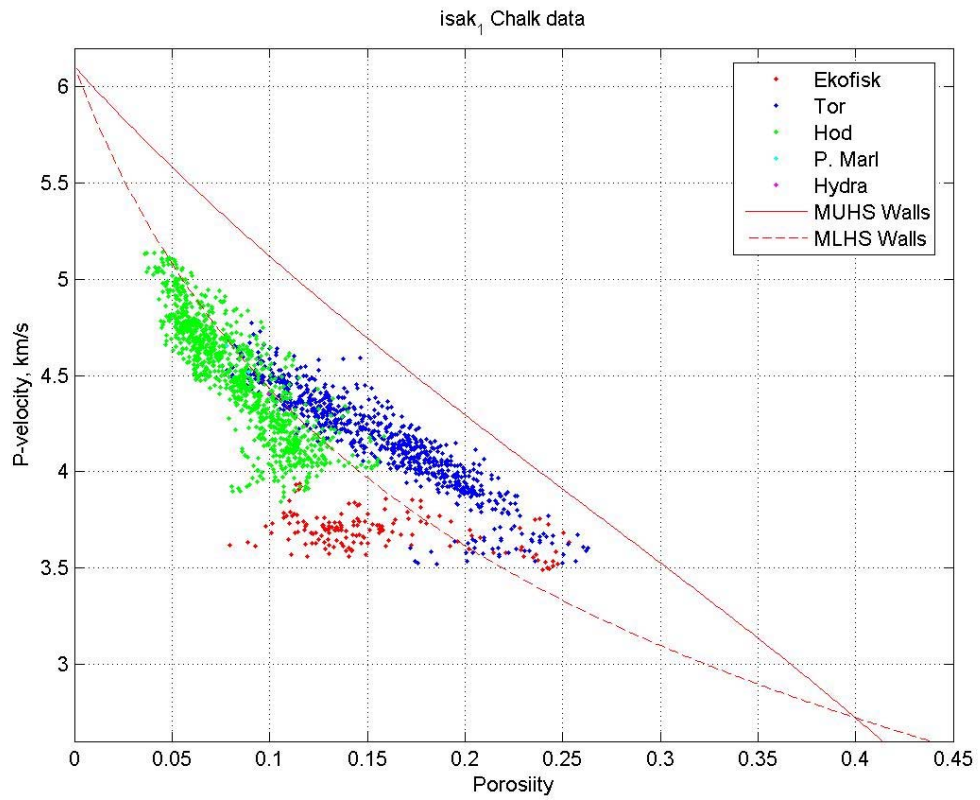
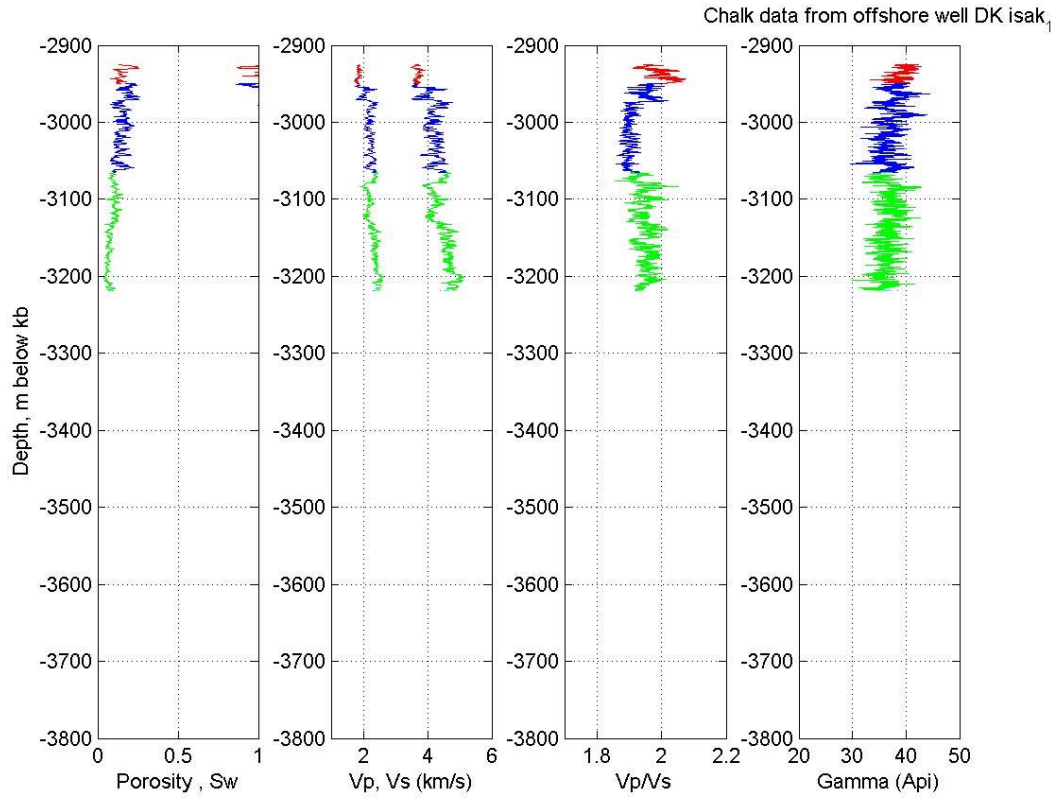




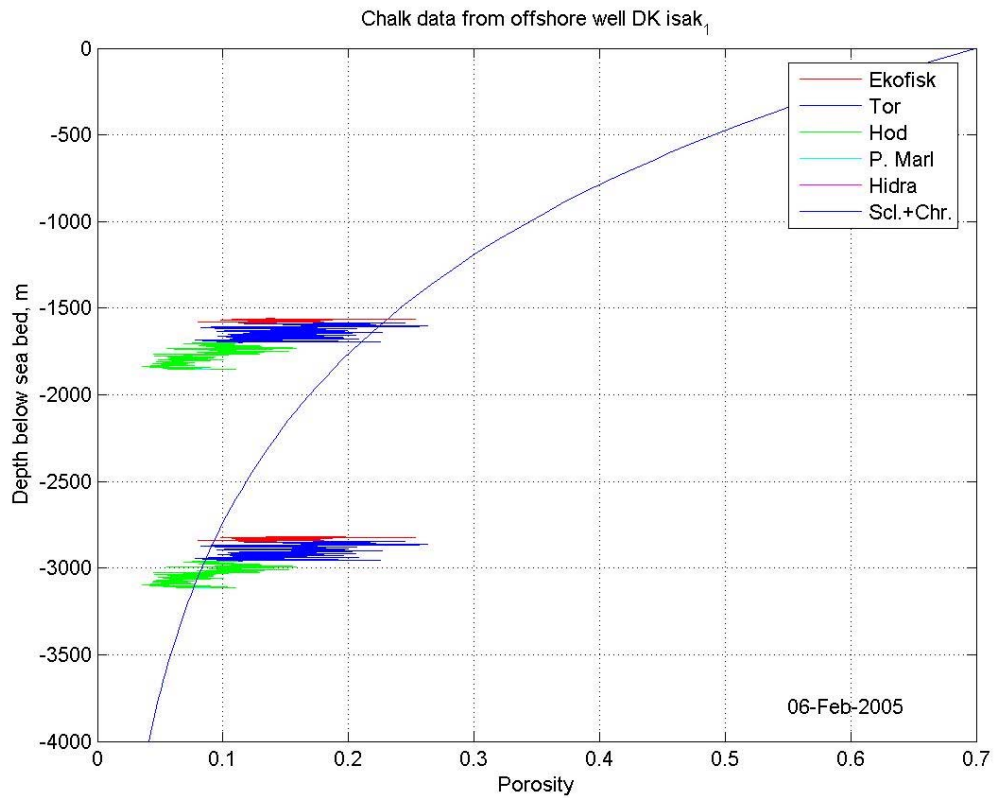
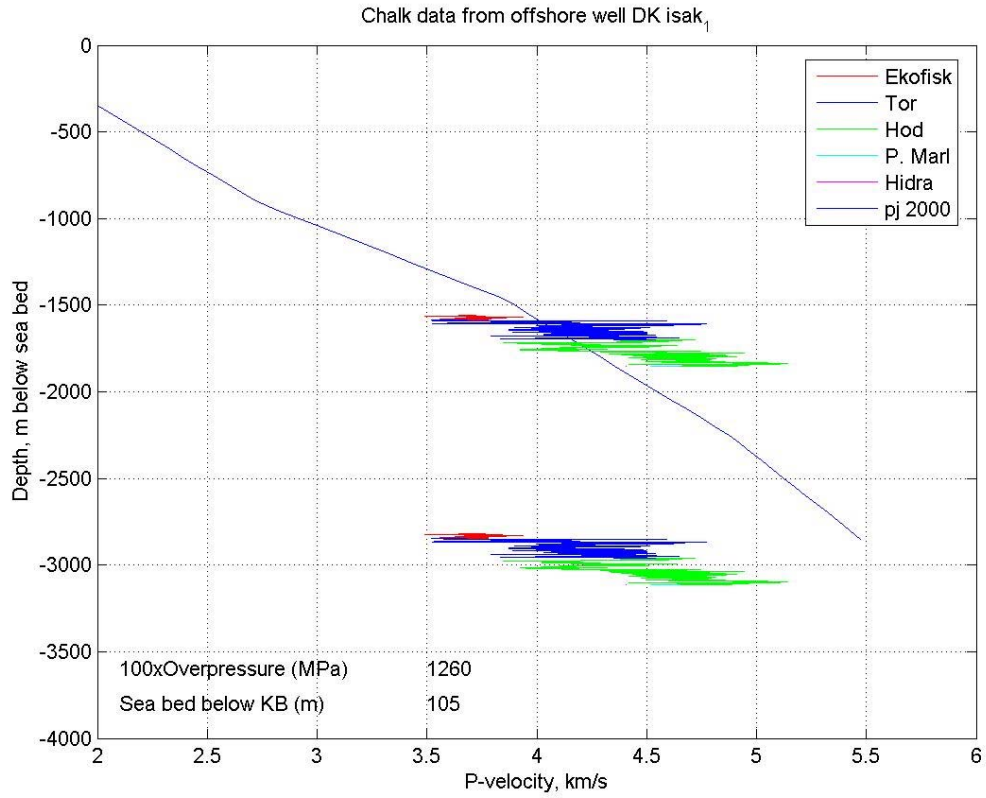
Iris-1



Iris-1

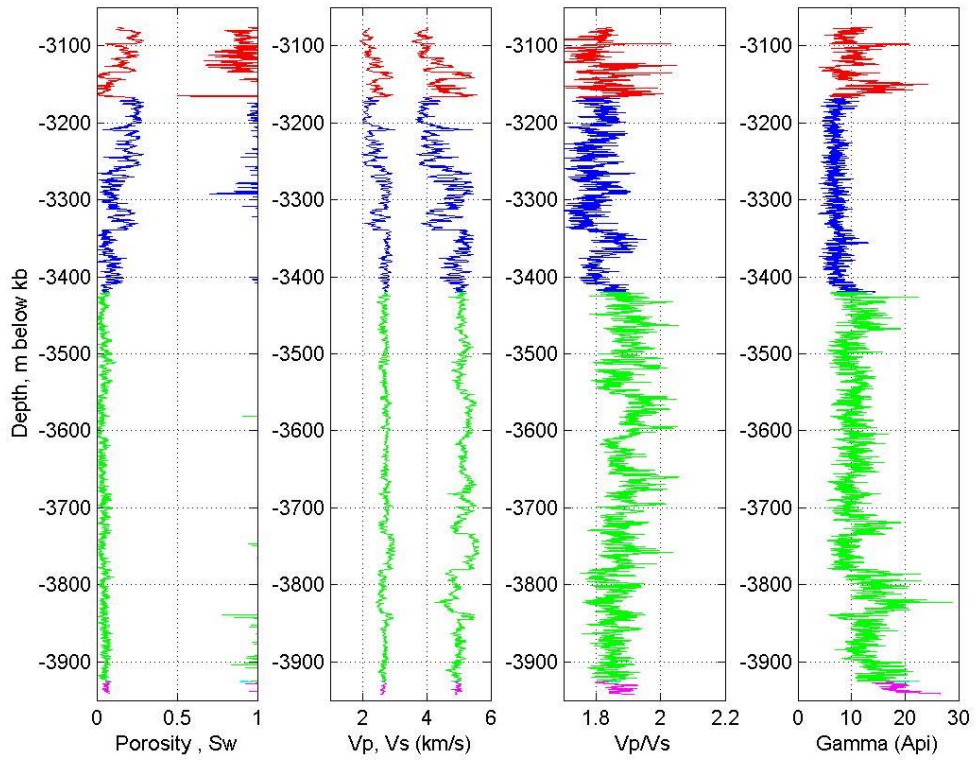


Isak-1

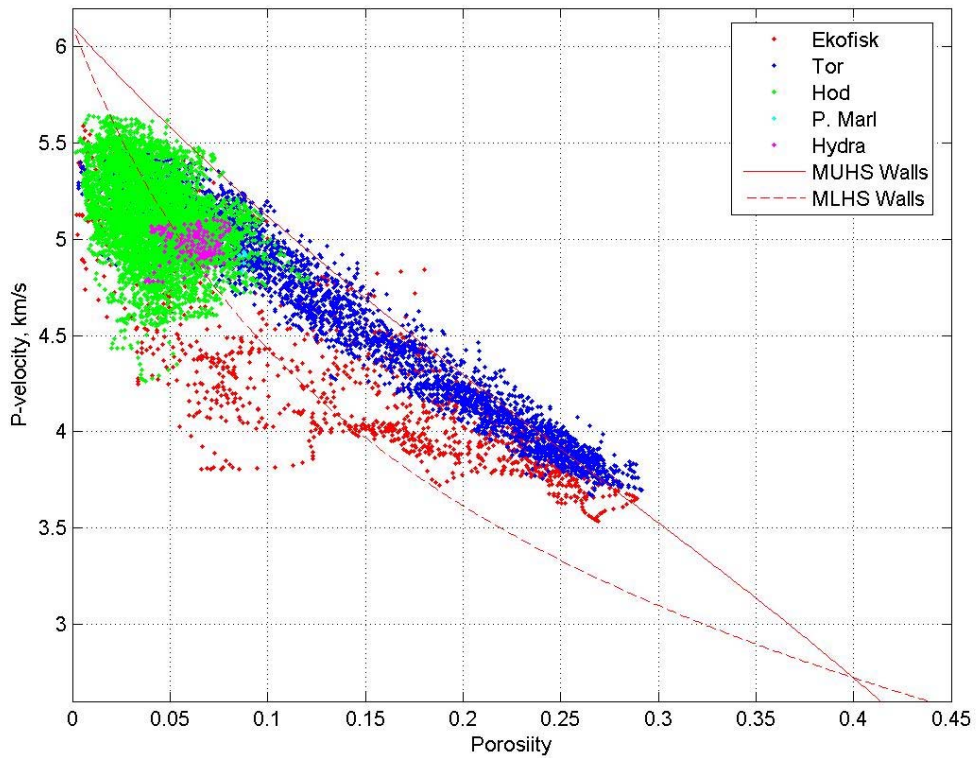


Isak-1

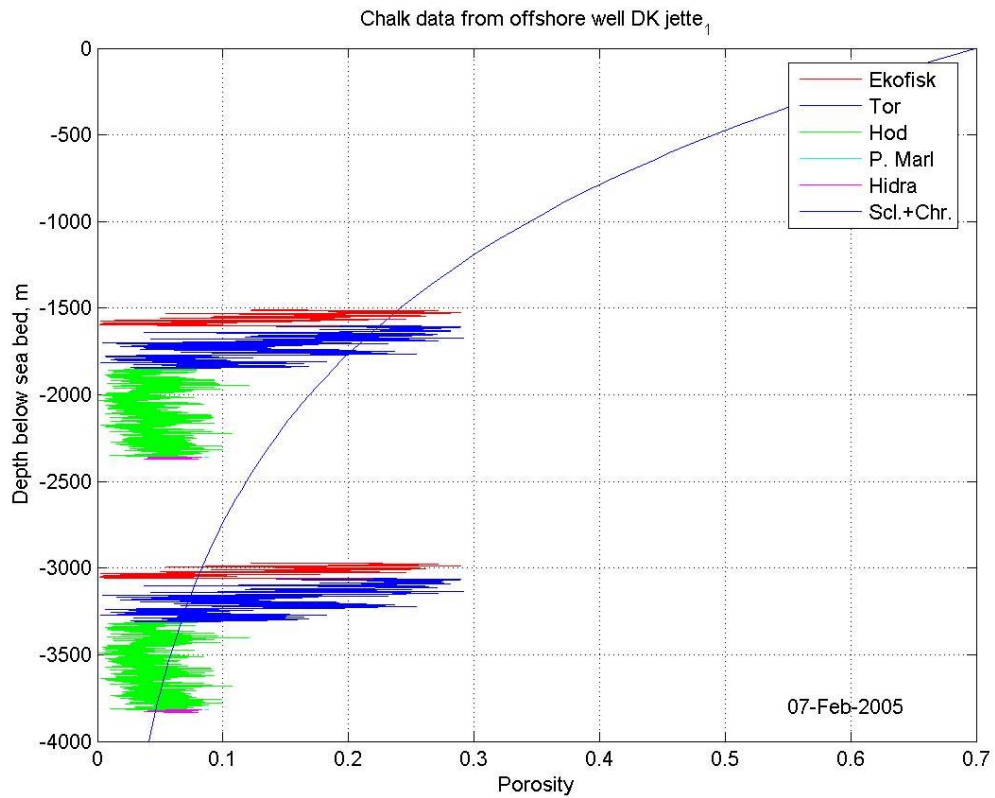
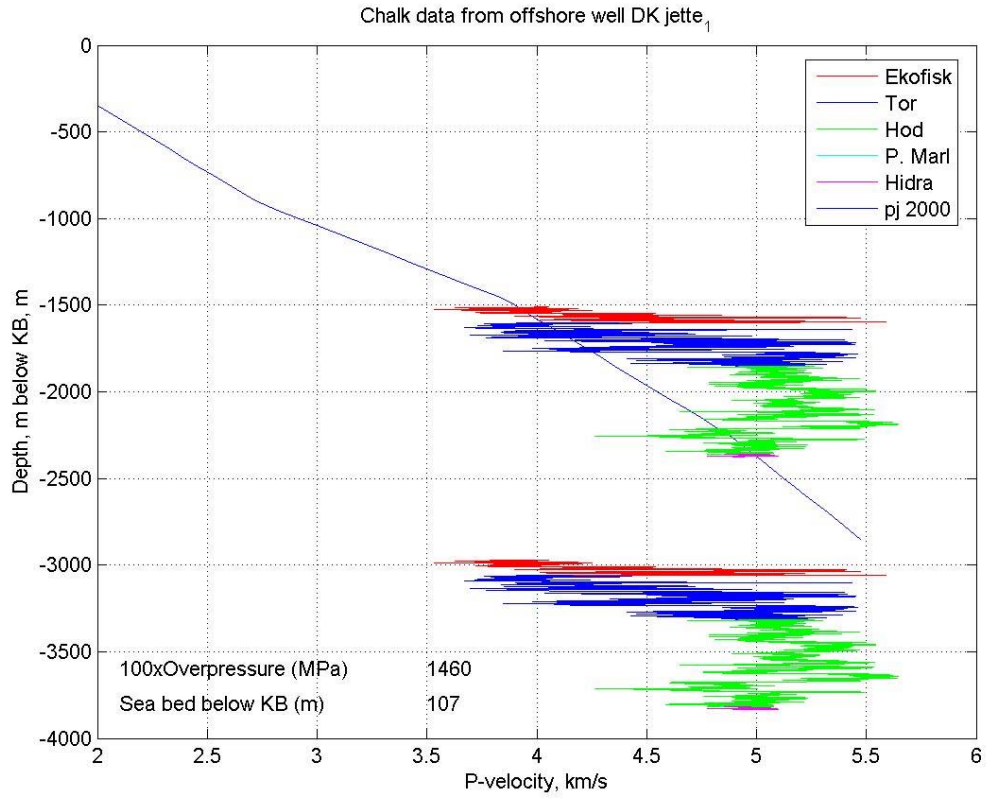
Chalk data from offshore well DK jette₁



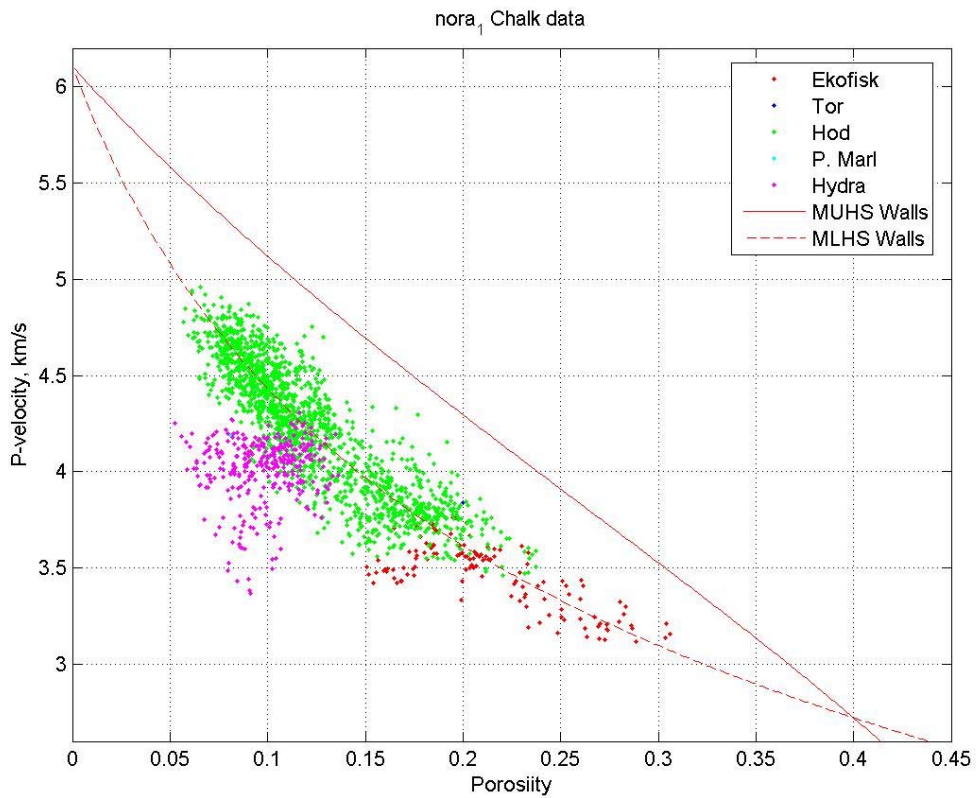
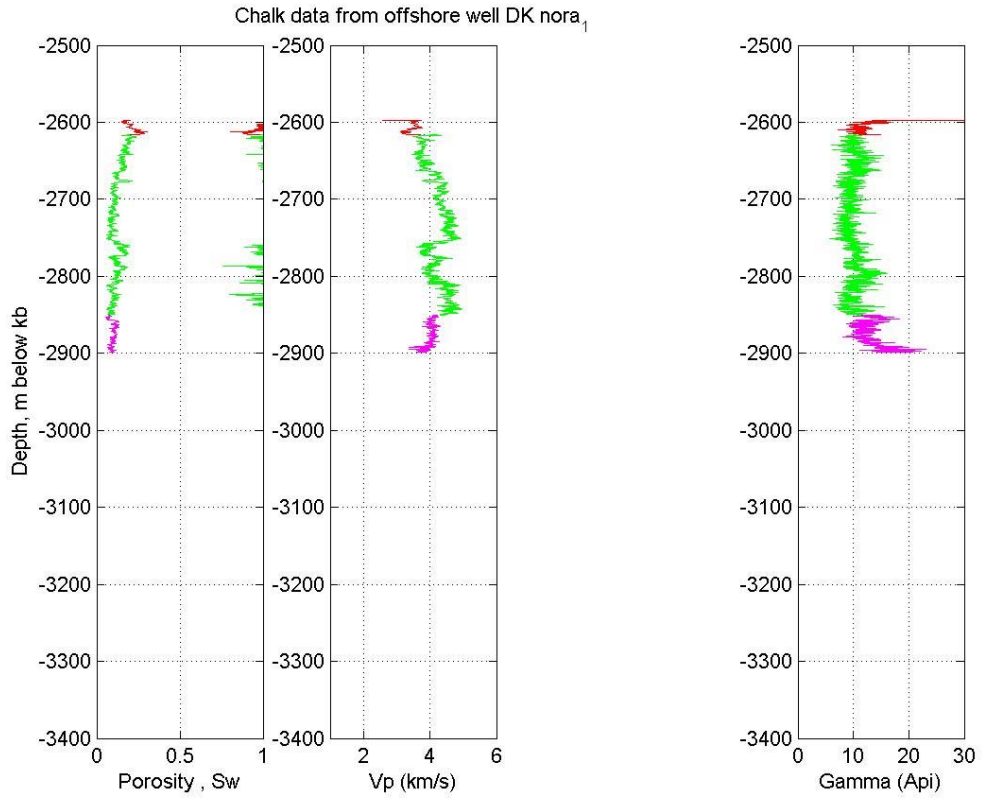
jette₁ Chalk data



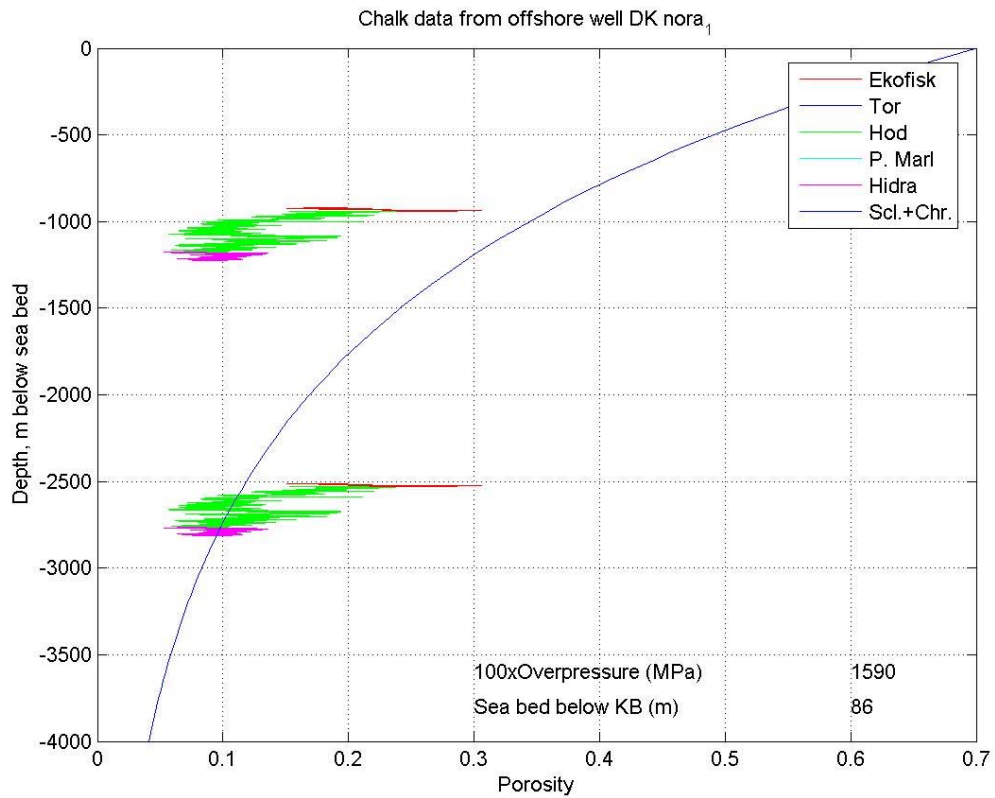
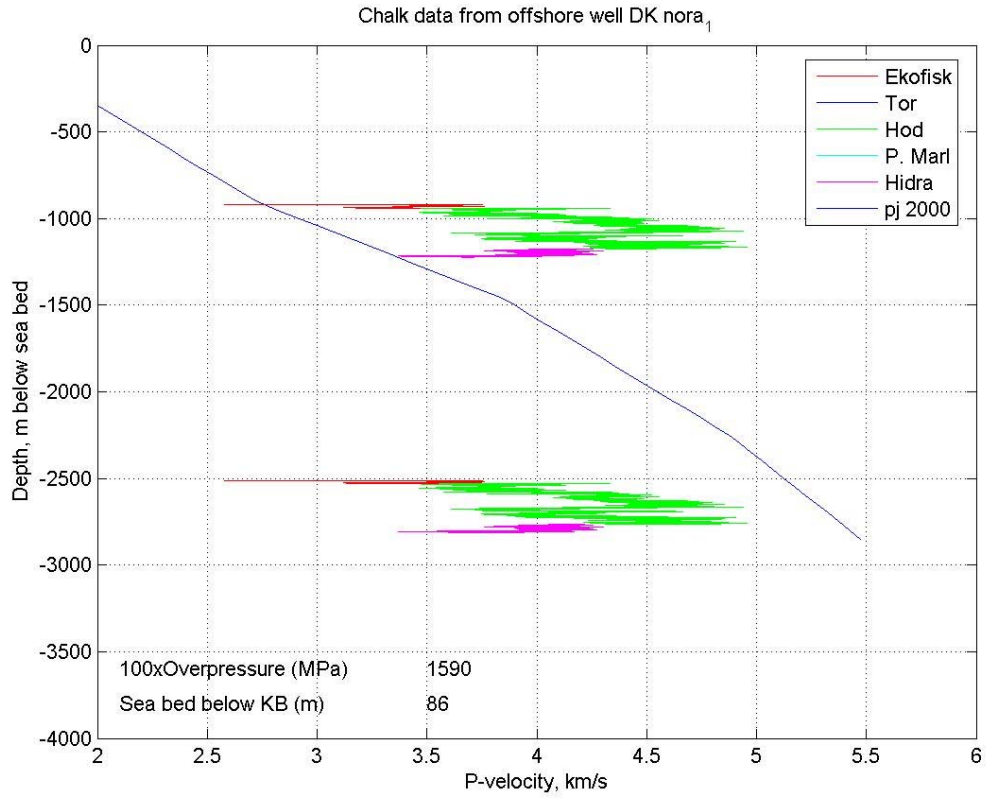
Jette-1



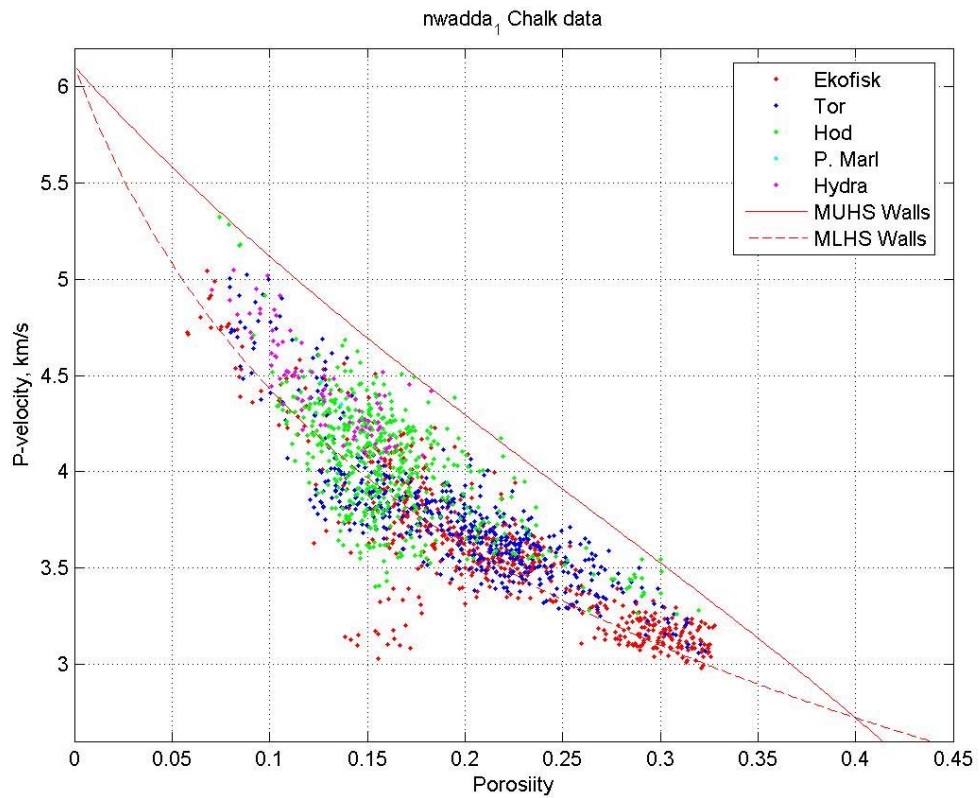
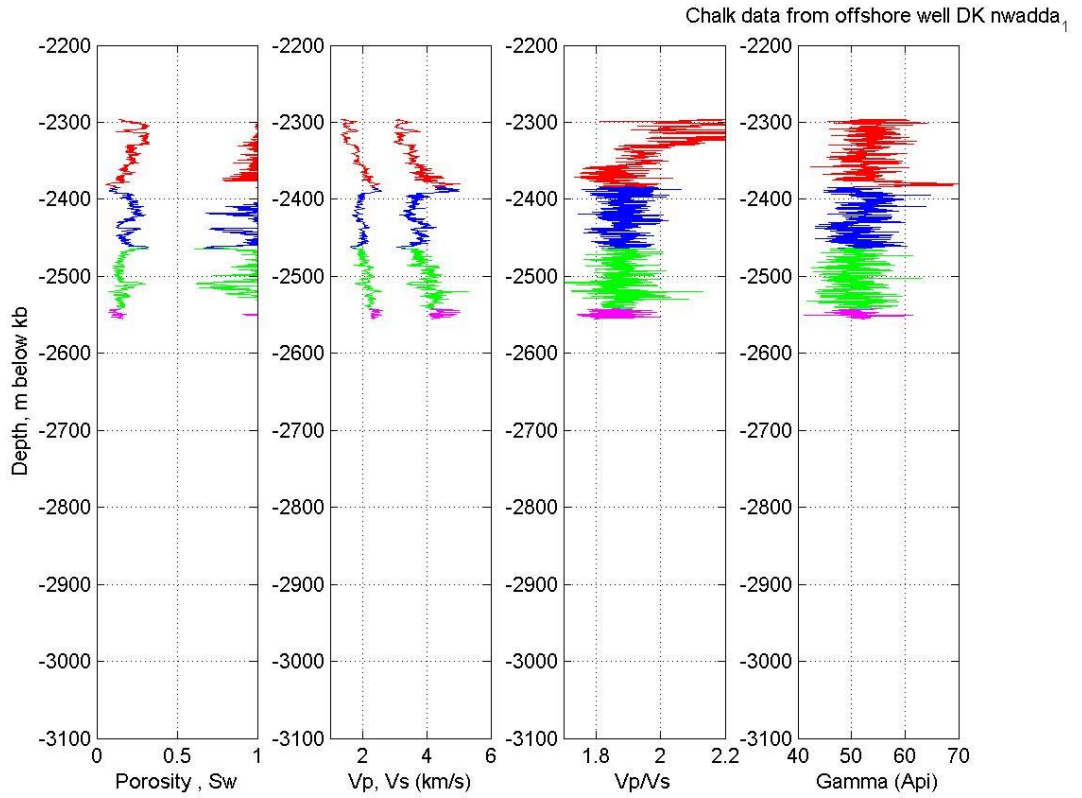
Jette-1



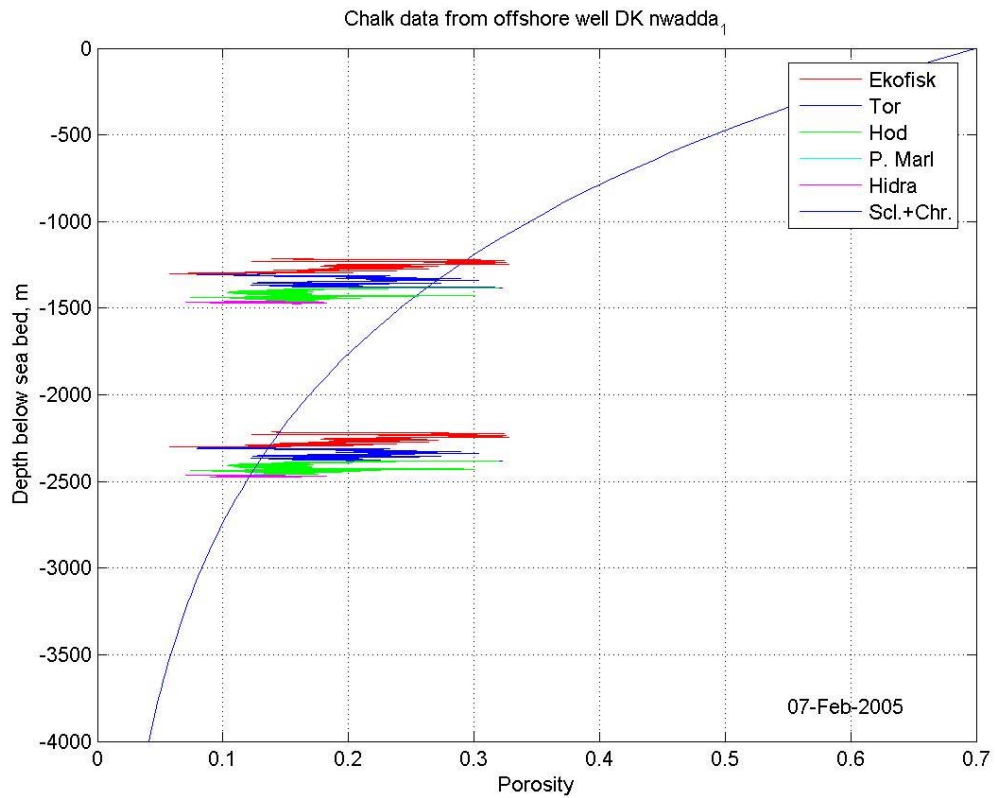
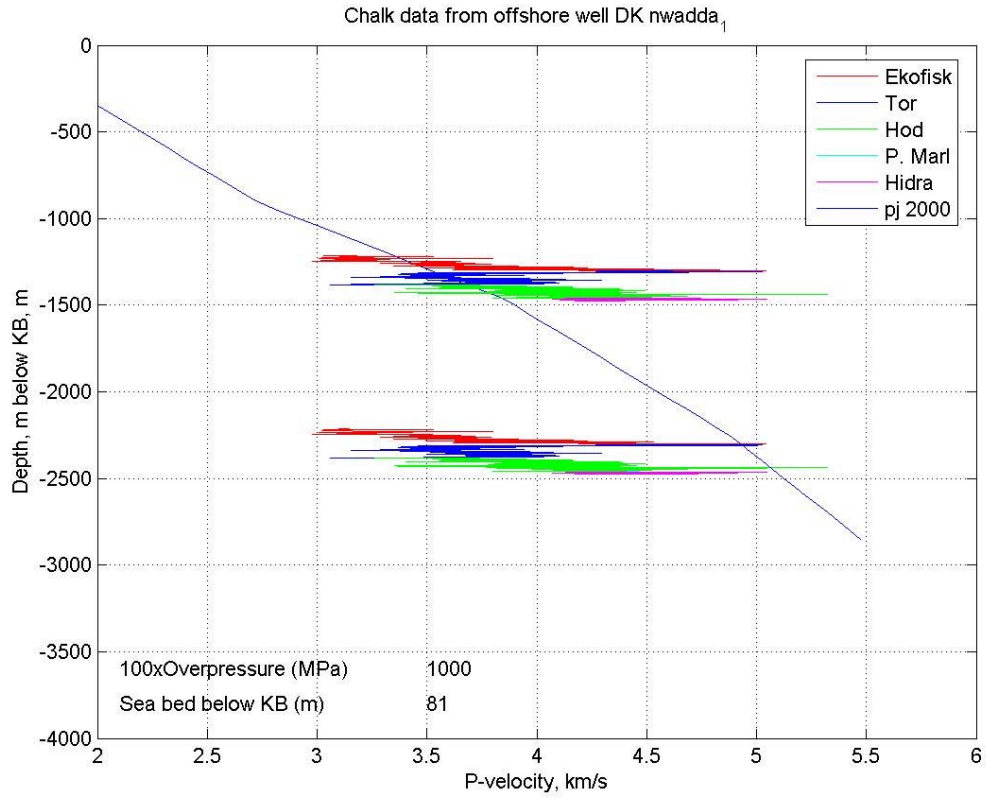
Nora-1



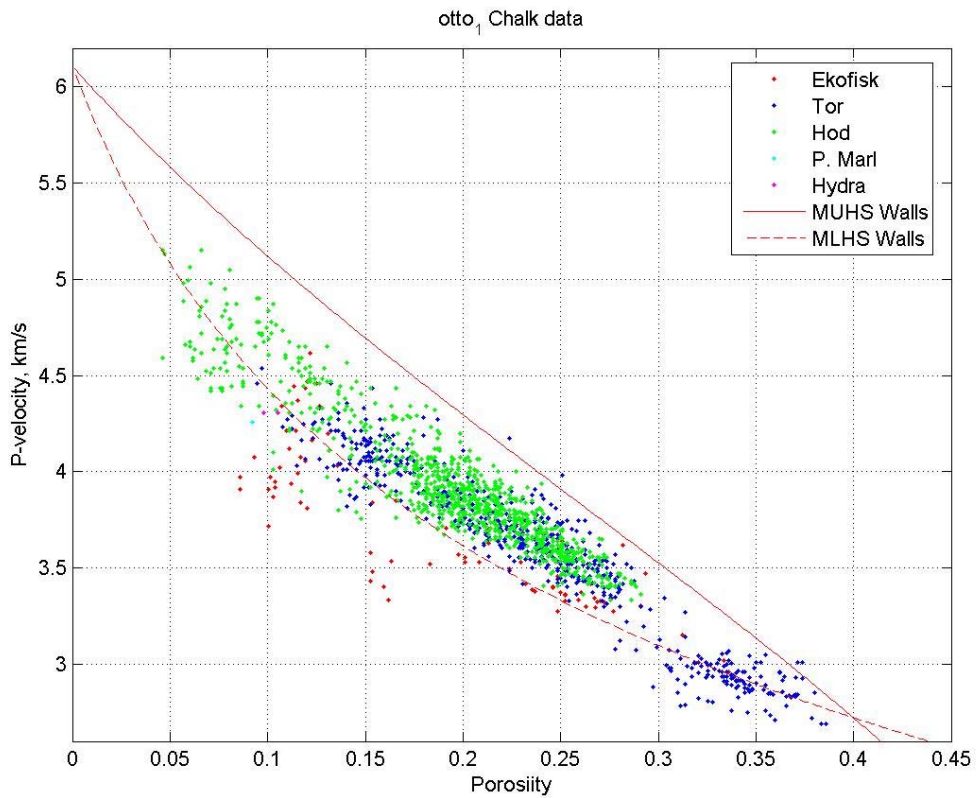
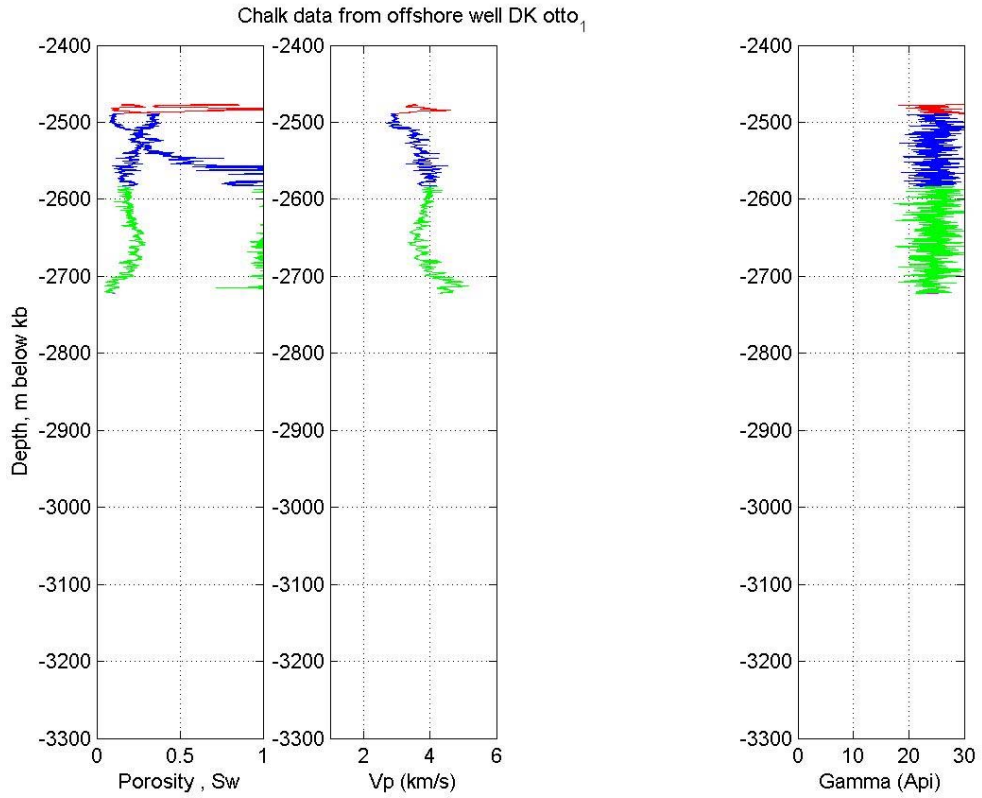
Nora-1



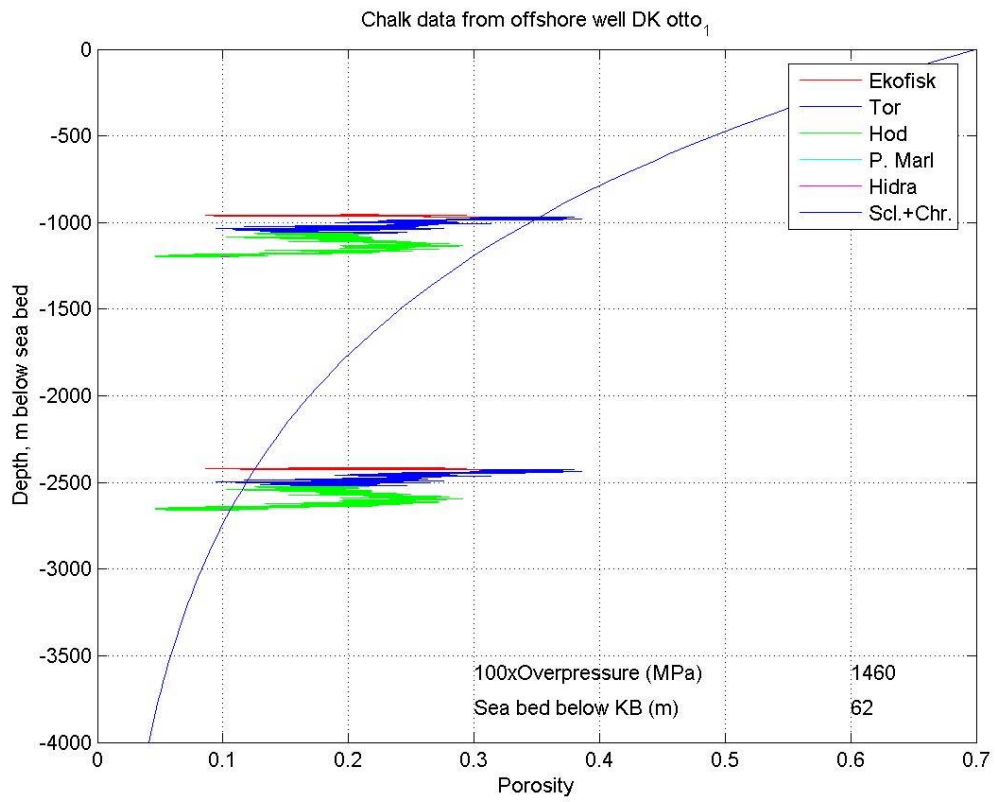
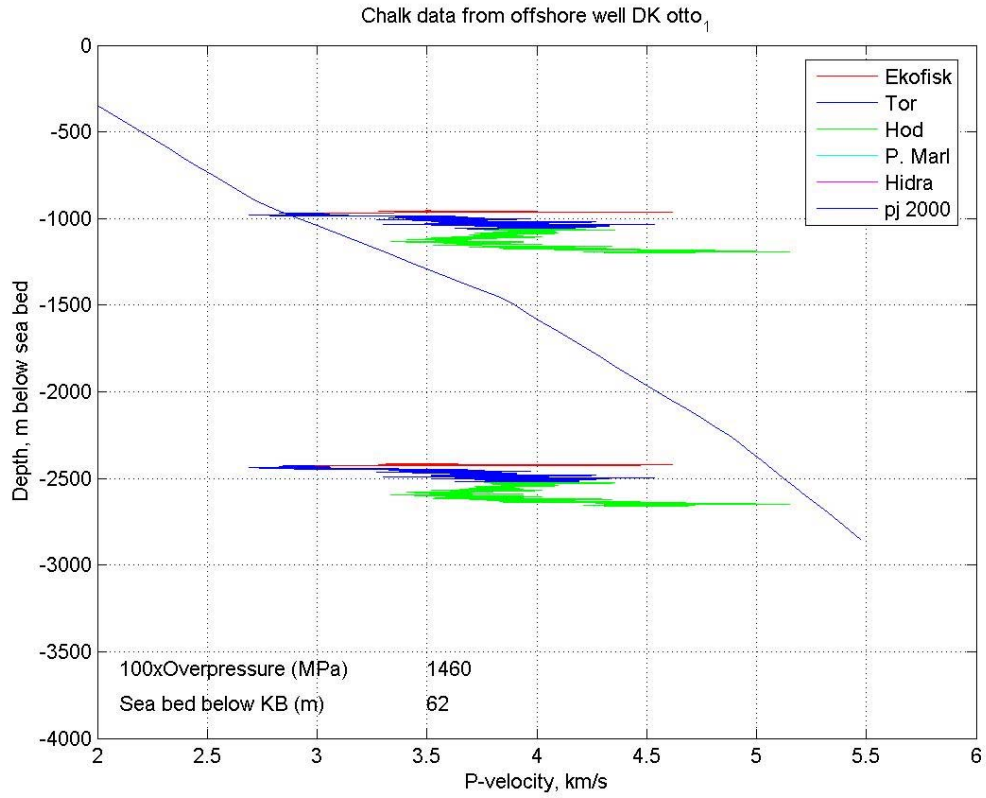
NW Adda-1



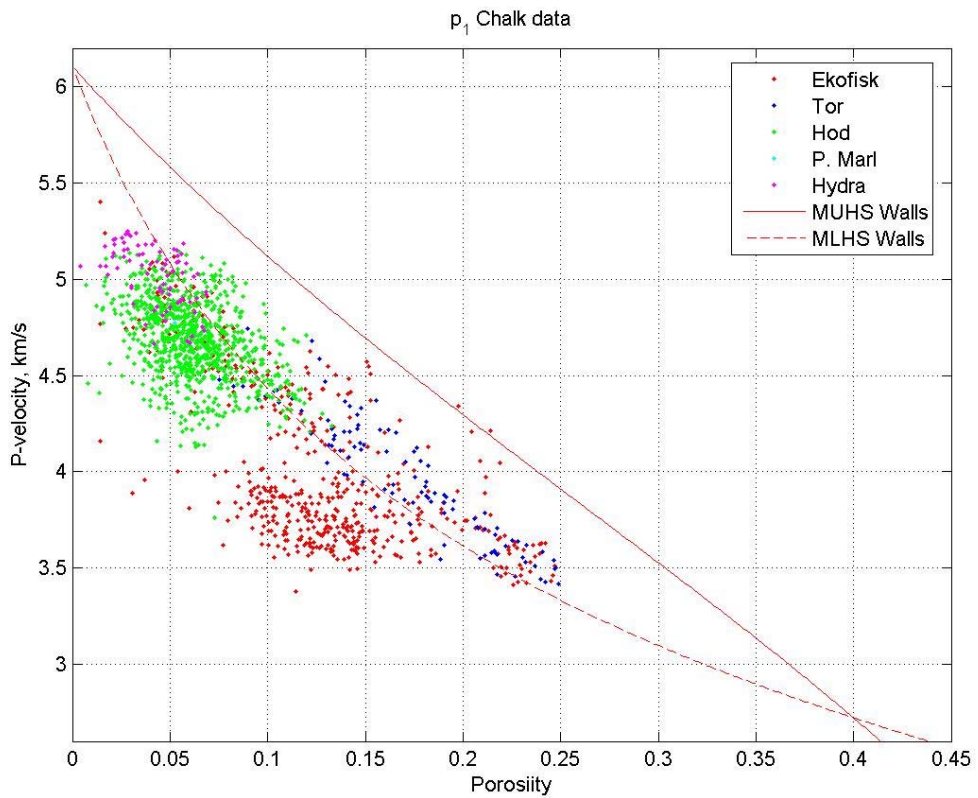
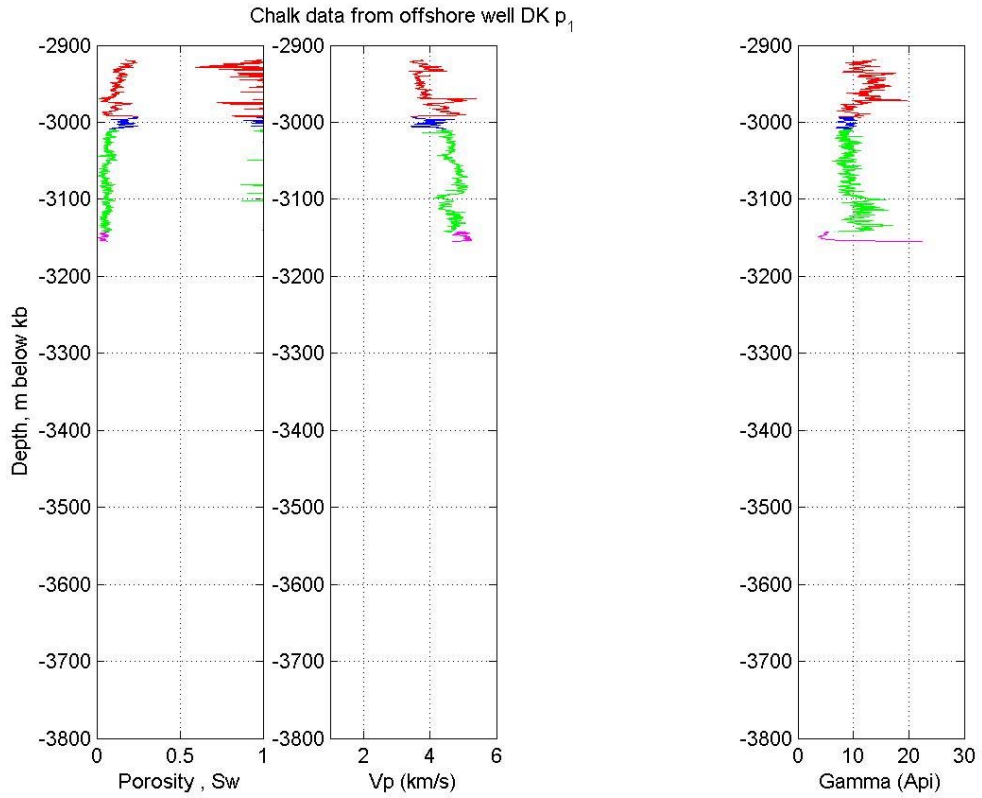
NW Adda-1



Otto-1

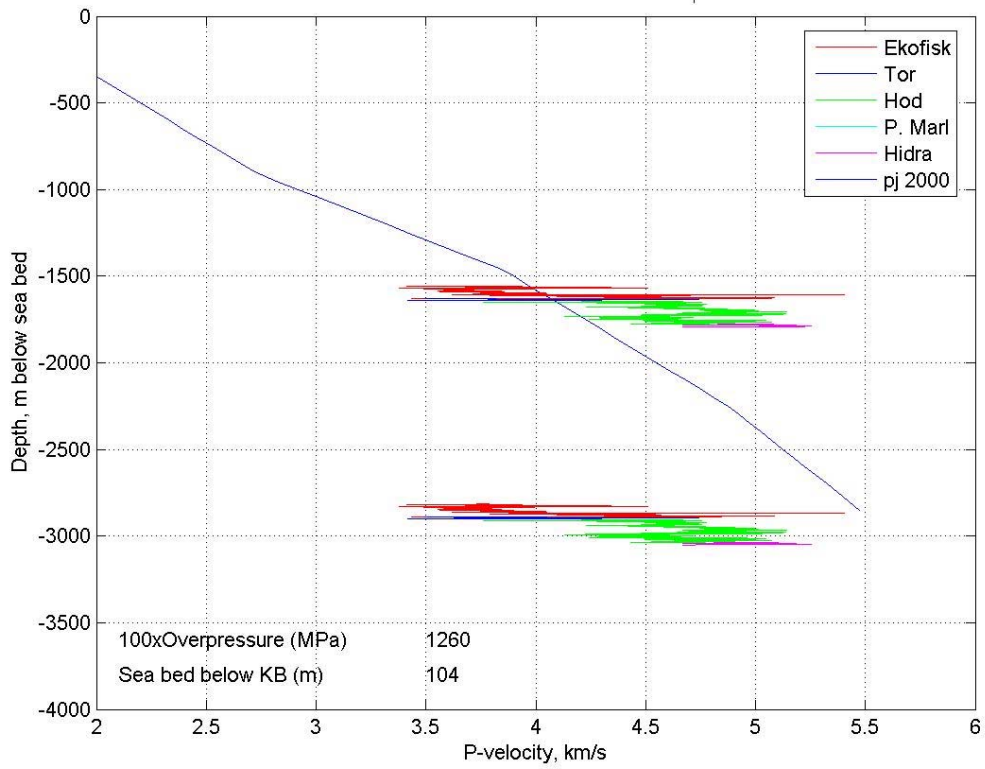


Otto-1

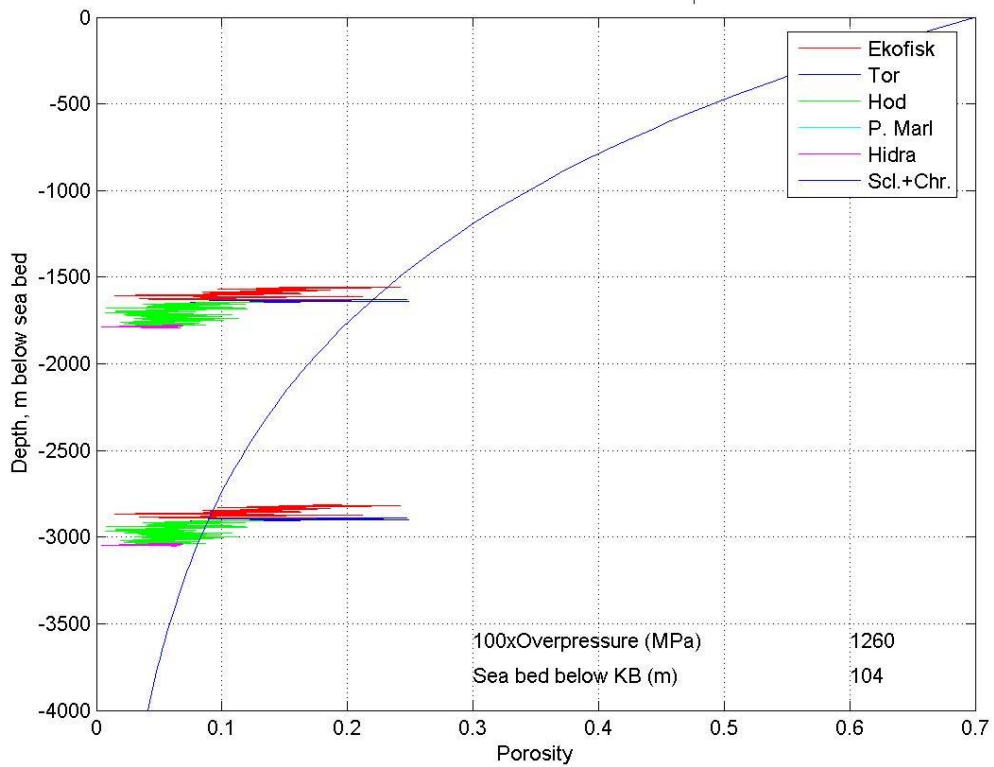


P-1

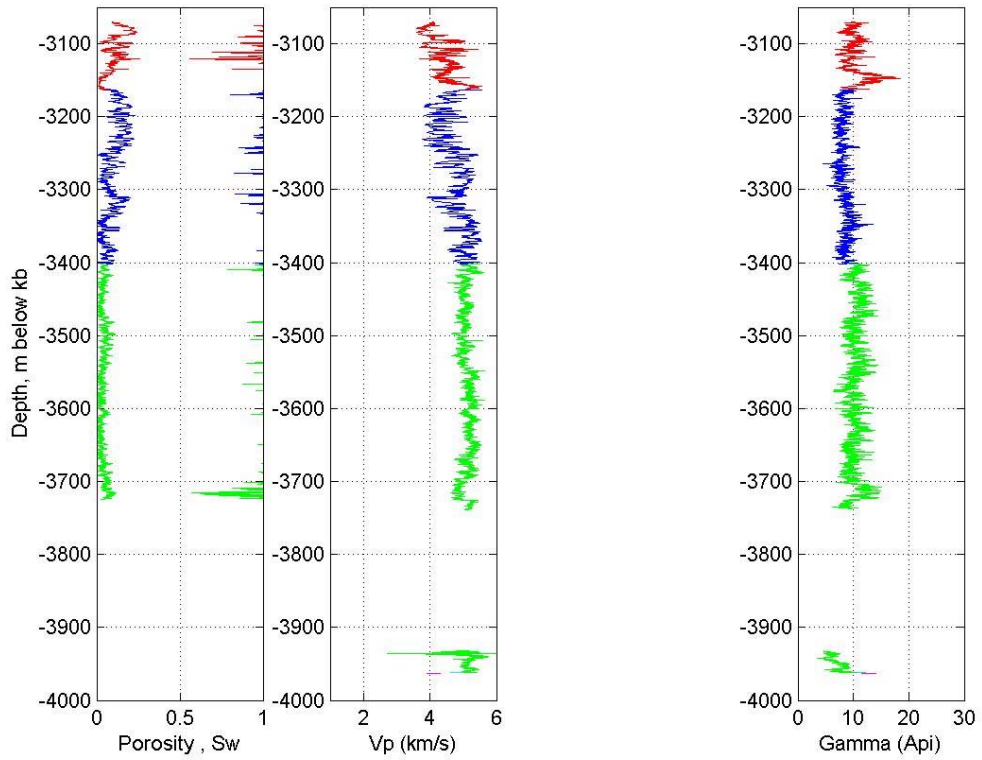
Chalk data from offshore well DK p₁



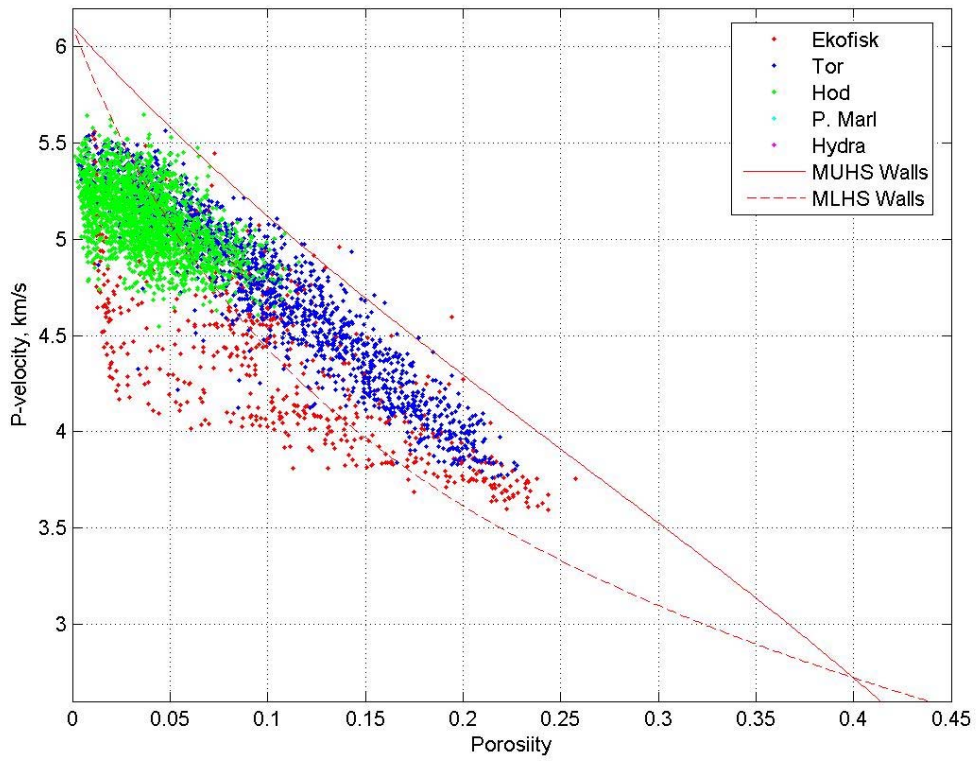
Chalk data from offshore well DK p₁



Chalk data from offshore well DK q₁

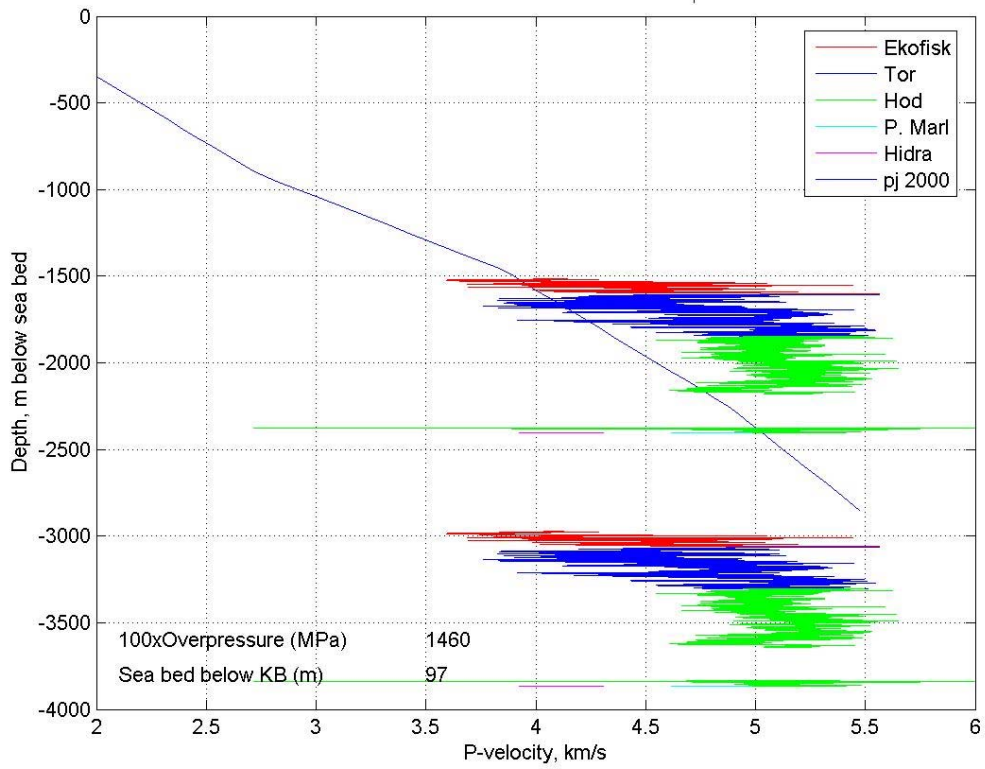


q₁ Chalk data

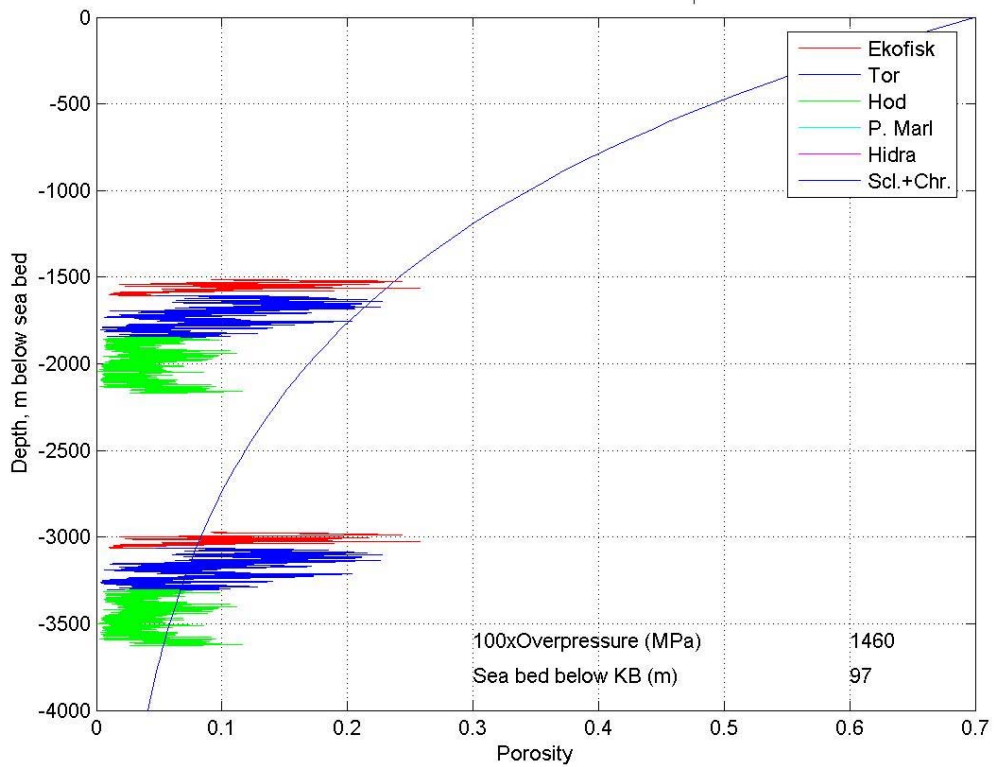


Q-1

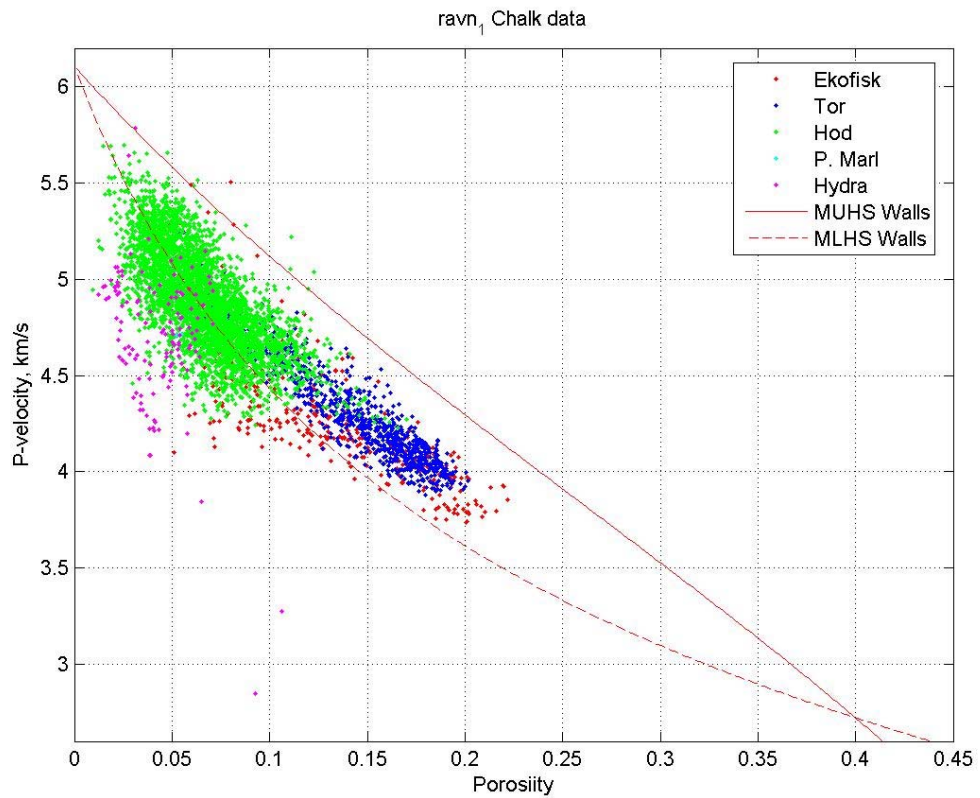
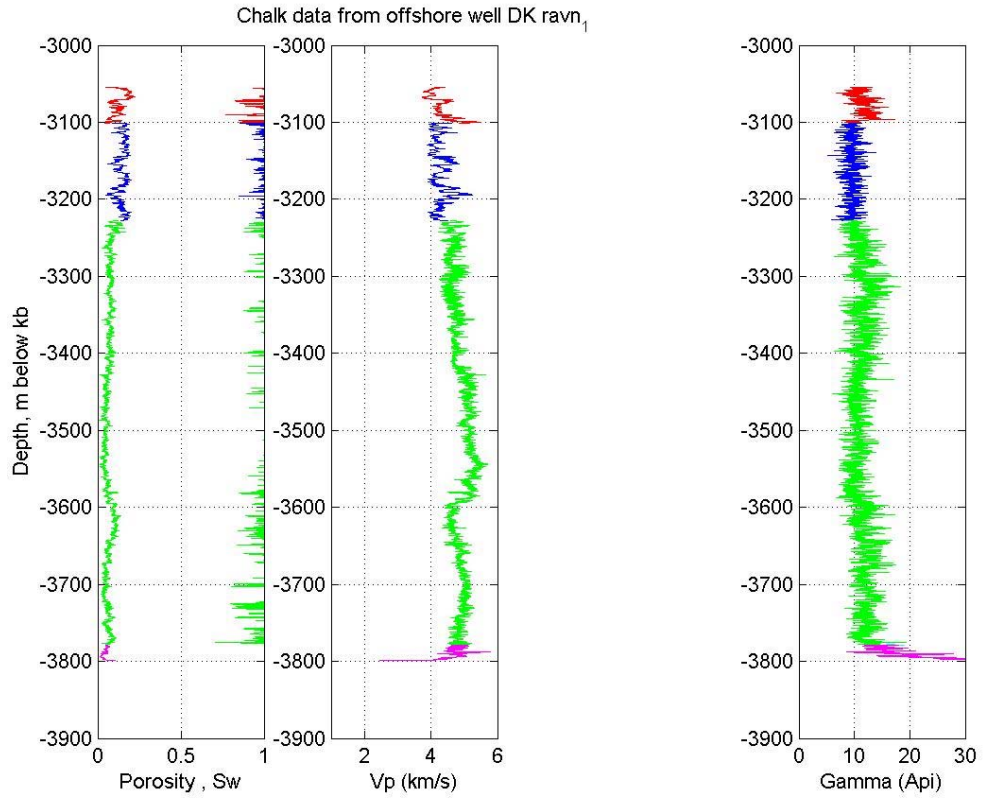
Chalk data from offshore well DK q₁



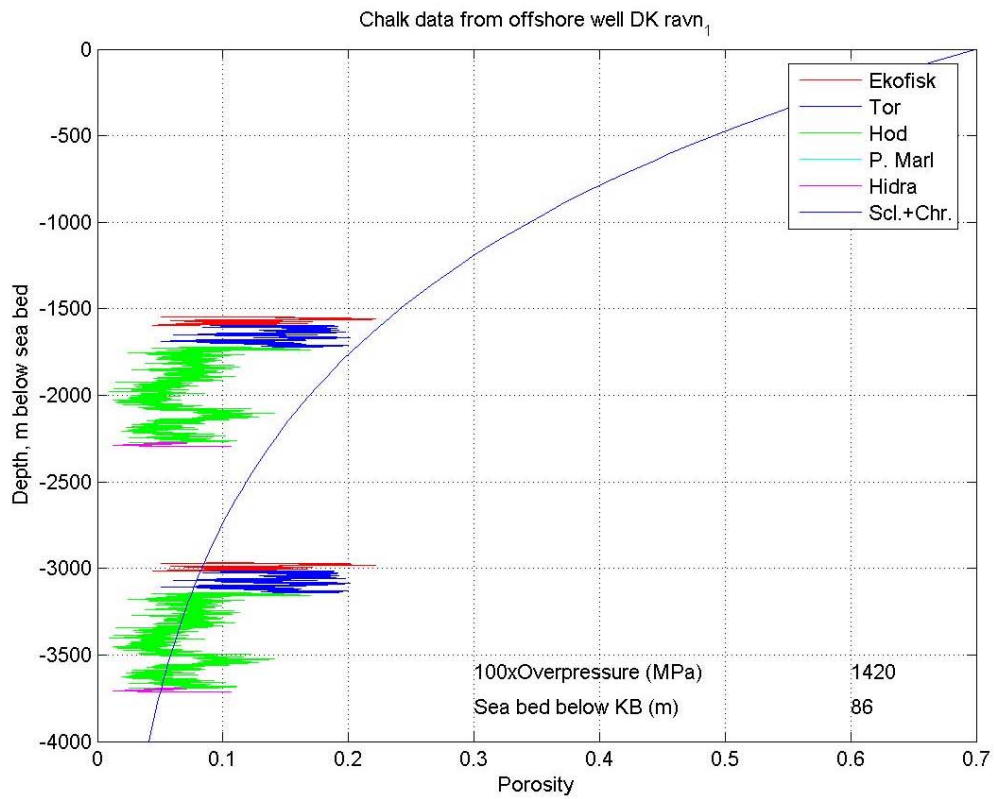
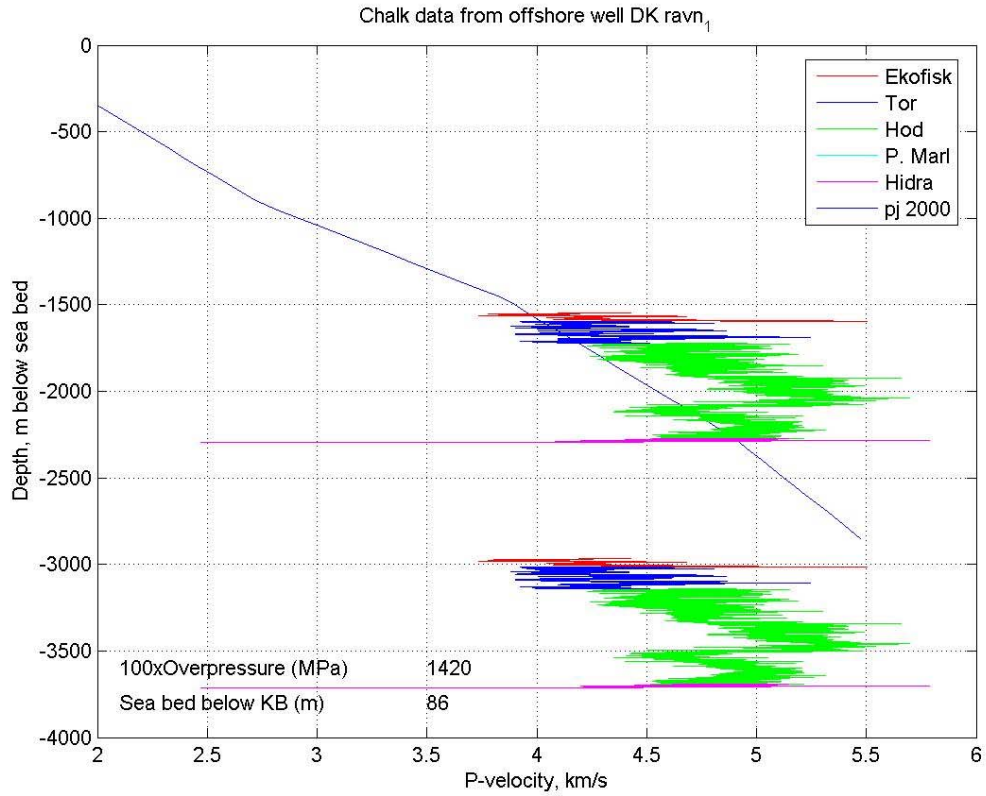
Chalk data from offshore well DK q₁



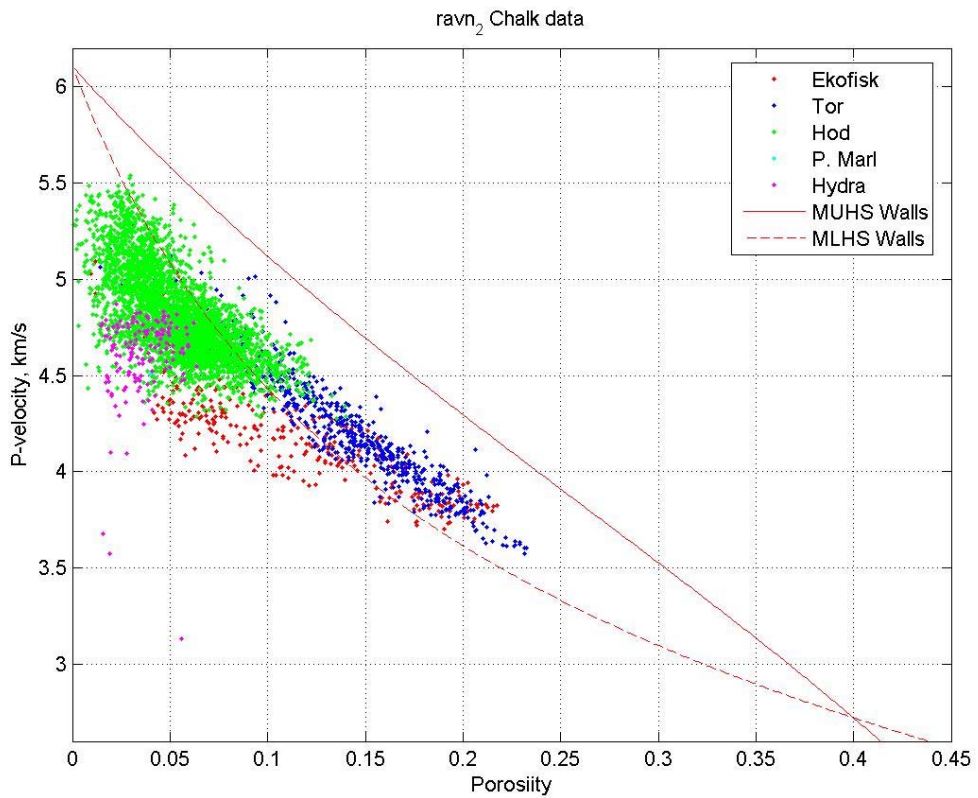
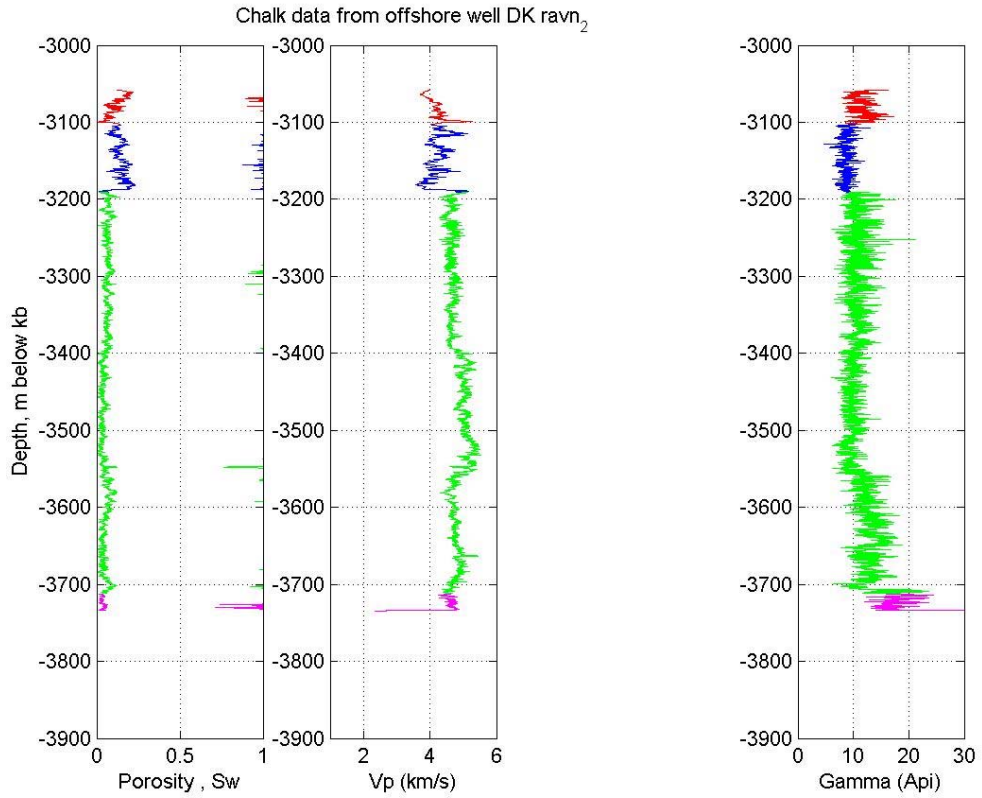
Q-1



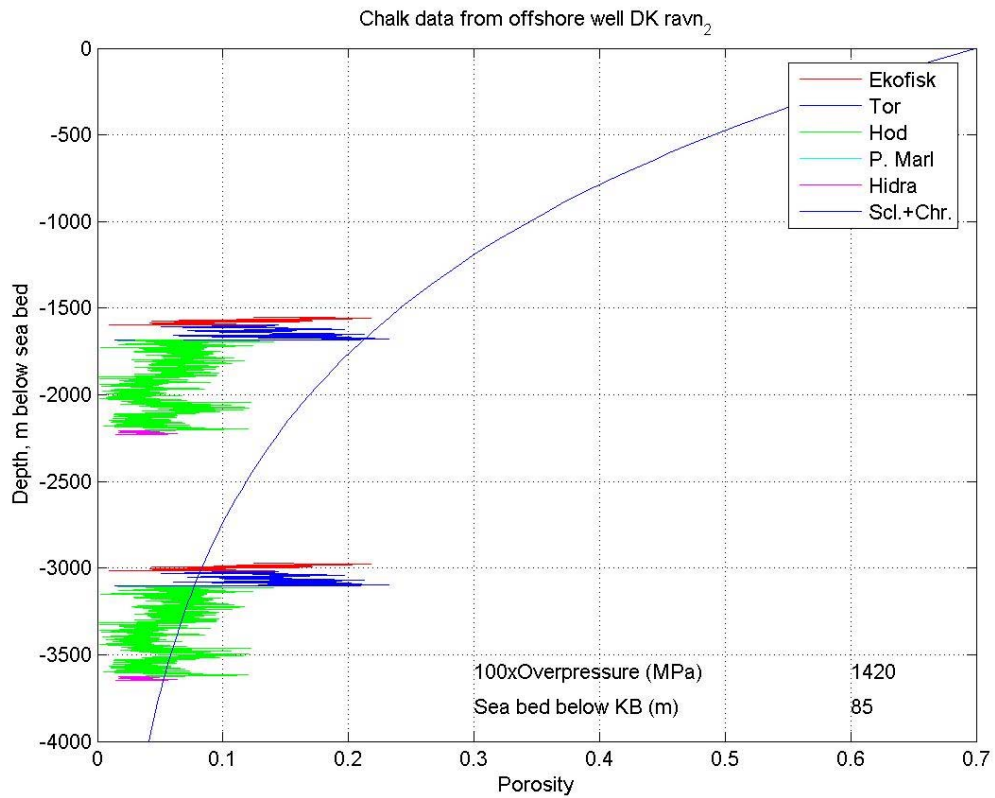
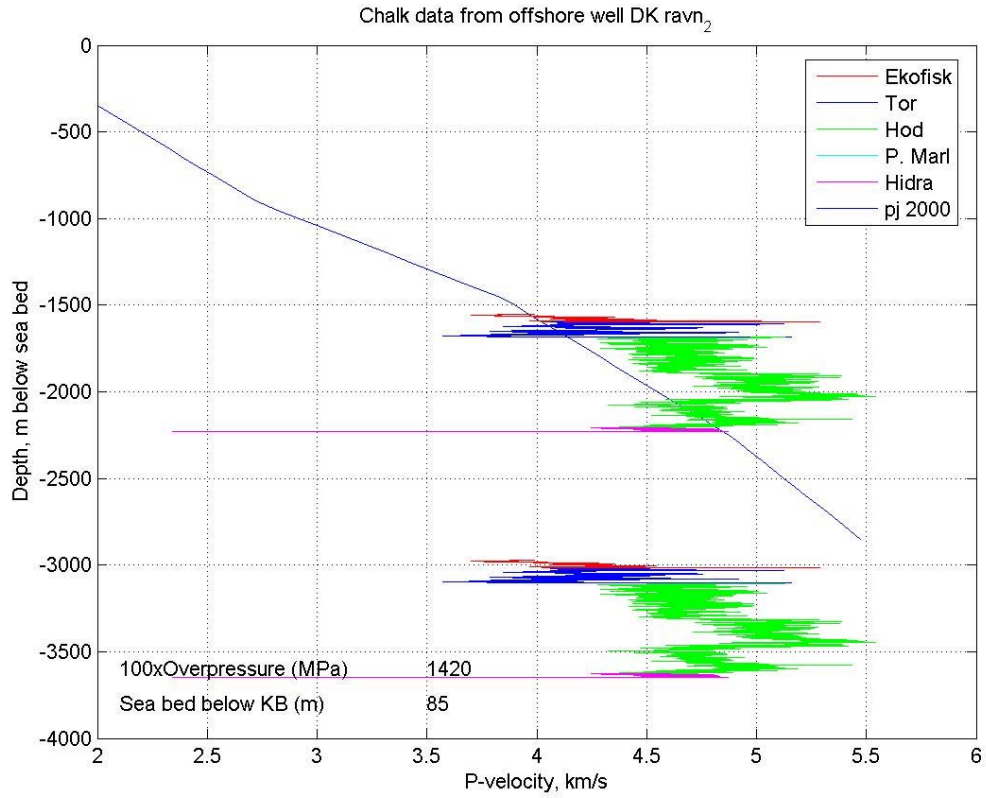
Ravn-1



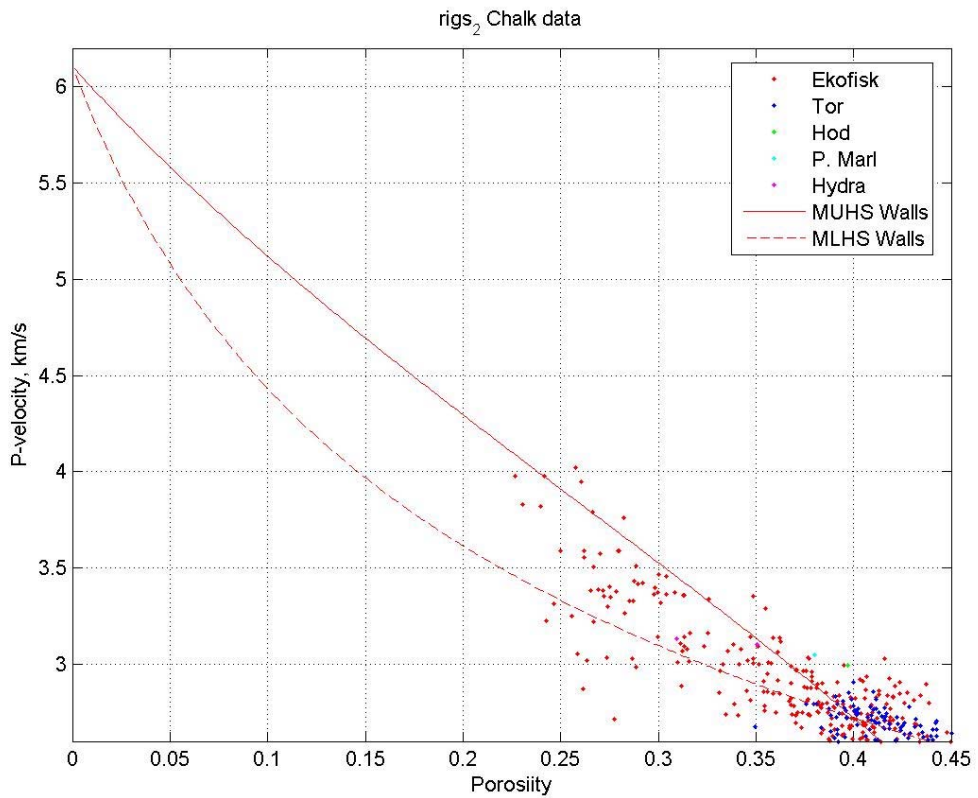
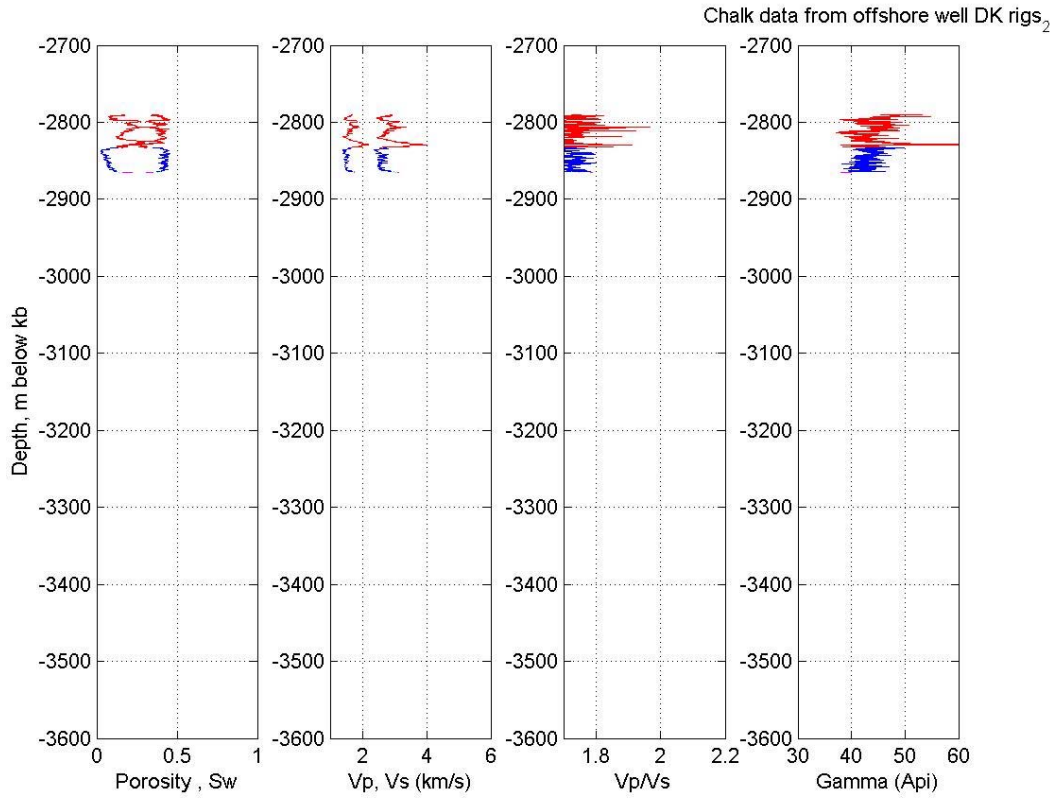
Ravn-1



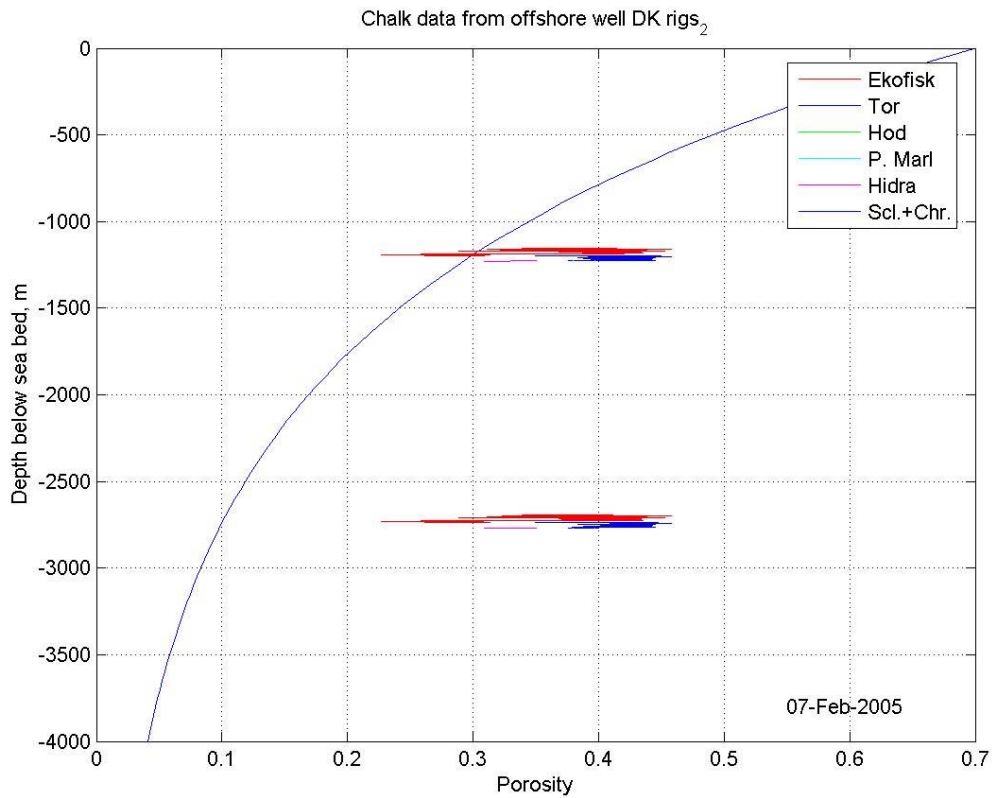
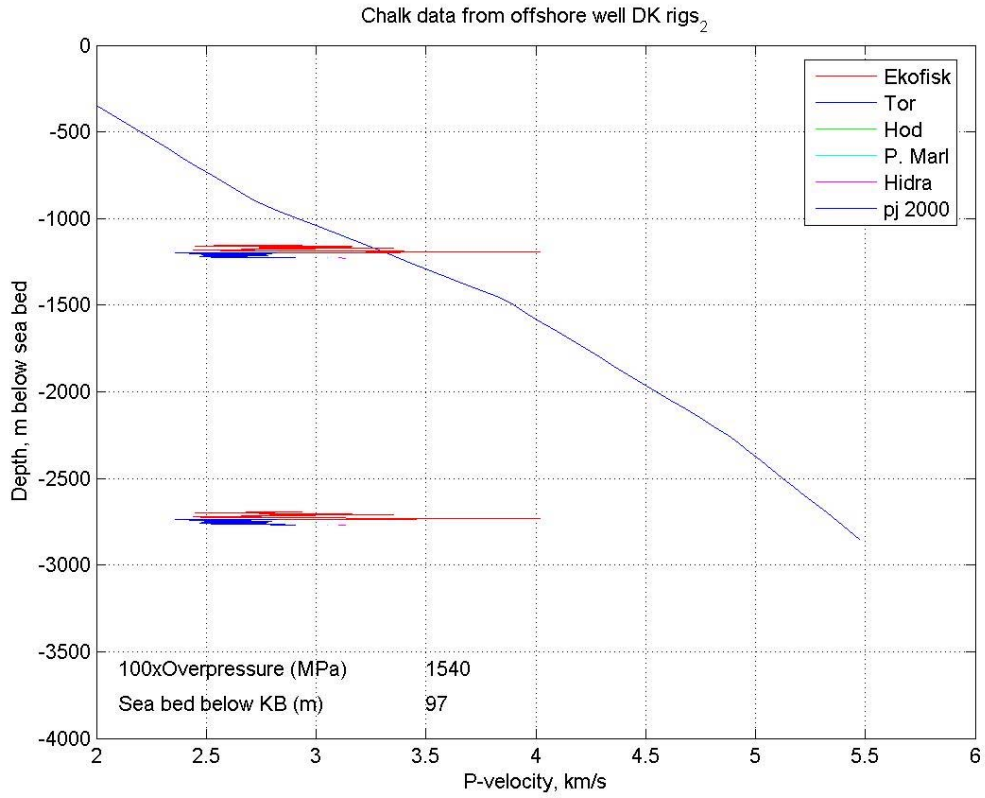
Ravn-2



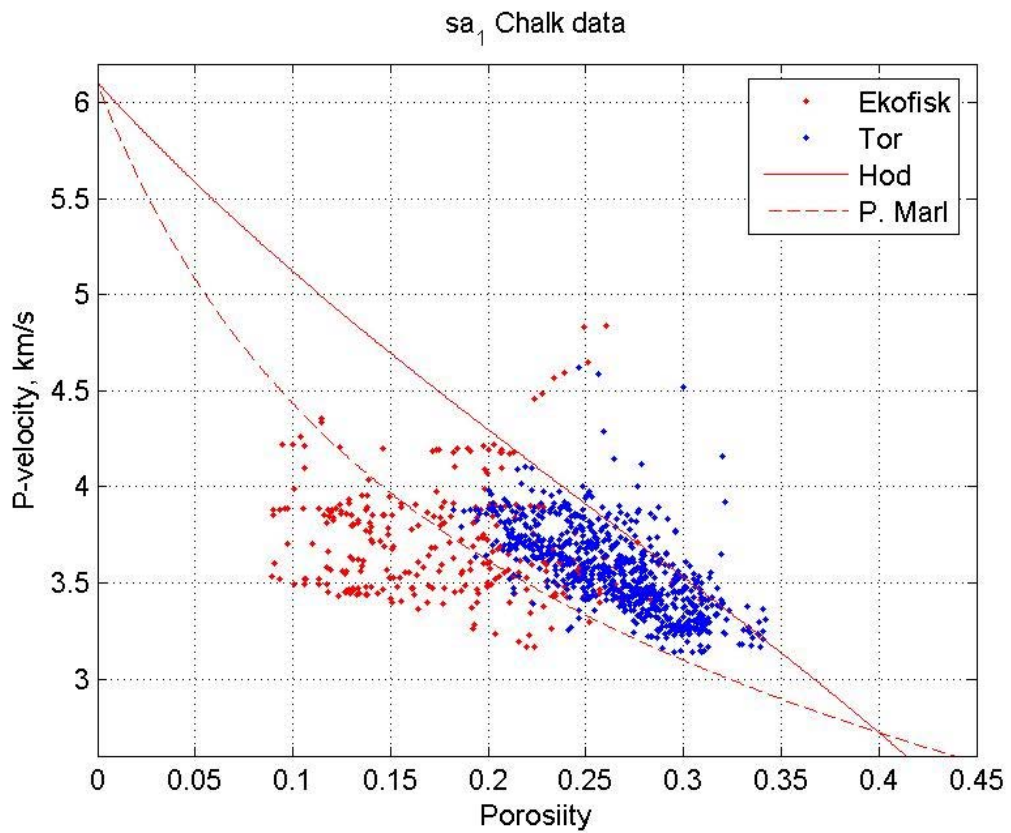
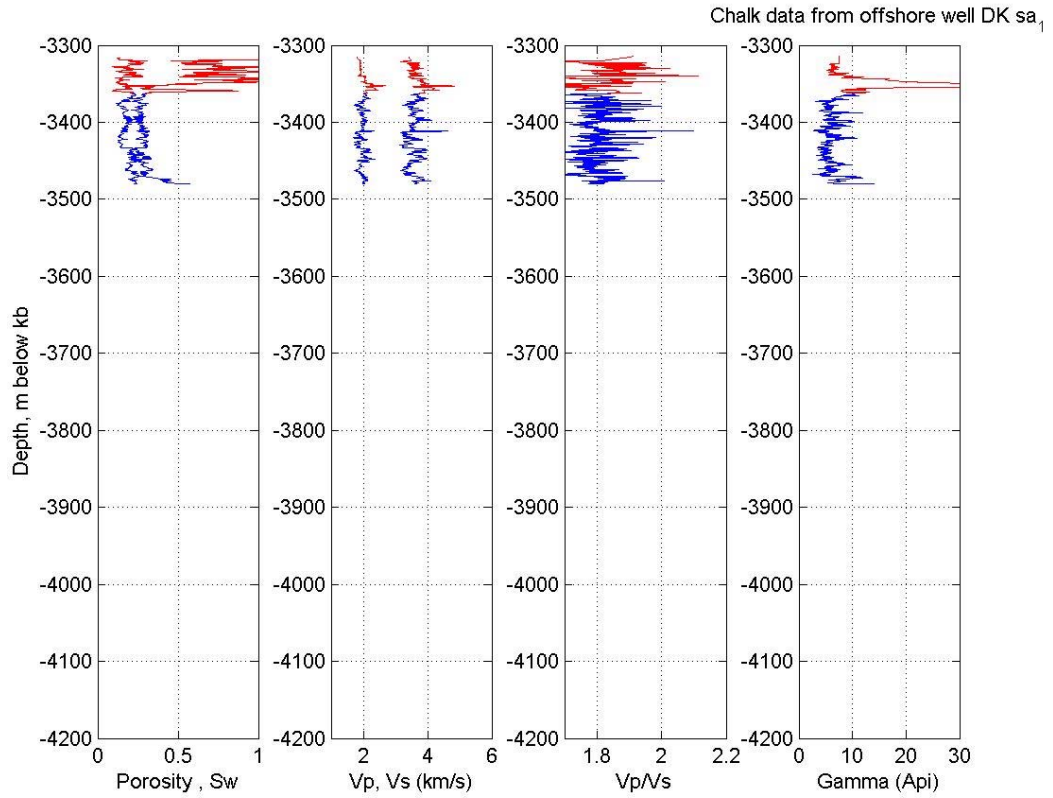
Ravn-2



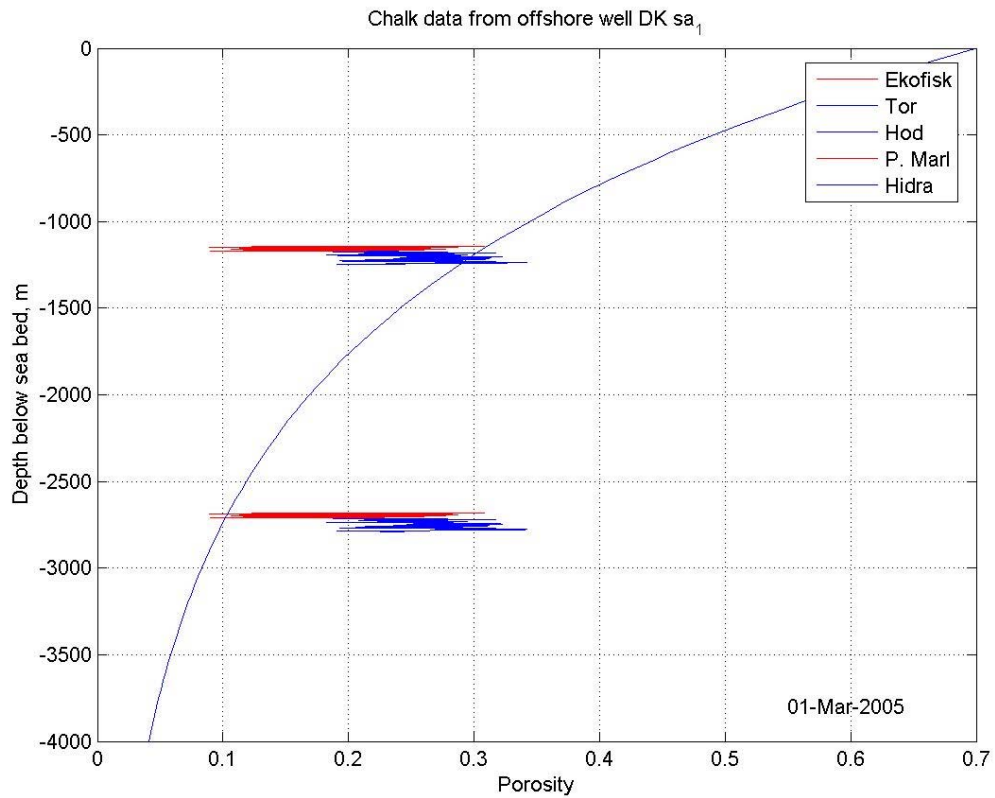
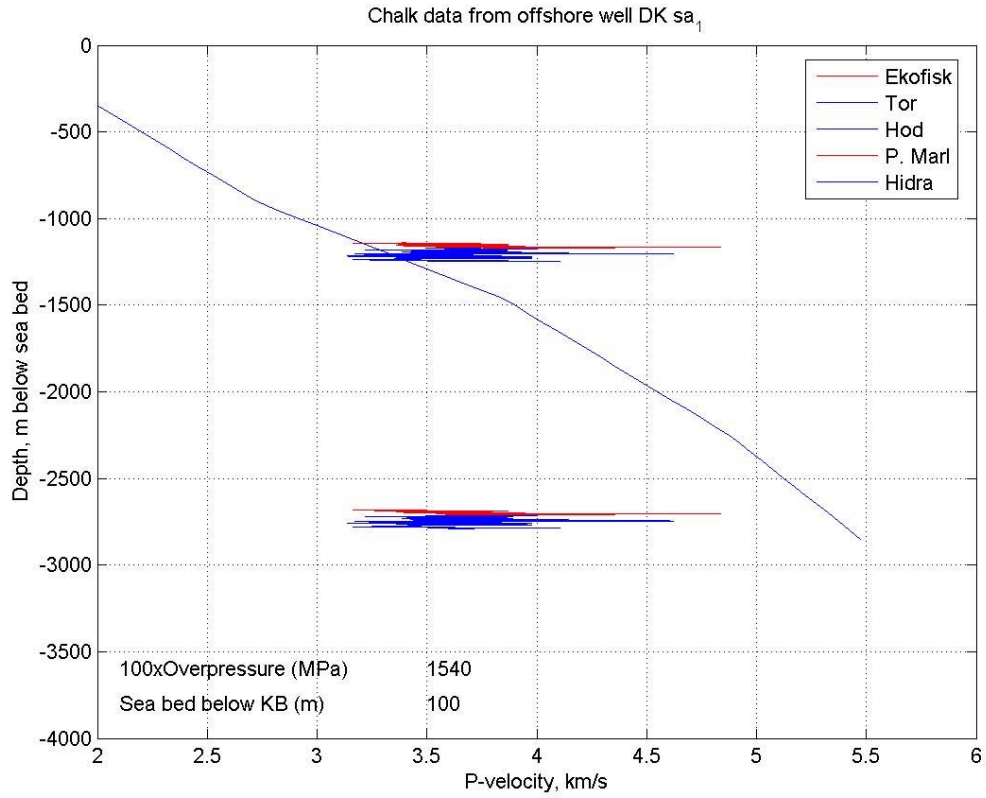
Rigs-2



Rigs-2

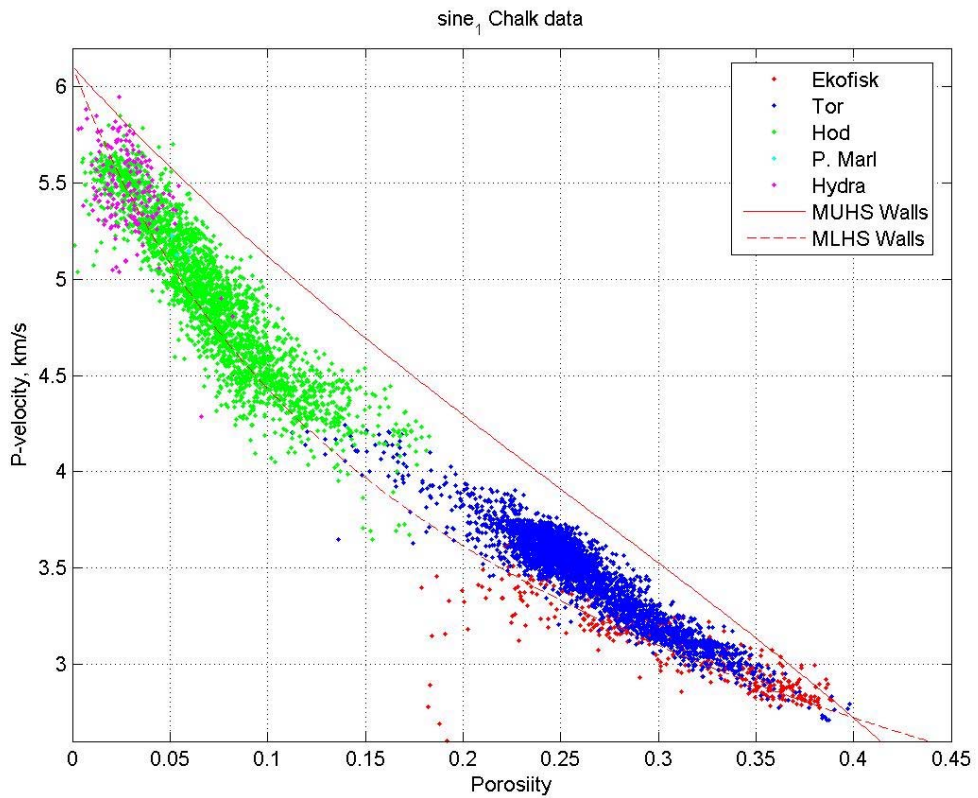
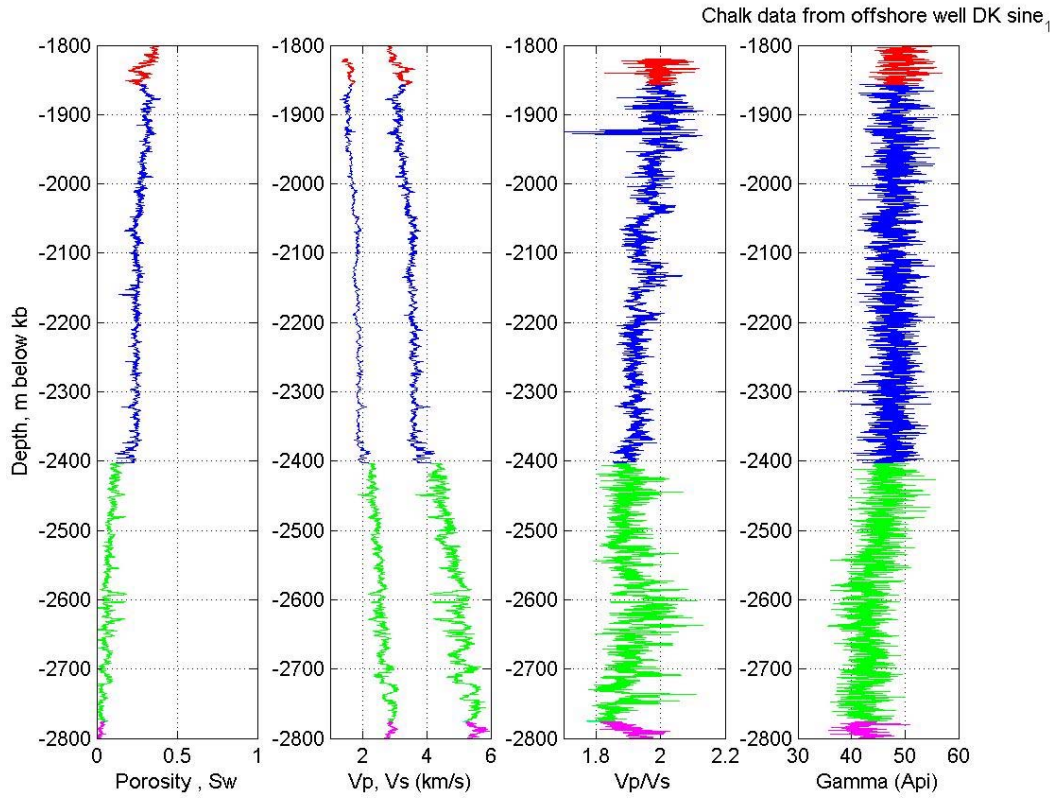


SA-1
Log plot in measured depths

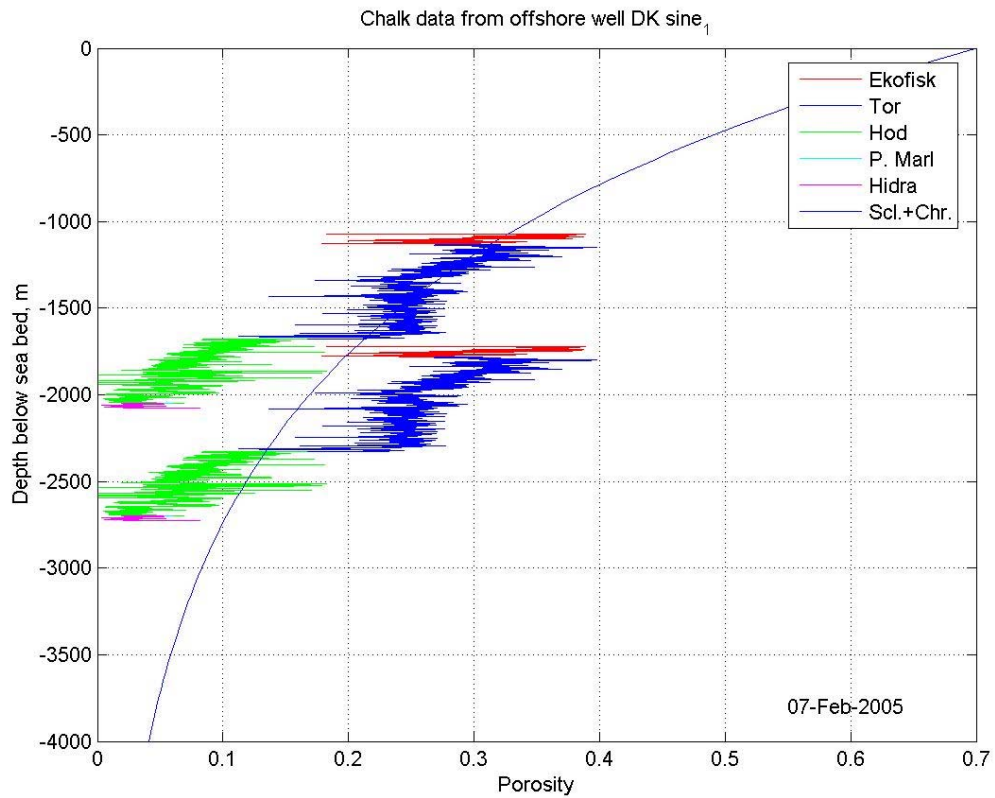
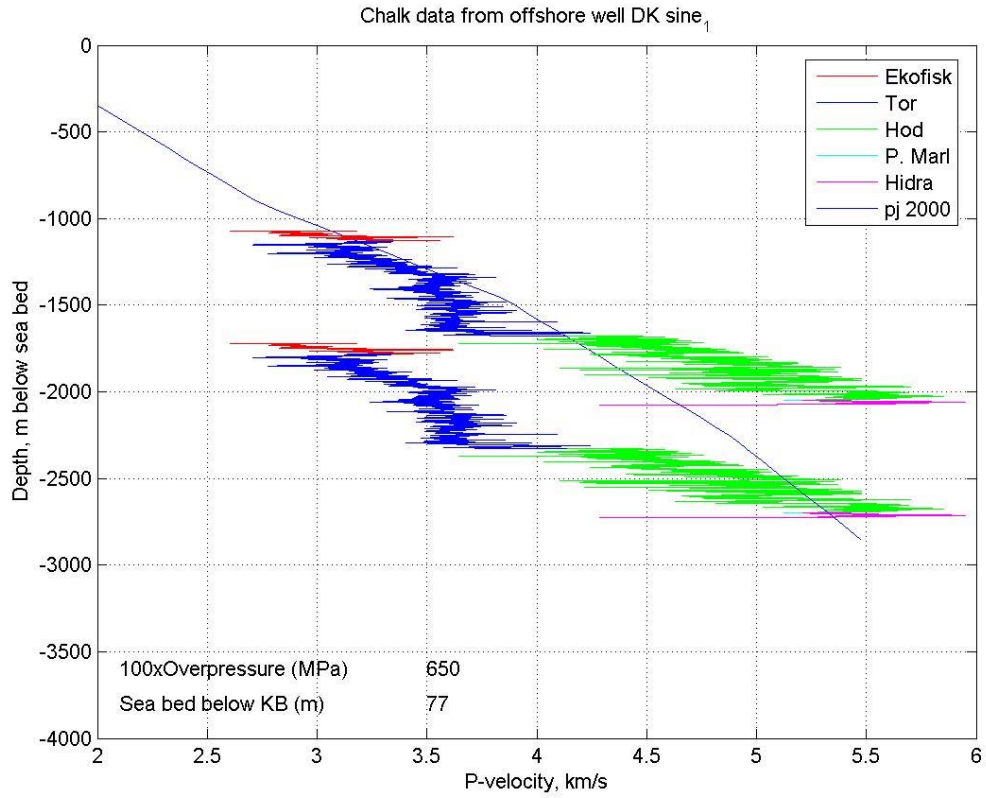


True vertical depths

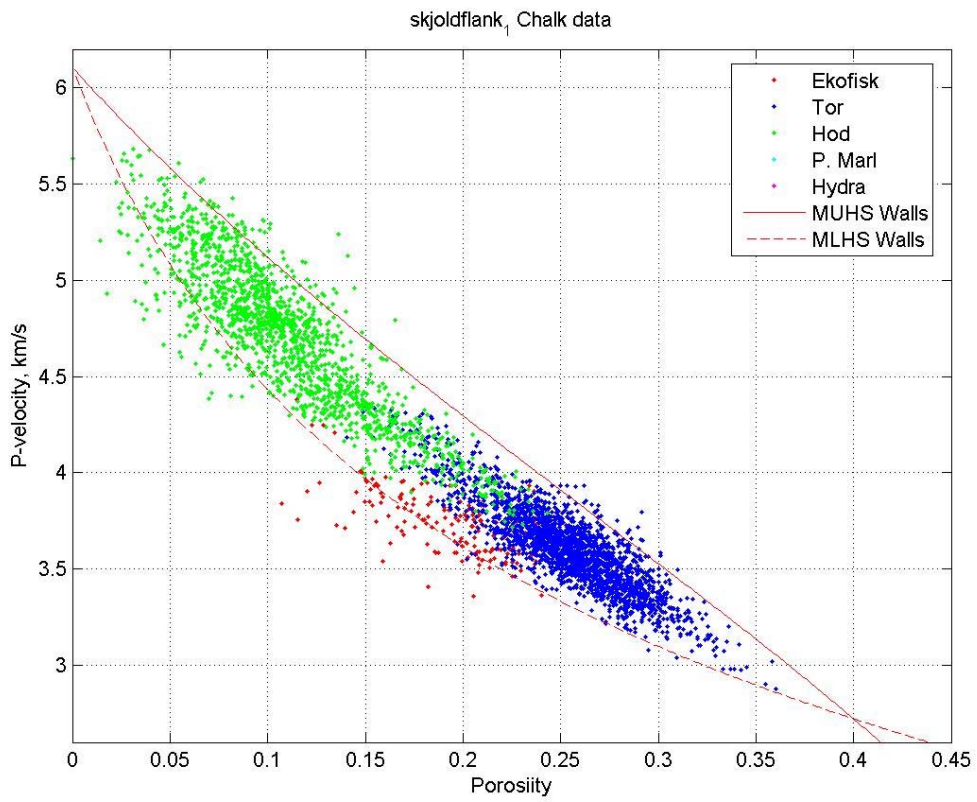
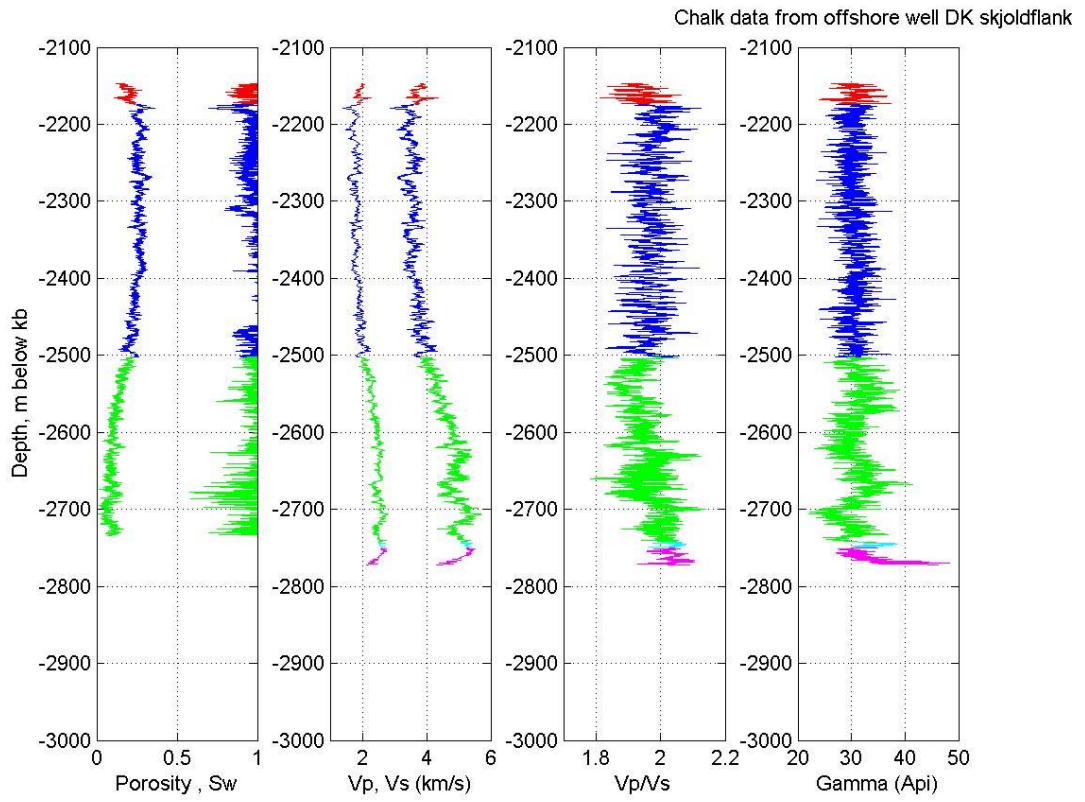
SA-1



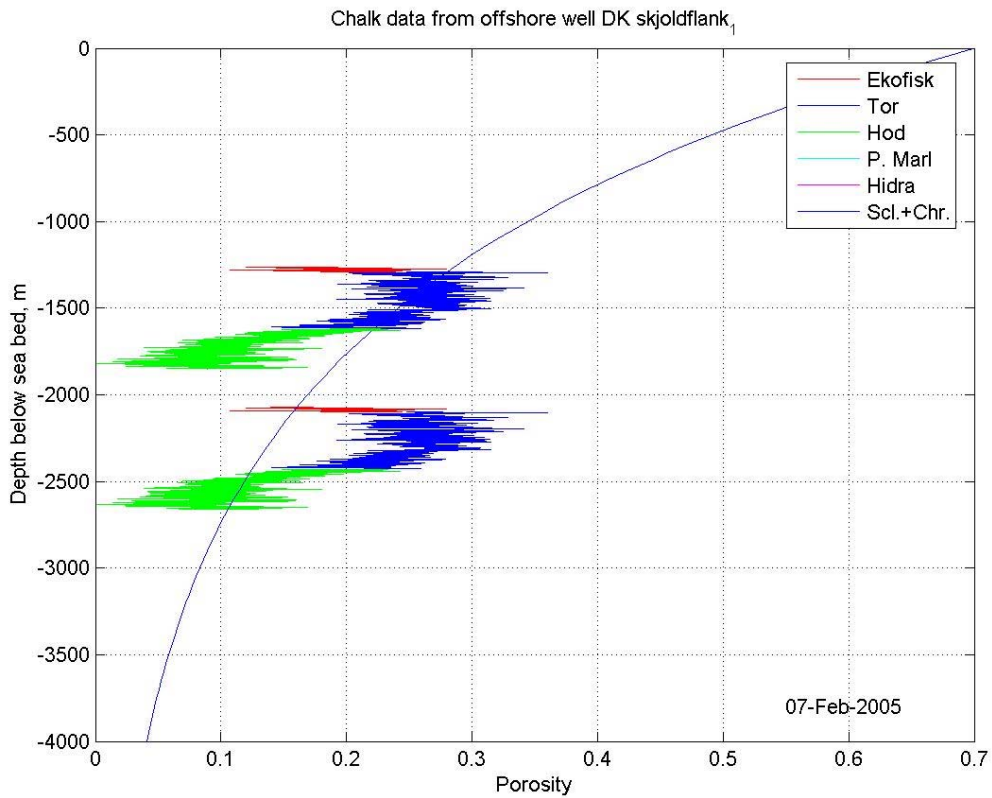
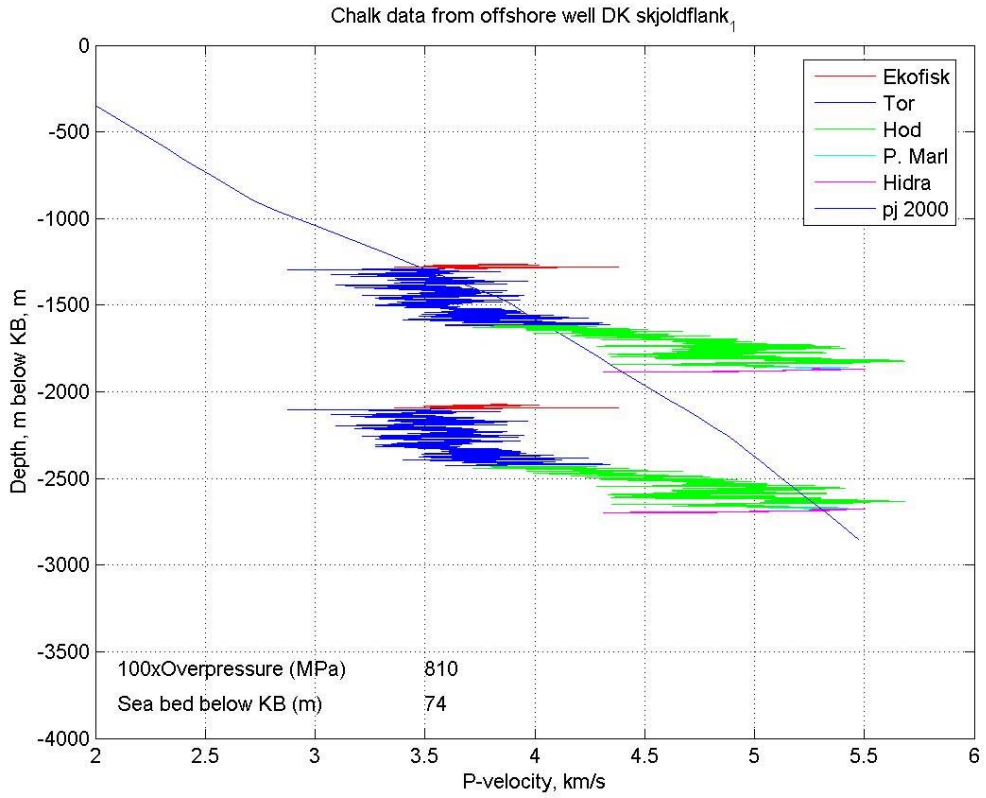
Sine-1



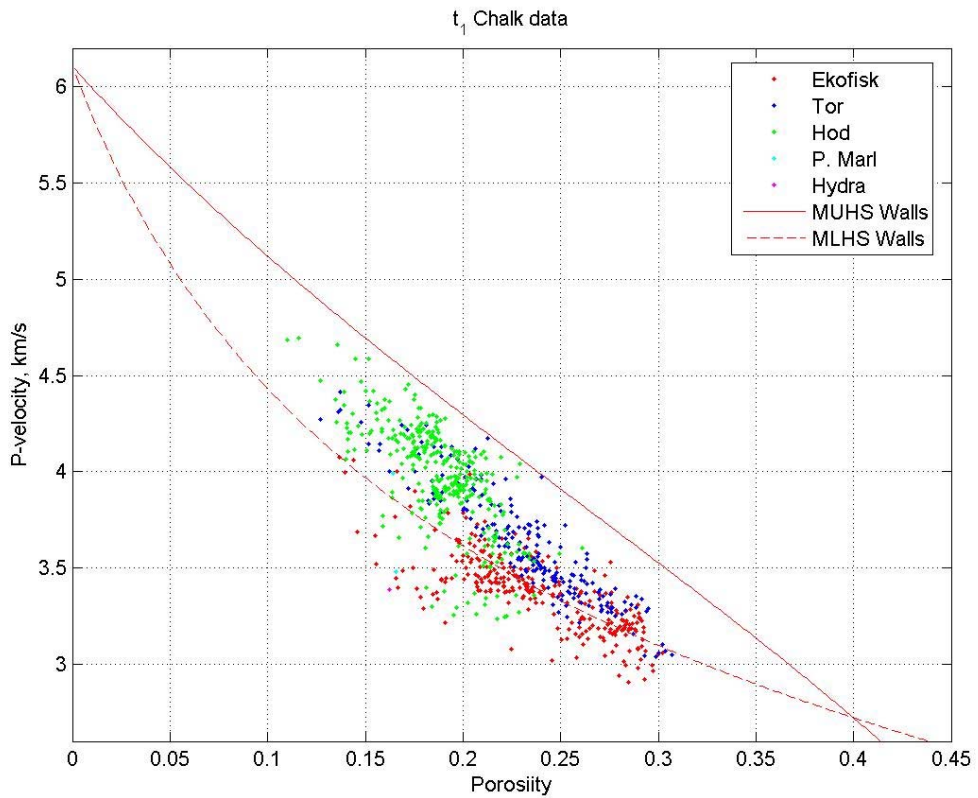
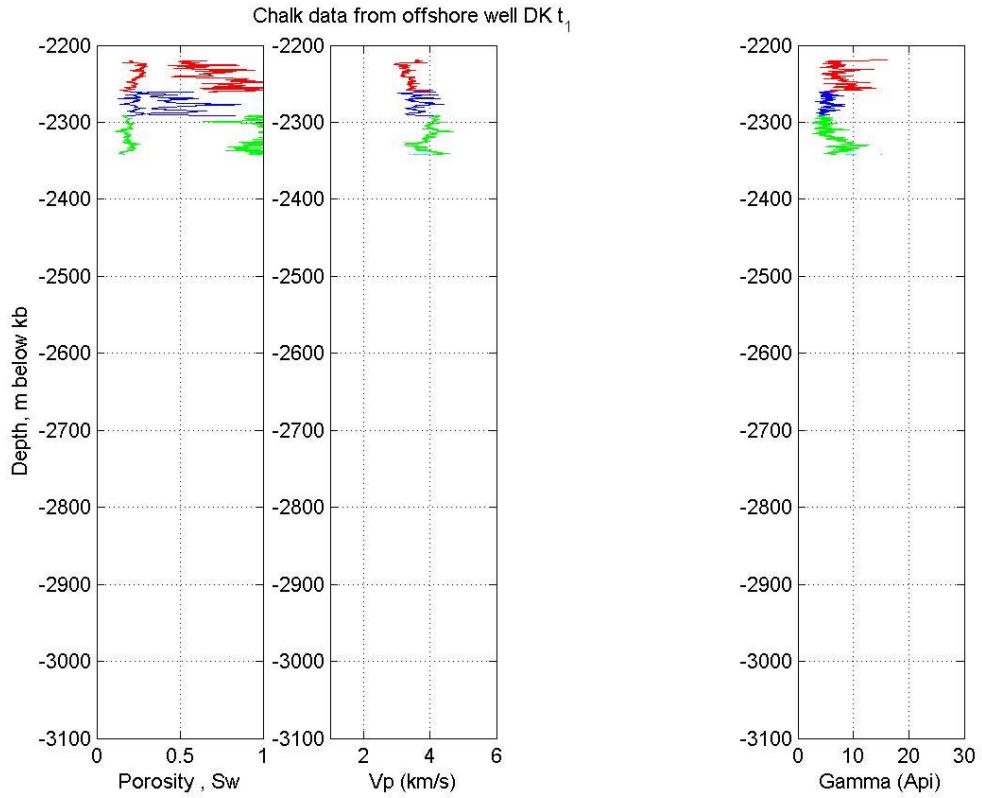
Sine-1



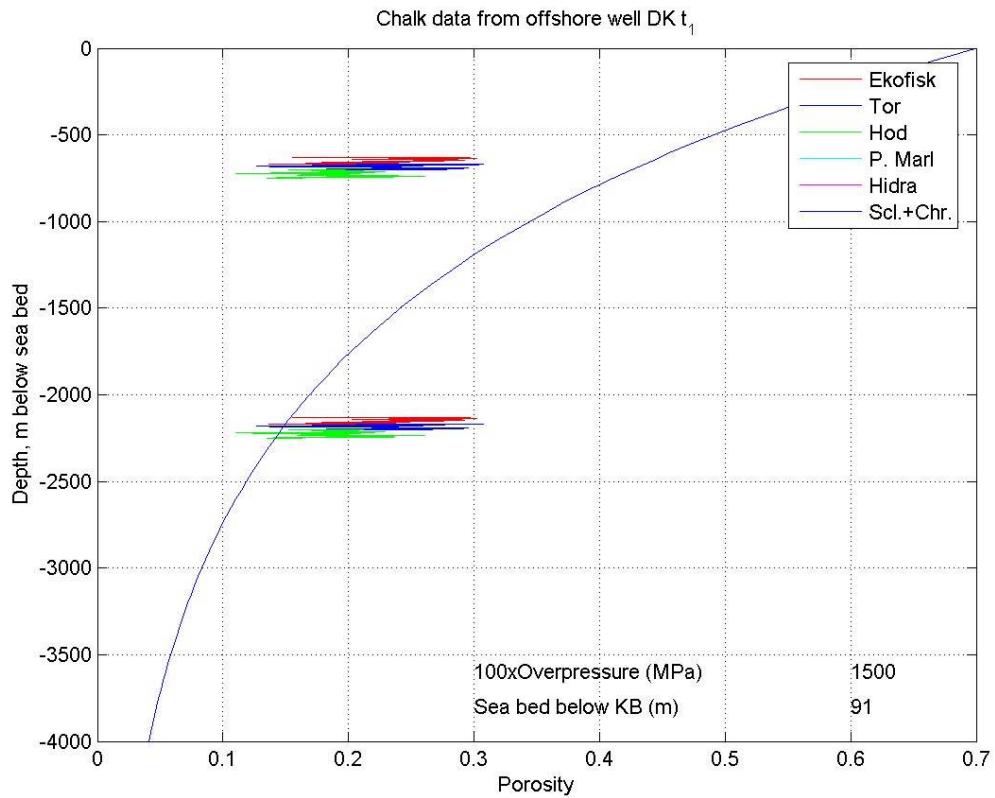
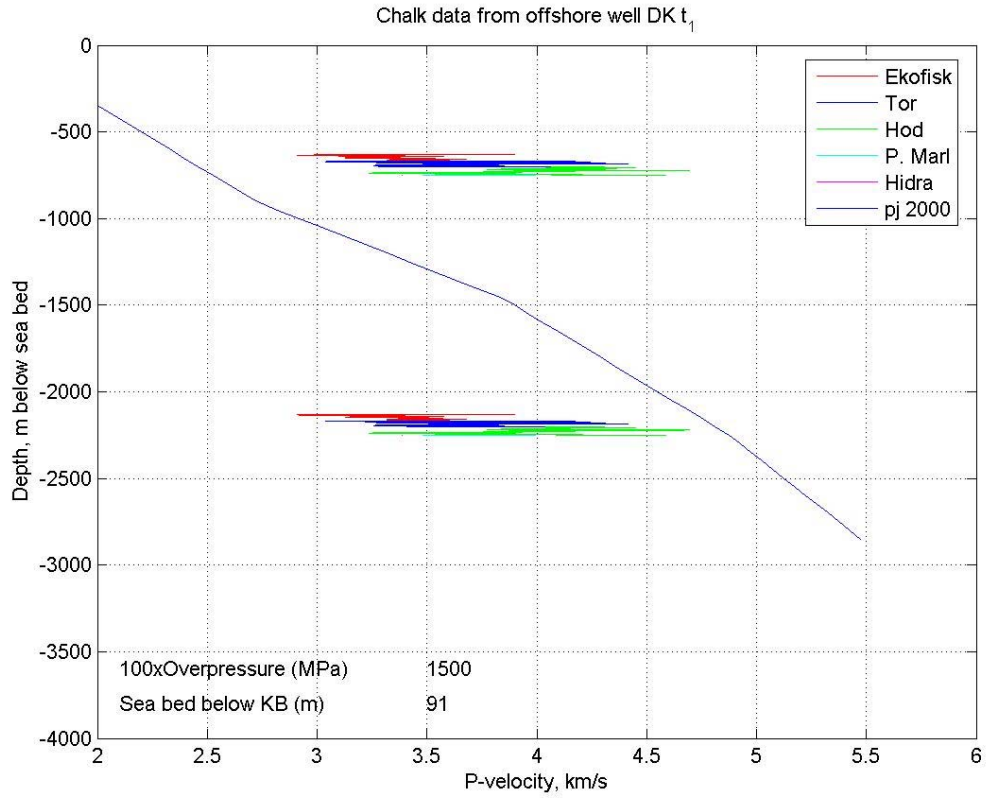
Skjold Flank-1



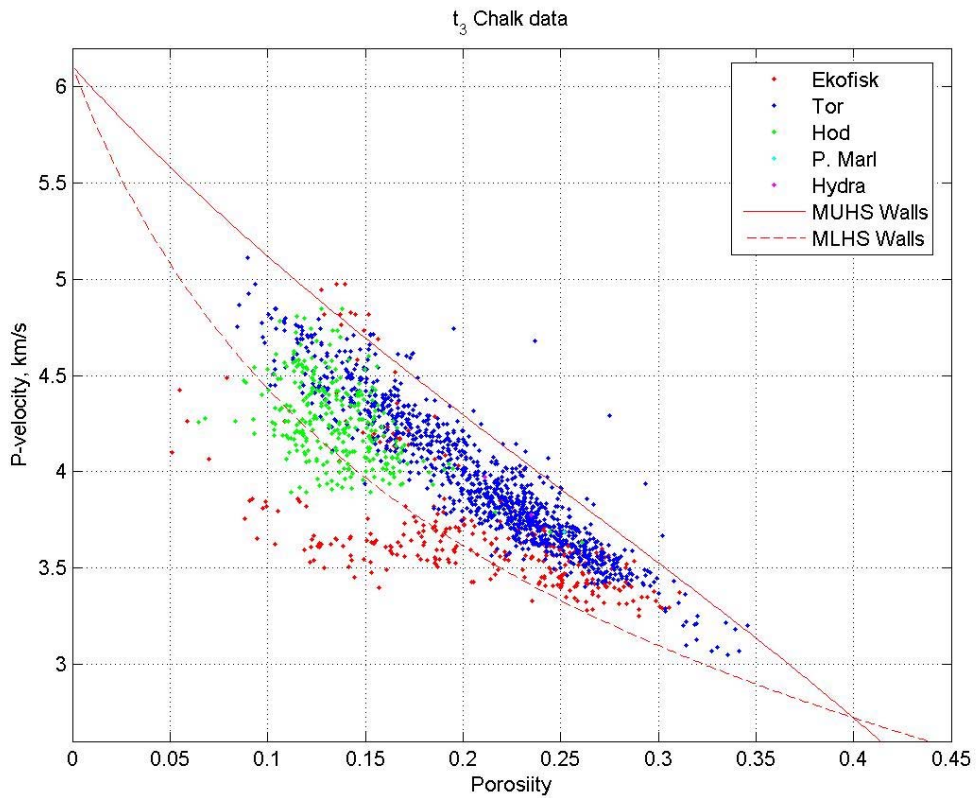
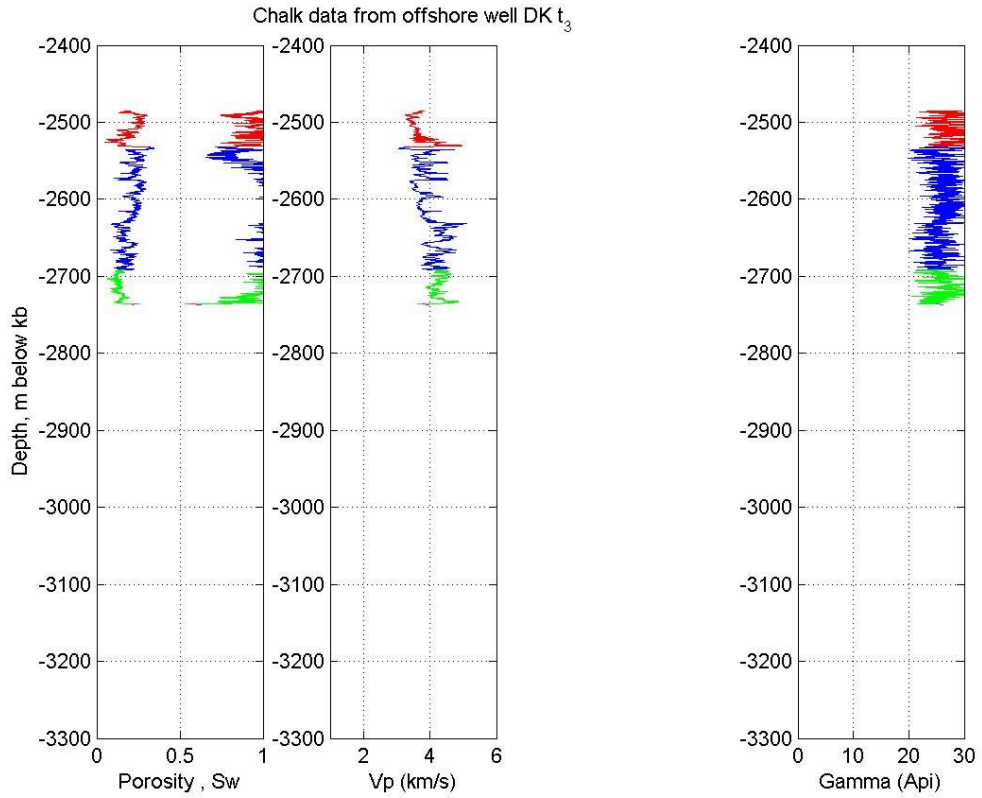
Skjold Flank-1



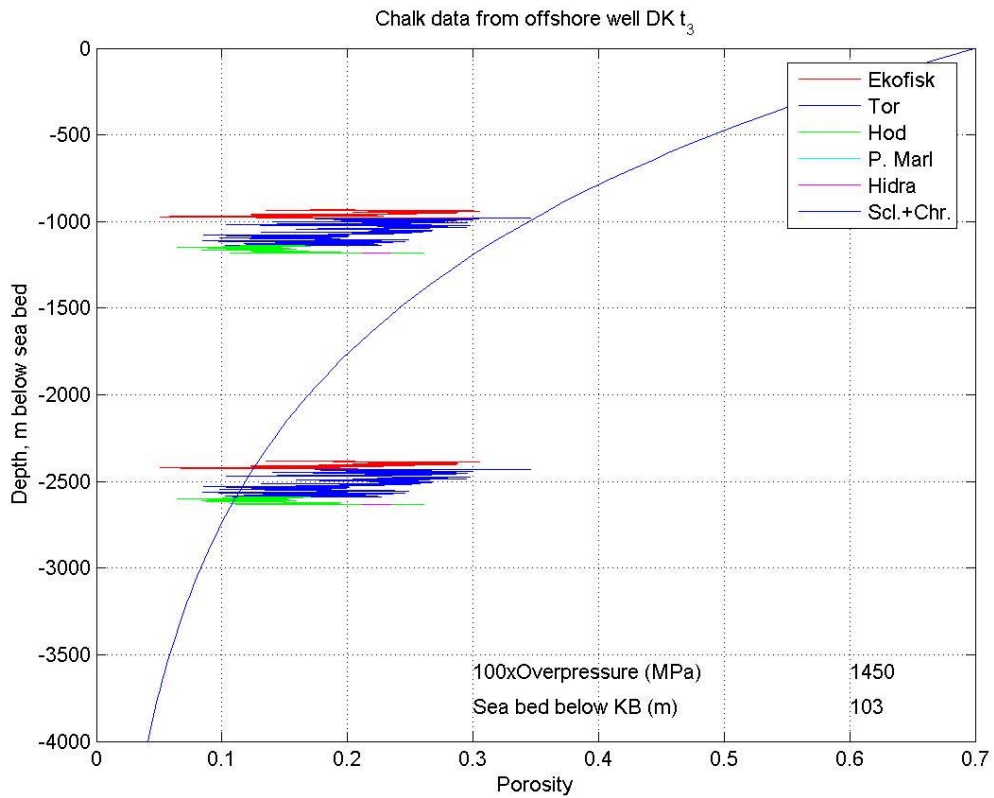
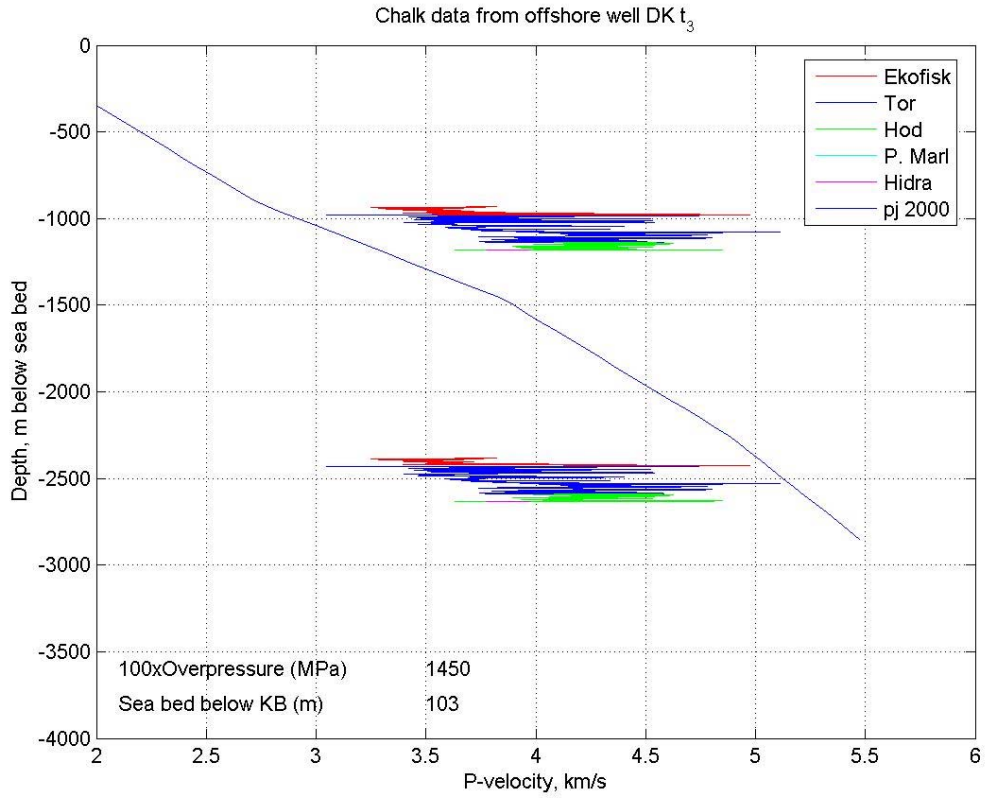
T-1



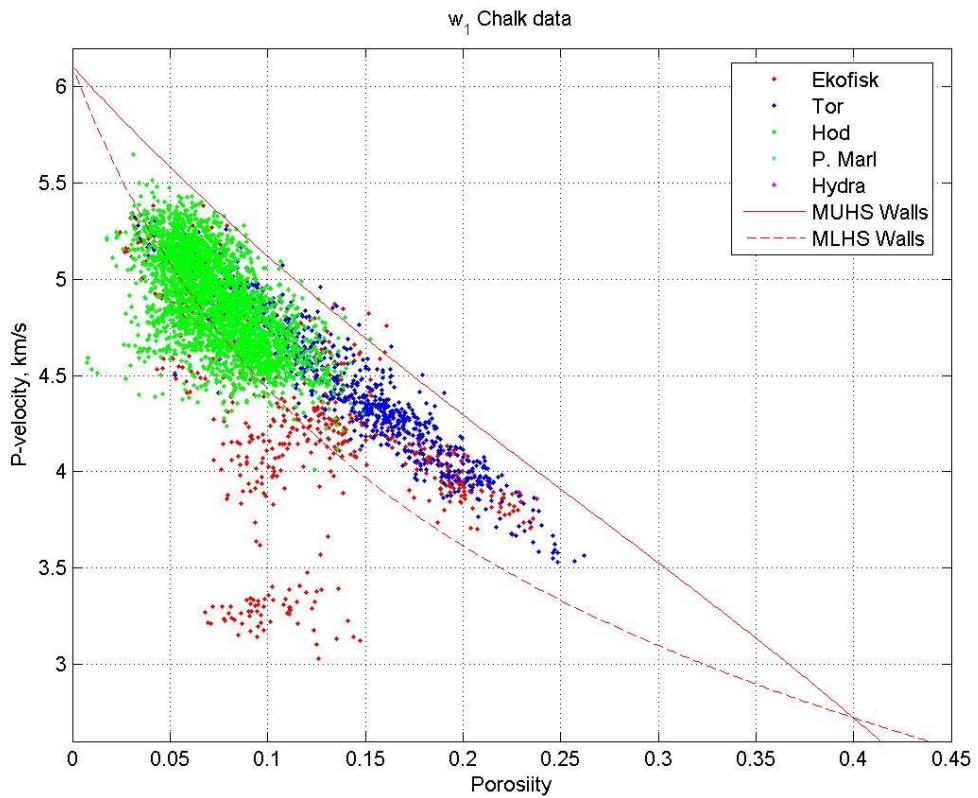
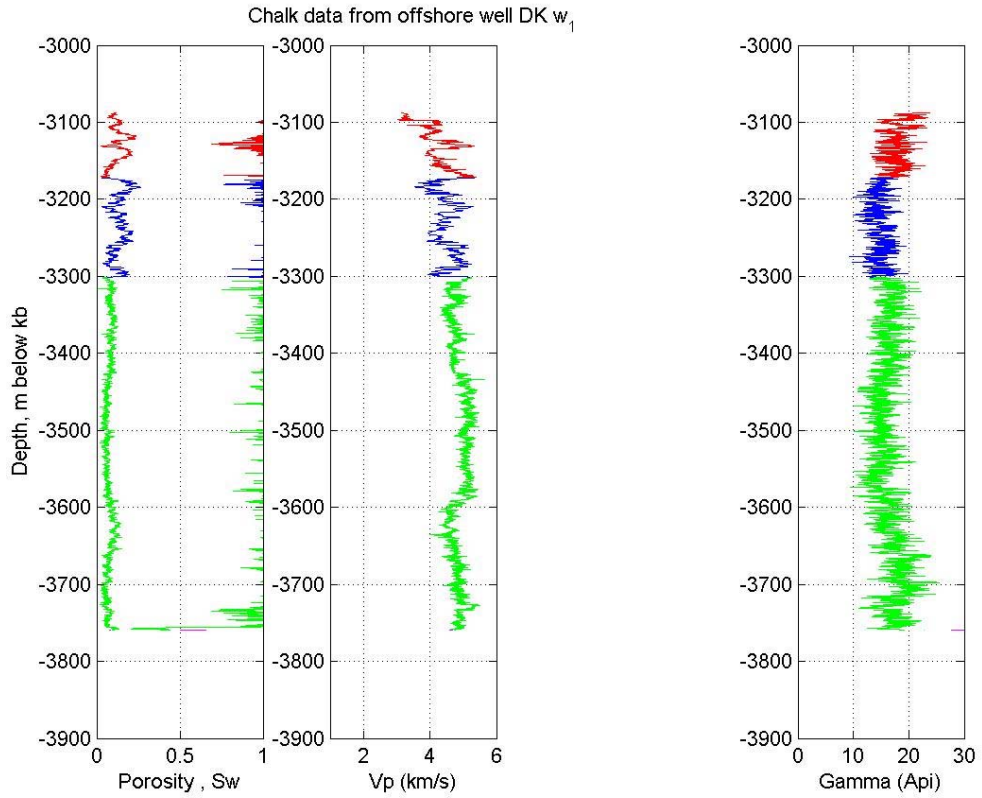
T-1



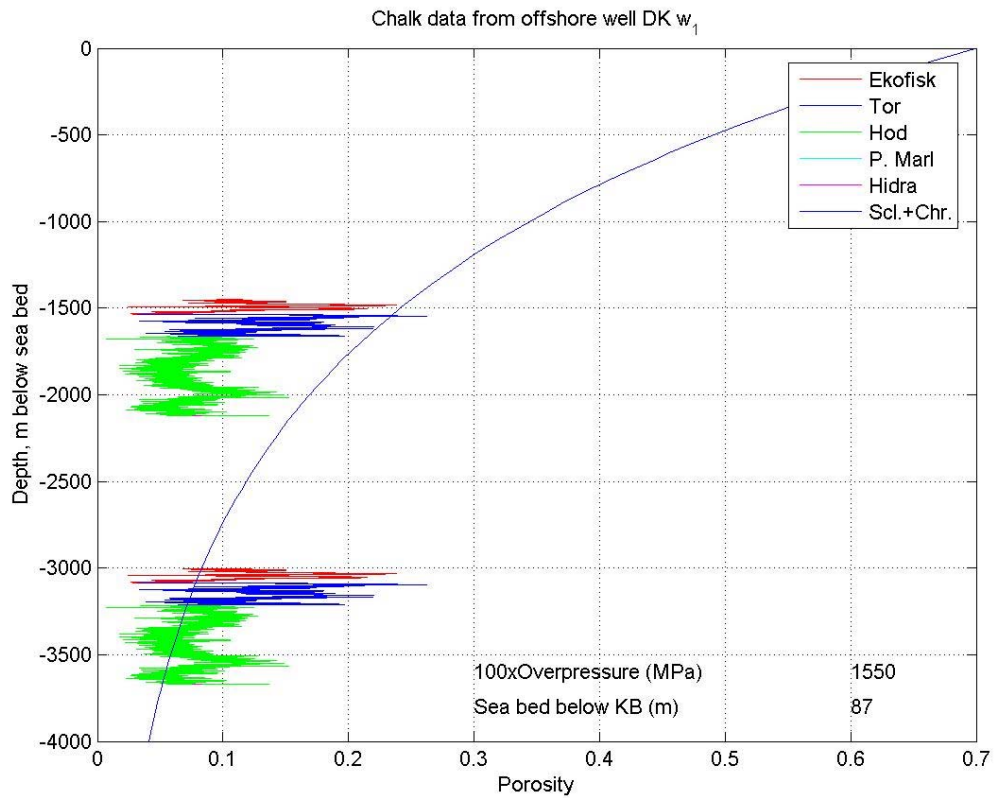
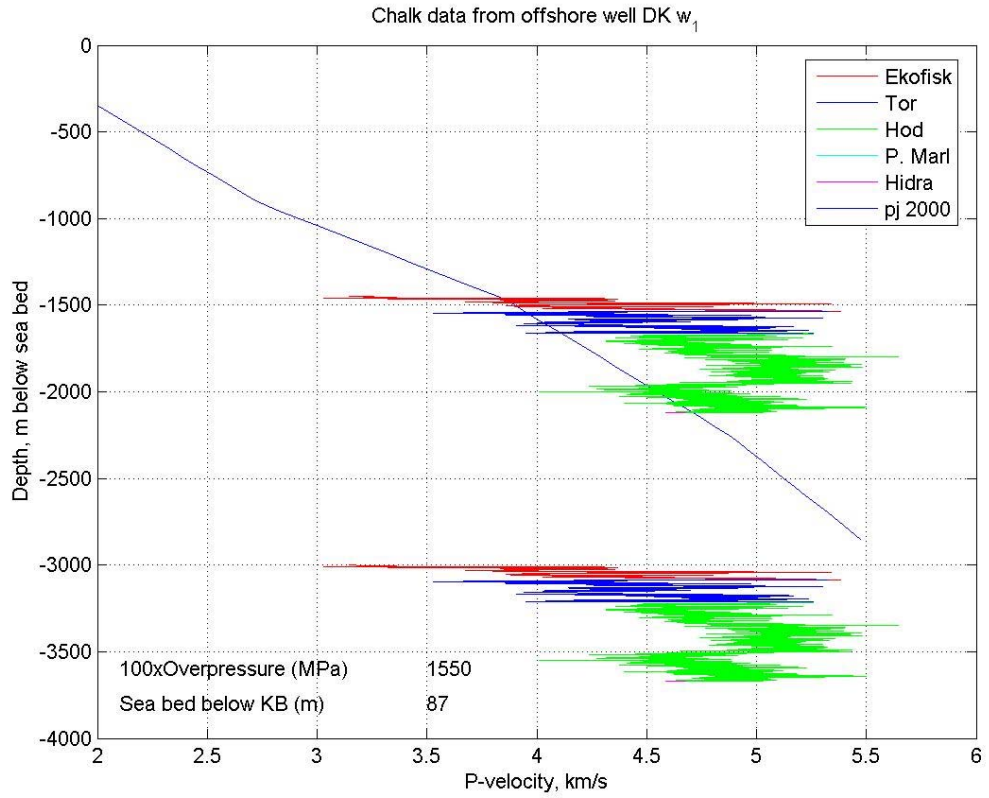
T-3



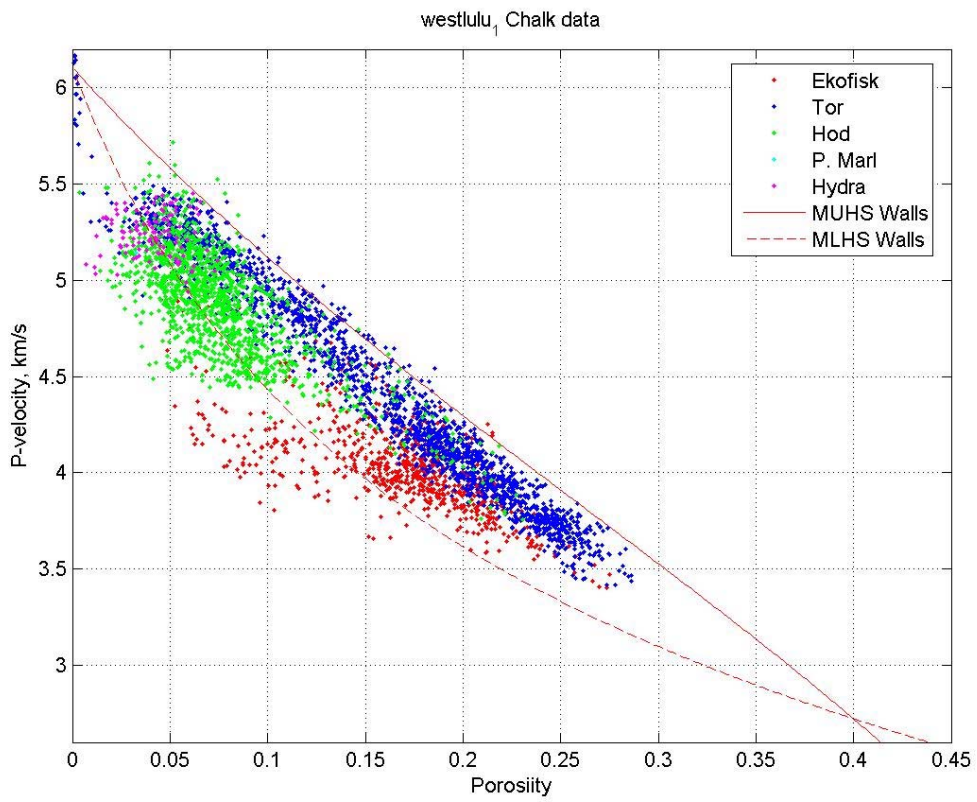
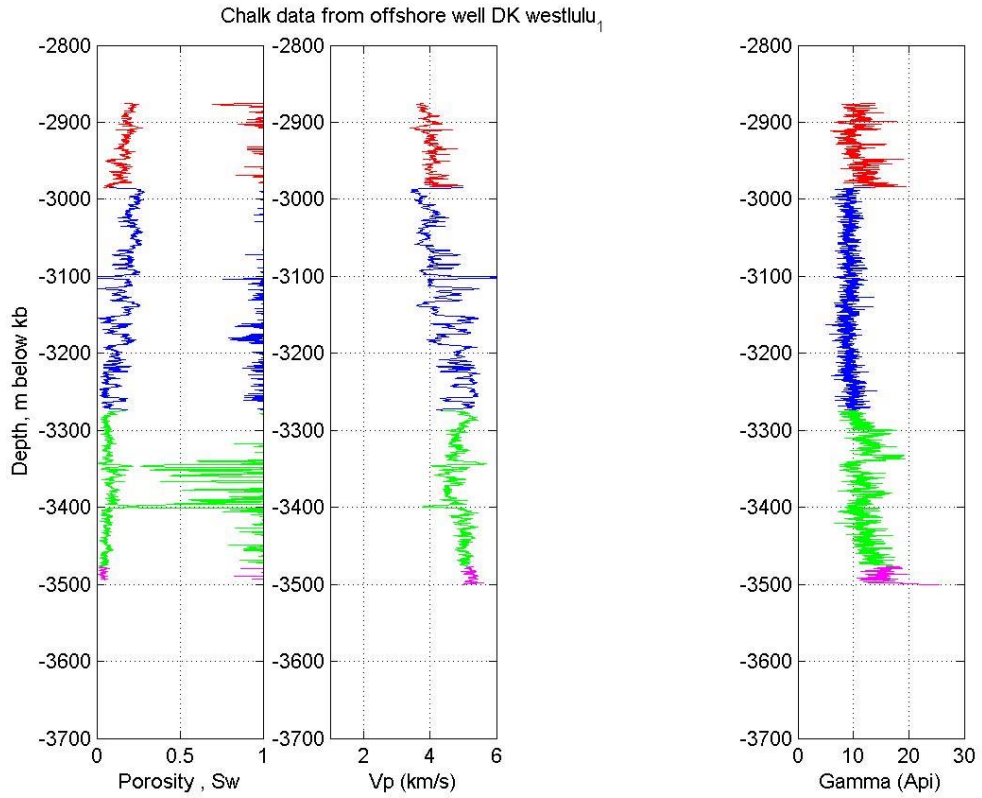
T-3



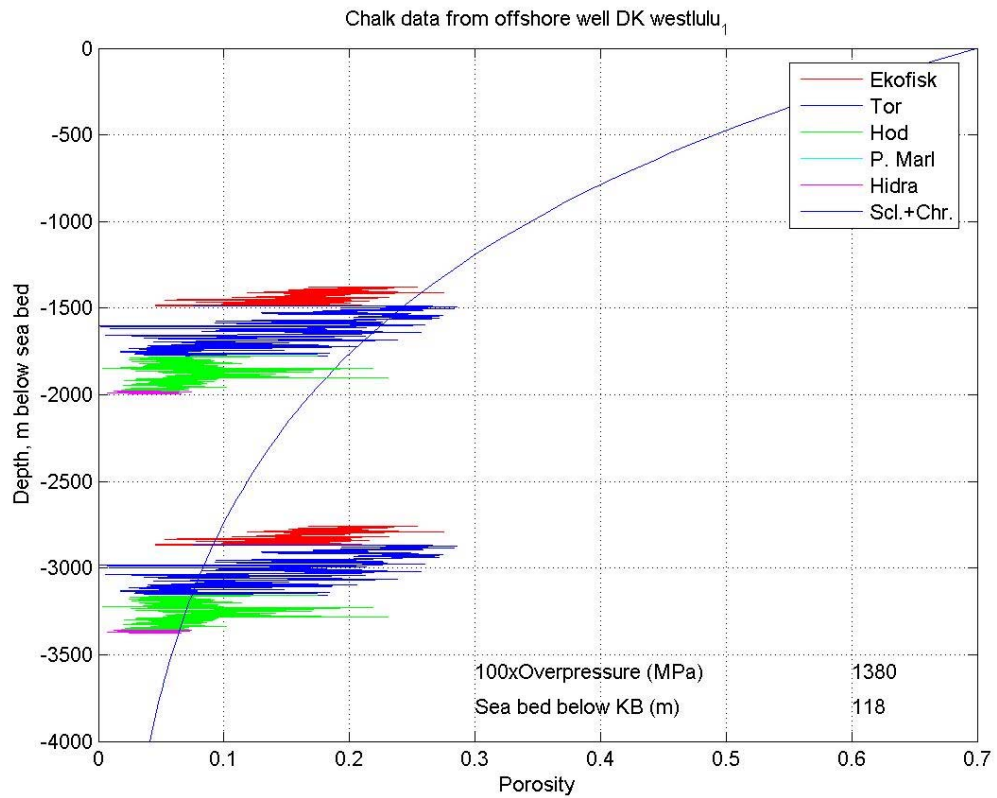
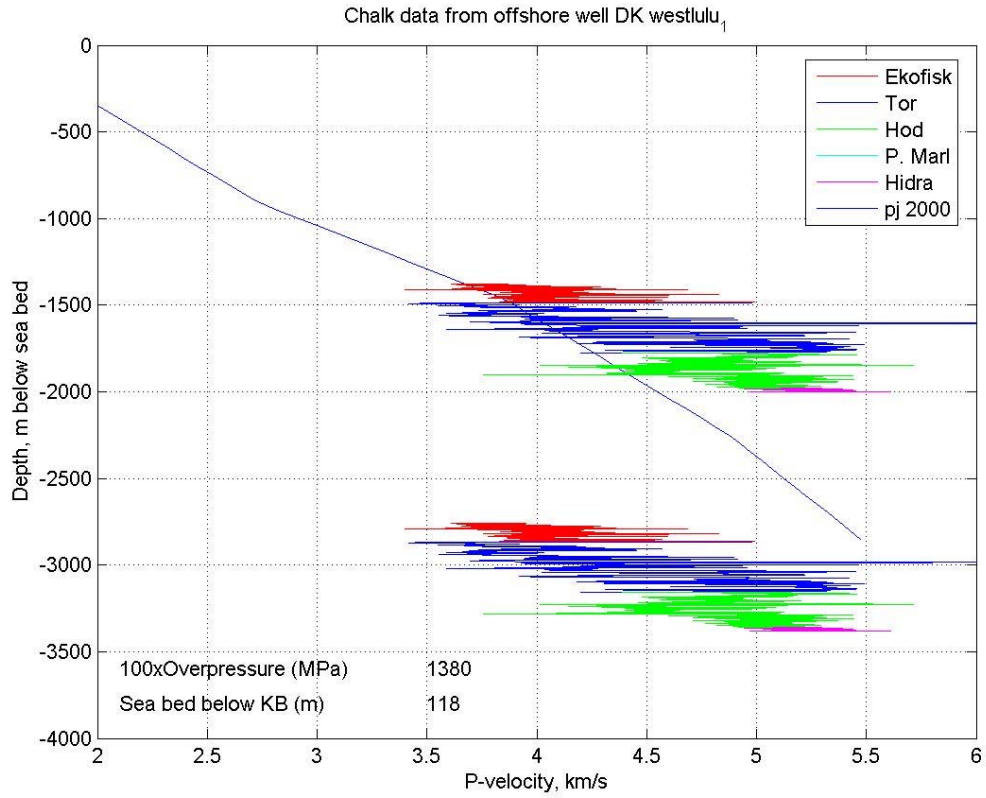
W-1



W-1

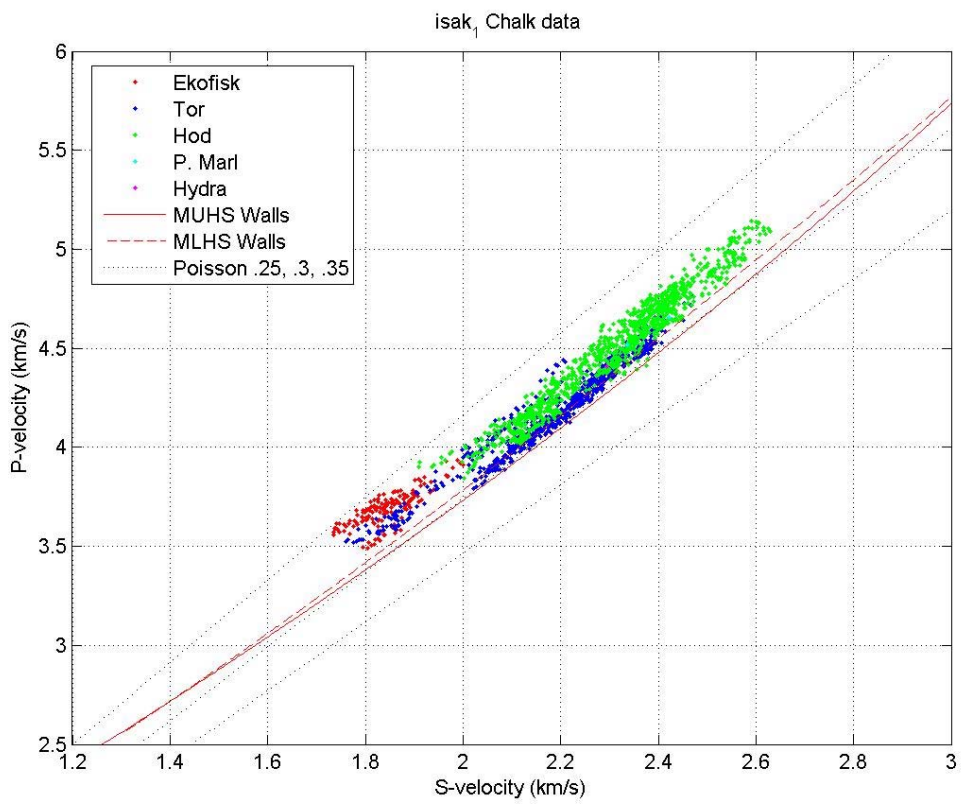
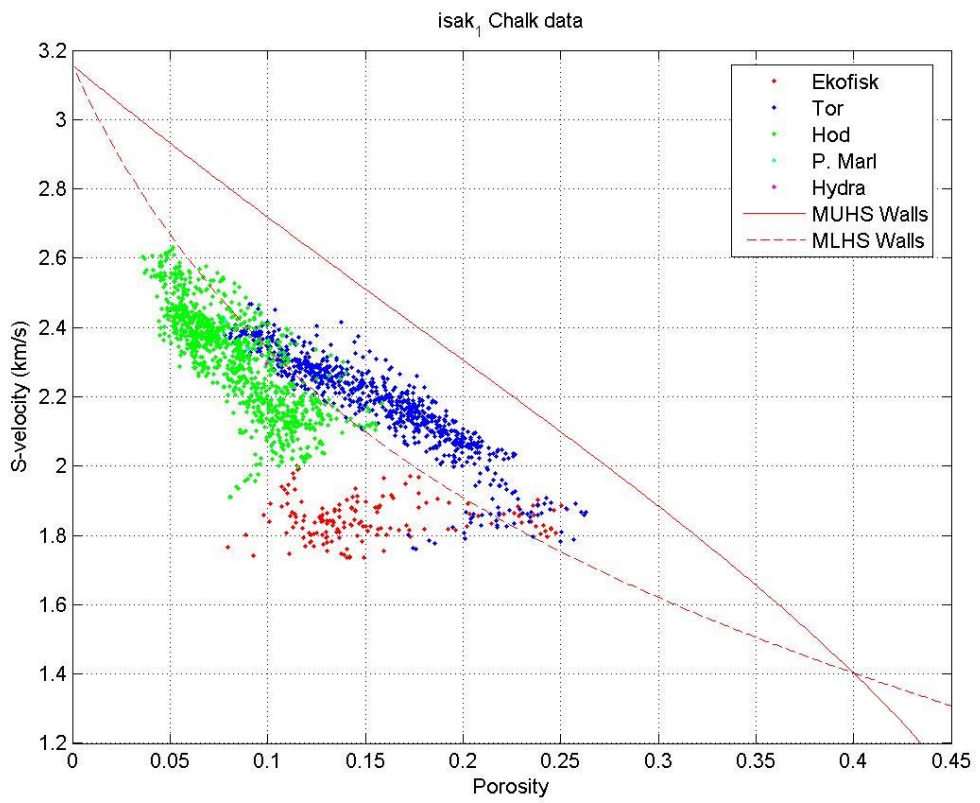


West Lulu-1



West Lulu-1

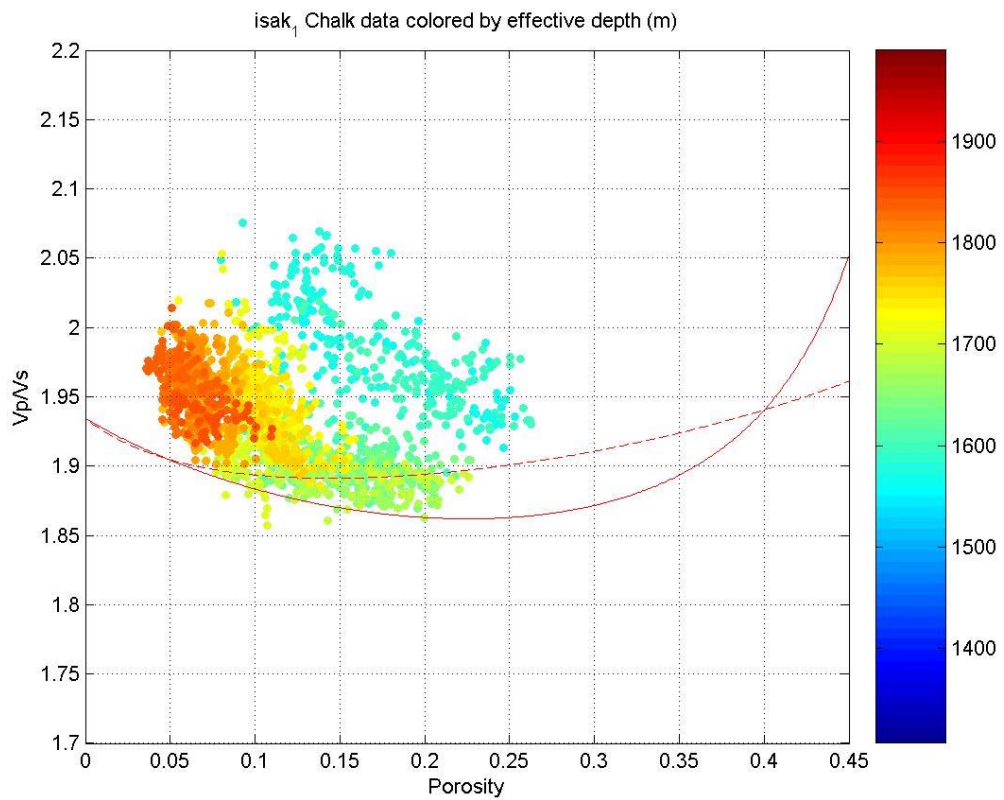
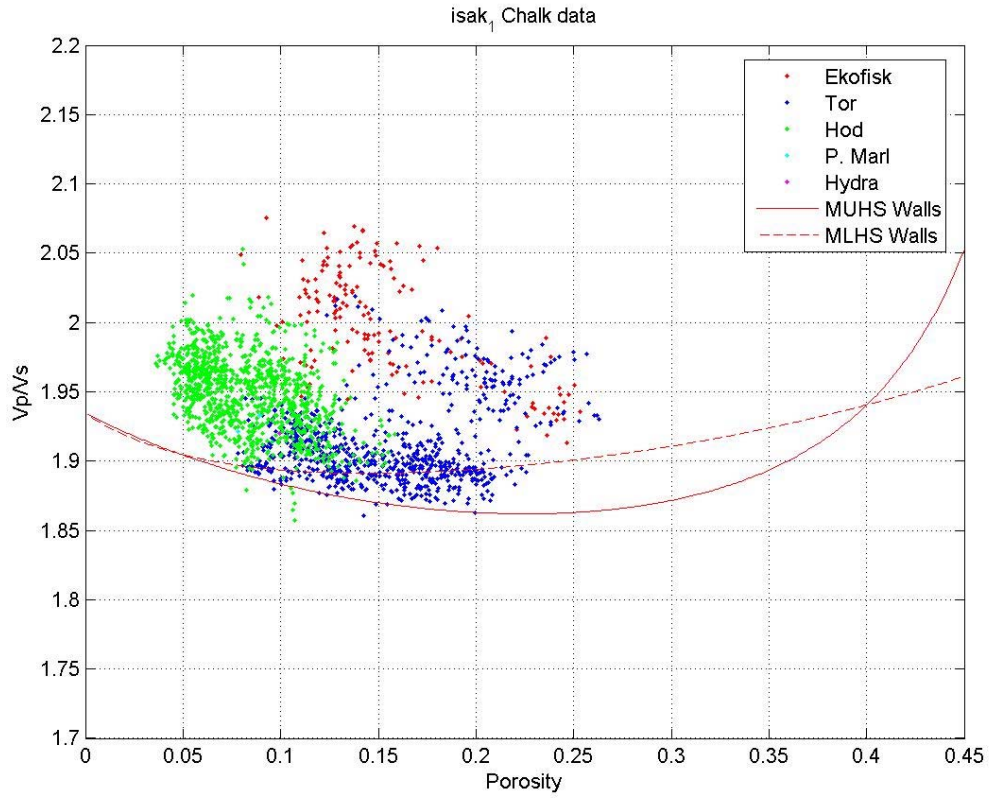
Vp-Vs plots



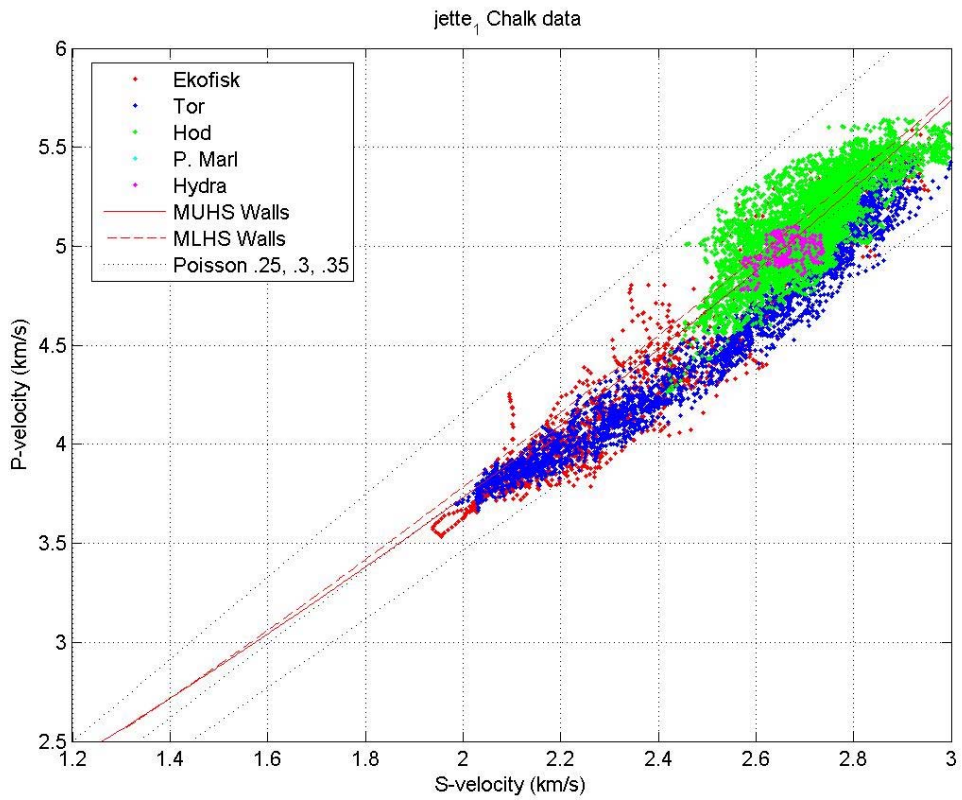
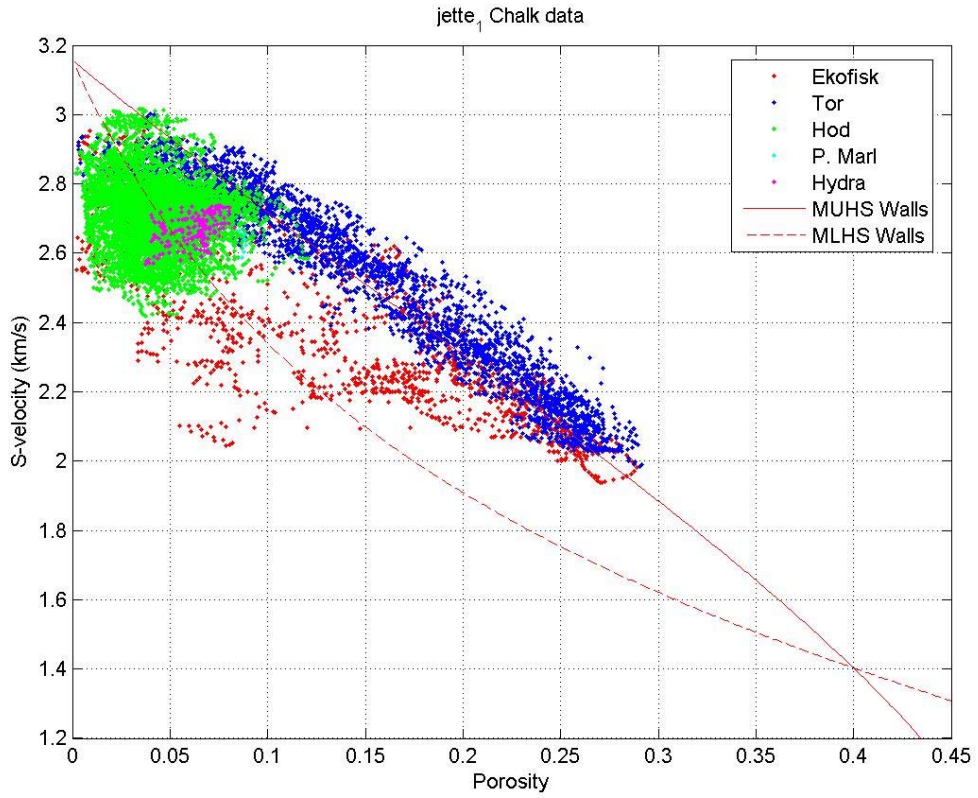
Isak-1

GEUS

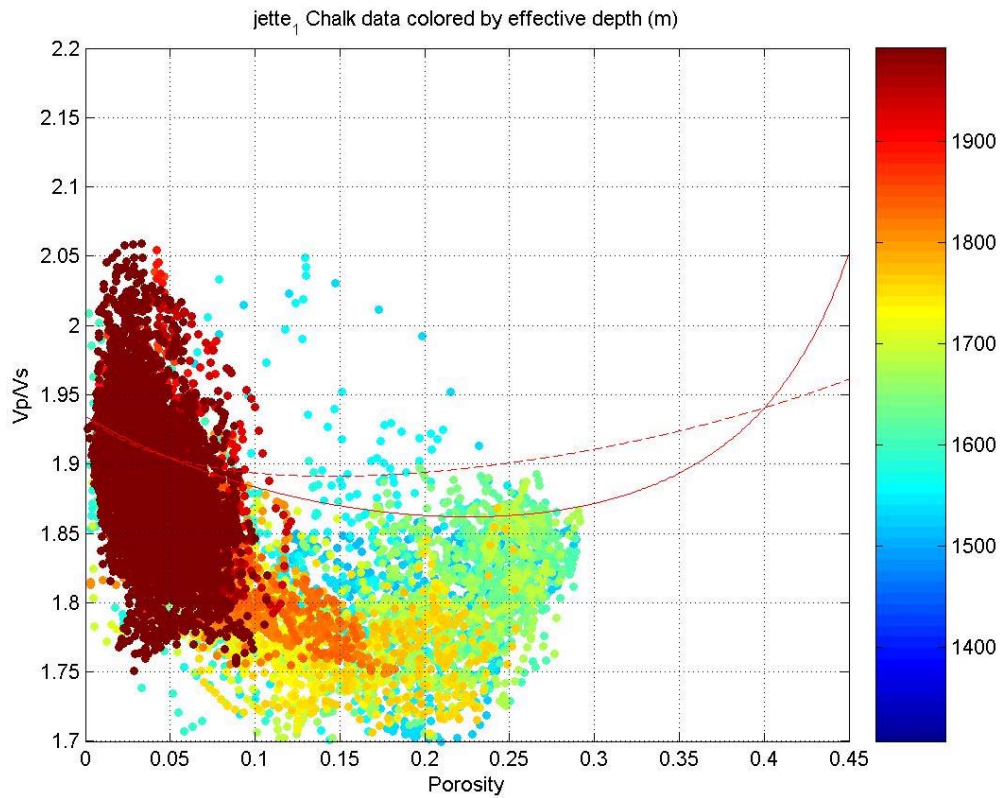
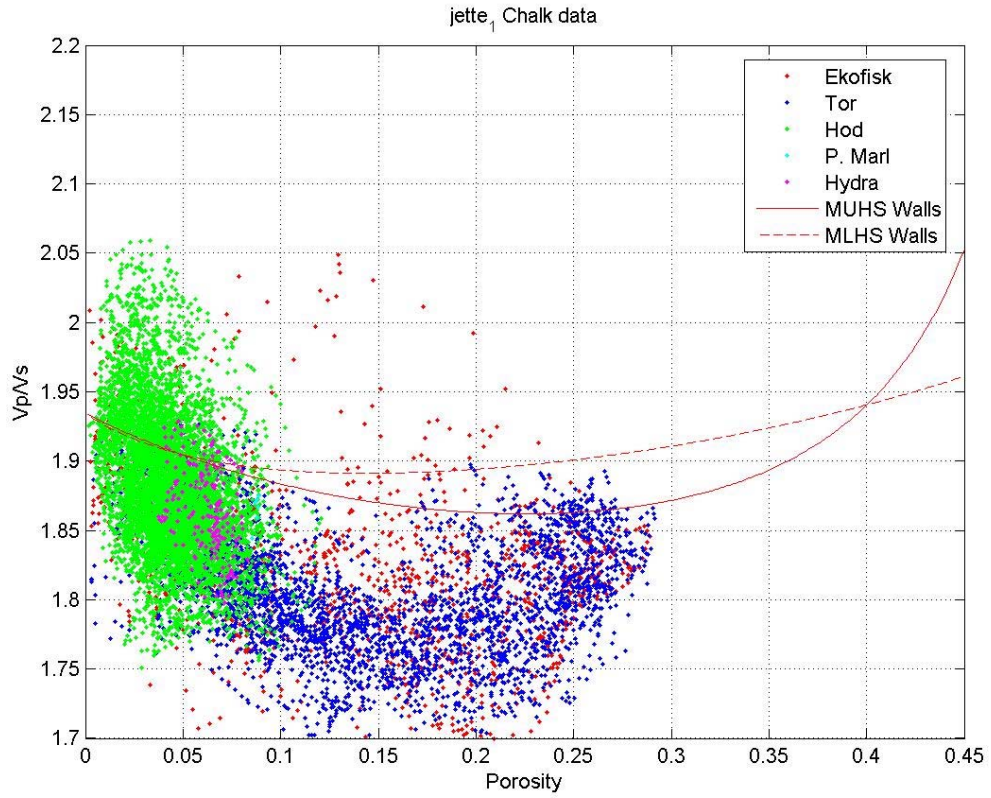
105



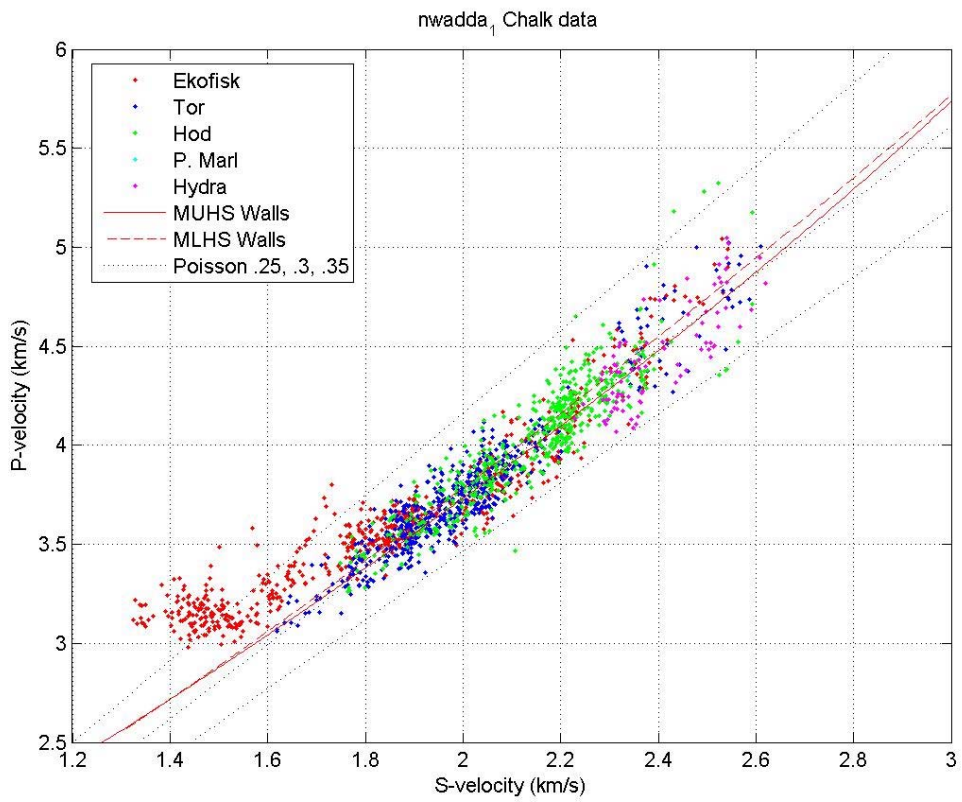
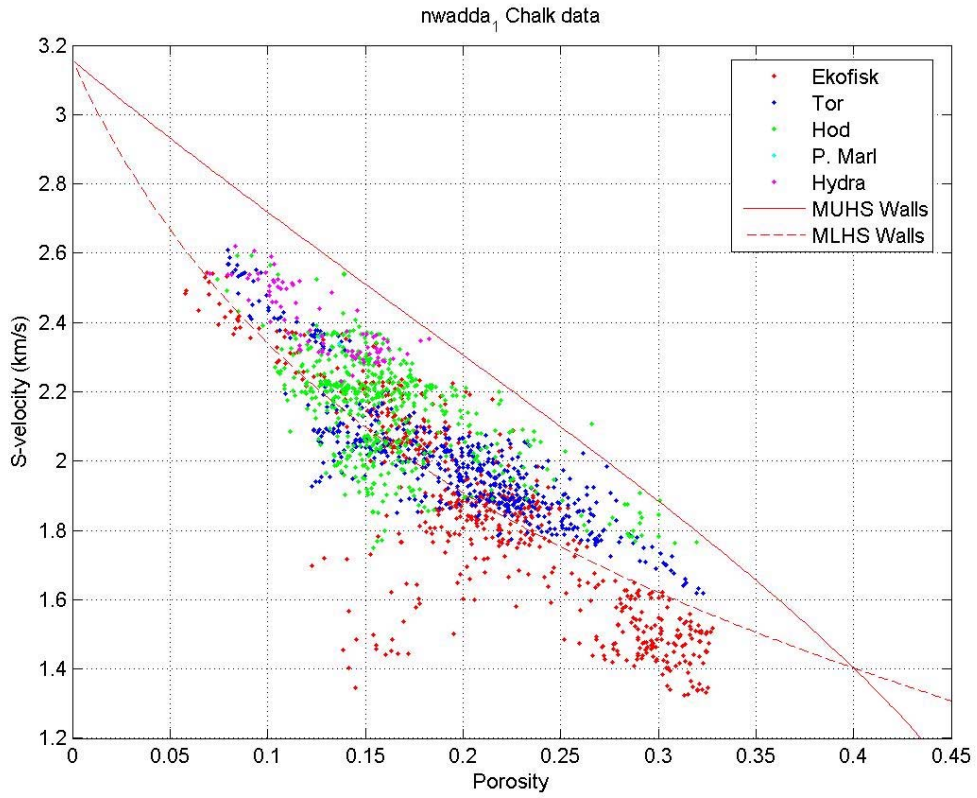
Isak-1



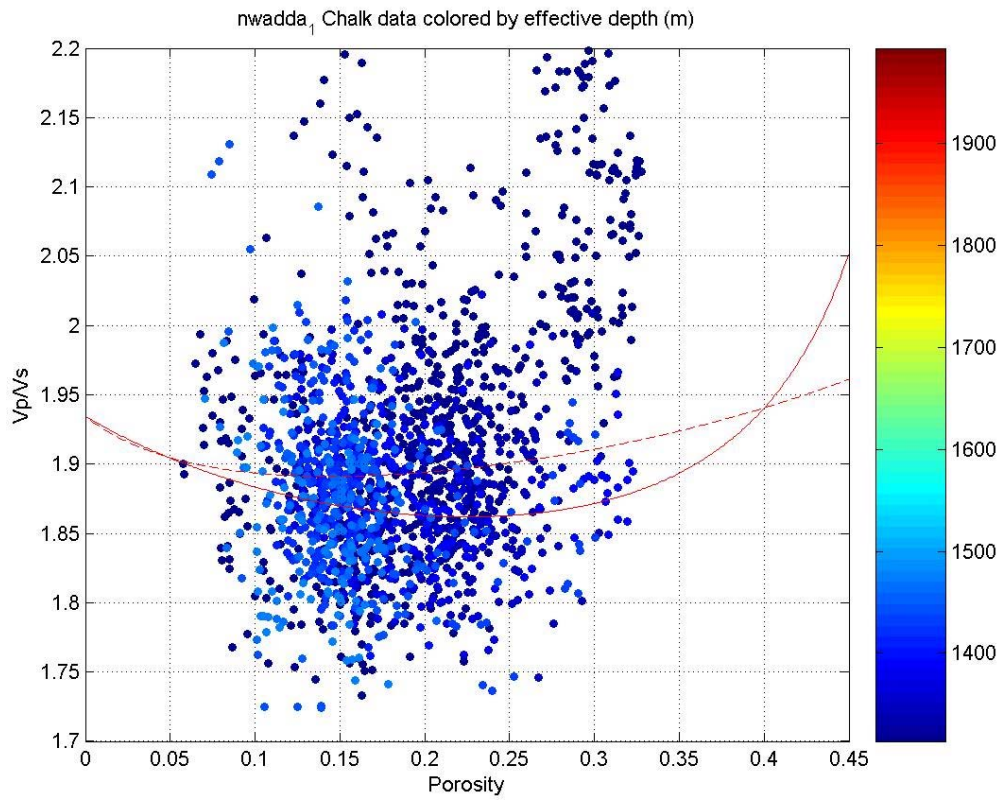
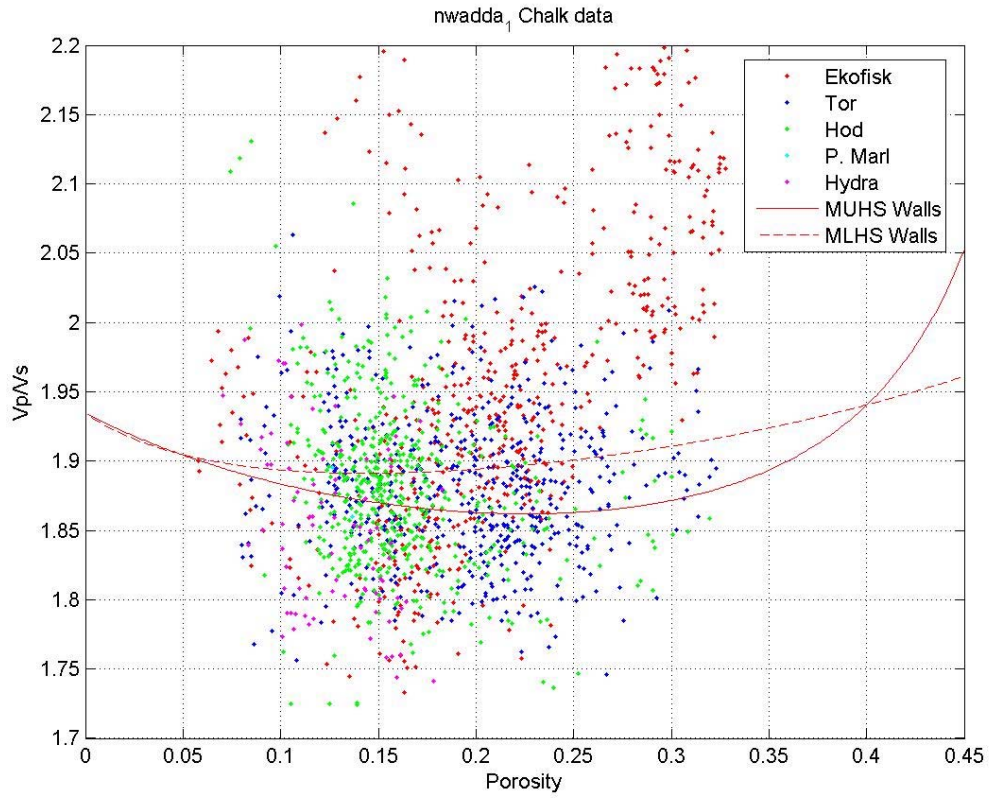
Jette-1



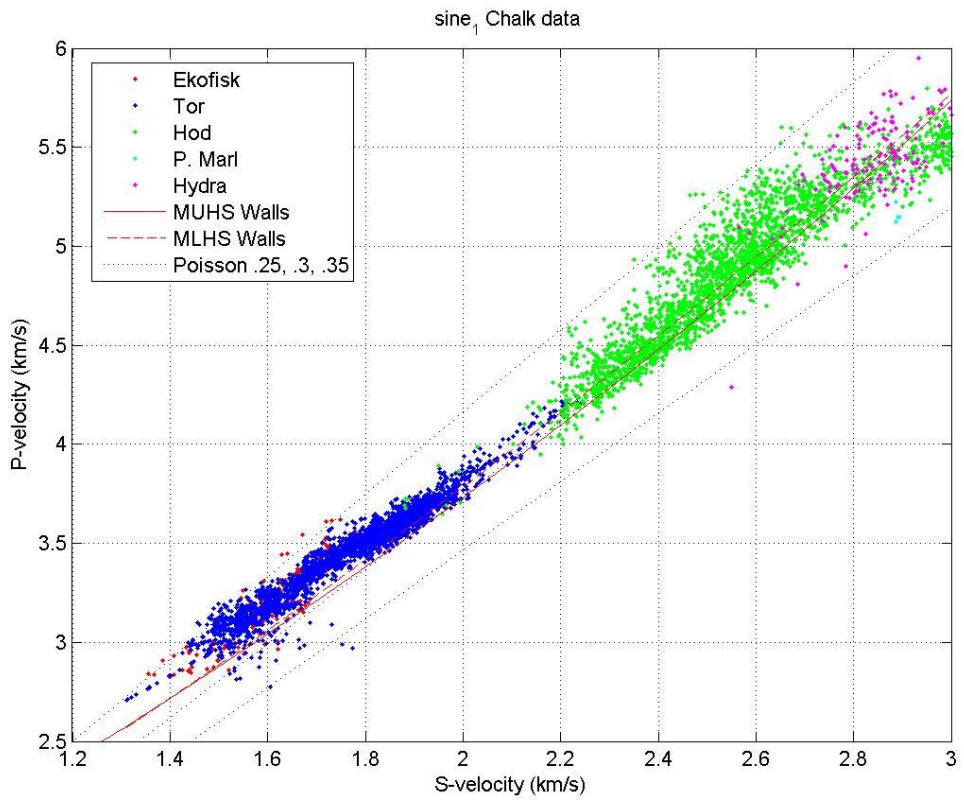
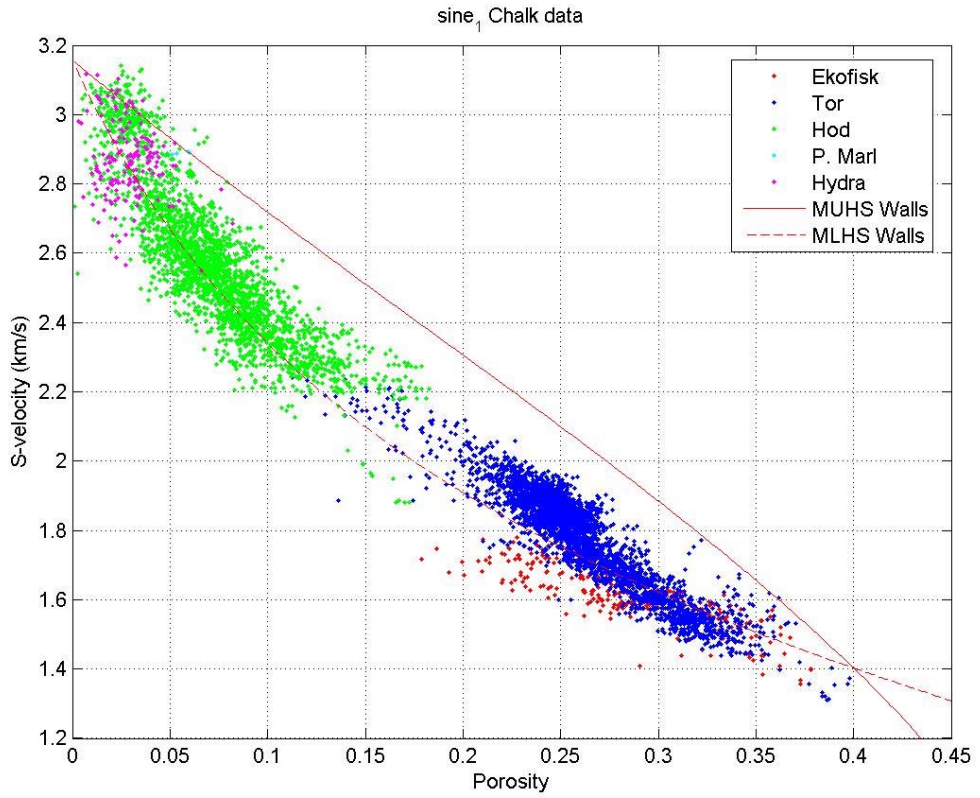
Jette-1



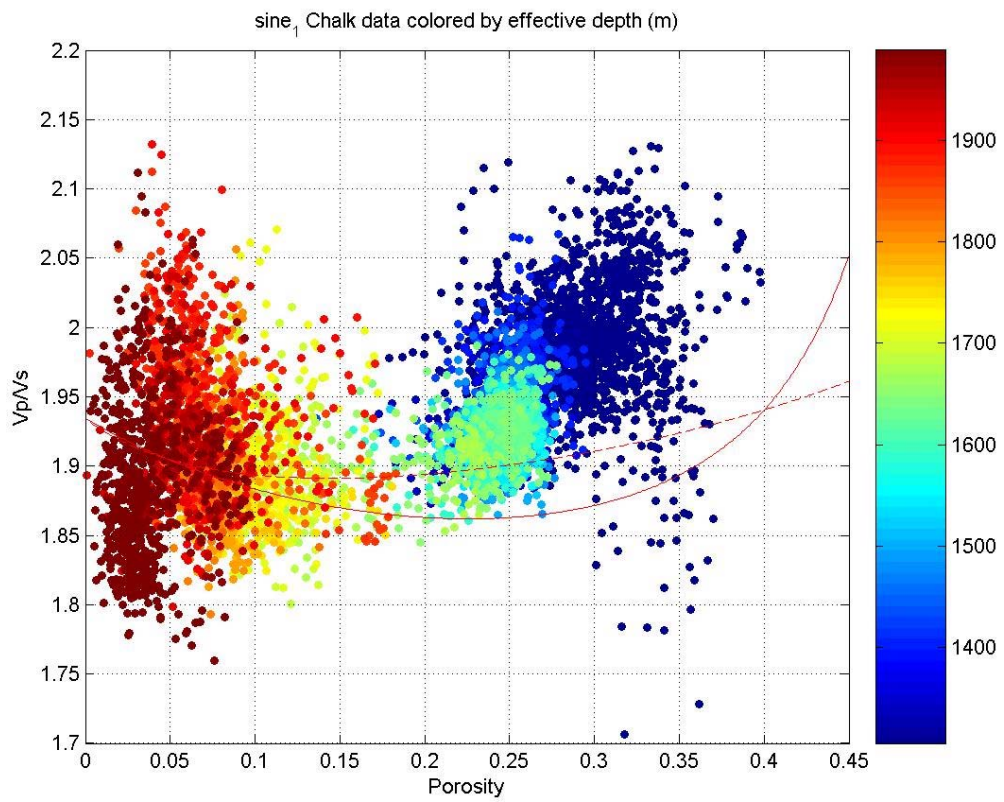
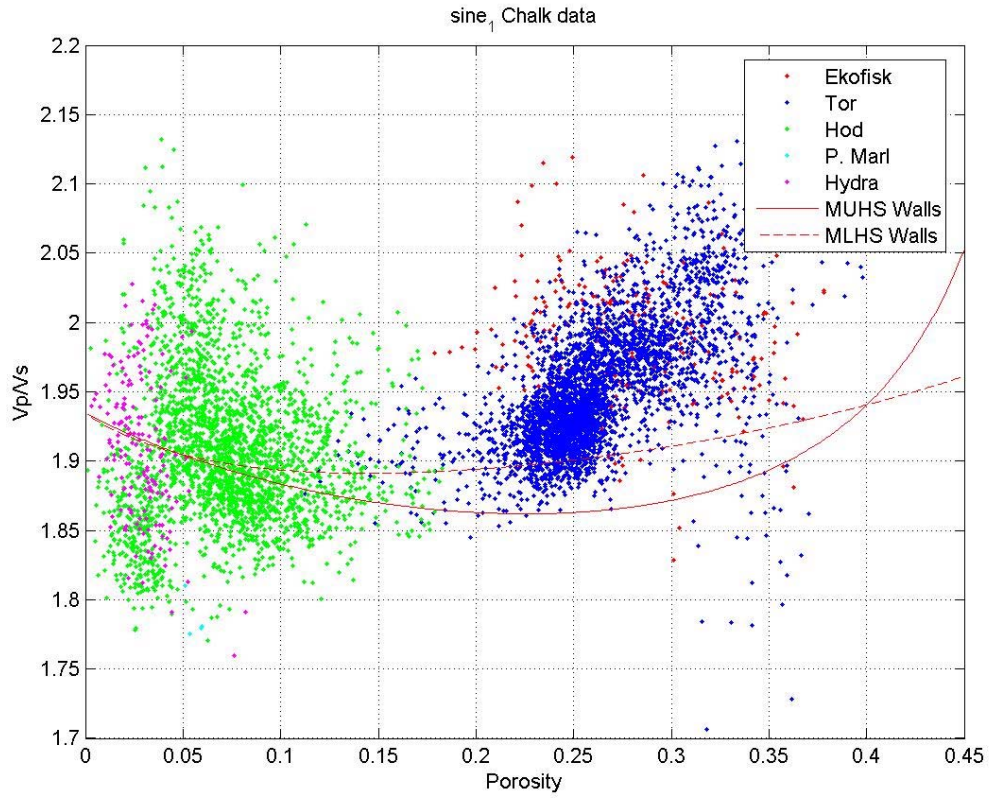
NW Adda-1



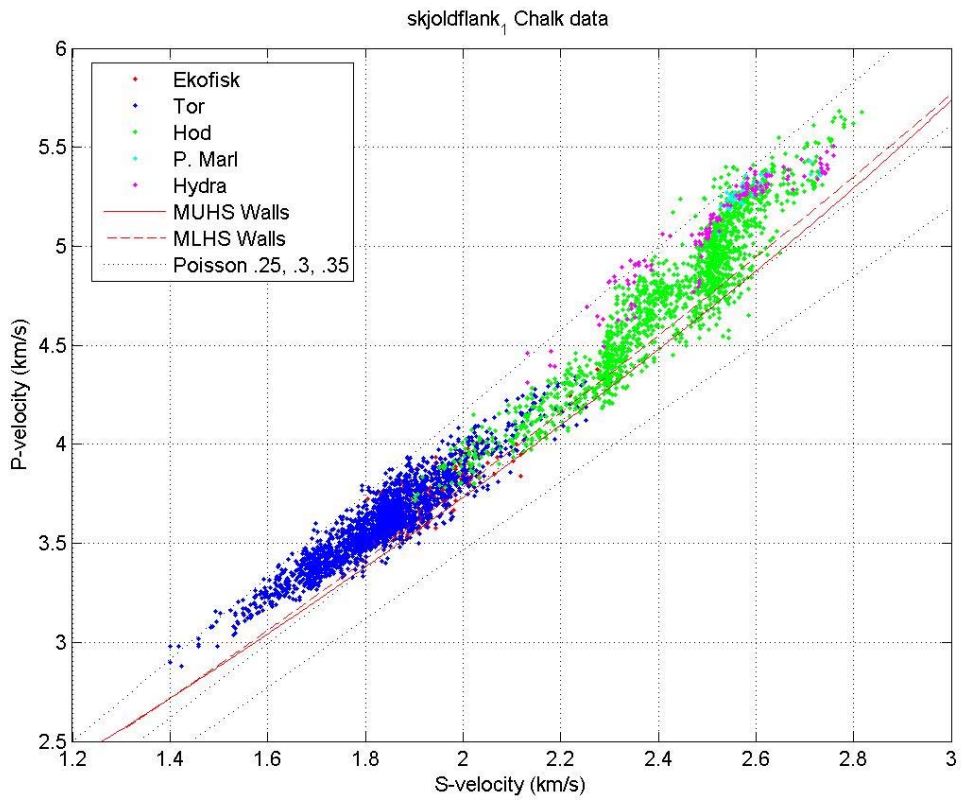
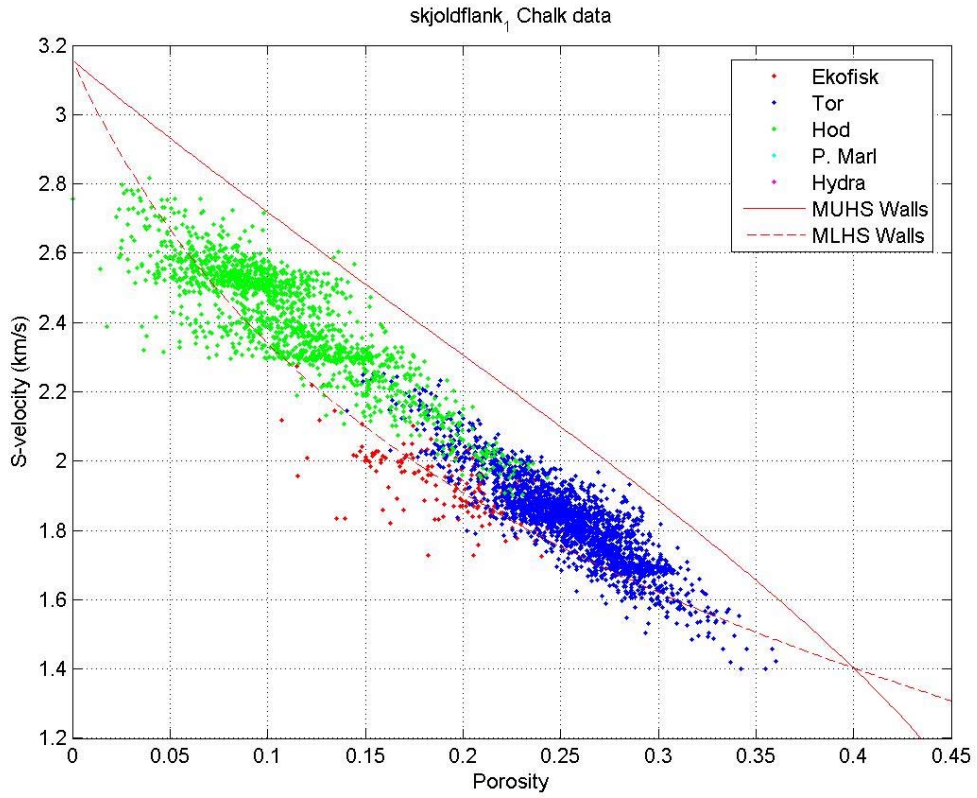
NW Ada-1



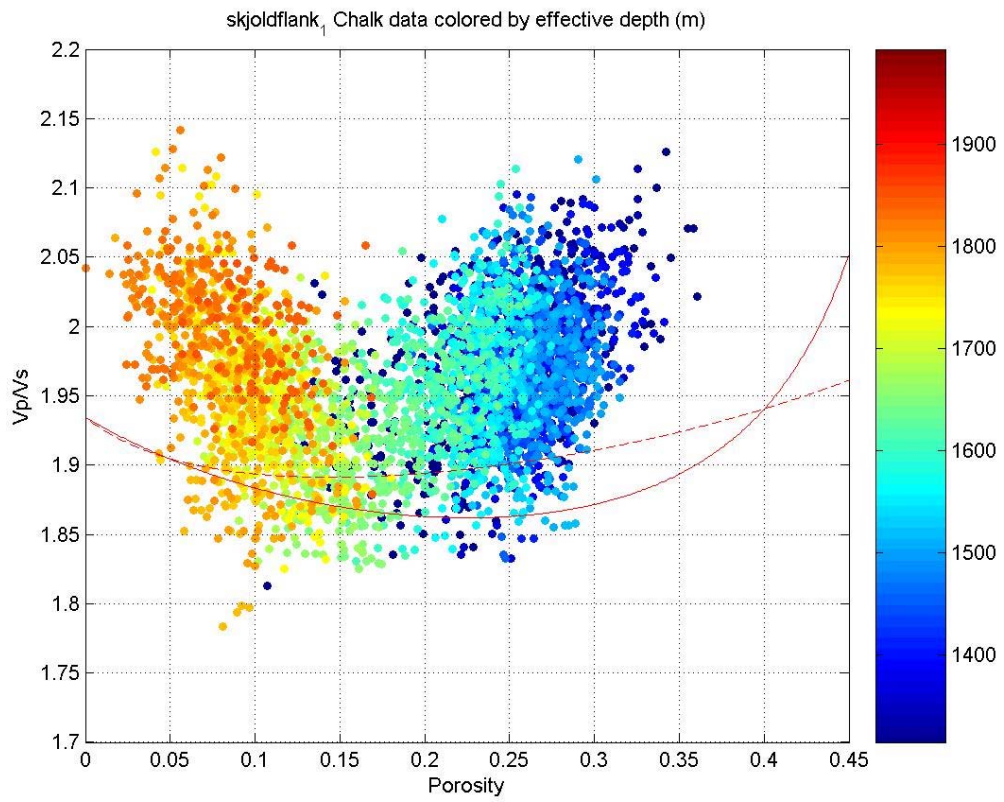
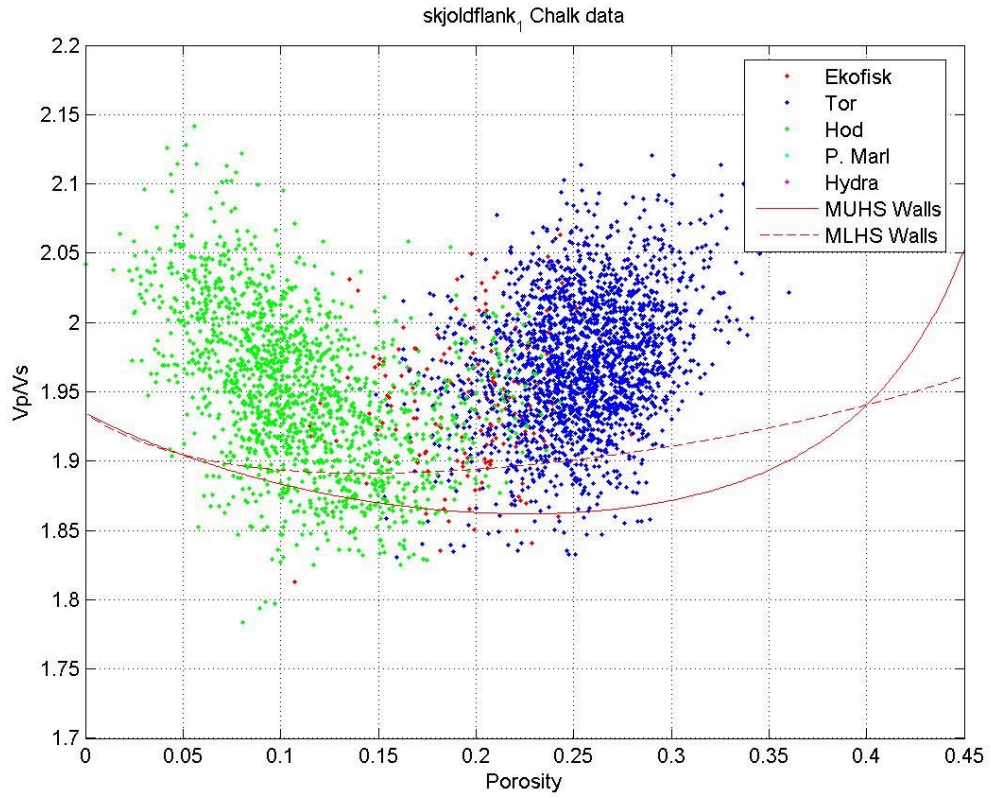
Sine-1



Sine-1



Skjold Flank-1



Skjold Flank-1

Special Core Analysis for Chalk Background Velocity Project

Ultrasonic velocity measurements on plug samples
of chalk from the wells Q-1, Otto-1, T-3, Gert-1,
West Lulu-1, Baron-2, I-1 and Cecilie-1B

Dan Olsen



Special Core Analysis for Chalk Background Velocity Project

Ultrasonic velocity measurements on plug samples
of chalk from the wells Q-1, Otto-1, T-3, Gert-1,
West Lulu-1, Baron-2, I-1 and Cecilie-1B

The Chalk Background Velocity Project
is funded by the South Arne Group

Dan Olsen

Contents

1. INTRODUCTION	2
2. SAMPLING AND ANALYTICAL PROCEDURE	3
2.1 SAMPLE MATERIAL	3
2.2 SAMPLE PREPARATION BEFORE ULTRASONIC MEASUREMENTS AND CONVENTIONAL CORE ANALYSIS	4
2.3 ULTRASONIC MEASUREMENTS OF HUMIDITY DRIED SAMPLES	5
2.4 ULTRASONIC MEASUREMENTS OF WATER SATURATED SAMPLES	6
2.5 PORE VOLUME REDUCTION AND LENGTH REDUCTION	8
2.6 PROCEDURE FOR THE ULTRASONIC MEASUREMENTS	9
2.7 CALIBRATION OF ULTRASONIC MEASUREMENTS	9
2.8 ANALYSIS OF THE ULTRASONIC SIGNAL	10
2.9 PRECISION AND REPRODUCIBILITY OF ULTRASONIC DATA	10
1. Precision evaluation of the actual analytical data for each sample	10
2. Measurements on standard Alu6061	11
3. Reproducibility of measurements on Rigs-1 samples	11
4. Reproducibility of measurements within the present work	12
Summary of precision and reproducibility	12
3. FLOW CHART OF THE ANALYTICAL PROCEDURE	13
4. ANALYTICAL METHODS	14
4.1 GAS PERMEABILITY	14
4.2 HE-POROSITY AND GRAIN DENSITY	14
4.3 PRECISION OF CONVENTIONAL CORE ANALYSIS DATA	14
4.4 ULTRASONIC MEASUREMENTS	14
4.5 THE ARRIVAL PICKER PROGRAM	15
Picking the arrival of the ultrasonic signal	16
The global uncertainty:	16
The local uncertainty (Error-band):	16
Amplitude at pick	16
5. RESULTS OF THE ULTRASONIC MEASUREMENTS	17
6. DOCUMENTATION OF DATA	28
7. REFERENCES	29
APPENDIX 1. BASIC DATA, RESULTS, AND PRECISION	30

1. Introduction

By request of Dr. Peter Japsen, GEUS on behalf of the Chalk Background Velocity Project (CBV Project), GEUS Core Laboratory has carried out conventional core analysis on 32 1.5" plug samples from 8 wells in the Danish Central Graben area. After conventional core analysis ultrasonic velocity determination was performed on a subset of 20 samples.

The analytical programme was specified by Dr. Peter Japsen and contained the following services:

- Conventional core analysis: gas permeability, He-porosity, and grain density.
- P and S velocities measured at reservoir overburden pressure on dry samples equilibrated at controlled humidity. All samples were measured at a hydrostatic confining pressure of 75 bar, and two samples, one from Gert-1 and one from Cecilie-1B, were also measured at hydrostatic confining pressures of 125 and 200 bar.
- P and S velocities measured on water saturated plugs at reservoir overburden pressure. All samples were measured at a hydrostatic confining pressure of 75 bar.

The measurements were conducted in the period from March 8th to June 30th 2004.

Presentations of preliminary results was given for the Chalk Background Velocity Project on 25th May 2004, 9th August 2004, and 29th September 2004.

The Chalk Background Velocity Project is funded by the Syd Arne Group.

2. Sampling and analytical procedure

2.1 Sample material

Thirty-two (32) new 1.5" plug samples of chalk were taken at the start of the project. A total of eight wells

Table 2.1. Basic sample data and conventional core analysis results.

Sample id.	Well id.	Depth	Formation or unit	Gas perm (mD)	Porosity (%)	Gr. dns. (g/ml)	Length (mm)	Diameter (mm)	Selected for sonic meas.
1	Q-1	10125.25 ft	Ekofisk ²⁾	0.003	14.35	2.721	38.43	37.62	+
2	Q-1	10132.50 ft	Ekofisk ²⁾	0.002	8.97	2.724	38.23	37.59	+
3	Q-1	10138.08 ft	Ekofisk ²⁾	0.018	14.43	2.720	38.18	37.70	+
4	Q-1	10147.25 ft	Ekofisk ²⁾	0.009	9.91	2.706	39.41	37.58	+
5	Otto-1	8473.84 ft	Tor ²⁾	0.43	19.06	2.720	40.39	37.61	
6	Otto-1	8495.00 ft	Hod ²⁾	0.33	19.23	2.716	38.68	37.59	+
7	Otto-1	8497.00 ft	Hod ²⁾	4.4	21.96	2.717	39.71	37.58	
8	Otto-1	8504.00 ft	Hod ²⁾	0.52	20.72	2.720	39.44	37.60	+
9	T-3	8440.33 ft	Tor ²⁾	0.42	19.10	2.718	38.38	37.57	+
10	T-3	8526.75 ft	Tor ²⁾	0.86	24.77	2.717	39.31	37.56	+
11	T-3	8532.08 ft	Tor ²⁾	0.77	24.69	2.717	39.24	37.50	
12	T-3	8568.33 ft	Tor ²⁾	1.62	24.24	2.719	31.05	37.58	
13	Gert-1	12838.90 ft	Hidra ²⁾	0.009	11.28	2.680	37.68	37.63	+
14	Gert-1	12846.42 ft	Hidra ²⁾	0.003	6.85	2.706	35.79	37.63	+
15	Gert-1	12854.50 ft	Hidra ²⁾	0.005	3.92	2.699	39.67	37.62	
16	Gert-1	12858.58 ft	Hidra ²⁾	0.005	3.70	2.698	35.80	37.59	+
17	West Lulu-1	11159.51 ft	Hod ²⁾	0.002	6.32	2.726	35.91	37.64	+
18	West Lulu-1	11187.33 ft	Hod ²⁾	0.003	6.68	2.724	38.49	37.59	
19	West Lulu-1	11213.33 ft	Hod ²⁾	0.004	8.01	2.723	37.94	37.63	+
20	West Lulu-1	11246.42 ft	Hod ²⁾	0.003	7.11	2.724	41.14	37.64	
21	Baron-2	2855.55 m	Ekofisk ²⁾	0.17	26.90	2.706	40.56	37.50	+
22	Baron-2	2858.55 m	Ekofisk ²⁾	0.057	24.69	2.708	39.30	37.56	+
23	Baron-2	2860.48 m	Ekofisk ²⁾	0.047	16.68	2.698	38.20	37.62	+
24	Baron-2	2867.03 m	Ekofisk ²⁾	0.070	21.87	2.704	35.53	37.55	+
25	I-1	9504.00 ft	Sola ¹⁾	0.056	24.80	2.701	33.01	37.58	
26	I-1	9508.50 ft	Tuxen ¹⁾	0.075	26.73	2.696	39.42	37.57	+
27	I-1	9523.90 ft	Tuxen ¹⁾	0.016	17.43	2.735	30.10	37.51	
28	I-1	9538.50 ft	Tuxen ¹⁾	0.019	16.95	2.716	21.75	37.55	
29	Cecilie-1B	2393.81 m	Våle ²⁾	- ³⁾	12.29	2.712	26.72	37.60	
30	Cecilie-1B	2402.61 m	Ekofisk ²⁾	0.011	14.90	2.709	34.18	37.60	
31	Cecilie-1B	2407.50 m	Ekofisk ²⁾	0.41	22.36	2.710	36.58	37.57	+
32	Cecilie-1B	2420.76 m	Ekofisk ²⁾	0.002	7.21	2.705	38.49	37.62	+

1) From Nielsen & Japsen (1991).

2) From Jakobsen (2004).

3) Measurement not possible – plug damaged.

were sampled with four plugs from each well. Table 2.1 presents the sample numbers, wells, and sample depths.

2.2 Sample preparation before ultrasonic measurements and conventional core analysis

The samples were cleaned in Soxhlet extractors by refluxing in turn with methanol and toluene. Then the plugs were trimmed to a length of approximately 1.5" and dried at 60 °C. They were stored in a desiccator until conventional core analysis.

All the samples underwent conventional core analysis with measurement of gas permeability, He-porosity, and grain density. Results are given in Table 2.1. Refer to Chapter 4 for a description of the conventional core analysis methods.

A subset of 20 plug samples was selected from the initial set of 32 plugs. The selected samples are indicated in

Table 2.2. Water saturation of samples at time of ultrasonic measurement in humidity dried state.

Sample id.	Weight at He-por determ. (g)	Bulk vol. at He-por determ. (ml)	Helium porosity (%)	Pore vol. at He-por determ. (ml)	Weight at sonic meas. in humidity dry state (g)	Weight increase in humidity dry state (g)	Sw at sonic meas. in humidity dry state (%)
1	99.77	42.81	14.35	6.14	100.17	0.40	6.5
2	105.61	42.60	8.97	3.82	106.13	0.52	13.6
3	98.81	42.71	14.43	6.16	99.12	0.31	5.0
4	107.41	44.04	9.91	4.36	107.60	0.19	4.4
6	94.68	43.15	19.23	8.30	94.74	0.06	0.7
8	94.72	43.91	20.72	9.10	94.77	0.05	0.6
9	93.99	42.74	19.10	8.16	94.05	0.06	0.7
10	89.40	43.73	24.77	10.83	89.44	0.04	0.4
13	99.67	41.90	11.28	4.73	99.84	0.17	3.6
14	100.66	39.94	6.85	2.74	100.96	0.30	11.2
16	102.25	39.83	4.86	1.94	102.61	0.36	18.6
17	102.16	40.00	6.32	2.53	102.31	0.15	5.9
19	105.99	42.30	8.01	3.39	106.18	0.19	5.6
21	88.63	44.80	26.90	12.05	88.82	0.19	1.6
22	89.17	43.72	24.69	10.79	89.43	0.26	2.4
23	95.84	42.64	16.68	7.11	96.08	0.24	3.4
24	83.43	39.49	21.87	8.64	83.71	0.28	3.2
26	86.49	43.77	26.73	11.70	86.73	0.24	2.1
31	85.63	40.69	22.36	9.10	85.57	-0.06	-0.7
32	107.83	42.96	7.21	3.10	108.27	0.44	14.2
Rigs213	60.31	27.91	20.43	5.70	60.32	0.01	0.2
Rigs220	57.47	31.11	31.66	9.85	n.a.	n.a.	n.a.

n.a. = Not analyzed

Weight, porosity, and bulk volume of sample Rigs1-213 from Høier (2002) Table 2.2

Weight, porosity, and bulk volume of sample Rigs1-220 from Høier (2000) Tables 2.1 and 2.2

the last column of Table 2.1. Further work was restricted to this subset of 20 plugs. Two samples from well Rigs-1 identified as Rigs213 and Rigs220 also measured by Høier (2000, 2002) were included for quality control purposes.

2.3 Ultrasonic measurements of humidity dried samples

After conventional core analysis the samples were placed in a humidity-controlled oven at 60 °C and 40 % relative humidity until weight measurements showed that an equilibrium state was established. Table 2.2 presents the equilibrium weights and the water saturations calculated from these weights. The uncertainty, ΔS , of the water saturation values is dependent i.a. on the porosity of the sample. An empirical estimate is given as

$$\Delta S \sim 15 / \Phi \quad \text{Eq. 2-1}$$

where Δ and Φ are in percent units (p.u.).

The water saturation values show a considerable scatter, ranging from zero to 19 %. The highest water saturation values tend to occur with the low porosity samples.

The humidity dried samples were mounted in a modified AutoLab 500 Ultrasonic core holder (New England Research) and the ultrasonic transit times were measured with a Tektronix Model TDS3012 2-channel digital phosphor oscilloscope connected to a PAR spike-generator. The ultrasonic transducers have centre frequencies at 700 kHz.

P- and S-waves were measured on the humidity-dried plugs at 75 bar hydrostatic confining pressure. Confining pressure was controlled with a Quizix SP-5400 high-pressure pump system. The confining pressure was initially increased to 20 bar in 5 minutes to secure a good seal of the confining rubber sleeve. Pressure was subsequently increased from 20 to 75 bar in 30 minutes, and the sample allowed to equilibrate at 75 bar for 30 minutes before measurement of the ultrasonic P- and S-signals. The ultrasonic data were saved digitally for later analysis. When unloading the core holder, the confining pressure was decreased continually from 75 to 0 bar during a time period of 30 minutes. A time schedule for the analysis is given in Table 2.3.

Table 2.3. Time schedule for ultrasonic measurements at hydrostatic confining pressure 75 bar on samples in humidity dried state.

Step no. Description	Cumulate time hh:mm
1 Mount sample in core holder	00:15
2 Increase pressure to 10 bar in 5 min	00:20
3 Increase pressure to 75 bar in 30 min	00:50
4 Equilibration at 75 bar for 30 minutes	01:20
5 Measure ultrasonic velocity at 75 bar	01:35
6 Decrease pressure to 0 bar in 20 min	01:55
7 Dismount sample	02:10

Table 2.4. Time schedule for ultrasonic measurements on samples 13 and 31: Measurement at three pressure steps, 75 bar, 125 bar, and 200 bar.

Step no. Description	Cumulate time hh:mm
1 Mount sample in core holder	00:15
2 Increase pressure to 10 bar in 5 min	00:20
3 Increase pressure to 75 bar in 30 min	00:50
4 Equilibration at 75 bar for 30 minutes	01:20
5 Measure ultrasonic velocity at 75 bar	01:35
6 Increase pressure to 125 bar in 30 minutes	02:05
7 Equilibration at 125 bar for 30 minutes	02:35
8 Measure ultrasonic velocity at 125 bar	02:50
9 Increase pressure to 200 bar in 30 minutes	03:20
10 Equilibration at 200 bar for 30 minutes	03:50
11 Measure ultrasonic velocity at 200 bar	04:05
12 Decrease pressure to 0 bar in 20 min	04:25
13 Dismount sample	04:40

Two of the samples, with identifications 13 and 31, were measured with an extended analytical programme that included ultrasonic measurements at the confining pressure steps 75, 125, and 200 bar (Table 2.4).

Ultrasonic repeat measurements were performed on a total of 9 samples.

Calibration of the ultrasonic measurements is described in Section 2.7, precision and reproducibility are described in Section 2.9, while the technique for analysing the ultrasonic signals are described in Sections 4.4 and 4.5.

2.4 Ultrasonic measurements of water saturated samples

After ultrasonic measurement in humidity dried state, the samples were cleaned briefly in a Soxhlet with methanol, and were dried at 60 °C.

Table 2.5. Water saturation of samples at time of ultrasonic measurement in $S_w = 100\%$ state.

Sample id.	Weight at He-por determ. (g)	Bulk vol. at He-por determ. (ml)	Helium porosity (%)	Pore vol. at He-por determ. (ml)	Weight at sonic meas. in $S_w=100\%$ state (g)	Weight increase in $S_w=100\%$ state (g)	S_w at sonic meas. in $S_w=100\%$ state (%)	Water vol. minus PV in $S_w=100\%$ state (ml)
1	99.77	42.81	14.35	6.14	105.95	6.18	100.8	-0.05
2	105.61	42.60	8.97	3.82	109.64	4.03	105.7	-0.22
3	98.81	42.71	14.43	6.16	104.81	6.00	97.5	0.15
4	107.41	44.04	9.91	4.36	111.57	4.16	95.5	0.20
6	94.68	43.15	19.23	8.30	102.76	8.08	97.6	0.20
8	94.72	43.91	20.72	9.10	103.57	8.85	97.5	0.23
9	93.99	42.74	19.10	8.16	101.89	7.90	97.0	0.25
10	89.40	43.73	24.77	10.83	99.94	10.54	97.5	0.27
13	99.67	41.90	11.28	4.73	104.21	4.54	96.3	0.18
14	100.66	39.94	6.85	2.74	103.26	2.61	95.4	0.13
16	102.25	39.83	4.86	1.94	104.22	1.97	102.0	-0.04
17	102.16	40.00	6.32	2.53	104.42	2.26	89.6	0.26
19	105.99	42.30	8.01	3.39	109.15	3.16	93.5	0.22
21	88.63	44.80	26.90	12.05	100.48	11.85	98.5	0.18
22	89.17	43.72	24.69	10.79	99.86	10.69	99.2	0.08
23	95.84	42.64	16.68	7.11	102.77	6.93	97.6	0.17
24	83.43	39.49	21.87	8.64	91.80	8.37	97.1	0.25
26	86.49	43.77	26.73	11.70	98.12	11.63	99.6	0.05
31	85.63	40.69	22.36	9.10	94.76	9.13	100.5	-0.05
32	107.83	42.96	7.21	3.10	110.74	2.91	94.1	0.18
Rigs213	60.31	27.91	20.43	5.70	65.82	5.51	96.8	0.18
Rigs220	57.47	31.11	31.66	9.85	67.17	9.70	98.7	0.13

n.a. = Not analyzed

Weight, porosity, and bulk volume of sample Rigs1-213 from Høier (2002) Table 2.2

Weight, porosity, and bulk volume of sample Rigs1-220 from Høier (2000) Tables 2.1 and 2.2

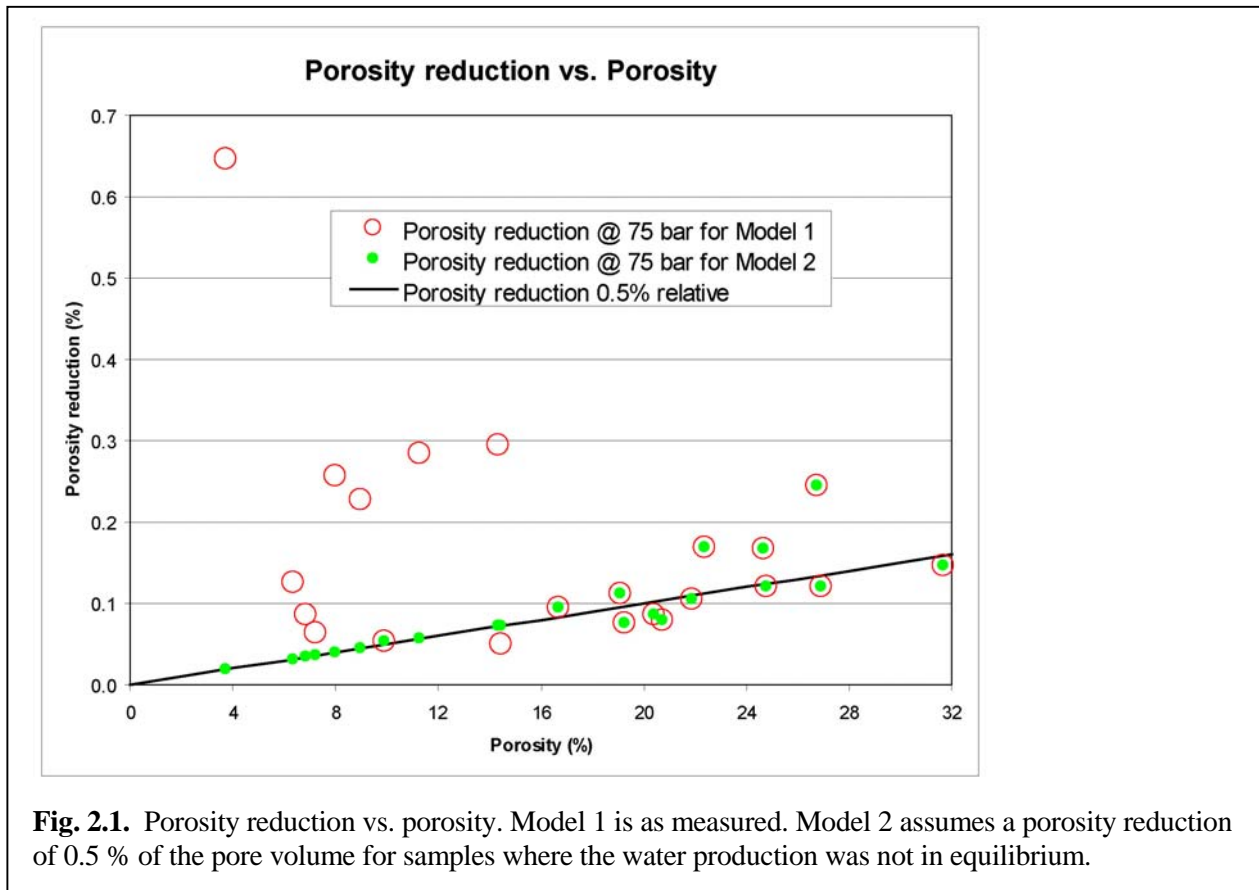
The samples were saturated with water by a vacuum/pressure saturation procedure, which included vacuum saturation for one day followed by pressure saturation at 100 bar for 2 days. The samples were weighed before and after the saturation procedure and Table 2.5 presents the calculated water saturations. The calculated deviation from a fully saturated state, i.e. $S_w=100\%$, may be given as the difference between the calculated water volume and the calculated pore volume of the sample. This value is given as the column *Water vol. minus PV in $S_w=100\%$ state* of Table 2.5. The mean value is 0.17 ml with a maximum of 0.27 ml. These values seem to be a reasonable representation of the combined uncertainties of the He-porosity, bulk volume, wet weight, and dry weight determinations. It is concluded that within the uncertainty the samples were fully saturated with water.

Table 2.6. Time schedule for ultrasonic measurements at hydrostatic confining pressure 75 bar on samples in water saturated state $S_w=100\%$.

Step no.	Description	Cumulative time hh:mm
1	Mount sample in core holder	00:15
2	Increase pressure to 20 bar in 5 min	00:20
3	Equilibration at 20 bar for 60 minutes	01:20
4	Increase pressure to 75 bar in 30 min	01:50
5	Equilibration at 75 bar for 30 minutes	02:20
6	Measure ultrasonic velocity at 75 bar	02:35
7	Decrease pressure to 0 bar in 20 min	02:55
8	Dismount sample	03:10

The water used for saturation of the samples was tap water equilibrated with crushed chalk and filtered.

The procedure for ultrasonic measurement of the samples in water saturated state was similar to the measurements in humidity dried state (Table 2.3) except that an equilibration period was added at a confining pressure of 20 bar. A time schedule for the analysis is given in Table 2.6.



2.5 Pore volume reduction and length reduction

During measurement of samples in water saturated state, the outlet from the ultrasonic core holder was connected with a Mettler balance and the production of water was continuously logged. From the water production data two models for the pore volume reduction were established.

Model 1 assumes that the amount of produced water, W_w corresponds to the pore volume reduction, ΔPV

$$\Delta PV = W_w / \rho_w \quad \text{Eq. 2-2}$$

where ρ_w is the water density. Model 1 is presented in Fig. 2.1 and it is evident that most of the low porosity samples show aberrant high porosity reduction values. Plotting the water production versus time reveals that for a number of samples the water production had not ceased when the ultrasonic measurement was conducted. Clearly, the water production had not reached equilibrium. On mounting a sample in the ultrasonic core holder an amount of water is inevitably trapped between the sample and the end fittings and sleeve. For samples with reasonable permeability this water escapes during the 60 minutes equilibration at 20 bar (Table 2.6), but for samples with very low permeability the production of this water continued during the whole measurement and spoiled the porosity reduction determination.

Model 2 then assumes the same expression as Model 1 for the samples that had reached equilibrium at the time of ultrasonic measurement (Eq. 2-2) but for the disequilibrium samples assumes

$$\Delta PV = PV * 0.005 \quad \text{Eq. 2-3}$$

Table 2.7. Calculated porosity reduction and length reduction at a confining pressure of 75 bar

Sample id.	State of fluid production	Gas perm. (mD)	Measured porosity (%)	Porosity reduction (%)	Reduced porosity (%)	Measured length (mm)	Length reduction (mm)	Reduced length (mm)
1	No equilibrium	0.003	14.35	0.07	14.28	38.38	0.01	38.37
2	No equilibrium	0.002	8.97	0.04	8.93	38.34	0.01	38.33
3	No equilibrium	0.018	14.43	0.07	14.36	38.34	0.01	38.33
4	Equilib. OK	0.009	9.91	0.05	9.86	39.41	0.01	39.40
6	Equilib. OK	0.33	19.23	0.08	19.15	38.63	0.01	38.62
8	Equilib. OK	0.52	20.72	0.08	20.64	39.39	0.01	39.38
9	Equilib. OK	0.42	19.10	0.11	18.99	38.40	0.01	38.39
10	Equilib. OK	0.86	24.77	0.12	24.65	39.40	0.02	39.38
13	No equilibrium	0.009	11.28	0.06	11.22	37.62	0.01	37.61
14	No equilibrium	0.003	6.85	0.03	6.82	35.86	0.00	35.86
16	No equilibrium	0.005	3.70	0.02	3.68	35.72	0.00	35.72
17	No equilibrium	0.002	6.32	0.03	6.29	35.76	0.00	35.76
19	No equilibrium	0.004	8.01	0.04	7.97	37.90	0.01	37.89
21	Equilib. OK	0.17	26.90	0.12	26.78	40.55	0.02	40.53
22	Equilib. OK	0.06	24.69	0.17	24.52	39.33	0.02	39.31
23	Equilib. OK	0.05	16.68	0.09	16.59	38.22	0.01	38.21
24	Equilib. OK	0.07	21.87	0.11	21.76	35.63	0.01	35.62
26	Equilib. OK	0.08	26.73	0.24	26.49	39.42	0.03	39.39
31	Equilib. OK	0.41	22.36	0.17	22.19	36.64	0.02	36.62
32	No equilibrium	0.002	7.21	0.04	7.17	38.49	0.00	38.49
Rigs213	Equilib. OK	0.3	20.43	0.09	20.34	24.76	0.01	24.75
Rigs220	Equilib. OK	1.25	31.66	0.15	31.51	27.88	0.01	27.87

i.e. the pore volume reduction is calculated as a fixed percentage, 0.5 %, of the pore volume. Model 2 completely removed the aberrant porosity reduction values of Model 1, cf. Fig. 2.1, and is thus adopted in this work. Table 2.7 reports the equilibrium state judged from the Mettler log, the measured He-porosity values and the calculated reduced porosity values.

The length of a sample is important for the calculation of the ultrasonic velocity. A model for calculation of the reduction in sample length, ΔL , is applied that assumes isotropic contraction of the pore volume without any change to the grain volume:

$$\Delta L = L \left(1 - \sqrt[3]{1 - \Delta\Phi} \right) \quad \text{Eq. 2-4}$$

where L is the length of the sample and $\Delta\Phi$ is the porosity reduction. Table 2.7 reports lengths measured without confining pressure at the time of humidity equilibration, and the reduced lengths according to Eq. 2-4. The reduced lengths of Table 2.7 are used for all ultrasonic velocity calculations.

2.6 Procedure for the ultrasonic measurements

A plug sample was mounted in an ultrasonic core holder with an ultrasonic transmitter at one end and an ultrasonic receiver at the other end. A rubber sleeve was mounted around the cylinder surface to isolate the plug sample from the hydrostatic pressure medium. The ultrasonic equipment is described in more detail in Chapter 4 Analytical methods. Contact paste was not used. Hydrostatic pressure was applied to the sample with a Quizix SP-5400 high-pressure pump system. Except for the initial pressure build-up, which must take place fairly rapidly to ensure a good seal of the rubber sleeve, all pressure changes were applied with the pressure ramping facility of the Quizix pump system, which provides a linear evolution of pressure vs. time. Time schedules for the pressurisation are given in Tables 2.3, 2.4, and 2.6.

If a water saturated sample was going to be measured, the outlet of the core holder was connected to a cuvette placed on a Mettler balance and data logging of the balance was started. This allowed quantification of the fluid production during sample pressurization and ultrasonic measurement and thus enabled determination of the pore volume reduction, and sample length reduction.

The temperature in the laboratory during the ultrasonic measurements was 23 ± 2 °C.

The P- and S-wave data were saved digitally in csv-format for later analysis. Screen-dumps from the oscilloscope were saved in tif-format. Cf. Chapter 6 for data documentation.

A number of repeat measurements were performed. These measurements are indicated in Tables A.1 to A.6 with a "_ch" attached to the sample identification. At repeat measurements care was taken to assure that the S1 and S2 directions were the same as in the original measurements. S1 and S2 velocity determinations are thus comparable.

2.7 Calibration of ultrasonic measurements

The AutoLab 500 Ultrasonic core holder has an inherent system delay, mainly due to the time required for the ultrasonic signal to travel through the ultrasonic transmitter and receiver units. It is determined by calculating a 4-point linear regression on 4 calibration standards of different lengths and constant ultrasonic velocity. Three of the calibration standards (Alu1, Alu2, and Alu3) are aluminium plug samples of known length; the fourth calibration standard is a configuration where the ultrasonic transducers are mounted head-to-head, i.e. with a sample length of zero. A total of four calibrations were performed during the present work. The system delays are listed in Table 2.8 and the correlation coefficients for the associated linear regressions are listed in Table 2.9. Cf. Chapter 6 for documentation of the full ultrasonic calibration.

2.8 Analysis of the ultrasonic signal

Analysis of the ultrasonic signal was done by the program *firstarrival* made by Ødegaard A/S that determines the arrival of the ultrasonic wave train from a table of amplitude versus time in a csv-file. Refer to Chapter 4 Analytical methods for a thorough description.

2.9 Precision and reproducibility of ultrasonic data

The precision of the ultrasonic results may be assessed from 1) precision evaluation of the actual analytical data for each sample and 2) measurements on secondary standard Alu6061. The reproducibility of the ultrasonic results may be assessed from 3) repeat measurements of two samples, Rigs213 and Rigs220, that were measured in an earlier study, and 4) repeat measurements within the present study.

1. Precision evaluation of the actual analytical data for each sample

The precision of the ultrasonic measurements may be assessed from the precision parameters reported by the program *firstarrival* and an estimate of the uncertainty of the plug length determination. Precision estimates for all measurements are presented in Tables A.1 to A.6 of Appendix 1. The uncertainty of the plug length is estimated to be 0.1 mm for all samples and this leads to the error given in the column “Error on velocity from length”. The *firstarrival* parameter "Global uncertainty", i.e. the precision of picking the right signal is listed in column “Global uncertainty”. The risk of picking a wrong signal for the ultrasonic velocity calculation increases with the value of this parameter. When the parameter "Global uncertainty" exceeds approximately 0.5 a significant risk of picking a wrong signal is probably present. For most of the picks with high "Global uncertainty" values the *firstarrival* program was guided by the *forced pick* procedure, cf. Section 4.5 "The arrival picker program". The *firstarrival* parameter "Local uncertainty", i.e. the error due to signal noise is listed in column “Error on velocity from noise”. The column “Total error” is the sum of the errors “Error on velocity from length” and “Error on velocity from noise”.

The mean total error for all the 166 measurements of P, S1 and S2 ultrasonic velocities is 0.34 %, cf. Tables A.1 to A.6. Errors of this size mainly reflect the uncertainty of the plug length measurements. Only two errors exceeds 1.0 %, namely an error of 1.4 % for the measurements of S1 on sample 17 in the water saturated state, and an error of 1.1 % for the measurement of S2 on sample 32 also in the water saturated state.

The errors listed in Tables A.1 to A.6 do not include possible systematic errors or calibration inaccuracies and shall thus only be regarded as minimum errors.

Table 2.8 System delay at confining pressure 75 bar.

Calibration id.	P signal (us)	S1 signal (us)	S2 signal (us)
Calib. mar-04	12.7024	23.6636	24.2939
Calib. apr-04	12.7268	23.7072	24.3240
Calib. may-04	12.7319	23.7151	24.3447
Calib jun-04	12.7205	23.6536	24.3153

Table 2.9 Correlation coefficient R^2 for system delay regressions at confining pressure 75 bar.

Calibration id.	P signal	S1 signal	S2 signal
Calib. mar-04	0.9989	0.9998	0.9998
Calib. apr-04	0.9991	0.9998	0.9998
Calib may-04	0.9994	0.9997	0.9997
Calib jun-04	0.9990	0.9998	0.9998

Table 2.10 Measurements on standard Alu6061.

Calibration id.	Deviation		Deviation		Deviation	
	Ultrasonic P velocity (m/s)	from nominal P velocity (%)	Ultrasonic S1 velocity (m/s)	from nominal S velocity (%)	Ultrasonic S2 velocity (m/s)	from nominal S velocity (%)
Nominal value	6396.0		3125.0		3125.0	
Calib. mar-04	6417.7	0.34	3129.4	0.14	3124.0	-0.03
Calib. apr-04	6499.6	1.62	3121.4	-0.12	3121.7	-0.11
Calib. may-04	6428.6	0.51	3117.9	-0.23	3121.1	-0.12
Calib. jun-04	n.a.	n.a.	n.a.	n.a.	n.a.	n.a.

n.a. = Not analyzed

2. Measurements on standard Alu6061

Standard Alu6061 is a secondary standard of aluminium provided by New England Research.. It was measured three times during the work. The results are listed in Table 2.10 together with the nominal sonic velocities for the standard. The results indicate a mean error of 0.82 % for P measurements, and a mean error of 0.13 % for S1 and S2 measurements.

3. Reproducibility of measurements on Rigs-1 samples

To check the reproducibility of the ultrasonic measurements two samples that have previously been measured during the Rock Physics Project (RPP project, Høier, 2000; Høier, 2002) financed by the EFP-98 research programme were included in the test programme. The new and the old measurements are compared in Table 2.11. The S1 and S2 directions of the samples in the RPP measurements are not known, therefore, to be comparable the S1 and S2 velocities are averaged.

Table 2.11. Comparison of ultrasonic measurements on samples Rigs213 and Rigs220 from the Rock Physics Project (RRP) and from the present work..

Sample id.	Saturation state	Ultrasonic P velocity, RPP project (m/s)	Ultrasonic P velocity, this project (m/s)	Deviation (%)	Ultrasonic S velocity, RPP project (m/s)	Ultrasonic S velocity, this project (m/s)	Deviation (%)
Rigs213 ¹⁾	Air saturated	4296 ³⁾	4311.90	0.4	2597 ³⁾	2570.33	-1.0
Rigs213 ¹⁾	Water saturated	4437 ⁴⁾	4412.52	-0.6	2486 ⁴⁾	2481.35	-0.2
Rigs220 ²⁾	Water saturated	3335 ⁵⁾	3344.61	0.3	1825 ⁵⁾	1837.29	0.7

Note 1: In Høier (2002) this sample is identified as sample 213 from well Rigs-1.

Note 2: In Høier (2000) this sample is identified as sample 220 from well Rigs-1.

Note 3: From Høier (2002) Table 5.1.

Note 4: From Høier (2002) Table 5.2.

Note 5: From Høier (2002) Table 5.4.

Table 2.12. Mean deviation of repeat measurements within the present project. The number of samples for each mean is given in parenthesis.

	Mean deviation of P measurements	Mean deviation of S1 measurements	Mean deviation of S2 measurements
Humidity dried samples	1.1 % (N=9)	1.7 % (N=5)	1.6 % (N=5)
Water saturated samples	0.4 % (N=6)	0.6 % (N=3)	0.6 % (N=4)

The conditions of the ultrasonic measurements in Høier (2000, 2002) and the present project were similar, but not identical. All measurements were performed with a hydrostatic confining pressure of 75 bar. Høier (2002) used the program *firstarrival* to pick the arrival of the ultrasonic signals same as the present project. Høier (2002) also recalculated the data from Høier (2000) with *firstarrival* to make them more comparable to the later data. In Table 2.11 the recalculated values of Høier (2002) have been used for sample Rigs220.

Høier (2002) dried sample Rigs213 at 110 °C and then allowed it to equilibrate at room condition in the laboratory for 2 weeks. During ultrasonic measurement a water saturation of 1 % was calculated (Table 2.2. of Høier, 2002). The ultrasonic results are referred in Table 2.11 under the heading "Air saturated". The comparable measurement in the present project refers to the same sample dried at 60 °C and then equilibrated at the same temperature and a controlled humidity of 40 % relative humidity. During ultrasonic measurement a water saturation of 0.2 % was calculated, cf. Table 2.2.

The conditions for the water saturated samples during ultrasonic measurement were very similar. They were saturated with formation water prepared by the same procedure, and saturated by the same combined vacuum and pressure saturation procedure, cf. Section 2.4. For sample Rigs213 Høier (2002) reports a water saturation of 98 %, while this study reports a water saturation of 96.8 % (cf. Table 2.5). For sample Rigs220 Høier (2000) reports a water saturation of 100.1 %, while this study reports a water saturation of 98.7 % (cf. Table 2.5). The saturation states of the samples are thus very comparable.

Table 2.11 indicates a mean reproducibility of 0.4 % for the P velocities and 0.6 % for the S velocities. This is considered very satisfactory as the numbers include any velocity variations relating to changes caused by sample handling, cleaning etc. during the time interval from the measurements of Høier (2000, 2002) and the measurements of the present project.

4. Reproducibility of measurements within the present work

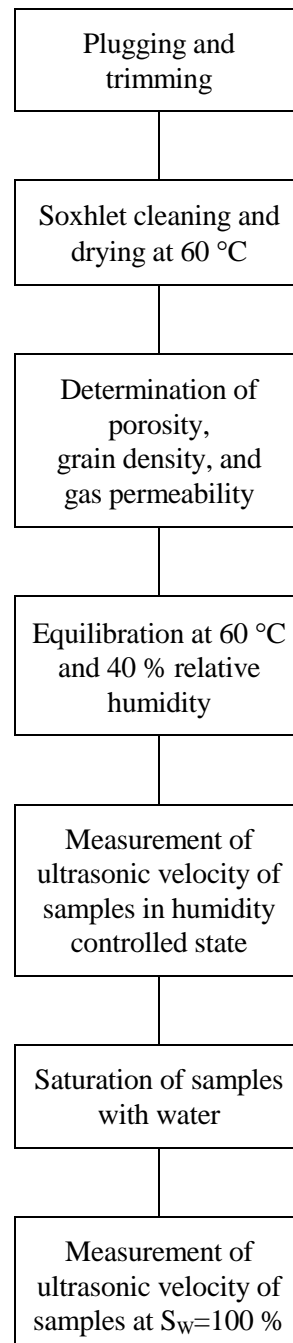
A total of 9 repeat measurements were performed on humidity dried samples, and a total of 6 repeat measurements were performed on water saturated samples. Table 2.12 summarises the results. The water saturated measurements is seen to have excellent reproducibility, while the humidity-dried measurements have much inferior reproducibility. This probably reflects the difficulty with controlling the saturation state of some of the humidity-dried samples.

The mean reproducibility for P determinations is generally 30 % better than for S determinations. This applies to both humidity dried samples and water saturated samples.

Summary of precision and reproducibility

Precision and reproducibility the ultrasonic velocity determinations are considered to be better than 1 %, except for some samples in humidity equilibrated state where precision and reproducibility may deteriorate to 2 %.

3. Flow chart of the analytical procedure



4. Analytical methods

The following is a short description of the methods used by GEUS Core Laboratory. For a more detailed description of methods, instrumentation and principles of calculation the reader is referred to API recommended practice for core analysis procedure (API RP 40, 1998).

4.1 Gas permeability

The plug is mounted in a Hassler core holder, and a confining pressure of 400 psi applied to the sleeve. The specific permeability to gas is measured by flowing nitrogen gas through a plug of known dimensions at differential pressures between 0 and 1 bar. No back pressure is applied. The readings of the digital gas permeameter are checked regularly by routine measurement of permeable steel reference plugs.

4.2 He-porosity and grain density

The porosity is measured on cleaned and dried samples. The porosity is determined by subtraction of the measured grain volume and the measured bulk volume. The Helium technique, employing Boyle's Law, is used for grain volume determination, applying a double chambered Helium porosimeter with digital readout, whereas bulk volume is measured by submersion of the plug in a mercury bath using Archimedes principle. Grain density is calculated from the grain volume measurement and the weight of the cleaned and dried sample.

4.3 Precision of conventional core analysis data

Table 4.1 gives the precision (= reproducibility) at the 68% level of confidence (+/- 1 standard deviation) for routine core analysis measurements performed at GEUS Core Laboratory.

Table 4.1. Precision of conventional core analysis data.

Measurement	Range, mD	Precision
Grain density		0.003 g/cc
Porosity		0.1 porosity-%
Gas Permeability	0.001-0.01	25%
	0.01-0.1	15%
	> 0.1	4%

4.4 Ultrasonic measurements

The transit time of P- and S-waves in a plug sample is measured by a Tektronix Model TDS3012 two-channel digital phosphor oscilloscope, connected to a spike-generator (PAR Scientific Instruments) and a modified AutoLab 500 Ultrasonic core holder from New England Research. The P- and S-wave transducers have nominal centre frequencies at 700 kHz.

The ultrasonic velocity, V , is calculated from the following equation.

$$V = \frac{L}{t_{transit} - t_{delay}} \dots\dots\dots \text{Eq. 4-1}$$

where L is the sample length, $t_{transit}$ is the measured total travel time, and t_{delay} is the system delay. The system delay is an inherent system property representing the time taken for the ultrasonic signal to travel through the transducers plus any delays caused by the electronics. One way to determine the system delay is by measuring the transit time of the system without any plugs. A more precise determination is obtained by measuring the transit time for a series of plugs with uniform velocity and known length. The system delay is then determined as the transit time at length zero as calculated by a linear regression. This principle is illustrated in Fig. 4.1. Depending on the task, GEUS uses either a series of three aluminium plugs of lengths 15, 25 and 36 mm or a series of three acrylic plugs of lengths 20, 35 and 50 mm for calibration. In addition a fourth data point is obtained for both series by including a measurement where the ultrasonic transducers are mounted head-on-head, equivalent to a plug of length zero.

The system is tested against a reference plug made from aluminium, Alu6061, with known P and S velocities, supplied by New England Research.

4.5 The arrival picker program

Whenever possible a program named *firstarrival* is used for determining the transit time of the ultrasonic signals. The program was developed by Ødegaard A/S. Compared to manual picking of the transit time the use of a computer program eliminates the subjectivity of manual picking, and objective information about precision becomes available. The input to the program consists of 1) a comma-separated file (csv-file) listing time and signal amplitude, 2) a search interval specifying the time interval to be searched, and 3) a parameter specifying whether a positive or a negative deflection from zero shall be picked.

firstarrival identifies the first amplitude extremum of the ultrasonic signal and determines the transit time, the amplitude and two uncertainty parameters, a global uncertainty and a local uncertainty, for the arrival event.

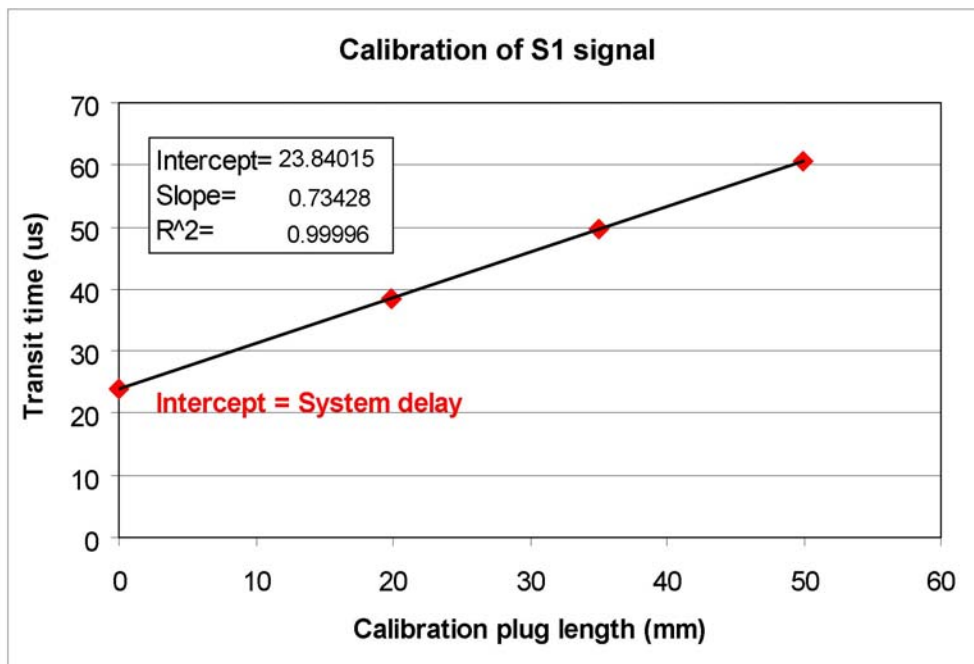


Fig. 4.1 Determination of the system delay from a regression on 4 data points.

The first amplitude extremum is used as the arrival event rather than the first deviation from the baseline because this causes the algorithm to be much more robust in case of noisy data. The difference between the two methods is negligible, because the same procedure is used for both calibration and sample measurements and because the width of signal peaks are nearly constant (being governed by the 700 kHz centre frequency).

On some occasions when the ultrasonic signal is very noisy the *firstarrival* program may pick a wrong signal peak and thus result in a wrong transit time. Or the program may fail to detect a signal peak at all. Therefore, the transit time determinations of the *firstarrival* program are always checked manually. In case they are deemed wrong it is first attempted to force *firstarrival* to pick the correct extremum by reducing the search interval – a procedure termed *forced picking*. If this procedure fails manual picking of the transit time is performed - a procedure termed *manual picking*. In case of forced picking objective information about precision is still available. In case of manual picking objective information about precision is not available.

The output from the *firstarrival* program consists of 1) a pick of the extremum identified as the arrival of the ultrasonic signal, 2) a global uncertainty parameter, 3) a local uncertainty parameter, and 4) an amplitude at the pick.

Picking the arrival of the ultrasonic signal

firstarrival looks for an event consisting of two consecutive local extrema with amplitudes of opposite sign. The search can be limited to a given time interval and to a given polarity, i.e. the sign of the first extremum. In a typical ultrasonic signal the desired event will give the maximum output in the following non-linear object function:

$$\frac{|FirstExtremumAmplitude - 2 * SecondExtremumAmplitude|}{HeadAmplitude} \quad \text{Eq. 4-2}$$

Where the HeadAmplitude denotes the maximum absolute amplitude of the signal in an interval ending just before the onset of the half period containing the first extremum. The length of the interval has been set to 5 mean periods, i.e. 5 divided by the mean frequency. The precise time of the first extremum is found using Newton-Raphson local optimisation starting from the solution determined previously and using sinc interpolation between the samples.

The global uncertainty:

To describe how easy it is to identify the desired event, the global uncertainty is defined as the ratio of the object function for the second largest value and the largest value. The global uncertainty takes values between 0 and 1, where 0 represents a very easy case and 1 means that two or more picks were equally good, in fact equally bad.

The local uncertainty (Error-band):

To describe how much the picked time could be wrong due to additive noise moving the chosen extremum of the observable signal, the local uncertainty is computed. The chosen HeadAmplitude is used as a noise estimate in that computation.

Amplitude at pick

The amplitude of the Newton-Raphson optimisation at the picked time is reported as the amplitude at the pick.

5. Results of the ultrasonic measurements

The results of the ultrasonic measurements are presented in the following tables and figures:

- Table 5.1: Ultrasonic results of 21 samples (incl. Rigs213) dried at humidity controlled conditions (60 °C, 40 % relative humidity) and measured with a confining pressure of 75 bar.
- Table 5.2: Ultrasonic results of 22 samples (incl. Rigs213 and Rigs220) fully saturated with water ($S_w=100\%$) and measured with a confining pressure of 75 bar.
- Table 5.3: Ultrasonic results of two samples (nos. 13 and 31) dried at humidity controlled conditions (60 °C, 40 % relative humidity) and measured in turn at confining pressures of 75, 125, and 200 bar.

Values reported in Tables 5.1 to 5.3 as "Mean S velocity" are the mean of S1 and S2 measurements. Basic data for the underlying P, S1 and S2 measurements are given in Tables A.1 to A.6.

In the following figures samples in the humidity-dried state are referred to as *Gas saturated samples*. The ultrasonic velocity have been plotted as follows:

- Fig. 5.1 V_S vs. V_P for samples in the *gas saturated* and *water saturated* state.
- Fig. 5.2. V_P vs. porosity for samples in the *gas saturated* and *water saturated* state.
- Fig. 5.3. V_S vs. porosity for samples in the *gas saturated* and *water saturated* state.
- Fig. 5.4. V_P in *water saturated* state vs. V_P in *gas saturated* state.
- Fig. 5.5. V_S in *water saturated* state vs. V_S in *gas saturated* state.
- Fig. 5.6. Ratio V_P/V_S for samples in the *gas saturated* and *water saturated* state.
- Fig. 5.7. V_P and V_S vs. confining pressure for sample nos. 13.
- Fig. 5.8. V_P and V_S vs. confining pressure for sample nos. 31.
- Fig. 5.9 V_S vs. V_P for sample 13.
- Fig. 5.10. V_S vs. V_P for sample 31.

In Figs. 5.1 to 5.6 the ultrasonic results are compared with the modified upper Hashin-Shtrikman ('MUHS') model presented by Walls et al. (1998). This model describes how the dry bulk and shear moduli, K and G increase as porosity is reduced from a maximum value, ϕ_{\max} , to zero porosity. Here the model is presented with the high-porosity parameters of Japsen et al. (2004) combined with the low-porosity parameters of Walls et al. (1998):

$$K_s = 65 \text{ GPa}, G_s = 27 \text{ GPa} \text{ for } \phi = 0\%$$

$$K_{\phi_{\max}} = 1.5 \text{ GPa}, G_{\phi_{\max}} = 2.5 \text{ GPa} \text{ for } \phi_{\max} = 45\%$$

where the low-porosity end-members, K_s and G_s , are moduli of the solid at zero porosity. The prediction of the MUHS model for the dry rock properties are used as input to Gassmann's equations for calculating the properties of fully water saturated chalk samples.

Table 5.1. Results of ultrasonic measurements – humidity dried samples 60 °C, 40 % relative humidity.

Sample id.	Well id.	Gas perm (mD)	Porosity (%)	Reduced porosity (%)	Grain density (g/ml)	P velocity (m/s)	S1 velocity (m/s)	S2 velocity (m/s)	Mean S velocity (m/s)	P / S Ratio
1	Q-1	0.003	14.35	14.28	2.721	3947.90	2470.08	2463.11	2466.60	1.601
2	Q-1	0.002	8.97	8.93	2.724	3809.06	2487.63	2484.25	2485.94	1.532
3	Q-1	0.018	14.43	14.36	2.720	4565.64	2689.62	2684.18	2686.90	1.699
4	Q-1	0.009	9.91	9.86	2.706	4999.22	2924.66	2910.07	2917.37	1.714
6	Otto-1	0.33	19.23	19.15	2.716	4011.13	2436.30	2431.91	2434.10	1.648
8	Otto-1	0.52	20.72	20.64	2.720	4042.53	2424.08	2423.21	2423.64	1.668
9	T-3	0.42	19.10	18.99	2.718	3924.27	2375.41	2378.52	2376.97	1.651
10	T-3	0.86	24.77	24.65	2.717	3560.11	2162.80	2158.41	2160.61	1.648
13	Gert-1	0.009	11.28	11.22	2.680	4921.17	2927.56	2924.84	2926.20	1.682
14	Gert-1	0.003	6.85	6.82	2.706	5079.40	3043.50	3044.33	3043.91	1.669
16	Gert-1	0.005	3.70	3.68	2.698	4699.53	2779.95	2790.49	2785.22	1.687
17	West Lulu-1	0.002	6.32	6.29	2.726	5524.85	3074.23	3066.46	3070.34	1.799
19	West Lulu-1	0.004	8.01	7.97	2.723	5234.62	2988.33	2987.47	2987.90	1.752
21	Baron-2	0.17	26.90	26.78	2.706	3587.62	2179.81	2185.08	2182.44	1.644
22	Baron-2	0.06	24.69	24.52	2.708	3469.73	2168.74	2158.69	2163.72	1.604
23	Baron-2	0.05	16.68	16.59	2.698	4404.68	2641.34	2635.04	2638.19	1.670
24	Baron-2	0.07	21.87	21.76	2.704	3764.95	2308.84	2307.02	2307.93	1.631
26	I-1	0.08	26.73	26.49	2.696	3155.82	2085.77	2080.65	2083.21	1.515
31	Cecilie-1B	0.41	22.36	22.19	2.710	3867.87	2328.33	2347.50	2337.91	1.654
32	Cecilie-1B	0.002	7.21	7.17	2.705	4852.66	2836.39	2837.12	2836.76	1.711
Rigs213	Rigs-1	0.3	20.43	20.34	2.716	4311.90	2587.22	2553.44	2570.33	1.678

Table 5.2. Results of ultrasonic measurements – water saturated state, $S_w=100\%$.

Sample id.	Well id.	Gas perm (mD)	Porosity (%)	Reduced porosity (%)	Grain density (g/ml)	P velocity (m/s)	S1 velocity (m/s)	S2 velocity (m/s)	Mean S velocity (m/s)	P / S Ratio
1	Q-1	0.003	14.35	14.28	2.721	3863.42	2007.58	2015.37	2011.47	1.921
2	Q-1	0.002	8.97	8.93	2.724	4001.06	n.u.	n.u.	n.u.	n.u.
3	Q-1	0.018	14.43	14.36	2.720	4469.80	2463.57	2477.63	2470.60	1.809
4	Q-1	0.009	9.91	9.86	2.706	4983.85	2756.79	2741.32	2749.06	1.813
6	Otto-1	0.33	19.23	19.15	2.716	4105.68	2264.49	2265.28	2264.89	1.813
8	Otto-1	0.52	20.72	20.64	2.720	4111.58	2263.13	2255.78	2259.45	1.820
9	T-3	0.42	19.10	18.99	2.718	3974.37	2179.71	2166.21	2172.96	1.829
10	T-3	0.86	24.77	24.65	2.717	3620.09	1950.22	1952.72	1951.47	1.855
13	Gert-1	0.009	11.28	11.22	2.680	4892.34	2797.13	2795.91	2796.52	1.749
14	Gert-1	0.003	6.85	6.82	2.706	5119.09	n.u.	n.u.	n.u.	n.u.
16	Gert-1	0.005	3.70	3.68	2.698	4849.78	n.u.	n.u.	n.u.	n.u.
17	West Lulu-1	0.002	6.32	6.29	2.726	5497.70	2962.01	2947.56	2954.79	1.861
19	West Lulu-1	0.004	8.01	7.97	2.723	5228.16	2838.16	2827.87	2833.01	1.845
21	Baron-2	0.17	26.90	26.78	2.706	3471.16	1865.75	1863.59	1864.67	1.862
22	Baron-2	0.06	24.69	24.52	2.708	3425.03	1829.15	1823.52	1826.33	1.875
23	Baron-2	0.05	16.68	16.59	2.698	4319.03	2432.66	2416.59	2424.62	1.781
24	Baron-2	0.07	21.87	21.76	2.704	3783.77	2062.67	2068.80	2065.73	1.832
26	I-1	0.08	26.73	26.49	2.696	3185.16	1756.03	1750.55	1753.29	1.817
31	Cecilie-1B	0.41	22.36	22.19	2.710	3807.16	2058.03	2071.97	2065.00	1.844
32	Cecilie-1B	0.002	7.21	7.17	2.705	4832.14	n.u.	2589.20	2589.20	1.866
Rigs213	Rigs-1	0.3	20.43	20.34	2.716	4412.52	2478.99	2483.70	2481.35	1.778
Rigs220	Rigs-1	1.25	31.66	31.51	2.703	3344.61	1839.94	1834.64	1837.29	1.820

n.u. Measurement not useful.

Table 5.3. Results of ultrasonic measurements – samples dried at 60 °C, 40 % relative humidity, and measured at confining pressures 75, 125 and 200 bar.

Sam- ple id.	Well id.	Con- fining pressure (bar)	Gas perm (mD)	Porosity (%)	Reduced porosity (%)	Grain density (g/ml)	P velocity (m/s)	S1 velocity (m/s)	S2 velocity (m/s)	Mean S velocity (m/s)	P / S Ratio
13	Gert-1	75	0.009	11.28	11.22	2.680	4921.17	2927.56	2924.84	2926.20	1.682
13	Gert-1	125	0.009	11.28	11.22	2.680	4941.08	2938.20	2932.66	2935.43	1.683
13	Gert-1	200	0.009	11.28	11.22	2.680	4937.70	2937.76	2932.18	2934.97	1.682
31	Cecilie-1B	75	0.41	22.36	22.19	2.710	3867.87	2328.33	2347.50	2337.91	1.654
31	Cecilie-1B	125	0.41	22.36	22.19	2.710	3903.28	2347.90	2362.08	2354.99	1.657
31	Cecilie-1B	200	0.41	22.36	22.19	2.710	3940.92	2359.99	2374.84	2367.42	1.665

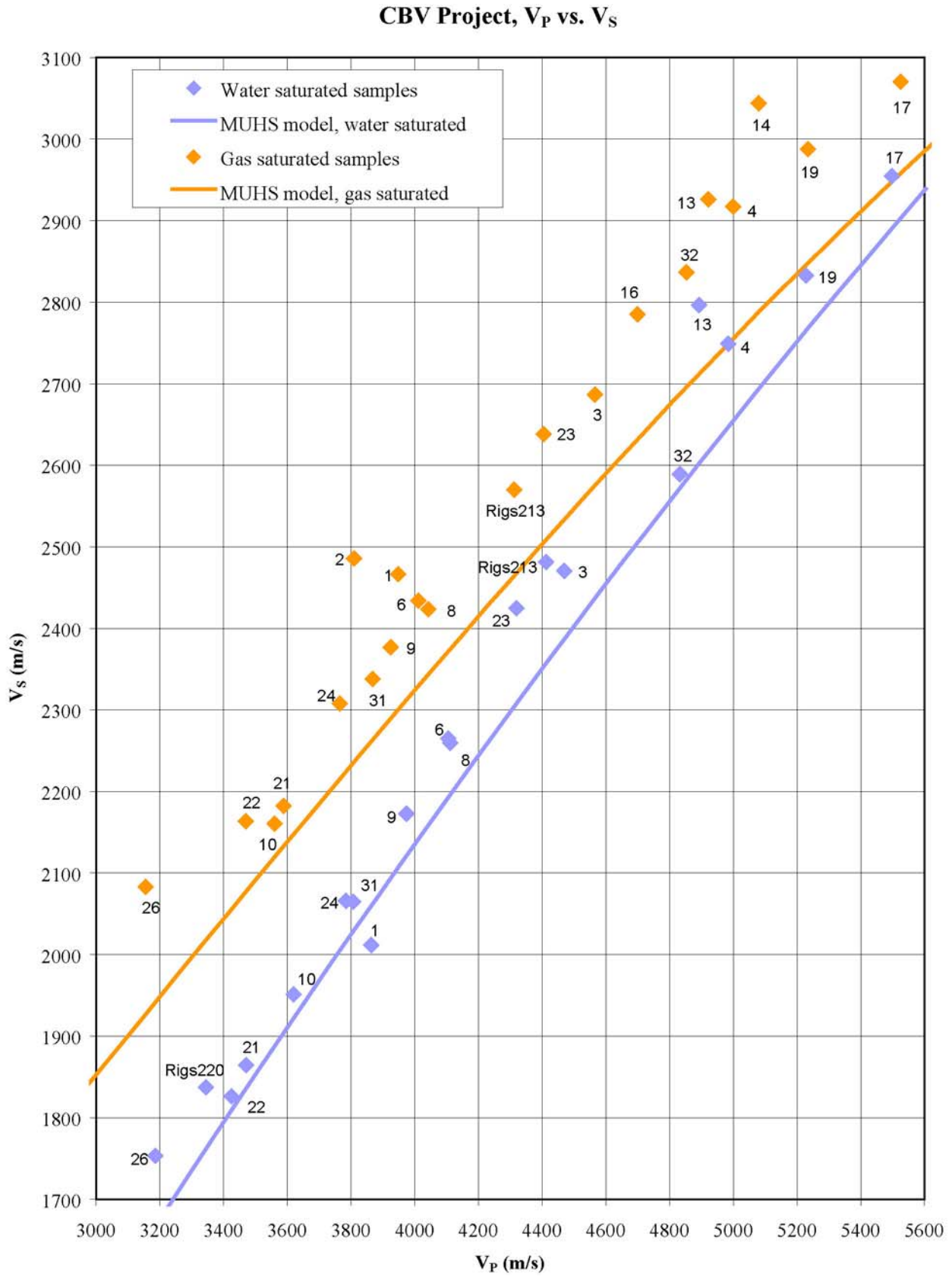


Fig. 5.1. V_S vs. V_P for samples in gas saturated and water saturated state..

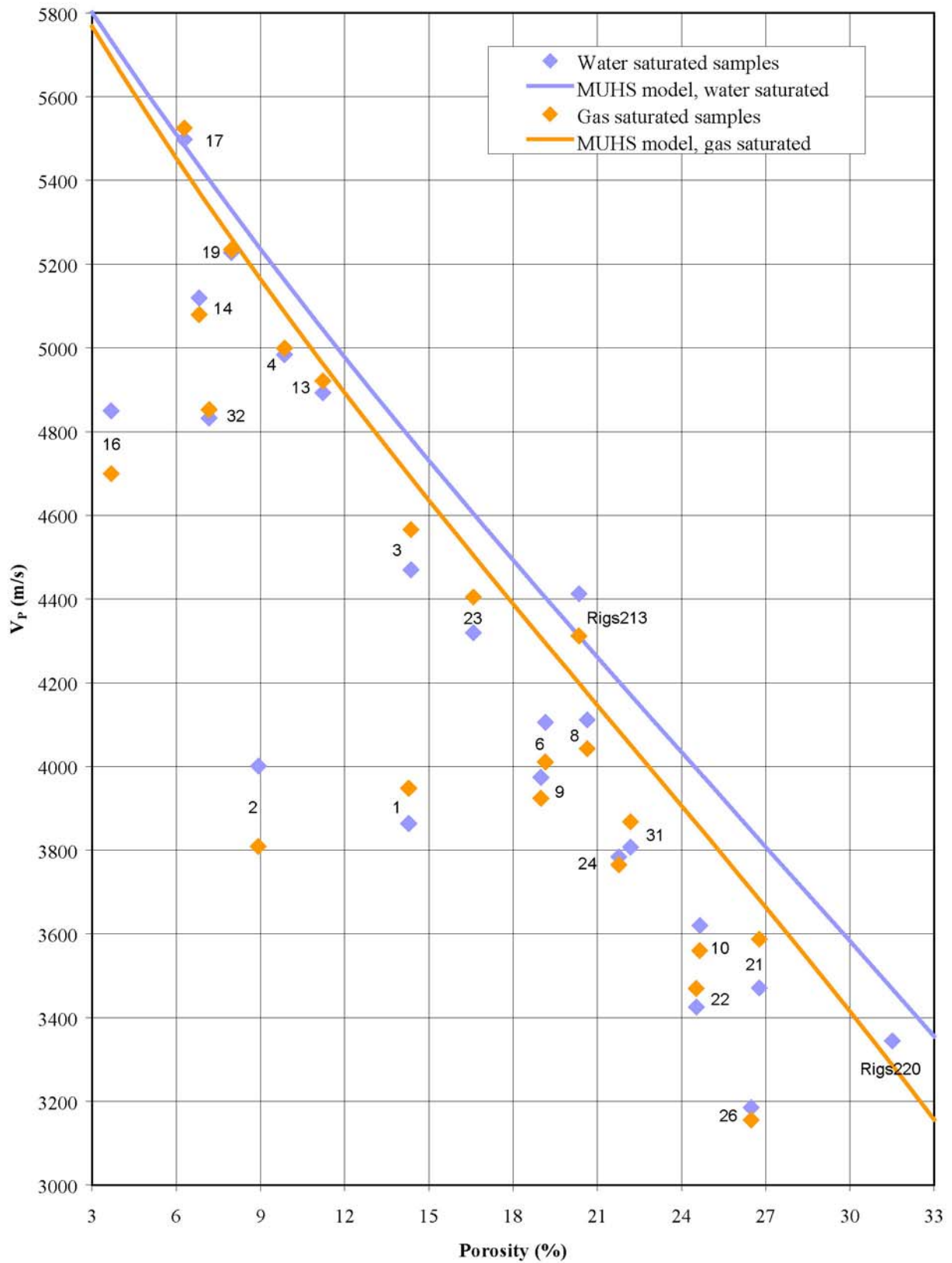
CBV Project, V_P vs. porosity

Fig. 5.2. V_P vs. porosity for samples in gas saturated and water saturated state. Please note that each sample is only labelled once, i.e. each label refers to both a gas saturated and a water saturated measurement, except for sample Rigs220 where only a water saturated measurement is available.

CBV Project, V_s vs. porosity

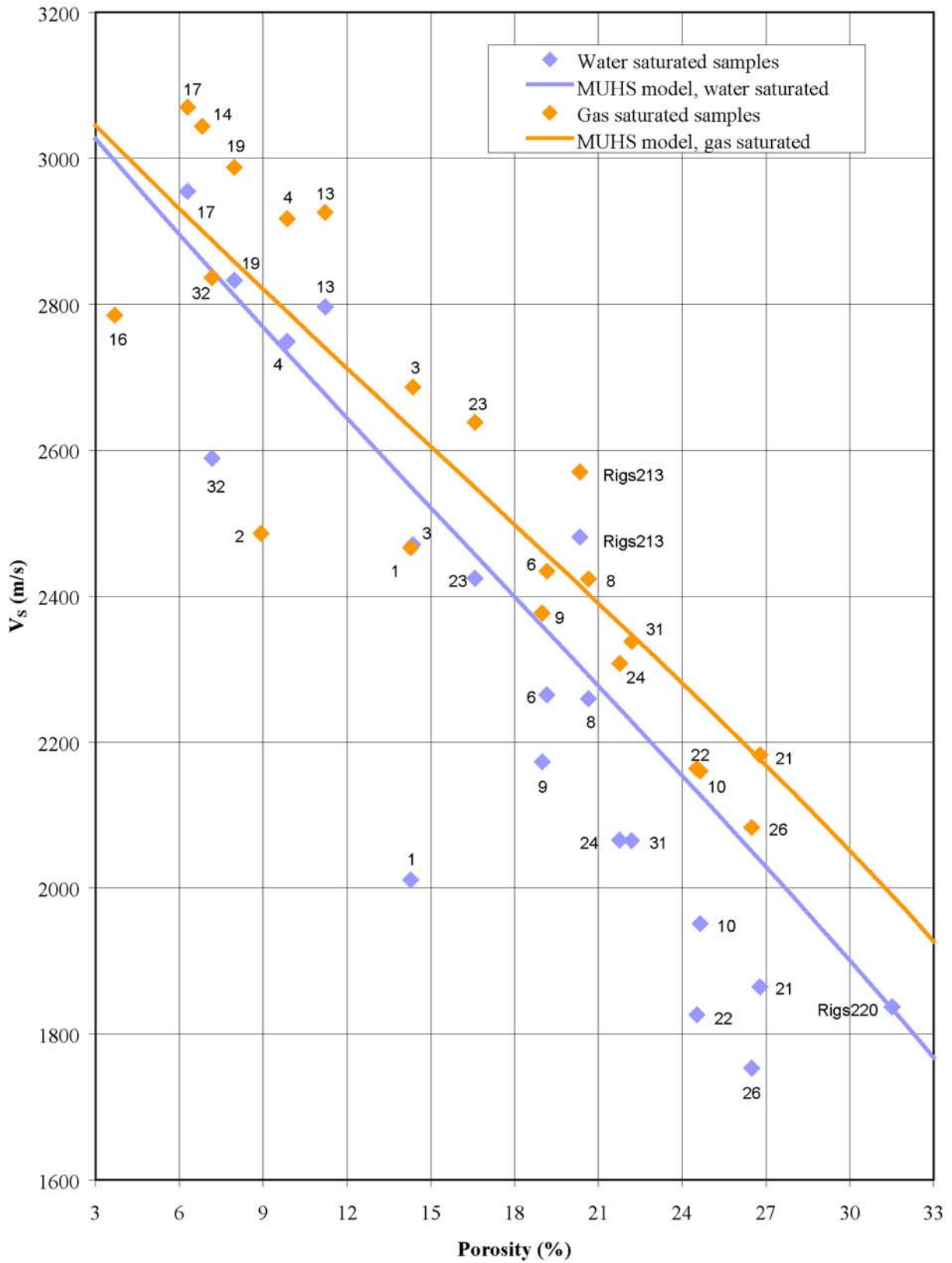


Fig. 5.3. V_s vs. porosity for samples in gas saturated and water saturated state.

CBV Project, V_P water saturated vs. V_P gas saturated

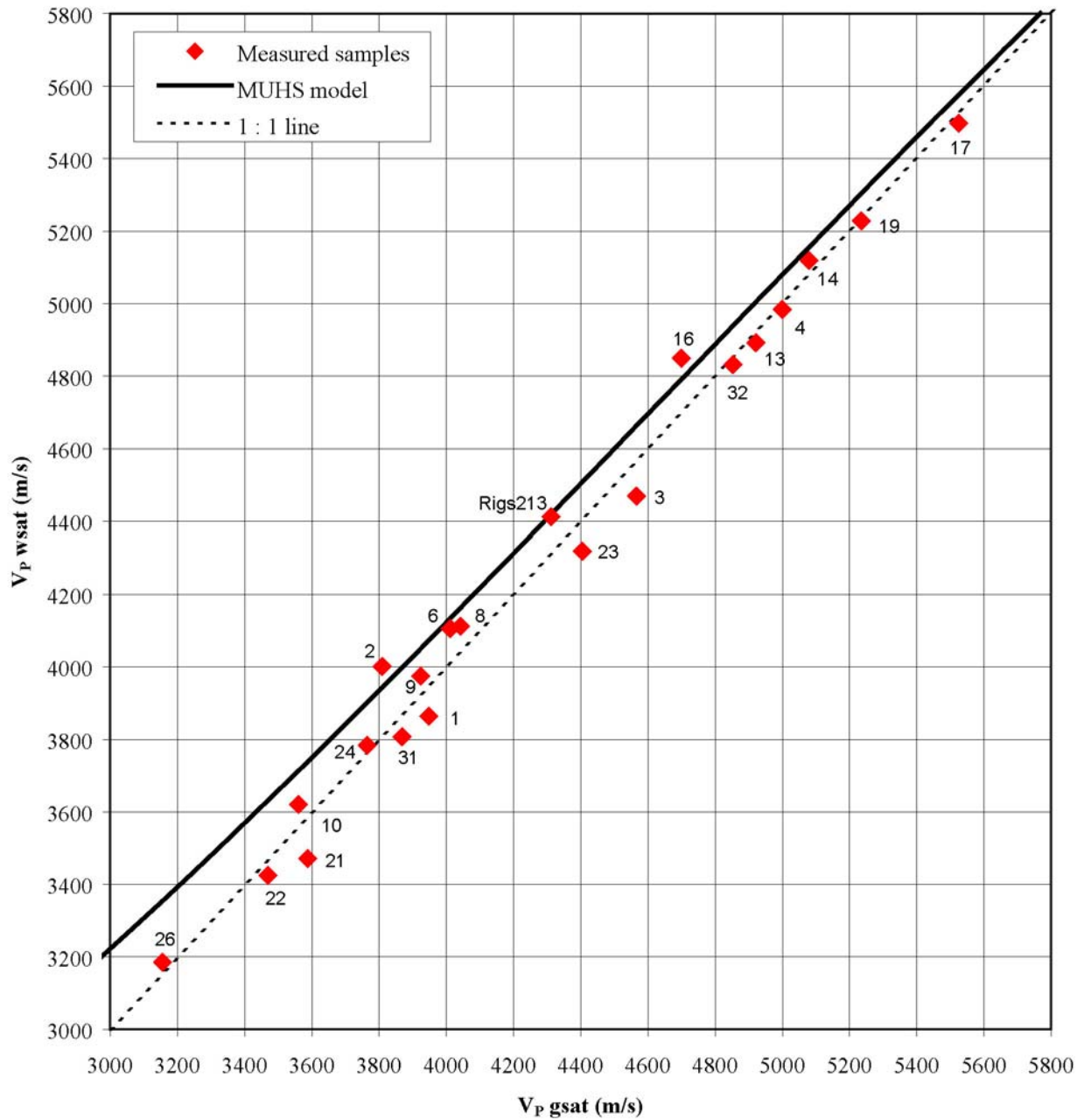


Fig. 5.4. V_P in water saturated state vs. V_P in gas saturated state.

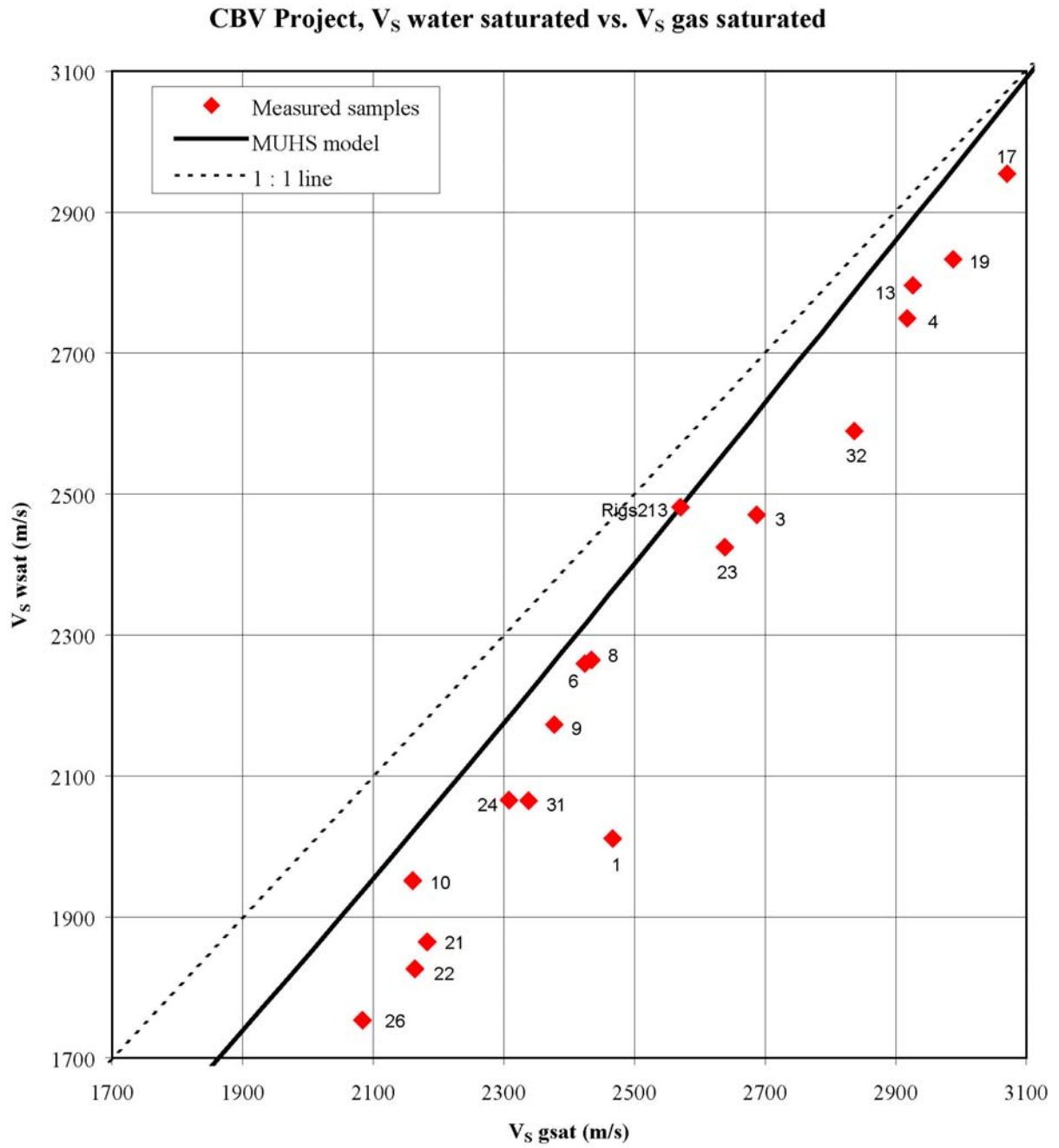


Fig. 5.5. V_s in water saturated state vs. V_s in gas saturated state.

CBV Project, V_p/V_s vs. porosity

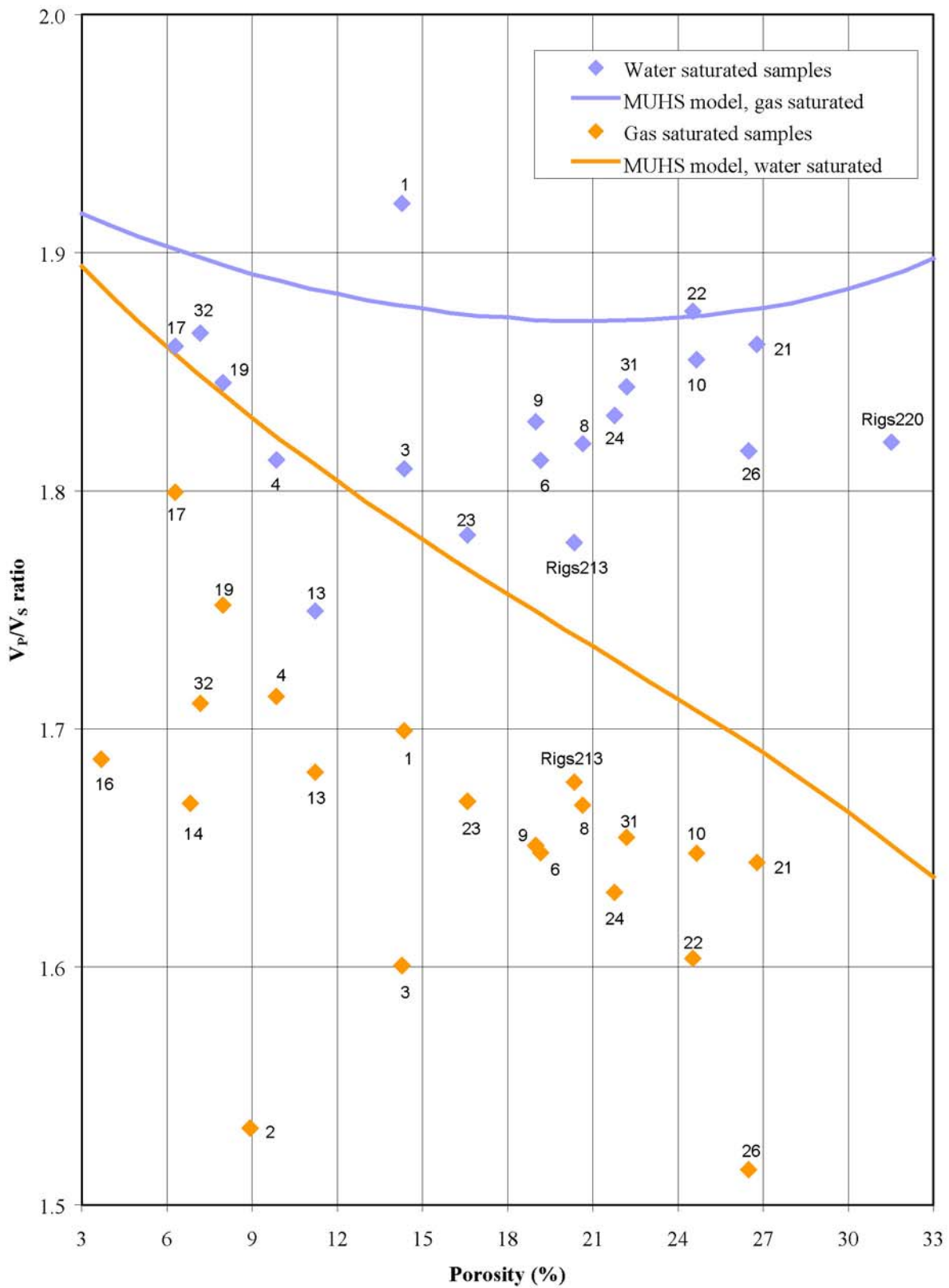


Fig. 5.6. V_p/V_s ratio vs. porosity for samples in gas saturated and water saturated state.

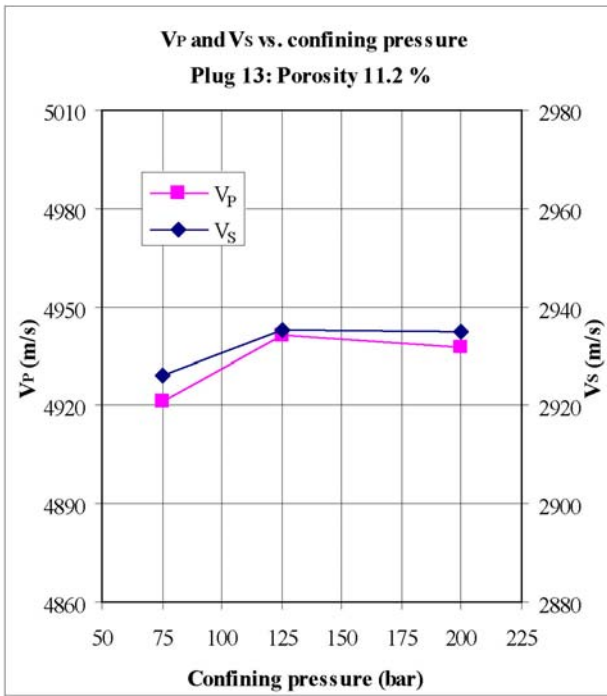


Fig. 5.7. Ultrasonic velocities V_P and V_S plotted against confining pressure for sample 13. Note that V_P and V_S are plotted on separate Y-axes.

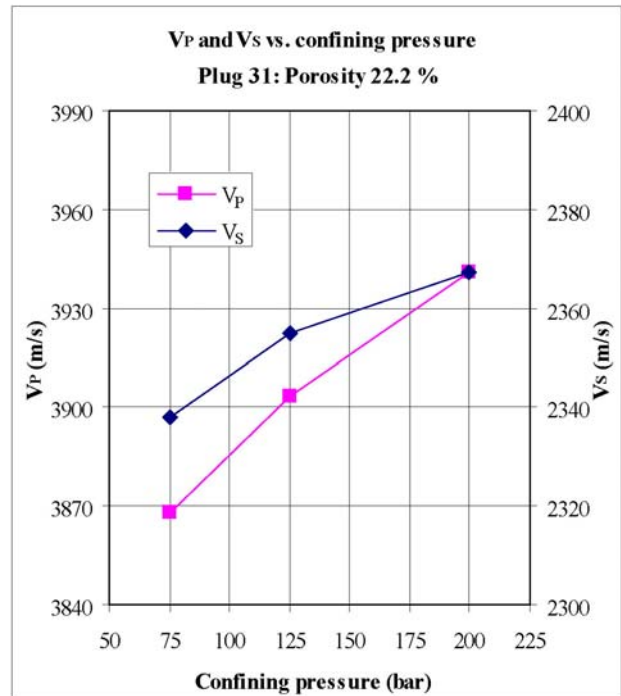


Fig. 5.8. Ultrasonic velocities V_P and V_S plotted against confining pressure for sample 31. Note that V_P and V_S are plotted on separate Y-axes.

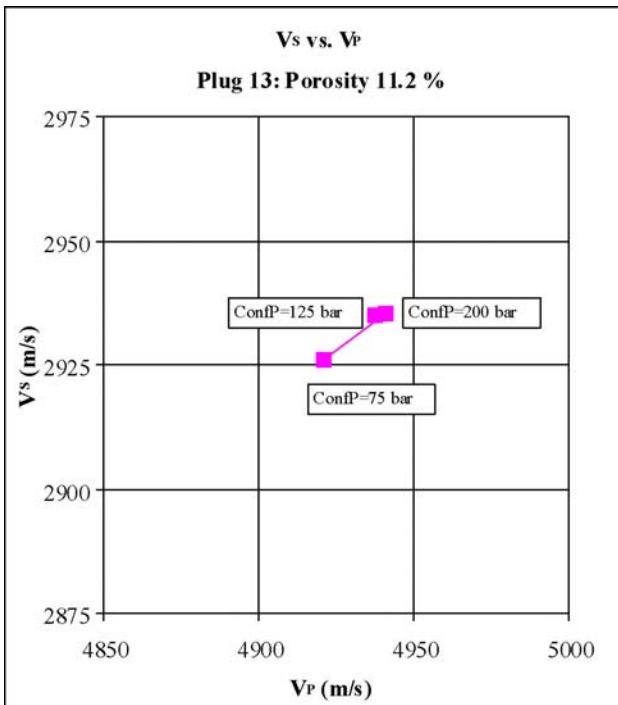


Fig. 5.9. Ultrasonic velocity V_S plotted against ultrasonic velocity V_P for sample 13. Measurements are labelled with confining pressure.

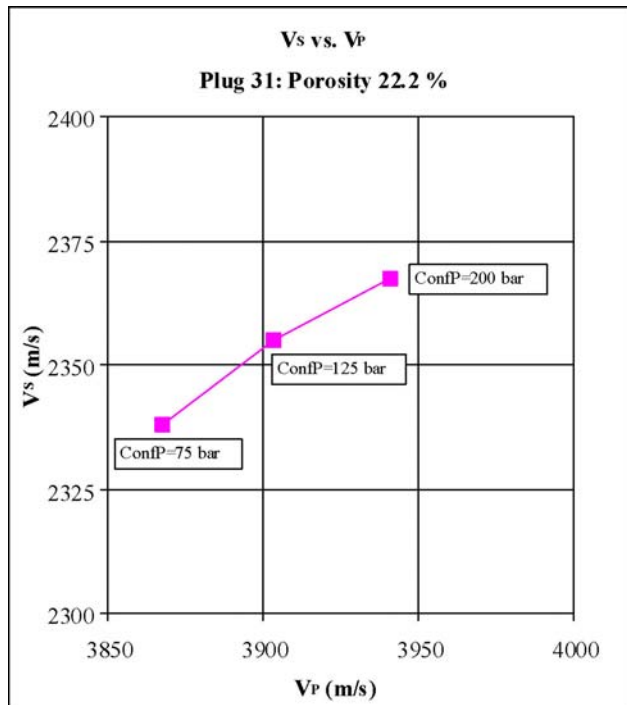


Fig. 5.10. Ultrasonic velocity V_S plotted against ultrasonic velocity V_P for sample 31. Measurements are labelled with confining pressure.

6. Documentation of data

This report comes in two versions: one with an attached CD and one without.

The CD contains all the ultrasonic data of the present work. The sample data for measurements in humidity dried state can be found in the "HumidityDry" folder, and the sample data for measurements in the $S_w=100\%$ state can be found in the "WaterSat" folder. The calibration data can be found in the "CalibrationData" folder. At the top level, all results and plots are placed in the spreadsheet *sonic_cbv.xls*, which is an Excel97 file.

Each folder "HumidityDry", "WaterSat", and "CalibrationData" contains a file *firstarrival_<id.>.doc*, which contains the output from the *firstarrival* program, cf. Section 4.5 for a description of the output.

In the folders "HumidityDry" and "WaterSat" sample folders contain the following files:

- 1) Files with wave train data stored in comma separated files (*.csv)
- 2) Screen-dumps of the oscilloscope in tif format (*.tif)

For these files the filenames are constructed as follows:

<sample id.>_<state_><measurement type>_<hydrostatic pressure>_<date>.<file type>

where

- <sample id.> is the identification of the sample
- <state_> is either missing indicating humidity dried state or *maet* indicating water saturated state
- <measurement type> is given as P (P-wave) or S1 (S1-wave) or S2 (S2-wave)
- <hydrostatic pressure> is the hydrostatic pressure in bar
- <date> is a shorthand date with format ddmmyy
- <file type> is csv or tif

Every sample folder for water saturated samples in addition contains

- 3) An Excel file <sample id.>.xls with a Mettler log and the calculation of pore volume reduction

The clock of the oscilloscope, the clock of the attached PC, and the clock of the Quizix pump system were kept synchronized within ½ minute within the data acquisition period April 5th to June 30th 2004 to allow comparison of the Mettler logs and the ultrasonic data.

7. References

- API RP40, 1998. Recommended practices for core analysis. *American Petroleum Institute, Recommended Practices 40, second edition.*
- Høier, C., 2002. Special core analysis for the Rock Physics project (EFP-2001) ENS J.nr. 1313/01-0006. Ultrasonic velocity measured on plugs from the Ekofisk and Tor formation. Samples taken from the wells: Rigs-1, Rigs-2 and SA-1, the South Arne Field. *Danmarks og Grønlands Geologiske Undersøgelse Rapport 2002/23*, 26 pp.
- Høier, C., 2000. Special core analysis for the Rock Physics project (EFP-98) ENS J.nr. 1313/98-0007. Ultrasonic velocity measured on plugs from the wells: Rigs-1, Rigs-2 and SA-1, the South Arne Field. *Danmarks og Grønlands Geologiske Undersøgelse Rapport 2000/19*, 71 pp.
- Jakobsen, F., 2004. *Unpublished work prepared for the Chalk Background Velocity project, GEUS.*
- Japsen, P., Bruun, A., Fabricius, I. L., Rasmussen, R., Mavko, G., Vejbæk, O. V. & Pedersen, J. M. 2004. Influence of porosity and pore fluid on acoustic properties of chalk: AVO-response from oil, South Arne Field, North Sea. *Petroleum Geoscience 10*, 319-330.
- Nielsen, L.H. & Japsen, P., 1991. Deep wells in Denmark 1935-1990, *Danm. Geol. Unders. Ser. A 31*, 178 pp.
- Walls, J. D., Dvorkin, J. & Smith, B. A. 1998. Modeling seismic velocity in Ekofisk Chalk. *Society of Exploration Geophysicists 68th annual conference*. 1016–1019.

Appendix 1. Basic data, results, and precision

Basic data, results and precision parameters for all measurements are presented in Tables A.1 to A.6.

These tables report the full output from the *firstarrival* program in the columns labelled *First arrival of <id.> signal*, *Local uncertainty*, *Global uncertainty*, and *Amplitude at pick*. This is true even for measurements where the identification of the ultrasonic signal, and thus the calculation of an ultrasonic velocity, failed. In these instance the output from *firstarrival* is reported but the velocity and precision parameters are marked with the Excel symbol #I/T denoting that the data values are absent. In addition the measurement is commented "Not useful".

Tables A.1 to A.3 reports data from measurement of the samples in humidity dried state, i.e. 60 °C and 40 % relative humidity.

Tables A.4 to A.6 reports data from measurement of the samples in fully water saturated state, i.e. $S_w = 100\%$.

Table A.1. Basic data, results, and precision of ultrasonic measurements.
Ultrasonic P signals, samples measured in humidity dried state, 60 °C, 40 % relative humidity

Sample id.	File id.	Reduced porosity (%)	Reduced length (mm)	First arrival of P signal (us)	Local uncertainty (us)	Global uncertainty	Amplitude at pick (mV)	P velocity (m/s)	Error on velocity				Total error (%)	Comment
									from length (m/s)	from noise (m/s)	Total error (m/s)	Total error (m/s)		
1	Plug1_P_75_por_080304	14.28	38.37	22.4542	0.0188	0.06	84.0	3934.74	10	3	14	0.3		
1_ch	Plug1_P_75_310304	14.28	38.37	22.3894	0.0121	0.04	97.2	3961.07	10	2	12	0.3		
2	Plug2_P_75_por_100304	8.93	38.33	22.5949	0.0176	0.05	53.6	3875.09	10	3	13	0.3		
2_ch	Plug2_P_75_010404	8.93	38.33	22.9439	0.0181	0.05	51.2	3743.03	10	3	13	0.3		
3	Plug3_P_75_por_110304	14.36	38.33	21.0759	0.0098	0.04	54.3	4577.63	12	2	14	0.3		
3_ch	Plug3_P_75_250304	14.36	38.33	21.1200	0.0148	0.06	49.7	4553.65	12	3	15	0.3		
4	Plug4_P_75_180304	9.86	39.40	20.6345	0.0206	0.08	53.2	4967.54	13	5	18	0.4		
4_ch	Plug4_P_75_010404	9.86	39.40	20.5346	0.0340	0.13	47.7	5030.90	13	8	21	0.4		
6	Plug6_P_75_180304	19.15	38.62	22.3307	0.0175	0.06	88.5	4011.13	10	3	14	0.3		
8	Plug8_P_75_por_100304	20.64	39.38	22.4429	0.0168	0.05	91.0	4042.88	10	3	13	0.3		
8_ch	Plug8_P_75_070404	20.64	39.38	22.4446	0.0102	0.03	111.6	4042.17	10	2	12	0.3		
9	Plug9_P_75_190304	18.99	38.39	22.4840	0.0234	0.08	65.9	3924.27	10	4	14	0.4		
10	Plug10_P_75_190304	24.65	39.38	23.7650	0.0102	0.03	126.3	3560.11	9	2	11	0.3		
13	Plug13_P_75_110304	11.22	37.61	20.3345	0.0191	0.07	54.1	4928.26	13	5	18	0.4		
13_3p	Plug13_P_75_290304	11.22	37.61	20.3565	0.0232	0.07	52.1	4914.09	13	6	19	0.4		
13_3p	Plug13_P_125_290304	11.22	37.61	20.3147	0.0142	0.05	86.2	4941.08	13	3	17	0.3	Pconf 125 bar	
13_3p	Plug13_P_200_290304	11.22	37.61	20.3199	0.0118	0.44	110.1	4937.70	13	3	16	0.3	Pconf 200 bar	
14	Plug14_P_75_120304	6.82	35.86	19.7689	0.0139	0.05	45.3	5074.07	14	4	18	0.3		
14_ch	Plug14_P_75_310304	6.82	35.86	19.7541	0.0248	0.08	49.3	5084.72	14	6	21	0.4		
16	Plug16_P_75_250304	3.68	35.72	20.3027	0.0408	0.13	23.2	4699.53	13	9	23	0.5		
17	Plug17_P_75_260304	6.29	35.76	19.1743	0.0121	0.04	59.2	5524.85	15	3	19	0.3		
19	Plug19_P_75_170304	7.97	37.89	19.9417	0.0175	0.06	44.5	5234.62	14	5	18	0.4		
21	Plug21_P_75_230304	26.78	40.53	24.0006	0.0107	0.03	114.1	3587.62	9	2	10	0.3		
22	Plug22_P_75_230304	24.52	39.31	24.0313	0.0191	0.07	65.1	3469.73	9	3	12	0.3		
23	Plug23_P_75_240304	16.59	38.21	21.3768	0.0113	0.04	55.0	4404.68	12	2	14	0.3		
24	Plug24_P_75_240304	21.76	35.62	22.1627	0.0238	0.07	47.2	3764.95	11	4	15	0.4		
26	Plug26_P_75_240304	26.49	39.39	25.3903	0.0117	0.03	87.4	3104.36	8	1	9	0.3		
26_ch	Plug26_P_75_060404	26.49	39.39	24.9832	0.0135	0.04	92.4	3207.27	8	2	10	0.3		
31_3p	Plug31_P_75_300304	22.19	36.62	22.1700	0.0254	0.09	61.5	3867.87	11	4	15	0.4		
31_3p	Plug31_P_125_300304	22.19	36.62	22.0841	0.0100	0.03	100.3	3903.28	11	2	12	0.3	Pconf 125 bar	
31_3p	Plug31_P_200_300304	22.19	36.62	21.9945	0.0099	0.03	118.5	3940.92	11	2	13	0.3	Pconf 200 bar	
32	Plug32_P_75_260304	7.17	38.49	20.6430	0.0214	0.07	29.0	4846.66	13	5	18	0.4		
32_ch	Plug32_P_75_060404	7.17	38.49	20.6234	0.0103	0.03	37.1	4858.65	13	2	15	0.3		
Rigs213	Rigs213_P_75_150304	20.34	24.75	18.4430	0.0271	0.07	50.7	4311.90	17	6	24	0.6	Por from GEUS rap. 2002/23	

Table A.2. Basic data, results, and precision of ultrasonic measurements.

Ultrasonic S1 signals, samples measured in humidity dried state, 60 °C, 40 % relative humidity

Sample id.	File id.	Reduced porosity (%)	Reduced length (mm)	First arrival of S1 signal (us)	Local uncertainty (us)	Global uncertainty	Amplitude at pick (mV)	S1 velocity (m/s)	Error on velocity				Comment
									from length (m/s)	from noise (m/s)	Total error (m/s)	Total error (%)	
1	Plug1_S1_75_por_080304	14.28	38.37	39.3545	0.0120	0.07	-172.5	2445.42	6	1	7	0.3	
1_ch	Plug1_S1_75_310304	14.28	38.37	39.0444	0.0138	0.03	-350.4	2494.73	7	1	7	0.3	
2	Plug2_S1_75_por_100304	8.93	38.33	41.9183	0.1331	0.88	-56.2	#I/T	#I/T	#I/T	#I/T	#I/T	S1 signal not useful
2_ch	Plug2_S1_75_010404	8.93	38.33	39.0736	0.0246	0.06	-266.2	2487.63	6	2	8	0.3	
3	Plug3_S1_75_por_110304	14.36	38.33	28.2630	0.1381	0.88	-8.4	#I/T	#I/T	#I/T	#I/T	#I/T	S1 signal not useful
3_ch	Plug3_S1_75_250304	14.36	38.33	37.9150	0.0122	0.03	-200.3	2689.62	7	1	8	0.3	
4	Plug4_S1_75_180304	9.86	39.40	37.2449	0.0160	0.04	-202.4	2901.28	7	1	9	0.3	
4_ch	Plug4_S1_75_010404	9.86	39.40	37.0294	0.0215	0.07	-184.0	2948.05	7	2	9	0.3	
6	Plug6_S1_75_180304	19.15	38.62	39.5157	0.0134	0.03	-355.7	2436.30	6	1	7	0.3	
8	Plug8_S1_75_por_100304	20.64	39.38	39.9445	0.0238	0.09	-332.4	2418.77	6	1	8	0.3	
8_ch	Plug8_S1_75_070404	20.64	39.38	39.8733	0.0129	0.03	-366.9	2429.39	6	1	7	0.3	
9	Plug9_S1_75_190304	18.99	38.39	39.8232	0.0174	0.04	-254.1	2375.41	6	1	7	0.3	
10	Plug10_S1_75_190304	24.65	39.38	41.8734	0.0152	0.05	-416.3	2162.80	5	1	6	0.3	
13	Plug13_S1_75_110304	11.22	37.61	27.0122	0.1912	0.78	-4.2	#I/T	#I/T	#I/T	#I/T	#I/T	S1 signal not useful
13_3p	Plug13_S1_75_290304	11.22	37.61	36.5115	0.0209	0.06	-209.2	2927.56	8	2	9	0.3	
13_3p	Plug13_S1_125_290304	11.22	37.61	36.4650	0.0149	0.04	-315.9	2938.20	8	1	9	0.3	Pconf 125 bar
13_3p	Plug13_S1_200_290304	11.22	37.61	36.4669	0.0168	0.04	-375.6	2937.76	8	1	9	0.3	Pconf 200 bar
14	Plug14_S1_75_120304	6.82	35.86	32.1044	0.1536	0.93	-30.6	#I/T	#I/T	#I/T	#I/T	#I/T	S1 signal not useful
14_ch	Plug14_S1_75_310304	6.82	35.86	35.4448	0.0199	0.08	-220.5	3043.50	8	2	10	0.3	
16	Plug16_S1_75_250304	3.68	35.72	36.5120	0.0304	0.07	-60.2	2779.95	8	2	10	0.4	
17	Plug17_S1_75_260304	6.29	35.76	35.2946	0.0268	0.13	-242.3	3074.23	9	2	11	0.4	
19	Plug19_S1_75_170304	7.97	37.89	36.3446	0.0096	0.02	-192.4	2988.33	8	1	9	0.3	
21	Plug21_S1_75_230304	26.78	40.53	42.2587	0.0328	0.04	-134.1	2179.81	5	2	7	0.3	
22	Plug22_S1_75_230304	24.52	39.31	41.7885	0.0112	0.03	-232.1	2168.74	6	1	6	0.3	
23	Plug23_S1_75_240304	16.59	38.21	38.1290	0.0172	0.04	-226.0	2641.34	7	1	8	0.3	
24	Plug24_S1_75_240304	21.76	35.62	39.0902	0.0213	0.04	-215.9	2308.84	6	1	8	0.3	
26	Plug26_S1_75_240304	26.49	39.39	42.8038	0.0139	0.03	-318.6	2057.86	5	1	6	0.3	
26_ch	Plug26_S1_75_060404	26.49	39.39	42.2983	0.0146	0.04	-345.6	2113.69	5	1	6	0.3	
31_3p	Plug31_S1_75_300304	22.19	36.62	39.3914	0.0222	0.08	-220.1	2328.33	6	1	8	0.3	
31_3p	Plug31_S1_125_300304	22.19	36.62	39.2603	0.0213	0.05	-300.5	2347.90	6	1	8	0.3	Pconf 125 bar
31_3p	Plug31_S1_200_300304	22.19	36.62	39.1804	0.0192	0.05	-329.0	2359.99	6	1	8	0.3	Pconf 200 bar
32	Plug32_S1_75_260304	7.17	38.49	37.3536	0.0282	0.07	-129.8	2811.21	7	2	9	0.3	
32_ch	Plug32_S1_75_060404	7.17	38.49	37.1127	0.0279	0.06	-154.3	2861.57	7	2	10	0.3	
Rigs213	Rigs213_S1_75_150304	20.34	24.75	33.2310	0.0407	0.23	-141.0	2587.22	10	3	14	0.5	Por from GEUS rap. 2002/23

Table A.3. Basic data, results, and precision of ultrasonic measurements.

Ultrasonic S2 signals, samples measured in humidity dried state, 60 °C, 40 % relative humidity

Sample id.	File id.	Reduced porosity (%)	Reduced length (mm)	First arrival of S2 signal (us)	Local uncertainty (us)	Global uncertainty	Amplitude at pick (mV)	S2 velocity (m/s)	Error on velocity				Total error (%)	Comment
									from length (m/s)	from noise (m/s)	Total error (m/s)	Total error (%)		
1	Plug1_S2_75_por_080304	14.28	38.37	40.0421	0.0103	0.02	-226.4	2436.51	6	1	7	0.3		
1_ch	Plug1_S2_75_310304	14.28	38.37	39.7056	0.0146	0.04	-215.8	2489.71	6	1	7	0.3		
2	Plug2_S2_75_por_100304	8.93	38.33	41.9227	0.1333	0.92	-56.2	#I/T	#I/T	#I/T	#I/T	#I/T	S2 signal not useful	
2_ch	Plug2_S2_75_010404	8.93	38.33	39.7248	0.0257	0.05	-150.2	2484.25	6	2	8	0.3		
3	Plug3_S2_75_por_110304	14.36	38.33	28.2713	0.1382	0.90	-8.5	#I/T	#I/T	#I/T	#I/T	#I/T	S2 signal not useful	
3_ch	Plug3_S2_75_250304	14.36	38.33	38.5741	0.0258	0.09	-95.1	2684.18	7	2	9	0.3		
4	Plug4_S2_75_180304	9.86	39.40	37.9310	0.0157	0.04	-132.1	2889.39	7	1	9	0.3		
4_ch	Plug4_S2_75_010404	9.86	39.40	37.7385	0.0150	0.03	-124.0	2930.76	7	1	9	0.3		
6	Plug6_S2_75_180304	19.15	38.62	40.1745	0.0130	0.03	-190.4	2431.91	6	1	7	0.3		
8	Plug8_S2_75_por_100304	20.64	39.38	40.5449	0.0120	0.03	-232.6	2423.21	6	1	7	0.3		
8_ch	Plug8_S2_75_070404	20.64	39.38	40.5449	0.0129	0.03	-240.0	2423.21	6	1	7	0.3		
9	Plug9_S2_75_190304	18.99	38.39	40.4323	0.0099	0.02	-142.1	2378.52	6	1	7	0.3		
10	Plug10_S2_75_190304	24.65	39.38	42.5406	0.0133	0.03	-242.0	2158.41	5	1	6	0.3		
13	Plug13_S2_75_110304	11.22	37.61	27.0486	0.1706	0.75	-4.5	#I/T	#I/T	#I/T	#I/T	#I/T	S2 signal not useful	
13_3p	Plug13_S2_75_290304	11.22	37.61	37.1537	0.0175	0.04	-106.1	2924.84	8	1	9	0.3		
13_3p	Plug13_S2_125_290304	11.22	37.61	37.1194	0.0113	0.03	-165.6	2932.66	8	1	9	0.3	Pconf 125 bar	
13_3p	Plug13_S2_200_290304	11.22	37.61	37.1215	0.0156	0.04	-203.4	2932.18	8	1	9	0.3	Pconf 200 bar	
14	Plug14_S2_75_120304	6.82	35.86	32.0831	0.1476	0.90	-30.9	#I/T	#I/T	#I/T	#I/T	#I/T	S2 signal not useful	
14_ch	Plug14_S2_75_310304	6.82	35.86	36.0718	0.0296	0.07	-132.9	3044.33	8	2	11	0.4		
16	Plug16_S2_75_250304	3.68	35.72	37.0937	0.0102	0.02	-123.3	2790.49	8	1	9	0.3		
17	Plug17_S2_75_260304	6.29	35.76	35.9543	0.0225	0.08	-176.7	3066.46	9	2	10	0.3		
19	Plug19_S2_75_170304	7.97	37.89	36.9785	0.0275	0.08	-110.0	2987.47	8	2	10	0.3		
21	Plug21_S2_75_230304	26.78	40.53	42.8440	0.0121	0.03	-400.4	2185.08	5	1	6	0.3		
22	Plug22_S2_75_230304	24.52	39.31	42.5031	0.0121	0.03	-158.2	2158.69	5	1	6	0.3		
23	Plug23_S2_75_240304	16.59	38.21	38.7938	0.0254	0.05	-120.4	2635.04	7	2	9	0.3		
24	Plug24_S2_75_240304	21.76	35.62	39.7326	0.0175	0.04	-144.1	2307.02	6	1	7	0.3		
26	Plug26_S2_75_240304	26.49	39.39	43.4808	0.0151	0.03	-207.4	2052.85	5	1	6	0.3		
26_ch	Plug26_S2_75_060404	26.49	39.39	42.9747	0.0137	0.03	-210.3	2108.46	5	1	6	0.3		
31_3p	Plug31_S2_75_300304	22.19	36.62	39.8932	0.0179	0.04	-173.2	2347.50	6	1	7	0.3		
31_3p	Plug31_S2_125_300304	22.19	36.62	39.7969	0.0132	0.03	-245.0	2362.08	6	1	7	0.3	Pconf 125 bar	
31_3p	Plug31_S2_200_300304	22.19	36.62	39.7136	0.0119	0.03	-270.6	2374.84	6	1	7	0.3	Pconf 200 bar	
32	Plug32_S2_75_260304	7.17	38.49	37.9648	0.0393	0.12	-78.0	2815.12	7	3	10	0.4		
32_ch	Plug32_S2_75_060404	7.17	38.49	37.7544	0.0298	0.11	-83.2	2859.12	7	2	10	0.3		
Rigs213	Rigs213_S2_75_150304	20.34	24.75	33.9878	0.0461	0.09	-61.0	2553.44	10	3	14	0.5	Por from GEUS rap. 2002/23	

Table A.4. Basic data, results, and precision of ultrasonic measurements – Samples measured in $S_w=100$ % state.
Ultrasonic P signals, samples measured in $S_w=100$ % state.

Sample id.	File id.	Reduced porosity (%)	Reduced length (mm)	First arrival of P signal (us)	Local uncertainty (us)	Global uncertainty	Amplitude at pick (mV)	P velocity (m/s)	Error on velocity				Total error (%)	Comment
									from length (m/s)	from noise (m/s)	Total error (m/s)	Total error (%)		
1	Plug1_maet_P_75_180504	14.28	38.37	22.6586	0.0168	0.05	53.1	3863.42	10	3	13	0.3		
2	Plug2_maet_P_75_180504	8.93	38.33	22.2529	0.0189	0.05	64.1	4024.12	10	3	14	0.3		
2_ch	Plug2ch_maet_P_75_210604	8.93	38.33	22.3685	0.0210	0.06	60.2	3978.00	10	4	14	0.4		
3	Plug3_maet_P_75_210404	14.36	38.33	21.2779	0.0108	0.03	86.1	4469.80	12	2	14	0.3		
4	Plug4_maet_P_75_190504	9.86	39.40	20.6329	0.0102	0.03	156.7	4983.85	13	2	15	0.3		
6	Plug6_maet_P_75_210404	19.15	38.62	22.1142	0.0110	0.03	124.1	4103.39	11	2	13	0.3		
6_ch	Plug6ch_maet_P_75_300604	19.15	38.62	22.1218	0.0116	0.04	134.7	4107.96	11	2	13	0.3		
8	Plug8_maet_P_75_190504	20.64	39.38	22.3045	0.0107	0.03	156.5	4111.58	10	2	12	0.3		
9	Plug9_maet_P_75_220404	18.99	38.39	22.3607	0.0118	0.03	122.1	3974.37	10	2	12	0.3		
10	Plug10_maet_P_75_220404	24.65	39.38	23.5817	0.0112	0.03	138.7	3620.09	9	2	11	0.3		
13	Plug13_maet_P_75_210504	11.22	37.61	20.4149	0.0098	0.03	174.8	4892.34	13	2	15	0.3		
14	Plug14_maet_P_75_210504	6.82	35.86	19.7249	0.0105	0.04	144.0	5123.64	14	3	17	0.3		
14_ch	Plug14ch_maet_P_75_220604	6.82	35.86	19.7425	0.0126	0.05	141.2	5114.55	14	3	18	0.3		
16	Plug16_maet_P_75_240504	3.68	35.72	20.0916	0.0138	0.04	84.0	4849.78	14	3	17	0.3		
17	Plug17_maet_P_75_240504	6.29	35.76	19.2317	0.0115	0.04	162.4	5496.79	15	3	19	0.3		
17_ch	Plug17ch_maet_P_75_220604	6.29	35.76	19.2347	0.0123	0.04	162.1	5498.62	15	4	19	0.3		
19	Plug19_maet_P_75_120504	7.97	37.89	19.9750	0.0112	0.04	154.4	5228.16	14	3	17	0.3		
21	Plug21_maet_P_75_120504	26.78	40.53	24.4040	0.0121	0.04	102.3	3471.16	9	2	10	0.3		
22	Plug22_maet_P_75_130504	24.52	39.31	24.2035	0.0174	0.05	72.1	3425.03	9	2	11	0.3		
23	Plug23_maet_P_75_130504	16.59	38.21	21.5732	0.0104	0.04	129.4	4319.03	11	2	13	0.3		
24	Plug24_maet_P_75_170504	21.76	35.62	22.1400	0.0119	0.04	104.2	3783.77	11	2	13	0.3		
26	Plug26_maet_P_75_250504	26.49	39.39	25.0928	0.0123	0.04	59.1	3185.16	8	2	10	0.3		
31	Plug31_maet_P_75_170504	22.19	36.62	22.3940	0.0161	0.05	62.1	3787.99	10	3	13	0.3		
31_ch	Plug31ch_maet_P_75_230604	22.19	36.62	22.3023	0.0198	0.07	75.3	3826.33	10	3	14	0.4	Fracture taped	
32	Plug32_maet_P_75_260504	7.17	38.49	20.6949	0.0136	0.04	91.1	4829.91	13	3	16	0.3		
32_ch	Plug32ch_maet_P_75_230604	7.17	38.49	20.6927	0.0138	0.05	96.0	4834.38	13	3	16	0.3		
Rigs213	Rigs213_maet_P_75_050404	20.34	24.75	18.3121	0.0169	0.05	58.4	4412.52	18	4	22	0.5	Por from GEUS rap. 2002/23	
Rigs220	Rigs220_*_75_maet_190404	31.51	27.87	21.0341	0.0113	0.03	132.2	3344.61	12	2	14	0.4	Por from GEUS rap. 2000/19	

Table A.5. Basic data, results, and precision of ultrasonic measurements.
Ultrasonic S1 signals, samples measured in $S_w=100$ % state.

Sample id.	File id.	Reduced porosity (%)	Reduced length (mm)	First arrival of S1 signal (us)	Local uncertainty (us)	Global uncertainty	Amplitude at pick (mV)	S1 velocity (m/s)	Error on velocity				Comment
									from length (m/s)	from noise (m/s)	Total error (m/s)	Total error (%)	
1	Plug1_maet_S1_75_180504	14.28	38.37	42.8202	0.0327	0.10	-53.6	2007.58	5	2	7	0.3	
2	Plug2_maet_S1_75_180504	8.93	38.33	34.6097	0.0875	0.57	-6.8	#I/T	#I/T	#I/T	#I/T	#I/T	
2_ch	Plug2ch_maet_S1_75_210604	8.93	38.33	34.7631	0.1140	0.83	-6.4	#I/T	#I/T	#I/T	#I/T	#I/T	
3	Plug3_maet_S1_75_210404	14.36	38.33	39.2227	0.0235	0.08	-146.2	2463.57	6	1	8	0.3	
4	Plug4_maet_S1_75_190504	9.86	39.40	38.0003	0.0266	0.06	-176.0	2756.79	7	2	9	0.3	
6	Plug6_maet_S1_75_210404	19.15	38.62	40.7650	0.0178	0.05	-322.7	2258.32	6	1	7	0.3	
6_ch	Plug6ch_maet_S1_75_300604	19.15	38.62	40.6620	0.0195	0.06	-330.1	2270.67	6	1	7	0.3	
8	Plug8_maet_S1_75_190504	20.64	39.38	41.1078	0.0202	0.05	-315.1	2263.13	6	1	7	0.3	
9	Plug9_maet_S1_75_220404	18.99	38.39	41.2741	0.0313	0.10	-190.3	2179.71	6	2	7	0.3	
10	Plug10_maet_S1_75_220404	24.65	39.38	43.8583	0.0166	0.04	-293.4	1950.22	5	1	6	0.3	
13	Plug13_maet_S1_75_210504	11.22	37.61	37.1542	0.0363	0.09	-173.9	2797.13	7	3	10	0.4	
14	Plug14_maet_S1_75_210504	6.82	35.86	31.9467	0.3842	0.90	-9.0	#I/T	#I/T	#I/T	#I/T	#I/T	
14_ch	Plug14ch_maet_S1_75_220604	6.82	35.86	26.2088	0.2198	0.98	-5.6	#I/T	#I/T	#I/T	#I/T	#I/T	
16	Plug16_maet_S1_75_240504	3.68	35.72	26.5214	0.1643	0.69	-6.5	#I/T	#I/T	#I/T	#I/T	#I/T	
17	Plug17_maet_S1_75_240504	6.29	35.76	35.7608	0.4159	0.96	-20.9	2966.45	8	35	43	1.4	
17_ch	Plug17ch_maet_S1_75_220604	6.29	35.76	35.8048	0.2503	0.66	-31.5	2957.57	8	21	29	1.0	
19	Plug19_maet_S1_75_120504	7.97	37.89	37.0592	0.0508	0.13	-116.6	2838.16	7	4	11	0.4	
21	Plug21_maet_S1_75_120504	26.78	40.53	45.4323	0.0235	0.07	-200.3	1865.75	5	1	6	0.3	
22	Plug22_maet_S1_75_130504	24.52	39.31	45.1971	0.0255	0.04	-109.7	1829.15	5	1	6	0.3	
23	Plug23_maet_S1_75_130504	16.59	38.21	39.4135	0.0348	0.12	-168.9	2432.66	6	2	9	0.4	
24	Plug24_maet_S1_75_170504	21.76	35.62	40.9749	0.0247	0.09	-208.5	2062.67	6	1	7	0.3	
26	Plug26_maet_S1_75_250504	26.49	39.39	46.1373	0.0259	0.05	-103.2	1756.03	4	1	5	0.3	
31	Plug31_maet_S1_75_170504	22.19	36.62	41.5978	0.0233	0.04	-190.2	2046.86	6	1	7	0.3	
31_ch	Plug31ch_maet_S1_75_230604	22.19	36.62	41.4125	0.0229	0.08	-196.1	2069.20	6	1	7	0.3	Fracture taped
32	Plug32_maet_S1_75_260504	7.17	38.49	40.6600	0.1271	0.88	-22.1	#I/T	#I/T	#I/T	#I/T	#I/T	
32_ch	Plug32ch_maet_S1_75_230604	7.17	38.49	27.1873	0.1079	0.94	-5.6	#I/T	#I/T	#I/T	#I/T	#I/T	
Rigs213	Rigs213_maet_S1_75_050404	20.34	24.75	33.6487	0.0840	0.45	-78.1	2478.99	10	6	16	0.7	Por from GEUS rap. 2002/23
Rigs220	Rigs220_*_75_maet_190404	31.51	27.87	38.8089	0.0164	0.04	-307.9	1839.94	7	1	7	0.4	Por from GEUS rap. 2000/19

Table A.6. Basic data, results, and precision of ultrasonic measurements.
Ultrasonic S2 signals, samples measured in $S_w=100$ % state.

Sample id.	File id.	Reduced porosity (%)	Reduced length (mm)	First arrival of S2 signal (us)	Local uncertainty (us)	Global uncertainty	Amplitude at pick (mV)	S2 velocity (m/s)	Error on velocity				Comment
									from length (m/s)	from noise (m/s)	Total error (m/s)	Total error (%)	
1	Plug1_maet_S2_75_180504	14.28	38.37	43.3631	0.0294	0.10	-27.0	2015.37	5	1	7	0.3	
2	Plug2_maet_S2_75_180504	8.93	38.33	35.1484	0.0419	0.88	-4.1	#I/T	#I/T	#I/T	#I/T	#I/T	
2_ch	Plug2ch_maet_S2_75_210604	8.93	38.33	35.3396	0.0413	1.00	-3.6	#I/T	#I/T	#I/T	#I/T	#I/T	
3	Plug3_maet_S2_75_210404	14.36	38.33	39.7646	0.0180	0.06	-92.1	2477.63	6	1	8	0.3	
4	Plug4_maet_S2_75_190504	9.86	39.40	38.6977	0.0180	0.04	-104.2	2741.32	7	1	8	0.3	
6	Plug6_maet_S2_75_210404	19.15	38.62	41.3922	0.0117	0.02	-163.7	2258.72	6	1	6	0.3	
6_ch	Plug6ch_maet_S2_75_300604	19.15	38.62	41.3148	0.0114	0.02	-172.5	2271.85	6	1	7	0.3	
8	Plug8_maet_S2_75_190504	20.64	39.38	41.7812	0.0151	0.03	-207.8	2255.78	6	1	7	0.3	
9	Plug9_maet_S2_75_220404	18.99	38.39	42.0140	0.0186	0.05	-134.3	2166.21	6	1	7	0.3	
10	Plug10_maet_S2_75_220404	24.65	39.38	44.4627	0.0114	0.02	-222.4	1952.72	5	1	5	0.3	
13	Plug13_maet_S2_75_210504	11.22	37.61	37.7768	0.0290	0.09	-132.0	2795.91	7	2	10	0.3	
14	Plug14_maet_S2_75_210504	6.82	35.86	38.9373	0.1257	0.62	-26.1	#I/T	#I/T	#I/T	#I/T	#I/T	
14_ch	Plug14ch_maet_S2_75_220604	6.82	35.86	38.8756	0.1199	0.74	-18.2	#I/T	#I/T	#I/T	#I/T	#I/T	
16	Plug16_maet_S2_75_240504	3.68	35.72	33.0051	0.1148	0.89	-6.0	#I/T	#I/T	#I/T	#I/T	#I/T	
17	Plug17_maet_S2_75_240504	6.29	35.76	36.4754	0.1334	0.44	-23.0	2942.55	8	11	19	0.6	
17_ch	Plug17ch_maet_S2_75_220604	6.29	35.76	36.4549	0.1185	0.69	-25.0	2952.57	8	10	18	0.6	
19	Plug19_maet_S2_75_120504	7.97	37.89	37.7245	0.0317	0.08	-72.4	2827.87	7	2	10	0.3	
21	Plug21_maet_S2_75_120504	26.78	40.53	46.0743	0.0249	0.05	-98.2	1863.59	5	1	6	0.3	
22	Plug22_maet_S2_75_130504	24.52	39.31	45.8802	0.0226	0.04	-72.1	1823.52	5	1	6	0.3	
23	Plug23_maet_S2_75_130504	16.59	38.21	40.1347	0.0201	0.05	-96.3	2416.59	6	1	8	0.3	
24	Plug24_maet_S2_75_170504	21.76	35.62	41.5405	0.0243	0.07	-111.0	2068.80	6	1	7	0.3	
26	Plug26_maet_S2_75_250504	26.49	39.39	46.8242	0.0183	0.03	-86.1	1750.55	4	1	5	0.3	
31	Plug31_maet_S2_75_170504	22.19	36.62	42.0833	0.0174	0.04	-120.2	2061.98	6	1	6	0.3	
31_ch	Plug31ch_maet_S2_75_230604	22.19	36.62	41.9336	0.0190	0.04	-134.3	2081.96	6	1	7	0.3	Fracture taped
32	Plug32_maet_S2_75_260504	7.17	38.49	39.1388	0.3223	0.00	-4.6	2597.76	7	21	28	1.1	
32_ch	Plug32ch_maet_S2_75_230604	7.17	38.49	39.2578	0.0890	0.71	-4.7	2580.64	7	6	13	0.5	
Rigs213	Rigs213_maet_S2_75_050404	20.34	24.75	34.2600	0.0668	0.16	-43.8	2483.70	10	5	15	0.6	Por from GEUS rap. 2002/23
Rigs220	Rigs220_*_75_maet_190404	31.51	27.87	39.4828	0.0226	0.05	-136.3	1834.64	7	1	8	0.4	Por from GEUS rap. 2000/19

Rock physics analysis of velocity differences in the chalks of wells Jette-1 and Isak-1

A contribution to the Chalk Background
Velocity project

Gary Mavko & Peter Japsen



Rock physics analysis of velocity differences in the chalks of wells Jette-1 and Isak-1

A contribution to the Chalk Background
Velocity project

The Chalk Background Velocity project
is funded by the South Arne Group

Gary Mavko¹ & Peter Japsen²

¹Stanford University, ²GEUS

Contents

Introduction – basic observations	3
Rock physics modeling	9
Effect of mineral properties on inclusion model predictions.....	10
Comparison of Jette-1 and Isak-1 in the velocity-porosity planes	15
Interpretations of differing mineral properties.....	18
Empirical models in the Vp-Vs plane.....	20
The acoustic impedance – Poisson’s ratio plane.....	27
Summary	30
References	31

Introduction – basic observations

In this note we discuss observations of P-wave sonic velocity differences between chalk intervals of the Jette-1 and Isak-1 wells. Questions of interest are, why are P-wave velocities higher in Jette-1 than in Isak-1? Why is the V_p/V_s ratio lower in Jette-1? We will show with rock physics models that these are consistent with different pore stiffnesses, though the mechanism for generating different pore stiffness is not clear.

Figure 1 compares well logs from the two wells. In both, the Ekofisk Formation is highlighted in red, the Tor Formation in blue, and the Hod Formation in green. The gamma ray log suggests differences between the two wells. In both wells, the Ekofisk tends to have relatively higher gamma ray than the cleaner Tor Formation. In Isak-1, the gamma ray in the Hod is comparable to the Tor, while in Jette-1 the gamma ray is significantly higher in the Hod than in the Tor. Overall, the gamma ray has significantly lower values in Jette-1 than in Isak-1, though the gamma ray is more variable in Jette-1 than in Isak-1, at least in the Ekofisk and Hod Formations.

Figure 2 shows sonic V_p vs. density porosity (Φ) for the Ekofisk, Tor, and Hod Formations in the two wells. For the Ekofisk and Tor Formations, we observe a wider range of porosities in Jette-1 than in Isak-1. Also, at a given porosity, the P-wave velocities in Jette-1 are higher than in Isak-1, for all formations. We also observe quite different velocity-porosity trends for the three formations. In Ekofisk, the velocity-porosity trend has a very low slope; the Tor slope is steeper; and the Hod slope is steeper still, though in Jette-1 the Hod slope is not so evident.

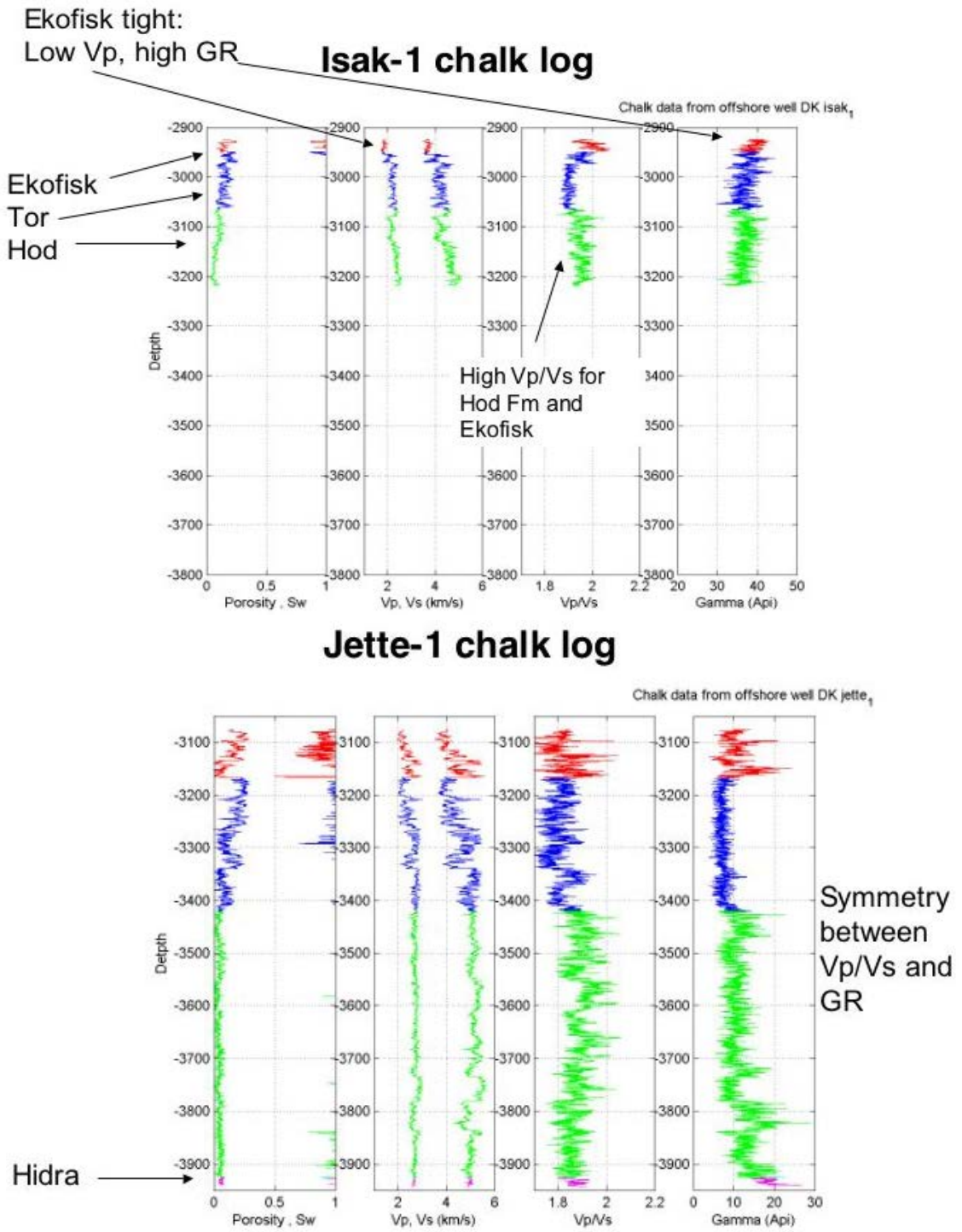


Figure 1. Logs in Isak-1 and Jette-1. Ekofisk Formation is highlighted in red, Tor in blue, and Hod in green.

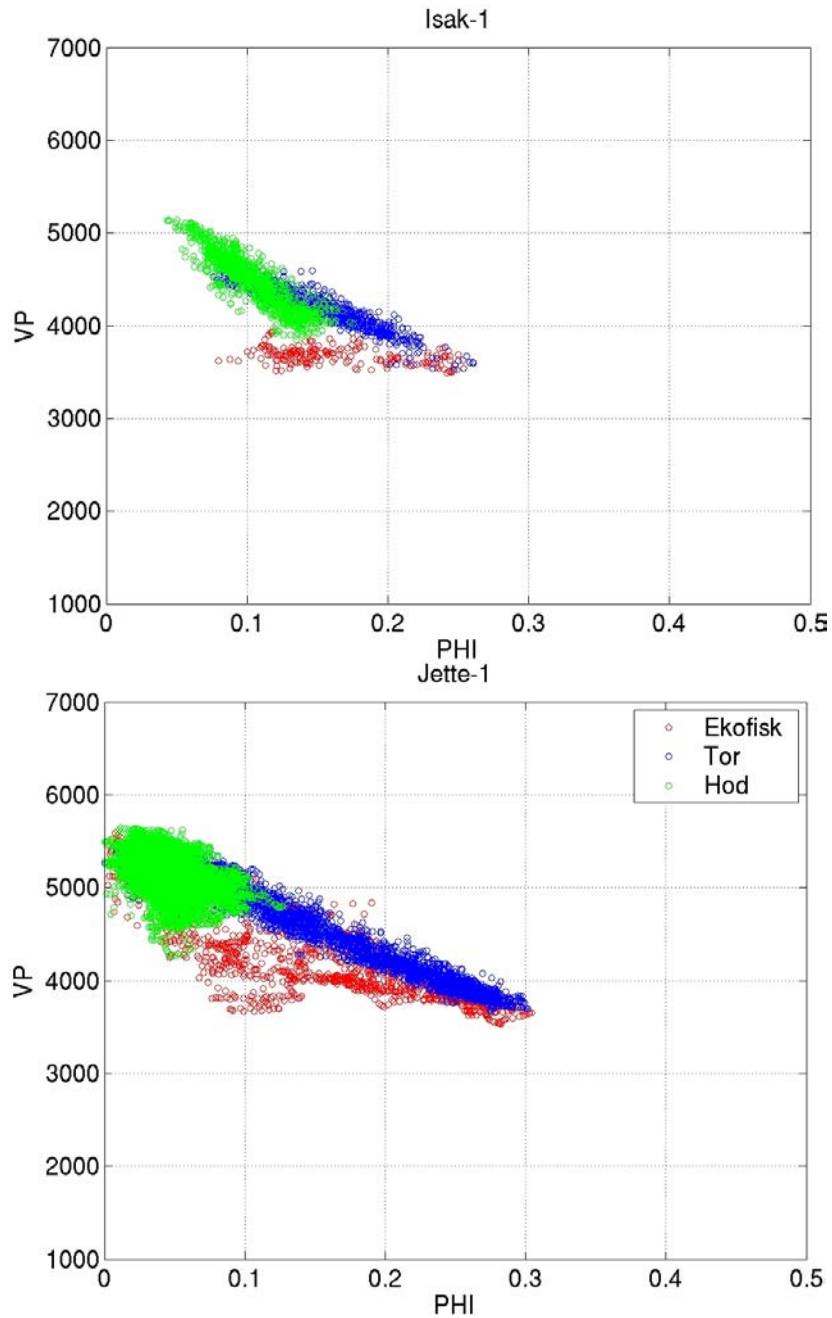


Figure 2. Log P-wave sonic velocity vs. density porosity (Φ) in Isak-1 and Jette-1. Ekofisk Formation is highlighted in red, Tor in blue, and Hod in green.

Figure 3 compares V_p/V_s ratio vs. Acoustic Impedance in Isak-1 and Jette-1. For the Ekofisk and Tor Formations, we observe a wider range of acoustic impedance in Jette-1 than in Isak-1. This mimics the porosity variation in Figure 2, since porosity and impedance tend to be highly correlated. At a given acoustic impedance, the V_p/V_s ratios in Jette-1 are lower than in Isak-1, for all formations, even though in Figure 2 we observed that V_p was higher in Jette-1.

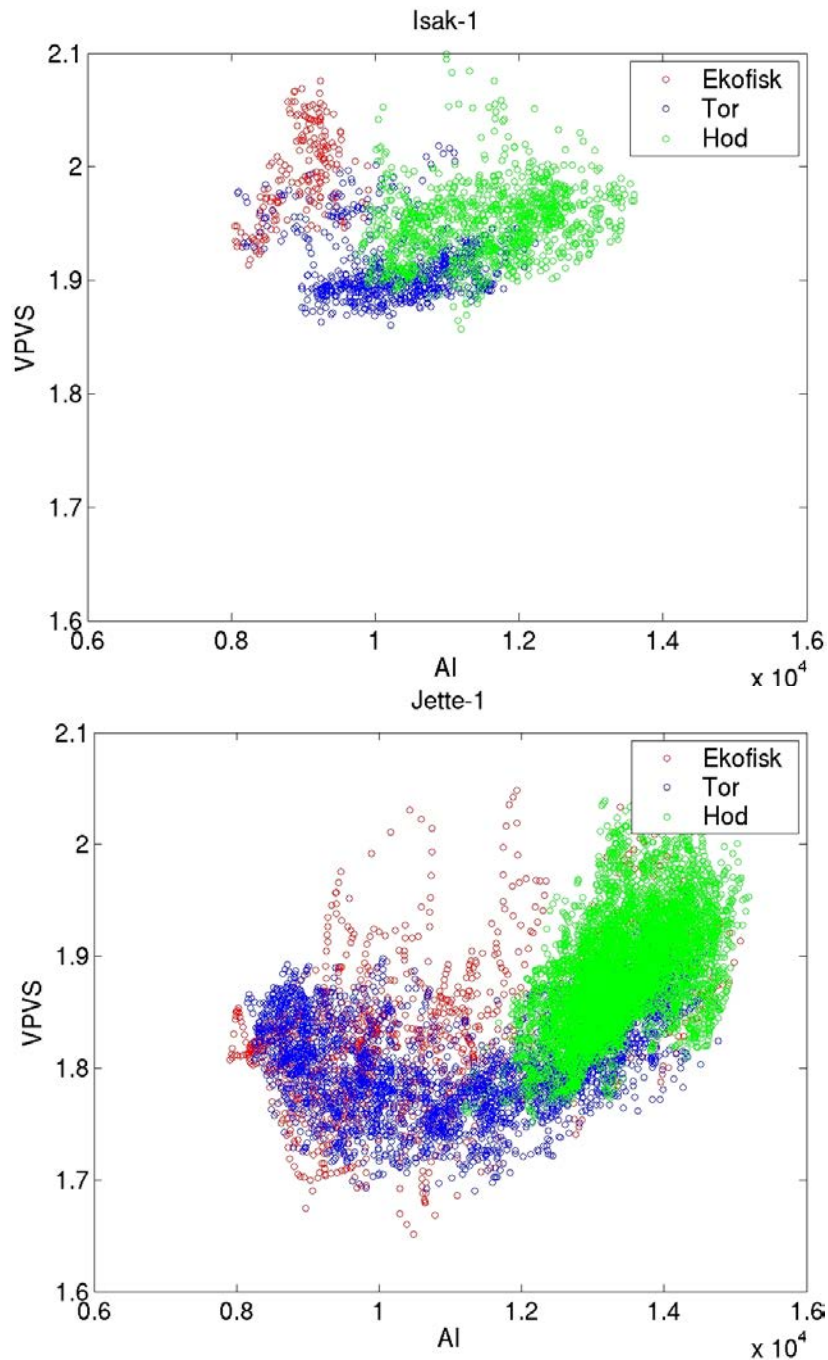


Figure 3. Log sonic V_p/V_s ratio vs. acoustic impedance in Isak-1 and Jette-1. Ekofisk Formation is highlighted in red, Tor in blue, and Hod in green.

Figure 4 compares sonic V_p vs. V_s in Isak-1 and Jette-1. The empirical Greenberg-Castagna (1992) lines for water-saturated sandstone (black line), shale (blue line), dolomite (magenta line) and limestone (green line) are shown for comparison. We also show a gas-saturated limestone line (dashed green), calculated from the water line using the Gassmann (1951) relations. Although none of the curves were developed explicitly for chalks, we see that the Jette-1 data mimic the limestone trend.

For each of the Greenberg-Castagna lithologic curves, the upper right extent can be interpreted as approximately the mineral point, at zero porosity. For pure calcite, this would correspond to ($V_p=6370$ m/s, $V_s=3330$ m/s). (Strictly, the Greenberg-Castagna curves do not pass exactly through this point. The reason is that they are empirical fits to data, and none of those data came close to zero porosity.) Moving to the lower left along each Greenberg-Castagna curve corresponds to increasing total porosity. The left-most intercept, at $V_s=0$ can be thought of as critical porosity, where the rock is falling apart. (Again, the precise V_p intercept value of the Greenberg-Castagna lines is not exactly what we would expect for a calcite-water suspension at critical porosity; the explanation again is that this high porosity limit is an extrapolation of the empirical Greenberg-Castagna curves beyond their range of validity.)

We observe in Figure 4 that the data from Isak-1 fall systematically above the Greenberg-Castagna carbonate line, while the data from Jette-1 fall along the line. That is, the Isak-1 data have systematically higher V_p/V_s ratios for all formations than the Jette-1 data. As discussed in later, this difference in V_p/V_s ratio appears to be consistent with rock textural or mineralogic differences between the two wells.

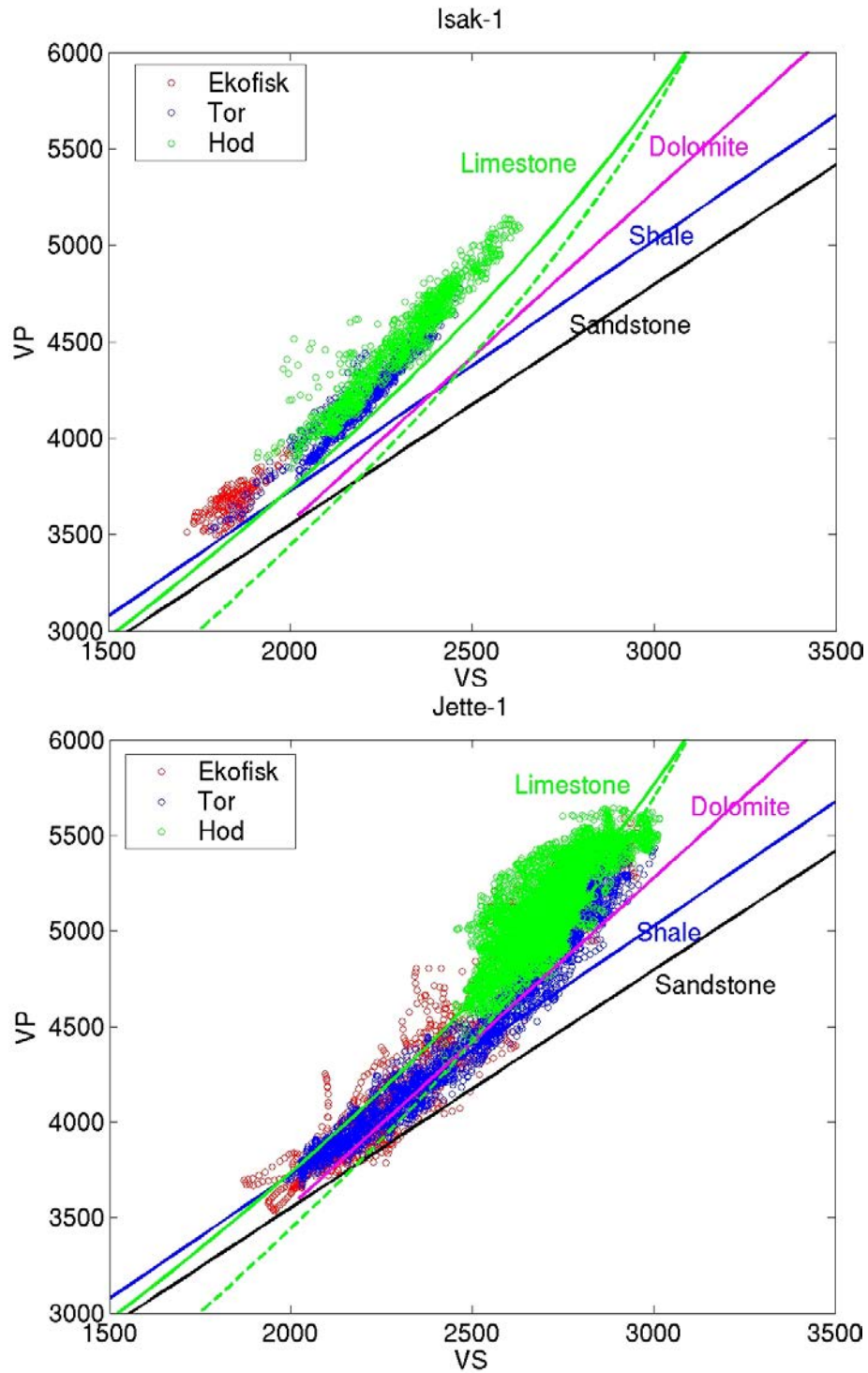


Figure 4. Log sonic Vp vs. Vs in Isak-1 and Jette-1. Ekofisk Formation is highlighted in red, Tor in blue, and Hod in green. Greenberg-Castagna lines are shown for comparison.

Rock physics modeling

In this section, we analyze the observations of Figures 2-4 by comparing them with rock physics models. One set of models represents the pore space as a collection of ellipsoidal inclusions, ranging from flat penny-shaped cracks to spherical pores. The equations that we implement are for the self-consistent formulation of Berryman (1995). The effective rock bulk and shear moduli of an N-phase composite are given by:

$$\sum_{i=1}^N x_i (K_i - K_{SC}^*) P^{*i} = 0$$

$$\sum_{i=1}^N x_i (\mu_i - \mu_{SC}^*) Q^{*i} = 0$$

where i refers to the i th material, x_i its volume fraction, P and Q are geometric factors given in Table 1, and the superscript $*i$ on P and Q indicates that the factors are for an inclusion of material i in a background medium with self-consistent effective moduli K_{SC}^* and μ_{SC}^* . These equations are coupled and must be solved by simultaneous iteration.

In the modeling, spherical pores are represented with an aspect ratio of 1; these are the stiffest possible shapes, leading to high velocities for a given porosity. Successively smaller aspect ratios represent flattened spherical pores (oblate spheroids), which are successively more compliant. Aspect ratios less than about 0.1 are often referred to as “penny-shaped” cracks. In our application, we assume two phases, calcite and water.

In using these inclusion models, it is important to remember that they are quite idealized, and should not be interpreted too literally. In real rocks there are no ellipsoidal pores. Also, the ellipsoidal models do not explicitly allow for pore connectivity. Nevertheless, these models are useful elastic analogs, and we believe that the trends predicted by them, such as from stiffer pores to more compliant pores, are valid. In our discussion below, the fact that Isak-1 data are consistent with a penny-shaped crack model does not mean that there must be cracks in the rocks. Poorly cemented, compliant grain contacts will yield the same elastic behavior.

Table 1. Coefficients P and Q for some specific shapes. The subscripts m and i refer to the background and inclusion materials [from Berryman (1995)].

Inclusion shape	P^{mi}	Q^{mi}
Spheres	$\frac{K_m + \frac{4}{3}\mu_m}{K_i + \frac{4}{3}\mu_m}$	$\frac{\mu_m + \zeta_m}{\mu_i + \zeta_m}$
Needles	$\frac{K_m + \mu_m + \frac{1}{3}\mu_i}{K_i + \mu_m + \frac{1}{3}\mu_i}$	$\frac{1}{5} \left(\frac{4\mu_m}{\mu_m + \mu_i} + 2 \frac{\mu_m + \gamma_m}{\mu_i + \gamma_m} + \frac{K_i + \frac{4}{3}\mu_m}{K_i + \mu_m + \frac{1}{3}\mu_i} \right)$
Disks	$\frac{K_m + \frac{4}{3}\mu_i}{K_i + \frac{4}{3}\mu_i}$	$\frac{\mu_m + \zeta_i}{\mu_i + \zeta_i}$
Penny cracks	$\frac{K_m + \frac{4}{3}\mu_i}{K_i + \frac{4}{3}\mu_i + \pi\alpha\beta_m}$	$\frac{1}{5} \left(1 + \frac{8\mu_m}{4\mu_i + \pi\alpha(\mu_m + 2\beta_m)} + 2 \frac{K_i + \frac{2}{3}(\mu_i + \mu_m)}{K_i + \frac{4}{3}\mu_i + \pi\alpha\beta_m} \right)$
$\beta = \mu \frac{(3K + \mu)}{(3K + 4\mu)}$		$\gamma = \mu \frac{(3K + \mu)}{(3K + 7\mu)}$
		$\zeta = \frac{\mu}{6} \frac{(9K + 8\mu)}{(K + 2\mu)}$

Effect of mineral properties on inclusion model predictions

When comparing theoretical curves with well log data, we find that the results are very sensitive to the assumed mineral properties. Figure 5 shows plots of V_p vs. V_s , V_p vs. Φ , and V_s vs. Φ for the Ekofisk, Tor, and Hod Formations of Isak-1. Superimposed are the predictions of the ellipsoidal inclusion model, for average pore aspect ratios of [1, 0.3, 0.1, 0.03, 0.01]. For these curves, we assumed mineral bulk modulus, $K = 65 \text{ GPa}$, shear modulus, $\mu = 27 \text{ GPa}$, and density, $\rho = 2.71 \text{ g/cm}^3$. From the top two plots, it appears that most of the data fall between aspect ratios ~ 0.03 and ~ 0.1 . Looking closer, we see that the V_p - Φ plot (top) shows data extending to about half way between the curves for aspect ratios 0.1 and 0.3; in contrast, the V_s - Φ plot (middle) shows data falling only slightly above the curve for aspect ratio 0.1. Hence, there is an inconsistency with the model – it does not make physical sense that the P-waves are seeing stiffer aspect ratios than the S-waves. The inconsistency is even more obvious in the plot of V_p - V_s (bottom).

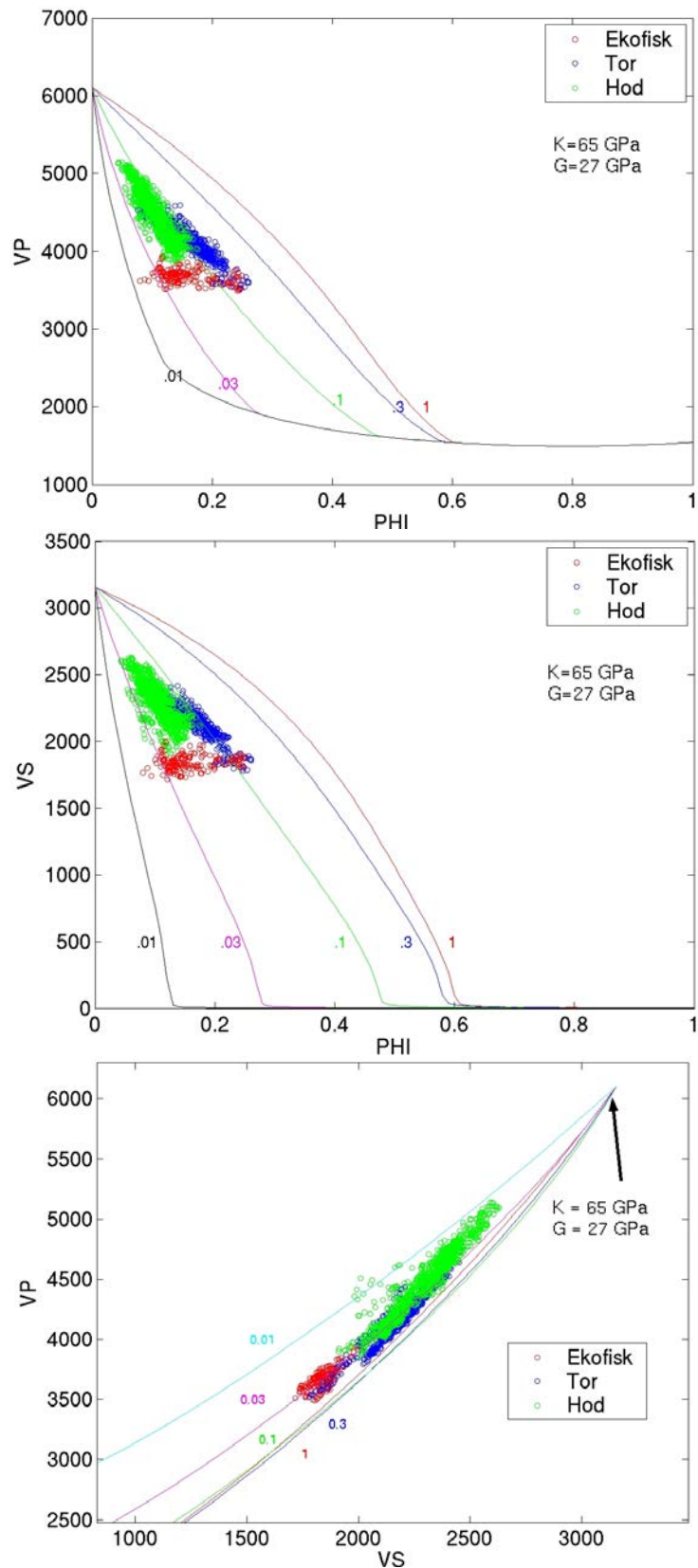


Figure 5. Plots for the Ekofisk, Tor, and Hod Formations of Isak-1, showing the model inconsistency resulting from a poor choice of mineral properties.

Note that data from the Hod Formation (green) extend to very small aspect ratios, ~ 0.01 , while in the Vp-Phi and Vs-Phi plots, the Hod always falls above the curve for 0.03. One way to explain this discrepancy is that the Poisson's ratio of the elastic mineral used for modeling is not consistent with the observed Poisson's ratio of the porous rocks.

Figure 6 shows the same type of plots as in Figure 5, but now with mineral properties adjusted to $K = 67 \text{ GPa}$, $\mu = 23 \text{ GPa}$, and density, $\rho = 2.71 \text{ g/cm}^3$. The moduli were adjusted empirically to find model predictions consistent with both P- and S-wave velocity data. We now observe that the plots of Vp vs. Phi (top) and Vs vs. Phi (middle) show data falling consistently in the aspect ratio range $\sim .03$ - $.2$. The plot of Vp vs. Vs (bottom) shows essentially the same range. (In this plot the curves for larger aspect ratios (.1, .3, and 1) cluster very close together, so it is difficult to conclude much about the higher end aspect ratio suggested by the data.) Hence, by adjusting the mineral moduli, we can find model aspect ratios that are consistent with both P- and S-wave velocities at Isak-1. It is interesting that this single adjustment improved the consistency for all three formations, even though the formations have different textures, pore shapes, and Poisson's ratios.

Figure 7 shows the same type of plots as in Figures 5 and 6, but now for Jette-1. Here, model consistency with both Vp and Vs requires a different set of mineral properties, $K = 60 \text{ GPa}$, $\mu = 27 \text{ GPa}$, and density, $\rho = 2.71 \text{ g/cm}^3$.

In summary, inference of pore shapes corresponding to the log data, based on the ellipsoidal inclusion model is very sensitive to the choice of mineral properties. We observed in Figures 5 and 6 for well Isak-1 that adjusting the moduli from ($K = 65 \text{ GPa}$, $\mu = 27 \text{ GPa}$) to ($K = 67 \text{ GPa}$, $\mu = 23 \text{ GPa}$) has a large effect on the consistency of the models with P- and S-wave data. This adjustment caused a change in mineral Vp of only about $\sim 1\%$, but a change in mineral Vs of $\sim 7\%$.

Similarly, model consistency required a change in mineral moduli between Isak-1 and Jette-1. Mineral Vp at Jette-1 is about 1% slower than at Isak-1, while mineral Vs at Jette-1 is about 7% faster than at Isak-1.

It is difficult to know how much of this discrepancy is a limitation of the idealized ellipsoidal inclusion model. Nevertheless, the Vp/Vs behavior of the data from the two wells shows different trends, with Vp/Vs at Jette-1 generally lower than Isak-1.

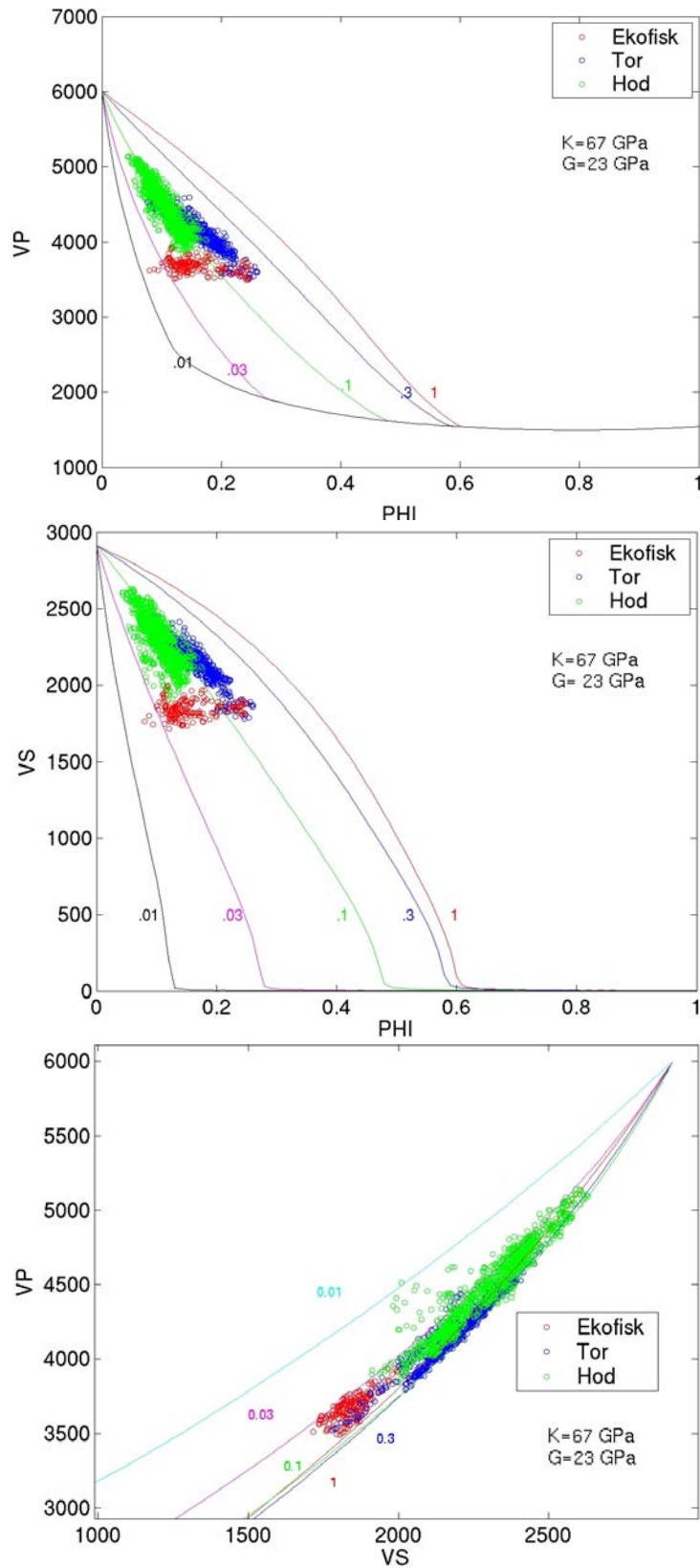


Figure 6. Plots for the Ekofisk, Tor, and Hod Formations of Isak-1, showing improved model consistency resulting from adjusted mineral properties. Mineral bulk and shear moduli used in the modeling are labeled in the figures.

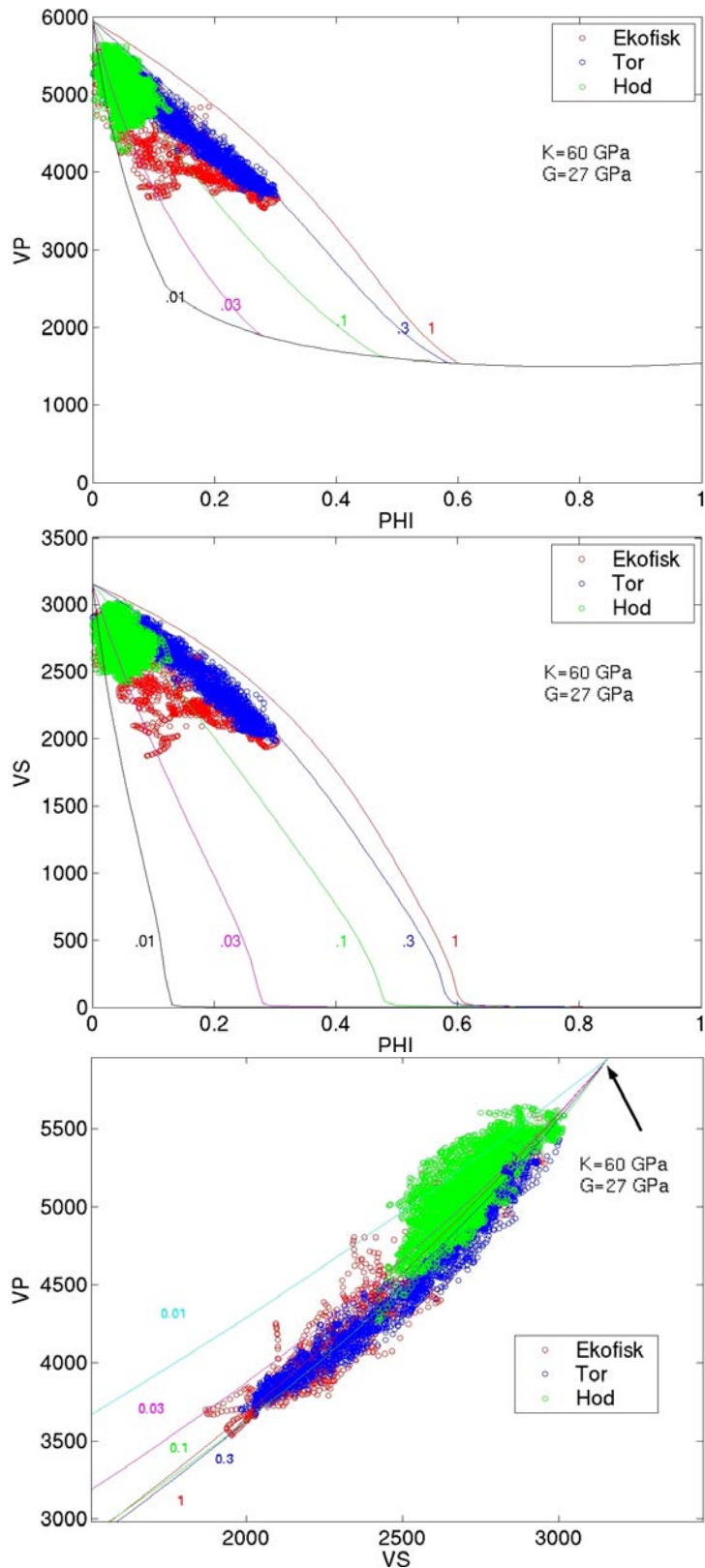


Figure 7. Plots for the Ekofisk, Tor, and Hod Formations of Jette-1, showing good model consistency resulting from adjusted mineral properties. Mineral bulk and shear moduli used in the modeling are labeled in the figures.

Comparison of Jette-1 and Isak-1 in the velocity-porosity planes

Figure 8 compares plots of sonic Vp vs. Phi and Vs vs. Phi for the Ekofisk, Tor, and Hod Formations in Isak-1 and Jette-1. Predictions of the ellipsoidal inclusion model are superimposed, for average pore aspect ratios of [1, 0.3, 0.1, 0.03, 0.01]. As discussed above, slightly different mineral moduli were used for each well, though the mineral Vp is virtually the same. The comparison suggests that the rocks from Jette-1 appear to span a much larger range of pore shapes than the rocks in Isak-1 (although we will show below that this is likely related to clay content). Rocks of the Tor Formation (blue) show the cleanest trend for both wells, and in Jette-1, the Tor seems to have significantly rounder, stiffer pores than in Isak-1. The Hod Formation in Isak-1 shows a very consistent Vp-Phi trend, with aspect ratios between .03-.1, while the Hod Formation in Jette-1 is quite variable, spanning from soft (~.01) to stiff (~1) pores (again, likely a clay effect). The Ekofisk Formation shows a range of pore aspect ratios in both wells, but the range is much larger in Jette-1, especially extending to stiffer pore shapes, similar to the Tor.

Figure 9 compares plots of sonic Vp vs. Vs for the Ekofisk, Tor, and Hod Formations in Isak-1 and Jette-1. Predictions of the ellipsoidal inclusion model are superimposed. Once again the Tor Formation in Jette-1 appears to have stiffer pore space (large aspect ratios) than in Isak-1, though in these axes the large aspect ratios are difficult to resolve.

What processes can lead to differences in pore stiffness? One hypothesis is that earlier in their burial histories, rocks from both the Isak-1 and Jette-1 wells had similar microstructures, with compliant grain-to-grain contacts. As time went on, rocks in the Ekofisk and Tor Formations of Jette-1 gained more cement preferentially deposited at the grain contacts. This would account for some stiffer rocks in the Tor and Ekofisk Formations, but it does not explain the overall larger range of porosities and the larger range of pore stiffnesses in Jette-1. A second hypothesis is that rocks in the different wells suffered different amounts of strain or pore pressure, which created microcracks resulting in a softer pore space. A third hypothesis is that we are seeing elastic effects of clay in the dirtier Ekofisk and Hod Formations.

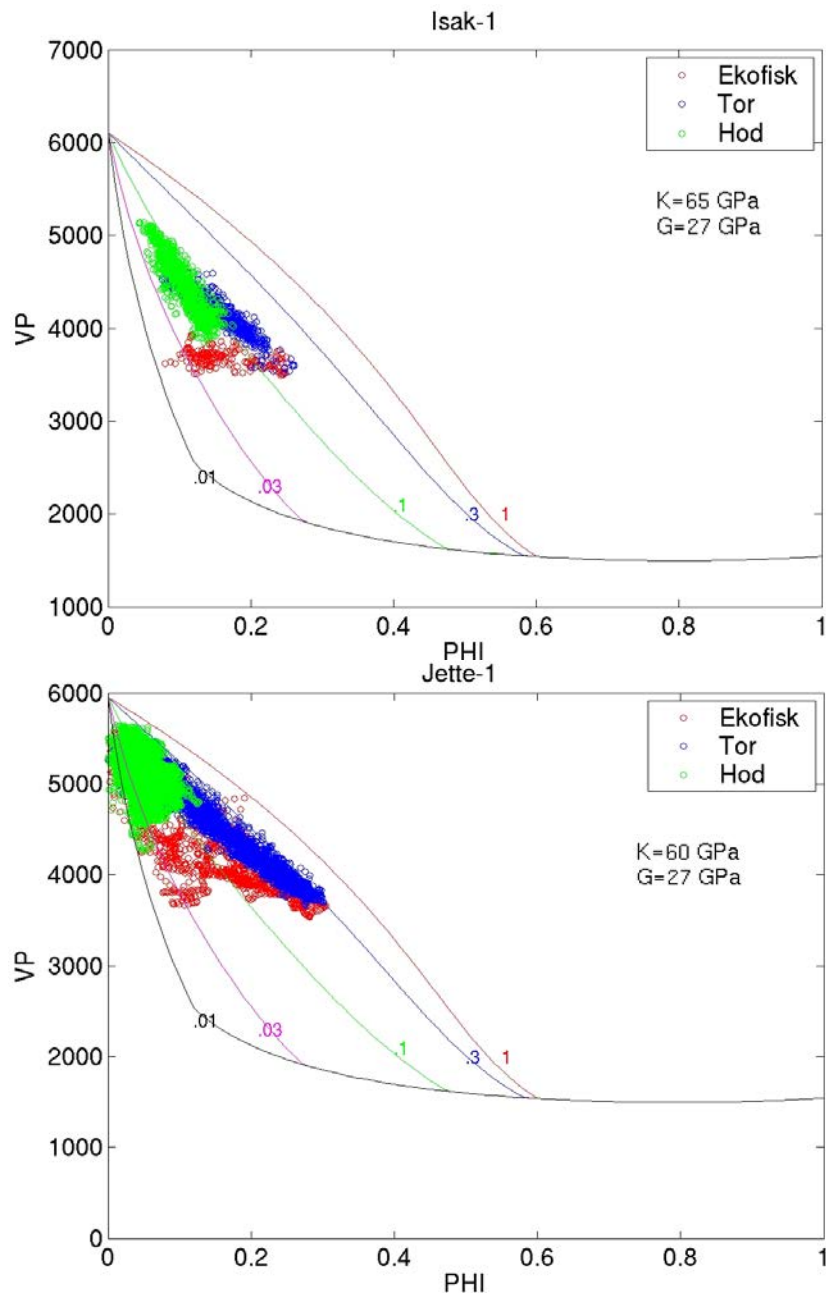


Figure 8. Comparison of V_p vs. porosity in Isak-1 (top) and Jette-1 (bottom). Predictions of a rock physics model representing pores of various aspect ratios (numbers next to the various curves) are superimposed. Ekofisk Formation is highlighted in red, Tor in blue, and Hod in green.

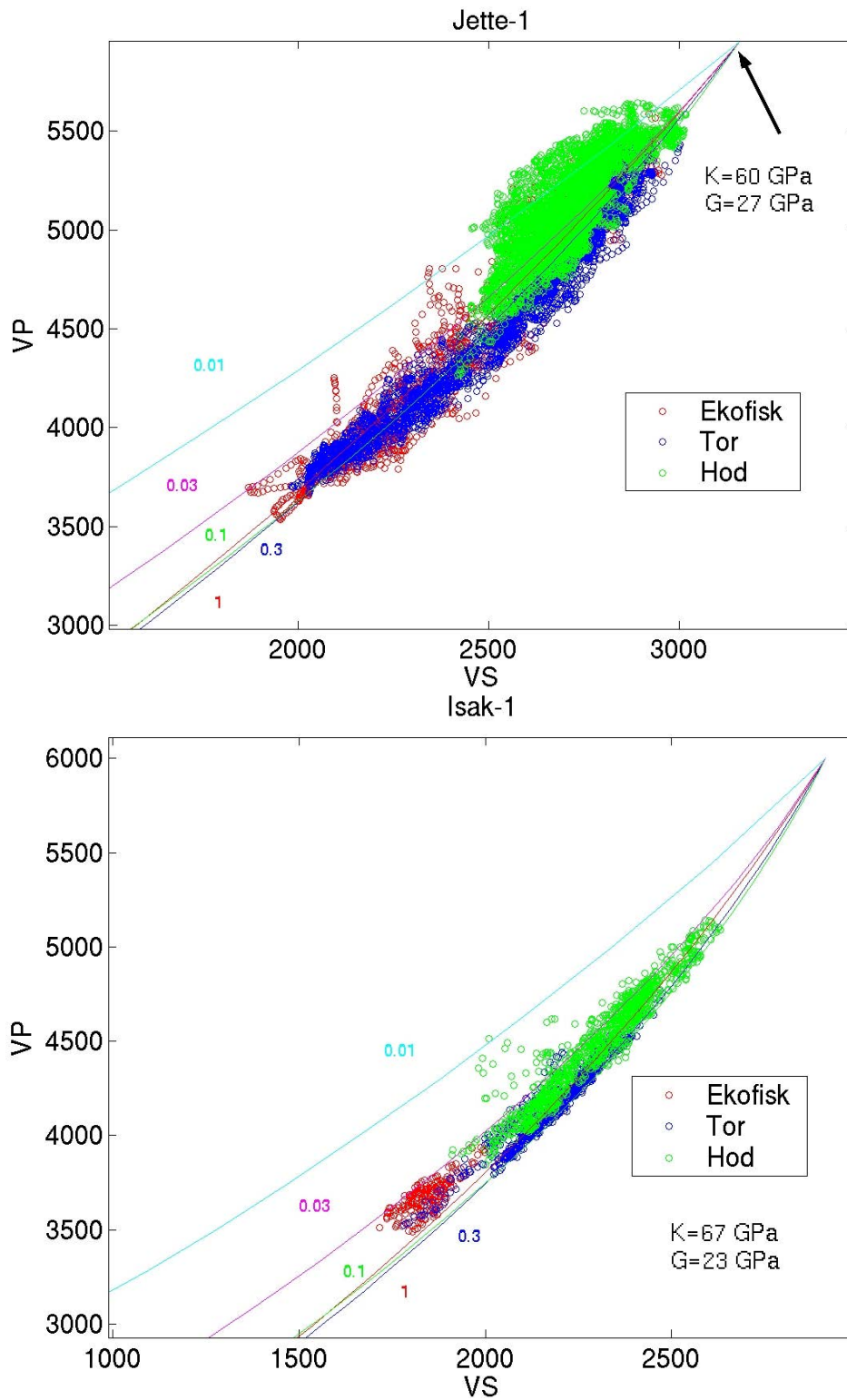


Figure 9. Log sonic V_p vs. V_s in Isak-1 and Jette-1. Predictions of a rock physics model representing pores of various aspect ratios (numbers next to the various curves) are superimposed. Ekofisk Formation is highlighted in red, Tor in blue, and Hod in green.

Interpretations of differing mineral properties

In the previous sections we illustrated that consistency between the well log data and the ellipsoidal inclusion models indicated different mineral properties in Isak-1 vs. Jette-1. For reference, the parameters that we used are shown in the table below.

Mineral properties used in elastic models of wells Isak-1 and Jette-1

	Bulk Modulus (GPa)	Shear Modulus (GPa)	Density (g/cm ³)
Isak-1	67	23	3.31
Jette-1	60	27	3.31

What might account for this difference? One scenario that we consider is that well Jette-1 has more quartz present in the mineral matrix, possibly the result of precipitation from pore fluids after deposition.

To test this idea, we modeled the average elastic properties for mixtures of quartz and calcite, as shown in Figure 10. In the figure, we plot average mineral bulk modulus vs. average mineral shear modulus. No porosity is included in the modeling; we are only considering the average properties of the mineral matrix. The average moduli were computed in two different ways. The thin black curves show the upper and lower Hashin-Shtrikman bounds. All mixtures of quartz and calcite, regardless of the way they are geometrically arranged, must fall between these two bounds. The bounds are very close to each other, because the properties of calcite and quartz end members are elastically similar – within a factor of two.

The red line shows the results of assuming a composite of equant grains of the two minerals, computed using the ellipsoidal inclusion model. As expected for a physically realizable model, the results fall between the Hashin-Shtrikman bounds. We found that the results were virtually independent of the assumed aspect ratios of the quartz and calcite, again the result of quartz and calcite being elastically similar. In both models, we took the properties of the Isak-1 mineral as the calcite end member (point on the upper left of the graph, labeled Quartz fraction = 0); the properties of quartz were assumed to be $K = 36\text{GPa}$ and $\mu = 45\text{GPa}$ (point on the lower right of the graph, label Quartz fraction = 1). The properties for the Jette-1 mineral that we determined by trial and error in the previous section, are shown by a black dot. Note that in fact, it corresponds very closely to the theoretically expected value for a mixture of 80% calcite and 20% quartz.

A second observation that we discussed in Figures 6 and 7 is that the rocks in Jette-1 appear to have stiffer pores than in Isak-1. This again could be the result of quartz cementation, particularly if the quartz fills the thinnest cracks and grain contacts, resulting in a more rigid pore space.

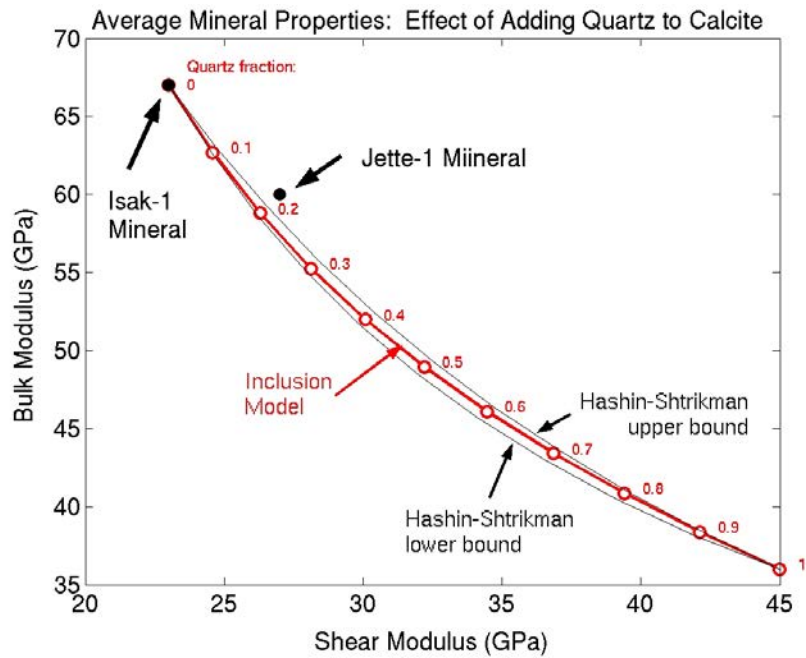


Figure 10. Theoretical predictions of the average modulus of calcite and quartz mixed in different proportions. The point on the upper left is for pure calcite and on the lower right, pure quartz. Predictions of the Hashin-Shtrikman bounds and the elastic inclusion model give essentially the same result. The Jette-1 mineral is consistent with 20% quartz.

Another aspect of the mineralogy is the effect of clay. In general, clay tends to soften both the bulk and shear moduli of rocks, and tends to increase the V_p/V_s ratio. One of the observations of Figure 7 is that the Hod Formation in Jette-1 has a large apparent range of aspect ratios, and a large V_p/V_s ratio. We also observed in Figure 7 that the data in the V_p vs. V_s plane have a large scatter relative to the ellipsoidal model curves.

Figure 11 shows the data from Jette-1, now color-coded by gamma ray. The data are shown for the Ekofisk, Tor, and Hod Formations together, as well as separately. The clean Tor Formation shows little variation with gamma ray. However, the clay-bearing Ekofisk and Hod Formations show a large variation in gamma ray, and a large variation in apparent aspect ratios. In fact, Figure 11 suggests that the data extending to the smallest aspect ratio curves are probably reflecting the presence of clay, rather than a systematic change in pore shape.

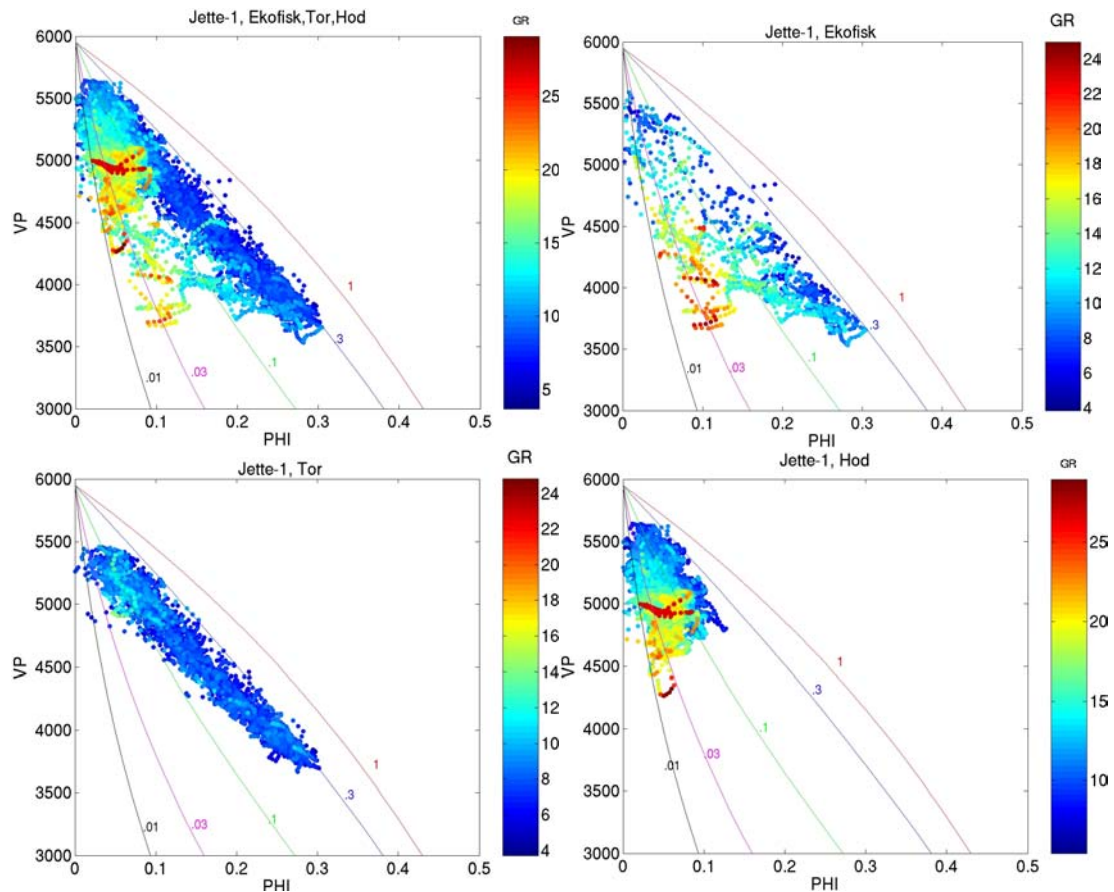


Figure 11. Plots of V_p vs. Φ in Jette-1, color-coded by gamma ray. Plots of Ekofisk, Tor, and Hod Formations are shown together (upper left) and separately.

Empirical models in the V_p - V_s plane

Additional insights into the effects of rock texture can be gotten by comparing Greenberg-Castagna curves for sand and limestone lithologies, as shown in Figure 12. Empirical studies on clastics almost always indicate a *linear* relation between V_p and V_s extending from the quartz mineral point, as illustrated by the blue Greenberg-Castagna sand line in Figure 12. In contrast, carbonates often show a quadratic relation, as illustrated by the *curved* green Greenberg-Castagna limestone line. A conceptual view of the corresponding rock textures is that sandstones are made from an assembly of *particles*, while limestones are calcite mineral, containing an assembly of *holes*.

Tsuneyama, et al. (2003) showed that, in contrast to most limestones, carbonate *grainstones* have V_p/V_s larger than expected from the usual Greenberg-Castagna curve; they found that grainstone V_p - V_s follows a straight line extending from the mineral point, as illustrated by the magenta line in Figure 12. Since grainstones can be thought of as an assembly of carbonate particles, texturally resembling a clastic, it is not surprising that the corresponding V_p - V_s relation is linear. In fact, we construct the grainstone line in Figure 12 by taking the sandstone line and scaling it by the ratio of calcite to quartz bulk and shear moduli.

Figure 13 shows V_p vs. V_s with the grainstone line (magenta) and Greenberg-Castagna carbonate line (green), similar to Figure 12. We now superimpose the Hashin-Shtrikman upper bound (red), computed for calcite ($K = 65 \text{ GPa}$, $\mu = 27 \text{ GPa}$, $\rho = 2.71 \text{ g/cm}^3$) and water ($K = 2.2 \text{ GPa}$, $\rho = 1.02 \text{ g/cm}^3$). We see that the curved Greenberg-Castagna line falls almost exactly along the upper bound, indicating that it represents essentially the stiffest possible pore space in calcite mineral. Points plotting anywhere above this line represent rocks with softer pore space.

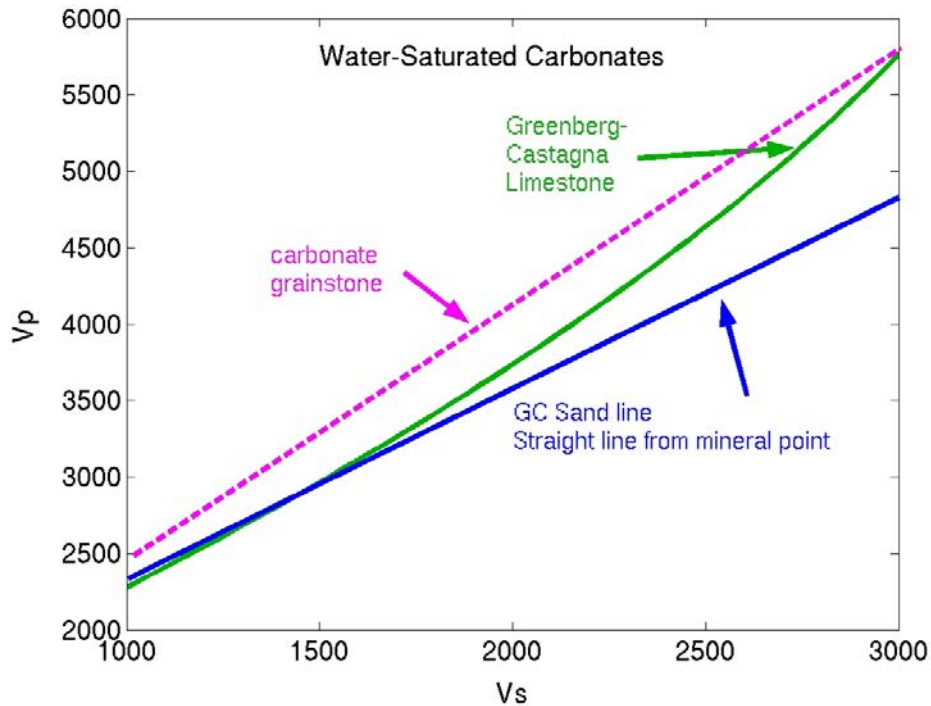


Figure 12. Comparison of empirical V_p - V_s relations for sands and carbonates. The empirical Greenberg-Castagna line for sandstone is shown in blue, the Greenberg-Castagna curve for limestones is shown in green, and a carbonate grainstone line is shown in dashed magenta.

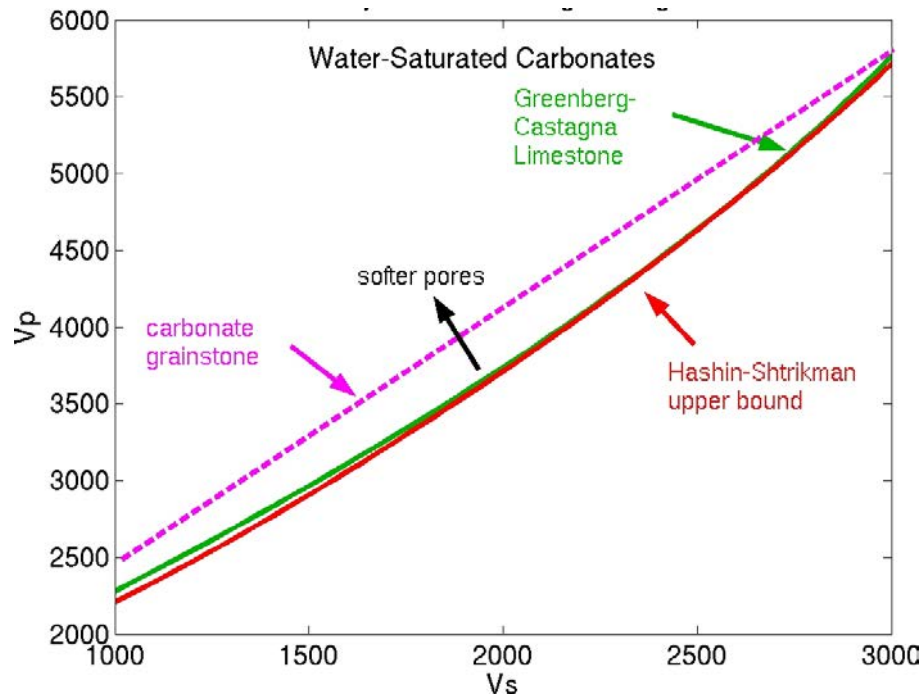


Figure 13. Comparison of empirical Greenberg-Castagna curve for limestones with Hashin-Shtrikman upper bound.

Figure 14 compares sonic V_p vs. V_s in Isak-1 and Jette-1, similar to Figure 4. The empirical Greenberg-Castagna (1992) line for limestone (dark green curve) is shown for comparison. We also show the carbonate grainstone line from Figure 12 (magenta; upper plot) and a gas-saturated line (dashed green; lower plot). We observe, as before, that the data from the Ekofisk and Tor in Jette-1 are fairly consistent with the limestone line, while data from Hod in Jette-1 and all formations in Isak-1 deviate in the direction of the grainstone line. This would suggest that a textural difference could account for the differences observed between the two wells.

Figure 15 compares data from Isak-1 and Jette-1, one formation at a time. The Greenberg-Castagna lines for water and gas-saturated limestones are shown for reference. In each case the rocks in Isak-1 have larger V_p/V_s ratio than the corresponding formation in Jette-1. Also striking is that in each case the rocks in Jette-1 tend to have higher velocities and span a larger range of velocities than the corresponding formations in Isak-1.

Figure 16 shows data for Isak-1 and Jette-1, color-coded by depth. In Isak-1, there is a fairly monotonic increase of velocities with depth. However in Jette-1, the depth variation is more complicated. Rocks from the shallower Ekofisk and Tor Formations span the entire range of velocities. Data from the Hod Formation fall in the upper half of the velocity range, though within the Hod, there is not a systematic increase of velocity with depth.

Figure 17 shows data from Isak-1 and Jette-1, again color-coded by depth. Ellipsoidal inclusion models are superimposed. In Isak-1, there is no apparent change of pore shape with depth, even though the velocities increase systematically with depth. This can correspond to a systematic decrease in porosity with depth, without a significant change in pore shape. In Jette-1, there is a stiffening of pore shape with depth within the Tor Formation,

and again within the Hod Formation. This stiffening within each of the formations seems to occur without a systematic decrease of porosity with depth.

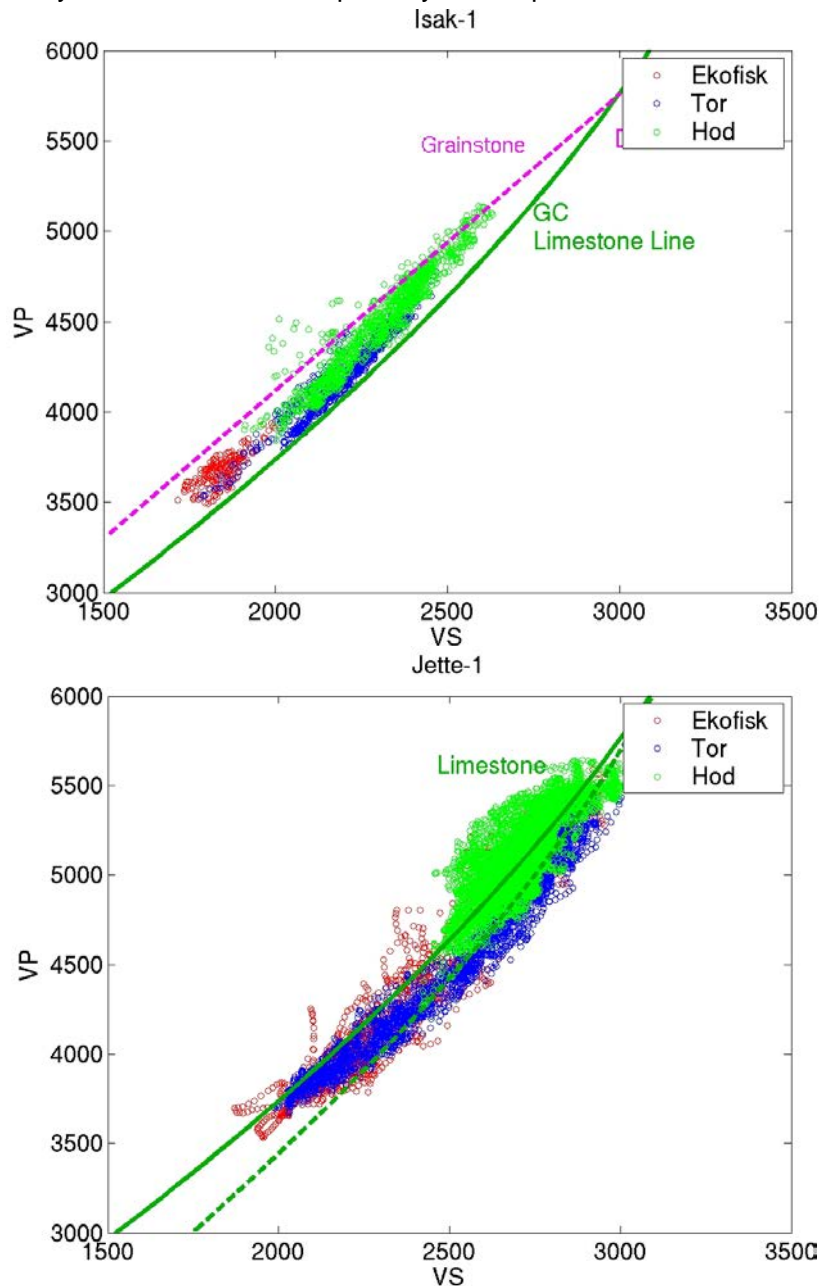


Figure 14. Comparison of empirical V_p - V_s relations for sands and carbonates. The empirical Greenberg-Castagna curve for limestones is shown in dark green (water-solid, gas-dashed), and a carbonate grainstone line is shown in dashed magenta. Data from the Ekofisk Formation is shown in red; the Tor in blue; and the Hod in green.

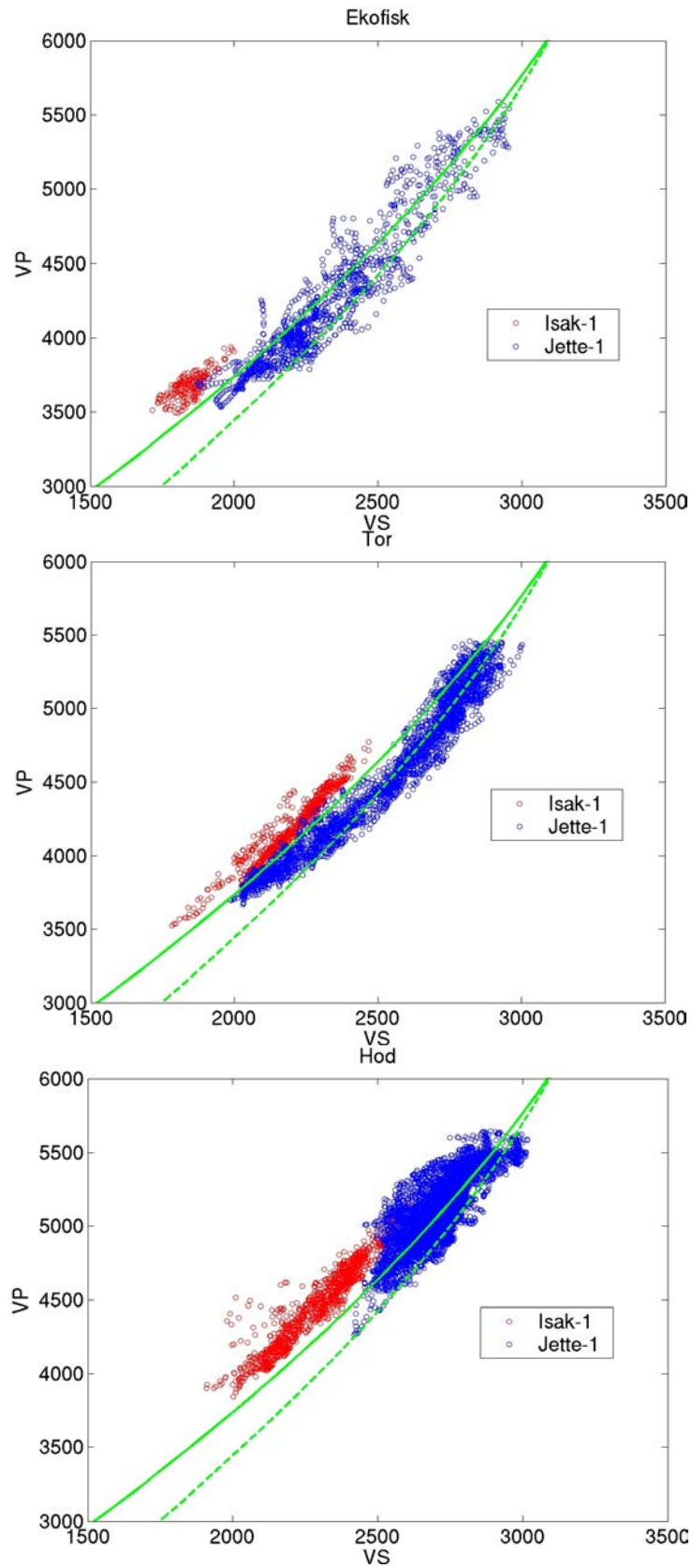


Figure 15. Comparison Isak-1 and Jette-1, for each Formation. Greenberg-Castagna curves for limestones (water: solid; gas: dashed) are superimposed.

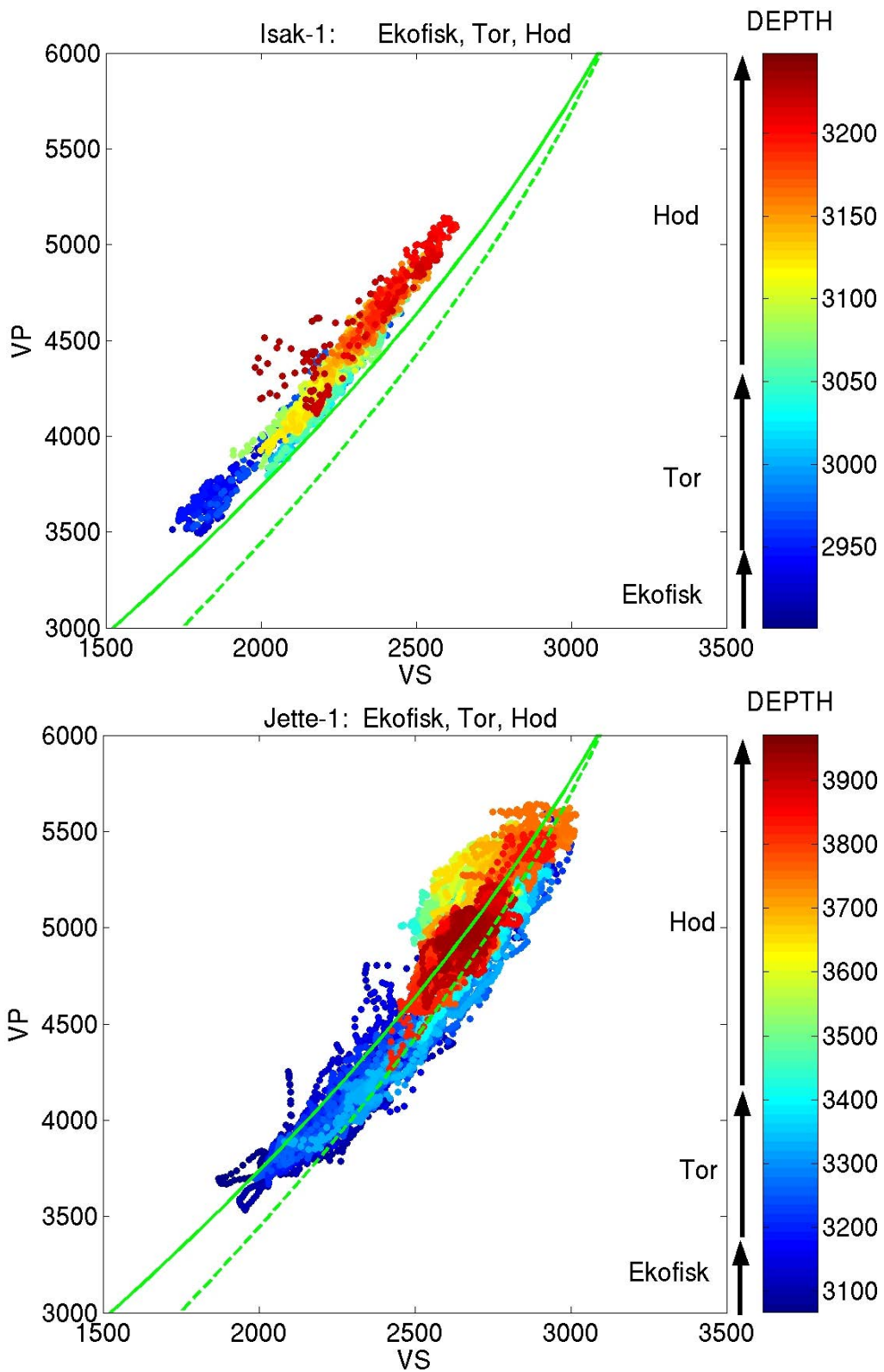


Figure 16. Comparison Isak-1 and Jette-1, color-coded by depth. Greenberg-Castagna curves for limestones (water: solid; gas: dashed) are superimposed.

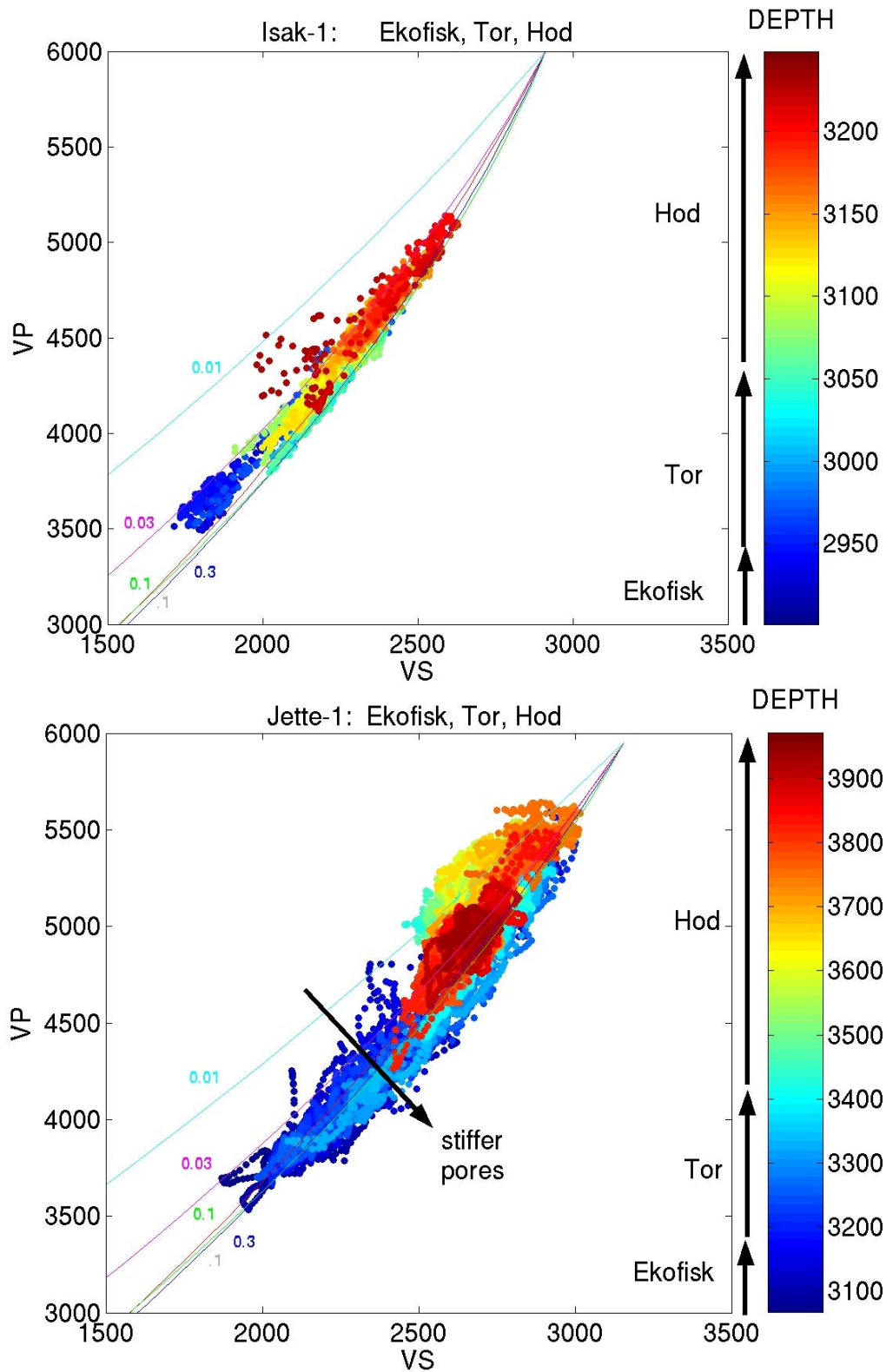


Figure 17. Comparison Isak-1 and Jette-1, color-coded by depth. Ellipsoidal inclusion models are superimposed.

The acoustic impedance – Poisson's ratio plane

Finally, we compare data from Isak-1 and Jette-1 plotted as acoustic impedance vs. V_p/V_s ratio (Figure 18) and Poisson's ratio (Figure 19). Both planes highlight the differences in apparent pore stiffness and velocity that we have been discussing.

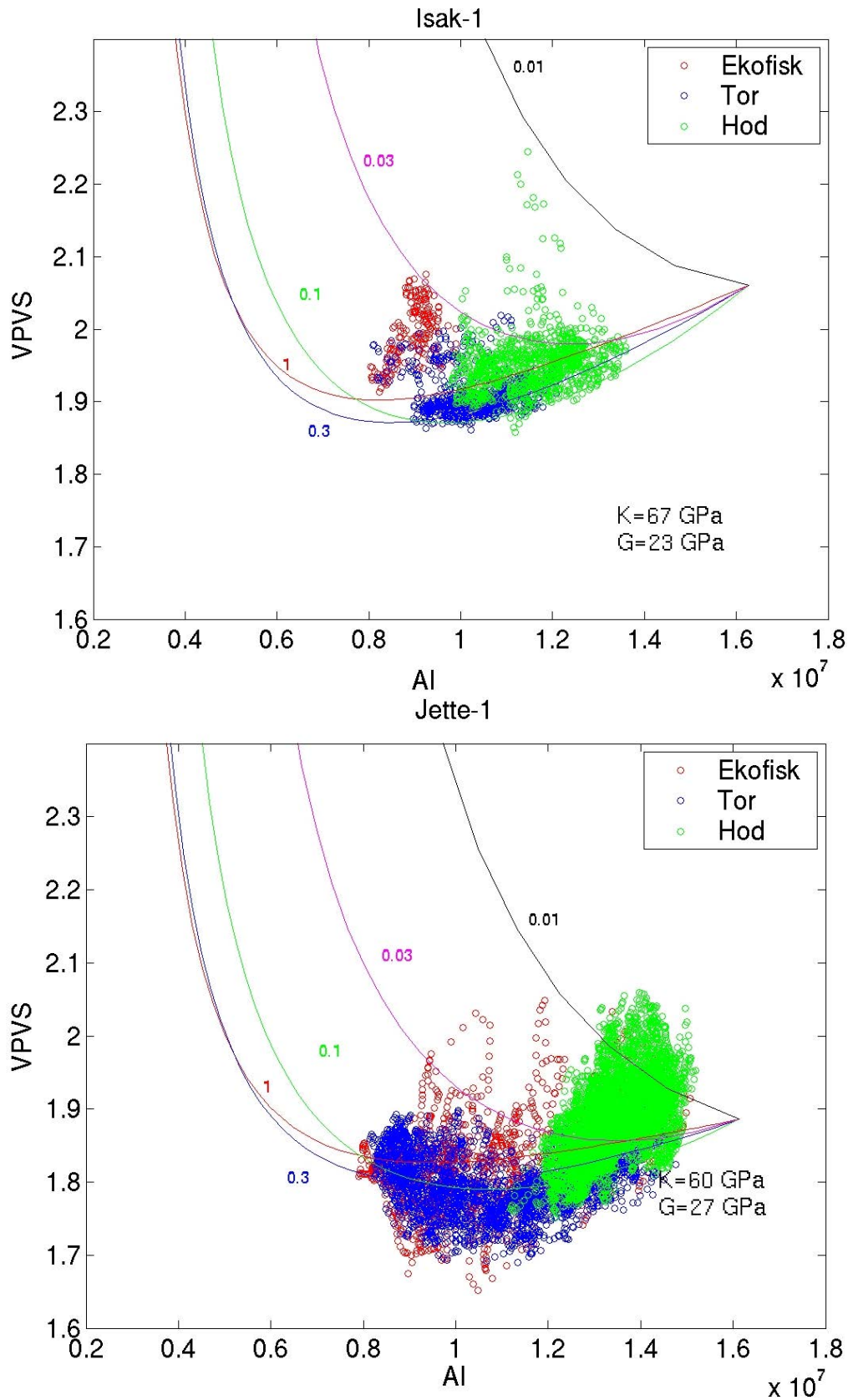


Figure 18. Log V_p/V_s vs. acoustic impedance in Isak-1 and Jette-1. Ekofisk Formation is highlighted in red, Tor in blue, and Hod in green. Ellipsoidal pore models are superimposed.

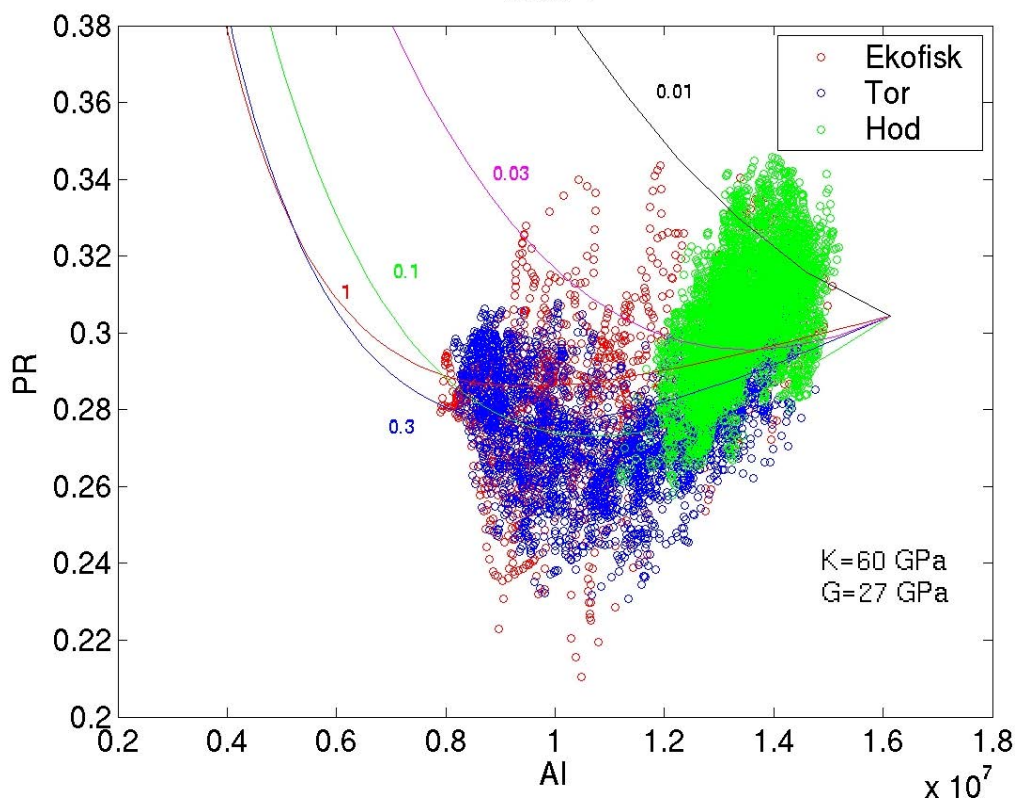
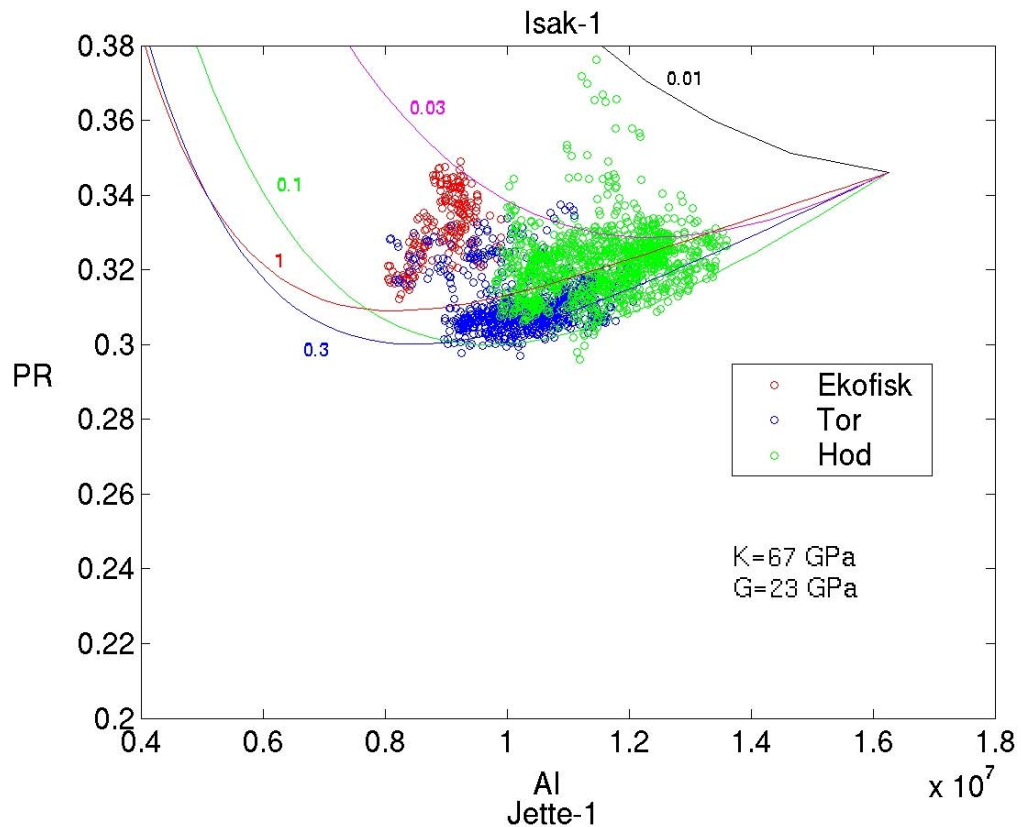


Figure 19. Log Poisson's ratio vs. density porosity in Isak-1 and Jette-1. Ekofisk Formation is highlighted in red, Tor in blue, and Hod in green. Ellipsoidal pore models are superimposed.

Summary

Differences between the sonic log data from wells Jette-1 and Isak-1 have been observed in the chinks of the Ekofisk, Tor, and Hod Formations. Both P- and S-wave velocities in Jette-1 tend to be larger than in Isak-1, while the V_p/V_s ratio is smaller in Jette-1. Comparison with rock physics ellipsoidal pore models suggest that the chalk in Jette-1 have stiffer pores than in Isak-1 and that the mineral end-point properties are different for the two wells. The moduli were adjusted empirically to find model predictions consistent with both P- and S-wave velocity data because the ellipsoidal inclusion model is very sensitive to the choice of mineral properties. The mineral moduli for Isak-1 were found to be $K=67$ GPa, $G=23$ GPa and those for Jette-1 $K=60$ GPa, $G=27$ GPa. Taking the properties of the Isak-1 mineral as the calcite end-member, the Jette-1 properties correspond to the theoretically expected value for a mixture of 80% calcite and 20% quartz. If the quartz fills the thinnest cracks and grain contacts the result would be a more rigid pore space and thus explain that the chalk in Jette-1 have stiffer pores than in Isak-1. The clean Tor Formation has little variation with gamma ray, whereas the clay-bearing Ekofisk and Hod Formations have a large variation in gamma ray and a corresponding spread in V_p vs porosity (apparent aspect ratios). This spread thus probably reflects the presence of clay, rather than a systematic change in pore shape. Velocities in Isak-1 increase monotonically with depth without a significant change of pore shape (porosities decreasing from 25% to less than 10%), while in Jette-1 the velocities are not well correlated with depth.

References

- Berryman, J.G., 1995, Mixture theories for rock properties, *in: A Handbook of Physical Constants*, Ahrens, T.J., ed., American Geophysical Union, Washington, 236 pp.
- Gassmann, F., 1951, Über die elastizität poroser medien, *Vier. der Natur Gesellschaft*, 96, 1-23.
- Greenberg, M.L. and Castagna, J.P., 1992, Shear-wave velocity estimation in porous rocks: theoretical formulation, preliminary verification and applications, *Geophysical Prospecting*, 40, 195-209.
- Tsuneyama, F., Nishida, A., Okamura, H., 2003, Vp/Vs as a rock frame indicator for a carbonate reservoir, *First Break*, 21, 22-27.

Seismic velocities in the chalk, NE part of the South Arne Field

Contribution to the Chalk Background Velocity project

Ole Vejbæk & Peter Japsen



Seismic velocities in the chalk, NE part of the South Arne Field

Contribution to the Chalk Background Velocity project

The Chalk Background Velocity project
is funded by the South Arne Group

Ole Vejbæk & Peter Japsen

Released 15.04.2010

Introduction

For the purpose of analysing the suitability of high resolution stacking velocities as support for the construction of low-frequency models, a subset a velocity cube has been investigated. Low-frequency models are needed in connection with inversion of seismic data for acoustic impedance, because low frequencies, and thus the absolute level of the acoustic impedance, are not directly contained in the seismic data. To overcome this problem, standard stacking velocities, horizontal velocity analysis (HVA) data or more sophisticated processed data (as used here) may be utilised in this construction. The velocity cube used in this study has been produced by GX-Technology EAME Ltd. in august 2003 in connection with a pre-stack depth migration (PSDM) processing of a 3-D seismic data set covering the entire South Arne Field. A subset of this cube covering the north-eastern quadrant around the Rigs-2 and Modi-1 wells has been selected for the analysis (Fig. 1).

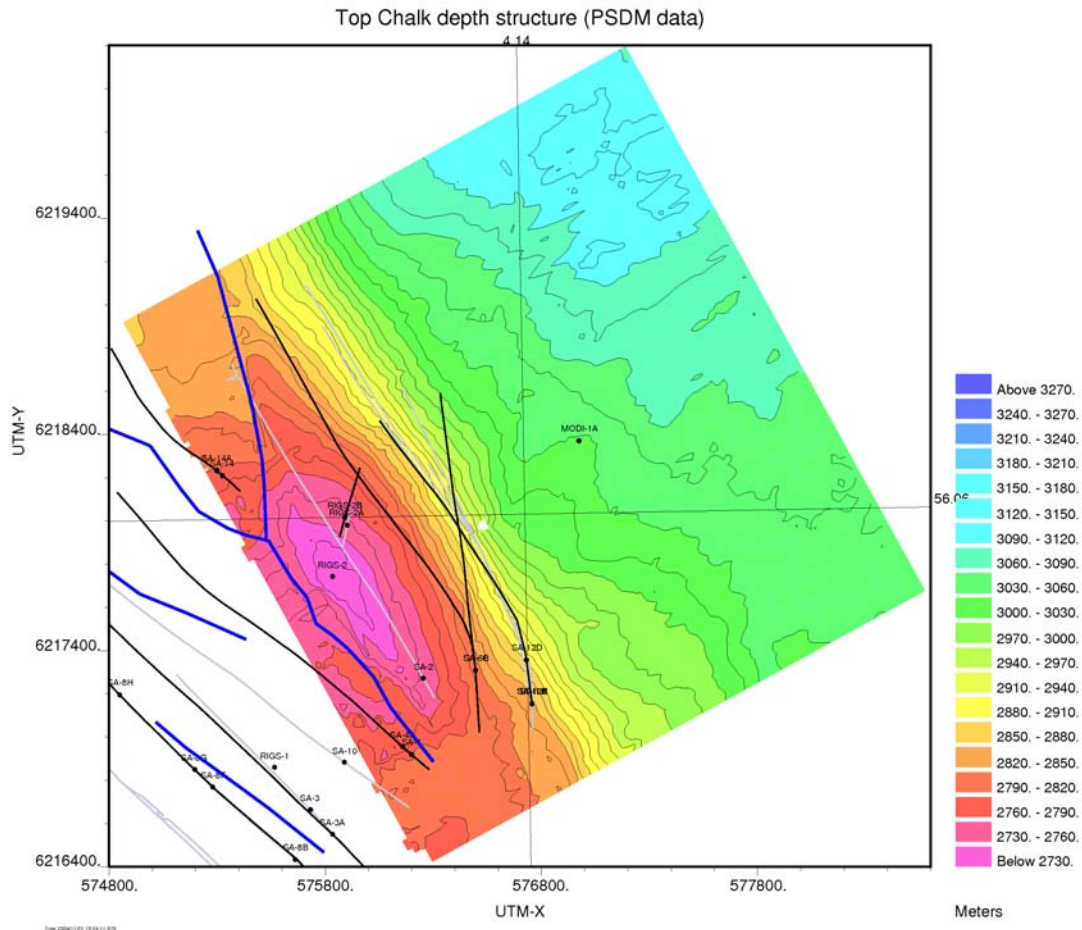


Figure 1. Top chalk depth structure map interpreted directly on PSDM data. The mapped area shows the extent of the subset 3-D velocity data-set analysed in this report.

In order to get a precise sampling of the velocity-cube, the Top Chalk, Top Tor and Base Chalk reflectors have been re-interpreted on the PSDM data that are depth converted with a velocity field contained in the analysed velocity cube. In order to reduce the data volume while still maintaining a representative sampling, only every eight trace has been included in the analysis (original line and trace interval is 12.5 m). The sample rate is 10 m, the line number interval is 2986 – 3216, and the trace interval is 1480 – 1690.

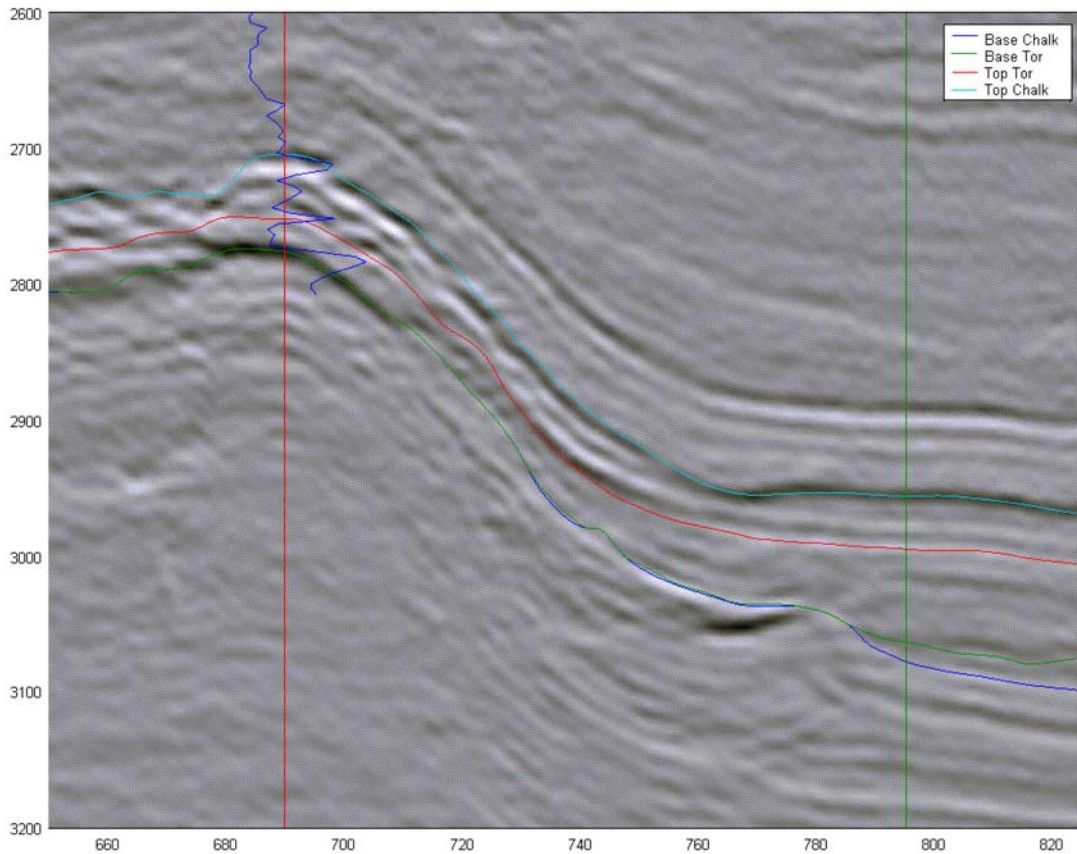


Figure 2. West – east seismic section across the analysed sub volume. As opposed to the data used in this report, this section is in two-way time. The red vertical line shows the position of the Rigs-2 well, and the green is the Modi-1 well location.

The selected seismic velocity data set covers a considerable depth range (Figs. 1 and 2), and the data should ideally capture any depth dependency of velocity. The volume also straddles fully oil saturated reservoir sections (around Rigs-2), residual oil saturations (around Modi-1) and presumably fully brine saturated rock (east of Modi-1). In order to give an impression of the data set Figure 3 shows the seismic traces included in the analysis.

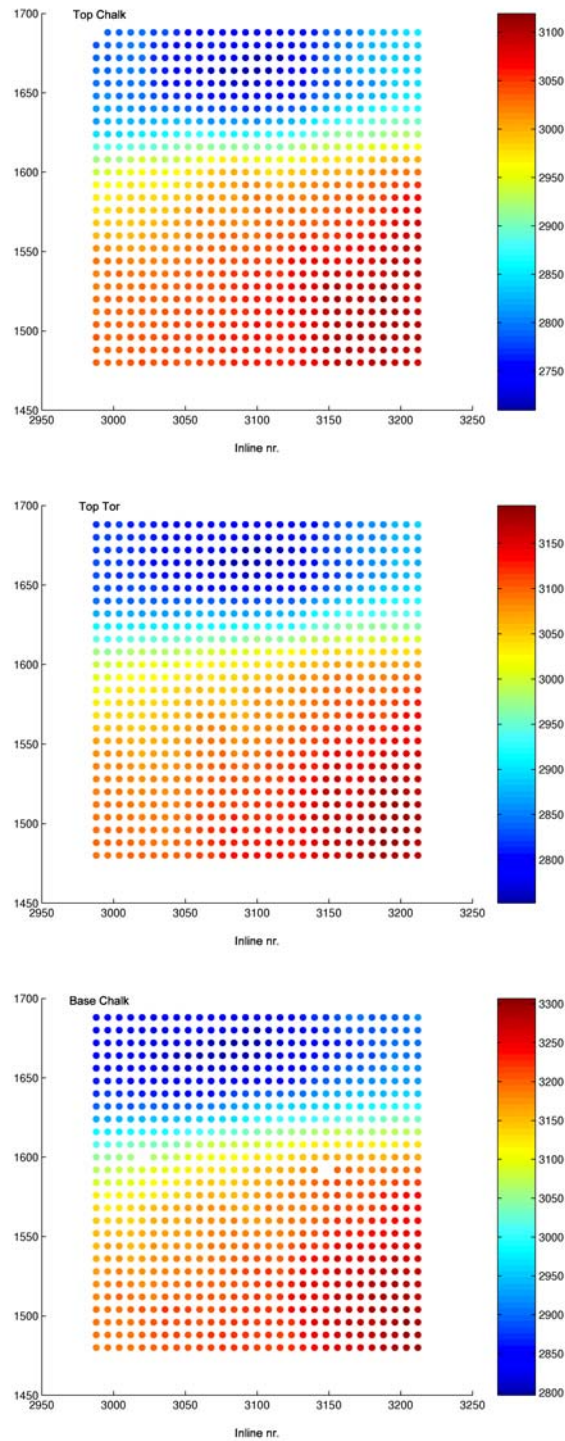


Figure 3. The analysed data set with colour-coding showing depth in metres to Top Chalk (upper), Top Tor (middle), and Base Chalk (lower). Every dot corresponds to a seismic trace included in the analysis (every 8th trace corresponding to 100 m intervals). NW is to the right. Y-axis is cross-line number.

The Tor Formation

The seismic velocities of the Tor Formation show the expected depth dependency from the depth-variation in the sample volume (compare Figs 1, 2 & 4). We can compute an average velocity-depth gradient, k (m/s/s = 1/s) from the densest parts of the data cloud in Figure 4:

$$k = \frac{3800 - 2900 \text{ (m/s)}}{3200 - 2800 \text{ (m)}} = \frac{900}{400} = 2.25 \text{ 1/s}$$

This estimate matches the normal velocity-depth trend of Japsen (1998, 2000) that predicts a gradient of 2 1/s for chalk velocities around 3000 – 3500 m/s.

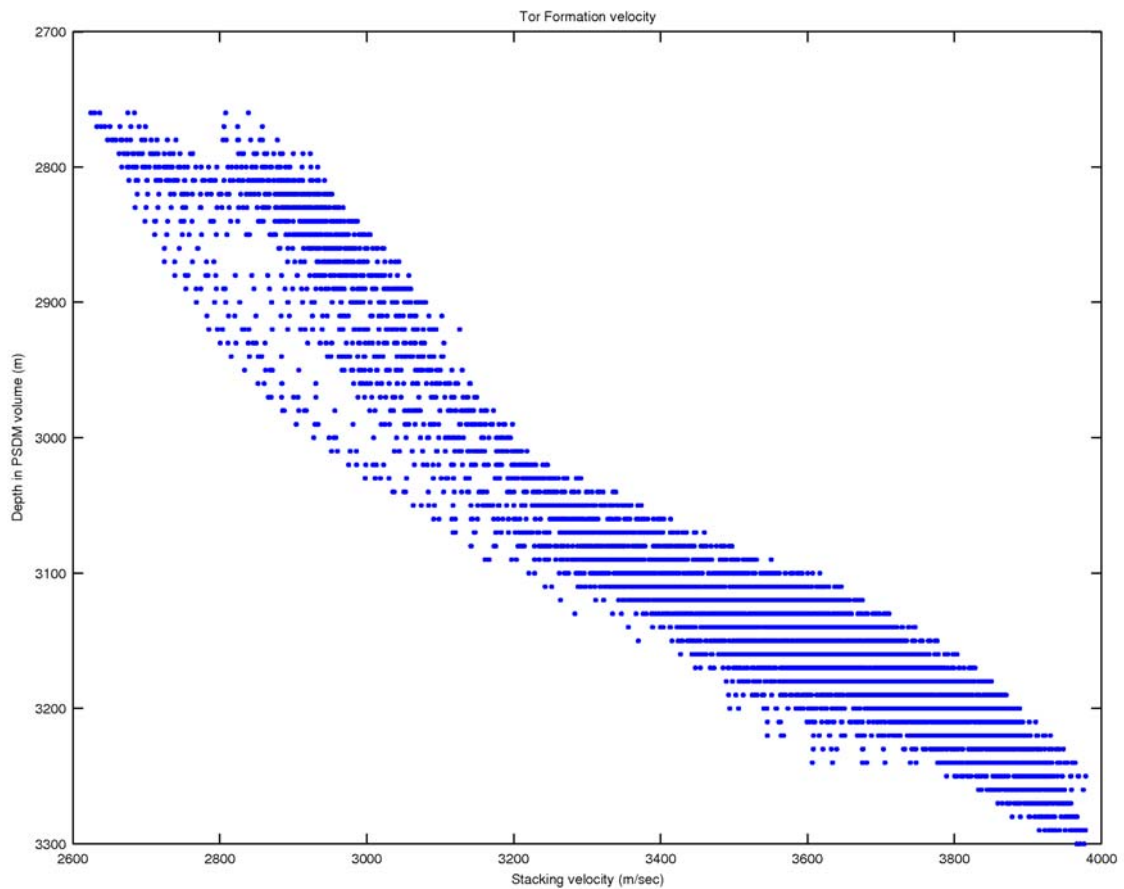


Figure 4. Seismic velocities from the Tor Formation in the 3-D data set within the studied sub volume. The analysed depth interval can also be seen on Fig. 3 top and middle panel. Horizontal striation is due to the 10 m sample rate in the traces.

The overall mean Tor Formation velocity in the extracted data set is 3477 m/sec, which is much below what would be expected from the present depth when compared to the normal velocity depth trend for chalk (Fig. 5; Japsen 2000). The chalk formation overpressure in the Rigs-2 well is in the order of 14.8 MPa according to the completion report and 14.5 according to Dennis et al. (2004). Assuming overburden densities of around 2000 kg/m³ and 1000 kg/m³ for bulk rock and water a correction for over-pressure would result in a depth

shift of 1450 m (see Japsen 1998). However, the depth shift of 1800 m is needed to obtain a match between the data and the normal velocity depth trend (Fig. 5). After this depth shift we observe that the depth trend in the stacking velocity data mimics that of the normal compaction depth trend.

Observed average Tor Formation velocity in the high-porous parts of the Rigs-2 well is around 2600 m/sec (117 ms/ft; Fig. 6) corresponding to porosities exceeding 40%. This velocity ties well with the stacking velocity (dot in Fig. 5), and it appears that the interpreted stacking velocities have been calibrated with the Rigs-2 data. The velocities are, however, too low as compared to the normal velocity-depth trend even after correction for overpressure. The discrepancy corresponds to a depth shift of c. 300 m (1800 m – 1500 m) that may reflect a considerable preservation-effect from early hydrocarbon invasion at a time when the effective stress was less (corresponding to 300 m more shallow burial). Likewise the high porosity in Rigs-2 may be interpreted to reflect early hydrocarbon migration (Hansen 2003, Vejbæk et al. 2005).

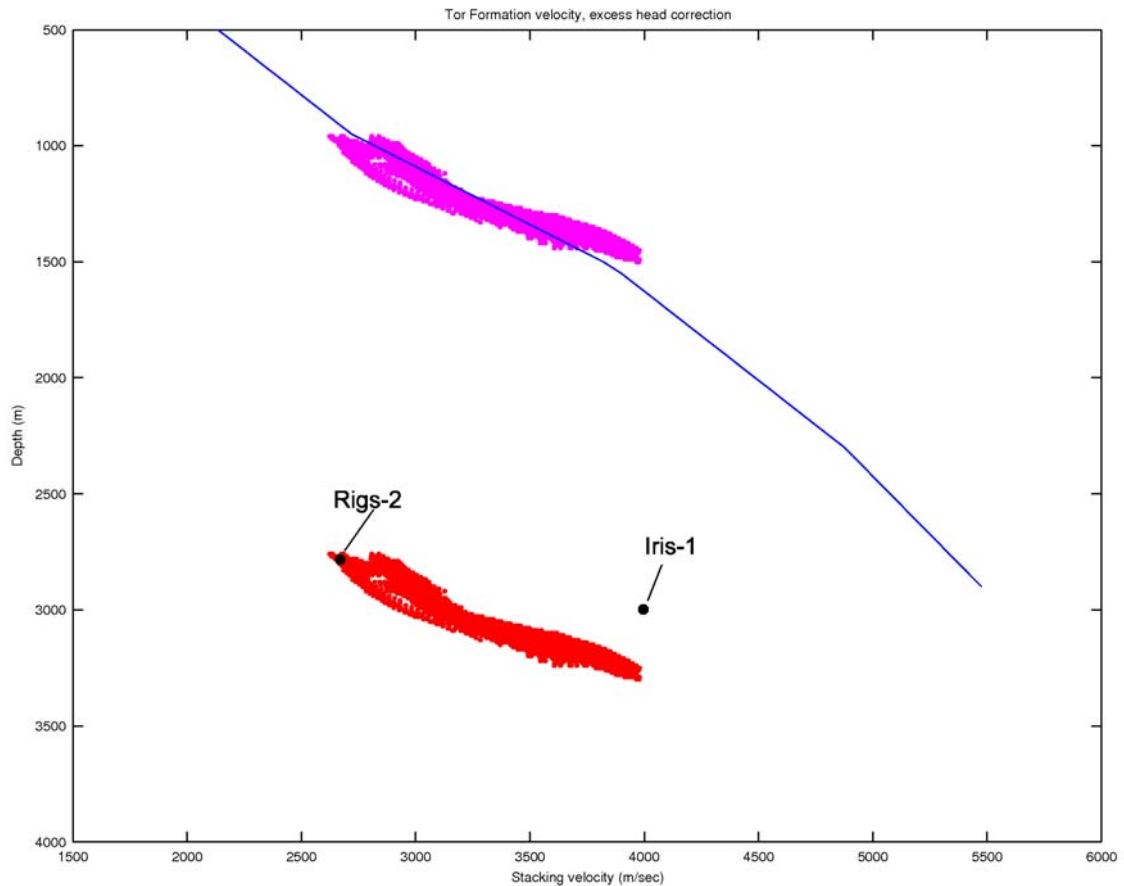


Figure 5. Original stacking velocities for Tor Formation data are here shown in red. After a depth shift of 1800 m, the population (in magenta) falls on the normal velocity – depth trend (from Japsen 2000).

In Figure 5 we observe that the velocity-level from Rigs-2 continues down-dip with a steady gradient. However, the nearby Iris-1 well does not match the level of the stacking velocities,

but is exactly consistent with the normal velocity-depth trend after correction for over-pressure.

Also studies by Hansen (2003) suggest the abnormally high porosities in Rigs-2 (and thus the low velocities), to result from early hydrocarbon invasion effects, and to vanish already in the Modi-1 well where porosities in the Tor Formation are around 20%. The Modi-1 well lacks sonic log data, and contain residual oil saturations ($S_w \sim 80\%$). It may be surmised that the transition from the crestal parts of the South Arne structure where hydrocarbon preserving effects are important to where they do not occur is likely to be rather abrupt. It is possible that the velocity analysis is incapable of handling such abrupt changes. It thus appears that too much emphasis has been placed on the Rigs-2 well in the construction of the velocity cube. A low-frequency model for acoustic inversion constructed on the basis of the velocity cube is thus expected to be erroneous.

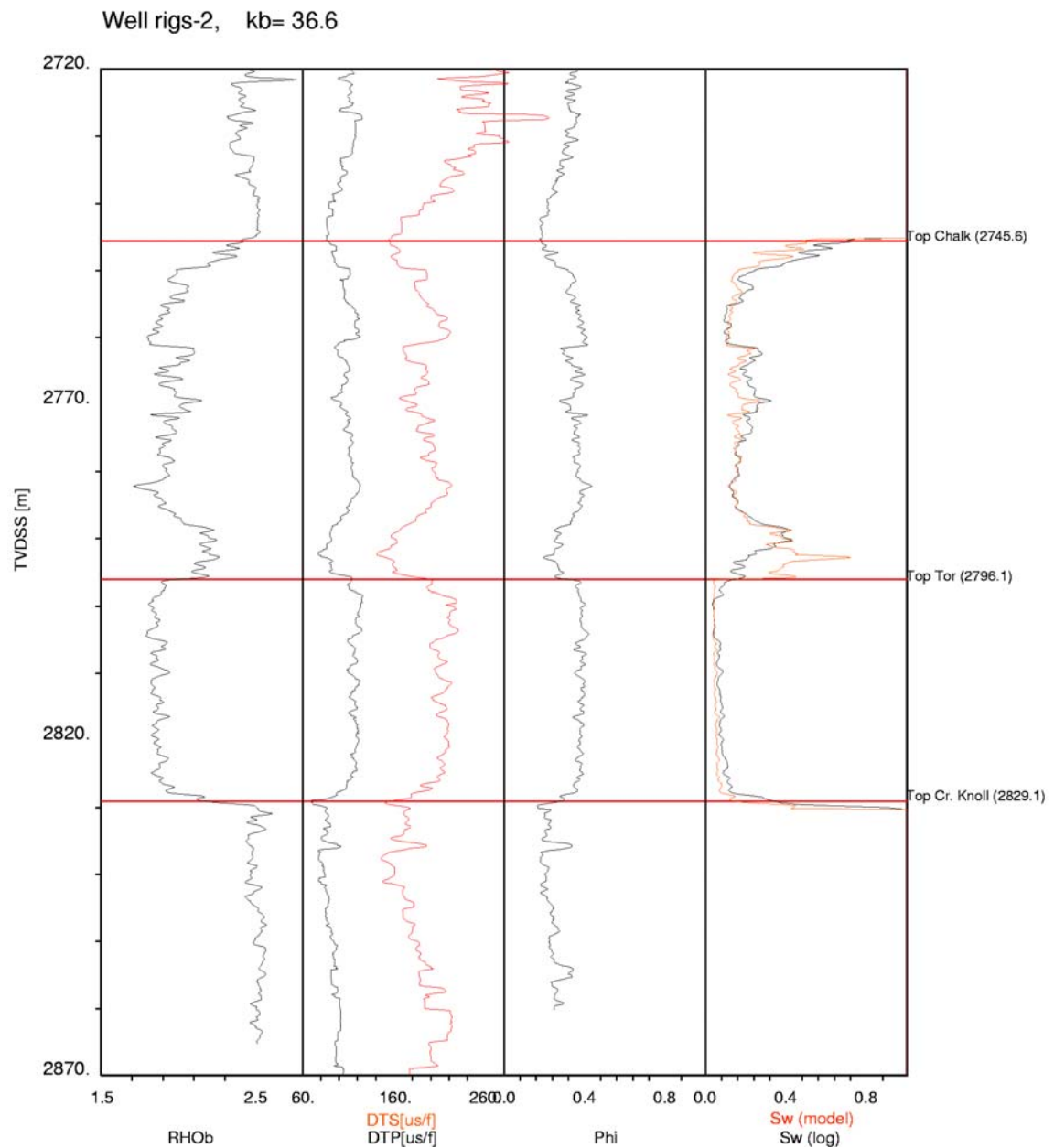


Figure 6. Rigs-2 logs. Note that sonic logs are reciprocal velocity values.

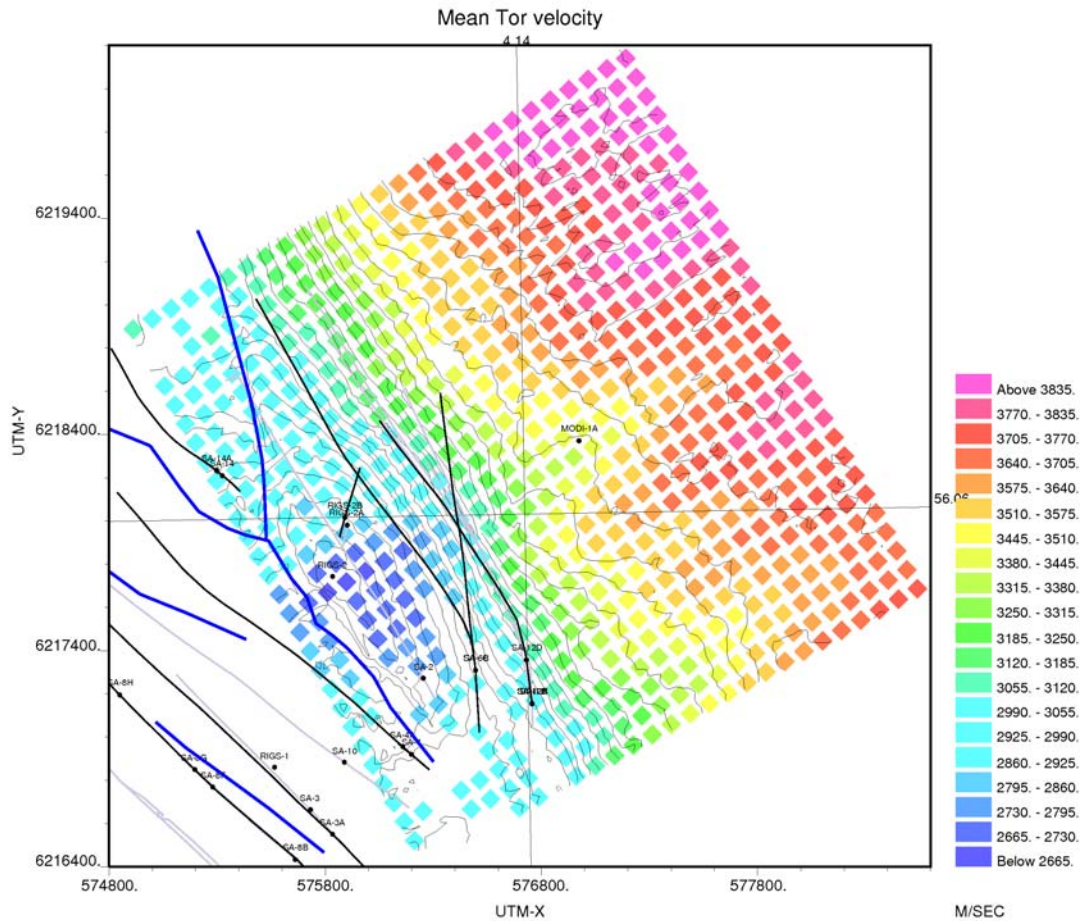


Figure 7. Mean Tor Formation stacking velocities with Top Chalk depth contours from Fig. 1 superimposed. Each square is the average velocity in one trace. Average velocities are clearly following depth variations smoothly.

The Ekofisk Formation

An analysis similar to that for the Tor Formation has been applied to the Ekofisk Formation (Fig. 8). The stacking velocities are also quite low, and a depth correction of 1800 m is needed to align the data with the normal velocity dept trend (Fig. 9). The velocities for the Ekofisk Formation are also below the expected for this depth, corresponding to too high porosities. Mean Ekofisk velocity in the cube is, however even lower than for the Tor Formation, at 2710 m/sec. When looking at the Rigs-2 well data, porosity is not quite as high on average as in the Tor Formation in spite of lower velocities. It may therefore be surmised that the stacking velocity cube, like the well-log velocity data (Fig. 6), are reflecting a higher clay content than the Tor Formation.

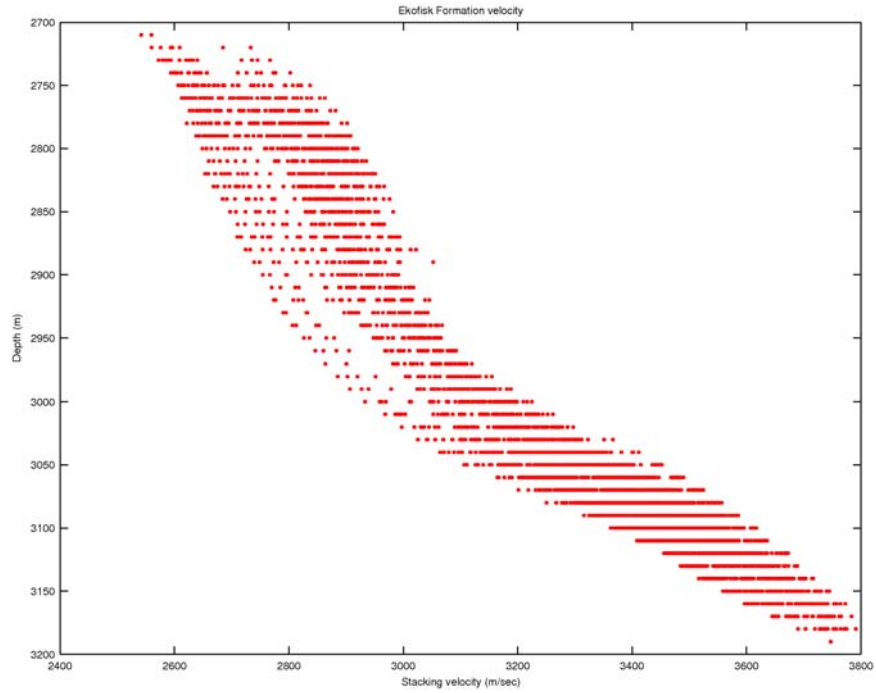


Figure 8. Stacking velocities for the Ekofisk Formation extracted from the velocity cube within the area depicted in Fig. 1. Horizontal striation is due to the 10 m sample rate in the traces.

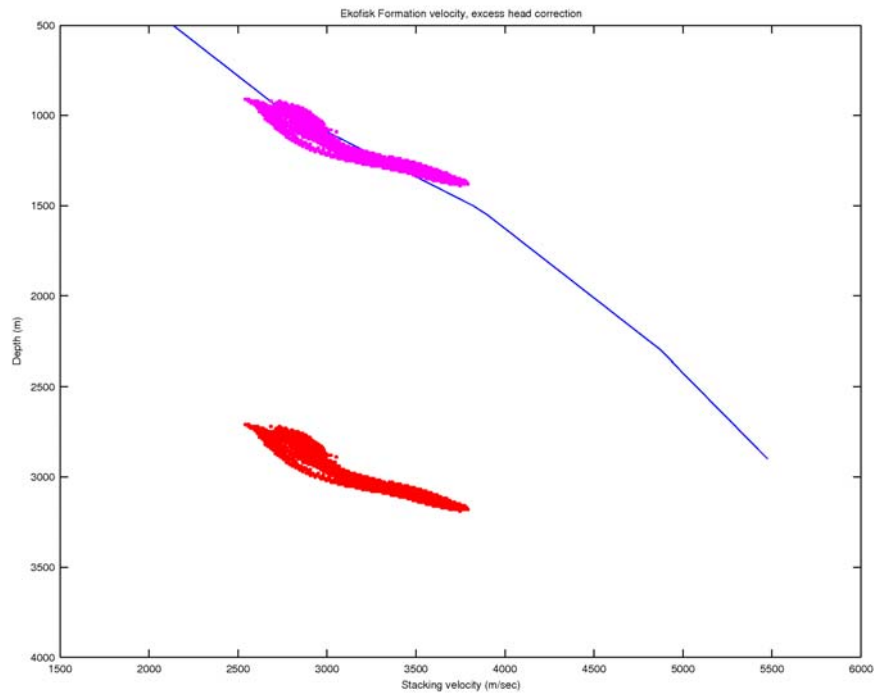


Figure 9. Original stacking velocities for Ekofisk Formation data are here shown in red. After a depth shift of 1800 m like for the Tor Formation, the population (in magenta) falls on the normal velocity – depth trend (from Japsen 2000).

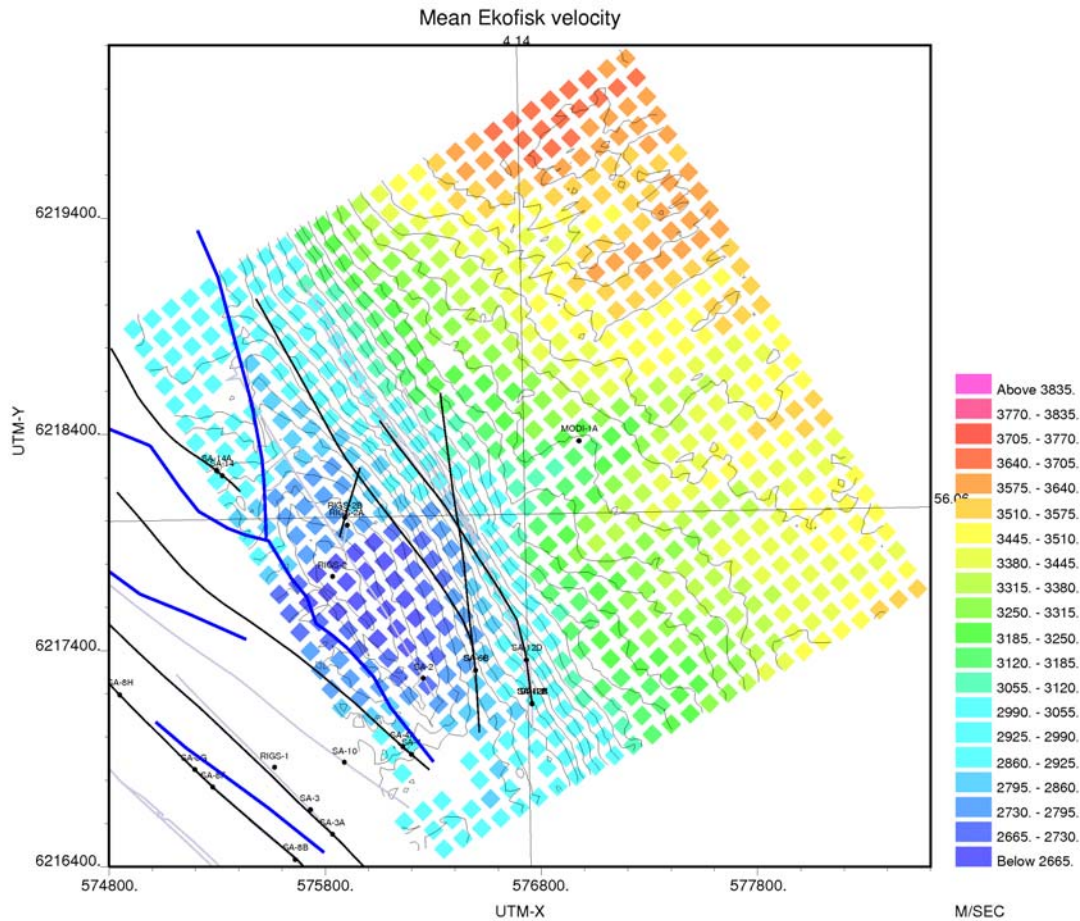


Figure 10. Mean Ekofisk Formation stacking velocities with Top Chalk depth contours from Fig. 1 superimposed. Each square is the average velocity in one trace. Average velocities are clearly following depth variations smoothly, but velocities are slightly lower than for the Tor Formation (compare Fig. 7).

Discussion

In the above analysis we have concluded that the velocity cube obviously is affected by the Rigs-2 well data, and that this well is likely to represent a local anomaly in terms of porosity and velocity. This porosity anomaly is suggested to be the result of early oil charging in the Rigs-2 well and its immediate vicinity. Therefore the down flank prediction of the Tor and Ekofisk formation velocities from the seismic data is expected to yield too low velocities as also hinted by the Iris-1 well velocities. However, it could be argued that the low velocities are just an effect of oil charging, and not hydrocarbon preserving effects. Even in Modi-1, residual oil saturations were encountered ($S_w \sim 80\%$) which due to the non-linear effect of mixed fluid compositions would lower moduli and velocity almost as much as the fully oil charged chalk ($S_w < 20\%$). In order to investigate this assertion, some simple fluid substitution calculations have been done using the properties listed in Table 1.

As stated above, the porosity in the Tor Formation in the Rigs-2 well is around 40% with a P-wave velocity close to 2600 m/sec. The water saturation in the well is well below 20%

and substitution to 80% brine has almost no effect as consistent with the highly non-linear effects of fluid mixtures on velocity. Replacing fluids to 100% brine has some effect by increasing to 2800 m/sec. The present Tor Formation depth in Rigs-2 is around 2800 m and a correction for over-pressure results in an effective depth of close to 1400 m. The normal velocity depth trend should be 3620 m/sec. The early hydrocarbon preserving effect on velocities in Rigs-2 may thus be estimated to be around 820 m/sec equivalent to around 400 m of burial. Fluid effects alone are thus not capable of explaining the too low velocities observed in the velocity cube down dip of the Rigs-2 well location.

	ρ (g/cm ³)	K (GPa)	G (Gpa)
Oil	0.633	0.52	0
Water	1.035	2.96	0
80% brine	0.955	1.53	0
Chalk 0%	2.710	71.00	30

Table.1: Properties in the form of density (ρ), bulk modulus (K), and shear modulus (G).

Porosity		100% brine	80% brine
0.2	Vp (m/s)	4400	4.277
	Vs (m/s)	2300	2.308
	Rho (g/ccm)	2.375	2.359
	K (GPa)	29.22833	26.405
	G (GPa)	12.56375	12.564
0.4	Vp (m/s)	2800	2.555
	Vs (m/s)	1400	1.411
	Rho (g/ccm)	2.04	2.008
	K (GPa)	10.6624	7.771
	G (GPa)	3.9984	3.998

Table 2: Calculated properties for Rigs-2 type chalk for two different porosities at two different fluid compositions.

Summary

The seismic velocity cube is clearly strongly tied up well data from the Rigs-2 well, and this may result in propagation of the properties of the chalk in this well down-flank. The velocity at the Rigs-2 well location is seen to be smoothly continuous with the entire east flank velocity distribution such that only a gradual depth dependency is seen. If velocities are depth shifted 1800 m, this depth dependency is nicely consistent with the normal velocity depth trend for chalk. However, the Rigs-2 well (and immediate vicinity) is most probably a local anomaly due to porosity preservation from early hydrocarbon invasion. The high porosity and low velocity encountered in both Tor and Ekofisk formations in this well are thus a local anomaly little lateral extent. The down flank velocity prediction from the seismic velocity

cube is therefore expected to be wrong. Velocities in the Rigs-2 well are over 1000 m/sec too low compared to a normal velocity depth trend even considering overpressuring. Of these 1000 m/sec about 200 is attributed to fluid effects (oil content) leaving about 800 m/sec to be attributed to porosity preservation from early hydrocarbon invasion. This figure corresponds to about 400 m of burial. The porosity preservation effect from early hydrocarbon invasion is removed by subtracting 400 m from the first depth shift of 1800 m (above). This leaves a depth shift of 1400 m consistent with observed overpressure.

References

Dennis, H., Bergmo, P., and Holt, T. 2004: Tilted oil-water contacts: modelling effects of aquifer heterogeneity. In A.G. Doré & B.A. Vining (eds.) *Petroleum Geology: North-West Europe and Global Perspectives*.

Hansen, S. 2003: Charging of the South Arne Field from porosity analysis and basin modelling, version II. Rep. No. 15677. DONG.25 p.

Japsen, P. 1998: Regional velocity-depth anomalies, North Sea Chalk; a record of overpressure and Neogene uplift and erosion. *AAPG Bulletin* v. 82, p. 2031-2074.

Japsen, P. 2000. Investigation of multi-phase erosion using reconstructed shale trends based on sonic data. Sole Pit axis, North Sea. *Global and Planetary Change* v. 24, 189–210.

Vejbæk, O. V., Rasmussen, R., Japsen, P., Bruun, A., Pedersen, J. M., Marsden, G., & Fabricius, I. L. 2005: Modelling seismic response from North Sea chalk reservoirs resulting from changes in burial depth and fluid saturation. 6th *Petroleum Geology Conference: North West Europe and Global Perspectives*.